UNIVERSITAT DE BARCELONA

Computational Analyses of CO_2 Electroreduction and C Interactions with Transition Metals

Oriol Piqué Caufapé

Computational Analyses of CO_2 Electroreduction and C Interactions with Transition Metals

Oriol Piqué Caufapé

UNIVERSITAT DE BARCELONA

Memòria presentada per

Oriol Piqué Caufapé

Per a optar al grau de Doctor per la

Universitat de Barcelona

Programa de doctorat en Química Teòrica i Computacional

Computational Analyses of CO_2 Electroreduction and C Interactions with Transition Metals

Dirigida per:

Dr. Federico Calle-Vallejo
Universitat de Barcelona

Dr. Francesc Viñes
Universitat de Barcelona

Tutor:

Prof. Francesc Illas Riera
Universitat de Barcelona

UNIVERSITAT DE BARCELONA

Barcelona, 2022

Al meu pare

Abstract

Catalysis is ubiquitous in chemical industries since it accelerates chemical reactions, thereby saving considerable amounts of energy. Most catalytic processes in industry are heterogeneous in nature, typically involving a solid catalyst and a gas or liquid phase containing the reactants and products. Although numerous types of materials are used, most heterogeneous catalysts are made of metals and/or metal oxides. Research towards improving the activity and selectivity of catalytic systems along with reducing the cost of the catalysts is crucial. In this thesis, different aspects regarding two relevant processes are investigated: (*i*) the improvement of CO_2 electroreduction catalytic systems and (*ii*) atomic carbon interactions with transition metals (TMs), often present in many heterogeneous catalysts.

In the first part, the electroreduction of CO_2 (CO_2RR) to valuable fuels for energy storage and environmental mitigation is studied through density functional theory (DFT) calculations on suitable models. Some findings are the result of collaborations with the experimental research groups of Prof. Boon Siang Yeo (NUS, Singapore) and Dr. Katsounaros (HI-ERN, Germany). Four-atom square islands on top of Cu(100) are identified as the active sites in oxide-derived Cu surfaces responsible for ethanol evolution. It is observed that the C_2 product selectivity at the late stages of the CO_2RR is dictated by the coordination of the different active sites. Moreover, adding Ag to Cu is shown to enhance the production of ethanol via the opening of an alternative pathway. Finally, it is shown how formic acid, usually considered a dead-end product of CO_2RR, can be electroreduced to methanol at the oxygen vacancies of anodized titanium catalysts.

In the second part, a broad and detailed atomistic view of the interaction of C with TM surfaces is given by determining its most stable sites, bond strength, possible subsurface stability, and diffusion kinetics, regarding the possible C poisoning or promoting role on the catalyst surface and the formation of TM carbides, also extendedly used as heterogeneous catalysts. Hundreds of simulations are performed within the DFT framework, and the resulting data are analyzed to find correlations and draw conclusions. Initially, it is observed that atomic C features preferential subsurface stability in the (111) facets of Cu, Ag, and Au surfaces and nanoparticles, which has important implications

when using those metals as catalysts. Dynamic simulations provided estimates of the lifetimes of surface and subsurface C species. Moreover, data analysis using different descriptors together with machine learning tools shows that both the thermodynamic and kinetic data are better described when using a combination of several descriptors.

Acknowledgements

The research featured in this thesis could only be possible thanks to many people. I shall first thank the tuition done by my supervisors Federico Calle-Vallejo and Francesc Viñes, and my tutor Francesc Illas, as without their guidance and expertise this thesis would have not been possible. Moreover, I would like to acknowledge the help of all my collaborators: Batyr Garlyyev, Johannes Fichtner, Oliver Schnerider, Aliaksandr S. Bandarenka, Louisa R. L. Ting, Si Ying Lim, Mohammad Tanhaei, Boon Siang Yeo, Iskra Z. Koleva, Hristiyan A. Aleksandrov, Georgi N. Vayssilov, Biel Martínez, Hèctor Prats, Iosif Mangoufis, Peyman Khanipour, Karl J. J. Mayrhofer, Ioannis Katsounaros, Qi Hang Low, Albertus D. Handoko, María Retuerto, Laura Pascual, Paula Kayser, Mohamed A. Salam, Mohamed Mokhtar, José Antonio Alonso, Miguel Peña, Sergio Rojas, Wei Jie The, Weihan Zhu, and Mario Löffler.

Per altra banda, m'agradaria fer una menció especial a totes aquelles persones que han conviscut amb mi durant aquesta etapa i que, de manera indirecta, també han estat involucrades en el desenvolupament d'aquesta tesi. Primerament, als companys de despatx, el Joan, l'Anabel, el Juanjo, el Raúl Morales, i el Martí. Ha sigut un veritable plaer compartir aquest espai amb vosaltres, he gaudit moltíssim de les innumerables converses, de les partides a la bolera, dels torneigs d'escacs, i de les nostres aventures en el món dels *Battlegrounds*. Més que companys m'enduc amics, espero que ens puguem retrobar més endavant i mantenir viu l'esperit del despatx 425.

Voldria agrair també el suport de la resta de companys de la universitat que, tot i no compartir despatx amb mi, han estat presents durant aquesta etapa, la Berta, la Cristina, el Genís, el Marc, el Pablo Blanco, el Pablo Lozano, el Toni, i especialment el Raúl Santiago, amb qui porto compartint camí des del màster i que sempre s'ha mostrat disposat a ajudar-me tant en l'acadèmic com en el personal.

No pot faltar també una menció especial al Daniel i el Roger. Les nostres excursions al *Glub* durant la pandèmia es van convertir en una mena de ritual alliberador, hem arreglat el món incomptables vegades, de poc no fundem un partit polític! Divertidíssimes també les nostres aventures en el món de les inversions... *To the moon!* Gràcies per tant.

A més a més, també voldria dedicar un agraïment especial a tots els amics i amigues de la colla de Vallfogona, que m'han acompanyat durant aquesta etapa, durant les passades, i de ben segur que també en les futures. Els viatges, les excursions, els dinars, els *tardeos*, i el temps que he gaudit al vostre costat, m'han fet una millor persona. Gràcies a tots! Altrament, també voldria dedicar una menció especial als innegociables *angelus* de dimecres amb l'Efe, el Pinyol, i el Roy. Les nostres pregàries, birra en mà, han sigut l'enveja de Còrsega; tot i que la veïna de sota potser hagués preferit que anéssim més sovint al *Malasang* a engolir una botifarra esparracada. Gràcies per aquesta glopada d'aire fresc setmanal, gràcies per ser increïbles, i gràcies també per aguantar totes les meves cabòries sobre la tesi, quin fart d'escoltar-me us heu fet!

Finalment, voldria agrair a la meva família la seva estima i suport incondicional. Especialment a la Lorena, que ja forma part d'aquesta, gràcies per la teva paciència i comprensió, encara no em faig creus de la sort que tinc de tenir-te al meu costat.

Abbreviations

DFT	**D**ensity **F**unctional **T**heory
LDA	**L**ocal **D**ensity **A**pproximation
GGA	**G**eneralized **G**radient **A**pproximation
PBE	**P**erdew-**B**urke-**E**rnzerhof
ZPE	**Z**ero-**P**oint **E**nergy
CHE	**C**omputational **H**ydrogen **E**lectrode
RHE	**R**eversible **H**ydrogen **E**lectrode
CI-NEB	**C**limbing **I**mage **N**udged **E**lastic **B**and
bcc	**B**ody **C**entered **C**ubic
fcc	**F**ace **C**entered **C**ubic
hcp	**H**exagonal **C**losed **P**acked
NP	**N**ano**p**article
TM	**T**ransition **M**etal
TMC	**T**ransition **M**etal **C**arbide
kMC	**K**inetic **M**onte **C**arlo
KM	**K**-**M**eans
CS	**C**rystallographic **S**tructure
ML	**M**achine **L**earning
MLR	**M**ultivariable **L**inear **R**egression
DTR	**D**ecision **T**ree **R**egressor
RFR	**R**andom **F**orest **R**egressor
CV	**C**ross **V**alidation
CO_2RR	**CO_2 R**eduction **R**eaction
CORR	**CO R**eduction **R**eaction
OD-Cu	**O**xide-**D**erived **Cu**
PLS	**P**otential-**L**imiting **S**tep
EC-RTMS	**E**lectrochemical **R**eal-**T**ime **M**ass **S**pectrometry
ARR	**A**cetaldehyde **R**eduction **R**eaction
EOR	**E**thylene **O**xide **R**eduction

HER	**H**ydrogen **E**volution **R**eaction
NW	**N**ano**w**ire
L-H	**L**angmuir-**H**inshelwood
E-R	**E**ley-**R**ideal
FAR	**F**ormic **A**cid **R**eduction
Ti_{an}	**An**odized **Ti**tanium
OV	**O**xygen **V**acancy
CUS	**C**oordinatively **Uns**aturated

Contents

Chapter 1

Introduction

Catalysis is the acceleration of the rate of a chemical reaction by a substance (the catalyst) that is neither consumed nor generated in the process. Specifically, a catalyst is defined by the IUPAC as:[1] "*A substance that increases the rate of a reaction without modifying the overall standard Gibbs energy change of the reaction. The catalyst is both a reactant and a product of the reaction.*" Practically speaking, a catalyst decreases the activation energy (E^a) of a given reaction. Catalysts interact with the reactants to give intermediate species that will ultimately lead to products and the regenerated catalyst. They essentially provide an alternative reaction mechanism involving different intermediates and different transition-state energies compared to the non-catalyzed reaction. Since reactants and products are the same for both the catalyzed and the non-catalyzed reactions, the thermodynamics of the reaction is not modified. Thus, catalysis relies on changes in the kinetics of chemical reactions. Figure 1 shows a schematic representation of a reaction energy profile with and without the effect of a catalyst.

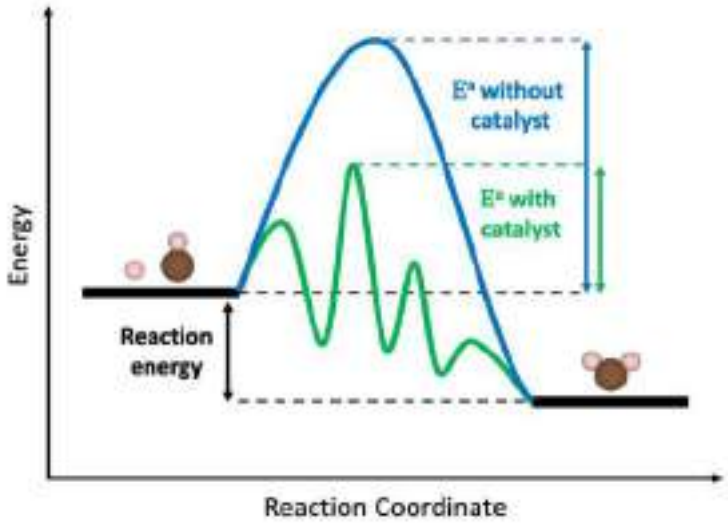

Figure 1. Schematic representation of a reaction energy profile. The activation energy (E^a) is reduced in the presence of a catalyst, but the reaction energy remains unchanged. The reaction coordinate represents the progress along a reaction pathway from reactants to products.

Applications based on catalysis can be traced back to thousands of years ago with the discovery of fermentation to produce wine and beer through processes known today as enzymatic catalysis.[2] However, it was not until 1835 that the term *catalysis* was coined by Berzelius. Later, in 1895, Ostwald was the first to scientifically define the term. Nowadays, catalysts are used in more than 90% of all chemical industrial processes, contributing directly or indirectly to around 35% of the world's gross domestic product (GDP).[3] Catalysis is key to numerous industrial applications, including the production of commodity, fine, and specialty chemicals as well as the manufacturing of pharmaceuticals, cosmetics, food, and polymers. Moreover, catalysis is central in the design of processes for clean energy provision and in environmental protection and remediation, both by eliminating environmental pollutants and providing alternative cleaner chemical synthetic procedures.[4]

Catalysis is deemed heterogeneous when the catalyst and the reactants are in different phases and its interaction happens at the interface between those phases. Countless catalytic processes are heterogeneous, typically including a solid catalyst and reactants in either a gaseous or liquid phase. To a large extent, heterogeneous catalysts are made of metals or metal oxides, although numerous other compounds are used for such purpose (*e.g.*, sulfides, phosphates, graphitic materials, carbides, and ion-exchange resins, among others).[5-8] Metal catalysts, particularly those containing transition metals, have been proven to be especially useful in industrial catalysis, since they can easily activate simple molecules like H_2, O_2, N_2, CO, and polyatomic organic molecules containing C-H, C-O, and C-N bonds.[9]

Heterogeneous catalytic reactions start with the adsorption of the reactants onto the catalyst surface. The adsorption and the subsequent conversion reactions take place at particular atoms or ensembles of atoms of the catalyst surface, often called active sites or active centers.[10] A particular atomic ensemble may be active or inactive for a given reaction by virtue of its specific structural arrangement of atoms. The electronic properties of the catalyst surface also play an important role in the adsorption and activation of the reactants. Therefore, the catalytic performance of a given catalyst is influenced by both its atomic structure and electronic properties. After the reactants have reached the active site, either through direct adsorption or by surface diffusion, they are converted into products. The products desorb from the catalyst regenerating it, that is, leaving the active sites available for new incoming reactants.[10] In this way, the catalytic cycle can be repeated several times in each of the surface active sites. Note that, according

to the *Sabatier* principle,[11] the interaction between the catalyst surface and the reactants should be neither too strong nor too weak. When the interaction is too weak, the reactants may not be able to adsorb on the surface and the reaction will not take place. On the other hand, when the interaction is too strong, either the reactants get completely decomposed on the surface or the products are not able to desorb and regenerate the active site, which ultimately deactivates the catalyst.[12]

Electrocatalysis can be defined as the heterogeneous catalysis of electrochemical reactions, which occurs at the electrode-electrolyte interface and where the electrode plays both the roles of electron donor/acceptor and catalyst. Electrochemical processes for clean energy production, conversion, and storage, are a promising strategy to relieve our modern society reliance on fossil fuels by converting chemical energy into electrical energy.[13-15] To take these promising technologies from the scale of fundamental research to real applications, active, selective, and durable catalysts are needed that facilitate the kinetics of electrochemical reactions.[16] However, several challenges related to unsatisfactory catalytic efficiency, low selectivity, or high costs still need to be addressed.[17] To do so, the electrocatalysis scientific community has devoted substantial efforts into revealing fundamental reaction mechanisms and structure-activity relationships, which are currently used to guide the fine-tuning of the composition, size, and morphology of electrocatalysts so as to achieve high activity and selectivity at reasonable costs.[18,19]

The research work presented in this thesis consists of a fundamental study of CO_2 electroreduction and C interactions with transition metal systems by means of theoretical and computational methods. The manuscript is divided into four well-differentiated parts. A brief introduction to catalysis, heterogeneous catalysis, and electrocatalysis (Chapter 1), a description of the theoretical methods used for the computational analysis of the systems of interest (Chapter 2), and two chapters showing the main results in the form of articles published in peer-reviewed journals (Chapters 3 and 4). Before each article, a summary is shown, mainly focused on the part of the work that I conducted. In Chapter 3, several studies on the electroreduction of CO_2 to valuable commodities are presented. Chapter 4 covers a detailed analysis of the interplay between C atoms and transition metal surfaces and nanoparticles. Finally, conclusions are drawn and a list of publications is provided.

Dr. Federico Calle-Vallejo supervised the projects included in Chapter 3 and proofread Chapters 1-3. Dr. Francesc Viñes supervised the projects in Chapter 4 and proofread Chapters 1, 2, and 4.

Chapter 2

Theoretical Methods

2.1 The Schrödinger Equation

The many-body Schrödinger equation governs the properties of any given chemical system through its wave function, which depends simultaneously on the positions of its nuclei and electrons. To understand chemistry at the microscopic level, it usually suffices to consider the non-relativistic time-independent Schrödinger equation:

$$\hat{H}\Psi(R,r) = E\Psi(R,r) \qquad (2.1),$$

where $\Psi(R,r)$ is the wavefunction of the system dependent on the positions of the nuclei, *R*, and electrons, *r*, and $\hat{H}$ is the Hamiltonian operator. For *M* nuclei and *N* electrons, the Hamiltonian operator expressed in atomic units is given by:

$$\hat{H} = -\sum_{i=1}^{N}\frac{1}{2}\nabla_i^2 - \sum_{A=1}^{M}\frac{1}{2m_A}\nabla_A^2 - \sum_{i=1}^{N}\sum_{A=1}^{M}\frac{Z_A}{r_{iA}} - \sum_{i=1}^{N}\sum_{j>i}^{N}\frac{1}{r_{ij}} - \sum_{A=1}^{M}\sum_{B>A}^{M}\frac{Z_A Z_B}{R_{AB}} \qquad (2.2),$$

where m_A and Z_A are the mass and charge of nucleus *A*, respectively. The ∇_i^2 and ∇_A^2 Laplacian operators involve second derivatives with respect to the coordinates of the i^{th} electron and the A^{th} nucleus, respectively. From left to right, the five terms of the Hamiltonian correspond to the kinetic energy of the electrons ($\hat{T}_e$), the kinetic energy of the nuclei ($\hat{T}_n$), the nucleus-electron attraction ($\hat{V}_{ne}$), the electron-electron repulsion ($\hat{V}_{ee}$), and the nucleus-nucleus repulsion ($\hat{V}_{nn}$).

To be able to solve the Schrödinger equation, the Born-Oppenheimer approximation is most often invoked.[20] This approximation proposes that, since nuclei are considerably heavier than electrons, they move more slowly. Hence, one can consider

electrons to be moving in the field generated by fixed nuclei at certain positions. Within this approximation, the nuclear kinetic energy ($\hat{T}_n$) can be considered zero and the repulsion between nuclei ($\hat{V}_{nn}$) constant for a specific nuclear configuration. The remaining terms form the electronic Hamiltonian, ($\hat{H}_{el}$), which can be used to obtain the electronic energy (E_{el}) of the system:

$$\hat{H}_{el} = -\sum_{i=1}^{N}\frac{1}{2}\nabla_i^2 - \sum_{i=1}^{N}\sum_{A=1}^{M}\frac{Z_A}{r_{iA}} - \sum_{i=1}^{N}\sum_{j>i}^{N}\frac{1}{r_{ij}} \quad (2.3),$$

$$\hat{H}_{el}\Psi_{el} = E_{el}\Psi_{el} \quad (2.4),$$

where Ψ_{el} is the electronic wavefunction, which still depends on the coordinates of electrons but has only a parametric dependence on the nuclear coordinates. The possible values of electronic energy in Equation 2.4 are not those corresponding to the solution of Equation 2.1. However, it can be shown that, once the $\hat{V}_{nn}$ term is included, the resulting quantity corresponds to the potential felt by the nuclei, which leads to the concept of potential energy surface, key to the microscopic mechanisms governing all chemistry in the ground or excited states.

Unfortunately, Equation 2.4 only has an analytical solution for up to three particles, and the high dimensionality of Ψ_{el} makes solving the equation numerically extremely difficult. Therefore, several different approximate methods have been developed to solve this problem, including Hartree-Fock,[21] Møller-Plesset perturbation theory,[22] Coupled Cluster,[23] Quantum Monte Carlo,[24] and Density Functional Theory (DFT), among others.

From all these different approaches one must choose the most adequate method for a target study. The nature and size of the system, the computational cost, and the accuracy of the method shall be considered when making the decision. Presently, DFT is the most widely used electronic-structure method in computational chemistry, as it provides a good compromise between computational cost and accuracy for a large number of systems, including the ones featured in this work.

2.2 Density Functional Theory

The foundations of DFT were laid by Hohenberg and Kohn in 1964.[25] They showed that the ground state energy, E_0, of a chemical system is a function of its electronic density, $\rho(r)$. Therefore, as far as ground-state chemistry is concerned, there is no need to know the wavefunction of the system. Specifically, they formulated and proved two theorems. The first theorem establishes that the electronic density of the ground state, $\rho_0(r)$, uniquely determines the external potential, $V(r)$, hence, the non-degenerate ground-state energy is determined as a function of $\rho_0(r)$:

$$E_0 = E_0[\rho_0(r)] \qquad (2.5).$$

The second theorem shows that the electronic density that minimizes the energy is that of the ground state. Therefore, within DFT, the ground-state energy and, consequently, the corresponding potential energy surface, can be determined from the ground-state electronic density.

$$E_0 = F_{HK}[\rho] + \int V(r)\,\rho(r)dr \qquad (2.6),$$

where F_{HK} is a universal, system-independent Hohenberg-Kohn functional of the electronic density ($\rho(r)$), hereafter referred to as (ρ) for simplicity.

However, the exact form of the F_{HK} functional remains unknown. As a practical solution, Kohn and Sham proposed to consider an auxiliary system of non-interacting electrons in an effective potential (V_{ext}), from which the ground-state energy can be approximated.[26] In this formalism, one has

$$E_{DFT}[\rho] = T[\rho] + \int V_{ext}(r)\rho dr + E_H[\rho] + E_{xc}[\rho] \qquad (2.7),$$

where $T[\rho]$ is the kinetic energy of the non-interacting electrons, $E_H[\rho]$ is the classical electron-electron Coulomb energy, and $E_{xc}[\rho]$ is the exchange-correlation energy which includes all the terms that are not accounted for by the other terms (exchange and

correlation energies, the auto-interaction correction to the classical Coulomb interaction, and the difference between interacting and non-interacting kinetic energies).

Note that finding the exact form of E_{xc} is as complicated as for F_{HK}, but $E_{xc}[\rho]$ is significantly smaller than $F_{HK}[\rho]$. Hence, any approximations made to $E_{xc}[\rho]$ have less of an effect in the calculated ground-state energy than on $F_{HK}[\rho]$.

Several different approaches have been used to approximate the E_{xc} term, commonly referred to as exchange-correlation functionals. The choice of using a particular functional depends on the model system, computational cost, and desired accuracy. Jacob's ladder is used to represent the different levels of exchange-correlation functionals, moving from the Hartree-Fock "earth" to the "heaven" of chemical accuracy, with errors smaller than or equal to 1 kcal/mol. From less to more complexity and computational cost, the rungs of the ladder include: (a) the local density approximation (LDA) functionals, which only depend on the local density, and offer an almost perfect description of a homogeneous electron gas (*e.g.* Vosko-Wilk-Nusair (VWN)),[27] (b) generalized gradient approximation (GGA) functionals, which include the local density and its gradient to account for spatial variations of the electronic density (*e.g.* Perdew-Burke-Ernzerhof (PBE)),[28] (c) meta-GGA functionals, which also include the second derivative of the local density or kinetic-energy density (*e.g.* Tao-Perdew-Staroverov-Scuseria (TPSS)),[29] and (d) hybrid exchange-correlation functionals, which include a certain amount of exact Hartree-Fock exchange (*e.g.* PBE0).[30]

Despite their simplicity and in view of the similarity between metals and homogeneous electron gases, LDA functionals can provide fairly accurate results of certain properties of metallic systems such as interatomic distances and lattice parameters. The main disadvantage of LDA functionals is that they usually overestimate bond energies and fail to describe highly correlated systems such as magnetic oxides.[31] GGA functionals generally provide better accuracy for bond energies but tend to overestimate bond distances.[32] Meta-GGA functionals usually involve an improvement in thermochemical estimates of molecules, but generally do not feature an accuracy enhancement with respect to GGA functionals when describing extended transition metals.[33]

Note that all these functionals suffer from self-interaction errors, since in these methods each electron interacts with its own electron density.[34] That leads to an overestimation of the energetic stability of electronic configurations with electrons delocalized over various atoms,[35] resulting in an accuracy loss when treating molecules,

clusters, or other strongly correlated systems. This problem may be solved by using hybrid functionals, since in Hartree-Fock the self-interaction is cancelled by the corresponding exchange term. However, including exact exchange highly increases the computational cost of the calculation and can lead to excessively localized electrons.[36] Based on the ideas of the so-called Hubbard Hamiltonian, a practical solution was proposed that includes contributions of on-site intra-atomic Coulomb interactions to the total energy.[37]

$$E = E_{DFT} + \frac{U_{eff}}{2} \sum n_i \, (1 - n_i) \qquad (2.8),$$

where U_{eff} is the effective on-site Coulomb interaction and n_i is the occupation of the atomic orbitals to which this correction is applied. Due to the associated difficulties in the determination of U_{eff} for each system,[38] the U_{eff} value is often obtained by trial and error to reproduce certain experimental observables.[39]

In this thesis, all the DFT calculations were performed using the Vienna *ab initio* simulation package (VASP)[40] with the Perdew-Burke-Ernzerhof (PBE) exchange-correlation functional, which is known to be among the best functionals for the description of transition-metal systems.[41] Occasionally, the Hubbard U approach was used for systems featuring localization problems. Note that all calculations were performed without spin polarization for non-magnetic metallic surfaces. As shown by Fajín *et al.*,[42] results obtained for heterogeneously catalyzed reactions on non-magnetic metallic surfaces with and without spin polarization lead to the same description of the potential energy surface. For magnetic surfaces, such as the ones containing Ni, Fe, and Co, spin polarization was considered.

In the Kohn-Sham formalism, the electron density is expressed as a single Slater determinant made of one-electron functions. This mathematic construction presents similarities with the orbitals derived from the Hartree-Fock theory. Hence, they are usually referred to as orbitals as well. In addition, as in the Hartree-Fock theory, the orbitals are chosen to minimize the energy in Equation 2.7. In practice, this is done by representing the one-electron Kohn-Sham orbitals as a linear combination of known and easy-to-treat functions to find a numerical solution of the Hartree-Fock equations. This set of functions is called a basis set and many families of them have been proposed. Local basis sets are the most popular choice for atoms and molecules, since they are highly

localized around each atom center. On the other hand, non-local basis sets are more appropriate for systems with highly delocalized electrons such as metals and other extended systems.

When dealing with periodic systems, plane-wave basis sets are the most common choice. Their general form in real space is e^{ikr}, where $\boldsymbol{k}$ is a vector in the reciprocal space. Plane waves are not centered at the nuclei since they extend throughout the complete space. Their periodicity makes them appropriate for extended systems with translational symmetry. However, a large number of plane waves is required to describe all electrons accurately. Since numerous chemical properties of molecules and solids are determined by their valence electrons, while core electrons remain basically unmodified for different chemical environments, to make DFT calculations more affordable, the effect of core electrons can be handled by means of an effective core potential or pseudopotential. Several different methodologies have been developed to construct pseudopotentials, but the most commonly used with planes waves on periodic models are norm-conserving pseudopotentials,[43] ultrasoft potentials,[44] and the projector augmented-wave (PAW)[45] method. For the calculations featured in this thesis, we make use of pseudopotentials built within the PAW formalism, since it restores the pseudo wavefunction obtained from the construction of the pseudopotential to the all-electron wavefunction, importing advantages from all-electron basis sets.

2.3 Periodic Solids

By definition, crystalline solids present a periodically ordered atomic structure. Their periodicity allows for their easy depiction, focusing the study on a portion of the system, which, translationally repeated in the three-dimensional space, reproduces the totality of the solid. The structural unit that is repeated translationally throughout the crystal is called the unit cell, which contains a certain number of atoms known as the atomic base. The Schrödinger equation only needs to be solved for the atoms in the unit cell, under the condition that the wavefunction or the electronic density in a given point remain invariant when a translational operator based on the periodic crystalline structure is applied. The

crystalline lattice is defined by the three orthogonal vectors of the unit cell (a_i), from which the translational operator ($\hat{T}$) is built:

$$\hat{T} = n_1\hat{a}_1 + n_2\hat{a}_2 + n_3\hat{a}_3 \qquad (2.9).$$

Note that the operator in Equation 2.9 is not to be confused with the kinetic energy operator for which we used the same symbol previously. Moreover, note that the infinite array of discrete points that can be generated in Equation 2.9 is called "Bravais lattice".

There are infinite ways in which we can build a unit cell that describes a given periodic solid, but there is smallest and irreducible unit cell is unique. Such a cell is called the primitive cell. The most common types of unit cell are cubic, body-centered cubic (*bcc*), face-centered cubic (*fcc*), and hexagonal closed packed (*hcp*). See Figure 2 for a schematic representation of the most common types of unit cell and Figure 3 for a depiction of the *fcc* primitive cell.

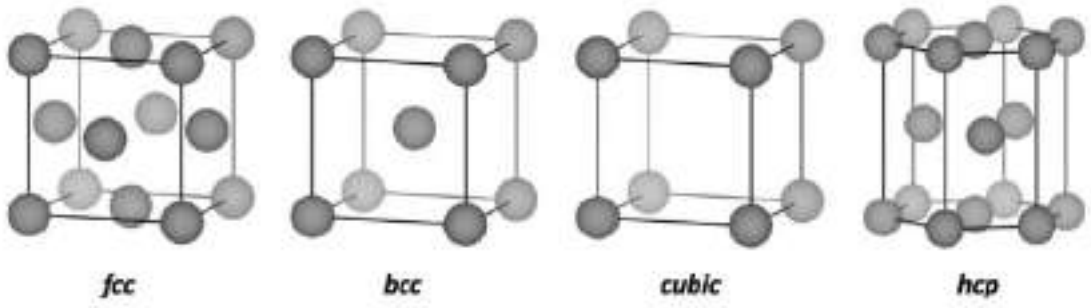

Figure 2. From left to right, a schematic representation of face-centered cubic, body-centered cubic, cubic, and hexagonal closed packed unit cells. Grey spheres denote atomic positions. Shades of grey are used to represent different depths.

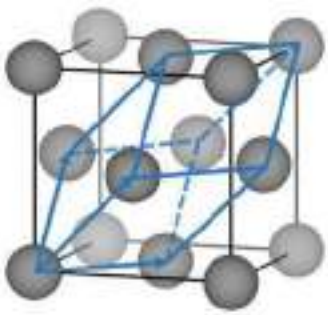

Figure 3. The *fcc* unit cell (in black) and its corresponding primitive cell (in blue). Shades of grey are used to represent different depths.

The use of the reciprocal space, also known as ***k***-space, is convenient for analyzing periodic systems. The reciprocal lattice is a mathematical construction that facilitates the study of the properties of periodic crystalline lattices. Each crystalline lattice $A = \{a_1, a_2, a_3\}$ has a corresponding reciprocal lattice $B = \{b_1, b_2, b_3\}$ that satisfies:

$$b_i = 2\pi \frac{a_j \times a_k}{a_i \cdot (a_j \times a_k)} \; \forall_{i,j,k} \in \{1,2,3\} \qquad (2.10),$$

$$a_i \cdot b_j = (2\pi)\delta_{i,j} \qquad (2.11).$$

Note that the volume of the unit cell of the reciprocal lattice is equal to $(2\pi)^3/V_c$, where V_c is the volume of the real space unit cell. Because the two volumes are inversely proportional, the larger the unit cell in the real space, the smaller in the reciprocal space.

When working with periodic models, the theoretical framework used to analyze the expansion of the wavefunction in the reciprocal space is based on Bloch's theorem.[46] Briefly, this theorem states that the values of all observables at a certain position of the unit cell are the same for the equivalent positions throughout the whole Bravais lattice. Thus, if a crystal is perfectly periodic, the potential in which the electrons move must satisfy:

$$\hat{T}V(\vec{r}) = V\left(\vec{r} + \vec{R}\right) = V(\vec{r}) \qquad (2.12).$$

Hence, when moving a given point $(\vec{r})$ to an equivalent point $\left(\vec{r} + \vec{R}\right)$ of a replicated cell using $\hat{T}$, the potential V remains identical.

A plane inside a Bravais lattice is determined by the position of three non-colinear points. The different possible planes inside the lattice are usually named using Miller indices. These indices are defined as the inverse of the reciprocal intersections between the plane and the coordinate axis, then multiplied by the least common multiple. For example, if the intersections between the plane and the coordinate axes are located at 2*x*, 3*y*, and 3*z*, the inverse values are 1/2, 1/3, and 1/3. If we then multiply by the least common multiple, we obtain the Miller indices, in this case (322). Note that if the plane does not intersect with one of the coordinate axes that index is 0. In Figure 4 the (100), (110), and (111) crystallographic planes inside a cubic unit cell are shown as an example.

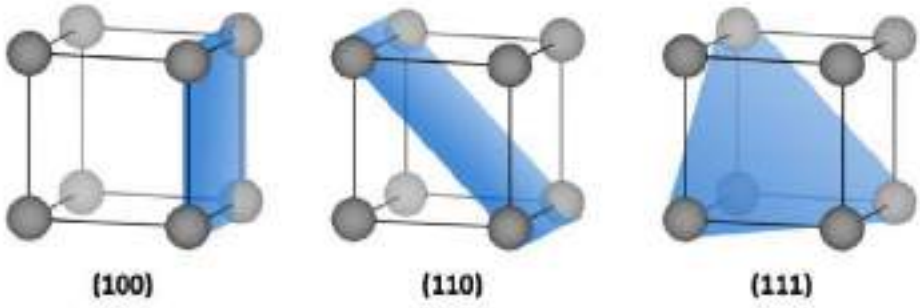

Figure 4. From left to right, the (100), (110), and (111) crystallographic planes inside a cubic unit cell in the Miller indices notation.

The study of solid surfaces is usually done using the periodic slab model. This model is easily built from the unit cell by increasing the size of the lattice vector perpendicular to the plane of interest. In this way, vacuum is introduced between replicas of the cell, avoiding interactions between them. Several atomic layers may be present in the slab to ensure a correct description of the bulk properties as well as the surface electronic properties. Usually, during optimization, the bottommost atomic layers are kept fixed at the converged bulk lattice constant to simulate the bulk environment, while the topmost ones are allowed to relax in all directions to represent the surface atoms. Note that when a perturbative element is to be introduced into the slab model (e.g., a surface defect or an adsorbed molecule) the slab model needs to be enlarged in the plane directions to ensure that there are no lateral interactions between the perturbative element and its replicas. An exemplary slab cell is shown in Figure 5.

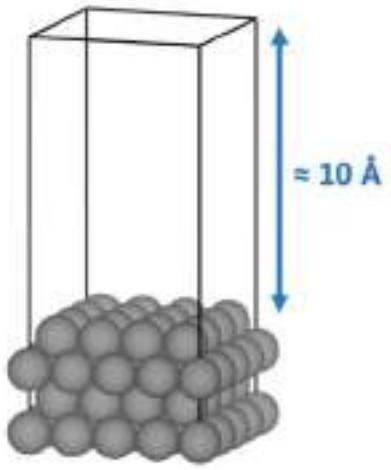

Figure 5. Schematic representation of a four-layered *fcc*(100) slab model unit cell with approximately 10 Å of vacuum.

2.4 Adsorption Energies

Most of the calculations featured in this thesis are based on DFT optimizations of the structure and position of adsorbed molecules on metallic surfaces. The main goal of these calculations is to obtain the adsorption energy (ΔE_{ads}) of the molecule on one particular surface (slab model), which is then used to assess different aspects of interest such as the catalytic activity of a certain catalyst. To do so, several geometry optimization calculations involving different molecule conformations on various sites of the slab must be performed. Once the most favorable conformation and adsorption site are obtained, one can then calculate ΔE_{ads} in the way shown in Equation 2.13.

$$\Delta E_{ads} = E_{M+S} - E_S - E_M \qquad (2.13),$$

where E_{M+S} is the energy of the system containing the slab and the molecule in its most favorable position, E_S is the energy of the slab, and E_M is the energy of the isolated molecule. The calculated energy of isolated molecules (E_M) within the generalized gradient approximation can present sizable errors. To correct these, a method where the errors are pinpointed based on the difference between calculated and experimentally determined formation energies is used.[47]

In order to relate these calculations to macroscopic experimental observables like the Gibbs free energy, thermal effects must be included. At the macroscopic level, nuclei are permanently moving, and molecular vibrations must be considered. The energy contribution of these vibrations at 0 K is known as the zero-point energy (*ZPE*):

$$ZPE = \frac{1}{2}\sum_i h\nu_i \qquad (2.14),$$

where h is the Planck constant and ν_i corresponds to each of the vibrational frequencies of the adsorbed molecule.

Moreover, entropy corrections (*TS*) for gas molecules have to be considered, which can be obtained from thermodynamic tables.[48] For adsorbed molecules, only the

vibrational contributions to the entropy (TS_{vib}) are considered. Those contributions are computed in the following way:[49]

$$TS_{vib} = k_B T \sum_i \ln\left(1 - e^{-\frac{h\nu_i}{k_B T}}\right) - \sum_i h\nu_i \left(\frac{1}{e^{\frac{h\nu_i}{k_B T}} - 1}\right) \qquad (2.15).$$

Thus, the adsorption Gibbs free energy is given by:

$$\Delta G_{ads} = \Delta E_{ads} + \Delta ZPE - T\Delta S \qquad (2.16).$$

Furthermore, in electrocatalysis, solvent effects can play a key role in adsorption free energies and catalytic activity assessment. Thus, they should be taken into account when looking for a more quantitative estimation of the catalytic activity of a given system.[50] Solute-solvent interactions can be computed mainly in two ways, with the explicit inclusion of solvent molecules or through an implicit continuum model. Both methods provide information on the electronic properties of the solute and its most stable geometry. The explicit approach involves adding a large number of solvent molecules into the calculation, making it more challenging and computationally expensive. On the other hand, treating the solvent as a continuum is more affordable but less accurate in cases when there are solute-solvent hydrogen bonds. When the solvent is treated implicitly, the solute is immersed in a bath of solvent the properties of which are determined by its electric permittivity (ϵ). An alternative, intermediate approach, aiming to preserve the explicit solvent accuracy but avoiding high computational costs, is the use of ad-hoc corrections to the adsorption free energies. It consists of calculating the contribution of solvation to the adsorption free energies using supercells covered with and without a few explicit water molecules. The difference between the calculated adsorption free energies gives a fair estimation of the magnitude of the solvation effect for one specific adsorbate. Then, these solvation values can be extrapolated to other adsorbates based on their chemical similarity to the ones the correction was calculated for.[51]

2.5 Computational Hydrogen Electrode

All the computational electrocatalysis studies in this thesis are based on the computational hydrogen electrode (CHE).[52] This method works on the basis that, at 1 atm, 0 V, and all pH values, protons and electrons are in equilibrium with gas-phase molecular hydrogen.

$$\frac{1}{2}H_{2(g)} \leftrightarrow H^{+}_{(aq)} + e^{-} \qquad (2.17).$$

Thus, under these conditions, the electrochemical potential of an aqueous proton-electron pair is equivalent to that of $\frac{1}{2}H_{2(g)}$. Hence, rather than using the energetics of $(H^{+} + e^{-})$ as an electrochemical reference, those of $\frac{1}{2}H_{2(g)}$ are used. The effect of the electrode potential can also be included into the equation as an eU term, where e is the charge of an electron and U is the electrode potential in V vs RHE.

$$\frac{1}{2}\mu(H_2) - eU = \mu(H^{+} + e^{-}) \qquad (2.18).$$

RHE stands for reversible hydrogen electrode, which is a widely used experimental reference electrode. Reference electrodes are electrodes with stable and well-known equilibrium potentials and are used to measure the potential in electrochemical experiments. RHE measured potentials do not change with pH.[53]

Most importantly, the CHE approach allows for the calculation of Gibbs free energies where proton-electron transfers are involved. In this way, free-energy diagrams can be built for reactions involving several proton-electron transfer steps. In Figure 6, one such diagram is shown featuring the energetics of 1-propanol oxidation to propanal on Pt(111) (orange) and PtRu(111) (blue). Note how all Gibbs free energies are referenced to the same molecule (1-propanol in this example) to be comparable between them. Moreover, different colors are used to depict the energetics of the reaction intermediates on different surfaces to ascertain those in which the reaction may proceed more favorably.

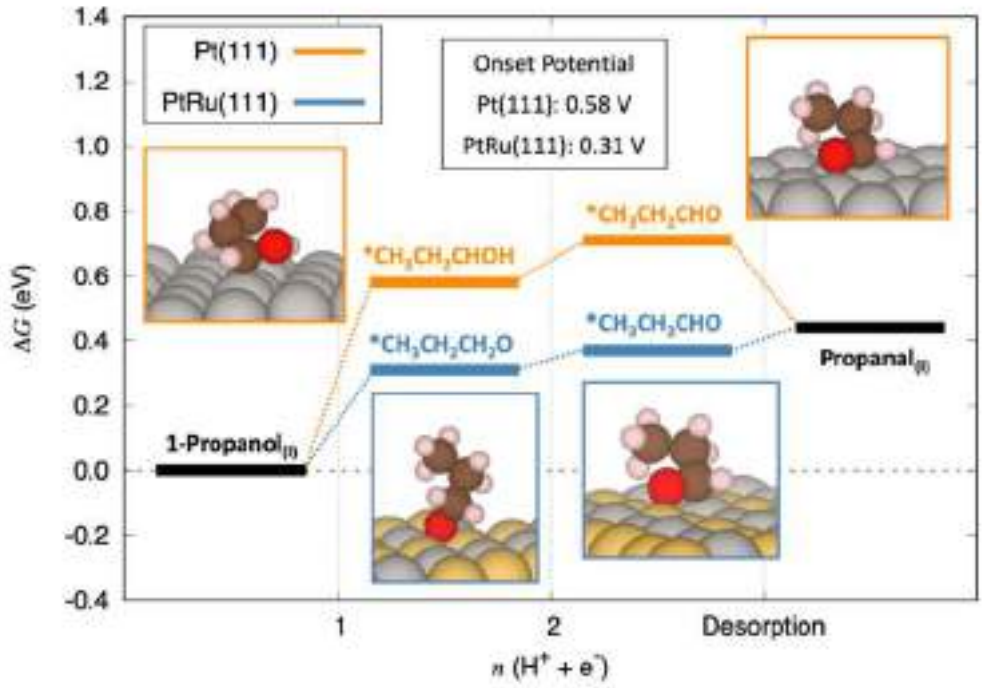

Figure 6. Free-energy diagram of the most favorable pathway at 0 V vs RHE for 1-propanol oxidation to propanal. In orange, Pt(111); in blue, PtRu(111). The calculated onset potentials and optimized geometries are also included. Pt, Ru, O, C, and H atoms are shown in grey, yellow, red, brown, and pink. This figure corresponds to panel a in Figure 4 of reference 54 and is included here to facilitate the reading of this thesis.

The activity of the catalyst can be tackled by determining limiting potentials (U_L), which are calculated based on the free energy of the largest uphill electrochemical step (ΔG_{max}) of a reaction involving several proton-electron transfers. In Figure 6 the limiting (or onset) potentials are shown as an inset. ΔG_{max} of the reaction on both surfaces is corresponds to the first step, namely, the deprotonation of 1-propanol to form a *CH_3CH_2CHOH intermediate on Pt(111) or a *$CH_3CH_2CH_2O$ intermediate on PtRu(111). This step is referred to as the potential-limiting step (PLS), and from its ΔG, U_L can be computed.

$$U_L = -\Delta G_{max}/e \qquad (2.19).$$

Finally, note that this is only a thermodynamic treatment and that electrochemical barriers are not considered. As noted recently by Rossmeisl et. al.,[55] there is "not (yet) a method to obtain electrochemical barriers between realistic states at constant electrochemical conditions". Hence, it is assumed that thermodynamics and kinetics are

proportional by virtue of Brønsted–Evans–Polanyi (BEP) relations, which linearly correlate a reaction step energy barrier (a kinetic quantity), E^a, with the corresponding reaction energy (a thermodynamic quantity), ΔE (see Figure 1).[56-58]

2.6 Phase Diagrams

In Chapter 4, where we analyze the interaction of C atoms with TM surfaces, we make use of pressure-temperature dependent phase diagrams to examine the most stable catalyst phase at working catalytic conditions. These are created following a a statistical thermodynamics approach from *ab initio* computed data.[59]. Briefly, for each calculated situation, one can obtain the adsorption or absorption free energy, ΔG^{ad} or ΔG^{ab}, respectively, as a function of the temperature (T) and gas pressure (p) of the system. For an example situation featuring the adsorption of a C atom on a (111) surface, the formula is:

$$\Delta G^{ad}(T,p) \approx -\frac{1}{A}\{E^{total}(N_C,N_M) - E^{total}(0,N_M) - N_C(E_C^{total} + E_C^{ZPE}) - N_C\Delta\mu_C(T,p)\} \quad (2.20),$$

where A is the surface area of the system, N_C the number of carbon atoms, N_M the number of metal atoms, and $\Delta\mu_C$ the chemical potential variation of carbon. Note the negative sign in front of Equation 2.20 is introduced just to turn most stable energies into the most positive ones, to facilitate the interpretation of the results. Moreover, it is worth noting that the $\frac{1}{A}$ factor is not indispensable, and only included here to obtain surface free energies as a result.

Equation 2.20 is only valid for a system with an invariant number of metal atoms, for a variant expression be referred to the literature.[59] Furthermore, note that, for the clean surface Equation 2.20 equals zero, since in that case $N_C = 0$, and $E^{total}(N_C,N_M) = E^{total}(0,N_M)$. As under working catalytic conditions it is not rigorous to consider a gas-phase C atom, a linear combination of gas-phase molecules is used to represent it.

Specifically, we used $\mu_C = \frac{1}{2}(\mu_{C_2H_2} - \mu_{H_2})$, $E_C^{total} = \frac{1}{2}\left(E_{C_2H_2}^{total} - E_{H_2}^{total}\right)$, and $E_C^{ZPE} = \frac{1}{2}\left(E_{C_2H_2}^{ZPE} - E_{H_2}^{ZPE}\right)$ as a reference. Employing this reference implies that $\Delta\mu_C = \frac{1}{2}(\Delta\mu_{C_2H_2} - \mu\Delta_{H_2})$. Thus, to calculate $\Delta\mu_C$, both C_2H_2 and H_2 (hereon referred to as *X* molecules) chemical potential variations are computed as:

$$\Delta\mu_X(T,p) = -k_BT\left\{ln\left[\left(\frac{2\pi m_X}{h^2}\right)^{\frac{3}{2}}\frac{(k_BT)^{\frac{5}{2}}}{p_X}\right] + \ln\left(\frac{k_BT}{\sigma_X^{sym}B_{0,X}}\right) - \sum_{i=1}^{n} ln\left[1 - \exp\left(\frac{-\hbar\omega_{i,X}}{k_BT}\right)\right] + \ln\left(I_X^{spin}\right)\right\} \quad (2.21),$$

where k_B is the Boltzmann constant, h is the Planck constant, m_X is the mass of the molecule *X*, p_X is the partial pressure of *X*, σ_X^{sym} is the classical symmetry number of *X*,[60] B_0 is the rotational constant, computed as $\frac{\hbar^2}{2I_X}$, where I_X is the moment of inertia of *X*, $I_X = \sum_i m_i r_i^2$. In the latter expression, m_i is the mass of the atoms in *X*, and r_i is the distance of the i atom to the centre of mass of *X*. Moreover, ω_i are each of the vibrational normal modes of *X*, and I_X^{spin} is the ground-state electronic spin degeneracy.

The first summand in Equation 2.21 stands for the translational free energy, computed as the translational partition function in the classical limit, assuming ideal gas-phase behaviour. The second summand corresponds to the rotational free energy, computed as the rotational partition function within the rigid rotator approximation. The third summand stands for the vibrational free energy, computed as the vibrational partition function in the harmonic approximation. Notice that in previous literature[59] there is a missing negative sign, which is duly incorporated in this work. Last, the fourth summand corresponds to the nuclear and electronic free energy, where the only significant term is the ground-state spin degeneracy.

In summary, ad/absorption free energies can be calculated as function of T and p using Equations 2.20 and 2.21. The ΔG^{ad} of the clean surface is zero. Hence, when the ΔG^{ad} of the system containing the adsorbate is negative, it is less stable than the clean surface, when positive it is more stable, and when null it is as stable as the clean surface, indicating a phase transition point in between clean and carbon-containing phases.

Figure 7 shows how adsorption and absorption free energies depend linearly on the carbon chemical potential variation, whereas the clean surface ΔG does not. The most stable scenario under a given chemical potential corresponds to the one with the highest positive ΔG, as shown by the thicker lines in Figure 7. The two C-containing scenarios described in it, C^{sur} and C_{sub}, have the same dependency on the chemical potential, hence the more stable of the two will remain the most stable under any T and p conditions. In this example, the point where the clean surface and C_{sub} cross corresponds to the chemical potential at which these two situations are equally stable, namely at a ΔG^{ab} of zero. Figure 7 is assembled at a constant temperature, *e.g.,* it could be at 1000 K, and a constant p_{H_2} of 10^{-7} Pa, mimicking ultra-high vacuum conditions. Considering a constant pressure of H_2 allows us to find the corresponding $p_{C_2H_2}$ for a ΔG^{ab} of zero. Finding the pressures and temperatures at which ad/absorption energies become zero allows us to construct a phase diagram by depicting these points in a T-$p_{C_2H_2}$ plot.

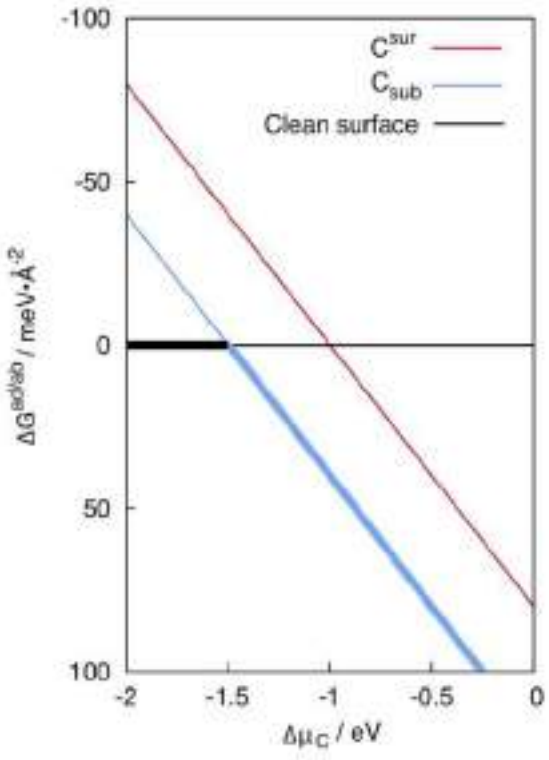

Figure 7. Illustrative scheme showing the variation of the adsorption or absorption free energies, $\Delta G^{ad/ab}$, across different variations of carbon chemical potential, $\Delta\mu_C$. The black line corresponds to the clean surface. Blue and red lines to C_{sub} and C^{sur} situations. This figure corresponds to Scheme 1 in the supporting information of reference 61 and is included here to facilitate the reading of this thesis.

2.7 Transition States

Transition-state theory was developed in parallel by Eyring and Polanyi. Their formulations from 1935 propose the existence of an activated complex or transition state assembled from the reactants, which is later decomposed to form the products of the reaction.[62,63] Looking back at Figure 1 (located in Chapter 1), the transition-state geometry for each elementary step (there are four of them in the catalytic pathway of Figure 1) would be found at the highest energy point of the reaction coordinate between two minima. More precisely, the transition state must fulfill two mathematic conditions. First, it must be a stationary point, hence, the gradient of the energy with respect to all coordinates of all atoms must be numerically zero. Second, the Hessian matrix must have one and only one negative eigenvalue corresponding to the pathway from reactants to products.[64] The difference in energy between the transition state and the reactants is called activation energy (E^a) or energy barrier (E_b) and is the main component influencing the reaction rate.

Numerous algorithms have been proposed to locate transition states,[65,66] here we used the climbing-image nudged elastic band (CI-NEB) method.[67] This method involves generating a set of images between the initial and final state geometries. Each image maintains equal spacing to neighboring images during the optimization, and are connected through spring forces, such that the structures of the images do not evolve towards a minimum, since the optimization is constrained by the chain of springs connecting them. At the same time, the highest-energy image is moved upwards along the reaction path until finding the alleged transition state. Still, note that this does not ensure that the located transition-state geometry is the correct one. When the set of images is created, we are assuming that the reaction pathway follows the path along them, which may not be the lowest-energy one. Hence, several different reaction paths must be studied to ensure that one has truly found the lowest-energy transition state.

Note that while we calculated coupling and diffusion barriers in some of the studies featured in this thesis, we did not perform calculations of proton-electron transfer barriers, since, as mentioned previously, there is not yet a method to obtain electrochemical barriers reliably.[55]

2.8 Machine Learning Algorithms

In Chapter 4, we make use of machine-learning algorithms to understand how our data are grouped and to perform multivariable regressions. For the first task, we employed the k-means (KM) algorithm as implemented in the *sklearn* Python library.[68] KM clusters data by dividing samples into *n* equal-variance groups, where *n* is determined beforehand. The algorithm finds *n* cluster centres that minimize the sum-of-squares within each cluster, also known as inertia, see Equation 2.22.

$$\sum_{i=0}^{n} \min_{\mu_j \in C} \left(\|x_i - \mu_j\| \right)^2 \qquad (2.22),$$

where μ_j is the mean of the sample, also known as cluster centroid, in the *C* disjoint clusters.

Inertia can be thought of as a quantitative measure of how coherent clusters are, but has some disadvantages. It performs poorly with elongated clusters because it assumes that clusters are isotropic and convex. Furthermore, inertia is a non-normalized metric, which means that smaller values are preferable and zero is ideal. As a result, it struggles in high-dimensional spaces, where Euclidean distances are prone to inflation. This issue can be mitigated by using a dimensionality reduction algorithm prior to the k-means analysis.

It is important to note that when *n* equals the number of data points, the minimum inertia of zero is obtained. In that regard, a criterion must be defined to limit the *n* number of clusters to a sensible and manageable size. This can be accomplished using the elbow method,[69] which consists of plotting the inertia as a function of *n* and selecting the curve elbow as the optimal number of clusters to utilize.

Furthermore, we also made use of machine learning regression algorithms, as implemented in the *sklearn* Python library.[68] Precisely, we employed the multivariable linear regression (MLR), which is the conventional least-squares linear regression but applied to two or more variables, as well as the decision tree regressor (DTR) and the random forest regressor (RFR). The DTR is a supervised learning algorithm which learns a set of binary rules derived from the data features to build a model that predicts the value of a target variable (*y*). DTR accomplishes this by creating a model in the shape of a tree

structure with branches, nodes, and leaves. The algorithm, which looks for the homogeneity of y values in a found subset and uses the standard deviation of y as an optimization criterion, automatically determines and optimizes the order of the questions (known as decision nodes) as well as their content. The model learns any relationships between the data and the target variable during training, identifying the optimal questions and their order to produce the most accurate estimations possible. When predicting the dependent variable value of a new datapoint, the point is navigated entirely through the tree branches, answering node questions until it reaches the final leaf, which contains the target variable estimation. This estimation corresponds to the y average value of all points meeting the same logic questions as the new point.

The complexity of the preceding explanation calls for an illustrative example to understand the fundamentals of the procedure. Let us define a dependent target variable, y, which depends on two features, x_1 and x_2. Figure 8 shows a scatter plot of x_2 *vs.* x_1. In it, dotted lines delimit zones defined by the nodes, such as one asking whether x_1 values are greater than 50, and others asking whether x_2 values are greater than 4 for x_1 values below 50, or x_2 values being greater than 12 when x_1 is greater than 50. As a result, four leaves are obtained with different average y values, $\bar{y}$, see Figure 9. If that were the result of a hypothetic training set, a new value from the test set with $x_1 = 25$ and $x_2 = 12$ would deliver a $\bar{y}$ value of 5.1. Note how this is done for a very simple, two-dimensional example, with y values depending only on two variables, but it may easily be applied to a case with a larger number of variables.

Although DTR is simple to interpret and requires little data preparation, the resulting tree is sensitive to the data used, meaning that little changes in the data can result in an entirely different tree. To alleviate this problem, an ensemble of trees (or forest) can be used. This is the foundation of the random forest regression (RFR), which involves the growth of an ensemble of decision trees. Each tree is built from a sample drawn randomly from the dataset. For each tree, the optimal split of each node can be obtained using either all the input features or a random subset of features, also known as *max_features*. These two sources of randomness assist in decreasing the variance of the estimator, since individual decision trees commonly feature high variance and tend to overfit. When a prediction is made on a dataset, such as for the x_1 and x_2 values mentioned above, distinct $\bar{y}_i$ values are obtained for $i = 1 - N$, where N is the number of trees of the forest, also known as *n_estimators*. The expected value of $\bar{y}$ is just the average of the expected $\bar{y}_i$ values across all N trees. By doing so, the tree forecasting accuracy is narrowed, and

possible possible extreme $\bar{y}$ forecasts are diluted. It is worth noting that RFR becomes DTR for $i = 1$, and that the more trees one has, the larger the accuracy. However, the computational expenses grow alongside the number of trees. Apart from that, the accuracy decreases as N increases, although the outcome rarely improves beyond a certain number of trees.

Finally, an appealing element of both DTR and RFR is the fact that the relative rank of a feature used as a decision node in a tree may be used to assess the relative importance of that feature regarding the target variable predictions. Features employed near the top of the tree have a greater impact, since they affect the final prediction of a bigger percentage of samples. Thus, the relative relevance of the features can be estimated as the expected fraction of samples they contribute to.

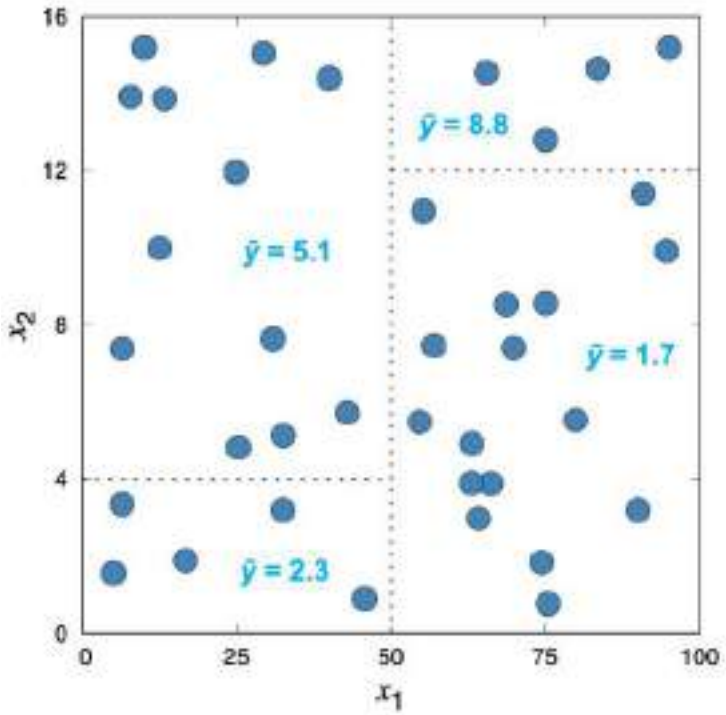

Figure 8. Exemplary scatter plot of values, shown as blue circles, of x_2 *vs.* x_1 variables, where black dotted lines represent the variable splitting decisions learned by the model. In light blue, the $\bar{y}$ average values for all those points belonging in each of the resulting sections inside the plot.

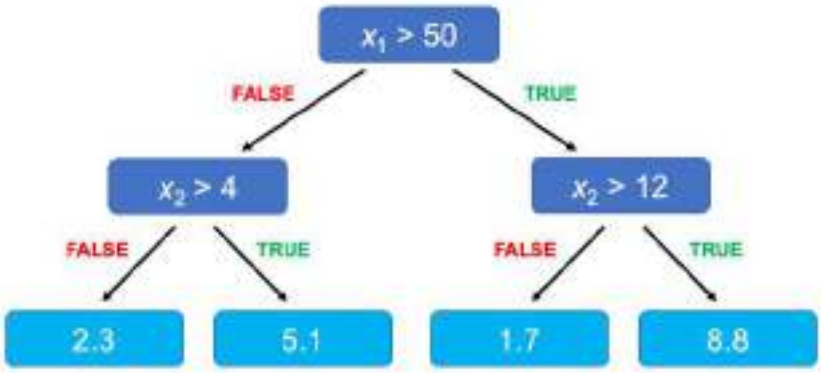

Figure 9. Exemplary decision tree from data shown in Figure 8.

2.9 Descriptors

In the field of computational heterogeneous catalysis and electrocatalysis, it is common to look for descriptors of DFT-calculated quantities related to the catalytic activity, such as ad/absorption energies, Gibbs free energies, energy barriers, and onset potentials, among others. Finding successful descriptors can have positive implications on future research, since it allows for estimating the catalytic activity of a certain material without performing all the costly DFT calculations necessary for it.

Several studies in the literature have been devoted to the study of electronic descriptors to predict material properties such as adsorption energies. Different descriptors have been proposed, such as surface energy,[70] work function,[71] number of outer electrons,[72] *d*-band center,[73] corrected *d*-band center,[74] highest Hilbert transform *d*-band peak,[75], and the electrochemical-step symmetry index,[76] among others. For transition metals, the most widely used one is the *d*-band center (ε_d), which generally exhibits a good linear correlation with adsorption energies.[77] To compute ε_d, the *d*-contribution of a surface atom to the projected density of states is obtained, thus, the surface first-layer *d*-projected density of states (*d*-PDOS). Specifically, ε_d is defined as the center of mass (or the weighted average) of the *d*-band density of states of a surface atom:

$$\varepsilon_d = \frac{\int_{E_i}^{E_f} (E - E_{Fermi})\, dPDOS}{\int_{E_i}^{E_f} dPDOS} \qquad (2.23),$$

where E_i is the *d*-band starting point and E_f is the energy point that would belong to a d^{10} electronic configuration.

The idea underlying this descriptor is that materials with higher (more positive) *d*-band center values are more reactive than those with lower (more negative) ε_d values. Hence, adsorption energies should be stronger the higher in energy ε_d is.

Geometric features are also used as descriptors, such as coordination numbers[78] and generalized coordination numbers.[79] They can capture the differences arising from different atomic arrangements of the same material, for example, between diverse surface terminations of the same TM. This is justified by the fact that low coordinated atoms are typically more reactive than those with higher coordination.

DFT-calculated properties can be correlated between themselves, for example, the usage of Brønsted–Evans–Polanyi (BEP) relations is widely extended, linearly expressing a reaction step energy barrier as a function of the corresponding reaction energy.[56-58] Moreover, linear relations have been observed between adsorption energies of adsorbates similarly bound to transition metal surfaces.[80] Such relations also hold on surfaces of nitrides, sulfides, oxides, and carbides, among others.[72,81] The general rule for scalability ($\Delta E_B = m\Delta E_A + b$, Figure 10, top-right panel) is that the extrema of two curves that correlate the adsorption energies of species A and B (ΔE_A and ΔE_B, Figure 10, top and bottom panels on the left) with the electronic structure of the surface coincide.[82,83] This can be seen in Figure 10, where we assume a quadratic correlation between a hypothetic descriptor *D* and ΔE_A and ΔE_b. As shown in Figure 10 (bottom-right panel), the offset of the linear correlation (*b*) depends on the slope value (*m*):[83,84] if $m = 1$, *b* is proportional to the coordination of the adsorption sites, if $m \neq 1$, *b* is surface independent.

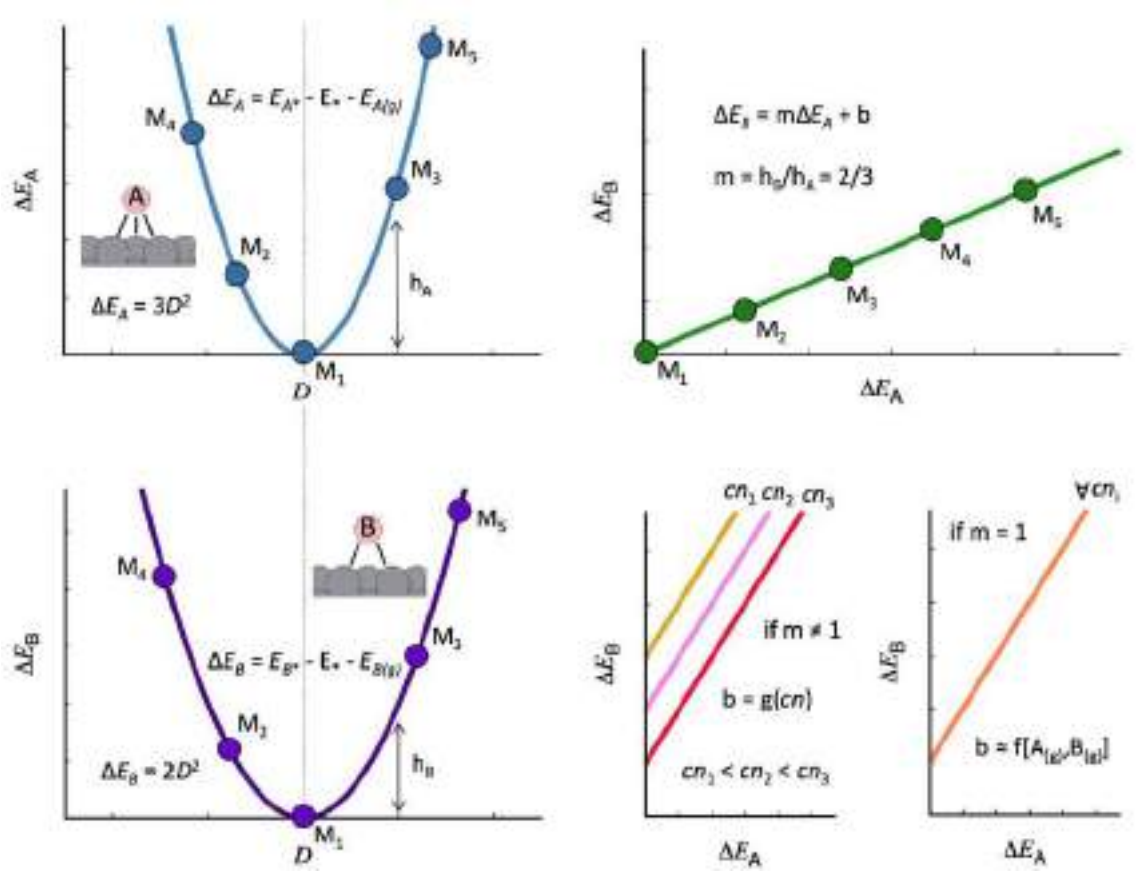

Figure 10. Generalities of adsorption-energy scaling relations. Left: the adsorption energies of species A (ΔE_A, top) and B (ΔE_B, bottom) for materials M_1 to M_5 scale with a hypothetical descriptor D and their minima coincide. A makes three bonds with the surface and B makes two. Top-right panel: because ΔE_A and ΔE_B scale similarly with descriptor D and the minima coincide, there is a linear scaling relation between them and the slope of the line is the ratio of the bonds made to the surface. Bottom-right panel: if $m \neq 1$, the offset of the scaling relation depends on the coordination number of the active sites. Conversely, if $m = 1$, the offset is surface-independent and proportional to the gas-phase energetics of A and B. This figure corresponds to Figure 1 in reference 85 and is included here to facilitate the reading of this thesis.

Finally, it is worth noting that the use of descriptors is not limited to linear correlations, one can perform multivariable linear (or polynomial) regressions to use multiple descriptors at the same time to correlate a desired quantity. Moreover, machine learning algorithms such as random forest regressors can also be used in this regard, obtaining an advanced predictive model capable of estimating a certain quantity when fed with the necessary descriptors for it.

Chapter 3

Electroreduction of CO_2 to Valuable Commodities

3.1 Introduction

Increasing the availability of renewable electricity and lowering its costs are pivotal to address climate change and rebalance the biogeochemical cycle of carbon. One of the major challenges in that respect is the inherent intermittency of renewable energy sources. It is necessary to develop means to store energy surpluses and use them in due time, according to the demand.[86]

To this end, the electroreduction of CO_2 (CO_2RR) to valuable fuels for energy storage and environmental mitigation has received great attention and experienced pronounced advances.[87-90] Although numerous catalysts are able to reduce CO_2 to 2-electron products such as CO or formic acid, further electroreduction of these products is needed to produce "electrofuels". The latter are fuels made by storing energy from renewable sources in the chemical bonds of liquid or gas molecules. Pioneering works by Hori and his coworkers showed that when Cu is used as a catalyst, further electroreduction of CO (CORR) to valuable commodities such as methane, ethylene, acetaldehyde, and ethanol is possible.[91-93] Thus, CO_2 and/or CO electrolyzers using Cu catalysts and renewable electricity hold promise as a carbon-neutral means to produce commodity chemicals. However, the large overpotentials required to reach appreciable current densities and conspicuous selectivity problems hinder global spread of such technology.[94,95]

3.2 Elucidating the Active Sites and Onset Potentials for CO_2RR and CORR at Oxide-Derived Cu Electrocatalysts

Introduction To address some of the challenges involved in CO_2RR and CORR on Cu catalysts, the redox treatment of Cu catalysts has been shown as a good solution. Oxide-derived Cu (OD-Cu) catalysts show lower overpotentials (< 0.4 V) and are more selective towards C_2 products, with higher ethanol production compared to regular Cu catalysts.[96,97] However, the structure of the active sites present in OD-Cu and the chemistry behind these improvements remains elusive. Previous studies showed that such sites could be located at grain boundaries.[97,98] Those works suggested that engineering the amount and structure of the gran boundaries by altering the oxide reduction method or varying the synthesis procedure could result in better OD-Cu catalysts with higher selectivity and activity towards C_2 products. Moreover, those studies showed that the OD-Cu active sites responsible for the high CORR activity bind CO more strongly than low-index and stepped Cu facets.[98]

Previous research showed that (a) square sites promote C-C coupling,[78,99] (b) Cu(100) has square sites and is selective to ethylene, [51,99] (c) the OD-Cu active sites bind CO stronger than step sites,[98] (d) undercoordinated sites favor acetaldehyde reduction to ethanol,[100] and acetaldehyde is a known intermediate of CORR to ethanol on OD-Cu catalysts,[51,101] and (e) isotopic labelling experiments show that ethylene and ethanol are produced on different active sites during CORR on OD-Cu catalysts.[102] Based on those observations, we argue that the active sites responsible for ethanol evolution on OD-Cu catalysts are square-symmetry four-atom islands sitting on top of neighboring Cu(100) hollow sites, which we refer to as 4AD@Cu(100), were AD stands for Cu adatoms.

This work led to the publication of two research articles.[103,104] The manuscripts are included at the end of this section. In the following pages, a summary of them is provided. My contributions to the research articles were: (a) Elaboration of the DFT calculations, (b) analysis of the computational results and making of the corresponding figures, and (c) writing an initial draft of both papers. I was not involved in the making of the experiments. The supporting information for "*Elucidating the structure of ethanol-producing active sites at oxide-derived electrocatalysts*" can be found in Appendix A. The optimized geometries have been removed from this document to save space but can be found online at: https://doi.org/10.1021/acscatal.0c01880. The supporting information for

"*Computational-Experimental study of the onset potentials for CO_2 reduction on polycrystalline and oxide-derived copper electrodes*" can be found in Appendix B.

Results To verify our hypothesis, we performed DFT calculations using the intermediates featured in the CORR mechanism proposed in Ref. 51. The thermodynamics of each proton-electron transfer were obtained for four different surface models: Cu(111), which is the most stable surface termination of Cu; Cu(100), which is known to facilitate C-C coupling; 4AD@Cu(100), which is our proposed ethanol production site on OD-Cu for the reasons explained above; and 4AD@Cu(111), to determine the effect of adding such atoms islands on top of the most stable Cu facet in a hexagonal symmetry. Figure 11 shows: (a) a top view of the surface models, and (b) the pathways studied toward C_2 products.

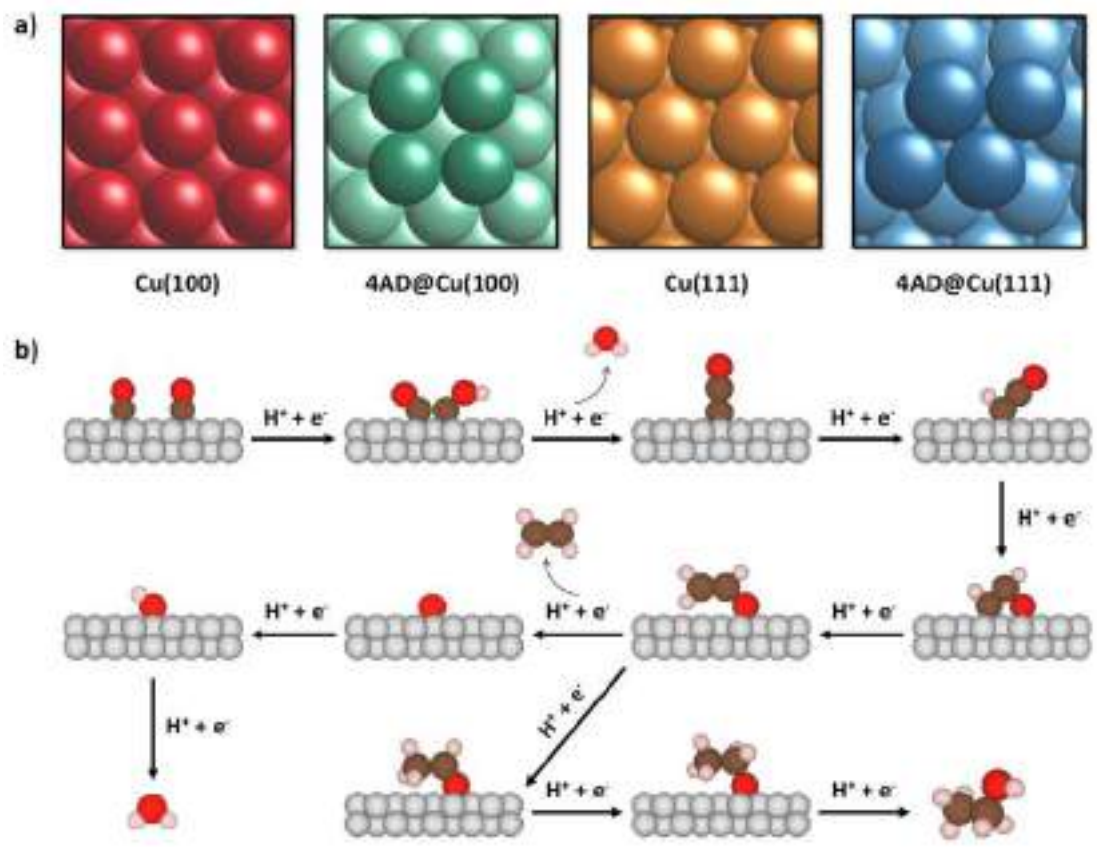

Figure 11. a) Schematics of the four different surface models used in this work. Cu(100), 4AD@Cu(100), Cu(111), and 4AD@Cu(111) surfaces are provided in red, green, orange, and blue, respectively. Island atoms are shown in darker colors. b) Reaction pathway for CORR to C_2 species. We depicted Cu, C, O, and H atoms as grey, brown, red, and pink spheres, respectively. This figure corresponds to Figure 1 in reference 103 and is included here to facilitate the reading of this thesis.

Previous studies have shown that alkaline cations can affect the product selectivity of the CORR.[105-107] Therefore, we included cation and solvent effects in our calculations to obtain a more realistic picture of the active sites. In Figure 12, we show the results in two different free-energy diagrams. The data for Cu(100) and 4AD@Cu(100) is depicted in panel a, while the data for Cu(111) and 4AD@Cu(111) appears in panel b. In these diagrams, the reaction coordinate for each of the four surface models is shown, with each of the sites depicted with a specific color. As seen in Figure 11b, the reaction pathway bifurcates at the sixth proton-electron transfer, with one path leading to ethylene and the other to ethanol. In the diagrams, a lighter version of each color indicates the respective ethanol pathway for each of the surface models. Likewise, the formula for each intermediate of the reaction is shown on the upper part of Figure 12, where black is used for the intermediates of the ethylene pathway and grey for those of the ethanol pathway.

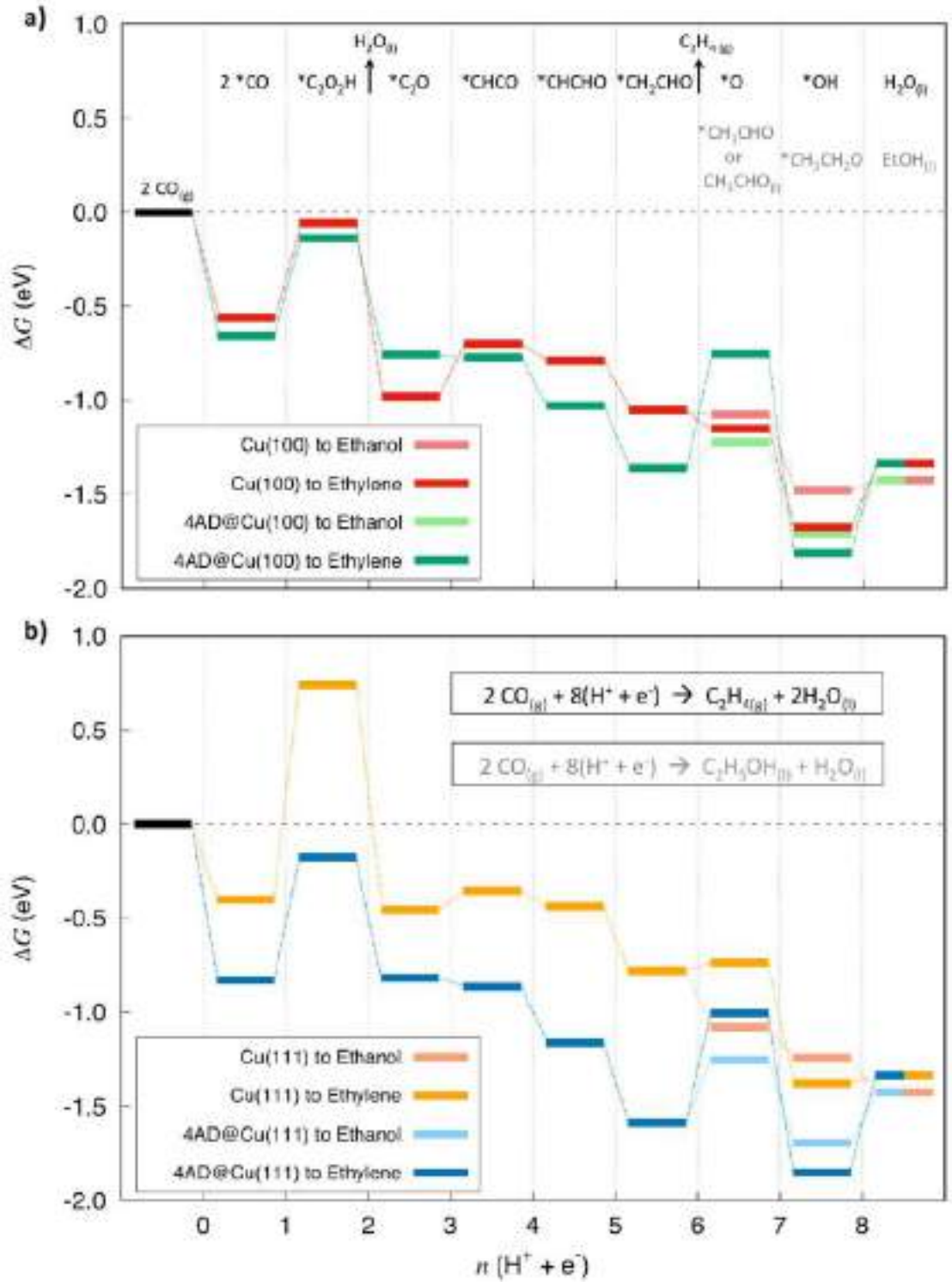

Figure 12. Free-energy diagrams including solvent and cation effects for all intermediates of the CORR on all four surfaces studied at 0 V vs RHE. a) Cu(100) (red) and 4AD@Cu(100) (green). b) Cu(111) (orange) and 4AD@Cu(111) (blue). The same colors in a lighter tone are used to represent the ethanol pathway, which drifts from that of ethylene upon the sixth proton-electron transfer. EtOH: ethanol. This figure corresponds to Figure 2 in reference 103 and is included here to facilitate the reading of this thesis.

Within the thermodynamic approach used here, the potential-limiting step (PLS) is the step with the largest positive free energy at 0 V vs RHE, which is close to the equilibrium potentials of ethylene and ethanol evolution. For all four surface models, the PLS is the first proton-electron transfer, which involves the C-C coupling between two adsorbed CO molecules and the protonation of the formed CO dimer. This C-C coupling step is experimentally known to be critical in the C_2 pathway of CORR.[93,94] Specifically, 0.50, 0.52, 1.14, and 0.66 eV are the PLS free energies for Cu(100), 4AD@Cu(100), Cu(111), and 4AD@Cu(111), respectively. Cu(111) is the surface model with the highest PLS free energy, which is consistent with previous calculations and experiments suggesting that this facet is the least active facet toward C_2 products and usually favors CH_4 production.[78,99,108] Comparing Cu(111) to 4AD@Cu(111), we observe that undercoordination helps in stabilizing $*C_2O_2H$, i.e. the hydrogenated CO dimer, therefore lowering the PLS free energy. However, the lowest PLS values correspond to Cu(100) and 4AD@Cu(100), indicating that square symmetry is key in enhancing CO dimerization and is more important than the coordination number of the active sites.

Figure 13 dissects the energetics of the first electrochemical step in Figure 12 ($2CO_{(g)} + * + H^+ + e^- \rightarrow *C_2O_2H$), including a *CO dimer configuration proposed previously.[109] We calculated the kinetic barriers for the formation of the dimer ($*C_2O_2$) and found them essentially equal to the thermodynamic energy difference between 2 *CO and $*C_2O_2$, implying a late transition state. The specific values are provided in the inset of Figure 13. Kinetic barriers at 0 V vs RHE of 1.52 for Cu(111) and 1.22 eV for 4AD@Cu(111), indicate that C-C coupling is not favored on hexagonal-symmetry surfaces. Lower values of 0.81 and 0.91 eV are calculated for Cu(100) and 4AD@Cu(100) at that potential. Therefore, regarding CO-CO coupling, 4AD@Cu(100) does not show a major improvement compared to Cu(100). However, CO dimerization is clearly favored at square-symmetry sites with respect to hexagonal sites.

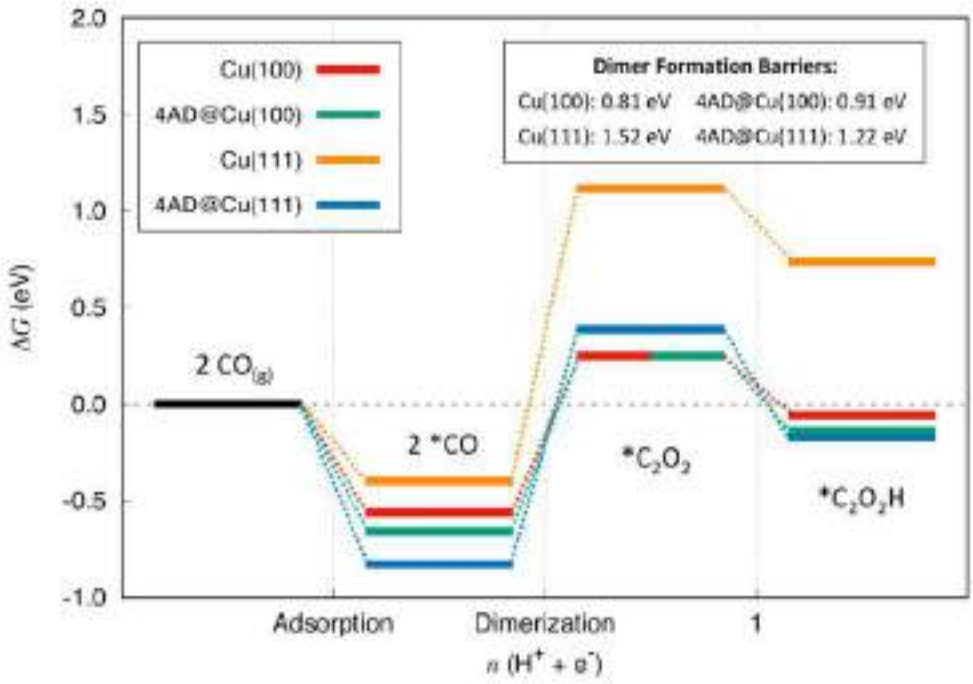

Figure 13. Free-energy diagram at 0 V vs RHE for CO dimerization at the four types of active sites under study. Color code as in Figure 11, see top left corner. Inset: *CO dimerization barriers at 0 V vs RHE for each active site. Note that the formation of $*C_2O_2$ takes place through a decoupled electron-then-proton transfer. This figure corresponds to Figure 3 in reference 103 and is included here to facilitate the reading of this thesis.

While CO dimerization energetics determines the C_1 vs. C_2 selectivity, it does not influence the selectivity among C_2 products, which is determined later in the reaction by the energetics of the concomitant intermediates. The sixth proton-electron transfer is key in this context, as it is the step where the ethylene and ethanol pathways bifurcate. Looking at Figure 12, we see than both hexagonal surfaces, Cu(111) and 4AD@Cu(111), have a clear preference for ethanol evolution, since after the sixth proton-electron transfer acetaldehyde is the most stable intermediate. However, unfavorable CO dimerization prevents these surfaces from producing multi-carbon products. Conversely, Cu(100) shows favorable C-C coupling energetics and is inclined toward ethylene formation. This leaves 4AD@Cu(100) as the only active site with preferential ethanol evolution that is able to couple two *CO at reasonably negative potentials.

A more detailed analysis shows that the ethylene vs ethanol selectivity is essentially modulated by the interplay of three different factors: the adsorption energy of acetaldehyde, the stability of acetaldehyde in solution, and the adsorption energy of an oxygen atom. In Figure 14, we show the dependence of these three factors with the

surface coordination number. We added the step edge of Cu(211), with a coordination number of 7, for completeness. Adsorbed acetaldehyde data are shown in green, and *O + $C_2H_{4(g)}$ values in blue. The stability of liquid acetaldehyde is independent of the surface model and is shown as a dotted black line at a free energy of zero, since all the data in the figure is referenced to it.

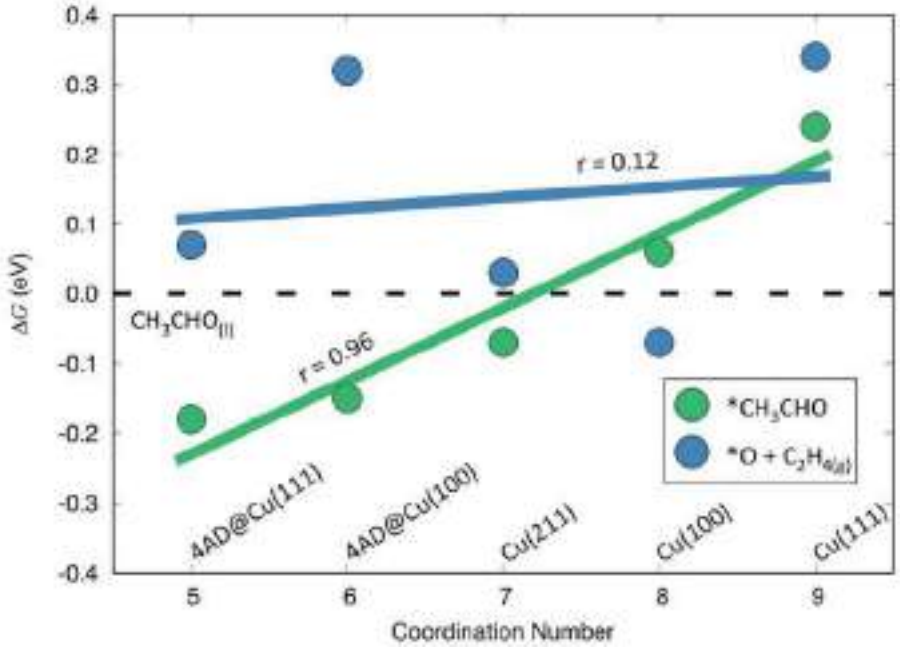

Figure 14. Free energies of adsorption of CH_3CHO (green) and *O + $C_2H_{4(g)}$ (blue) versus the coordination number (*cn*) of the active sites at different surface models. The linear regression for each set of values is provided together with the corresponding Pearson regression coefficient (r). The linear equations are $\Delta G = -0.76 + 0.11cn$ and $\Delta G = 0.03 + 0.02cn$ for the green and blue lines, respectively. All energies are referenced to liquid acetaldehyde (black dashed line). This figure corresponds to Figure 4 in reference 103 and is included here to facilitate the reading of this thesis.

Ethanol evolution is thermodynamically preferred when either adsorbed or liquid acetaldehyde is more stable than *O + $C_2H_{4(g)}$, otherwise, ethylene formation would be preferred. Active sites that bind acetaldehyde strongly, namely those with a coordination number of 7 or lower, are promising candidates for enhancing ethanol selectivity. Moreover, sites that bind *O weakly will also favor ethanol evolution. Usually, less coordinated metal sites bind adsorbates stronger than the more coordinated ones, however, this is not the case for all adsorbates. As seen in Figure 14, there is no clear correlation between the adsorption energy of *O and the coordination number of different

Cu sites. Hence, while we conclude that weak *O binding leads to favored ethanol production, we observe that it is difficult to predict the atomic structure needed to fulfill this requisite.

After finalizing the exposed analysis, another study in collaboration with our experimental colleagues from the Helmholtz Institute in Germany started. We compared our computationally obtained onset potentials for C_2 products, with those experimentally determined by them. To do that, we used our calculated data from the first study, but this time adding new calculations, since the mechanism is now starting from CO_2, which reduces to *CO via a *COOH intermediate. Concretely, they obtained the onset potentials for seven different products from CO_2RR on polycrystalline Cu (Cu-poly) and OD-Cu electrodes: methane, ethylene, ethanol, acetaldehyde, 1-propanol, propionaldehyde, and allyl alcohol. Particularly, they made use of a recently developed experimental technique called electrochemical real-time mass spectrometry (EC-RTMS). This novel technique allows for accurate and *in operando* detection of reaction products and displays better sensitivity than chromatography techniques or nuclear magnetic resonance.[110,111] Moreover, the low limits of detection of this technique allow for a more accurate determination of the onset potentials, since it can detect products at low formation rates during potential sweep experiments. This is especially useful for CO_2RR, where different compounds are produced as a function of the applied potential, and some of them appear at similar potentials.

The results from the EC-RTMS experiments show that, on Cu-poly, methane is the product with the most negative onset potential (-0.88 ± 0.02 V_{RHE}). Products with 2 or 3 carbon atoms show similar negative onset potentials, ranging from -0.70 to -0.86 V_{RHE}, suggesting that their onset potential is determined by a common potential-limiting step (PLS) early in the reaction pathway. Acetaldehyde electroreduction (ARR), performed as a side experiment, showed that ethanol is produced from ARR at a clearly less negative onset potential than from CO_2, -0.51 ± 0.03 V_{RHE} versus -0.82 ± 0.03 V_{RHE}. This result further supports that the onset potential for ethanol evolution from CO_2RR through acetaldehyde[101,111] is determined by another step earlier in the reaction sequence, as shown previously in the previous analysis and in other DFT-based models.[51,100,112]

On OD-Cu, methane is not detected, but all the other products see their onset potential shifted to more positive values, spanning now from -0.49 ± 0.01 V_{RHE} for ethanol to -0.59 ± 0.02 V_{RHE} for allyl alcohol. Since the onset potentials are similar among

all C_{2+} products, we conclude that on OD-Cu they also share an early common PLS as observed in Cu-poly. In view of the more positive onset potential values on OD-Cu, we deduce that this common early PLS is more favorable on OD-Cu than on Cu-poly. The onset potential for ethanol from ARR shifts accordingly to more positive values, -0.27 ± 0.04 V_{RHE}, on OD-Cu, again more positive than from CO_2RR on the same electrode, in line with the finding on Cu-poly.

The calculated onset potentials for CO_2RR to both ethanol and ethylene are -0.50, -0.52, -1.14, and -0.66 V_{RHE} for Cu(100), 4AD@Cu(100), Cu(111), and 4AD@Cu(111), respectively. DFT calculations show that the PLS of the reaction for ethylene and ethanol production is the hydrogenation of adsorbed CO molecules ($2*CO + H^+ + e^- \rightarrow C_2O_2H$). A depiction of the catalytic pathways can be seen in Figure 15. Among the 4 different models studied only Cu(100) and 4AD@Cu(100) are able to perform C-C coupling favorably, such that free-energy diagrams featuring results only from the latter two surfaces are shown in Figure 16. The fact that C-C coupling is involved in the PLS for C_2 products is also in agreement with the similar onset potentials determined experimentally with EC-RTMS for C_2 and C_3 products, bearing in mind that C_3 products are formed via a chemical reaction between C_1 and C_2 species.[95,113,114] We also note here that *CO hydrogenation to either *CHO or *COH is also the PLS for CO_2RR to methane.[84,115-118] Finally, we note that (a) the calculated onset potentials for Cu(100) and 4AD@Cu(100) are in agreement with those determined experimentally with EC-RTMS for ethylene and ethanol on OD-Cu, and (b) Cu(100) is selective to ethylene and 4AD@Cu(100) is selective to ethanol. Thus, we reaffirm our previous conclusions, with more solid indications that the active sites present at OD-Cu responsible for ethylene and ethanol formation resemble Cu(100) terraces and 4AD@Cu(100) islands, respectively.

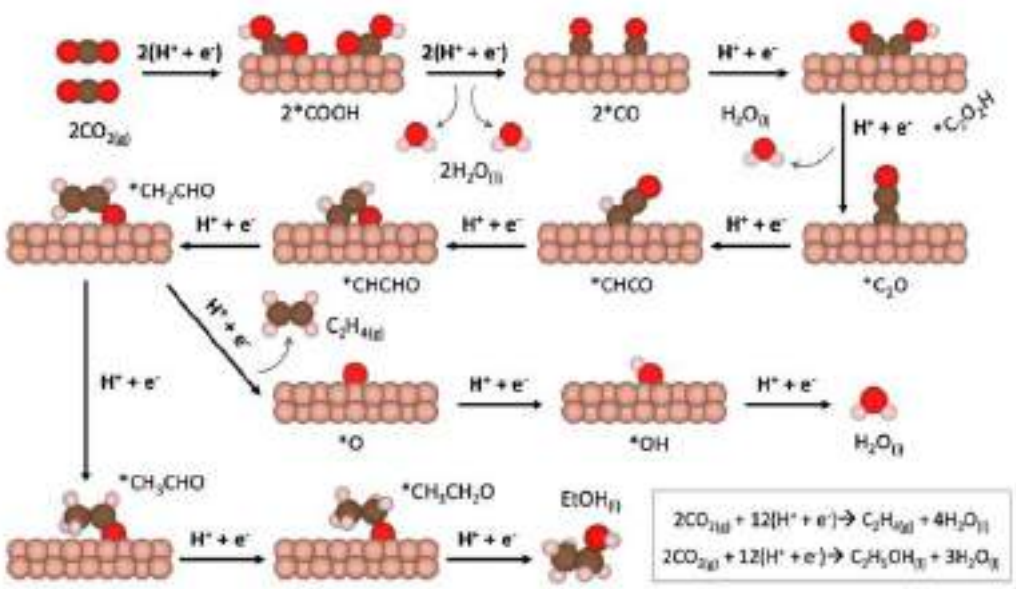

Figure 15. Schematic representation of the reaction pathways for CO_2RR to C_2 species. Cu, C, O, and H atoms are depicted in grey, brown, red, and pink. EtOH: ethanol. This figure corresponds to Figure 3 in reference 104 and is included here to facilitate the reading of this thesis.

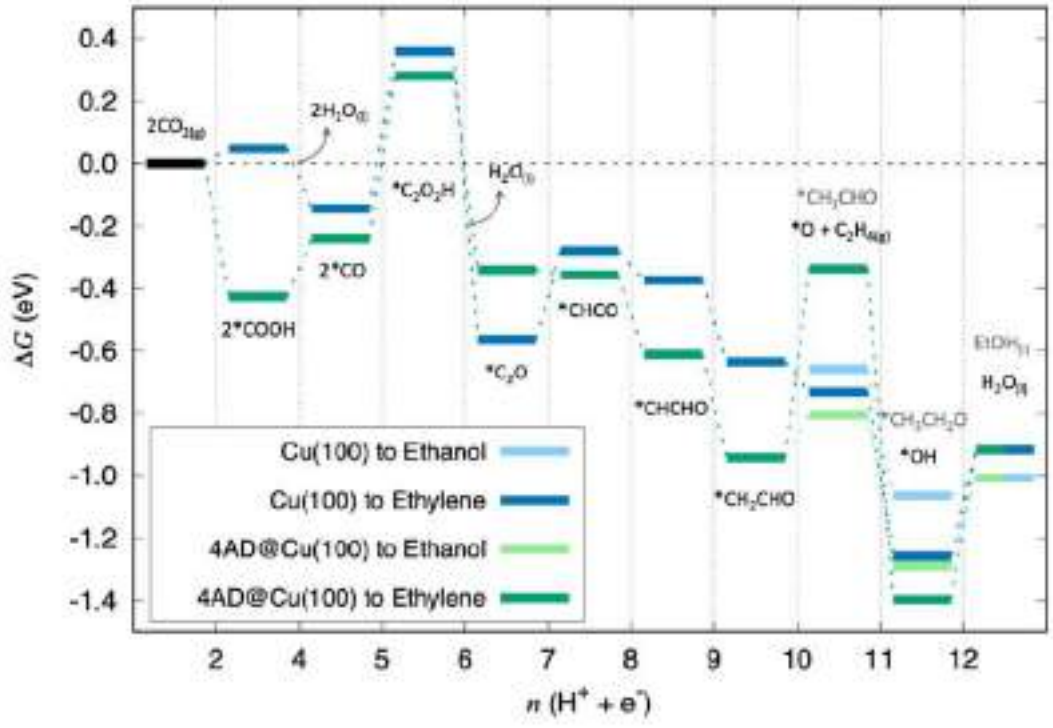

Figure 16. Free-energy diagrams including solvent and cation effects for all intermediates of the CO_2RR to C_2 species on Cu(100) (blue) and 4AD@Cu(100) (green) at 0 V_{RHE}. The same colors in a lighter tone are used to represent the ethanol pathway, which drifts away from that of ethylene upon the tenth proton-electron transfer. The corresponding intermediates toward ethylene are noted for each proton-electron transfer in black (grey for the ethanol pathway). EtOH: Ethanol. This figure corresponds to Figure 4 in reference 104 and is included here to facilitate the reading of this thesis.

Conclusions These results, together with additional data and analyses shown in the research articles below, lead to the following conclusions:

- Square four-atom islands on top of Cu(100) facets are identified as the active sites responsible for ethanol evolution on OD-Cu.
- These sites enhance *CO dimerization due to their square shape and are selective to ethanol owing to their undercoordination.
- Hexagonal-symmetry sites are probably not the active sites responsible for ethanol production, regardless of their coordination number.
- The relative thermodynamic stability of adsorbed or liquid acetaldehyde versus adsorbed oxygen may determine the selectivity of the active sites towards ethylene or ethanol in CORR.
- While acetaldehyde adsorption energy does correlate with the coordination number of the active sites, that of oxygen does not. Thus, other structural descriptors must be considered when aiming at engineering ethanol-selective active sites.
- The hydrogenation of *CO is the potential-limiting step of CO_2 electroreduction to produce both C_1 and C_2 molecules. Given that more negative onset potentials are required to produce C_1 molecules compared to those required for C_2 molecules, we conclude that the hydrogenation of a *CO dimer is easier than that of a *CO monomer.
- These two previous observations are the reason why the onset potentials for C_{2+} CO_2RR products are similar to each other and are produced at more positive potentials than C_1 molecules.
- The differences observed between experimentally determined onset potentials on Cu-poly and OD-Cu indicate that the latter has a unique set of active sites that enhance the production of C_2 molecules.

ACS Catalysis

pubs.acs.org/acscatalysis

Research Article

Elucidating the Structure of Ethanol-Producing Active Sites at Oxide-Derived Cu Electrocatalysts

Oriol Piqué, Francesc Viñes, Francesc Illas, and Federico Calle-Vallejo*

Cite This: ACS Catal. 2020, 10, 10488−10494

Read Online

ACCESS | Metrics & More | Article Recommendations | Supporting Information

ABSTRACT: The discovery of oxide-derived copper (OD-Cu) catalysts for CO_2 electroreduction is a remarkable advancement in the field of electrocatalysis. Their low overpotentials and improved selectivity toward C_2 products make them unique. However, the structure of the active sites responsible for these improvements remains unclear. Herein, by means of a computational model including thermodynamic, kinetic, solvent, and cation effects, we outline the atomic structure of the active sites responsible for ethanol evolution in OD-Cu catalysts. We also point out the specific features that determine selectivity and pinpoint the design criteria that should be fulfilled to enhance the selectivity of the catalysts toward ethanol. Specifically, we propose that square, four-atom Cu islands are the active sites of OD-Cu for CO electroreduction to ethanol as they display favorable *CO dimerization energetics and ethanol selectivity by virtue of their square, undercoordinated structure.

KEYWORDS: *CO and CO_2 electroreduction, ethanol production, oxide-derived Cu, electrocatalysis, selectivity*

INTRODUCTION

In recent years, the electroreduction of CO_2 (CO_2RR) to high-value fuels for energy storage and environmental mitigation has received great attention and experienced pronounced advances.[1−4] Although numerous electrocatalysts are able to reduce CO_2 to CO, further reduction of CO (CORR) is needed to produce "electrofuels". Pioneering studies by Hori and co-workers showed that Cu is the most active metal toward CO_2RR and CORR to valuable commodities and fuels such as methane, ethylene, acetaldehyde, ethanol, and other minor products.[1−7] In spite of the great insight and important advances, some issues still hinder a large-scale implementation of CO_2 electrolyzers, namely, large overpotentials and copper's low selectivity and faradaic efficiency.

Among the strategies devised to address these challenges, we highlight the redox treatment of metal electrodes.[7,8,9] In particular, oxide-derived copper (OD-Cu) catalysts display relatively low overpotentials (<0.4 V) and enhanced selectivity toward C_2 products, with ethanol appearing in substantial quantities,[10,11] compared to regular Cu catalysts. In spite of the significant enhancement and clear synthesis routes, the structure of the active sites at OD-Cu remains elusive. Some authors have proposed that such sites are located at grain boundaries.[11,12] According to them, engineering the grain boundaries by altering the oxide reduction method or modifying the synthesis procedure could yield catalysts with higher selectivity and activity toward multi-carbon products. Moreover, by using different kinds of OD-Cu catalysts, they show that high CORR activity on OD-Cu is concomitant to surface sites that bind CO more strongly than low-index and stepped Cu facets.[12]

Other authors have proposed that the presence of subsurface oxygen (O_{sb}) is the reason behind the noteworthy catalytic properties of OD-Cu.[13−15] Their works suggest that O_{sb} increases the CO binding energy to Cu surfaces. They argue that larger CO surface coverage results in more frequent C−C coupling, hence promoting the formation of C_2 products. However, recent computational and experimental works on the matter concluded that the stability of O_{sb} in OD-Cu catalysts is insufficient for it to stay at the subsurface under reaction conditions. It was also claimed that if O_{sb} were indeed present, it would have a negligible effect on CORR.[16−18] Instead, the results support the idea that the activity and selectivity improvements of OD-Cu versus metallic Cu are due to undercoordinated sites at rough surfaces, that is, grain boundaries.

Received: April 27, 2020
Revised: August 13, 2020
Published: August 21, 2020

https://dx.doi.org/10.1021/acscatal.0c01880
ACS Catal. 2020, 10, 10488−10494

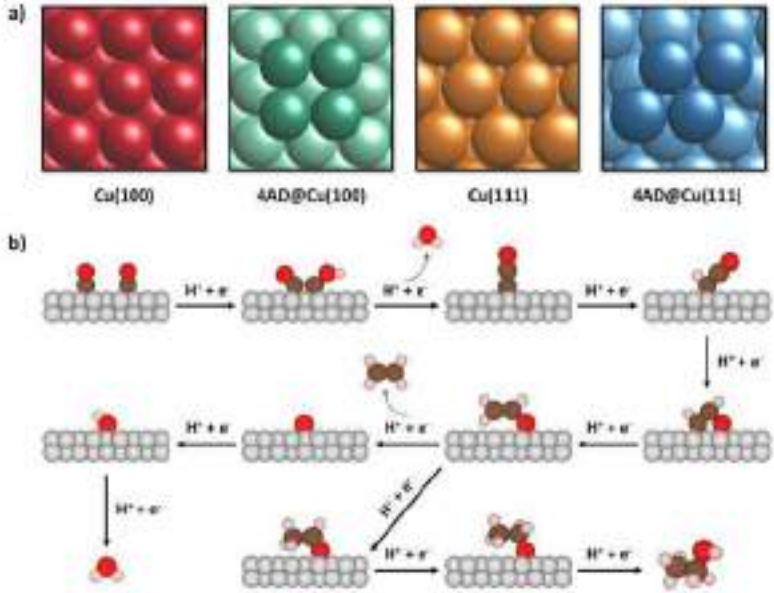

Figure 1. (a) Schematics of the four different surface models used in this work. The Cu(100), 4AD@Cu(100), Cu(111), and 4AD@Cu(111) surfaces are provided in red, green, orange, and blue, respectively. Island atoms are shown in darker colors. (b) Reaction pathway for CORR to C_2 species. We depicted Cu, C, O, and H atoms as gray, brown, red, and pink spheres, respectively. Figures S1−S4 show the optimized, minimum-energy geometries for each intermediate on each active site.

Because an atomic-scale understanding of OD-Cu catalysts remains elusive, we aim in this work at providing insights into the structure of their ethanol-producing sites. Specifically, we propose that the active sites are square-symmetry four-atom islands sitting on neighboring fourfold hollow sites of Cu(100) facets (hereon denoted as 4AD@Cu(100), where AD stands for Cu adatoms). This is justified by the following observations: (I) It has been shown experimentally and computationally that square sites promote C−C coupling;[19,20] (II) Cu(100) features square sites and is selective to ethylene,[20,21] whereas OD-Cu catalysts have enhanced ethanol selectivity;[13] (III) the active sites on OD-Cu bind CO more strongly than terraces and typical step-edge sites, and their number grows alongside the amount of grain boundaries;[12] (IV) acetaldehyde reduction to ethanol is enhanced at undercoordinated sites,[22] and acetaldehyde is an intermediate of CO reduction to ethanol on Cu catalysts;[21,23] and (V) experiments suggest that ethanol and ethylene are produced on different active sites on OD-Cu.[24]

For completeness, we supplemented the study with a nonsquare island [4AD@Cu(111)] and two common flat terraces [Cu(111) and Cu(100)]. Our calculations indicate that 4AD@Cu(100) fulfills all the requirements set in I−V, as apart from being square and undercoordinated, it binds CO more strongly than terraces and step-edge sites and, more importantly, is selective to ethanol.

■ COMPUTATIONAL DETAILS

The density functional theory (DFT) calculations were performed using the Vienna ab initio simulation package (VASP)[25] with the Perdew−Burke−Ernzerhof (PBE) exchange−correlation functional,[26] which is known to be among the best functionals for the description of transition-metal systems.[27] In addition, we used the projector augmented-wave method[28] to describe the effect of the inner cores on the valence electron density. The Cu(100) surfaces and the 4AD@Cu(100) model site were represented by a $(4\sqrt{2} \times 4\sqrt{2})R45°$ supercell slab including 32 atoms per layer, while for Cu(111) and 4AD@Cu(111) [a four-atom island sitting on four neighboring face-centered cubic sites on Cu(111)], a $p(4 \times 4)$ supercell including 16 atoms per layer was used. Cu(211) was modeled as a 3×1 supercell. These large supercells avoid lateral interactions between atom islands, adsorbates, and cations. All slab models were composed of four metal layers and modeled with the converged PBE lattice constant of Cu, namely, 3.64 Å. The topmost two layers, the Cu islands, and the adsorbates were relaxed in all directions, while the bottom-most two layers were fixed at the bulk equilibrium distances to provide an adequate bulk environment to the surface region. On average, around 10 different initial geometries for each adsorbate on each active site were optimized, including monodentate, bidentate, and tridentate structures, when possible. A plane-wave cutoff of 450 eV was used, and the Fermi level was smeared following the Methfessel−Paxton approach[29] with k_BT = 0.2 eV to facilitate convergence, always extrapolating the total energies to 0 K. The conjugate-gradient optimization scheme was used to search for the minimum-energy structures with iterations carried out until the maximal force on any atom was below 0.05 eV·Å^{-1}. Monkhorst−Pack meshes of $2 \times 2 \times 1$ for Cu(100) and 4AD@Cu(100) were used to carry out the numerical integration in the reciprocal space, while for Cu(111) and 4AD@Cu(111), we used $3 \times 3 \times 1$ meshes, which ensured convergence of adsorption energies within 0.05 eV. For Cu(211), a $4 \times 5 \times 1$ mesh was used. The distance between repeated images in the vertical direction was larger than 13 Å, and dipole corrections were applied. Isolated molecules were calculated in boxes of 9 Å × 10 Å × 11 Å using Gaussian smearing with k_BT = 0.001 eV, with further extrapolation to 0 K and considering the Γ point only. Transition-state geometries were located using the climbing-image nudged elastic band method,[30] ensuring that only one

https://dx.doi.org/10.1021/acscatal.0c01888
ACS Catal. 2020, 10, 10488−10494

imaginary frequency along the reaction coordinate was obtained at the saddle point. The potential-dependent barriers were approximated as described in Section S8.

The reaction free energies were approximated as $\Delta G \approx \Delta E_{DFT} + \Delta ZPE - T\Delta S + \Delta E_{solvation}$, where ΔE_{DFT} is the DFT-calculated reaction energy, ΔZPE is the zero-point energy change between reactants and products, $T\Delta S$ is the corresponding entropy change at 298.15 K, and $\Delta E_{solvation}$ is a solvation correction to the free energy. The ZPE and TS_{vib} values were obtained from vibrational frequency calculations within the harmonic approximation. ΔS includes only the vibrational entropy for adsorbates and all contributions for free molecules. The TS values of the free molecules were extracted from thermodynamic tables.[31] Solvation contributions to the free energies ($\Delta E_{solvation}$) were modeled as an external correction depending on the chemical nature of the adsorbates. Specific values calculated in previous works are given in Table S2 in the Supporting Information.[21,32] For a brief summary on the assessment and use of such ad hoc solvation corrections, we refer the reader to ref 33.

Considering previous reports on OD-Cu,[13−15] we performed a number of calculations including subsurface oxygen on 4AD@Cu(100) and 4AD@Cu(111). Most optimizations resulted in distorted slabs and/or the oxygen atom at the surface.

The computational hydrogen electrode was used to model proton−electron pairs.[24] Cation effects were modeled by explicit inclusion of a K atom on top of the slabs. Its most stable position was found by evaluating different possible sites around the adsorbate, as seen in Section S6. Although we calculated CO coupling barriers, we did not compute proton−electron transfer barriers because as noted recently by Rossmeisl et al.,[35] there is "not (yet) a method to obtain electrochemical barriers between realistic states at constant electrochemical conditions". Furthermore, we stress that Bronsted−Evans−Polanyi relations exist for reactions where C-, H-, and O-containing species are involved.[36,37] Thus, we assume that the kinetics and thermodynamics are well correlated for the reaction steps considered in this work.

Further computational details appear in the Supporting Information (Sections S1−S3), and all the adsorption energies and corrections are reported in Section S4. Electrochemical stability considerations for 4AD@Cu(111) and 4AD@Cu(100) are provided in Section S5. The coordinates of all the optimized systems appear in Section S9, and the corresponding images appear in Figures S1−S4.

RESULTS AND DISCUSSION

We computed the thermodynamics of each proton−electron transfer of the CORR to C_2 products (see Figure 1b) for the four different slab models described in the Computational Details section and shown in Figure 1a. Cu(100) was selected in view of the known ability of its square sites to catalyze C−C coupling.[3,19,21,38−41] 4AD@Cu(100) features favorable C−C coupling energetics in view of its square symmetry and presumably enhanced ethanol selectivity by virtue of its undercoordination.[20,22] Thermodynamically, Cu(111) is the most stable facet of Cu and is probably abundant in polycrystalline Cu and OD-Cu. We note, however, that Cu(111) is not ostensibly active for the production of C_2 species,[3,28,38] and its selectivity is inclined toward methane. 4AD@Cu(111) is included to show that hexagonal-symmetry defects increase the activity of Cu(111) for C_2 production but are less active for C−C coupling than square facets. The analysis in Section S5 suggests that 4AD@Cu(100) and 4AD@Cu(111) are stable under CORR conditions. We modeled the reaction pathway in Figure 1b,[21,39] which is known to comply with several key experimental observations.[3,40] However, we note that some other pathways have been proposed in the literature,[42−45] and we analyze some of them in Section S7. We conclude that within our computational approach, the pathway in Figure 1b is thermodynamically more favorable.

Previous studies have shown that alkaline cations affect the product selectivity of the CORR.[40,46,47] Thus, we included solvent and cation effects in our calculations to obtain a more realistic picture of the active sites. In the following, only the most stable situation for each adsorbate is considered, either solvated, with cations, or both in some specific cases (see Table S3 and Section S4).

Figure 2 shows the results in two separate free-energy diagrams: (a) shows the data for Cu(100) and 4AD@Cu(100), and (b) shows the data for Cu(111) and 4AD@Cu(111). In these diagrams, the advancement of the reaction can be followed for each of the four surface models, and each one is depicted with a specific color. As also seen in Figure 1b, the reaction pathway bifurcates at the sixth proton−electron transfer, where one path leads to ethylene and the other to

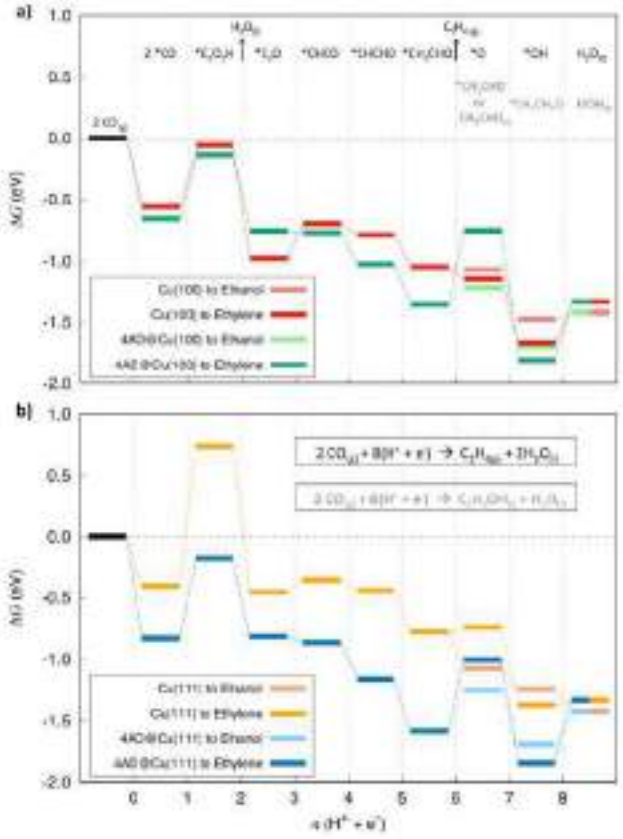

Figure 2. Free-energy diagrams including solvent and cation effects for all intermediates of CORR to C_2 species on all four surfaces studied at 0 V vs RHE. (a) Cu(100) (red) and 4AD@Cu(100) (green). (b) Cu(111) (orange) and 4AD@Cu(111) (blue). The same colors in a lighter tone are used to represent the ethanol pathway, which drifts from that of ethylene upon the sixth proton−electron transfer. EtOH: ethanol.

https://dx.doi.org/10.1021/acscatal.0c01888
ACS Catal. 2020, 10, 10488−10494

ethanol. This branching is represented in the diagrams by introducing a lighter version of each color that indicates the respective ethanol pathway. Similarly, the formula of each intermediate is depicted on the upper part of Figure 2, where black corresponds to ethylene-pathway intermediates and gray to ethanol-pathway intermediates.

Within the thermodynamic approach used here, the potential-limiting step (PLS) is the step with the largest positive free energy. In all four model active sites, the PLS is the first proton−electron transfer. Indeed, this C−C coupling step is experimentally known to be critical in the C_2 pathway.[41,48] Concretely, 0.50, 0.52, 1.14, and 0.66 eV are the free energies of the PLS for the Cu(100), 4AD@Cu(100), Cu(111), and 4AD@Cu(111) surface models, respectively. The considerably larger value for Cu(111) is consistent with previous experiments and calculations, which showed that this facet is probably one of Cu's least active facets toward C_2 products, and usually favors CH_4 evolution.[19,20,49] Comparing the 4AD@Cu(111) model with Cu(111), we observe that undercoordination helps in lowering the free energy of the PLS by appreciably stabilizing $*C_2O_2H$, that is, the hydrogenated *CO dimer. However, the least endothermic energies correspond to the square-symmetry slabs Cu(100) and 4AD@Cu(100), which display similar values, indicating that the presence of square sites is a more important factor for *CO dimerization than surface coordination.

Figure 3 shows the energetics of the first electrochemical step in Figure 2 ($2CO_{(g)} + * + H^+ + e^- \rightarrow *C_2O_2H$), including

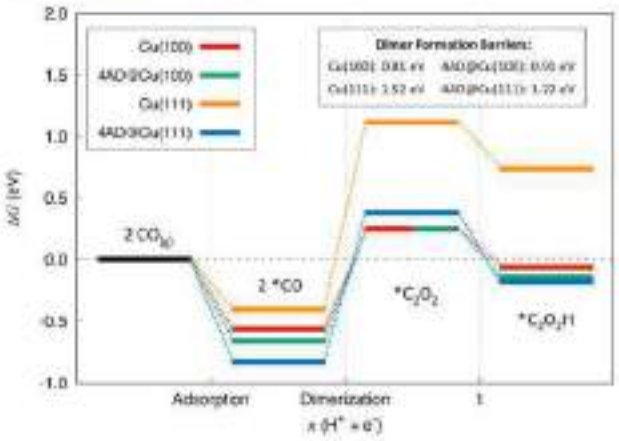

Figure 3. Free-energy diagram at 0 V vs RHE for CO dimerization at the four types of active sites under study. Color code is as in Figure 1; see top left corner. Inset: *CO dimerization barriers at 0 V vs RHE for each active site. Note that the formation of $*C_2O_2$ takes place through a decoupled electron-then-proton transfer.

a *CO dimer configuration proposed previously.[50] The kinetic barriers for the formation of the dimer ($*C_2O_2$) were calculated and found to be essentially equal to the thermodynamic energy difference between 2*CO and $*C_2O_2$, implying a late transition state. These values are provided in the inset of Figure 3. Kinetic barriers at 0 V versus reversible hydrogen electrode (RHE) of 1.52 and 1.22 eV for Cu(111) and 4AD@Cu(111), respectively, confirm that C−C coupling is not favored on hexagonal-symmetry surfaces. Lower values of 0.81 and 0.91 eV are calculated for Cu(100) and 4AD@Cu(100), respectively, at this potential. Note in passing that in the formation of $*C_2O_2H$, the proton−electron transfer is known to be decoupled[7,21,38,41] such that the electron is transferred first, and the proton transfer follows. This explains an important experimental observation of CO reduction: on Cu(100), CH_4 formation depends on the pH in the standard hydrogen electrode (SHE) scale, while C_2H_4 formation does not.[7,21,51]

Moreover, this decoupled transfer implies that the activation barrier for *CO dimerization is potential-dependent and pH-independent in the SHE scale.[21] Through Bader analysis,[52] we determined that at the transition state, ~0.9 e^- have been transferred to the activated complex. Following the method described in Section S8, at a potential of −0.4 V versus RHE, where C_2 species are typically reported to start evolving from Cu electrodes,[3,41,53] the dimer formation barriers are 0.45 and 0.55 eV for Cu(100) and 4AD@Cu(100), respectively. At such a potential, the barriers for Cu(111) and 4AD@Cu(111) are 1.16 and 0.86 eV, respectively. Typically, surmountable barriers at room temperature are below 0.75 eV.[53] All this information suggests that regarding CO−CO coupling, 4AD@Cu(100) does not feature an improvement with respect to Cu(100). However, CO dimerization is favored at square-symmetry sites [Cu(100) and 4AD@Cu(100)] with respect to hexagonal sites [Cu(111) and 4AD@Cu(111)], and the barriers are surmountable under experimental conditions.

Although CO dimerization energetics is paramount for C_1 versus C_2 selectivity, it does not influence the selectivity among C_2 products. The sixth proton−electron transfer is key in this context as it is the step where the ethanol and ethylene pathways bifurcate. As shown in Figure 2, both hexagonal surfaces [Cu(111) and 4AD@Cu(111)] have a clear preference for ethanol formation because after the sixth proton−electron transfer, acetaldehyde is the thermodynamically more stable intermediate. However, as mentioned before, unfavorable CO dimerization prevents these surfaces from producing significant amounts of multi-carbon products, which can be mitigated by opening alternative pathways upon processes such as alloying Cu with Ag.[54,55] Conversely, Cu(100) features favorable energetics for C−C coupling and is inclined toward ethylene formation. This leaves 4AD@Cu(100) as the only model active site able to couple two *CO at reasonably negative potentials and exhibiting a clear preference for ethanol evolution.

A closer look at the free-energy diagram of 4AD@Cu(100) in Figure 2a reveals that the ethylene pathway requires an energy input of 0.61 eV at the sixth proton−electron transfer. This value is slightly larger than the energy needed for producing $*C_2O_2H$ from 2*CO, indicating that for these specific sites, the ethylene and ethanol pathways have different PLSs and ethylene formation likely requires a more negative onset potential than ethanol evolution. This is yet another reason to postulate this atomic configuration as a plausible atomic configuration for the ethanol-producing active sites at OD-Cu catalysts, although the main reason is explained in detail below.

Analyzing the energetics of the sixth proton−electron transfer, we observed that the ethanol versus ethylene selectivity is essentially modulated by the interplay of three factors: the adsorption energy of acetaldehyde, the stability of acetaldehyde in solution, and the *O adsorption energy. Note in passing that the adsorption energy of $*CH_2CHO$ is not a determining factor because it is the reference for the formation of both $*O + C_2H_{4(g)}$ and CH_3CHO. In Figure 4, a closer look at the dependence of the aforementioned three factors with the

https://dx.doi.org/10.1021/acscatal.0c01888
ACS Catal. 2020, 10, 10488−10494

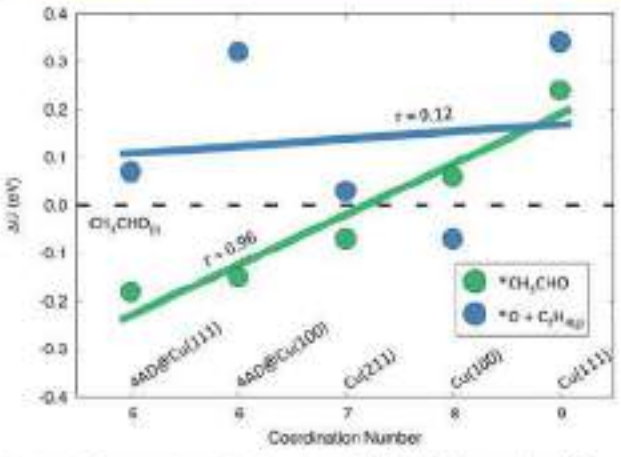

Figure 4. Free energies of adsorption of CH_3CHO (green) and $*O + C_2H_{4(g)}$ (blue) vs the coordination number of the active sites at different surface models. The linear regression for each set of values is provided together with the corresponding Pearson regression coefficient (r). The linear equations are $y = -0.76 + 0.11x$ and $y = 0.03 + 0.02x$ for the green and blue lines, respectively. All energies are referenced to liquid acetaldehyde (black dashed line).

surface coordination number is displayed. The step edge of Cu(211) slabs, with a coordination number of 7, is also featured in the plot for completeness, and we emphasize that essentially any site with such a coordination number might have been added. Adsorbed acetaldehyde values are shown in green, and $*O + C_2H_{4(g)}$ data are shown in blue. The stability of liquid acetaldehyde is independent of the surface structure and is shown as a dotted black line at a free energy of 0 since all the data in the figure are referenced to it.

If adsorbed or liquid acetaldehyde is more stable than $*O + C_2H_{4(g)}$, the ethanol pathway is thermodynamically preferred; otherwise, ethylene evolution would be preferred. Liquid acetaldehyde is usually more stable than its adsorbed counterpart at high-coordination sites, as is the case of Cu(100) and Cu(111) surfaces, with coordination numbers 8 and 9, respectively. However, undercoordinated sites bind acetaldehyde strong enough to prevent its desorption once formed, inclining the selectivity toward ethanol production. Hence, active sites that tend to bind acetaldehyde strongly, that is, sites with coordination number 7 or lower, are good candidates for enhancing ethanol selectivity.

Furthermore, ethanol evolution will be favored when the active sites bind *O weakly. It is known that less coordinated sites at metals generally bind adsorbates more strongly than the more coordinated ones (e.g., Figure S5 for 2*CO),[58−59] but this is not forcedly the case for all metals and adsorbates. In the case of *O at Cu, as seen in Figure 4, there is no clear correlation between adsorption energies and coordination numbers. Conversely, the correlation is evident for acetaldehyde, which exhibits a good correlation coefficient. Thus, we conclude that weak *O adsorption enhances ethanol evolution, but it is difficult to predict what atomic structure is needed to fulfill this requisite. According to Figure 4, 4AD@Cu(100) sites bind *O more weakly than Cu(100), indicating that the square, four-atom islands incline the selectivity toward ethanol. In fact, $*CH_3CHO$ is more stable than $*O + C_2H_4$ by 0.46 eV at 4AD@Cu(100) (see Table S3). Note in passing that this type of comparison (i.e., ΔG_2 vs ΔG_1) is habitually used in computational electrocatalysis to predict/rationalize the selectivity of reactions.[40,41] Moreover, in line with Lum and Ager conclusions,[24] Figure 4 suggests that in OD-Cu catalysts in which a multiplicity of sites coexists, 4AD@Cu(100) is primarily responsible for producing ethanol, whereas other sites such as (100) terraces mainly produce ethylene.

CONCLUSIONS

Oxide-derived copper (OD-Cu) catalysts are remarkably active for CO electroreduction (CORR) to C_2 species. In spite of the extensive research devoted to exploit and enhance their electrocatalytic activity and selectivity, the atomic-scale nature of their active sites has not been fully identified yet. On the basis of a computational model including thermodynamic and kinetic data and solvent and cation effects, we proposed square, four-atom islands [4AD@Cu(100)] as the active sites of OD-Cu for CORR to ethanol. These sites feature favorable *CO dimerization energetics by virtue of their square shape, and ethanol selectivity granted by their undercoordination. We ruled out active sites with hexagonal symmetry, with either high or low surface coordination numbers.

Finally, we pointed out that the relative thermodynamic stability of adsorbed and liquid acetaldehyde with respect to *O may determine the CORR selectivity of the active sites toward ethylene or ethanol. Because we found no apparent correlation between *O adsorption and coordination numbers on Cu sites with enhanced selectivity need to be engineered with great caution and using more advanced structural descriptors. We hope that this study provides insightful guidelines for the design of CO and CO_2 reduction active sites with enhanced ethanol selectivity.

ASSOCIATED CONTENT

Supporting Information

The Supporting Information is available free of charge at https://pubs.acs.org/doi/10.1021/acscatal.0c01880.

Details on gas-phase corrections, liquid-phase corrections, solvation contributions to the free energies, adsorption energy values, stability of the four-atom Cu islands, cation effects, alternative pathways, CO coupling kinetics, and coordinates of the optimized systems (PDF)

AUTHOR INFORMATION

Corresponding Author

Federico Calle-Vallejo − *Departament de Ciència de Materials i Química Física & Institut de Química Teòrica i Computacional (IQTCUB), Universitat de Barcelona, 08028 Barcelona, Spain;* orcid.org/0000-0001-5147-8635; Email: f.calle.vallejo@ub.edu

Authors

Oriol Piqué − *Departament de Ciència de Materials i Química Física & Institut de Química Teòrica i Computacional (IQTCUB), Universitat de Barcelona, 08028 Barcelona, Spain;* orcid.org/0000-0002-6995-5927

Francesc Viñes − *Departament de Ciència de Materials i Química Física & Institut de Química Teòrica i Computacional (IQTCUB), Universitat de Barcelona, 08028 Barcelona, Spain;* orcid.org/0000-0001-9987-8654

Francesc Illas − *Departament de Ciència de Materials i Química Física & Institut de Química Teòrica i*

https://dx.doi.org/10.1021/acscatal.0c01880
ACS Catal. 2020, 10, 10488−10494

Computacional (IQTCUB), Universitat de Barcelona, 08028 Barcelona, Spain; orcid.org/0000-0003-2104-6123

Complete contact information is available at: https://pubs.acs.org/10.1021/acscatal.0c01880

Notes

The authors declare no competing financial interest.

■ ACKNOWLEDGMENTS

This work has been supported by Spanish MICIUN's RTI2018-095460-B-I00 and María de Maeztu MDM-2017-0767 grants and, in part, by Generalitat de Catalunya 2017SGR13 grant and by COST Action 18234, supported by the COST (the European Cooperation in Science and Technology). F.C.-V. thanks the Spanish MICIUN for a Ramón y Cajal research contract (RYC-2015-18996), and F.I. acknowledges additional support from the 2015 ICREA Academia Award for Excellence in University Research. O.P. thanks the Spanish MICIUN for an FPI PhD grant (PRE2018-083811). F.V. thanks the Spanish MICIUN for a Ramón y Cajal research contract (RYC-2012-10129). We are thankful to Red Española de Supercomputación (RES) for supercomputing time at SCAYLE (projects QS-2019-3-0018, QS-2019-2-0023, and QCM-2019-1-0034). The use of supercomputing facilities at SURFsara was sponsored by NWO Physical Sciences. F.C.-V. thanks Dr. Ioannis Katsounaros for insightful discussions. Patricia Verdugo is gratefully acknowledged for her help with the design of the table of contents figure.

■ REFERENCES

(1) Bushuyev, O. S.; De Luna, P.; Dinh, C. T.; Tao, L.; Saur, G.; van de Lagemaat, J.; Kelley, S. O.; Sargent, E. H. What Should We Make with CO_2 and How Can We Make It? *Joule* **2018**, *2*, 825−832.

(2) Gao, D.; Arán-Ais, R. M.; Jeon, H. S.; Roldan Cuenya, B. Rational Catalyst and Electrolyte Design for CO_2 Electroreduction towards Multicarbon Products. *Nat. Catal.* **2019**, *2*, 198−210.

(3) Birdja, Y. Y.; Pérez-Gallent, E.; Figueiredo, M. C.; Göttle, A. J.; Calle-Vallejo, F.; Koper, M. T. M. Advances and Challenges in Understanding the Electrocatalytic Conversion of Carbon Dioxide to Fuels. *Nat. Energy* **2019**, *4*, 732−745.

(4) Handoko, A. D.; Wei, F.; Jenndy; Yeo, B. S.; Seh, Z. W. Understanding Heterogeneous Electrocatalytic Carbon Dioxide Reduction through Operando Techniques. *Nat. Catal.* **2018**, *1*, 922−934.

(5) Hori, Y.; Murata, A.; Takahashi, R.; Suzuki, S. Electroreduction of Carbon Monoxide to Methane and Ethylene at a Copper Electrode in Aqueous Solutions at Ambient Temperature and Pressure. *J. Am. Chem. Soc.* **1987**, *109*, 5022−5023.

(6) Hori, Y.; Murata, A.; Takahashi, R. Formation of Hydrocarbons in the Electrochemical Reduction of Carbon Dioxide at a Copper Electrode in Aqueous Solution. *J. Chem. Soc., Faraday Trans. 1* **1989**, *85*, 2309−2326.

(7) Hori, Y.; Takahashi, R.; Yoshinami, Y.; Murata, A. Electrochemical Reduction of CO at a Copper Electrode. *J. Phys. Chem. B* **1997**, *101*, 7075−7081.

(8) Chen, Y.; Li, C. W.; Kanan, M. W. Aqueous CO_2 Reduction at Very Low Overpotential on Oxide-Derived Au Nanoparticles. *J. Am. Chem. Soc.* **2012**, *134*, 19969−19972.

(9) Ma, M.; Trześniewski, B. J.; Xie, J.; Smith, W. A. Selective and Efficient Reduction of Carbon Dioxide to Carbon Monoxide on Oxide-Derived Nanostructured Silver Electrocatalysts. *Angew. Chem., Int. Ed.* **2016**, *55*, 9748−9752.

(10) Li, C. W.; Kanan, M. W. CO_2 Reduction at Low Overpotential on Cu Electrodes Resulting from the Reduction of Thick Cu_2O Films. *J. Am. Chem. Soc.* **2012**, *134*, 7231−7234.

(11) Li, C. W.; Ciston, J.; Kanan, M. W. Electroreduction of Carbon Monoxide to Liquid Fuel on Oxide-Derived Nanocrystalline Copper. *Nature* **2014**, *508*, 504−507.

(12) Verdaguer-Casadevall, A.; Li, C. W.; Johansson, T. P.; Scott, S. B.; McKeown, J. T.; Kumar, M.; Stephens, I. E. L.; Kanan, M. W.; Chorkendorff, I. Probing the Active Surface Sites for CO Reduction on Oxide-Derived Copper Electrocatalysts. *J. Am. Chem. Soc.* **2015**, *137*, 9808−9811.

(13) Eilert, A.; Cavalca, F.; Roberts, F. S.; Osterwalder, J.; Liu, C.; Favaro, M.; Crumlin, E. J.; Ogasawara, H.; Friebel, D.; Pettersson, L. G. M.; Nilsson, A. Subsurface Oxygen in Oxide-Derived Copper Electrocatalysts for Carbon Dioxide Reduction. *J. Phys. Chem. Lett.* **2017**, *8*, 285−290.

(14) Cavalca, F.; Ferragut, R.; Aghion, S.; Eilert, A.; Diaz-Morales, O.; Liu, C.; Koh, A. L.; Hansen, T. W.; Pettersson, L. G. M.; Nilsson, A. Nature and Distribution of Stable Subsurface Oxygen in Copper Electrodes during Electrochemical CO_2 Reduction. *J. Phys. Chem. C* **2017**, *121*, 25003−25009.

(15) Liu, C.; Lourenço, M. P.; Hedström, S.; Cavalca, F.; Diaz-Morales, O.; Duarte, H. A.; Nilsson, A.; Pettersson, L. G. M. Stability and Effects of Subsurface Oxygen in Oxide-derived Cu Catalyst for CO_2 Reduction. *J. Phys. Chem. C* **2017**, *121*, 25010−25017.

(16) Garza, A. J.; Bell, A. T.; Head-Gordon, M. Is Subsurface Oxygen Necessary for the Electrochemical Reduction of CO_2 on Copper? *J. Phys. Chem. Lett.* **2018**, *9*, 601−606.

(17) Fields, M.; Hong, X.; Nørskov, J. K.; Chan, K. Role of Subsurface Oxygen on Cu Surfaces for CO_2 Electrochemical Reduction. *J. Phys. Chem. C* **2018**, *122*, 16209−16215.

(18) Scott, S. B.; Hogg, T. V.; Landers, A. T.; Maagaard, T.; Bertheussen, E.; Lin, J. C.; Davis, R. C.; Beeman, J. W.; Higgins, D.; Drisdell, W. S.; Hahn, C.; Mehta, A.; Seger, B.; Jaramillo, T. F.; Chorkendorff, I. Absence of Oxidized Phases in Cu under CO Reduction Conditions. *ACS Energy Lett.* **2019**, *4*, 803−804.

(19) Li, H.; Li, Y.; Koper, M. T. M.; Calle-Vallejo, F. Bond-Making and Breaking between Carbon, Nitrogen, and Oxygen in Electrocatalysis. *J. Am. Chem. Soc.* **2014**, *136*, 15694−15701.

(20) Hori, Y.; Takahashi, I.; Koga, O.; Hoshi, N. Electrochemical Reduction of Carbon Dioxide at Various Series of Copper Single Crystal Electrodes. *J. Mol. Catal. A: Chem.* **2003**, *199*, 39−47.

(21) Calle-Vallejo, F.; Koper, M. T. M. Theoretical Considerations on the Electroreduction of CO to C_2 Species on Cu(100) Electrodes. *Angew. Chem.* **2013**, *125*, 7423−7426.

(22) Ledezma-Yanez, I.; Gallent, E. P.; Koper, M. T. M.; Calle-Vallejo, F. Structure-Sensitive Electroreduction of Acetaldehyde to Ethanol on Copper and its Mechanistic Implications for CO and CO_2 Reduction. *Catal. Today* **2016**, *262*, 90−94.

(23) Bertheussen, E.; Verdaguer-Casadevall, A.; Ravasio, D.; Montoya, J. H.; Trimarco, D. B.; Roy, C.; Meier, S.; Wendland, J.; Nørskov, J. K.; Stephens, I. E. L.; Chorkendorff, I. Acetaldehyde as an Intermediate in the Electroreduction of Carbon Monoxide to Ethanol on Oxide-Derived Copper. *Angew. Chem., Int. Ed.* **2016**, *55*, 1450−1454.

(24) Lum, Y.; Ager, J. W. Evidence for Product-Specific Active Sites on Oxide-Derived Cu Catalysts for Electrochemical CO_2 Reduction. *Nat. Catal.* **2019**, *2*, 86−93.

(25) Kresse, G.; Furthmüller, J. Efficient Iterative Schemes for *Ab Initio* Total-Energy Calculations using a Plane-Wave Basis Set. *Phys. Rev. B: Condens. Matter Mater. Phys.* **1996**, *54*, 11169−11186.

(26) Perdew, J. P.; Burke, K.; Ernzerhof, M. Generalized Gradient Approximation Made Simple. *Phys. Rev. Lett.* **1996**, *77*, 3865−3868.

(27) Vega, L.; Ruvireta, J.; Viñes, F.; Illas, F. Jacob's Ladder as Sketched by Escher: Assessing the Performance of Broadly Used Density Functionals on Transition Metal Surface Properties. *J. Chem. Theory Comput.* **2018**, *14*, 395−403.

(28) Kresse, G.; Joubert, D. From Ultrasoft Pseudopotentials to the Projector Augmented-Wave Method. *Phys. Rev. B: Condens. Matter Mater. Phys.* **1999**, *59*, 1758−1775.

(29) Methfessel, M.; Paxton, A. T. High-Precision Sampling for Brillouin-Zone Integration in Metals. *Phys. Rev. B: Condens. Matter Mater. Phys.* **1989**, *40*, 3616−3621.
(30) Henkelman, G.; Uberuaga, B. P.; Jónsson, H. A Climbing Image Nudged Elastic Band Method for Finding Saddle Points and Minimum Energy Paths. *J. Chem. Phys.* **2000**, *113*, 9901−9904.
(31) Lide, D. R. *CRC Handbook of Chemistry and Physics*, 85th ed.; CRC Press, 2005.
(32) He, Z.-D.; Hanselman, S.; Chen, Y.-X.; Koper, M. T. M.; Calle-Vallejo, F. Importance of Solvation for the Accurate Prediction of Oxygen Reduction Activities of Pt-based Electrocatalysts. *J. Phys. Chem. Lett.* **2017**, *8*, 2243−2246.
(33) Granda-Marulanda, L. P.; Builes, S.; Koper, M. T. M.; Calle-Vallejo, F. Influence of Van der Waals Interactions on the Solvation Energies of Adsorbates at Pt-based Electrocatalysts. *ChemPhysChem* **2019**, *20*, 2968−2972.
(34) Nørskov, J. K.; Rossmeisl, J.; Logadottir, A.; Lindqvist, L.; Kitchin, J. R.; Bligaard, T.; Jónsson, H. Origin of the Overpotential for Oxygen Reduction at a Fuel-Cell Cathode. *J. Phys. Chem. B* **2004**, *108*, 17886−17892.
(35) Bagger, A.; Arnarson, L.; Hansen, M. H.; Spohr, E.; Rossmeisl, J. Electrochemical CO Reduction: A Property of the Electrochemical Interface. *J. Am. Chem. Soc.* **2019**, *141*, 1506−1514.
(36) Wang, S.; Petzold, V.; Tripkovic, V.; Kleis, J.; Howalt, J. G.; Skúlason, E.; Fernández, E. M.; Hvolbæk, B.; Jones, G.; Toftelund, A.; Falsig, H.; Björketun, M.; Studt, F.; Abild-Pedersen, F.; Rossmeisl, J.; Nørskov, J. K.; Bligaard, T. Universal Transition State Scaling Relations for (De)Hydrogenation over Transition Metals. *Phys. Chem. Chem. Phys.* **2011**, *13*, 20760−20765.
(37) Wang, S.; Temel, B.; Shen, J.; Jones, G.; Grabow, L. C.; Studt, F.; Bligaard, T.; Abild-Pedersen, F.; Christensen, C. H.; Nørskov, J. K. Universal Brønsted-Evans-Polanyi Relations for C-C, C-O, C-N, N-O, N-N, and O-O Dissociation Reactions. *Catal. Lett.* **2011**, *141*, 370−373.
(38) Schouten, K. J. P.; Pérez Gallent, E.; Koper, M. T. M. Structure Sensitivity of the Electrochemical Reduction of Carbon Monoxide on Copper Single Crystals. *ACS Catal.* **2013**, *3*, 1292−1295.
(39) Hanselman, S.; Koper, M. T. M.; Calle-Vallejo, F. Computational Comparison of Late Transition Metal (100) Surfaces for the Electrocatalytic Reduction of CO to C_2 Species. *ACS Energy Lett.* **2018**, *3*, 1062−1067.
(40) Pérez-Gallent, E.; Marcandalli, G.; Figueiredo, M. C.; Calle-Vallejo, F.; Koper, M. T. M. Structure- and Potential-Dependent Cation Effects on CO Reduction at Copper Single-Crystal Electrodes. *J. Am. Chem. Soc.* **2017**, *139*, 16412−16419.
(41) Gattrell, M.; Gupta, N.; Co, A. A Review of the Aqueous Electrochemical Reduction of CO_2 to Hydrocarbons at Copper. *J. Electroanal. Chem.* **2006**, *594*, 1−19.
(42) Garza, A. J.; Bell, A. T.; Head-Gordon, M. Mechanism of CO_2 Reduction at Copper Surfaces: Pathways to C_2 Products. *ACS Catal.* **2018**, *8*, 1490−1499.
(43) Cheng, T.; Xiao, H.; Goddard, W. A., III Full Atomistic Reaction Mechanism with Kinetics for CO Reduction on Cu(100) from *Ab Initio* Molecular Dynamics Free-Energy Calculations at 298 K. *Proc. Natl. Acad. Sci. U.S.A.* **2017**, *114*, 1795−1800.
(44) Lum, Y.; Cheng, T.; Goddard, W. A.; Ager, J. W. Electrochemical CO Reduction Builds Solvent Water into Oxygenate Products. *J. Am. Chem. Soc.* **2018**, *140*, 9337−9340.
(45) Clark, E. L.; Wong, J.; Garza, A. J.; Lin, Z.; Head-Gordon, M.; Bell, A. T. Explaining the Incorporation of Oxygen Derived from Solvent Water into the Oxygenated Products of CO Reduction over Cu. *J. Am. Chem. Soc.* **2019**, *141*, 4191−4193.
(46) Murata, A.; Hori, Y. Product Selectivity Affected by Cationic Species in Electrochemical Reduction of CO_2 and CO at a Cu Electrode. *Bull. Chem. Soc. Jpn.* **1991**, *64*, 123−127.
(47) Singh, M. R.; Kwon, Y.; Lum, Y.; Ager, J. W.; Bell, A. T. Hydrolysis of Electrolyte Cations Enhances the Electrochemical Reduction of CO_2 over Ag and Cu. *J. Am. Chem. Soc.* **2016**, *138*, 13006−13012.
(48) Hori, Y.; Takahashi, R.; Yoshinami, Y.; Murata, A. Electrochemical Reduction of CO at a Copper Electrode. *J. Phys. Chem. B* **1997**, *101*, 7075−7081.
(49) Durand, W. J.; Peterson, A. A.; Studt, F.; Abild-Pedersen, F.; Nørskov, J. K. Structure Effects on the Energetics of the Electrochemical Reduction of CO_2 by Copper Surfaces. *Surf. Sci.* **2011**, *605*, 1354−1359.
(50) Montoya, J. H.; Shi, C.; Chan, K.; Nørskov, J. K. Theoretical Insights into a CO Dimerization Mechanism in CO_2 Electroreduction. *J. Phys. Chem. Lett.* **2015**, *6*, 2032−2037.
(51) Schouten, K. J. P.; Kwon, Y.; van der Ham, C. J. M.; Qin, Z.; Koper, M. T. M. A New Mechanism for the Selectivity to C_1 and C_2 Species in the Electrochemical Reduction of Carbon Dioxide on Copper Electrodes. *Chem. Sci.* **2011**, *2*, 1902−1909.
(52) Tang, W.; Sanville, E.; Henkelman, G. A Grid-Based Bader Analysis Algorithm Without Lattice Bias. *J. Phys.: Condens. Matter* **2009**, *21*, 084204.
(53) Nitopi, S.; Bertheussen, E.; Scott, S. B.; Liu, X.; Engstfeld, A. K.; Horch, S.; Seger, B.; Stephens, I. E. L.; Chan, K.; Hahn, C.; Nørskov, J. K.; Jaramillo, T. F.; Chorkendorff, I. Progress and Perspectives of Electrochemical CO_2 Reduction on Copper in Aqueous Electrolyte. *Chem. Rev.* **2019**, *119*, 7610−7672.
(54) Ting, L. R. L.; Piqué, O.; Lim, S. Y.; Tanhaei, M.; Calle-Vallejo, F.; Yeo, B. S. Enhancing CO_2 Electroreduction to Ethanol on Copper−Silver Composites by Opening an Alternative Catalytic Pathway. *ACS Catal.* **2020**, *10*, 4059−4069.
(55) Lee, S.; Park, G.; Lee, J. Importance of Ag−Cu Biphasic Boundaries for Selective Electrochemical Reduction of CO_2 to Ethanol. *ACS Catal.* **2017**, *7*, 8594−8604.
(56) Jiang, T.; Mowbray, D. J.; Dobrin, S.; Falsig, H.; Hvolbæk, B.; Bligaard, T.; Nørskov, J. K. Trends in CO Oxidation Rates for Metal Nanoparticles and Close-Packed, Stepped, and Kinked surfaces. *J. Phys. Chem. C* **2009**, *113*, 10548−10553.
(57) Calle-Vallejo, F.; Martínez, J. I.; García-Lastra, J. M.; Sautet, P.; Loffreda, D. Fast Prediction of Adsorption Properties for Platinum Nanocatalysts with Generalized Coordination Numbers. *Angew. Chem., Int. Ed.* **2014**, *53*, 8316−8319.
(58) Calle-Vallejo, F.; Bandarenka, A. S. Enabling Generalized Coordination Numbers to Describe Strain Effects. *ChemSusChem* **2018**, *11*, 1824−1828.
(59) Garlyyev, B.; Fichtner, J.; Piqué, O.; Schneider, O.; Bandarenka, A. S.; Calle-Vallejo, F. Revealing the Nature of Active Sites in Electrocatalysis. *Chem. Sci.* **2019**, *10*, 8060−8075.
(60) Bagger, A.; Ju, W.; Varela, A. S.; Strasser, P.; Rossmeisl, J. Electrochemical CO_2 Reduction: A Classification Problem. *ChemPhysChem* **2017**, *18*, 3266−3273.
(61) Johnson, L. R.; Sridhar, S.; Zhang, L.; Fredrickson, K. D.; Raman, A. S.; Jang, J.; Leach, C.; Padmanabhan, A.; Price, C. C.; Frey, N. C.; Raizada, A.; Rajaraman, V.; Saiprasad, S. A.; Tang, X.; Vojvodic, A. MXene Materials for the Electrochemical Nitrogen Reduction—Functionalized or Not? *ACS Catal.* **2020**, *10*, 253−264.

https://dx.doi.org/10.1021/acscatal.0c01488
ACS Catal. 2020, 10, 10488−10494

Electrochimica Acta 380 (2021) 138247

Contents lists available at ScienceDirect

Electrochimica Acta

journal homepage: www.elsevier.com/locate/electacta

Computational-experimental study of the onset potentials for CO_2 reduction on polycrystalline and oxide-derived copper electrodes

Oriol Piqué [a], Mario Löffler [b,c], Ioannis Katsounaros [b,*], Federico Calle-Vallejo [a,*]

[a] Department of Materials Science and Physical Chemistry & Institute of Theoretical and Computational Chemistry (IQTCUB), University of Barcelona, Martí i Franquès 1, 08028 Barcelona, Spain
[b] Helmholtz Institute Erlangen-Nürnberg for Renewable Energy (IEK-11), Forschungszentrum Jülich GmbH, Egerlandstr. 3, 91058 Erlangen, Germany
[c] Department of Chemical and Biological Engineering, Friedrich-Alexander-Universität Erlangen-Nürnberg (FAU), Egerlandstr. 3, 91058 Erlangen, Germany

ARTICLE INFO

Article history:
Received 11 December 2020
Revised 8 February 2021
Accepted 20 March 2021
Available online 26 March 2021

Keywords:
CO_2 electroreduction
onset potential
polycrystalline Cu
Oxide-derived Cu
DFT
Real time quantification

ABSTRACT

The electrocatalytic reduction of CO_2 (CO_2RR) is a promising yet intricate process to alleviate the alarming imbalance in the carbon cycle. One of the intricacies of CO_2RR is its structural sensitivity, which is illustrated by the varying onset potentials and selectivities of the reaction products depending on the electrode morphology. Here, using electrochemical real-time mass spectrometry (EC-RTMS), we accurately determine the onset potentials for seven CO_2RR products including C_1, C_2, and C_3 species on polycrystalline and oxide-derived Cu electrodes. Density functional theory calculations affordably including solvent and cation effects produce onset potentials of C_2 species matching those obtained with EC-RTMS. Our analysis leads us to conclude that the elusive active sites at oxide-derived Cu, known to enhance ethanol production, are undercoordinated square ensembles of Cu atoms.

1. Introduction

Powered by renewable electricity, the electrochemical reduction of CO_2 (CO_2RR) is a plausible approach to help compensate the tremendous global imbalance of the carbon cycle. In doing so, the alarming amounts of CO_2 in the environment can be transformed into valuable chemical compounds such as methane, ethanol and ethylene [1–3]. As shown by the pioneering works of Hori et al., copper is capable of reducing CO_2 beyond the two-electron products (CO or formic acid) observed on most metals [4–6]. However, the predominance of the competing hydrogen evolution, the low selectivity toward specific products, and the large overpotentials needed to obtain fair current densities still hinder a large-scale implementation of Cu-based CO_2 electrolyzers. Interestingly, the redox treatment of Cu electrodes holds promise for addressing some of these issues [7,8].

In fact, oxide-derived copper (OD-Cu) electrocatalysts show lower overpotentials and enhanced selectivity toward C_2 products, with higher faradaic efficiencies of ethanol compared to regular Cu electrodes [7,8]. In spite of some hints, the active sites responsible for such improvements have not been ascertained yet in experiments. For instance, it is known that the presence and extent of grain boundaries are connected with the activity improvements of OD-Cu [7,9]. Furthermore, isotopic labelling experiments of CO_2RR on OD-Cu showed that ethylene and ethanol, the two major C_2 products, are produced on different active sites [10]. On the other hand, ethylene is more abundant than ethanol on pristine Cu(100) facets [11], while increasing amounts of ethanol are observed at rough Cu surfaces.

The recent development of the electrochemical real-time mass spectrometry technique (EC-RTMS) allows for accurate, *in operando* detection of CO_2RR products on OD-Cu and polycrystalline Cu (Cu-poly) [12,13]. The sensitivity of this real-time technique for reaction products and intermediates is remarkably high compared to established chromatography techniques or nuclear magnetic resonance, which are compatible with steady-state electrolysis [13]. The low limits of detection enable a more accurate determination of onset potentials based on the detection of products at low formation rates during potential sweep experiments. This is rather useful for CO_2RR, as different compounds are produced as a function of the applied potential and, in some cases, some products appear at similar if not identical potentials.

Furthermore, computational studies have shown that solvation and cation effects are key to accurately predict the CO_2RR activity and selectivity of Cu electrodes [1,14–18]. Remarkably, several experimental investigations have shown that alkaline cations enhance the production of multi-carbon species [19–22]. Different

* Corresponding authors.
E-mail addresses: i.katsounaros@fz-juelich.de (I. Katsounaros), f.calle.vallejo@ub.edu (F. Calle-Vallejo).

https://doi.org/10.1016/j.electacta.2021.138247
0013-4686/

approaches have been used to model these effects. Using static calculations, solvation can be modelled using implicit solvent models [23], ad hoc corrections [14,24,25], explicit water layers [17,26], or using micro-solvation models in which explicit water molecules are added in the vicinity of the adsorbates to capture their hydrogen bonds [27,28]. On the other hand, (solvated) cations can be modelled through an electric field [29], by including them within an explicit water bilayer [26,30], by adsorbing them next to the adsorbates [16,22,31], or by means of continuum models of the double-layer [32]. Specific choices for the modelling of these effects depend on the system size and complexity, usually attempting to compromise computational expenses and accuracy.

In this work, we provide the onset potentials for seven CO_2RR products including C_1, C_2, and C_3 species using EC-RTMS experiments. In addition, we show that calculations affordably including solvent and cation effects produce onset potentials of C_2 species matching those obtained experimentally with EC-RTMS. This helps in outlining a plausible geometric structure of the active sites at OD-Cu and leads to interesting mechanistic conclusions.

2. Methods

2.1. Experimental details

Details on the analysis of gaseous and liquid products with electrochemical real-time mass spectrometry (EC-RTMS) have been described previously [13,33]. Linear sweep voltammetry at a scan rate of 3 mV s^{-1} was conducted from −0.4 to −1.1 V_{RHE} for Cu-poly and from −0.1 to −0.8 V_{RHE} for OD-Cu, always in the negative direction of the potential (V_{RHE} denotes potentials in the reversible hydrogen electrode scale). The starting potentials were such that neither CO_2 reduction nor extensive hydrogen evolution takes place, while the surface oxidation state remains unaltered until the measurement starts. Parallel to the electrochemical data of current and potential versus time, information on the formed products was obtained versus time as well, with a data acquisition frequency of ca. 1.7 Hz for the gas analysis and 2 Hz for the liquid analysis. The mass spectrometric data were synchronized with the electrochemical data after the measurement, taking into account the time needed for the formed products to reach the corresponding mass spectrometer, and eventually the intensities for each product were expressed as a function of the applied potential after post-correction for the remaining 36–41 Ω after 85% positive feedback compensation. The evaluation procedure to determine the onset potential of each product from the respective mass spectrometry signals is described in section S1 of the Supporting Information (SI).

For the preparation of Cu-poly and OD-Cu electrodes, we employed the same procedure described in a previous work [13]. The thermally oxidized electrodes were reduced electrochemically at −1.2 V_{RHE} for 10 min before the linear sweep voltammetry was applied, to make sure that the oxide reduction did not interfere with the product evolution during the linear sweep. Ultrapure water (18.2 MΩ cm, TOC <5 ppb, Merck Milli-Q IQ 7000) was used for the preparation of the electrolyte, right before each measurement. For the CO_2 reduction experiments, the electrolyte was 0.1 M $KHCO_3$ (analysis grade, Merck) saturated in CO_2 (99.998%, Air Liquide) and the resulting pH of the solution was 6.8. For the acetaldehyde reduction experiments, the electrolyte was 0.05 M Na_2HPO_4 (99%, VWR), 0.05 M $NaH_2PO_4{\cdot}2H_2O$ (99%, VWR) (pH set to 6.8 equal to the pH of 0.1 M $KHCO_3$ saturated in CO_2) and 1 mM acetaldehyde (≥99.0%, VWR) saturated in Argon (99.998%, Air Liquide). In either case, the electrolyte was sparged with the respective gas for 30 min before the measurement started, and sparging was maintained throughout the entire measurement.

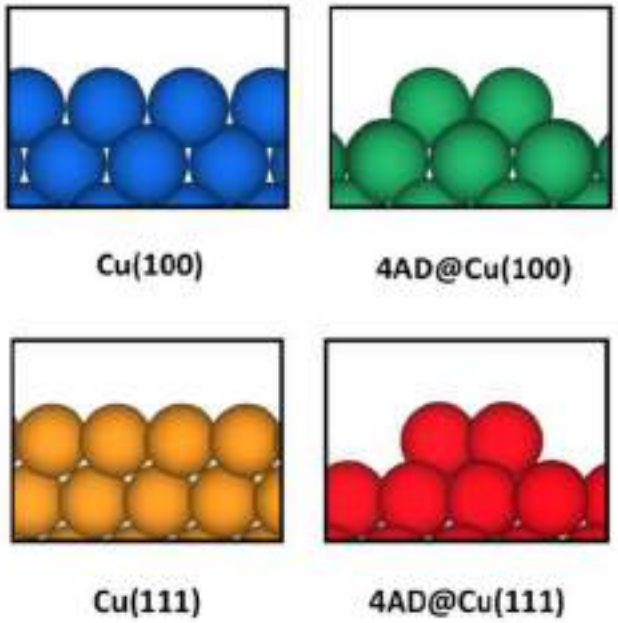

Fig. 1. Side views of the four different slab models used in this work. Top: Cu(100) (blue), 4AD@Cu(100) (green). Bottom: Cu(111) (orange), and 4AD@Cu(111) (red). Details on the number of atoms per layer and the number of layers in the slabs are provided in the Computational Methods section. (For interpretation of the references to color in this figure legend, the reader is refered to the web version of this article.)

2.2. Computational details

The DFT simulations were carried out using the VASP code [34] with the Perdew-Burke-Ernzerhof (PBE) exchange-correlation functional [35], and the PAW method [36]. To model Cu-poly and OD-Cu, we studied four different types of active sites: Cu(111) terraces; Cu(100) terraces; 4AD@Cu(100) and 4AD@Cu(111), which contain 4-atom islands on top of (100) and (111) terraces, respectively. A side view of the active sites is shown in Fig. 1. A $(4\sqrt{2} \times 4\sqrt{2})R45°$ supercell slab of 32 atoms per layer was used to model the Cu(100) and 4AD@Cu(100) surfaces. For Cu(111) and 4AD@Cu(111) a p(4 × 4) supercell including 16 atoms per layer was used. These large supercells help avoid lateral interactions between atom islands, adsorbates, and cations. All the slabs were modelled with the converged PBE lattice constant of Cu (3.64 Å) and were composed of four atomic layers. The adsorbates, Cu islands, and the top two layers of the slabs were allowed to relax in all directions, while the bottom layers were fixed at the bulk equilibrium distances. The plane-wave cutoff was 450 eV. The Methfessel-Paxton approach was used to smear the Fermi level with an electronic temperature of 0.2 eV, always extrapolating the total energies to 0 K. The numerical integration in the reciprocal space was carried out using Monkhorst-Pack grids of 2 × 2 × 1 for Cu(100) and 4AD@Cu(100) and 3 × 3 × 1 for Cu(111) and 4AD@Cu(111), which guaranteed convergence of the adsorption energies within ±0.05 eV. Periodically repeated images in the vertical direction were separated by more than 13 Å of vacuum and dipole corrections were also applied. The conjugate-gradient optimization algorithm was used for the geometry optimizations, with iterations performed until the maximal force on all atoms was below 0.05 eV $Å^{-1}$. Boxes of 9 × 10 × 11 $Å^3$ were used to calculate the isolated molecules in this study, considering the Γ-point only, using Gaussian smearing and an electronic temperature of 0.001 eV with further extrapolation to 0 K. On average, 10 different initial configurations were relaxed for each adsorbate on each active site.

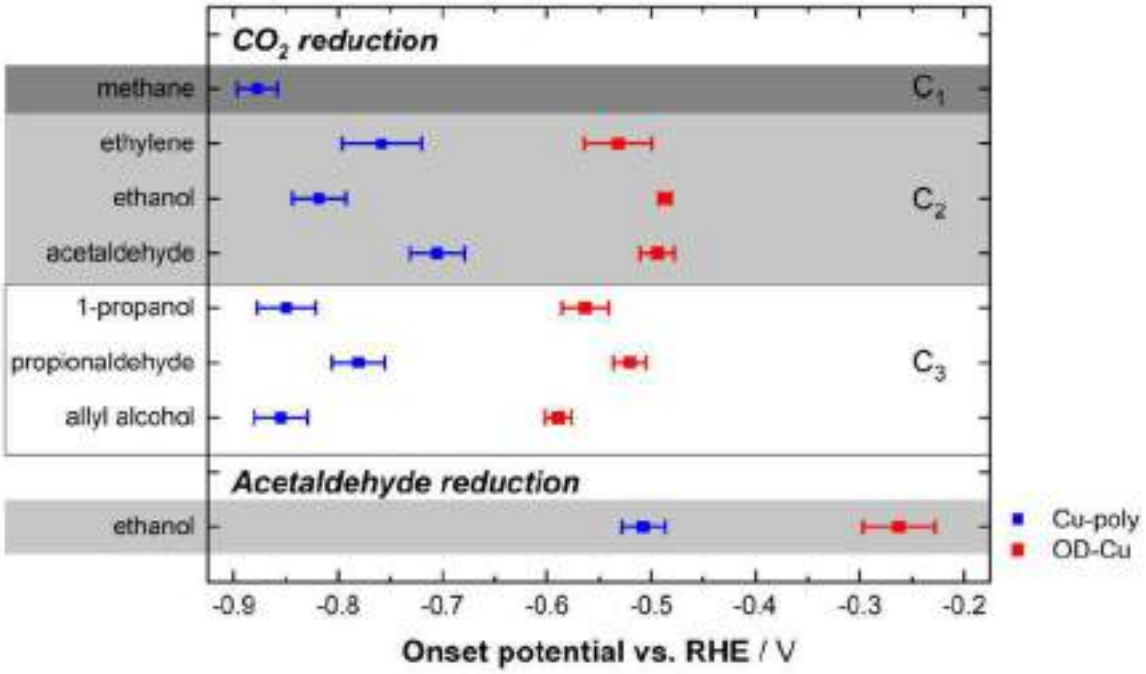

Fig. 2. Onset potentials of seven compounds from the reduction of CO_2, and onset of ethanol from the reduction of acetaldehyde. Error bars show the standard deviation of three independent measurements.

including, when possible, monodentate, bidentate, and tridentate configurations.

Reaction free energies were approximated as $\Delta G \approx \Delta E_{DFT} + \Delta ZPE - T\Delta S + \Delta E_{solvation}$, where ΔE_{DFT} is the DFT-calculated reaction energy, ΔZPE is the zero-point energy change, $T\Delta S$ is the corresponding entropy change at 298.15 K, and $\Delta E_{solvation}$ contains ad-hoc solvation corrections depending on the chemical nature of the adsorbates [14,25]. For free molecules, all contributions are considered in ΔS and the values were obtained from thermodynamic tables, while for adsorbates ΔS only includes the vibrational entropies. ZPE and TS_{vib} values are obtained from DFT calculations of vibrational frequencies making use of the harmonic-oscillator approximation.

Proton-electron pairs were modelled using the computational hydrogen electrode [37]. Cation effects were modelled by the explicit inclusion of a potassium atom over the slabs. In each case, we found around each adsorbate the most favorable position of the cation by relaxing different initial geometries. We did not compute proton-electron transfer barriers in this study, as Rossmeisl et al. recently noted that there is "not (yet) a method to obtain electrochemical barriers between realistic states at constant electrochemical conditions" [38]. Nevertheless, CO-CO coupling happens upon an electron transfer, so its barrier was assessed by means of the climbing-image nudged elastic band method [39], verifying that only one imaginary frequency along the reaction coordinate was present at the saddle point.

3. Results and discussion

We employed EC-RTMS together with linear sweep voltammetry to determine experimentally the onset potentials from the reduction of CO_2 for the following seven liquid and gaseous compounds: methane, ethylene, ethanol, acetaldehyde, 1-propanol, propionaldehyde and allyl alcohol. We also determined the onset potential for ethanol from the reduction of acetaldehyde. Fig. 2 shows the results for Cu-poly and OD-Cu electrodes, while a representative dataset can be found in the SI, Figure S2. All onset potentials are characterized by a small and constant standard deviation determined by three independent measurements, underlining the high reproducibility of the experiments.

On Cu-poly, methane shows the most negative onset potential with -0.88 ± 0.02 V_{RHE}. Different C_2 compounds (ethylene, ethanol) as well as C_3 compounds (1-propanol, propionaldehyde, allyl alcohol) show similarly negative onset potentials, ranging from -0.70 to -0.86 V_{RHE}, the least negative being the onset for acetaldehyde (-0.70 ± 0.03 V_{RHE}). Small deviations in these measurements might arise from different sensitivity of the instrumental method toward the detection of individual compounds. The fact that the experimental onset potentials are relatively similar for all C_{2+} products on Cu-poly suggests that their onset is controlled by a common potential-limiting step, early in the reaction pathway.

Interestingly, ethanol is produced from acetaldehyde reduction at a clearly less negative onset potential than from CO_2 (-0.51 ± 0.03 V_{RHE} versus -0.82 ± 0.03 V_{RHE}), which further supports that the onset potential for CO_2 reduction to ethanol through the acetaldehyde intermediate [13,40] is determined by another step, earlier in the reaction sequence, as shown by DFT-based models [14,16,25,41].

On OD-Cu, the onset potentials for all products of CO_2 reduction (except for methane, which is not detected) are shifted substantially to more positive values, spanning now from -0.49 ± 0.01 V_{RHE} for ethanol to -0.59 ± 0.02 V_{RHE} for allyl alcohol. As the onset potentials are similar among all C_{2+} products, we conclude that they likely still share a common potential-limiting step on OD-Cu, as is the case on Cu-poly. The onset potential for ethanol from the reduction of acetaldehyde shifts accordingly to more positive values (-0.27 ± 0.04 V_{RHE}) on OD-Cu, again more positive than from CO_2 on the same electrode, in line with the finding on Cu-poly. The significant shift of 250 mV on average for the onset potential of all reactions on OD-Cu compared to Cu-poly is ascribed to the creation of new active sites after the thermal treatment and subsequent oxide reduction [7–10,42,43]. We note that changes in the local pH or the local concentration of CO_2, which can be induced at the interface due to the higher roughness of OD-Cu and modify

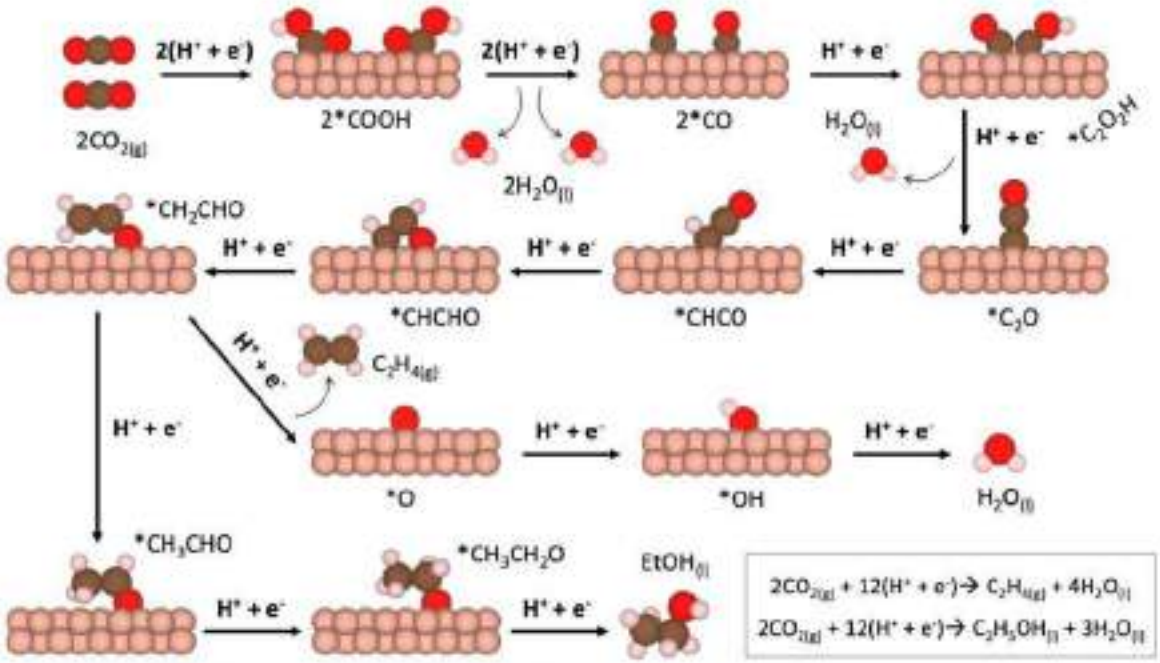

Fig. 3. Schematic representation of the reaction pathways for CO_2RR to C_2 species. Cu, C, O, and H atoms are depicted in grey, brown, red, and pink. EtOH: ethanol. (For interpretation of the references to color in this figure legend, the reader is referred to the web version of this article.)

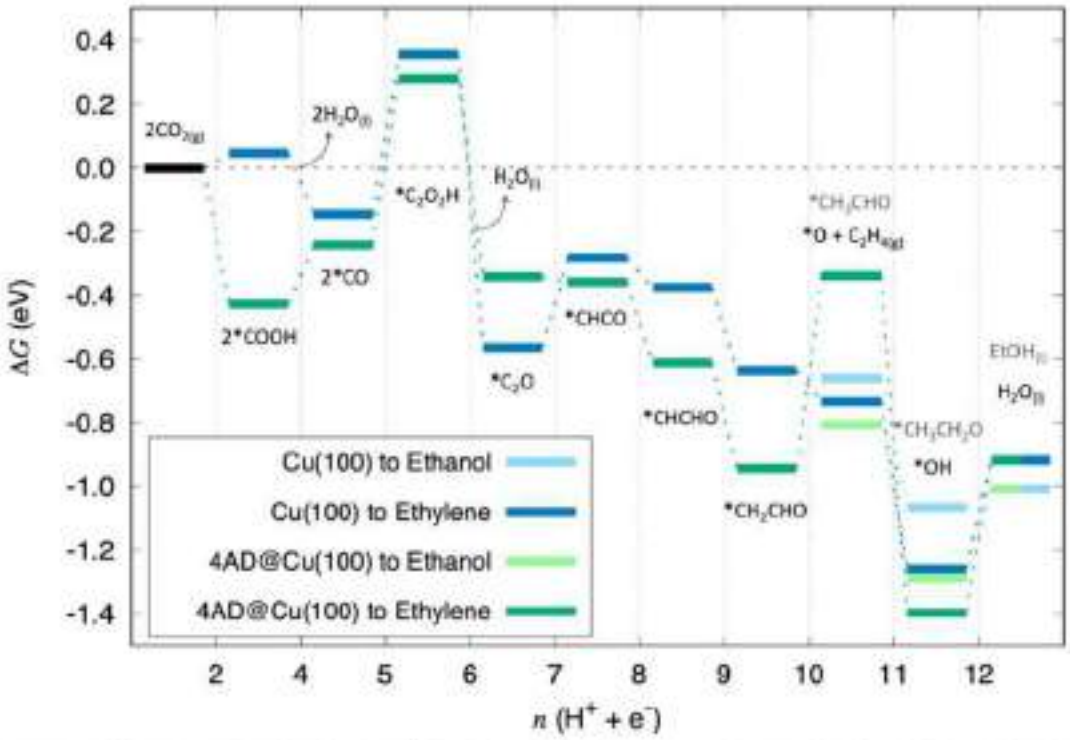

Fig. 4. Free-energy diagrams including solvent and cation effects for all intermediates of the CO_2RR to C_2 species on Cu(100) (blue) and 4AD@Cu(100) (green) at 0 V_{RHE}. The same colors in a lighter tone are used to represent the ethanol pathway, which drifts away from that of ethylene upon the tenth proton-electron transfer. The corresponding intermediates toward ethylene are noted for each proton-electron transfer in black (gray for the ethanol pathway). EtOH: Ethanol. (For interpretation of the references to color in this figure legend, the reader is referred to the web version of this article.)

the product distribution [44–47], are negligible here because the onsets were determined at rather low current densities and continuous electrolyte flow was employed.

Furthermore, the thermodynamics of each proton-electron transfer of CO_2RR to C_2 products (ethylene and ethanol) were calculated for four different active sites by combining well-known CO_2 reduction pathways to *CO via *COOH [27,48–51] with *CO reduction pathways that comply with several experimental observations [14,16,25]. The active sites selected for this study were Cu(111), as it is the most stable surface termination; Cu(100), known to facilitate C-C coupling and for being ethylene selective [14]; 4AD@Cu(100), a square, four-atom island likely present in

OD-Cu, the surface of which is extremely rough [52] and ethanol selective [16]; and, for completeness, 4AD@Cu(111), a four-atom island with hexagonal symmetry, which, as shown in previous works [16] and in Table S3, enhances CO dimerization with respect to Cu(111) but is not as active as the studied square sites, namely Cu(100) and 4AD@Cu(100).

A schematic representation of the modelled pathway is shown in Fig. 3. We find that the hydrogenation of adsorbed CO molecules ($2^*CO + H^+ + e^- \rightarrow {}^*C_2O_2H$) is the potential-limiting step of the reaction for ethylene and ethanol production on the analyzed active sites, in line with previous experimental and computational studies [6,14,53]. The fact that C-C coupling is involved in the potential-limiting step for C_2 products is also in agreement with the similar onset potentials determined experimentally with EC-RTMS for C_2 and C_3 products, bearing in mind that C_3 products are formed via a chemical reaction between C_1 and C_2 species [54–56]. We note here that *CO hydrogenation to either *COH or *CHO is also the potential-limiting step for CO_2RR to methane [17,24,27,57,58]. The onset potentials for CO_2RR to both ethylene and ethanol are −0.50, −0.52, −1.14, and −0.66 V_{RHE} for Cu(100), 4AD@Cu(100), Cu(111), and 4AD@Cu(111), respectively, calculated based on values from Table S3.

In Fig. 4, we show the calculated free-energy diagrams for these two surface models using the pathways in Fig. 3. After noting that (i) the calculated onset potentials for Cu(100) and 4AD@Cu(100) agree well with those determined experimentally for ethylene and ethanol on OD-Cu, and (ii) Cu(100) is selective to ethylene and 4AD@Cu(100) is selective to ethanol, we believe that the active sites present at OD-Cu responsible for ethylene and ethanol evolution resemble Cu(100) terraces and 4AD@Cu(100) islands, respectively. Cu(111) and 4AD@Cu(111) are not shown in Fig. 4 because they are not active toward C_2 products, given their unfavorable energetics of CO dimerization (see Table S3).

4. Conclusions

Because it is energy-intensive, the hydrogenation of *CO impedes an efficient CO_2 electroreduction. Hydrogenating *CO monomers is more difficult than hydrogenating *CO dimers on Cu electrodes. These two observations help explain why the onset potentials for all C_{2+} reaction products at a given electrode are similar and why more negative potentials are required for producing C_1 species compared to C_2 and C_3 species.

Furthermore, the notable differences in the experimental onset potentials between polycrystalline and oxide-derived copper electrodes, indicate the presence of a unique set of active sites in the latter. Based on DFT calculations affordably including solvent and cation effects, we propose that such sites are formed by square, four-atom ensembles of Cu atoms. Such configuration renders onset potentials for C_2 products that match the experimental values and complies with several experimental facts, namely that (i) oxide-derived Cu electrodes are extremely rough, (ii) square facets facilitate *CO coupling, and (iii) undercoordination favors ethanol production.

With all this in mind, we conclude that the selective production of a given multi-carbon product from CO_2RR requires not only engineering the C-C coupling step, which takes place early in the reaction mechanism, but also the bifurcation step, in which either the path toward oxygenates or hydrocarbons is followed.

Declaration of Competing Interest

The authors declare that they have no known competing financial interests or personal relationships that could have appeared to influence the work reported in this paper.

Credit authorship contribution statement

Oriol Piqué: Formal analysis, Investigation, Visualization, Writing – original draft. **Mario Löffler:** Formal analysis, Investigation, Visualization, Writing – original draft. **Ioannis Katsounaros:** Conceptualization, Formal analysis, Writing – review & editing, Supervision, Project administration. **Federico Calle-Vallejo:** Conceptualization, Formal analysis, Writing – review & editing, Supervision, Project administration, Funding acquisition.

Acknowledgments

F.C.-V. acknowledges funding from Spanish MICIUN RTI2018-095460-B-I00, Ramón y Cajal RyC-2015-18996 and María de Maeztu MDM-2017-0767 grants and partly by Generalitat de Catalunya 2017SGR13. O.P. thanks the Spanish MICIUN for a PhD grant (PRE2018-083811). We thank Red Española de Supercomputación (RES) for supercomputing time at SCAYLE (projects QS-2019-3-0018, QS-2019-2-0023, and QCM-2019-1-0034), MareNostrum (project QS-2020-1-0012), and CENITS (project QS-2020-2-0021). The use of supercomputing facilities at SURFsara was sponsored by NWO Physical Sciences, with financial support by NWO.

Supplementary materials

Supplementary material associated with this article can be found, in the online version, at doi:10.1016/j.electacta.2021.138247.

References

[1] S. Nitopi, E. Bertheussen, S.B. Scott, X. Liu, A.K. Engstfeld, S. Horch, B. Seger, I.E.L. Stephens, K. Chan, C. Hahn, J.K. Nørskov, T.F. Jaramillo, I. Chorkendorff, Progress and perspectives of electrochemical CO_2 reduction on copper in aqueous electrolyte, Chem. Rev. 119 (2019) 7610–7672, doi:10.1021/acs.chemrev.8b00705.

[2] O.S. Bushuyev, P.D. Luna, C.T. Dinh, L. Tao, G. Saur, J. van de Lagemaat, S.O. Kelley, E.H. Sargent, What should we make with CO_2 and how can we make it?, Joule 2 (2018) 825–832, doi:10.1016/j.joule.2017.09.003.

[3] Y.Y. Birdja, E. Pérez-Gallent, M.C. Figueiredo, A.J. Göttle, F. Calle-Vallejo, M.T.M. Koper, Advances and challenges in understanding the electrocatalytic conversion of carbon dioxide to fuels, Nat. Energy 4 (2019) 732–745, doi:10.1038/s41560-019-0450-y.

[4] Y. Hori, A. Murata, R. Takahashi, S. Suzuki, Electroreduction of carbon monoxide to methane and ethylene at a copper electrode in aqueous solutions at ambient temperature and pressure, J. Am. Chem. Soc. 109 (1987) 5022–5023, doi:10.1021/ja00250a044.

[5] Y. Hori, A. Murata, R. Takahashi, Formation of hydrocarbons in the electrochemical reduction of carbon dioxide at a copper electrode in aqueous solution, J. Chem. Soc., Faraday Trans. 1. 85 (1989) 2309–2326, doi:10.1039/F19898502309.

[6] Y. Hori, R. Takahashi, Y. Yoshinami, A. Murata, Electrochemical reduction of CO at a copper electrode, J. Phys. Chem. B. 101 (1997) 7075–7081, doi:10.1021/jp970284i.

[7] C.W. Li, J. Ciston, M.W. Kanan, Electroreduction of carbon monoxide to liquid fuel on oxide-derived nanocrystalline copper, Nature 508 (2014) 504–507, doi:10.1038/nature13249.

[8] C.W. Li, M.W. Kanan, CO_2 reduction at low overpotential on Cu electrodes resulting from the reduction of thick Cu_2O films, J. Am. Chem. Soc. 134 (2012) 7231–7234, doi:10.1021/ja3010978.

[9] A. Verdaguer-Casadevall, C.W. Li, T.P. Johansson, S.B. Scott, J.T. McKeown, M. Kumar, I.E.L. Stephens, M.W. Kanan, I. Chorkendorff, Probing the active surface sites for CO reduction on oxide-derived copper electrocatalysts, J. Am. Chem. Soc. 137 (2015) 9808–9811, doi:10.1021/jacs.5b06227.

[10] Y. Lum, J.W. Ager, Evidence for product-specific active sites on oxide-derived Cu catalysts for electrochemical CO_2 reduction, Nature Catalysis 2 (2019) 86–93, doi:10.1038/s41929-018-0201-7.

[11] Y. Hori, I. Takahashi, O. Koga, N. Hoshi, Electrochemical reduction of carbon dioxide at various series of copper single crystal electrodes, J. Mol. Catal. A: Chem. 199 (2003) 39–47, doi:10.1016/S1381-1169(03)00016-5.

[12] P. Kharipour, M. Löffler, A.M. Reichert, E.T. Haase, K.J.J. Mayrhofer, I. Katsounaros, Electrochemical real-time mass spectrometry (EC-RTMS): monitoring electrochemical reaction products in real time, Angewandte Chemie International Edition 58 (2019) 7273–7277, doi:10.1002/anie.201901923.

[13] M. Löffler, P. Kharipour, N. Kulyk, K.J.J. Mayrhofer, I. Katsounaros, Insights into liquid product formation during carbon dioxide reduction on copper and oxide-derived copper from quantitative real-time measurements, ACS Catal. 10 (2020) 6735–6740, doi:10.1021/acscatal.0c01388.

[14] F. Calle-Vallejo, M.T.M. Koper, Theoretical considerations on the electroreduction of CO to C_2 species on Cu(100) electrodes, Angewandte Chemie International Edition 52 (2013) 7282–7285, doi:10.1002/anie.201301470.
[15] A. Rendón-Calle, S. Builes, F. Calle-Vallejo, A brief review of the computational modeling of CO_2 electroreduction on Cu electrodes, Curr. Opin. Electrochem. 9 (2018) 158–165, doi:10.1016/j.coelec.2018.03.012.
[16] O. Piqué, F. Viñes, F. Illas, F. Calle-Vallejo, Elucidating the structure of ethanol-producing active sites at oxide-derived Cu electrocatalysts, ACS Catal. 10 (2020) 10488–10494, doi:10.1021/acscatal.0c01880.
[17] J. Hussain, H. Jónsson, E. Skúlason, Calculations of product selectivity in electrochemical CO_2 reduction, ACS Catal. 8 (2018) 5240–5249, doi:10.1021/acscatal.7b03308.
[18] T. Cheng, H. Xiao, W.A. Goddard, Full atomistic reaction mechanism with kinetics for CO reduction on Cu(100) from ab initio molecular dynamics free-energy calculations at 298 K, PNAS (2017), doi:10.1073/pnas.1612106114.
[19] A. Murata, Y. Hori, Product selectivity affected by cationic species in electrochemical reduction of CO_2 and CO at a Cu electrode, BCSJ 64 (1991) 123–127, doi:10.1246/bcsj.64.123.
[20] J. Resasco, L.D. Chen, E. Clark, C. Tsai, C. Hahn, T.F. Jaramillo, K. Chan, A.T. Bell, Promoter effects of alkali metal cations on the electrochemical reduction of carbon dioxide, J. Am. Chem. Soc. 139 (2017) 11277–11287, doi:10.1021/jacs.7b06765.
[21] M.R. Singh, Y. Kwon, Y. Lum, J.W. Ager, A.T. Bell, Hydrolysis of electrolyte cations enhances the electrochemical reduction of CO_2 over Ag and Cu, J. Am. Chem. Soc. 138 (2016) 13006–13012, doi:10.1021/jacs.6b07612.
[22] E. Pérez-Gallent, G. Marcandalli, M.C. Figueiredo, F. Calle-Vallejo, M.T.M. Koper, Structure- and potential-dependent cation effects on CO reduction at copper single-crystal electrodes, J. Am. Chem. Soc. 139 (2017) 16412–16419, doi:10.1021/jacs.7b10142.
[23] Y. Basdogan, A.M. Maldonado, J.A. Keith, Advances and challenges in modeling solvated reaction mechanisms for renewable fuels and chemicals, WIREs Comput. Mol. Sci. 10 (2020) e1446, doi:10.1002/wcms.1446.
[24] A.A. Peterson, F. Abild-Pedersen, F. Studt, J. Rossmeisl, J.K. Nørskov, How copper catalyzes the electroreduction of carbon dioxide into hydrocarbon fuels, Energy Environ. Sci. 3 (2010) 1311–1315, doi:10.1039/C0EE00071J.
[25] S. Hanselman, M.T.M. Koper, F. Calle-Vallejo, Computational comparison of late transition metal (100) surfaces for the electrocatalytic reduction of CO to C_2 Species, ACS Energy Lett 3 (2018) 1062–1067, doi:10.1021/acsenergylett.8b00326.
[26] J.H. Montoya, C. Shi, K. Chan, J.K. Nørskov, Theoretical Insights into a CO Dimerization Mechanism in CO_2 Electroreduction, J. Phys. Chem. Lett. 6 (2015) 2032–2037, doi:10.1021/acs.jpclett.5b00722.
[27] A. Rendón-Calle, S. Builes, F. Calle-Vallejo, Substantial improvement of electrocatalytic predictions by systematic assessment of solvent effects on adsorption energies, Appl. Catal. B: Environ. (2020) 119147, doi:10.1016/j.apcatb.2020.119147.
[28] S.A. Akhade, W. Luo, X. Nie, A. Asthagiri, M.J. Janik, Theoretical insight on reactivity trends in CO_2 electroreduction across transition metals, Catal. Sci. Technol. 6 (2016) 1042–1053, doi:10.1039/C5CY01338A.
[29] L.D. Chen, M. Urushihara, K. Chan, J.K. Nørskov, Electric field effects in electrochemical CO_2 reduction, ACS Catal 6 (2016) 7133–7139, doi:10.1021/acscatal.6b02209.
[30] T. Ludwig, J.A. Gauthier, C.F. Dickens, K.S. Brown, S. Ringe, K. Chan, J.K. Nørskov, Atomistic insight into cation effects on binding energies in Cu-catalyzed carbon dioxide reduction, J. Phys. Chem. C. 124 (2020) 24765–24775, doi:10.1021/acs.jpcc.0c07004.
[31] S.A. Akhade, I.T. McCrum, M.J. Janik, The impact of specifically adsorbed ions on the copper-catalyzed electroreduction of CO_2, J. Electrochem. Soc. 163 (2016) F477, doi:10.1149/2.0581606jes.
[32] D. Bohra, J.H. Chaudhry, T. Burdyny, E.A. Pidko, W.A. Smith, Modeling the electrical double layer to understand the reaction environment in a CO_2 electrocatalytic system, Energy Environ. Sci. 12 (2019) 3380–3389, doi:10.1039/C9EE02485A.
[33] N. Martić, C. Reller, C. Macauley, M. Löffler, A.M. Reichert, T. Reichbauer, K.-M. Vetter, B. Schmid, D. McLaughlin, P. Leidinger, D. Beinsch, C. Vogl, K.J.J. Mayrhofer, I. Katsounaros, G. Schmid, $Ag_2Cu_2O_3$ – a catalyst template material for selective electroreduction of CO to C_2+ products, Energy Environ. Sci. 13 (2020) 2999–3006, doi:10.1039/D0EE01100B.
[34] G. Kresse, J. Furthmüller, Efficient iterative schemes for ab initio total-energy calculations using a plane-wave basis set, Phys. Rev. B. 54 (1996) 11169–11186, doi:10.1103/PhysRevB.54.11169.
[35] J.P. Perdew, K. Burke, M. Ernzerhof, Generalized gradient approximation made simple, Phys. Rev. Lett. 77 (1996) 3865–3868, doi:10.1103/PhysRevLett.77.3865.
[36] G. Kresse, D. Joubert, From ultrasoft pseudopotentials to the projector augmented-wave method, Phys. Rev. B. 59 (1999) 1758–1775, doi:10.1103/PhysRevB.59.1758.
[37] J.K. Nørskov, J. Rossmeisl, A. Logadottir, L. Lindqvist, J.R. Kitchin, T. Bligaard, H. Jónsson, Origin of the overpotential for oxygen reduction at a fuel-cell cathode, J. Phys. Chem. B. 108 (2004) 17886–17892, doi:10.1021/jp047349j.
[38] A. Bagger, L. Arnarson, M.H. Hansen, E. Spohr, J. Rossmeisl, Electrochemical CO reduction: a property of the electrochemical interface, J. Am. Chem. Soc. 141 (2019) 1506–1514, doi:10.1021/jacs.8b08839.
[39] G. Henkelman, B.P. Uberuaga, H. Jónsson, A climbing image nudged elastic band method for finding saddle points and minimum energy paths, J. Chem. Phys. 113 (2000) 9901–9904, doi:10.1063/1.1329672.
[40] E. Bertheussen, A. Verdaguer-Casadevall, D. Ravasio, J.H. Montoya, D.B. Trimarco, C. Roy, S. Meier, J. Wendland, J.K. Nørskov, I.E.L. Stephens, I. Chorkendorff, Acetaldehyde as an intermediate in the electroreduction of carbon monoxide to ethanol on oxide-derived copper, Angewandte Chemie International Edition 55 (2016) 1450–1454, doi:10.1002/anie.201508853.
[41] I. Ledezma-Yanez, E.P. Gallent, M.T.M. Koper, F. Calle-Vallejo, Structure-sensitive electroreduction of acetaldehyde to ethanol on copper and its mechanistic implications for CO and CO_2 reduction, Catal Today 262 (2016) 90–94, doi:10.1016/j.cattod.2015.09.029.
[42] X. Feng, K. Jiang, S. Fan, M.W. Kanan, Grain-boundary-dependent CO_2 electroreduction activity, J. Am. Chem. Soc. 137 (2015) 4606–4609, doi:10.1021/ja5130513.
[43] R.G. Mariano, K. McKelvey, H.S. White, M.W. Kanan, Selective increase in CO_2 electroreduction activity at grain-boundary surface terminations, Science 358 (2017) 1187–1192, doi:10.1126/science.aao3691.
[44] M. Ma, K. Djanashvili, W.A. Smith, Controllable hydrocarbon formation from the electrochemical reduction of CO_2 over Cu nanowire arrays, Angewandte Chemie International Edition 55 (2016) 6680–6684, doi:10.1002/anie.201601282.
[45] Y. Lum, B. Yue, P. Lobaccaro, A.T. Bell, J.W. Ager, Optimizing C–C coupling on oxide-derived copper catalysts for electrochemical CO_2 reduction, J. Phys. Chem. C. 121 (2017) 14191–14203, doi:10.1021/acs.jpcc.7b03673.
[46] F.L.P. Veenstra, N. Ackerl, A.J. Martin, J. Pérez-Ramírez, Laser-microstructured copper reveals selectivity patterns in the electrocatalytic reduction of CO_2, Chem 6 (2020) 1707–1722, doi:10.1016/j.chempr.2020.04.001.
[47] H. Song, J.T. Song, B. Kim, Y.C. Tan, J. Oh, Activation of C_2H_4 reaction pathways in electrochemical CO_2 reduction under low CO_2 partial pressure, Appl. Catal. B: Environmental 272 (2020) 119049, doi:10.1016/j.apcatb.2020.119049.
[48] H.A. Hansen, J.B. Varley, A.A. Peterson, J.K. Nørskov, Understanding trends in the electrocatalytic activity of metals and enzymes for CO_2 reduction to CO, J. Phys. Chem. Lett. 4 (2013) 388–392, doi:10.1021/jz302035r.
[49] W. Zhu, Y.-J. Zhang, H. Zhang, H. Lv, Q. Li, R. Michalsky, A.A. Peterson, S. Sun, Active and selective conversion of CO_2 to CO on ultrathin Au nanowires, J. Am. Chem. Soc. 136 (2014) 16132–16135, doi:10.1021/ja5095099.
[50] J. Rosen, G.S. Hutchings, Q. Lu, S. Rivera, Y. Zhou, D.G. Vlachos, F. Jiao, Mechanistic insights into the electrochemical reduction of CO_2 to CO on nanostructured Ag surfaces, ACS Catal. 5 (2015) 4293–4299, doi:10.1021/acscatal.5b00840.
[51] L. Granda-Marulanda, A. Rendon-Calle, S. Builes, F. Illas, M.T.M. Koper, F. Calle-Vallejo, A semiempirical method to detect and correct DFT-based gas-phase errors and its application in electrocatalysis, ACS Catal 10 (2020) 6900–6907, doi:10.1021/acscatal.0c01075.
[52] M. Fields, X. Hong, J.K. Nørskov, K. Chan, Role of subsurface oxygen on Cu surfaces for CO_2 electrochemical reduction, J. Phys. Chem. C. 122 (2018) 16209–16215, doi:10.1021/acs.jpcc.8b04983.
[53] M. Gattrell, N. Gupta, A. Co, A review of the aqueous electrochemical reduction of CO_2 to hydrocarbons at copper, J. Electroanal. Chem. 594 (2006) 1–19, doi:10.1016/j.jelechem.2006.05.013.
[54] Y. Pang, J. Li, Z. Wang, C.-S. Tan, P.-L. Hsieh, T.-T. Zhuang, Z.-Q. Liang, C. Zou, X. Wang, P. De Luna, J.P. Edwards, Y. Xu, F. Li, C.-T. Dinh, M. Zhong, Y. Lou, D. Wu, L.-J. Chen, E.H. Sargent, D. Sinton, Efficient electrocatalytic conversion of carbon monoxide to propanol using fragmented copper, Nat. Catal. 2 (2019) 251–258, doi:10.1038/s41929-019-0225-7.
[55] R. Kortlever, J. Shen, K.J.P. Schouten, F. Calle-Vallejo, M.T.M. Koper, Catalysts and reaction pathways for the electrochemical reduction of carbon dioxide, J. Phys. Chem. Lett. 6 (2015) 4073–4082, doi:10.1021/acs.jpclett.5b01559.
[56] X. Chang, A. Malkani, X. Yang, B. Xu, Mechanistic insights into electroreductive C–C coupling between CO and Acetaldehyde into multicarbon products, J. Am. Chem. Soc. 142 (2020) 2975–2983, doi:10.1021/jacs.9b12817.
[57] X. Nie, M.R. Esopi, M.J. Janik, A. Asthagiri, Selectivity of CO_2 reduction on copper electrodes: the role of the kinetics of elementary steps, Angewandte Chemie International Edition 52 (2013) 2459–2462, doi:10.1002/anie.201208120.
[58] F. Calle-Vallejo, M.T.M. Koper, Accounting for bifurcating pathways in the screening for CO_2 reduction catalysts, ACS Catal. 7 (2017) 7345–7351, doi:10.1021/acscatal.7b02017.

3.3 Selectivity Map for the Late Stages of CO and CO_2 Reduction to C_2 Species on Cu Electrodes

Introduction Based on previous works,[51] the intermediate formed in the fifth proton-electron transfer of the C_2 pathway during CORR is $*CH_2CHO$. Depending on which of the two carbon atoms is hydrogenated, ethylene or acetaldehyde will be produced. Concretely, if the alpha carbon is hydrogenated, acetaldehyde ($*CH_2CHO + H^+ + e^- \rightarrow *CH_3CHO$) will be produced, which has been detected as a CORR intermediate on OD-Cu,[101] and shown to further reduce selectively to ethanol on Cu electrodes.[100,119] On the other hand, if the carbon atom of the carbonyl group is hydrogenated, adsorbed oxygen and ethylene will be formed ($*CH_2CHO + H^+ + e^- \rightarrow *O + C_2H_{4(g)}$). Note that this step involves both the hydrogenation of the carbon atom and the scission of the C-O bond. Previous studies have shown that the barrier for such scission is large,[120,121] indicating that adsorbed ethylene oxide might form at the surface ($*OCH_2CH_2$). Hence, electrochemical ethylene oxide reduction (EOR) can be regarded as part of the late stages of CO_2RR and CORR to ethylene on Cu electrodes.

Previous works by Schouten et. al. investigated this possibility.[119,122] They examined various candidate precursors to ethylene, such as glycolaldehyde, glyoxal, ethylene glycol, and ethylene oxide. They observed that only ethylene oxide was reduced to ethylene on polycrystalline Cu.[119] They also found that the EOR onset potential occurs earlier on Cu(100) than on Cu(111), indicating that EOR is more efficiently catalyzed by Cu(100).[122] This observation agrees with previous results for CO_2RR and CORR showing that ethylene forms on Cu(100) with lower onset potentials than on Cu(111).[89,105,122,123] Given that some intermediates are possibly shared but ethylene is usually more abundantly produced than ethanol during CO_2RR and CORR on Cu, it is important to understand what drives the selectivity of Cu catalysts toward specific C_2 molecules.

In this section, we investigate EOR on Cu electrodes by performing DFT calculations on Cu(111), Cu(100), and four non flat surfaces, namely, Cu(311), Cu(211), 4AD@Cu(100), and 4AD@Cu(111), hereon referred as defective surfaces. A side view of all the modelled surfaces is shown in Figure 17a. Moreover, in collaboration with our experimental colleagues of the National University of Singapore, the onset potentials for EOR on Cu(111), Cu(100), Cu(311), and Cu(211) single-crystal electrodes are determined. We then compare the obtained results with previous calculations of

acetaldehyde electroreduction (ARR) to build a selectivity map of the late stages of CO_2 and CO electroreduction to C_2 species on Cu electrodes.

This work led to the publication of a research article.[124] The manuscript is included at the end of this section. In the following pages, a summary of it is given. My contribution to the research article was: (a) Elaboration of the DFT calculations, (b) analysis of the computational results and making of the corresponding figures, and (c) writing a first draft of the manuscript. I was not involved in the making of the experiments. The supporting information for this article can be found in Appendix C. The optimized geometries were removed from this document to save space but can be found online at: https://doi.org/10.1002/anie.202014060.

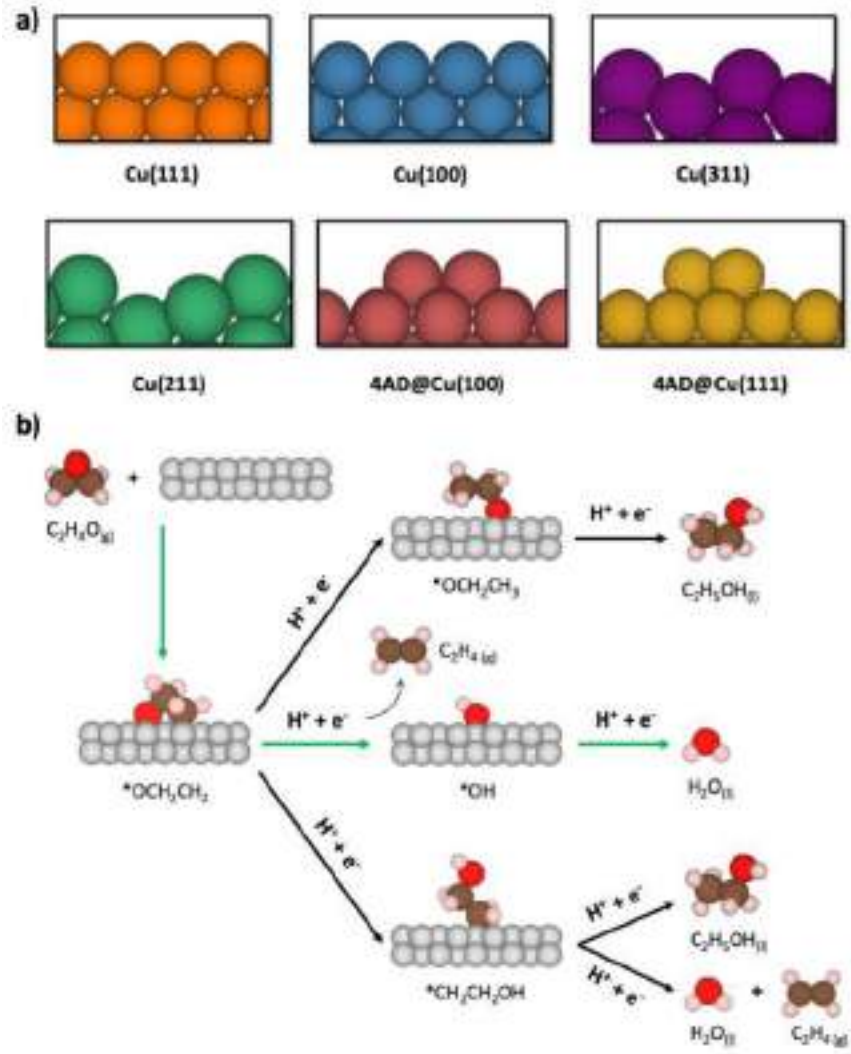

Figure 17. a) Side views of the surface models used in this work. b) Schematics of the different reaction pathways for ethylene oxide reduction to ethylene and ethanol on Cu electrodes. The first step is the chemisorption of ethylene oxide, whereas the other steps are electrochemical hydrogenations. The green arrows mark the lowest-energy pathway. Color code: Cu (gray), C (brown), O (red), H (pink). This figure corresponds to Figure 1 in reference 124 and is included here to facilitate the reading of this thesis.

Results The possible pathways through which EOR can produce ethylene ($C_2H_4O_{(g)}$ + $2H^+ + 2e^- \rightarrow C_2H_{4(g)} + H_2O_{(l)}$) or ethanol ($C_2H_4O_{(g)} + 2H^+ + 2e^- \rightarrow C_2H_5OH_{(l)}$) are shown in Figure 17b. We concluded that the most favorable pathway for all the studied surface sites is the one leading to ethylene via *OH, shown in green in Figure 17b. In such pathway, *OH is at least 0.2 eV more stable than the other two intermediates (*CH_2CH_2OH and *OCH_2CH_3). In addition, the first step is the adsorption of ethylene oxide, then *OH and ethylene are formed after the first proton-electron transfer, and finally *OH is reduced to $H_2O_{(l)}$ upon the second proton-electron transfer, such that the active sites is regenerated to start a new catalytic cycle.

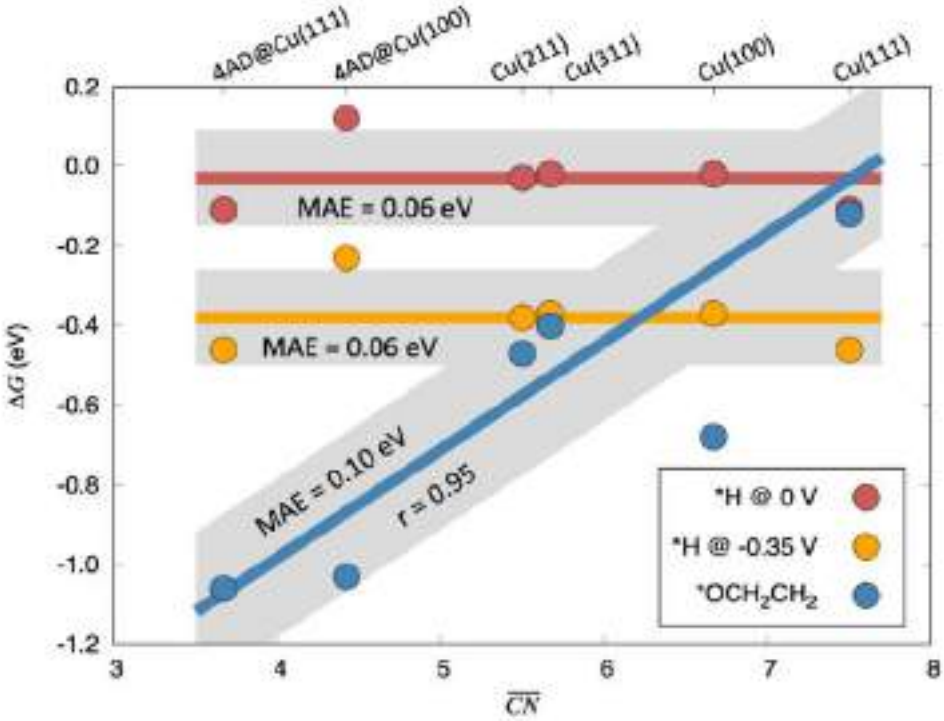

Figure 18. Free energies of adsorption of *OCH_2CH_2 (blue), *H at 0 V vs RHE (red, with respect to $H^+ + e^-$), and *H at -0.35 V vs RHE (orange), as a function of the generalized coordination number ($\overline{CN}$) of the active sites. -0.35 V vs RHE represents the least negative experimental onset potential in Figure 20. A linear regression for *OCH_2CH_2 along with the corresponding Pearson correlation coefficient is shown, without including Cu(100) in view of its known ensemble effects.[78,125] The red and orange lines are the arithmetic mean of the respective *H adsorption energies. A gray band of ± 2 MAE is provided around the lines. MAE: mean absolute error of the points with respect to the linear fit. This figure corresponds to Figure 2 in reference 124 and is included here to facilitate the reading of this thesis.

Competitive adsorption of *H, involved in the hydrogen evolution reaction (HER), could hinder the chemisorption of ethylene oxide. Hence, before we analyze the two electrochemical steps, a comparison between ethylene oxide and atomic hydrogen adsorption energies is pertinent. In Figure 18, these adsorption energies are plotted as a function of the generalized coordination number ($\overline{CN}$)[79,126] of the active sites. Their behavior is markedly different, since the adsorption energy of *H is potential-dependent, and only the adsorption energy of ethylene oxide displays structural sensitivity. Note that, at 0 V vs RHE, the adsorption energies of $*OCH_2CH_2$ and *H are comparable on Cu(111) terrace sites, consequently, Cu(111) will have a higher *H coverage than other Cu facets under experimental reaction conditions, since all the other surfaces adsorb ethylene oxide more strongly than *H at the two potentials analyzed in Figure 18. Moreover, since ethylene oxide requires binding to several surface atoms, its adsorption will likely be hindered by the high *H coverage on Cu(111).

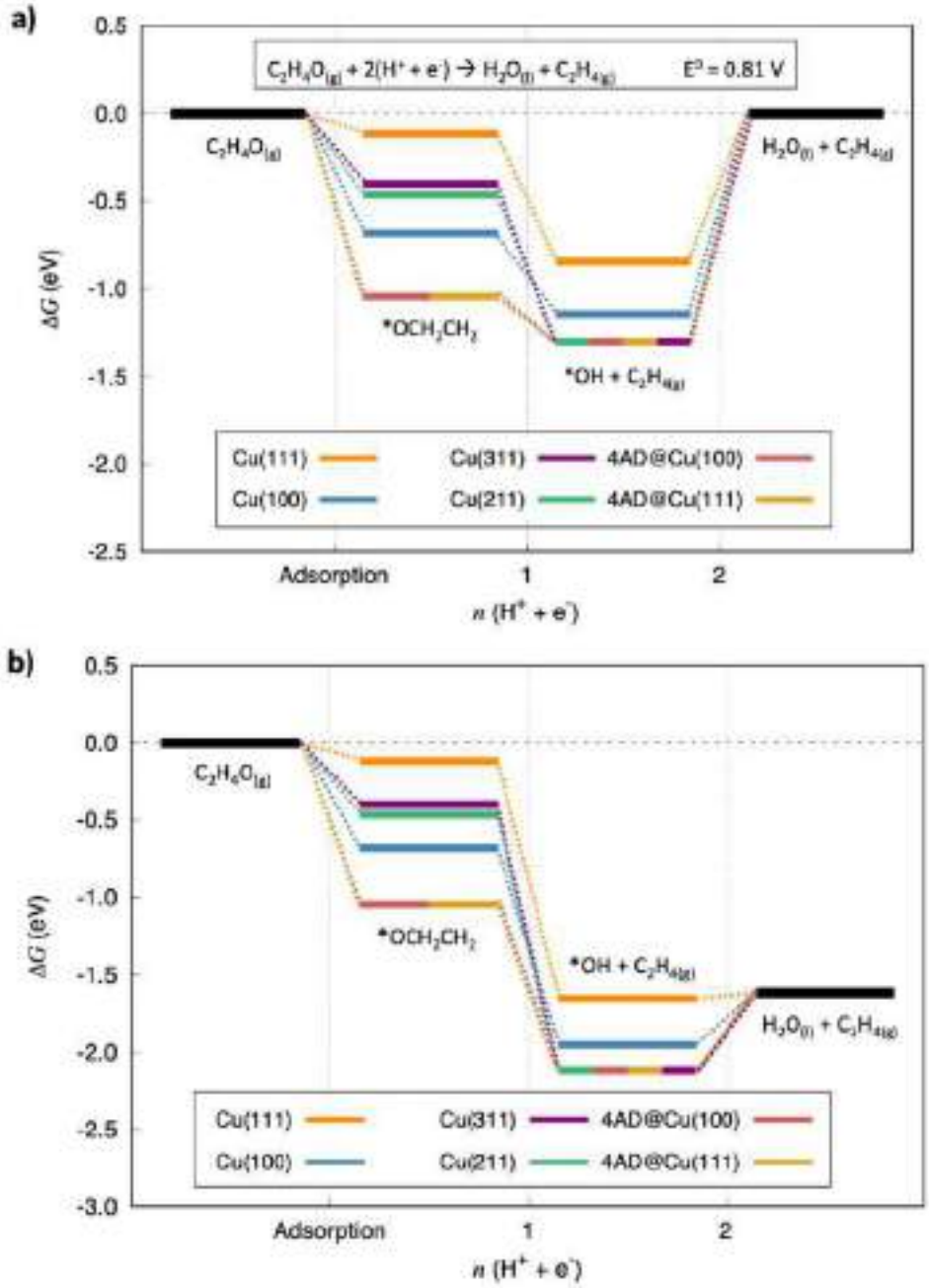

Figure 19. Free-energy diagrams for the lowest-energy pathways of ethylene oxide reduction to ethylene at a) the equilibrium potential (0.81 V vs RHE) and b) 0 V vs RHE. The free energies of the intermediates with respect to ethylene oxide, protons and electrons are given for Cu(111) (orange), Cu(100) (blue), Cu(311) (purple), Cu(211) (green), 4AD@Cu(100) (red), and 4AD@Cu(111) (yellow). This figure corresponds to Figure S9 in the supporting information of reference 124 and is included here to facilitate the reading of this thesis.

In Figure 19, the free-energy diagrams including the relative stability of each of the intermediates are shown for all the surfaces studied in this work. In panel a, the free energies are shown at the standard potential of the reaction, namely 0.81 V vs RHE. In panel b, the free energies are shown at 0 V vs RHE. At first glance, it can be noticed that

the potential-limiting step (PLS) is the same for all the different surfaces and corresponds to the second electrochemical step of the reaction. In Figure 20, we show a coordination-activity plot including the calculated onset potentials for each site correlated with its respective generalized coordination number. The top of the coordination-activity plot, found by extrapolating the blue line, is located at $\overline{CN}$ = 16.6. Since $\overline{CN}_{max}$ = 12 for an *fcc* crystal, neither the top nor the weak-binding side of the plot are accessible on Cu. Hence, we conclude that all Cu sites (also those not included in this work) share the same potential-limiting step, namely, the hydrogenation of *OH to form $H_2O_{(l)}$. Moreover, the experimental onset potentials from experiments are also included in Figure 20 as green squares. Note that, in those experiments, ethylene was the only EOR product detected, while ethanol was not observed, in agreement with the most favorable DFT-calculated pathway and its considerable energetic differences with respect to the pathways leading to ethanol. The experimental onset potentials are in agreement with those determined with DFT, except for Cu(111). Judging by the DFT-calculated onset potentials for the four defective surfaces (4AD@Cu(111), 4AD@Cu(100), Cu(211), and Cu(311)), which are all in the narrow range of -0.46 to -0.52 V vs RHE, we conclude that the discrepancy could stems from the fact that defects on the Cu(111) crystal, rather than the Cu(111) terraces themselves, catalyze the EOR. This is confirmed by the experimentally measured onset potentials for Cu(211) and Cu(311) of -0.50 and -0.45 V vs RHE, respectively. Note how Cu(111) and Cu(211) have an identical onset potential of -0.50 V vs RHE in experiments. Overall, Cu(100) produces the highest amount of ethylene from EOR among all the facets studied, followed by Cu(311), Cu(211), and lastly Cu(111). This finding highlights the importance of (100) facets for the EOR, indicating that square sites are key in the formation of ethylene rather than the defect sites, as postulated in previous works.[127-129]

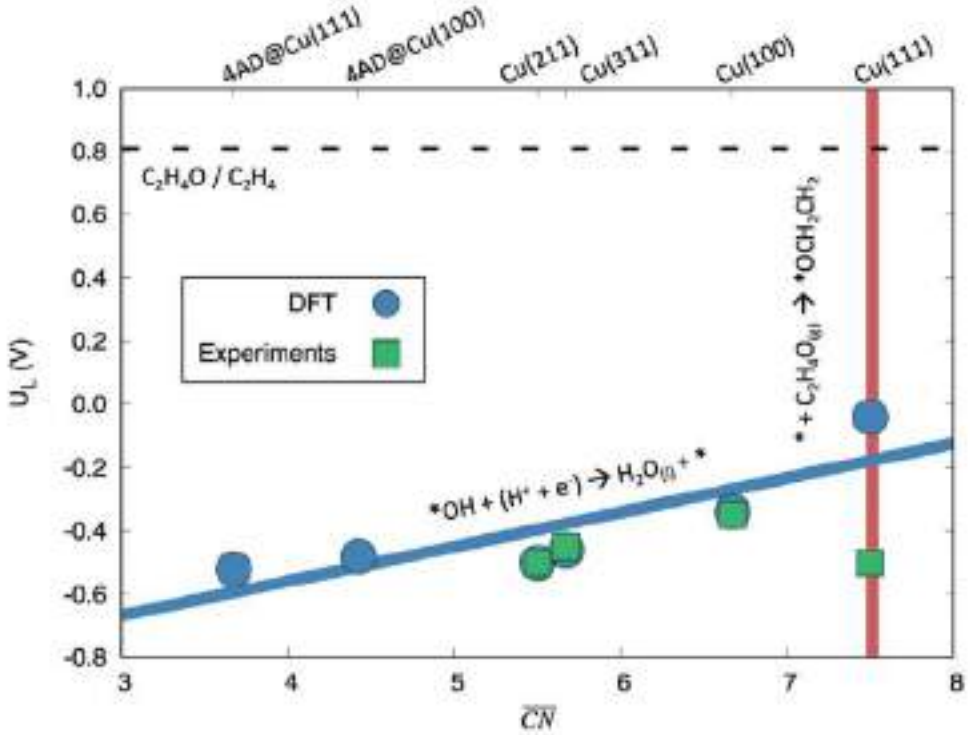

Figure 20. Coordination-activity plot for ethylene oxide reduction to ethylene. The calculated (blue) and measured (green) onset potentials are plotted as a function of generalized coordination numbers ($\overline{CN}$) for various electrodes. The dashed line is the equilibrium potential (0.81 V vs RHE) and the red line marks the point where *OCH_2CH_2 adsorbs more strongly than *H for surfaces with decreasing $\overline{CN}$. The large departure of the experimental datapoint for Cu(111) from the trends suggests that its actice sites are undercoordinated defects rather than terraces. This figure corresponds to panel a of Figure 3 in reference 124 and is included here to facilitate the reading of this thesis.

Finally, we compare our EOR results with previous ones from ARR.[100,119] Experimentally, ARR leads exclusively to ethanol ($CH_3CHO_{(l)} + 2H^+ + 2e^- \rightarrow C_2H_5OH_{(l)}$) and its equilibrium potential is 0.24 V vs RHE. In Figure 21, we provide a selectivity map of Cu sites for ARR, EOR, and HER. The map correlates the $\overline{CN}$ of the active sites to the preferred reaction products and limiting potentials (U_L). We identify highly uncoordinated sites ($\overline{CN} < 5.9$) as the active sites for ARR, moderately coordinated sites ($5.9 < \overline{CN} > 7.5$) as active toward EOR, and highly coordinated sites ($\overline{CN} > 7.5$) as inactive or selectively active toward the hydrogen evolution reaction (HER).

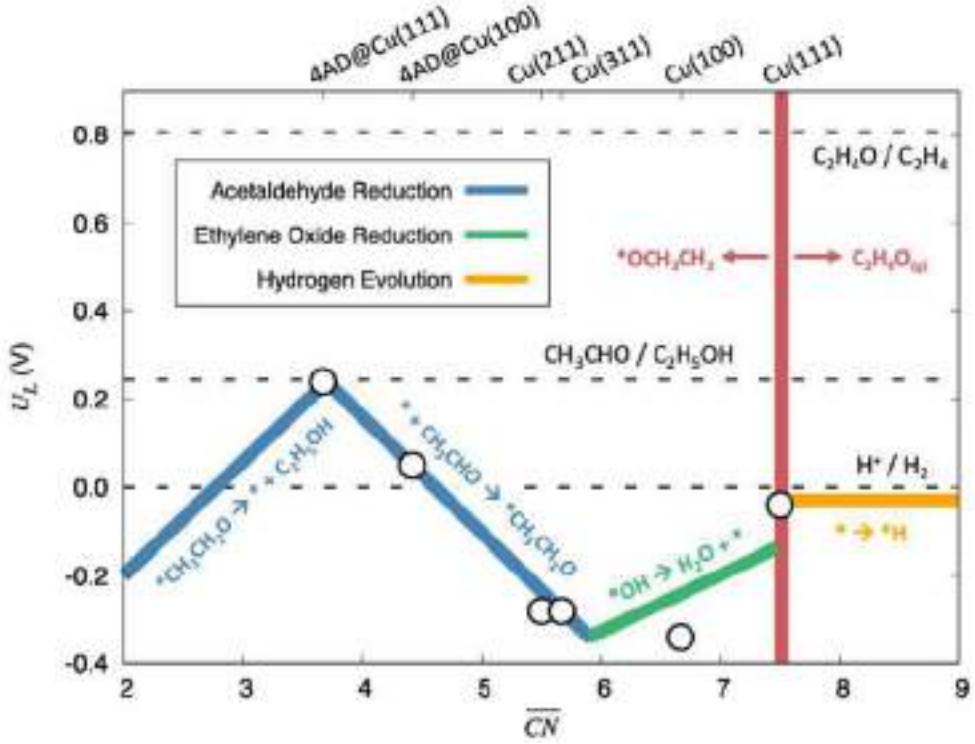

Figure 21. Selectivity map of the late stages of CO and CO_2 electroreduction on Cu electrodes. The calculated limiting potentials (U_L) are plotted as a function of the generalized coordination number ($\overline{CN}$) of the active sites. The marks on the upper *x*-axis show the studied active sites. To the left of the red line ($\overline{CN}$ = 7.5), the catalytic sites adsorb ethylene oxide more strongly than *H. The dashed lines mark the equilibrium potentials; the potential-limiting steps are written next to each line. This figure corresponds to panel a of Figure 4 in reference 124 and is included here to facilitate the reading of this thesis.

Conclusions These results, together with additional data and analyses shown in the research article below, lead to the following conclusions:

- The hydrogenation of *OH is the potential-limiting step of EOR on all the studied Cu surfaces.
- Cu(100) is the most efficient surface for catalyzing EOR, featuring an onset potential of -0.35 V vs RHE.
- Since the DFT-calculated EOR onset potentials of Cu(111) and Cu(211) were found to have an identical value of -0.50 V vs RHE but the experimental current density was smaller on the former, we conclude that only the defect sites on Cu(111) are active toward EOR.
- Highly uncoordinated sites ($\overline{CN}$ < 5.9) are the most active sites for ARR, sites featuring a $\overline{CN}$ between 5.9 and 7.5 are active toward EOR, and sites with a $\overline{CN}$ beyond 7.5 are selective to HER.

- The active sites for CO_2RR and CORR are different for each C_2 molecule. Product selectivity on Cu electrodes is dictated by the site-specific formation of either ethylene oxide or acetaldehyde.

CO_2 Reduction Reaction Hot Paper

How to cite: Angew. Chem. Int. Ed. 2021, 60, 10784–10790
International Edition: doi.org/10.1002/anie.202014060
German Edition: doi.org/10.1002/ange.202014060

Selectivity Map for the Late Stages of CO and CO_2 Reduction to C_2 Species on Copper Electrodes

Oriol Piqué[+], Qi Hang Low[+], Albertus D. Handoko, Boon Siang Yeo, and Federico Calle-Vallejo**

Abstract: *The electrochemical CO and CO_2 reduction reactions (CORR and CO_2RR) using copper catalysts and renewable electricity hold promise as a carbon-neutral route to produce commodity chemicals and fuels. However, the exact mechanisms and structure sensitivity of Cu electrodes toward C_2 products are still under debate. Herein, we investigate ethylene oxide reduction (EOR) as a proxy to the late stages of CORR to ethylene, and the results are compared to those of acetaldehyde reduction to ethanol. Density functional theory (DFT) calculations show that ethylene oxide undergoes ring opening before exclusively reducing to ethylene via *OH formation. Based on generalized coordination numbers ($\overline{CN}$), a selectivity map for the late stages of CORR and CO_2RR shows that sites with moderate coordination ($5.9 < \overline{CN} < 7.5$) are efficient for ethylene production, with pristine Cu(100) being more active than defective surfaces such as Cu(311). In contrast, kinks and edges are more active for ethanol production, while (111) terraces are relatively inert.*

Introduction

The electrochemical reduction of carbon monoxide and carbon dioxide (CORR and CO_2RR) using solar electricity has the potential to supply useful chemicals and liquid fuels sustainably while maintaining carbon neutrality.[1–3] Pioneering works from Hori and co-workers showed that copper is a unique catalyst capable of catalyzing the production of a variety of hydrocarbons and alcohols from CORR[4] and CO_2RR.[5] Interestingly, the relative abundance of certain products depends strongly on the catalyst's morphology and the applied potential. Specifically, methane tends to abound when Cu electrodes have hexagonal symmetry (e.g. pristine and stepped Cu(111)) (for the side view of different facets, see Figure 1a). On the other hand, electrodes with square symmetry, for example Cu(100), favor C_2 products such as ethylene and ethanol. Additionally, methane evolution commences at considerably more negative potentials than those required to form C_2 compounds.[6–9] Such dissimilar behavior indicates that the C_1 and C_2 reaction pathways are likely mediated by different species.

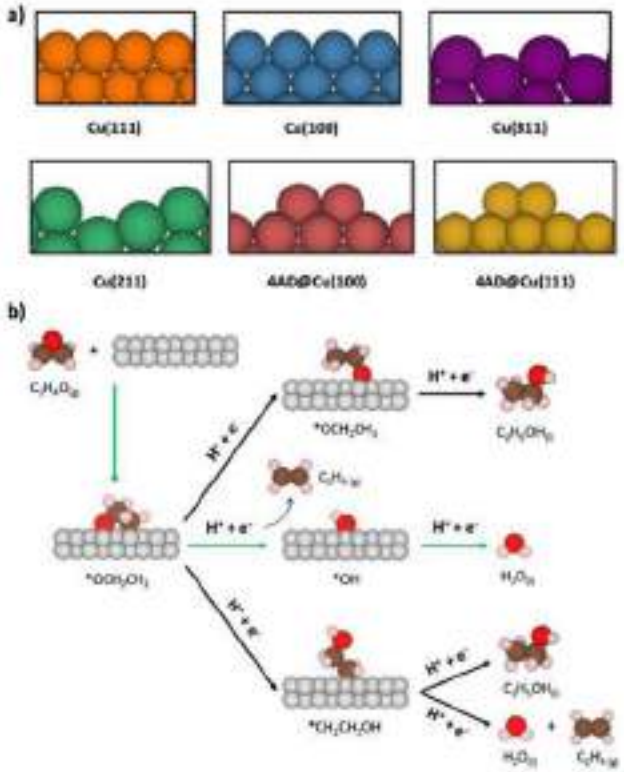

Figure 1. a) Side views of the surface models used in this work. b) Schematics of the different reaction pathways for ethylene oxide reduction to ethylene and ethanol on Cu electrodes. The first step is the chemisorption of ethylene oxide, whereas the other steps are electrochemical. The green arrows mark the lowest-energy pathway. Atom key: Cu (gray), C (brown), O (red), H (pink).

[*] O. Piqué[+], Dr. F. Calle-Vallejo
Departament de Ciència de Materials i Química Física & Institut de Química Teòrica i Computacional (IQTCUB)
Universitat de Barcelona
Martí i Franquès 1, 08028 Barcelona (Spain)
E-mail: f.calle.vallejo@ub.edu
Q. H. Low,[+] Prof. Dr. B. S. Yeo
Department of Chemistry, Faculty of Science, National University of Singapore, 3 Science Drive 3, Singapore 117543 (Singapore)
and
Solar Energy Research Institute of Singapore (SERIS)
National University of Singapore (NUS)
7 Engineering Drive 1, Building E3A, #06-01, Singapore 117574 (Singapore)
E-mail: chmyeos@nus.edu.sg
Dr. A. D. Handoko
Institute of Materials Research and Engineering
Agency for Science, Technology and Research (A*STAR)
2 Fusionopolis Way, Innovis, Singapore 138634 (Singapore)
[+] These authors contributed equally to this work.
Supporting information and the ORCID identification number(s) for the author(s) of this article can be found under: https://doi.org/10.1002/anie.202014060.

The C_2 pathways seem to proceed via several common intermediates, as evidenced by the experimental observation that the Faradaic efficiencies of ethylene and ethanol shift similarly when different alkaline cations are used in the electrolyte.[10] Ethylene and ethanol are also known to have identical or similar onset potentials,[11–13] which suggests that they share a common potential-limiting step. Further insight can be extracted from the pH independence in the standard hydrogen electrode (SHE) scale of the CORR to ethylene and ethanol.[4] This observation suggests that C–C bonds are made via *CO coupling through an electron transfer followed by a proton transfer.

Indeed, computational studies have indicated that during CORR on Cu(100) to C_2 species, the coupling of two *CO mediated by an electron transfer to form $*C_2O_2^-$ is potential-limiting.[14] Besides, ethylene and ethanol were found to share the same intermediates up to the fifth proton-electron transfer. The pathways to ethanol and ethylene then bifurcate, with the latter being the dominant product on that facet. To improve the selectivity toward acetaldehyde and ethanol, modified Cu catalysts such as oxide-derived Cu (OD-Cu)[15–18] or CuAg composites have been used.[19–22]

The intermediate formed upon the fifth proton-electron transfer in the C_2 pathway during CORR is $*CH_2CHO$. If the alpha carbon is hydrogenated, acetaldehyde (CH_3CHO) is produced. This molecule has been experimentally detected as a CORR intermediate on OD-Cu,[15] and shown to reduce selectively to ethanol on Cu electrodes.[23] If the carbonyl carbon is hydrogenated, adsorbed oxygen (*O) and gaseous ethylene are formed ($*CH_2CHO + H^+ + e^- \rightarrow *O + C_2H_{4(g)}$).[14] A closer inspection of the latter electrochemical step shows that it convolutes the hydrogenation of the carbonyl carbon and the scission of the C–O bond. As the kinetic barrier for the scission has been shown to be large,[24,25] $*OCH_2CH_2$ might form at the surface of the electrodes. Such an oxametallacycle species, known in gas-phase heterogeneous catalysis,[26] is a bidentate, adsorbed form of ethylene oxide in which the epoxy ring has opened (Figure 1b). Thus, the final stages of CO_2RR and CORR to ethylene on Cu may be regarded as the electrochemical ethylene oxide reduction (EOR).[7]

A previous study by Schouten et al. showed this possibility when they examined various possible precursors to ethylene, such as glyoxal, glycolaldehyde, ethylene glycol and ethylene oxide. They found that only ethylene oxide was reduced to ethylene on polycrystalline Cu.[7] Additionally, they showed that the onset potential for the EOR occurs earlier on Cu(100) as compared to Cu(111), which indicates that EOR is more efficiently catalyzed by Cu(100).[27] This observation agrees with the results for CO_2RR and CORR, where ethylene forms on Cu(100) with lower onset potentials than on Cu(111).[1,3,11,27] It has been hypothesized that the reason behind the lower EOR onset potential on Cu(100) is the enhanced stability of the oxametallacycle intermediate formed during ethylene oxide reduction on this surface.[7] Given that some intermediates are possibly shared, but ethylene is usually more abundantly produced than ethanol during CO_2RR and CORR,[28] it is critical to understand what drives the functionality of Cu catalysts toward specific C_2 molecules.

Herein, we provide a computational-experimental study of EOR to ethylene on copper electrodes. The onset potentials for ethylene formation were determined for Cu(111), Cu(100), Cu(211) and Cu(311) single-crystal electrodes. We find a quantitative correlation between the experimental and calculated onset potentials and the geometric structure of the active sites. Furthermore, we elucidate the most likely reaction pathway for EOR to ethylene, where *OH protonation is the potential-limiting step for all the studied surface sites. More importantly, we build a selectivity map for the late stages of CO_2RR and CORR to C_2 products at Cu surfaces. The map shows how the selectivity toward either ethanol or ethylene is modulated by the geometric structure of the active sites.

Results and Discussion

Active sites and reaction pathways. The pathways through which ethylene oxide may be reduced to either ethylene ($C_2H_4O_{(g)} + 2H^+ + 2e^- \rightarrow C_2H_{4(g)} + H_2O_{(l)}$) or ethanol ($C_2H_4O_{(g)} + 2H^+ + 2e^- \rightarrow C_2H_5OH_{(l)}$) via 2-electron catalytic processes are shown in Figure 1b. We computed the possible pathways on Cu(100), Cu(111) and four defective Cu surfaces, namely, Cu(211), Cu(311), 4AD@Cu(100) (four Cu adatoms on Cu(100)) and 4AD@Cu(111) (four Cu adatoms on Cu(111)). A depiction of the different active sites under study is shown in Figure 1a and the calculated adsorption energies are presented in the Supporting Information, Table S10. We concluded that the most favorable pathway in all cases is the one that leads to ethylene via *OH, as shown in Equations (1) to (3) (green pathway in Figure 1b). *OH is at least ≈ 0.2 eV more stable than the other two intermediates ($*OCH_2CH_2$ and $*CH_2CH_2OH$). Free-energy diagrams comparing these three pathways for each surface model are found in the Supporting Information, Figures S10–S15.

$$C_2H_4O_{(g)} + * \rightarrow *OCH_2CH_2 \quad (1)$$

$$*OCH_2CH_2 + H^+ + e^- \rightarrow *OH + C_2H_{4(g)} \quad (2)$$

$$*OH + H^+ + e^- \rightarrow H_2O_{(l)} \quad (3)$$

Where * is a free surface site. The first step is the chemisorption of ethylene oxide, which involves the opening of the epoxy ring and a bidentate adsorption configuration [Equation (1)]. Ethylene and *OH are formed after the first proton-electron transfer [Equation (2)]. Finally, *OH is reduced to $H_2O_{(l)}$ upon the second proton-electron transfer, such that the active site is free again to start a new catalytic cycle [Equation (3)].

It is important to note that if a given site does not bind ethylene oxide strong enough [Equation (1)], it would be difficult for EOR to proceed. This could occur as a result of the competitive adsorption of *H, which is involved in the hydrogen evolution reaction. Hence, before we analyze the electrochemical steps in Equations (2) and (3), a comparison

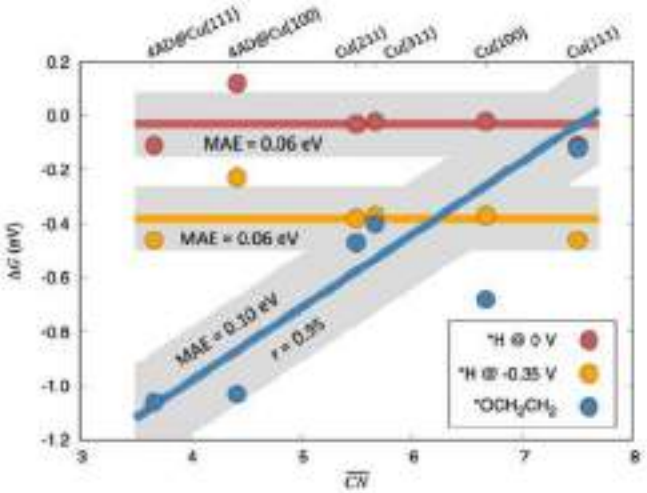

Figure 2. Adsorption free energies of $^*OCH_2CH_2$ (blue; see [Equation (1)]), *H at 0 V vs. RHE (red; with respect to $H^+ + e^-$), and *H at −0.35 V vs. RHE (orange), as a function of the generalized coordination number ($\overline{CN}$) of the active sites. −0.35 V vs. RHE represents the least negative experimental onset potential in Figure 3. A linear regression for $^*OCH_2CH_2$ along with the corresponding Pearson correlation coefficient is shown, without including Cu(100) in view of its known ensemble effects.[27,28] The red and orange lines are the arithmetic mean of the respective *H adsorption energies. A gray band of ±2 MAE is provided around the lines. MAE: mean absolute error of the points with respect to the linear fit.

between hydrogen and ethylene oxide adsorption is necessary. These adsorption energies are plotted in Figure 2 as a function of the generalized coordination number ($\overline{CN}$) of the active sites (for details on the assessment of $\overline{CN}$, see the Supporting Information, Section S7). *H and $^*OCH_2CH_2$ behave differently, as the adsorption energies of the former are potential dependent (Figure 2), and only the latter displays strong structural sensitivity. Interestingly, at 0 V vs. RHE, the adsorption energies of *H and $^*OCH_2CH_2$ are comparable on Cu(111) terrace sites. Consequently, Cu(111) will probably have a higher *H coverage as compared to the other Cu facets, since these latter surfaces adsorb $^*OCH_2CH_2$ more strongly than *H at the two potentials analyzed in Figure 2. As ethylene oxide adsorption requires binding to several surface atoms, its adsorption is likely hindered to a large extent by the high coverage of *H on Cu(111).

Furthermore, we note that the adsorption energy of ethylene oxide on Cu(100) noticeably departs from the linear trend in Figure 2. As $^*OCH_2CH_2$ is a bidentate adsorbate, this departure can be attributed to the ensemble effects originating from its double-bridge adsorption configuration (Supporting Information, Figure S8), in line with previous reports for similar bidentate adsorbates at square-symmetry sites.[29–31] According to those works, ensemble effects should generally be present on (100)-like sites but tend to be less pronounced at undercoordinated sites. Indeed, we observe this for 4AD@Cu(100) in Figure 2, whereby the deviation from the linear trend is within a confidence interval of 83% set at ±2 MAE (MAE: mean absolute error).

Experimental and computational onset potentials. The free-energy diagrams with the relative stability of the reaction intermediates in Equations (1) to (3) for the six surface models under study are shown in the Supporting Information, Figure S9. In Figure 3a, we condense these data in the form of a coordination-activity plot, in which the limiting potential for each site is correlated with its respective generalized coordination number. Extrapolating the blue line in Figure 3a, we find that the top of the coordination-activity plot for EOR on Cu is at $\overline{CN} = 16.6$. Since $\overline{CN}_{max} = 12$ for a face-centered cubic crystal, neither the top nor the weak-binding side of the EOR coordination-activity plot are accessible on Cu. Consequently, all Cu sites share the same potential-limiting step, namely *OH hydrogenation to H_2O [Equation (3)]. In Figure 3a, the

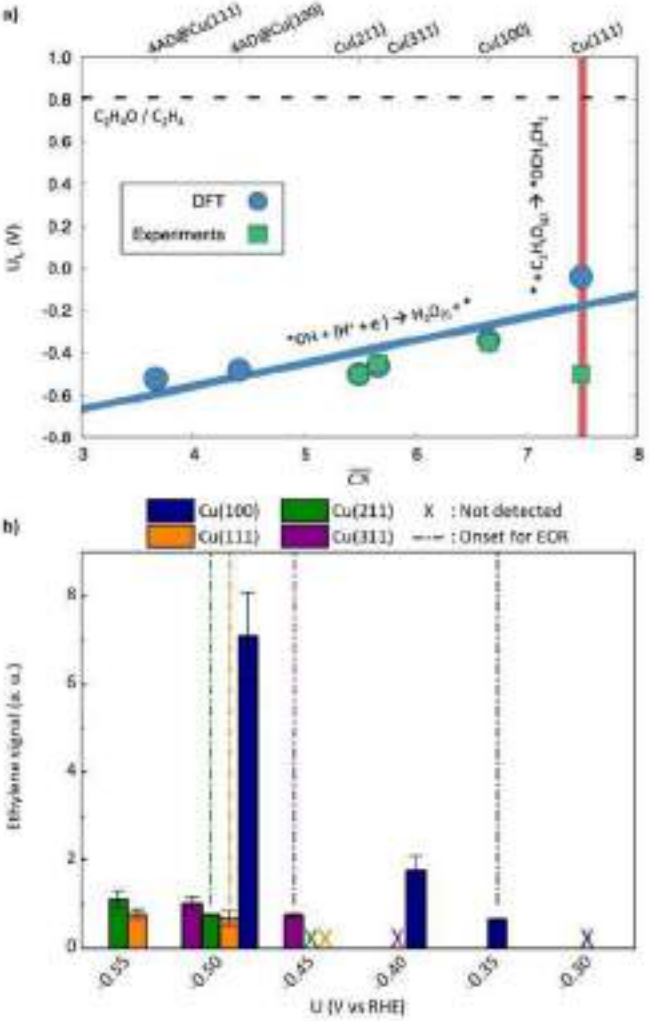

Figure 3. a) Coordination-activity plot for ethylene oxide reduction to ethylene. The calculated (blue) and measured (green) onset potentials are plotted as a function of generalized coordination numbers ($\overline{CN}$) for various electrodes. The dashed line is the equilibrium potential (0.81 V vs. RHE) and the red line marks the separating point, whereby $^*OCH_2CH_2$ adsorbs more strongly than *H for surfaces with $\overline{CN}$ on the left side of the red line. Detailed free-energy diagrams are provided in Figure S9. The large departure of experimental Cu(111) from the trends suggests that its activity originates from defect sites. b) Ethylene signals during EOR on Cu(111), Cu(100), Cu(311), and Cu(211) at different applied potentials in 0.1 M potassium phosphate buffer solution (pH 7). X marks the potentials where ethylene evolved from EOR was not generated in detectable amounts.

calculated onset potentials for Cu(111), Cu(100), Cu(311), Cu(211), 4AD@Cu(100) and 4AD@Cu(111) are, respectively, −0.04, −0.34, −0.46, −0.50, −0.48, and −0.52 V vs. RHE.

Next, we determined experimentally the onset potentials for EOR on copper surfaces (Figure 3; Table S2). The reaction was performed at pH 7 in 0.1 M potassium phosphate buffer electrolyte. An electrolyte with neutral pH was chosen to avoid the side reactions of ethylene oxide to give ethylene glycol and polyethylene glycol under acidic and basic conditions.[31] The surfaces of the Cu electrodes used were characterized using cyclic voltammetry and X-ray diffraction (XRD; Supporting Information, Figures S1–S4). During electrolysis, ethylene oxide (2.5 mol% in N_2 gas balance) was constantly bubbled into the cathodic compartment. The EOR products were analyzed by gas and liquid chromatography. Ethylene was the only EOR product detected, while ethanol was not observed, even at considerably more negative potentials such as −1.00 V vs. RHE (Supporting Information, Figure S6). This agrees with the DFT results, which show that ethylene is the more favorable EOR product (Figure 1; Table S10).

The experimental EOR onset potential was determined to be the potential at which the ethylene signal begins to be stronger than the baseline signal (Supporting Information, Section S3). The onset potentials for Cu(100) and Cu(111) were −0.35 and −0.50 V vs. RHE respectively (Figure 3b). Compared to the calculated values of −0.34 and −0.04 V vs. RHE on these two surfaces, it is striking that there is only good agreement for Cu(100). Judging by the simulated onset potentials for the four defective surfaces, which are all in the narrow range of −0.46 to −0.52 V vs. RHE (Figure 3a), we hypothesized that the discrepancy could stem from the fact that defects on the Cu(111) crystal, rather than the Cu(111) terraces themselves, catalyze the EOR.

We evaluated this hypothesis by performing EOR on Cu(211) and Cu(311). These two surfaces have, respectively 3-atom- and 2-atom-wide (111) terraces, separated by monoatomic (100) steps. The experimental EOR onset potential on Cu(211) was −0.50 V vs. RHE (Figure 3b), which is the same as that of Cu(111). For Cu(311), the EOR onset potential, which was at −0.45 V vs. RHE, is slightly earlier than that on Cu(211) and Cu(111) (Figure 3b). This result is in good agreement with the presence of a higher density of step edges on Cu(311), which can increase the amount of ethylene formed from EOR, thus resulting in a somewhat earlier EOR onset. Overall, similar onset potentials were determined for Cu(111), Cu(211) and Cu(311), which strongly indicates that the "discrepancy" between the experimental and calculated onset of EOR on Cu(111) was due to (i) the presence of defective sites such as step edges, and (ii) the inability of Cu(111) to sustain an appreciable coverage of adsorbed ethylene oxide.

In this context, the ethylene signals obtained on the different facets at −0.50 V vs. RHE are noteworthy (Figure 3b): Cu(100) produces the highest amount of ethylene from EOR amongst all the facets studied, followed by Cu(311), Cu(211) and lastly Cu(111). This finding further highlights the importance of (100) facets for the EOR to ethylene and the fact that (111) terraces are likely inactive. This conclusion goes along the same lines of previous studies for similar organic reactions, for example, acetone reduction, where (111) terraces were also observed to be rather inactive in view of the competition of the adsorbates with *H for adsorption sites at potentials close to 0 V vs. RHE.[23,32–34]

Implications for CO_2RR and CORR. Numerous works on roughened and oxide-derived Cu catalysts have invoked the presence of step and defect sites as being responsible for enhanced ethylene formation from CO_2RR or CORR.[35–37] Our experimental and computational onset potentials in Figure 3 suggest that this general claim is likely inaccurate, as Cu(311), which has abundant step edges, actually catalyzed ethylene formation less readily than Cu(100). This observation also concurs with a previous work on CuCl-derived Cu mesocrystals.[38] The surfaces of these catalysts, which consist mainly of various atomic steps and (100) terraces, reduced CO_2 to ethylene more selectively than Cu nanoparticles. Unlike the Cu mesocrystals, the Cu nanoparticle surfaces were found to have high-index planes composed of abundant steps, but with no terraces. The present results further stress the importance of Cu(100) terraces for the selective formation of ethylene during CO_2 electrolysis.

The standard potential for the reduction of ethylene oxide to ethylene is 0.81 V vs. RHE. Judging by the calculated and measured onset potentials, we conclude that, despite its apparent simplicity, the EOR on Cu requires large overpotentials of no less than ≈ 1.15 V. Knowing that Equation (3) ($^*OH + H^+ + e^- \rightarrow H_2O_{(l)}$) is the potential-limiting step for all the studied models (Figure 3a), destabilizing *OH would likely lead to lower overpotentials. Different strategies may be used to this end, for example, changing Cu-Cu distances via strain,[39–41] making use of different electrolytes so that cation and/or anion effects modify *OH adsorption energies,[42,43] using nonaqueous solvents such as acetonitrile to avoid the stabilization granted by *OH-H_2O hydrogen bonds,[44,45] and alloying a noble metal such as Pt with Cu, as the former binds *OH more weakly than the latter.

These strategies are also important for the CORR to ethylene on Cu(100), as the onset potential is around −0.40 V vs. RHE and is usually attributed to the formation of a *CO dimer.[1,14] Once the dimer formation is experimentally optimized so as to require a significantly less negative potential, the next target will probably be *OH, as its conversion to H_2O requires −0.35 V vs. RHE according to Figure 3. However, we note that the adsorption energies of *OH and $^*OCH_2CH_3$ are roughly correlated in a linear fashion (Supporting Information, Figure S7), such that if *OH adsorption is too weak, ethylene oxide might not adsorb on the surface of the catalyst.

Finally, we compare the EOR results to those of the acetaldehyde reduction reaction (ARR) on Cu.[23] Experimentally, the ARR leads exclusively to ethanol ($CH_3CHO_{(l)} + 2H^+ + 2e^- \rightarrow C_2H_5OH_{(l)}$) and its equilibrium potential is 0.24 V vs. RHE. On Cu electrodes, the ARR is limited by the formation of a monodentate, O-bound ethoxy intermediate ($^* + CH_3CHO_{(l)} + H^+ + e^- \rightarrow {}^*OCH_2CH_3$), the hydrogenation of which is usually downhill in energy to produce ethanol ($^*OCH_2CH_3 + H^+ + e^- \rightarrow {}^* + C_2H_5OH_{(l)}$).

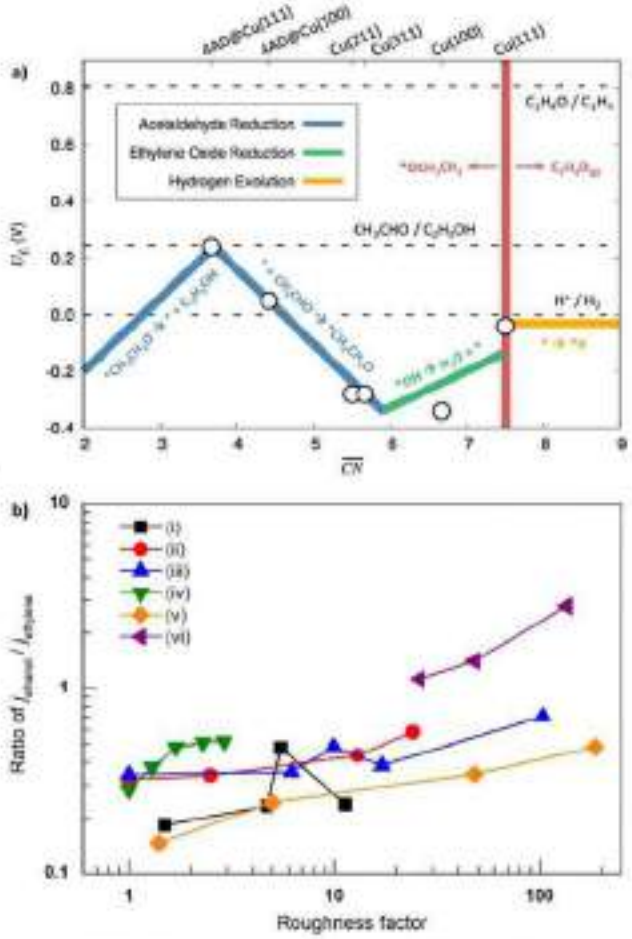

Figure 4. a) Selectivity map for the late stages of CO and CO_2 electroreduction on Cu electrodes. The calculated limiting potentials (U_L) are plotted as a function of the generalized coordination number ($\overline{CN}$) of the active sites. The upper *x*-axis shows the studied active sites. Acetaldehyde reduction (blue) to ethanol is most favorable on low-coordination sites ($\overline{CN} < 5.9$), whereas ethylene oxide reduction (green) to ethylene is most favorable on intermediate coordination sites ($5.9 < \overline{CN} < 7.5$). For $\overline{CN} > 7.5$, only hydrogen evolution (orange) proceeds. To the left of the red line ($\overline{CN} = 7.5$), the catalytic sites adsorb ethylene oxide more strongly than *H. The dashed lines mark the equilibrium potentials; the potential-limiting steps are provided in each case. b) Ratio of $j_{ethanol}/j_{ethylene}$ of various Cu catalysts plotted as a function of catalysts' roughness factor. All data used are obtained from previous CO_2RR (i–v) or CORR (vi) studies (Supporting Information, Section S4): (i) reference [13], (ii) reference [47], (iii) reference [48], (iv) reference [49], (v) reference [50], (vi) reference [16].

In Figure 4a, we provide a selectivity map of Cu sites for the ARR, EOR and hydrogen evolution reaction (HER). The map connects the generalized coordination of the active sites to the preferred reaction products and limiting potentials (U_L). ARR is thermodynamically more favorable than EOR at highly undercoordinated Cu sites ($\overline{CN} < 5.9$), which are characteristic of step edges and kinks. Note that this result helps to explain why in a recent work, Cu_3 and Cu_4 clusters could reduce CO_2 to ethanol with Faradaic efficiencies of up to 91%.[48] On the other hand, ethylene formation is favorable at moderate-coordination sites ($5.9 < \overline{CN} < 7.5$). Cu(100) terraces belong to this category and introducing undercoordinated defects onto facets within this category makes the limiting potential more negative. This is what we observed experimentally in Figure 3b. Finally, adsorbed hydrogen prevails over adsorbed ethylene oxide on Cu(111) terraces and more coordinated sites ($\overline{CN} > 7.5$), which renders them inactive for the EOR. This is also in line with the experimental results shown in Figure 3b.

We note in Figure 4a that the opposite slopes for the right leg of ARR (in blue, $3.7 < \overline{CN} < 5.9$) and the EOR region (in green, $5.9 < \overline{CN} < 7.5$) suggest that undercoordination has opposite effects on the catalytic activities. Interestingly, these observations coincide with many previous findings for CO_2RR and CORR: (I) Pristine Cu(100) is usually selective toward ethylene.[6,27,28] (II) A rougher Cu surface, which intuitively is a surface with more defective sites such as steps and kinks, will enhance the relative production of ethanol over ethylene as compared to smoother Cu surfaces (Figure 4b; Supporting Information, Section S4).[13,16,47,50] (III) Cu(111) produces small amounts of C_2 species.[6,27,28] In this order of ideas, electrodes where a multiplicity of sites coexist, will likely lead to a mix of C_2 products from CO_2RR and CORR.

Conclusion

Despite extensive research on CO_2RR and CORR, there is not yet a consensus about the complete reaction mechanism. Herein, we studied the ethylene oxide reduction (EOR) as a proxy for the late stages of the CO_2RR and CORR pathway to ethylene on Cu. *OH hydrogenation is the potential-limiting step in all studied cases, and the most efficient surface for EOR is Cu(100), with an onset potential of −0.35 V vs. RHE. The EOR onsets for Cu(111) and Cu(211) were identical at −0.50 V vs. RHE, but the measured current densities were smaller on the former, suggesting that only defect sites on Cu(111) are active.

Comparing the acetaldehyde reduction reaction (ARR) with EOR on Cu, we conclude that the former is favored at highly undercoordinated sites ($\overline{CN} < 5.9$, typical of step edges and kinks), the latter is preferred at moderately undercoordinated sites ($5.9 < \overline{CN} < 7.5$, for example, Cu(100)), and hydrogen adsorption precludes ethylene oxide reduction on Cu(111) and more coordinated sites ($\overline{CN} > 7.5$).

In broader terms, our findings indicate that the most active sites for CO_2RR and CORR are different for each C_2 product. Cu(100) terraces favor ethylene formation, while steps, kinks and akin undercoordinated defects favor ethanol evolution. As the EOR and the ARR lead exclusively to ethylene and ethanol, respectively, we conclude that the lack of CO_2RR product selectivity on Cu stems from surface inhomogeneities and is dictated by the site-specific formation of either $*OCH_2CH_3$ or CH_3CHO.

Acknowledgements

F.C.-V. acknowledges funding from Spanish MICIUN RTI2018-095460-B-I00, RYC-2015-18996 and María de

Maeztu MDM-2017-0767 grants, and partly by Generalitat de Catalunya 2017SGR13. O.P. thanks the Spanish MICIUN for a PhD grant (PRE2018-083811). We thank Red Española de Supercomputación (RES) for supercomputing time at SCAYLE (projects QS-2019-3-0018, QS-2019-2-0023, and QCM-2019-1-0034), MareNostrum (project QS-2020-1-0012), and CENITS (project QS-2020-2-0021). The use of supercomputing facilities at SURFsara was sponsored by NWO Physical Sciences, with financial support by NWO. Q.H.L. and B.S.Y. acknowledge funding from the National University of Singapore (R-143-000-B52-114 and R-143-000-A64-114), National University of Singapore Flagship Green Energy Program (R-143-000-A55-733 and R-143-000-A55-646), and the Solar Energy Research Institute of Singapore (SERIS).

Conflict of interest

The authors declare no conflict of interest.

Keywords: coordination-activity plot · copper · density functional calculations · electrocatalysis · ethylene oxide reduction

[1] S. Nitopi, E. Bertheussen, S. B. Scott, X. Liu, A. K. Engstfeld, S. Horch, B. Seger, I. E. L. Stephens, K. Chan, C. Hahn, J. K. Nørskov, T. F. Jaramillo, I. Chorkendorff, *Chem. Rev.* **2019**, *119*, 7610 – 7672.
[2] O. S. Bushuyev, P. D. Luna, C. T. Dinh, L. Tao, G. Saur, J. van de Lagemaat, S. O. Kelley, E. H. Sargent, *Joule* **2018**, *2*, 825 – 832.
[3] Y. Y. Birdja, E. Pérez-Gallent, M. C. Figueiredo, A. J. Gottle, F. Calle-Vallejo, M. T. M. Koper, *Nat. Energy* **2019**, *4*, 732 – 745.
[4] Y. Hori, R. Takahashi, Y. Yoshinami, A. Murata, *J. Phys. Chem. B* **1997**, *101*, 7075 – 7081.
[5] Y. Hori, H. Wakebe, T. Tsukamoto, O. Koga, *Electrochim. Acta* **1994**, *39*, 1833 – 1839.
[6] K. J. P. Schouten, Z. Qin, E. Pérez Gallent, M. T. M. Koper, *J. Am. Chem. Soc.* **2012**, *134*, 9864 – 9867.
[7] K. J. P. Schouten, Y. Kwon, C. J. M. van der Ham, Z. Qin, M. T. M. Koper, *Chem. Sci.* **2011**, *2*, 1902 – 1909.
[8] G. L. De Gregorio, T. Burdyny, A. Loiudice, P. Iyengar, W. A. Smith, R. Buonsanti, *ACS Catal.* **2020**, *10*, 4854 – 4862.
[9] Y. Huang, A. D. Handoko, P. Hirunsit, B. S. Yeo, *ACS Catal.* **2017**, *7*, 1749 – 1756.
[10] A. Murata, Y. Hori, *Bull. Chem. Soc. Jpn.* **1991**, *64*, 123 – 127.
[11] E. Pérez-Gallent, G. Marcandalli, M. C. Figueiredo, F. Calle-Vallejo, M. T. M. Koper, *J. Am. Chem. Soc.* **2017**, *139*, 16412 – 16419.
[12] K. P. Kuhl, E. R. Cave, D. N. Abram, T. F. Jaramillo, *Energy Environ. Sci.* **2012**, *5*, 7050 – 7059.
[13] D. Ren, Y. Deng, A. D. Handoko, C. S. Chen, S. Malkhandi, B. S. Yeo, *ACS Catal.* **2015**, *5*, 2814 – 2821.
[14] F. Calle-Vallejo, M. T. M. Koper, *Angew. Chem. Int. Ed.* **2013**, *52*, 7282 – 7285; *Angew. Chem.* **2013**, *125*, 7423 – 7426.
[15] E. Bertheussen, A. Verdaguer-Casadevall, D. Ravasio, J. H. Montoya, D. B. Trimarco, C. Roy, S. Meier, J. Wendland, J. K. Nørskov, I. E. L. Stephens, I. Chorkendorff, *Angew. Chem. Int. Ed.* **2016**, *55*, 1450 – 1454; *Angew. Chem.* **2016**, *128*, 1472 – 1476.
[16] C. W. Li, J. Ciston, M. W. Kanan, *Nature* **2014**, *508*, 504 – 507.
[17] Y. Lum, J. W. Ager, *Nat. Catal.* **2019**, *2*, 86 – 93.
[18] O. Piqué, F. Viñes, F. Illas, F. Calle-Vallejo, *ACS Catal.* **2020**, *10*, 10488 – 10494.
[19] L. R. L. Ting, O. Piqué, S. Y. Lim, M. Tanhaei, F. Calle-Vallejo, B. S. Yeo, *ACS Catal.* **2020**, *10*, 4059 – 4069.
[20] E. L. Clark, C. Hahn, T. F. Jaramillo, A. T. Bell, *J. Am. Chem. Soc.* **2017**, *139*, 15848 – 15857.
[21] L. Wang, D. C. Higgins, Y. Ji, C. G. Morales-Guio, K. Chan, C. Hahn, T. F. Jaramillo, *Proc. Natl. Acad. Sci. USA* **2020**, *117*, 12572 – 12575.
[22] D. Higgins, A. T. Landers, Y. Ji, S. Nitopi, C. G. Morales-Guio, L. Wang, K. Chan, C. Hahn, T. F. Jaramillo, *ACS Energy Lett.* **2018**, *3*, 2947 – 2955.
[23] I. Ledezma-Yanez, E. P. Gallent, M. T. M. Koper, F. Calle-Vallejo, *Catal. Today* **2016**, *262*, 90 – 94.
[24] W. Luo, X. Nie, M. J. Janik, A. Asthagiri, *ACS Catal.* **2016**, *6*, 219 – 229.
[25] D. Torres, N. Lopez, F. Illas, R. M. Lambert, *J. Am. Chem. Soc.* **2005**, *127*, 10774 – 10775.
[26] S. Linic, M. A. Barteau, *J. Am. Chem. Soc.* **2002**, *124*, 310 – 317.
[27] K. J. P. Schouten, E. Pérez Gallent, M. T. M. Koper, *ACS Catal.* **2013**, *3*, 1292 – 1295.
[28] Y. Hori, I. Takahashi, O. Koga, N. Hoshi, *J. Mol. Catal. Chem.* **2003**, *199*, 39 – 47.
[29] H. Li, F. Calle-Vallejo, M. J. Kolb, Y. Kwon, Y. Li, M. T. M. Koper, *J. Am. Chem. Soc.* **2013**, *135*, 14329 – 14338.
[30] H. Li, Y. Li, M. T. M. Koper, F. Calle-Vallejo, *J. Am. Chem. Soc.* **2014**, *136*, 15694 – 15701.
[31] G. A. Melhem, A. Gianetto, M. E. Levin, H. G. Fisher, S. Chippett, S. K. Singh, P. I. Chipman, *Process Saf. Prog.* **2001**, *20*, 231 – 246.
[32] C. J. Bondue, F. Calle-Vallejo, M. C. Figueiredo, M. T. M. Koper, *Nat. Catal.* **2019**, *2*, 243 – 250.
[33] Y.-J. Zhang, V. Sethuraman, R. Michalsky, A. A. Peterson, *ACS Catal.* **2014**, *4*, 3742 – 3748.
[34] Z. P. Jovanov, H. A. Hansen, A. S. Varela, P. Malacrida, A. A. Peterson, J. K. Nørskov, I. E. L. Stephens, I. Chorkendorff, *J. Catal.* **2016**, *343*, 215 – 231.
[35] Y. Hori, I. Takahashi, O. Koga, N. Hoshi, *J. Phys. Chem. B* **2002**, *106*, 15 – 17.
[36] W. Tang, A. A. Peterson, A. S. Varela, Z. P. Jovanov, L. Bech, W. J. Durand, S. Dahl, J. K. Nørskov, I. Chorkendorff, *Phys. Chem. Chem. Phys.* **2012**, *14*, 76 – 81.
[37] R. Kas, R. Kortlever, A. Milbrat, M. T. M. Koper, G. Mul, J. Baltrusaitis, *Phys. Chem. Chem. Phys.* **2014**, *16*, 12194 – 12201.
[38] C. S. Chen, A. D. Handoko, J. H. Wan, L. Ma, D. Ren, B. S. Yeo, *Catal. Sci. Technol.* **2015**, *5*, 161 – 168.
[39] F. Calle-Vallejo, A. S. Bandarenka, *ChemSusChem* **2018**, *11*, 1824 – 1828.
[40] A. Khorshidi, J. Violet, J. Hashemi, A. A. Peterson, *Nat. Catal.* **2018**, *1*, 263 – 268.
[41] M. Escudero-Escribano, P. Malacrida, M. H. Hansen, U. G. Vej-Hansen, A. Velázquez-Palenzuela, V. Tripkovic, J. Schiøtz, J. Rossmeisl, I. E. L. Stephens, I. Chorkendorff, *Science* **2016**, *352*, 73 – 76.
[42] B. Garlyyev, S. Xue, M. D. Pohl, D. Reinisch, A. S. Bandarenka, *ACS Omega* **2018**, *3*, 15325 – 15331.
[43] K. Holst-Olesen, M. Reda, H. A. Hansen, T. Vegge, M. Arenz, *ACS Catal.* **2018**, *8*, 7104 – 7112.
[44] A. Fortunelli, W. A. Goddard, Y. Sha, T. H. Yu, L. Sementa, G. Barcaro, O. Andreussi, *Angew. Chem. Int. Ed.* **2014**, *53*, 6669 – 6672; *Angew. Chem.* **2014**, *126*, 6787 – 6790.
[45] F. Calle-Vallejo, A. Krabbe, J. M. García-Lastra, *Chem. Sci.* **2017**, *8*, 124 – 130.
[46] H. Xu, D. Rebollar, H. He, L. Chong, Y. Liu, C. Liu, C.-J. Sun, T. Li, J. V. Muntean, R. E. Winans, D.-J. Liu, T. Xu, *Nat. Energy* **2020**, *5*, 623 – 632.

[47] D. Ren, N. T. Wong, A. D. Handoko, Y. Huang, B. S. Yeo, *J. Phys. Chem. Lett.* **2016**, *7*, 20–24.
[48] Y. Lum, B. Yue, P. Lobaccaro, A. T. Bell, J. W. Ager, *J. Phys. Chem. C* **2017**, *121*, 14191–14203.
[49] Y. Kwon, Y. Lum, E. L. Clark, J. W. Ager, A. T. Bell, *ChemElectroChem* **2016**, *3*, 1012–1019.
[50] D. Ren, J. Fong, B. S. Yeo, *Nat. Commun.* **2018**, *9*, 925.

Manuscript received: October 20, 2020
Revised manuscript received: January 16, 2021
Accepted manuscript online: February 1, 2021
Version of record online: April 1, 2021

3.4 Enhancing CO_2 Electroreduction to Ethanol on Copper–Silver Composites by Opening an Alternative Catalytic Pathway

Introduction As described in the previous sections, the rational control of the catalytic selectivity of CO_2RR and CORR is a central question in electrocatalysis. For instance, the addition of a CO-producing co-catalyst such as Zn or Ag to Cu electrodes helps in inclining the latter's CO_2RR selectivity toward C_2 products.[130-137] For CuAg systems, the enhancement has been attributed to the suppression of the competing hydrogen evolution reaction,[132,133] optimized binding of reaction intermediates such as *CO,[135,138] and increased surface population of *CO intermediates on the catalysts.[134,136,137] Moreover, experimental observations are often conflicting: some works showed an enhancement of the Faradaic efficiencies of both ethylene and ethanol,[139] some showed enhancements only for ethylene,[134,136] and others suppressed ethylene production while improving ethanol selectivity.[131,138] These discrepancies suggest that the atomic-scale configuration of these bimetallic catalysts strongly determines their CO_2RR product distribution and call for mechanistic studies to gain a deeper understanding of CO_2RR on CuAg systems.

Herein, we quantified the CO_2RR activity and selectivity of a series of CuAg composite catalysts containing Ag particles and OD-Cu nanowires (OD-Cu NW), again in collaboration with our experimental colleagues at the National University of Singapore. We assessed the impact of increasing the local amount of CO on ethylene and ethanol production during CO_2RR and complemented the analysis with DFT calculations.

This work led to the publication of a research article.[140] The manuscript is included at the end of this section. In the following pages, a summary of it is given. My contribution to the research article was: (a) Elaboration of the DFT calculations, (b) analysis of the computational results and making of the corresponding figures, and (c) collaboration in the writing of the manuscript. I was not involved in the making of the experiments. The supporting information for this article can be found in Appendix D. The optimized geometries were removed from this document to save space but can be found online at: https://doi.org/10.1021/acscatal.9b05319.

Results Experimental measurements of the CO_2RR activities of OD-Cu NW, Ag 20 nm particles (Ag-20), and a mixed catalyst containing OD-Cu NW and Ag-20 particles with an Ag/Cu molar ratio of 20 ($Cu(Ag\text{-}20)_{20}$), were evaluated. Note that, as determined by

means of different characterization techniques, the Cu and Ag phases in CuAg composites are segregated, and do not modify each other electronically. The results show that more C_2 molecules were produced from the Cu(Ag-20)$_{20}$ catalyst compared to OD-Cu NW. It is also observed by performing experiments on composites with Ag/Cu molar ratios of 5, 9, and 15, that increasing the Ag/Cu ratio improves the amount of C_2 molecules produced. Ethanol featured the most pronounced enhancement, 8 times larger than for ethylene, suggesting that ethanol evolution is more sensitive to the presence of the CO molecules produced at Ag particles as compared with ethylene production. Moreover, further experiments involving bigger Ag particles showed that ethanol evolution was significantly increased with Ag surface area, while ethylene production did not show a sizable increase.

To understand in better detail the working principle of CuAg catalysts, we performed DFT calculations on model systems. We divided the entire CO_2RR to ethanol into three separate parts. First, we considered the electroreduction of 2 CO_2 molecules to 2*CO. This is followed by the reduction of 2*CO to *CHCO. Finally, we close the analysis with the reduction of *CHCO to ethanol.

Computationally, we first inspected the thermodynamic stability of CuAg bulk alloys with different copper/silver proportions. Alloys of CuAu were also investigated as a control system. As shown in Figure 22, the formation energies for the CuAu alloys are negative for all the considered proportions, in line with previous studies.[141] On the other hand, the alloy formation energies are positive for all the studied proportions of CuAg alloys. Hence, we propose that Cu and Ag likely exist as separated phases in the catalyst, as also observed in the characterization results of our CuAg composite catalyst.

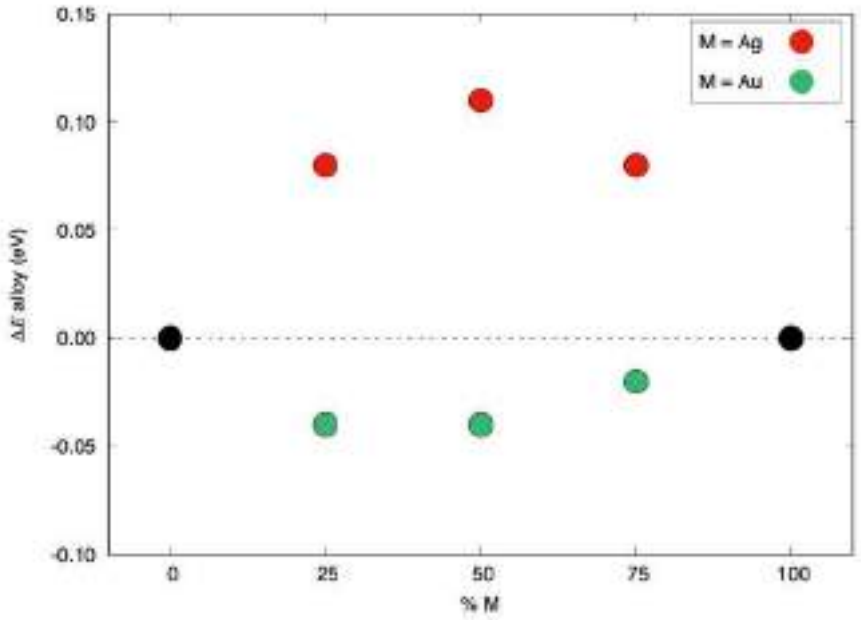

Figure 22. DFT-calculated alloy formation energies versus the % of M in CuM alloys. M = Au (green), Ag (red). This figure corresponds to Figure S11 in the supporting information of reference 140 and is included here to facilitate the reading of this thesis.

CO_2RR to CO was studied on Cu(111) (copper's most stable surface termination), a Ag cluster on top of Cu(111) (named Ag@Cu), and Cu(211). As seen in the top panel of Figure 23, the desorption of *CO to CO(g) is not favorable on Cu(111) and Cu(211), hence, *CO will further reduce to *CH_x species at negative enough potentials, eventually leading to CH_4.[116] On the other hand, *CO at Ag@Cu sites is so weakly adsorbed that it cannot undergo further reduction. Instead, it will either diffuse into the solution or migrate to neighboring Cu sites. Concretely, *CO to CO(g) is stabilized by 0.11 eV upon desorption from Ag, whereas it is stabilized by 0.39 eV when migrating to the Cu(111) surface. The kinetic barrier for the diffusion of *CO from the Ag cluster to Cu(111) is of 0.17 eV only, which is easily surmountable at room temperature (surmountable barriers at 298.15 K are usually below 0.75 eV).[123] Cu(211) step-edge sites are probably covered by reaction intermediates because of their undercoordination. However, weakly adsorbing Cu(111) sites coverage will remain low when there is no excess *CO. Thus, we hypothesize that ethanol evolves from Cu(111) sites near Ag particles.

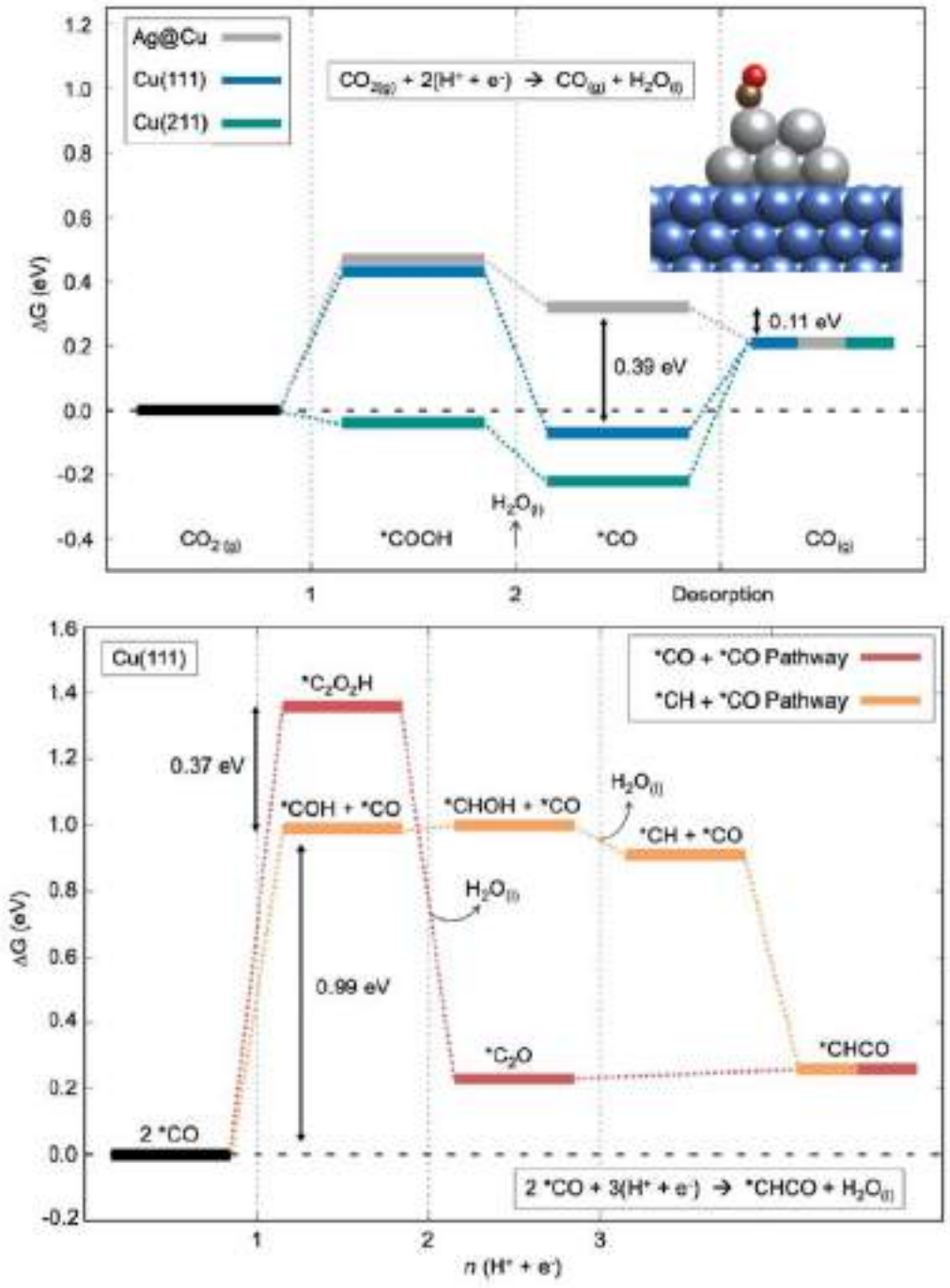

Figure 23. Top: Free-energy diagram of $CO_{2(g)}$ electroreduction to $CO_{(g)}$ on Cu(111) (blue), Cu(211) (cyan), and Ag@Cu (gray), which is a Ag cluster on top of a Cu(111) slab. All energies are referenced to $CO_{2(g)}$ and proton-electron pairs. Inset: CO adsorbed on the Ag@Cu cluster; Cu, Ag, C, and O atoms are shown in blue, gray, brown, and red, respectively. Bottom: Free-energy diagram on Cu(111) featuring two different C-C coupling pathways to *CHCO from 2*CO. In red, the *CO dimerization pathway. In orange, the energetics of the *CH + *CO pathway. All energies are referenced to 2*CO adsorbed on Cu(111) and proton-electron pairs. This figure corresponds to Figure 4 in reference 140 and is included here to facilitate the reading of this thesis.

As seen in the bottom panel of Figure 23, the reduction of 2*CO to C_2 species can proceed in two different ways, trough the conventional *CO dimerization pathway or via the coupling of *CO with CH_x species. To determine which species are able to couple with *CO, we calculated several coupling barriers on Cu(111) through both Langmuir-Hinshelwood (L-H) and Eley-Rideal (E-R) routes. The lower barriers are those featuring a L-H coupling between *CH and CO or *CH_2 and *CO, with values of 0.70 and 0.71 eV, respectively. The bottom panel of Figure 23 shows that the *CH + *CO coupling pathway is more favorable than *CO dimerization on Cu(111) by 0.37 eV. As concluded in previous sections, *CO dimerization energetics on Cu(111) are prohibitive.

Finally, we studied the further reduction of *CHCO species. In the top panel of Figure 24, the most favorable reduction pathway to ethanol is shown in green. The atomic structure of the intermediates involved in the most favorable pathway is depicted in the bottom panel of Figure 24. In Figure 25, we show all the pathways investigated for the formation of ethanol and ethylene from *CHCO, also including *CH_2CO and *CH_3CO. Further reduction of *CH_2CO and *CH_3CO also resulted in favorable ethanol formation. Regardless of whether *CHCO or *CH_2CO is the result of the coupling step (or even *CH_3CO), the pathways always incline toward ethanol instead of ethylene. This leads to a simple conclusion: once *CO + *CH_x coupling takes place on CuAg composite catalysts, ethanol is selectively produced. This is consistent with the experimental findings, where ethanol production is enhanced when CO availability increases. In summary, these results show that an alternative pathway to *CO dimerization is opened that produces ethanol selectively in the presence of excess *CO on the otherwise inert Cu(111) terraces.

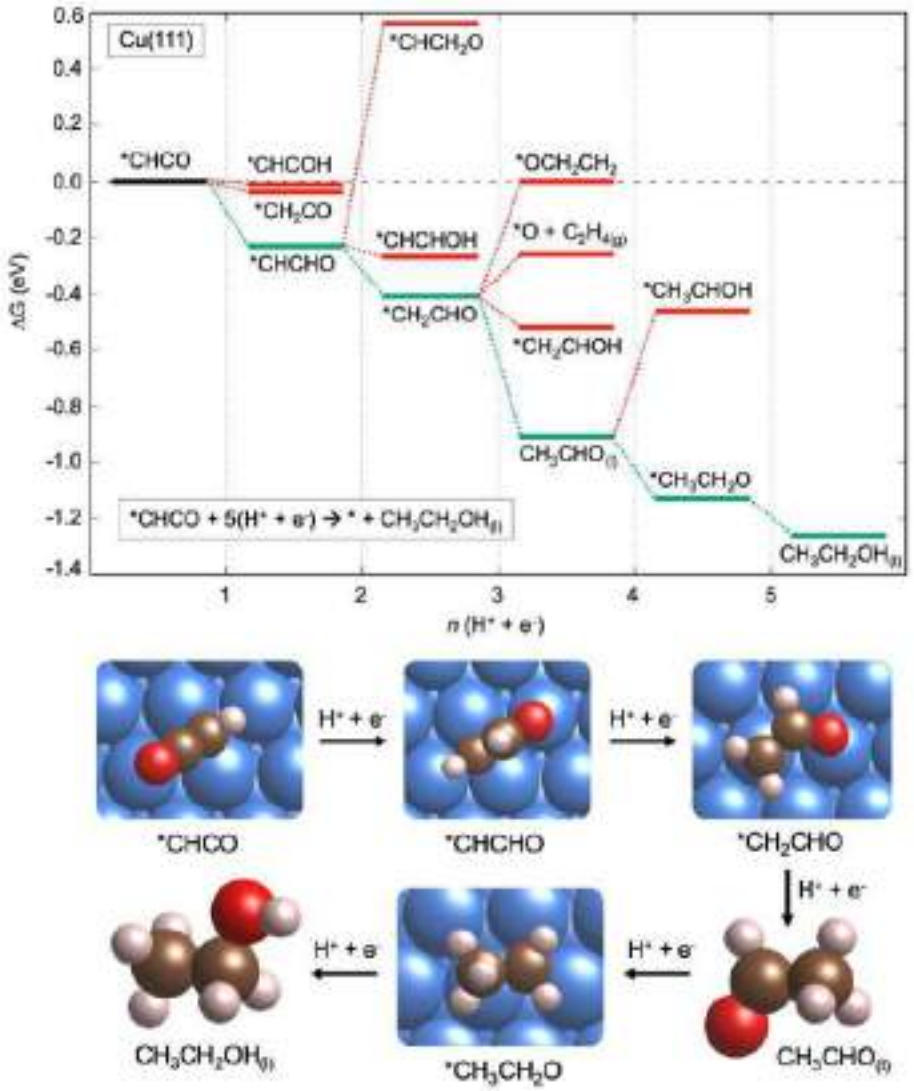

Figure 24. Reduction of *CHCO to ethanol on Cu sites. Top: Free-energy diagram for the electroreduction of *CHCO on Cu(111). The preferred pathway is shown in green, whereas less-stable intermediates are shown in red. Note that ethylene production is considerably less favorable than that of ethanol. All energies are referenced to *CHCO and proton-electron pairs. Bottom: Atomic structures of the species in the *CHCO preferred electroreduction pathway. Cu, C, O, and H atoms are shown in blue, brown, red, and pink, respectively. This figure corresponds to Figure 5 in reference 140 and is included here to facilitate the reading of this thesis.

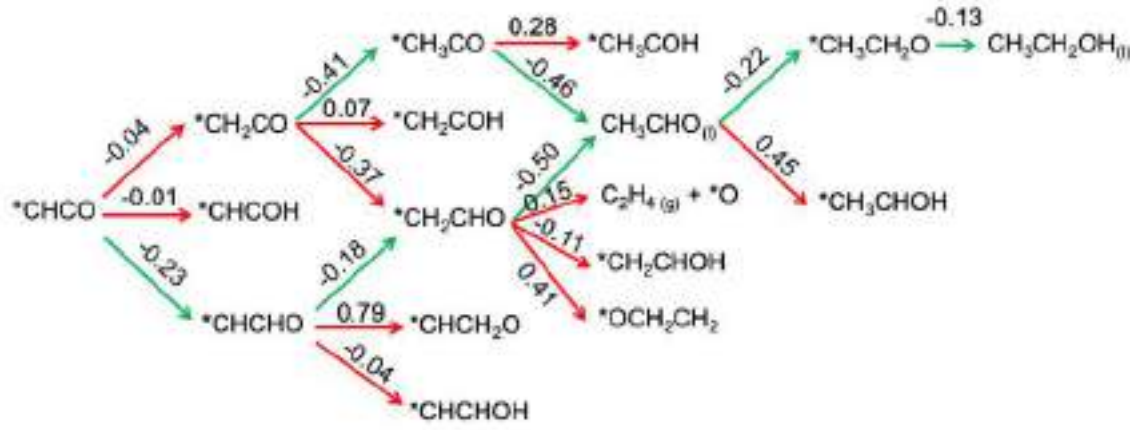

Figure 25. Pathways inspected for ethanol and ethylene production from *CHCO, including as well *CH_2CO, and *CH_3CO. The values over the arrows are the reaction free energies in eV. Green arrows lead in each case to the most stable intermediate, and red arrows are used for the least favorable intermediates. This figure corresponds to Figure S10 in the supporting information of reference 140 and is included here to facilitate the reading of this thesis.

Conclusions These results, together with additional data and analyses shown in the research article below, lead to the following conclusions:

- CuAg composite electrocatalysts show enhanced production of C_2 molecules from CO_2RR as compared to OD-Cu. Ethanol evolution features a more pronounced enhancement than ethylene production.
- When in presence of excess *CO, an alternative pathway to reduce CO_2 selectively to ethanol is opened. This pathway does not proceed via *CO dimerization but through *CO + *CH_x (x = 1, 2) coupling at Cu-Ag boundaries. The species resulting from such coupling are then reduced to ethanol.
- In perspective, our works shows that certain sites at catalytic surfaces are inactive because of their inability to stabilize certain adsorbates, but can become active via the opening of an alternative pathway that circumvents the formation of such troublesome species. This is the case of Cu(111) sites, which are not active toward C_2 species for CO_2RR; but when there is excess *CO, they can selectively reduce it to ethanol.

ACS Catalysis

pubs.acs.org/acscatalysis

Research Article

Enhancing CO_2 Electroreduction to Ethanol on Copper–Silver Composites by Opening an Alternative Catalytic Pathway

Louisa Rui Lin Ting,[†] Oriol Piqué,[†] Si Ying Lim, Mohammad Tanhaei, Federico Calle-Vallejo,* and Boon Siang Yeo*

Cite This: ACS Catal. 2020, 10, 4059−4069

Read Online

ACCESS | Metrics & More | Article Recommendations | Supporting Information

ABSTRACT: A fundamental question in the electrochemical CO_2 reduction reaction (CO_2RR) is how to rationally control the catalytic selectivity. For instance, adding a CO-selective cocatalyst like Ag to Cu shifts the latter's CO_2RR selectivity toward C_2 products, but the underlying cause of the change is unclear. Herein, we show that, during CO_2RR, the abundant CO availability at Cu−Ag boundaries facilitates C-C coupling on Cu to selectively generate ethanol through an otherwise closed pathway. Oxide-derived Cu nanowires mixed with 20 nm Ag particles (Cu:Ag mole ratio of 1:20) catalyzed CO_2 reduction to ethanol with a maximum current density of −4.1 mA/cm^2 and ethanol/ethylene Faradaic efficiency ratio of 1.1 at −1.1 V vs RHE. These figures of merit are, respectively, 5 and 3 times higher than those for pure oxide-derived Cu nanowires. CO_2RR on CuAg composite catalysts with different Ag:Cu ratios and Ag particle sizes reveals that ethanol production scales with the amount of CO evolved from Ag sites and the abundance of Cu−Ag boundaries, and, very interestingly, without significant modifications to ethylene formation. Computational modeling shows selective ethanol generation via Langmuir−Hinshelwood *CO + *CH_x (x = 1, 2) coupling at Cu−Ag boundaries and that the formation of energy-intensive CO dimers is circumvented.

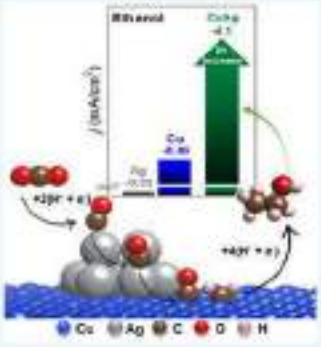

KEYWORDS: *electrochemical CO_2 reduction, electrocatalysis, ethanol, copper−silver, reaction mechanism*

1. INTRODUCTION

The electrochemical reduction of carbon dioxide (CO_2RR), when driven by renewable electricity, provides a carbon-neutral route to generate fuels and chemical feedstock.[1] Metallic copper foils can catalyze the electroreduction of CO_2 to hydrocarbons, such as methane and ethylene, and oxygenates such as ethanol.[2] Regrettably, they are not particularly selective toward C_1 molecules.[3] Oxidizing the Cu electrodes prior to their use as catalysts enhances their selectivity toward C_2 products, with ethylene more prevalently formed over ethanol.[4−6] This raises the question of how to strategically steer the conversion of CO_2 toward ethanol, which is both a widely used commodity chemical and a fuel with one of the highest gravimetric energy densities.[7] Techno-economic analyses also highlight the importance of good ethanol selectivity in order to increase the technology readiness level (TRL) of CO_2-to-ethanol electrolyzers.[7,8] In this context, elucidating the reaction intermediates and pathways of CO_2RR to ethanol is a key requisite.

For the production of C_2 molecules on Cu surfaces, *CO dimerization has been identified as the key step in the reaction pathway.[9,10] Theoretical simulations on Cu(100) further suggested that in the late stages of the pathway, there is a selectivity-determining intermediate, namely *CH_3CHO.[11] The hydrogenation of this intermediate leads to either ethylene or acetaldehyde,[11] which is readily electroreduced to ethanol.[9,12,13] The idea of a shared ethanol/ethylene pathway is supported by the Faradaic efficiencies (FE) of the two products being modified similarly in the presence of alkaline cations.[14]

An alternative pathway for the reduction of CO_2 to ethanol involving the coupling of CO and CH_x intermediates to give acetaldehyde, which again reduces to ethanol, has also been proposed.[15] This pathway has been postulated to occur when there is an excess of CO on the working catalyst.[16] Previously, zinc, which is selective for CO_2RR to CO, was added as a cocatalyst to copper. The Zn sites would produce CO molecules in situ, which would combine with *CH_x moieties on the Cu sites to produce C_2 species.[16] By increasing the amount of Zn in the bimetallic catalysts, it was found that the selectivity of ethanol over ethylene, defined by the ratio of their Faradaic efficiencies ($FE_{ethanol}/FE_{ethylene}$), could increase by a factor of up to ~12.5. Ethanol formation was maximized on Cu_xZn at −1.05 V vs RHE, with a Faradaic efficiency and current density of 29.1% and −8.2 mA/cm^2, respectively. Lee

Received: December 10, 2019
Revised: February 27, 2020
Published: March 16, 2020

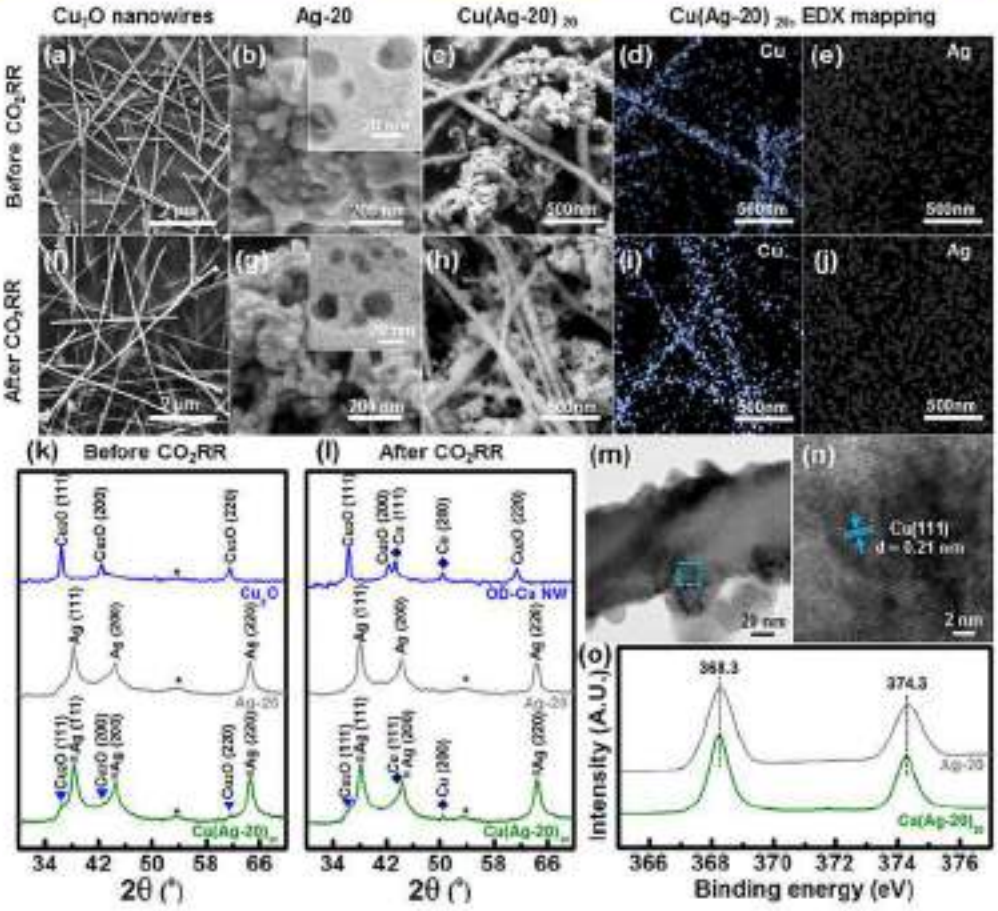

Figure 1. SEM images of as-prepared (a) Cu_2O nanowires (b) Ag-20, (c) $Cu(Ag\text{-}20)_{20}$ composite catalysts. (d) and (e) are, respectively, the Cu and Ag EDX maps of $Cu(Ag\text{-}20)_{20}$. (f)−(j) are the SEM images and EDX maps of the catalysts after 1 h of CO_2 reduction at −1.1 V vs RHE. TEM images of Ag-20 are shown in the insets of (b) and (g). XRD patterns of Cu_2O (blue lines), Ag-20 (gray lines), and $Cu(Ag\text{-}20)_{20}$ (green lines) (k) before and (l) after 1 h of CO_2 reduction at −1.1 V vs RHE. The peaks are assigned using standard XRD patterns JCPDS 01-071-3645 (Cu_2O), JCPDS 01-070-3038 (Cu), and 03-065-8428 (Ag). We note that Cu (111) and Ag (200) peaks overlap. Peaks from the graphite substrate are indicated with *. (m) TEM image of OD-Cu NW after CO_2 reduction at −1.1 V vs RHE. (n) HRTEM analysis of OD-Cu NW after electrolysis. The analysis region is indicated in blue on Figure 1m. (o) Ag 3d XPS spectra of Ag-20 and $Cu(Ag\text{-}20)_{20}$ after CO_2 reduction at −1.1 V vs RHE.

et al. further studied oxide-derived CuAg catalysts and reported a maximum $FE_{ethanol}$ of 34.8% at −1.2 V vs RHE.[17] At the same potential, ethylene was produced with a FE of 9.5%. Maximizing the number of biphasic Cu−Ag boundaries was hypothesized to facilitate the migration of CO produced on the Ag sites to the Cu sites, where ethanol could be eventually formed.

Recently, various CuAg catalysts have been reported to exhibit enhanced CO_2RR selectivity and activity toward multicarbon products. The enhancement has been attributed to the suppression of the competing hydrogen evolution reaction,[18,19] optimized binding of reaction intermediates such as *CO,[20,21] and increased surface population of *CO intermediates on the catalysts.[22−24] Propositions to improve multicarbon product selectivity include optimizing copper−silver interfaces to boost CO migration from silver to copper sites,[17,23,24] and mixing copper and silver phases to suppress hydrocarbon production and promote the formation of oxygenated products.[18,19]

While it is clear that adding silver influences the CO_2RR product distribution of copper, the experimental observations on the CuAg systems were often conflicting: some enhanced the Faradaic efficiencies of both ethylene and ethanol,[25] some showed enhancement only for ethylene,[22,23] while others improved the ethanol selectivity while suppressing ethylene.[17,21] Furthermore, despite commendable efforts in demonstrating the CO-spillover phenomenon from Ag to Cu, it is still unclear how the CO that spilled over from the Ag sites could modify the CO_2RR selectivity of Cu.[26,27] All these suggest that the atomic-scale configuration of CuAg catalysts strongly determines their CO_2RR product distribution and calls for detailed mechanistic studies in order to gain a deeper understanding of CO_2RR on CuAg systems.

Herein, we probe the CO_2RR catalytic activity of a series of composite catalysts consisting of Ag particles and oxide-derived Cu nanowires (OD-Cu NW). We assessed the impact of increasing the amount of CO in the system on ethanol and ethylene production during CO_2RR, and supplemented our analysis with density functional theory (DFT) calculations. Our results indicate that at Cu−Ag boundaries, an alternative pathway that allows the selective production of ethanol is open. Interestingly, the pathway remains locked when CO is not profusely evolved, indicating that CO availability is a key parameter to modulate the selectivity of copper catalysts.

https://dx.doi.org/10.1021/acscatal.8b05119
ACS Catal. 2020, 10, 4059−4069

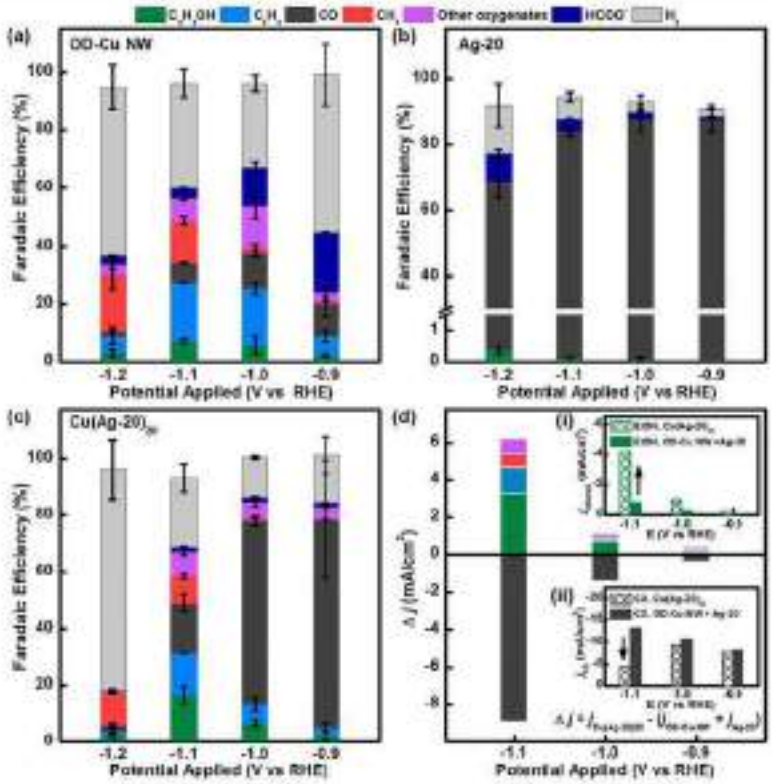

Figure 2. Faradaic efficiencies of CO_2 electrolysis products on (a) OD-Cu NW, (b) Ag-20, and (c) $Cu(Ag\text{-}20)_{20}$. (d) Difference in partial current densities ($\Delta j = j_{Cu(Ag\text{-}20)20} - (j_{OD\text{-}Cu\ NW} + j_{Ag\text{-}20})$) of major CO_2RR products formed on $Cu(Ag\text{-}20)_{20}$ and on OD-Cu + Ag-20. The other oxygenates include acetaldehyde, *n*-propanol, propionaldehyde, methanol, and allyl alcohol. The insets show the partial current densities of (i) ethanol and (ii) CO on $Cu(Ag\text{-}20)_{20}$ compared with the partial current densities from OD-Cu NW + Ag-20.

2. RESULTS AND DISCUSSION

2.1. Characterization of Materials. We synthesized Cu_2O nanowires using a published procedure.[28] Scanning electron microscopy (SEM) revealed that these nanowires had diameters of 50−100 nm and lengths of tens of micrometers (Figure 1a). SEM and transmission electron microscopy (TEM) analyses of the Ag powder (used as purchased) showed ~20 nm-sized particles (Figure 1b).

The Cu_2O nanowires and 20 nm Ag powders were physically mixed as a catalyst ink and dropcasted onto graphite substrates (see the Supporting Information, SI, Section S1). We labeled the composite catalyst as $Cu(Ag\text{-}D)_M$, where D is the diameter (in nanometers) of the Ag particles and M is the nominal molar ratio of Ag/Cu. The SEM image of as-prepared $Cu(Ag\text{-}20)_{20}$ showed that the Cu_2O nanowires and Ag particles were well mixed (Figure 1c), as confirmed by elemental mapping from energy-dispersive X-ray spectroscopy (EDX; Figure 1d,e). The morphologies of all these materials did not change significantly after they were used as catalysts for 1 h CO_2RR in 0.1 M $KHCO_3$ electrolyte at a representative potential of −1.1 V vs RHE (reversible hydrogen electrode; all potentials hereafter are referenced to the RHE; Figure 1f−j). EDX analysis indicates that after electrolysis, the Ag/Cu ratio of $Cu(Ag\text{-}20)_{20}$ increased from 18 ± 2 to 22 ± 2 (SI Section S2.1). This suggests that some Cu dissolution might have occurred.

The identities of the as-prepared catalysts were confirmed by X-ray diffraction (XRD) (Figure 1k). Ag peaks dominated the diffraction pattern of $Cu(Ag\text{-}20)_{20}$ because of its high Ag content. After electrolysis, both metallic Cu (with Cu(111) as the strongest peak) and Cu_2O signals were observed on OD-Cu NW (Figure 1l). TEM analysis of the OD-Cu NW (Figure 1m,n) after electrolysis confirms that its surface was reduced to metallic Cu. This observation is consistent with previous works which showed that the surface of copper oxides was reduced to metallic Cu under CO_2 reduction conditions.[5,19,31] Both Cu and Cu_2O signals were also observed in the XRD pattern of $Cu(Ag\text{-}20)_{20}$ after 1 h of CO_2 electrolysis (Figure 1l). TEM analysis of postreduced $Cu(Ag\text{-}20)_{20}$ confirms that, similar to OD-Cu NW, the surface of the Cu_2O nanowires in the composite catalyst was reduced to metallic Cu (Figure S1b).

It is noteworthy that $Cu(Ag\text{-}20)_{20}$, both before and after electrolysis, did not exhibit XRD peaks that could be assigned to CuAg alloys. This observation is consistent with Cu and Ag being immiscible in the solid state.[31] Furthermore, TEM analysis of $Cu(Ag\text{-}20)_{20}$ after electrolysis revealed that the Ag particles were not strongly adhered to the OD-Cu NW and that the OD-Cu NW surface consisted of only metallic Cu and was not incorporated with Ag (Section S2.2). X-ray photoelectron spectroscopy (XPS) was also performed on $Cu(Ag\text{-}20)_{20}$ and Ag-20, after they were used for CO_2RR. The Ag_{3d} peaks of both catalysts exhibited the same binding energies at 368.3 and 374.3 eV, which can be assigned to metallic Ag^0 (Figure 1o).[32] This observation is consistent with the metallic Ag peaks observed in the XRD of both catalysts (Figure 1l) and the pure Ag phase (no Cu incorporated) observed in the TEM analysis of $Cu(Ag\text{-}20)_{20}$ after electrolysis (Figure S1d). Collectively, these evidences demonstrate that the Cu and Ag

https://dx.doi.org/10.1021/acscatal.8b05119
ACS Catal. 2020, 10, 4059−4069

phases in $Cu(Ag\text{-}20)_{20}$ are segregated, and they do not modify each other electronically. This important piece of information will be used later to devise the DFT calculations.

2.2. CO_2RR Activity of OD-Cu NW, Ag-20 Particles, and $Cu(Ag\text{-}20)_{20}$ Composites. The CO_2RR activities of OD-Cu NW, Ag-20 particles, $Cu(Ag\text{-}20)_{20}$ catalysts were evaluated using chronoamperometry from −0.9 to −1.2 V vs RHE in 0.1 M $KHCO_3$ electrolyte (SI Section S3). The CO_2RR product distributions are presented in Figure 2a−c and Section S3 of the SI.

On OD-Cu NW, the optimal FEs of ethanol and ethylene were 7.3% and 20.1% respectively at −1.1 V ($FE_{ethanol}/FE_{ethylene}$ = 0.4; Figure 2a and Table S4). Methane became the dominant CO_2RR product (FE = 20.1% at −1.2 V) as more negative potentials were applied. Ag-20 reduced CO_2 to CO with FE of 80−90% from −0.9 to −1.1 V (Figure 2b and Table S5). At −1.2 V, FE_{CO} decreased significantly to 68.1%, while FE_{H_2} increased to 14.7% (Table S5), indicating that CO_2 mass transport limitations to the working electrode had occurred. We also detected minute amounts of methane (FE < 0.3%) and ethanol (FE < 0.4%) on Ag-20. This finding is consistent with earlier experimental and theoretical CO_2 electroreduction studies on Ag foils.[33,34]

On $Cu(Ag\text{-}20)_{20}$, CO_2RR to ethanol and ethylene peaked at −1.1 V, with FEs of 16.5 and 14.9% respectively ($FE_{ethanol}/FE_{ethylene}$ = 1.1; Figure 2c and Table S6). The increase in $FE_{ethanol}/FE_{ethylene}$ from 0.4 to 1.1 indicates that the addition of Ag to OD-Cu NW enhances the selectivity of the composite catalyst toward ethanol. Note that control CO_2 electrolyses on pristine graphite substrates produced mainly H_2 (71 to 79% FE), some HCOOH (FE < 17%), and CO (FE < 4.1%) (Table S7). Neither hydrocarbons nor alcohols were detected.

We also evaluate the difference in the geometric partial current densities ($\Delta j = j_{Cu(Ag\text{-}20)20} - (j_{OD\text{-}Cu\ NW} + j_{Ag\text{-}20})$) of major CO_2RR products formed on $Cu(Ag\text{-}20)_{20}$ and its two components (Figure 2d). Methane, ethylene, ethanol, and other oxygenates (excluding formic acid) showed a positive Δj, with ethanol exhibiting the greatest value of Δj. Specifically, at −1.1 V, the $j_{ethanol}$ on OD-Cu NW + Ag-20 and $Cu(Ag\text{-}20)_{20}$ were −0.87 and −4.14 mA/cm^2 respectively, representing a near 5-fold change (Figure 2d inset (i), SI Section S3). In contrast, $j_{ethylene}$ and $j_{methane}$ increased by less than a factor of 1.6 from −2.35 to −3.76 mA/cm^2, and −1.73 to −2.39 mA/cm^2, respectively (SI Section S3). CO had a negative Δj, with the largest change also observed at −1.1 V (Figure 2d and inset (ii)). These observations suggest that on the $Cu(Ag\text{-}20)_{20}$ catalyst, CO produced at Ag sites could be consumed at other sites to yield more reduced products, especially ethanol.

The stability of $Cu(Ag\text{-}20)_{20}$ was evaluated over 5 h (SI Section S4). We observed that the FEs of ethanol and ethylene decreased slightly from 16.4 to 12.2% and 13.4 to 11.0%, respectively, while the FE_{CO} increased from 27.5% to 41.4%. Inductively coupled plasma-optical emission spectrometry (ICP-OES) analysis detected only 0.1 ppm of Cu (and no Ag) in the used electrolyte, indicating Cu dissolution. EDX analysis of $Cu(Ag\text{-}20)_{20}$ after the electrolysis showed that the Ag/Cu ratio had increased to 26 ± 5 (Table S8). EDX mapping reveals that some of the dissolved Cu had redeposited as nanoparticles onto the catalyst surface (Figure S3), which is consistent with structural changes expected from the dissolution-redeposition processes on Cu.[9] These findings indicate that the Cu catalysts partially dissolved during CO_2 electrolysis, which resulted in less Cu catalytic sites for the conversion of CO to C_2 molecules. Consequently, ethylene and ethanol formation concurrently decreased, while more CO (produced on Ag) was detected. Interestingly, $FE_{ethanol}/FE_{ethylene}$ remained stable at about 1.1−1.2 across the 5 h duration of the experiment (Figure S2). This observation suggests that, rather than the catalyst structure, the availability of CO for further reduction on Cu is the main factor influencing the $FE_{ethanol}/FE_{ethylene}$.

To sum up, we observe that more C_2 molecules were produced from the $Cu(Ag\text{-}20)_{20}$ composite than on OD-Cu because of the utilization of CO molecules produced from the Ag sites. Ethanol was the most enhanced product from this CO utilization process.

2.3. Effect of Increased CO Production and Abundance of Cu−Ag Boundaries. The analysis in the preceding section indicates that among the CO_2RR products, ethanol benefits the most from the CO produced at Ag sites. Thus, we systematically studied how its production might be impacted by the amount of CO introduced into the catalytic system.

During CO_2RR, the amount of CO produced can be modulated by the loading of Ag particles in the catalyst. Composites with Ag/Cu mole ratios of 5, 9, and 15 were prepared (Figures S4 and S5, Table S9). The loading of Cu in all composites was kept constant, so that the Ag/Cu ratios increased because of the progressive addition of Ag. CO_2RR was performed at −1.1 V and ethanol enhancement was evaluated by normalizing $j_{ethanol}$ from the CuAg composites by $j_{ethanol}$ from OD-Cu NW (Tables S10−S12). Ethylene enhancement was determined analogously. We found that ethanol enhancement strongly correlates with Ag/Cu, reaching a value of ∼5 when Ag/Cu = 20 (i.e., the most Ag-rich sample; Figure 3a). In contrast, the enhancement of ethylene was smaller, having a maximum value of 1.6. The slope of ethanol enhancement against Ag/Cu was ∼8 times larger than the slope for ethylene enhancement, which suggests that ethanol production is appreciably more sensitive to the presence of CO, as compared with ethylene production.

Recent theoretical and experimental works on CuAg catalysts have suggested that CO produced on Ag sites can diffuse to Cu sites and be further reduced to C_2−C_3 products.[26,35] We hypothesized that this migration could be facilitated by increasing the amount of adjacent Cu−Ag sites. To test this, we performed CO_2RR at −1.1 V on $Cu(Ag\text{-}100)_{20}$ and $Cu(Ag\text{-}1000)_{20}$. These two composites were prepared by mixing Cu_2O nanowires with either 100 or 1000 nm diameter Ag particles (SI Section S6). With a constant Ag loading, the use of larger Ag particles decreases the total Ag surface area in the CuAg composites. This, in turn, decreases the abundance of adjacent Cu−Ag sites. Although the Ag particles studied have different sizes (20 to 1000 nm), they reduced CO_2 to CO with similar partial current densities between −9.5 to −13.2 mA/cm^2 at −1.1 V (Tables S5, S16, and S17). The ethanol and ethylene enhancement plotted against the total surface area of Ag particles shows that ethanol production significantly increases with Ag surface area. When the latter was increased by a factor of 50, the ethanol enhancement increased from 2 to 5 (Figure 3b). In contrast, ethylene production did not show a sizable increase. Thus, increasing the size of Cu−Ag boundaries favors the production of ethanol but not ethylene.

We have also prepared a $Cu(Ag\text{-}20)_{20}$-S sample, which contained the same Cu and Ag loading as $Cu(Ag\text{-}20)_{20}$ but had the Cu_2O and Ag components coated sequentially onto the

https://dx.doi.org/10.1021/acscatal.8b05119
ACS Catal. 2020, 10, 4059−4069

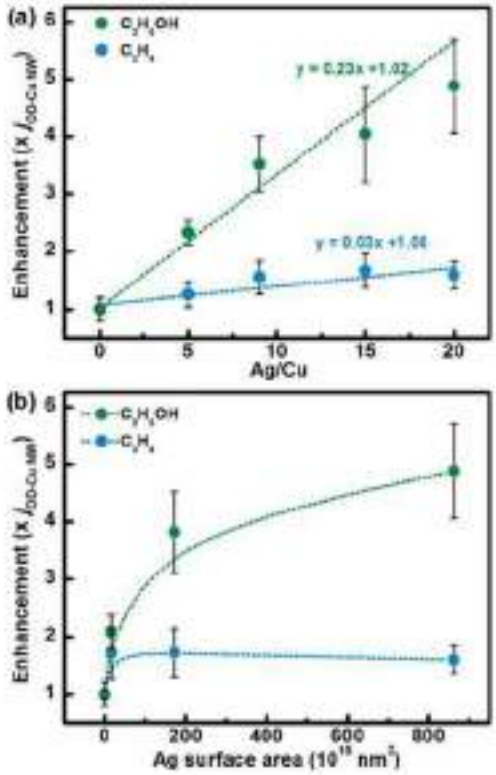

Figure 3. Dependence of ethanol and ethylene enhancement during CO_2 reduction at −1.1 V vs RHE on (a) Ag/Cu ratio and (b) total Ag surface area (dashed lines are included as a guide to the eye).

working electrode (SI Section S7). SEM analysis of this poorly mixed catalyst clearly reveals a lowering of the density of Cu−Ag boundaries. CO_2RR on this sample yielded ~30% higher j_{CO} but less than 50% $j_{ethanol}$ than that observed on $Cu(Ag\text{-}20)_{20}$ (Figure S7, Table S18). This shows that when the density of Cu−Ag boundaries is decreased, CO migrates less efficiently to the Cu sites for further reaction to form ethanol. Further control experiments performed on Ag nanoclusters galvanically deposited onto electropolished Cu foils also show that the enhancement of ethanol was affected more significantly than ethylene by the length of Cu−Ag boundaries (Section S8).

Some studies suggest that oxide-derived copper differs from metallic copper catalysts due to the presence of residual oxides, which improve *CO binding and facilitate C−C coupling.[36,37] However, others maintain that metallic copper is the active catalyst in oxide-derived copper because residual oxides are unstable and inactive for catalysis under CO_2RR conditions.[38,38,39] In view of this contention, we prepared a $Cu(Ag\text{-}20)_{20}$-M composite, which consisted of metallic Cu nanowires (Cu NW) well-mixed with Ag-20 (SI Section S9). CO_2RR at −1.1 V on $Cu(Ag\text{-}20)_{20}$-M revealed that, compared with Cu NW, $j_{ethanol}$ had increased 20 times, while $j_{ethylene}$ increased 4 times. This shows that the ethanol-selective enhancement due to the presence of CO is not unique to oxide-derived Cu surfaces but also applies to metallic Cu surfaces.

Since our results hint toward the importance of CO in enhancing ethanol production, we electroreduced CO directly on OD-Cu NW and $Cu(Ag\text{-}20)_{20}$ at −0.75, −0.80, and −0.90 V (SI Section S10). Unexpectedly, in this potential range, $FE_{ethylene}$ was higher than $FE_{ethanol}$ on both OD-Cu NW and $Cu(Ag\text{-}20)_{20}$. We hypothesized that this apparent discrepancy could be due to the lack of CO reactants at the electrode, due to its low solubility. To assess this hypothesis, we estimate using Fick's law that the flux of CO reaching the electrode during electrolysis is ~2.0 nmol cm^{-2} s^{-1} (SI Section S10.1). This value is about 1 order of magnitude smaller than the 68 nmol cm^{-2} s^{-1} of CO generated in situ by Ag sites in the composite during CO_2RR at −1.1 V, that is, the potential where we observed the largest enhancement of ethanol on $Cu(Ag\text{-}20)_{20}$ (SI Section S10.2). Our calculations show that under CO reduction conditions at −0.75 to −0.90 V, there is insufficient CO to enable selective ethanol production. During CO_2RR, therefore, a CO-selective cocatalyst in tandem with Cu is crucial to provide a large enough flux of CO for further reduction to ethanol.

Unlike several previously reported CuAg catalysts, the formation of hydrocarbons on our CuAg composites was not suppressed in favor of enhanced ethanol production.[17,19] We attribute this to the clear phase separation between copper and silver sites in our composites (Figure 1). This differs from the catalysts studied in earlier works, which showed miscibility between those two metals.[17,19] These catalysts were prepared by procedures using complexing agents[17] as well as by electron-beam physical vapor deposition,[19] which helped to preserve the metastable CuAg miscibility. Mixed-phase catalysts have been suggested to be less oxophilic and thus exhibit a higher propensity for suppressing hydrocarbon production.[18,19] Furthermore, recent isotope-labeling studies of CO_2RR on oxide-derived copper suggested the presence of distinctively different catalytic sites for ethanol and ethylene production.[40] This is in line with our experimental observation regarding ethanol enhancement and the idea that the selective electroreduction of CO_2 to ethanol can occur on active sites different from those for *CO dimerization, which mainly produces ethylene.

2.4. Computational Modeling of CO_2RR at Cu−Ag Boundaries. To understand in greater detail the working principle of the CuAg catalysts, we performed density functional theory (DFT) calculations on model systems. First, to decide on the characteristics of the model system, we calculated the thermodynamic stability of bulk CuAg alloys for different Cu/Ag proportions. Bulk CuAu alloys, which have been extensively studied,[41,42] were also analyzed as a control system. For the latter, we find that the alloy formation energy is negative for all the studied proportions, in line with experimental results from the literature.[41,42] Conversely, for the CuAg system, the alloy formation energies were positive in all cases, indicating that it is not thermodynamically favorable to alloy Cu and Ag in any of the studied proportions (Figure S11). This leads us to conclude that Ag and Cu likely exist as two separated phases in our catalyst, which is also supported by the characterization results of our CuAg composite catalyst.

In view of the current controversy regarding the presence of oxygen on oxide-derived Cu electrodes,[37−39] we performed calculations featuring surface and subsurface oxygen on both Cu(111) and Ag(111) (Table S30). We observe that while subsurface oxygen is metastable on both metals, surface oxygen is more stable by 1.5 and 0.7 eV, respectively. In view of its low stability and negligible effect on the adsorption energies of *CO, we did not include subsurface *O in our model. Neither did we include the effects of surface *O in our calculations as previous works have shown that it is unlikely for surface *O to

https://dx.doi.org/10.1021/acscatal.8b05119
ACS Catal. 2020, 10, 4059−4069

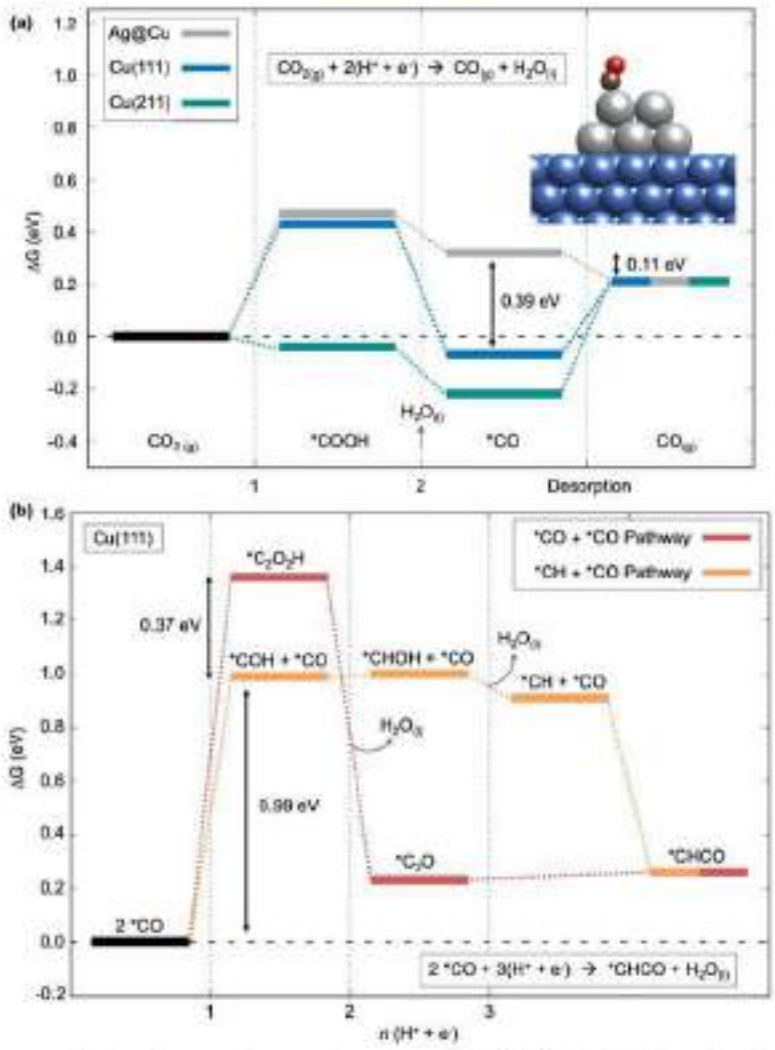

Figure 4. (a) Free energy diagram of $CO_{2(g)}$ electroreduction to $CO_{(g)}$ on Cu(111) (blue), Cu(211) (cyan), and Ag@Cu (gray), which is a Ag cluster on top of a Cu(111) slab. All energies are referenced to $CO_{2(g)}$ and proton−electron pairs. Inset: CO adsorbed on the Ag@Cu cluster; Cu, Ag, C, and O atoms are shown in blue, gray, brown, and red, respectively. (b) Free energy diagram on Cu(111) featuring two different C−C coupling pathways to *CHCO from 2*CO. In red, the *CO dimerization pathway. In orange, the energetics of the *CH + *CO pathway. All energies are referenced to 2*CO adsorbed on Cu(111) and proton−electron pairs, see section S15.

be present on Cu and Ag surfaces when they are subjected to the negative potentials needed for electrochemical CO_2RR.[43,44]

After outlining the model systems, we performed a mechanistic study. For clarity, we divided the entire CO_2RR to ethanol, which requires 12 proton−electron transfers ($2CO_2 + 12(H^+ + e^-) \rightarrow CH_3CH_2OH + 3H_2O$), into three separate yet interconnected parts. First, we consider the reduction of two CO_2 molecules to 2*CO, where four protons and electrons are transferred. This is followed by the reduction of 2*CO to *CHCO, which takes three proton−electron transfers and a C−C coupling. Finally, we close the analysis with *CHCO reduction to ethanol, where five protons and electrons are transferred.

CO_2RR to CO via *COOH was studied on Cu(111) (copper's closest-packed surface), a Ag cluster on top of Cu(111) (hereon referred to as Ag@Cu, see the inset of Figure 4a), and Cu(211), which is composed of (111) terraces separated by (100) steps. Cu(211) is chosen because models based on its step-edge sites reproduce well the experimental features of CO_2RR to C_1 and C_2 products.[45,46] On Cu(111) and Cu(211), the desorption of *CO to $CO_{(g)}$ is not favorable (Figure 4a). Hence, *CO will further reduce to $*CH_x$ species at negative enough potentials, eventually leading to CH_4.[45] In contrast, Ag@Cu sites reduce CO_2 to *CO, which is so weakly adsorbed on Ag that it cannot undergo further reduction. Thus, these *CO will either diffuse into the solution or migrate to neighboring Cu sites. The vertical differences in Figure 4a indicate that *CO is stabilized by 0.11 eV upon desorption from Ag to the solution, whereas it is stabilized by 0.39 eV when it migrates to the Cu(111) surface. The kinetic barrier for *CO diffusion from the Ag cluster to Cu(111) is only 0.17 eV (Table S29), which is easily surmountable at room temperature (surmountable barriers are typically below 0.75 eV).[47] Because of their strong adsorption energies, the Cu(211) step-edge sites are probably covered by reaction intermediates irrespective of *CO abundance. In contrast, the coverage of reaction intermediates at weakly adsorbing Cu(111) sites remains relatively low when there is no excess

https://dx.doi.org/10.1021/acscatal.9b05319
ACS Catal. 2020, 10, 4059−4069

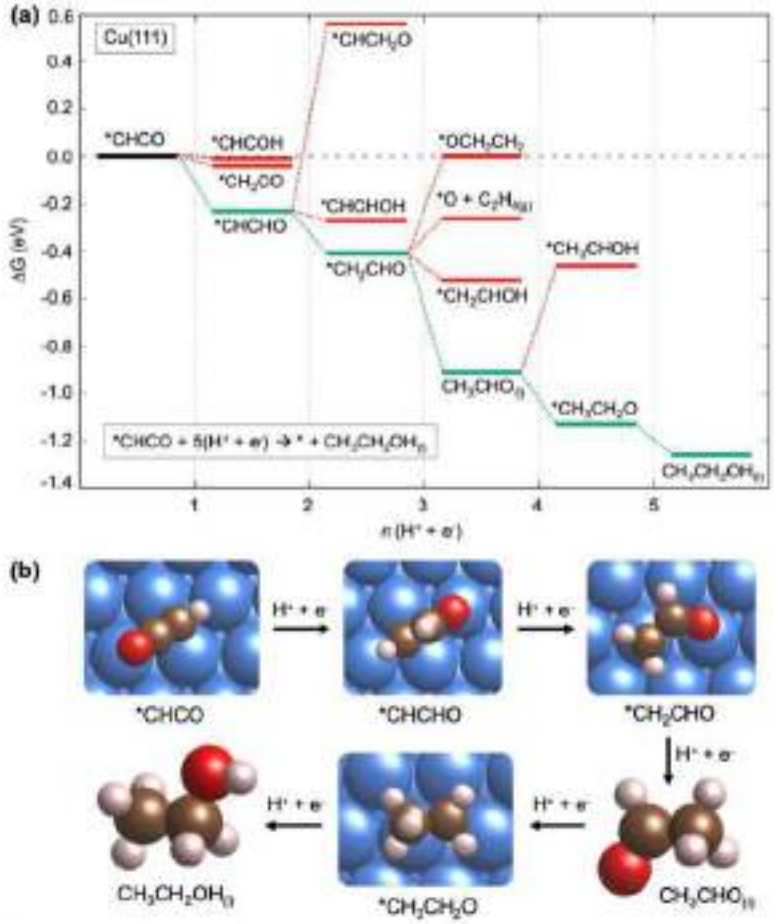

Figure 5. Reduction of *CHCO to ethanol on Cu sites. (a) Free energy diagram of the electroreduction of *CHCO on Cu(111). The preferred pathway is shown in green, whereas less-stable intermediates are shown in red. Note that ethylene production is considerably less favorable than that of ethanol. All energies are referenced to *CHCO and proton−electron pairs, see Section S15. (b) Atomic structures of the species in the *CHCO preferred electroreduction pathway. Cu, C, O, and H atoms are shown in blue, brown, red, and white.

*CO. Thus, we postulate that ethanol evolves from Cu(111) sites near Ag nanoparticles. This implies that Cu−Ag boundaries are dual active sites, in that $CO_{(g)}$ formed at Ag particles diffuses to unoccupied Cu(111) sites, where it is then further reduced.

As shown in Figure 4b, the reduction of 2*CO to C_2 species can proceed in two ways, namely, through the conventional *CO dimerization pathway or via the coupling of *CO and $*CH_x$ species. To ascertain the actual species which are likely to couple with *CO to produce ethanol, we calculated several coupling barriers on Cu(111). A summary of all values obtained for the different coupling reactions can be found in Section S15 of the SI. For *CH + *CO ($x = 1$), $*CH_2$ + *CO ($x = 2$), and $*CH_3$ + *CO ($x = 3$) through a Langmuir−Hinshelwood (L-H) mechanism on Cu(111), we obtained barriers of 0.70, 0.71, and 1.20 eV, respectively, which are commensurate with those in the literature.[48] Earlier studies have also suggested an Eley−Rideal (E-R) mechanism for the coupling of CO and $*CH_x$.[15−17,49] To assess this possibility, we calculated the energy barriers of the *CH + $CO_{(g)}$ and $*CH_2$ + $CO_{(g)}$ couplings via an E-R mechanism. The respectively obtained values are 1.40 and 1.49 eV, which are appreciably higher than the L-H values on Cu(111). Judging by all of the calculated barrier heights, the reaction may proceed through L-H routes coupling *CH and *CO, or $*CH_2$ and *CO, but not between $*CH_3$ and *CO. Note that while we calculated coupling and diffusion barriers, we did not perform calculations of proton−electron transfer barriers, since, as noted recently by Rossmeisl et al.,[50] there is "not (yet) a method to obtain electrochemical barriers between realistic states at constant electrochemical conditions". We further note that other authors have extensively studied the Bronsted−Evans−Polanyi (BEP) relations for reactions where C, H, and O-containing species are involved and have shown that thermodynamics and kinetics are generally well correlated for such reactions on transition metal surfaces.[51,52]

Figure 4b shows that, in terms of the potential-limiting step (i.e., *CO hydrogenation), the *CH + *CO coupling pathway is more favorable than that of *CO dimerization on Cu(111) by ~0.37 eV. This means that *CO is likely reduced to *COH on Cu(111), and not to its hydrogenated dimer $*C_2O_2H$. On Cu(111) without any vicinal Ag nanoparticles, this preference has two justifications: (1) the low coverage makes it statistically difficult for *CO to couple, and (2) the thermodynamics and kinetics of *CO dimerization are energetically prohibitive. If and when *CO is abundant on Cu(111), (1) is solved but (2) is not, so that the coupling likely takes place between *CH and *CO, or $*CH_2$ and *CO.

https://dx.doi.org/10.1021/acscatal.8b05119
ACS Catal. 2020, 10, 4059−4069

In agreement with experiments, Figure 4b indicates that opening the *CH + *CO pathway requires potentials of at least −0.99 V vs RHE (we explain how to calculate limiting potentials from free energies in Section 4: Computational Details).

Finally, we studied the fate of the *CHCO moieties upon further reduction (Figure 5). The most favorable reduction pathway to ethanol is colored in green in Figure 5a, whereas less favorable species are displayed in red at each stage of the reaction. For convenience, the atomic structures of the most favorable reduction path are depicted in Figure 5b. A more extended analysis, including the further reduction of $*CH_2CO$ and $*CH_3CO$ species, is depicted in Figure S10. It is striking that regardless of whether *CHCO or $*CH_2CO$ is the result of the coupling step, the pathway always inclines toward ethanol, instead of ethylene. The same holds for $*CH_3CO$. This leads to a simple conclusion: once *CO + $*CH_x$ coupling takes place on CuAg catalysts, ethanol is selectively produced. This is consistent with our experimental findings (Figure 3), wherein enhanced CO availability increases ethanol production. This is also supported by our results from using $Cu(Ag\text{-}20)_{20}$ for the electroreduction of acetaldehyde (Section S11), an isolable intermediate in our proposed mechanism. Ethanol was the major reduction product, while ethylene was not detected. Besides, several previous theoretical and experimental studies have shown that acetaldehyde is a precursor of ethanol.[9,12,15,53] This result also helped us to exclude a previously proposed pathway implicating solvent water as the oxygen source for ethanol.[54] In that mechanism, ethanol production did not proceed via acetaldehyde, and the pathway with the lowest energy barrier leads to ethylene formation.

In summary, bare Cu(111) terraces are relatively inactive for the production of C_2 molecules, in view of the low *CO coverage and the comparatively easier formation of C_1 adsorbed species.[55,56] However, the calculations in Figures 4 and 5 show that abundant *CO facilitates the formation of C−C bonds at Cu(111) terraces and the selective formation of ethanol, without the energy-intensive formation of CO dimers.[11,26,57]

3. CONCLUSIONS

A series of CuAg composite catalysts showed enhanced CO_2 reduction selectivity toward ethanol. A 5-fold improvement in $j_{ethanol}$ was observed on an optimized $Cu(Ag\text{-}20)_{20}$ sample (−4.1 mA/cm^2; compared to −0.87 mA/cm^2 on OD-Cu NW + Ag-20). In contrast, $j_{methane}$ only increased slightly by a factor of ∼1.6. These observations indicate the opening of a second pathway to reduce CO_2 selectively to ethanol, which is likely activated in excess of *CO. Unlike ethylene production, which is usually thought to proceed via *CO dimerization, the alternative pathway proceeds via *CO + $*CH_x$ (x = 1, 2) coupling at Cu−Ag boundaries, and the formed $*CH_2CO$ species are in all cases shown to preferably reduce to ethanol.

In a broader context, our work hints toward the fact that certain sites at catalytic surfaces are usually inactive because of their inability to stabilize particular adsorbate(s). If and when a workaround is found, catalytic activity and selectivity can be sizably enhanced. This is the case of Cu(111) sites, on which it is typically hard to produce C_2 molecules but, in excess of *CO, are able to reduce CO_2 selectively to ethanol. We hope this rationale opens up new possibilities in designing electrocatalysts with enhanced product selectivities for CO_2 reduction.

4. METHODS

Synthesis of Cu_2O Nanowires. First, 120 μL of *o*-anisidine (Aldrich) was added to 60 mL of deionized water containing 0.3 g of copper(II) acetate monohydrate (Sigma-Aldrich). The solution was stirred for 5 min until its color turned olive green. It was then transferred into a stainless-steel autoclave and heated at 200 °C for 14 h to yield Cu_2O nanowires. The product was decanted, washed with ethanol, and dried in the oven at 60 °C overnight.[28]

Preparation of $Cu(Ag\text{-}D)_M$ Composite Catalysts. Ag powders with diameters of 20 nm (US Research Nanomaterials), 100 nm (American Elements), and 1000 nm (Goodfellow) were purchased and used as received. The Cu-to-Ag ratios of the composite catalysts were controlled by using different mass ratios of the Cu_2O nanowires and Ag powders, with the loading of Cu_2O fixed at 1 mg (Table S1). The powders were dispersed in 1 mL of solvent (75% water, 15% ethanol, 10% Nafion) and sonicated until a homogeneous ink was obtained. Twenty-five μL of the ink was dropcasted onto polished graphite discs (15 mm diameter, Ted Pella) and dried in air.

Physical Characterization of Catalysts. Scanning electron microscopy and energy dispersive X-ray spectroscopy were performed using a JEOL JSM-6701F SEM. Transmission electron microscopy was performed using a JEOL 3010 TEM. The catalysts were removed from the graphite substrates and dispersed in ∼1 mL of methanol by sonication. Then 20 μL of the dispersion was drop-casted onto 300 mesh nickel grid coated with lacey carbon (LC325-Ni, Electron Microscopy Sciences) for TEM analysis. Powder X-ray diffraction was made using a Siemens 5005 (Cu Kα radiation with graphite monochromator), in locked θ-2θ scan mode from 15 to 100° 2θ with 0.1° resolution step and 1 s acquisition time per step. X-ray photoelectron spectroscopy analysis was performed using a Theta Probe (Thermo Scientific) XPS instrument with a monochromatic Al Kα (1486.6 eV) X-ray source. The binding energies were calibrated on the basis of the C_{1s} peak at 285 eV.

Electrochemical CO_2 Reduction Experiments. Electrolyses (1 h) were performed in 0.1 M $KHCO_3$ (Merck, 99.7%), using a two-compartment Teflon cell separated by an anion-exchange membrane (Selemion AMV, AGC Asahi Glass). The cathodic compartment contained 12 mL of electrolyte and housed the working electrode (exposed geometric surface area: 0.785 cm^2) and the reference electrode (Ag/AgCl, saturated KCl, Pine), while the anodic compartment contained 8 mL of electrolyte and a graphite rod (Ted Pella) as counter electrode. The electrolyte was purged with CO_2 gas (99.999%, Linde Gas) at 20 cm^3/min. The pH of the electrolyte was 6.8. The electrochemical measurements were performed using a Gamry Reference 600 potentiostat/galvanostat. The current interrupt method was used to compensate for the iR drop. The headspace of the cathodic compartment was continuously flowed into a gas chromatograph (GC, Agilent 7890A) for online detection of gas products. Liquid products were analyzed after the electrolysis experiments. Aldehydes, ketones and alcohols were detected using headspace GC (HSGC, Agilent, 7890B and 7697A). Formate and acetate were detected using high performance liquid chromatography (Agilent 1260 Infinity) with an Aminex HPX-87H column, variable wavelength detector, and 0.5 mM H_2SO_4 mobile phase.

https://dx.doi.org/10.1021/acscatal.8b05319
ACS Catal. 2020, 10, 4059−4069

Computational Details. The DFT simulations were made with the VASP[58] code using the PBE exchange-correlation functional[59] and the projector augmented-wave method.[60] Cu(111) was modeled with a 3 × 3 supercell, and Cu(211) with a 3 × 1 one. All Cu slab models contained four metal layers and were modeled with a lattice constant of 3.64 Å, typical of PBE. The topmost two layers and the adsorbates were relaxed in all directions, while the bottommost layers were fixed at the bulk equilibrium distances. Cu−Ag boundaries were modeled with a 7-atom Ag cluster (made of a layer of five atoms in contact with Cu and two Ag atoms on top of it) situated in adjacent fcc hollows of a 4 × 4 supercell Cu(111) slab. Such slab size avoids lateral interactions between Ag clusters. We used a plane-wave cutoff of 450 eV, k_BT = 0.2 eV (extrapolating total energies to 0 K), and the conjugate-gradient optimization scheme until the maximal force on any atom was below 0.05 eV Å^{-1}. Monkhorst−Pack meshes[61] of 4 × 4 × 1, 4 × 5 × 1, and 3 × 3 × 1 for Cu(111), Cu(211), and Cu−Ag boundaries ensured convergence of the adsorption energies within 0.05 eV. The distance between repeated images in the vertical direction was larger than 16 Å and dipole corrections were applied. Isolated molecules were calculated in boxes of 9 Å x 10 Å x 11 Å using k_BT = 0.001 eV and the gamma point.

The reaction free energies were approximated as $\Delta G \approx \Delta E_{DFT} + \Delta ZPE - T\Delta S + \Delta E_{solvation}$, where ΔE_{DFT} is the DFT-calculated reaction energy, ΔZPE is the zero-point energy change, and $T\Delta S$ is the entropy change at 298.15 K. ΔS includes only the vibrational entropy for the adsorbates and all the contributions for free molecules. The computational hydrogen electrode was used to model proton−electron pairs. Solvation was modeled as an external correction depending on the chemical nature of the adsorbates (specific values are given in Table S25).[11,62] Transition state geometries were found using the climbing image nudged elastic band method,[63] ensuring that at the saddle point, only one imaginary frequency along the reaction coordinate was observed. In this case, the limiting potentials U_L were calculated based on the largest positive free energies of reaction: $U_L = -\Delta G_{max}/e^-$, where e^- is the magnitude of the charge of an electron.

Detailed information on gas-phase, liquid-phase, and solvation corrections; specific values of adsorption free energies and kinetic energy barriers; and the optimized geometries coordinates of all the calculations featured in this work can be found in the SI, Sections S12−S16.

■ ASSOCIATED CONTENT

Supporting Information

The Supporting Information is available free of charge at https://pubs.acs.org/doi/10.1021/acscatal.9b05319.

Catalyst loadings, physical characterisations and electrolysis data of all catalysts tested, including electrolysis of intermediates; gas-phase and liquid-phase corrections, solvent contributions to free energies, adsorption energies, kinetic barriers, and optimized geometries used in DFT calculations (PDF)

■ AUTHOR INFORMATION

Corresponding Authors

Boon Siang Yeo − *Department of Chemistry and Solar Energy Research Institute of Singapore, National University of Singapore, Singapore 117543;* orcid.org/0000-0003-1609-0867; Email: chmyeos@nus.edu.sg

Federico Calle-Vallejo − *Departament de Ciència de Materials i Química Física & Institut de Química Teòrica i Computacional (IQTCUB), Universitat de Barcelona, 08028 Barcelona, Spain,* orcid.org/0000-0001-5147-8635; Email: f.calle.vallejo@ub.edu

Authors

Louisa Rui Lin Ting − *Department of Chemistry and Solar Energy Research Institute of Singapore, National University of Singapore, Singapore 117543*

Oriol Piqué − *Departament de Ciència de Materials i Química Física & Institut de Química Teòrica i Computacional (IQTCUB), Universitat de Barcelona, 08028 Barcelona, Spain*

Si Ying Lim − *Department of Chemistry and Solar Energy Research Institute of Singapore, National University of Singapore, Singapore 117543*

Mohammad Tanhaei − *Institute of Materials Research and Engineering, Agency for Science, Technology and Research, Singapore 138634*

Complete contact information is available at: https://pubs.acs.org/10.1021/acscatal.9b05319

Author Contributions

[¶](L.R.L.T., O.P.) These authors contributed equally to this work.

Notes

The authors declare no competing financial interest.

■ ACKNOWLEDGMENTS

This work is supported by an academic research fund (R-143-000-683-112) from the Ministry of Education, Singapore and the National University of Singapore Flagship Green Energy Program (R-143-000-A55-646 and R-143-000-A55-733). F.C.-V acknowledges funding from Spanish MICIUN RTI2018-095460−B-I00 and Maria de Maeztu MDM-2017-0767 grants and, in part, by Generalitat de Catalunya 2017SGR13. O.P. thanks the Spanish MICIUN for a PhD grant (PRE2018-083811). We thank Red Española de Supercomputación (RES) for supercomputing time at SCAYLE (projects QS-2019-3-0018, QS-2019-2-0023 and QCM-2019-1-0034). The use of supercomputing facilities at SURFsara was sponsored by NWO Physical Sciences, with financial support by NWO. We also thank Cheryldine Lim from the SERIS for assisting with SEM and EDX mapping experiments, and Futian You and Ka Yau Lee from the NUS for assisting with TEM imaging.

■ REFERENCES

(1) Lu, Q.; Jiao, F. Electrochemical CO_2 Reduction: Electrocatalyst, Reaction Mechanism, and Process Engineering. *Nano Energy* **2016**, *29*, 439−456.

(2) Hori, Y.; Murata, A.; Takahashi, R. Formation of Hydrocarbons in the Electrochemical Reduction of Carbon Dioxide at a Copper Electrode in Aqueous Solution. *J. Chem. Soc., Faraday Trans. 1* **1989**, *85*, 2309−2326.

(3) Kuhl, K. P.; Cave, E. R.; Abram, D. N.; Jaramillo, T. F. New Insights into the Electrochemical Reduction of Carbon Dioxide on Metallic Copper Surfaces. *Energy Environ. Sci.* **2012**, *5*, 7050−7059.

(4) Handoko, A. D.; Ong, C. W.; Huang, Y.; Lee, Z. G.; Lin, L.; Panetti, G. B.; Yeo, B. S. Mechanistic Insights into the Selective Electroreduction of Carbon Dioxide to Ethylene on Cu_2O-Derived Copper Catalysts. *J. Phys. Chem. C* **2016**, *120*, 20058−20067.

(5) Ren, D.; Deng, Y.; Handoko, A. D.; Chen, C. S.; Malkhandi, S.; Yeo, B. S. Selective Electrochemical Reduction of Carbon Dioxide to Ethylene and Ethanol on Copper (I) Oxide Catalysts. *ACS Catal.* **2015**, *5*, 2814−2821.
(6) Lum, Y.; Yue, B.; Lobaccaro, P.; Bell, A. T.; Ager, J. W. Optimizing C-C Coupling on Oxide-Derived Copper Catalysts for Electrochemical CO_2 Reduction. *J. Phys. Chem. C* **2017**, *121*, 14191−14203.
(7) Bushuyev, O. S.; De Luna, P.; Dinh, C. T.; Tao, L.; Saur, G.; van de Lagemaat, J.; Kelley, S. O.; Sargent, E. H. What Should We Make with CO_2 and How Can We Make It? *Joule* **2018**, *2*, 825−832.
(8) Spurgeon, J. M.; Kumar, B. A Comparative Technoeconomic Analysis of Pathways for Commercial Electrochemical CO_2 Reduction to Liquid Products. *Energy Environ. Sci.* **2018**, *11*, 1536−1551.
(9) Schouten, K. J. P.; Kwon, Y.; van der Ham, C. J. M.; Qin, Z.; Koper, M. T. M. A New Mechanism for the Selectivity to C_1 and C_2 Species in the Electrochemical Reduction of Carbon Dioxide on Copper Electrodes. *Chem. Sci.* **2011**, *2*, 1902−1909.
(10) Gattrell, M.; Gupta, N.; Co, A. A Review of the Aqueous Electrochemical Reduction of CO_2 to Hydrocarbons at Copper. *J. Electroanal. Chem.* **2006**, *594*, 1−19.
(11) Calle-Vallejo, F.; Koper, M. T. M. Theoretical Considerations on the Electroreduction of CO to C_2 Species on Cu(100) Electrodes. *Angew. Chem., Int. Ed.* **2013**, *52*, 7282−7285.
(12) Bertheussen, E.; Verdaguer-Casadevall, A.; Ravasio, D.; Montoya, J. H.; Trimarco, D. B.; Roy, C.; Meier, S.; Wendland, J.; Nørskov, J. K.; Stephens, I. E. L.; Chorkendorff, I. Acetaldehyde as an Intermediate in the Electroreduction of Carbon Monoxide to Ethanol on Oxide-Derived Copper. *Angew. Chem., Int. Ed.* **2016**, *55*, 1450−1454.
(13) Ledezma-Yanez, I.; Gallent, E. P.; Koper, M. T. M.; Calle-Vallejo, F. Structure-Sensitive Electroreduction of Acetaldehyde to Ethanol on Copper and Its Mechanistic Implications for CO and CO_2 Reduction. *Catal. Today* **2016**, *262*, 90−94.
(14) Murata, A.; Hori, Y. Product Selectivity Affected by Cationic Species in Electrochemical Reduction of CO_2 and CO at a Cu Electrode. *Bull. Chem. Soc. Jpn.* **1991**, *64*, 123−127.
(15) Hori, Y.; Takahashi, R.; Yoshinami, Y.; Murata, A. Electrochemical Reduction of CO at a Copper Electrode. *J. Phys. Chem. B* **1997**, *101*, 7075−7081.
(16) Ren, D.; Ang, B. S.-H.; Yeo, B. S. Tuning the Selectivity of Carbon Dioxide Electroreduction Toward Ethanol on Oxide-Derived Cu_xZn Catalysts. *ACS Catal.* **2016**, *6*, 8239−8247.
(17) Lee, S.; Park, G.; Lee, J. Importance of Ag−Cu Biphasic Boundaries for Selective Electrochemical Reduction of CO_2 to Ethanol. *ACS Catal.* **2017**, *7*, 8594−8604.
(18) Clark, E. L.; Hahn, C.; Jaramillo, T. F.; Bell, A. T. Electrochemical CO_2 Reduction over Compressively Strained CuAg Surface Alloys with Enhanced Multi-Carbon Oxygenate Selectivity. *J. Am. Chem. Soc.* **2017**, *139*, 15848−15857.
(19) Higgins, D.; Landers, A. T.; Ji, Y.; Nitopi, S.; Morales-Guio, C. G.; Wang, L.; Chan, K.; Hahn, C.; Jaramillo, T. F. Guiding Electrochemical Carbon Dioxide Reduction toward Carbonyls Using Copper Silver Thin Films with Interphase Miscibility. *ACS Energy Lett.* **2018**, *3*, 2947−2955.
(20) Chang, Z.; Huo, S.; Zhang, W.; Fang, J.; Wang, H. The Tunable and Highly Selective Reduction Products on Ag@Cu Bimetallic Catalysts toward CO_2 Electrochemical Reduction Reaction. *J. Phys. Chem. C* **2017**, *121*, 11368−11379.
(21) Li, Y. C.; Wang, Z.; Yuan, T.; Nam, D.-H.; Luo, M.; Wicks, J.; Chen, B.; Li, J.; Li, F.; de Arquer, F. P. G.; Wang, Y.; Dinh, C.-T.; Voznyy, O.; Sinton, D.; Sargent, E. H. Binding Site Diversity Promotes CO_2 Electroreduction to Ethanol. *J. Am. Chem. Soc.* **2019**, *141*, 8584−8591.
(22) Hoang, T. T. H.; Verma, S.; Ma, S.; Fister, T. T.; Timoshenko, J.; Frenkel, A. I.; Kenis, P. J. A.; Gewirth, A. A. Nanoporous Copper−Silver Alloys by Additive-Controlled Electrodeposition for the Selective Electroreduction of CO_2 to Ethylene and Ethanol. *J. Am. Chem. Soc.* **2018**, *140*, 5791−5797.
(23) Wang, J.; Li, Z.; Dong, C.; Feng, Y.; Yang, J.; Liu, H.; Du, X. Silver/Copper Interface for Relay Electroreduction of Carbon Dioxide to Ethylene. *ACS Appl. Mater. Interfaces* **2019**, *11*, 2763−2767.
(24) Lum, Y.; Ager, J. W. Sequential Catalysis Controls Selectivity in Electrochemical CO_2 Reduction on Cu. *Energy Environ. Sci.* **2018**, *11*, 2935−2944.
(25) Huang, J.; Mensi, M.; Oveisi, E.; Mantella, V.; Buonsanti, R. Structural Sensitivities in Bimetallic Catalysts for Electrochemical CO_2 Reduction Revealed by Ag−Cu Nanodimers. *J. Am. Chem. Soc.* **2019**, *141*, 2490−2499.
(26) Gurudayal; Perone, D.; Malani, S.; Lum, Y.; Haussener, S.; Ager, J. W. Sequential Cascade Electrocatalytic Conversion of Carbon Dioxide to C-C Coupled Products. *ACS Appl. Energy Mater.* **2019**, *2*, 4551−4559.
(27) Gao, J.; Zhang, H.; Guo, X.; Luo, J.; Zakeeruddin, S. M.; Ren, D.; Grätzel, M. Selective C−C Coupling in Carbon Dioxide Electroreduction via Efficient Spillover of Intermediates As Supported by Operando Raman Spectroscopy. *J. Am. Chem. Soc.* **2019**, *141*, 18704−18714.
(28) Tan, Y.; Xue, X.; Peng, Q.; Zhao, H.; Wang, T.; Li, Y. Controllable Fabrication and Electrical Performance of Single Crystalline Cu_2O Nanowires with High Aspect Ratios. *Nano Lett.* **2007**, *7*, 3723−3728.
(29) Mandal, L.; Yang, K. R.; Motapothula, M. R.; Ren, D.; Lobaccaro, P.; Patra, A.; Sherburne, M.; Batista, V. S.; Yeo, B. S.; Ager, J. W.; Martin, J.; Venkatesan, T. Investigating the Role of Copper Oxide in Electrochemical CO_2 Reduction in Real Time. *ACS Appl. Mater. Interfaces* **2018**, *10*, 8574−8584.
(30) Scholten, F.; Sinev, I.; Bernal, M.; Roldan Cuenya, B. Plasma-Modified Dendritic Cu Catalyst for CO_2 Electroreduction. *ACS Catal.* **2019**, *9*, 5496−5502.
(31) Nag, S.; Mahdak, K. C.; Devaraj, A.; Gohil, S.; Ayyub, P.; Banerjee, R. Phase Separation in Immiscible Silver−Copper Alloy Thin Films. *J. Mater. Sci.* **2009**, *44*, 3393−3401.
(32) Lu, Q.; Rosen, J.; Zhou, Y.; Hutchings, G. S.; Kimmel, Y. C.; Chen, J. G.; Jiao, F. A Selective and Efficient Electrocatalyst for Carbon Dioxide Reduction. *Nat. Commun.* **2014**, *5*, 3242.
(33) Hatsukade, T.; Kuhl, K. P.; Cave, E. R.; Abram, D. N.; Jaramillo, T. F. Insights into the Electrocatalytic Reduction of CO_2 on Metallic Silver Surfaces. *Phys. Chem. Chem. Phys.* **2014**, *16*, 13814−13819.
(34) Hansen Ian, S.; Koper, M. T. M.; Calle-Vallejo, F. Computational Comparison of Late Transition Metal (100) Surfaces for the Electrocatalytic Reduction of CO to C_2 Species. *ACS Energy Lett.* **2018**, *3*, 1062−1067.
(35) Zhang, H.; Chang, X.; Chen, J. G.; Goddard, W. A.; Xu, B.; Cheng, M.-J.; Lu, Q. Computational and Experimental Demonstrations of One-Pot Tandem Catalysis for Electrochemical Carbon Dioxide Reduction to Methane. *Nat. Commun.* **2019**, *10*, 3340.
(36) Cavalca, F.; Ferragut, R.; Aghion, S.; Eilert, A.; Diaz-Morales, O.; Liu, C.; Koh, A. L.; Hansen, T. W.; Pettersson, L. G. M.; Nilsson, A. Nature and Distribution of Stable Subsurface Oxygen in Copper Electrodes During Electrochemical CO_2 Reduction. *J. Phys. Chem. C* **2017**, *121*, 25003−25009.
(37) Liu, C.; Lourenço, M. P.; Hedström, S.; Cavalca, F.; Diaz-Morales, O.; Duarte, H. A.; Nilsson, A.; Pettersson, L. G. M. Stability and Effects of Subsurface Oxygen in Oxide-Derived Cu Catalyst for CO_2 Reduction. *J. Phys. Chem. C* **2017**, *121*, 25010−25017.
(38) Garza, A. J.; Bell, A. T.; Head-Gordon, M. Is Subsurface Oxygen Necessary for the Electrochemical Reduction of CO_2 on Copper? *J. Phys. Chem. Lett.* **2018**, *9*, 601−606.
(39) Fields, M.; Hong, X.; Nørskov, J. K.; Chan, K. Role of Subsurface Oxygen on Cu Surfaces for CO_2 Electrochemical Reduction. *J. Phys. Chem. C* **2018**, *122*, 16209−16215.
(40) Lum, Y.; Ager, J. W. Evidence for Product-Specific Active Sites on Oxide-Derived Cu Catalysts for Electrochemical CO_2 Reduction. *Nat. Catal.* **2019**, *2*, 86−93.

https://dx.doi.org/10.1021/acscatal.8b05119
ACS Catal. 2020, 10, 4059−4069

(41) Okamoto, H.; Chakrabarti, D. J.; Laughlin, D. E.; Massalski, T. B. The Au-Cu (Gold-Copper) System. *J. Phase Equilib.* **1987**, *8*, 454−473.
(42) Sauthoff, G. *Intermetallics*; Wiley-VCH Verlag GmbH & Co. KGaA.: Weinheim, Germany, 2006; pp 646−766.
(43) Bagger, A.; Arán-Ais, R. M.; Halldin Stenlid, J.; Campos dos Santos, E.; Arnarson, L.; Degn Jensen, K.; Escudero-Escribano, M.; Roldan Cuenya, B.; Rossmeisl, J. Ab Initio Cyclic Voltammetry on Cu(111), Cu(100) and Cu(110) in Acidic, Neutral and Alkaline Solutions. *ChemPhysChem* **2019**, *20*, 3096−3105.
(44) Mistry, H.; Choi, Y.-W.; Bagger, A.; Scholten, F.; Bonifacio, C. S.; Sinev, I.; Divins, N. J.; Zegkinoglou, I.; Jeon, H. S.; Kisslinger, K.; Stach, E. A.; Yang, J. C.; Rossmeisl, J.; Roldan Cuenya, B. Enhanced Carbon Dioxide Electroreduction to Carbon Monoxide over Defect-Rich Plasma-Activated Silver Catalysts. *Angew. Chem., Int. Ed.* **2017**, *56*, 11394−11398.
(45) Peterson, A. A.; Abild-Pedersen, F.; Studt, F.; Rossmeisl, J.; Nørskov, J. K. How Copper Catalyzes the Electroreduction of Carbon Dioxide into Hydrocarbon Fuels. *Energy Environ. Sci.* **2010**, *3*, 1311−1315.
(46) Jiang, K.; Sandberg, R. B.; Akey, A. J.; Liu, X.; Bell, D. C.; Nørskov, J. K.; Chan, K.; Wang, H. Metal Ion Cycling of Cu Foil for Selective C−C Coupling in Electrochemical CO_2 Reduction. *Nat. Catal.* **2018**, *1*, 111−119.
(47) Nitopi, S.; Bertheussen, E.; Scott, S. B.; Liu, X.; Engstfeld, A. K.; Horch, S.; Seger, B.; Stephens, I. E. L.; Chan, K.; Hahn, C.; Nørskov, J. K.; Jaramillo, T. F.; Chorkendorff, I. Progress and Perspectives of Electrochemical CO_2 Reduction on Copper in Aqueous Electrolyte. *Chem. Rev.* **2019**, *119*, 7610−7672.
(48) Wang, J.; Sun, Q.; Chan, S.; Su, H. The Acceleration of Methanol Synthesis and C_2 Oxygenates Formation on Copper Grain Boundary from Syngas. *Appl. Catal., A* **2016**, *509*, 97−104.
(49) Ma, S.; Sadakiyo, M.; Luo, R.; Heima, M.; Yamauchi, M.; Kenis, P. J. A. One-Step Electrosynthesis of Ethylene and Ethanol from CO_2 in an Alkaline Electrolyzer. *J. Power Sources* **2016**, *301*, 219−228.
(50) Bagger, A.; Arnarson, L.; Hansen, M. H.; Spohr, E.; Rossmeisl, J. Electrochemical CO Reduction: A Property of the Electrochemical Interface. *J. Am. Chem. Soc.* **2019**, *141*, 1506−1514.
(51) Wang, S.; Petzold, V.; Tripkovic, V.; Kleis, J.; Howalt, J. G.; Skúlason, E.; Fernández, E. M.; Hvolbæk, B.; Jones, G.; Toftelund, A.; Falsig, H.; Björketun, M.; Studt, F.; Abild-Pedersen, F.; Rossmeisl, J.; Nørskov, J. K.; Bligaard, T. Universal Transition State Scaling Relations for (De)hydrogenation over Transition Metals. *Phys. Chem. Chem. Phys.* **2011**, *13*, 20760−20765.
(52) Wang, S.; Temel, B.; Shen, J.; Jones, G.; Grabow, L.; Studt, F.; Bligaard, T.; Abild-Pedersen, F.; Christensen, C.; Nørskov, J. Universal Brønsted-Evans-Polanyi Relations for C-C, C-O, C-N, N-O, N-N, and O-O Dissociation Reactions. *Catal. Lett.* **2011**, *141*, 370−373.
(53) Clark, E. L.; Wong, J.; Garza, A. J.; Lin, Z.; Head-Gordon, M.; Bell, A. T. Explaining the Incorporation of Oxygen Derived from Solvent Water into the Oxygenated Products of CO Reduction over Cu. *J. Am. Chem. Soc.* **2019**, *141*, 4191−4193.
(54) Lum, Y.; Cheng, T.; Goddard, W. A.; Ager, J. W. Electrochemical CO Reduction Builds Solvent Water into Oxygenate Products. *J. Am. Chem. Soc.* **2018**, *140*, 9337−9340.
(55) Li, H.; Li, Y.; Koper, M. T. M.; Calle-Vallejo, F. Bond-Making and Breaking between Carbon, Nitrogen, and Oxygen in Electrocatalysis. *J. Am. Chem. Soc.* **2014**, *136*, 15694−15701.
(56) Durand, W. J.; Peterson, A. A.; Studt, F.; Abild-Pedersen, F.; Nørskov, J. K. Structure Effects on the Energetics of the Electrochemical Reduction of CO_2 by Copper Surfaces. *Surf. Sci.* **2011**, *605*, 1354−1359.
(57) Montoya, J. H.; Peterson, A. A.; Nørskov, J. K. Insights into C-C Coupling in CO_2 Electroreduction on Copper Electrodes. *ChemCatChem* **2013**, *5*, 737−742.
(58) Kresse, G.; Furthmüller, J. Efficient Iterative Schemes for Ab Initio Total-Energy Calculations Using a Plane-Wave Basis Set. *Phys. Rev. B: Condens. Matter Mater. Phys.* **1996**, *54*, 11169−11186.
(59) Perdew, J. P.; Burke, K.; Ernzerhof, M. Generalized Gradient Approximation Made Simple. *Phys. Rev. Lett.* **1996**, *77*, 3865−3868.
(60) Kresse, G.; Joubert, D. From Ultrasoft Pseudopotentials to the Projector Augmented-Wave Method. *Phys. Rev. B: Condens. Matter Mater. Phys.* **1999**, *59*, 1758−1775.
(61) Monkhorst, H. J.; Pack, J. D. Special Points for Brillouin-Zone Integrations. *Phys. Rev. B* **1976**, *13*, 5188−5192.
(62) He, Z.-D.; Hanselman, S.; Chen, Y.-X.; Koper, M. T. M.; Calle-Vallejo, F. Importance of Solvation for the Accurate Prediction of Oxygen Reduction Activities of Pt-Based Electrocatalysts. *J. Phys. Chem. Lett.* **2017**, *8*, 2243−2246.
(63) Henkelman, G.; Uberuaga, B. P.; Jónsson, H. A Climbing Image Nudged Elastic Band Method for Finding Saddle Points and Minimum Energy Paths. *J. Chem. Phys.* **2000**, *113*, 9901−9904.

https://dx.doi.org/10.1021/acscatal.8b05119
ACS Catal. 2020, 10, 4059−4069

3.5 Toward Efficient Tandem Electroreduction of CO_2 to Methanol Using Anodized Titanium

Introduction Annually, by reacting syngas (a mix of H_2 and CO) over Cu-Zn oxide catalysts, 95 million tons of methanol (CH_3OH) are produced worldwide.[142] High temperatures and pressures are required to produce syngas and synthesize CH_3OH. Overall, the production of one kg of methanol leads to the emission of approximately 0.5 kg of CO_2.[143] Therefore, a greener solution for CH_3OH production is needed. Powered by renewable electricity, CO_2RR is a sustainable route to produce methanol. However, to date, there are no electrocatalysts with enough stability, selectivity, and activity to implement this process industrially.[144,145]

To address these challenges, a strategy involving a tandem electroreduction where CO_2 is first reduced to formic acid (HCOOH) and then to CH_3OH could be a good alternative. The first step has been completed successfully with Faradaic efficiencies close to 100% using catalysts such as lead,[146] tin,[147] and indium.[148] The second step, the reduction of formic acid to methanol (FAR, in acid: $HCOOH + 4H^+ + 4e^- \rightarrow CH_3OH + H_2O$, $E^0 = 0.11$ V vs RHE), is more challenging due to the electrochemical inertness of formic acid,[149] which is considered a dead-end CO_2RR product on transition metal electrodes.[119] Previous efforts to reduce HCOOH to CH_3OH featured low current densities or high applied overvoltages.[150,151]

In this work, in collaboration with the group of Prof. Boon Siang Yeo at the National University of Singapore, we identified anodized titanium (Ti_{an}) as an active electrocatalyst for FAR. With the complementary data obtained from both experiments and DFT calculations we elucidated the active sites responsible for such an activity and provide useful guidelines for the future enhancement of FAR catalysts.

This work led to the publication of a research article.[152] The manuscript is included at the end of this section. In the following pages, a summary of it is given. My contribution to the research article was: (a) Elaboration of the DFT calculations, (b) analysis of the computational results and making of the corresponding figures, and (c) collaboration in the writing of the manuscript. I was not involved in the making of the experiments. The supporting information for this article can be found in Appendix E. The optimized geometries were removed from this document to save space but can be found online at: https://doi.org/10.1021/acscatal.1c01725.

Results Experimental measurements show that HCOOH can be reduced to methanol with an optimal Faradaic efficiency of 12.6% and a j_{CH3OH} of -2.0 mA/cm^2 at -1.0 V vs RHE on Ti_{an}. We noted that FAR to methanol could not be extended to other metal electrodes, even when anodized. Experiments suggest that the active sites for FAR on Ti_{an} are located at oxygen vacancies or Ti^{3+} sites (hereon denoted as TOVs), since a positive correlation between the amount of TOVs and j_{CH3OH} was found. Moreover, Ti_{an} catalysts anodized longer times, hence having an increased number of TOVs, show lower selectivity for HER, reducing the Faradaic efficiency of H_2 down to 70%.

DFT calculations were performed to elucidate the FAR reaction pathway to methanol and gain information on the active sites. Note that we used the Hubbard approach with a U_{eff} of 5 eV, to help in localizing the *d* states of Ti atoms. We modelled the most stable surface termination of titania, namely, TiO_2(110). This surface is composed of alternating rows of coordinatively unsaturated (CUS) and bridge sites. As seen in Figure 26a, CUS sites have exposed undercoordinated Ti atoms available to interact with adsorbates, while bridge sites do not. However, bridge sites have twofold-coordinated oxygen atoms (O_{2c}), which are known to leave TOVs on TiO_2.[153] To include the heterogeneity observed in experiments, we also modelled two stepped surfaces: CUS-terminated TiO_2(120) (denoted TiO_2(120)-CT) and bridge-terminated TiO_2(120) (denoted TiO_2(120)-BT). These surfaces have similar alternating rows of CUS and bridge sites as in TiO_2(110) but feature a unique type of O_{2c} located at edge sites (denoted E-O_{2c}). Calculated TOV formation energies show that TOVs are more facilely formed on stepped TiO_2 surfaces, and that in those, vacancies are easier to form by removing an O_{2c} oxygen atom than an E-O_{2c} oxygen atom.

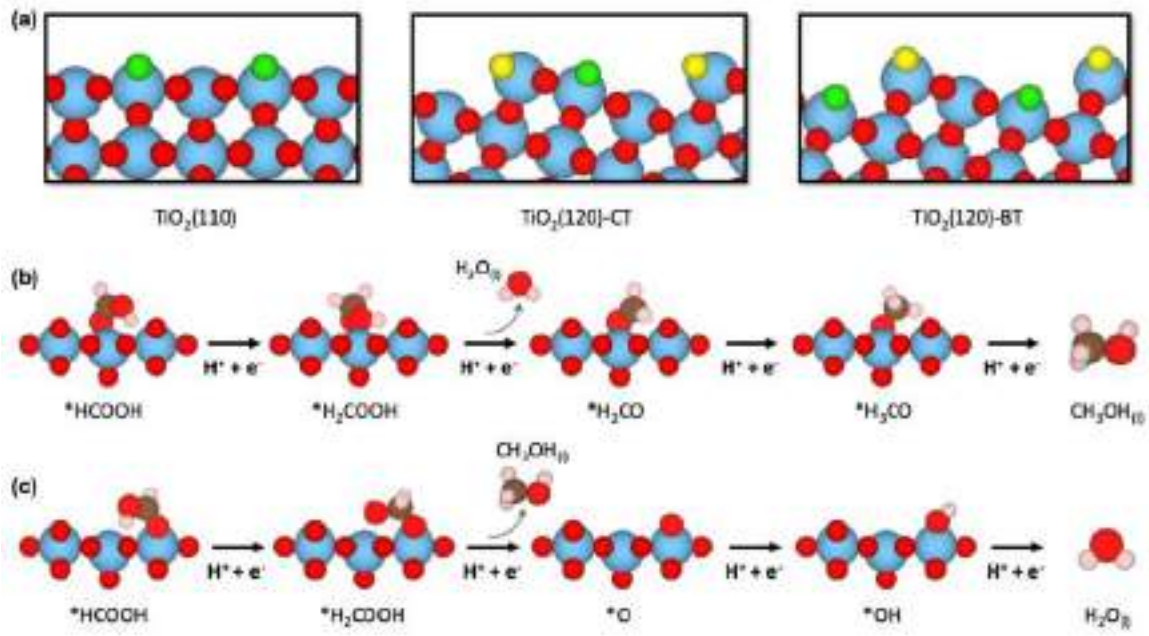

Figure 26. (a) Schematics of the slab models used in this work. Ti atoms are shown in blue, O atoms in red, bridge site oxygen atoms (O_{2c}) in green, and edge site oxygen atoms (E-O_{2c}) in yellow. The lowest-energy pathway for FAR to CH_3OH is shown in (b) CUS sites and (c) TOVs. In panels (b) and (c), Ti, O, C, and H atoms are shown in blue, red, brown, and pink, respectively. This figure corresponds to Figure 4 in reference 152 and is included here to facilitate the reading of this thesis.

The most favorable pathway for FAR to CH_3OH is shown in Figure 26b for CUS sites and Figure 26c for TOVs. On both sites the hydrogenation of *HCOOH leads to the formation of *H_2COOH, but the pathways bifurcate from that point on. On CUS sites, *H_2COOH is hydrogenated to produce *H_2CO + $H_2O_{(l)}$, while at TOVs, CH_3OH is directly produced from the protonation of *H_2COOH, leaving the TOV filled with *O. Free-energy diagrams featuring both pathways on the three studied surfaces are shown in Figure 27a. The potential-limiting step at CUS sites is the hydrogenation of *HCOOH to H_2COOH, with calculated onset potentials of -1.27, -1.57, and -1.21 V vs RHE for TiO_2(110), TiO_2(120)-CT, and TiO_2(120)-BT, respectively. In contrast, the electroreduction of HCOOH on TOVs (denoted TiO_2(110)-O, TiO_2(120)-CT-O, and TiO_2(120)-BT-O) proceeds via the exothermic formation of *H_2COOH. At TOVs, the potential-limiting step corresponds to the regeneration of the vacancy, namely, the protonation of *OH to $H_2O_{(l)}$. The calculated onset potentials are -1.17, -0.77, and -0.54 V vs RHE for TiO_2(110)-O, TiO_2(120)-CT-O, and TiO_2(120)-BT-O, respectively. The onset potentials at TOVs are clearly lower than those calculated at CUS sites, due to the favorable formation of the *H_2COOH intermediate at TOVs and the opening of an

alternative catalytic pathway. The most active sites toward FAR are those TOVs located at steps, namely TiO_2(120)-CT-O and TiO_2(120)-BT-O.

Figure 27b features a Sabatier-type activity plot using the free energy of $*H_2COOH$ (a common intermediate for both TOVs and CUS sites) with respect to $HCOOH_{(l)}$ as a descriptor. CUS sites are located at the right leg (i.e., weak-binding side) of the volcano, where the potential-limiting step is the formation of $*H_2COOH$. On the other hand, TOVs are on the strong-binding (left) leg, where the hydrogenation of *OH is the potential-limiting step. The peak of the volcano (where $\Delta G_{H_2COOH} \approx 0$) is close to the equilibrium potential, indicating that it is thermodynamically feasible to synthesize nearly ideal FAR electrocatalysts following $\Delta G_{H_2COOH} \approx 0$ as a guiding principle.

We also identified the free energy of adsorption of HCOOH as a suitable descriptor of FAR activity. As shown in Figure 27c, the weaker ΔG_{HCOOH}, the more positive the calculated limiting potential (U_L). However, this correlation is to be taken with caution: if the free energy of adsorption of HCOOH is too weak, it might not adsorb at all onto the catalyst surface, and no activity will be observed. Moreover, we found that TOV formation energies, ΔE_{TOV}, are inversely correlated with U_L (inset of Figure 27c). Hence, surface sites with more positive ΔE_{TOV} have simultaneously more stable *OH adsorption energies.

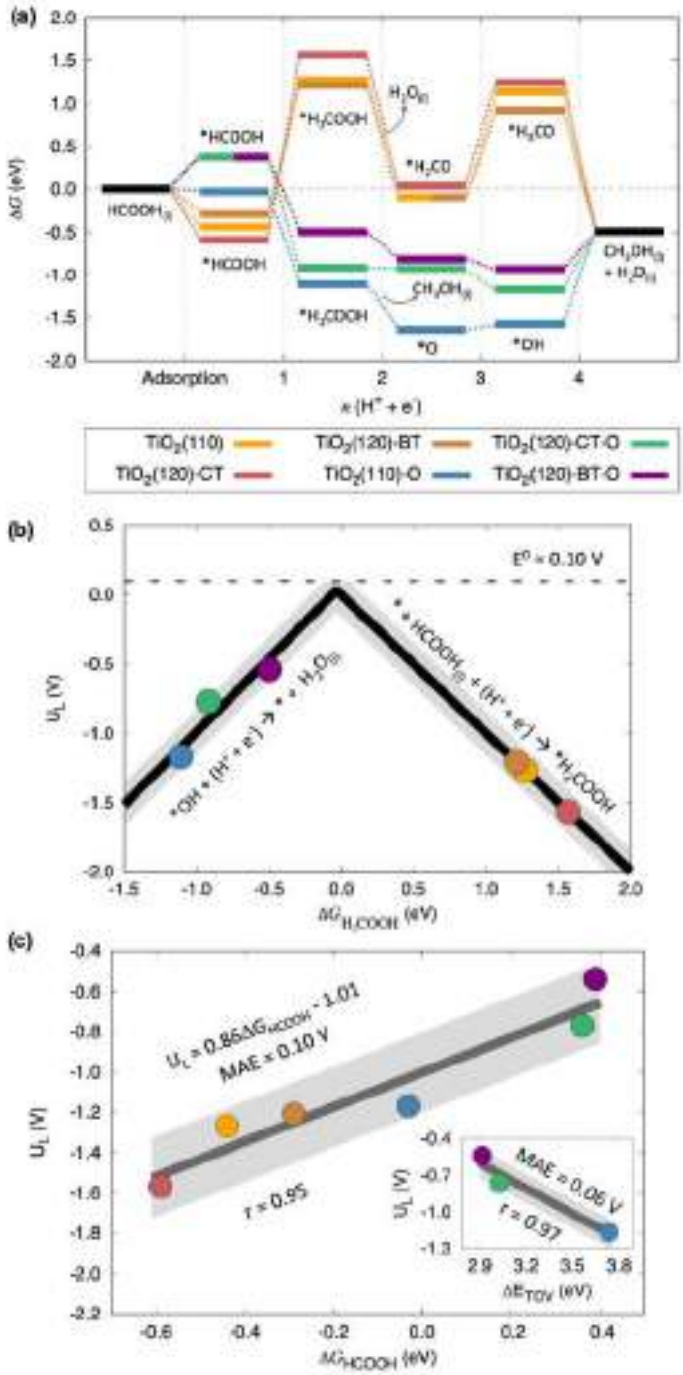

Figure 27. a) Free-energy diagrams at 0 V vs RHE for FAR to CH_3OH at CUS and TOV sites. The intermediates and active sites are shown in Figure 26. b) Volcano plot correlating the onset potential for FAR with the free energy of $*H_2COOH$ with respect to $HCOOH_{(l)}$. The dashed line corresponds to the calculated equilibrium potential (0.10 V vs RHE). Gray bands of ±0.16 V around the black lines correspond to ±2 MAE (MAE: mean absolute error) of the scaling relation between $*H_2COOH$ and *OH. c) Calculated onset potential as a function of the free energy of adsorption of formic acid. The MAE and the Pearson coefficient are also provided together with a linear regression in dark gray and a light gray zone of ±2 MAE. The inset shows the calculated onset potential as a function of the formation energies of oxygen vacancies at TOV sites. The color code for each active site is the same in all panels and is shown in (a). This figure corresponds to Figure 5 in reference 152 and is included here to facilitate the reading of this thesis.

Conclusions These results, together with additional data and analyses shown in the research article below, lead to the following conclusions:

- FAR to CH_3OH can be performed at -1.0 V vs RHE with a satisfactory Faradaic efficiencies and current densities using anodized titanium.
- Experimental measurements indicate that the amount of oxygen vacancies (TOVs) present in the catalyst is correlated with an increase in methanol production. DFT calculations indicate that the TOVs at steps are the most active sites for FAR to CH_3OH.
- The most favorable reaction pathway goes through the protonation of a $*H_2COOH$ intermediate that produces methanol and fills the TOV with *O. Subsequent hydrogenation to *OH and H_2O regenerates the TOV and enables the restart of the catalytic cycle.
- The free energies of adsorption of *HCOOH and $*H_2COOH$, as well as the formation energy of TOVs, can be used as descriptors to guide the design of enhanced FAR electrocatalysts.

ACS Catalysis

pubs.acs.org/acscatalysis

Research Article

Toward Efficient Tandem Electroreduction of CO_2 to Methanol using Anodized Titanium

Wei Jie Teh, Oriol Piqué, Qi Hang Low, Weihan Zhu, Federico Calle-Vallejo,* and Boon Siang Yeo*

Cite This: ACS Catal. 2021, 11, 8467−8475

Read Online

ACCESS | Metrics & More | Article Recommendations | Supporting Information

ABSTRACT: The electroreduction of CO_2 (CO_2RR) using renewable electricity is an appealing route to synthesize methanol (CH_3OH), a valuable C_1 feedstock and fuel. Unfortunately, there are still no workhorse electrocatalysts with suitable activity and selectivity for this reaction. Currently, formic acid (HCOOH), CO, and methane are the most common C_1 products. Since multielectron electrocatalytic reactions can be severely affected by adsorption-energy scaling relations, a tandem process likely offers a higher efficiency. Therefore, we strategized to reduce CO_2 to HCOOH and then reduce HCOOH to CH_3OH. While the former step can be accomplished with ease using post-transition metals, the latter is extremely difficult due to the electrochemical inertness of HCOOH. Herein, we develop anodized titanium catalysts containing Ti^{3+} sites and oxygen vacancies (termed as TOVs), which can reduce HCOOH to CH_3OH with a remarkable Faradaic efficiency of 12.6% and a partial current density of −2 mA/cm^2 at −1.0 V versus reversible hydrogen electrode (RHE). Using electron paramagnetic resonance spectroscopy and cyclic voltammetry, we show that the population of TOVs on the catalyst is positively correlated with the production of CH_3OH. Density functional theory (DFT) calculations identify TOVs at defects as the active sites in a vacancy-filling pathway mediated by $*H_2COOH$. We further provide holistic screening guidelines based on the *HCOOH and $*H_2COOH$ binding energies alongside TOV formation energies. These can open the path for the high-throughput automated design of catalysts for CH_3OH synthesis from tandem CO_2 electrolysis.

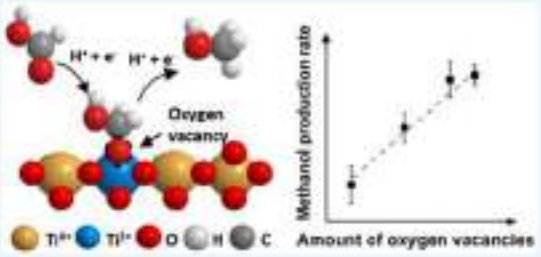

KEYWORDS: *formic acid reduction, electrocatalysis, oxygen vacancies, density functional theory, methanol*

1. INTRODUCTION

Methanol (CH_3OH) is a major transportation fuel and chemical feedstock, and 95 million tons of it are produced worldwide annually.[1] Currently, CH_3OH is produced industrially by reacting syngas (CO and H_2) over copper−zinc oxide catalysts. However, high temperatures and pressures are required to synthesize CH_3OH (200−300 °C and 50−100 bar)[2] and the syngas reactant (via the steam reforming of natural gas at ~850 °C and ~30 bar over a nickel catalyst).[3] Overall, the typical industrial production of 1 kg of CH_3OH leads to a net positive emission of ~0.5 kg of CO_2.[4] For these reasons, a greener pathway toward CH_3OH production is needed.

A sustainable route to CH_3OH production is through the electrochemical CO_2 reduction reaction (CO_2RR), which can be powered by renewable electricity. However, there are to date no workhorse electrocatalysts that can directly reduce CO_2 to CH_3OH with industrially relevant activity, selectivity, and stability.[5,6] To overcome this obstacle, one can resort to a tandem strategy in which CO_2 is first reduced to formic acid (HCOOH) and the latter is then reduced to CH_3OH. The first step has already been achieved with Faradaic efficiencies (FEs) for HCOOH production close to 100% using catalysts based on post-transition metals such as tin,[7] indium,[8] and lead.[9]

The second step, namely, formic acid reduction (FAR) to CH_3OH ($HCOOH + 4H^+ + 4e^- \rightarrow CH_3OH + H_2O$, E^0 = +0.11 V vs RHE),[10] is more challenging because of the electrochemical inertness of HCOOH. This is caused by the low electrophilicity of the carbonyl carbon that is part of a conjugated carboxylic acid functional group.[11] Thus, while ketones and aldehydes formed from CO_2RR can be further reduced to give alcohols,[12,13] HCOOH and other carboxylic acids are dead-end CO_2RR products on transition metal electrodes.[14]

Early efforts to reduce formic acid to CH_3OH were from Russell et al., whose team employed an electro-etched Sn catalyst.[15] While the reported Faradaic efficiency for CH_3OH (FE_{CH3OH}) was nearly 100%, its partial current density (j_{CH3OH}) was 3.6 μA/cm^2, which limits the practicality of the process. Kyriacou et al. found that HCOOH could be reduced to CH_3OH on a Cr foil catalyst (FE_{CH3OH} = 37.4%) in an 85%

Received: April 15, 2021
Revised: May 26, 2021
Published: June 28, 2021

https://doi.org/10.1021/acscatal.1c01725
ACS Catal. 2021, 11, 8467−8475

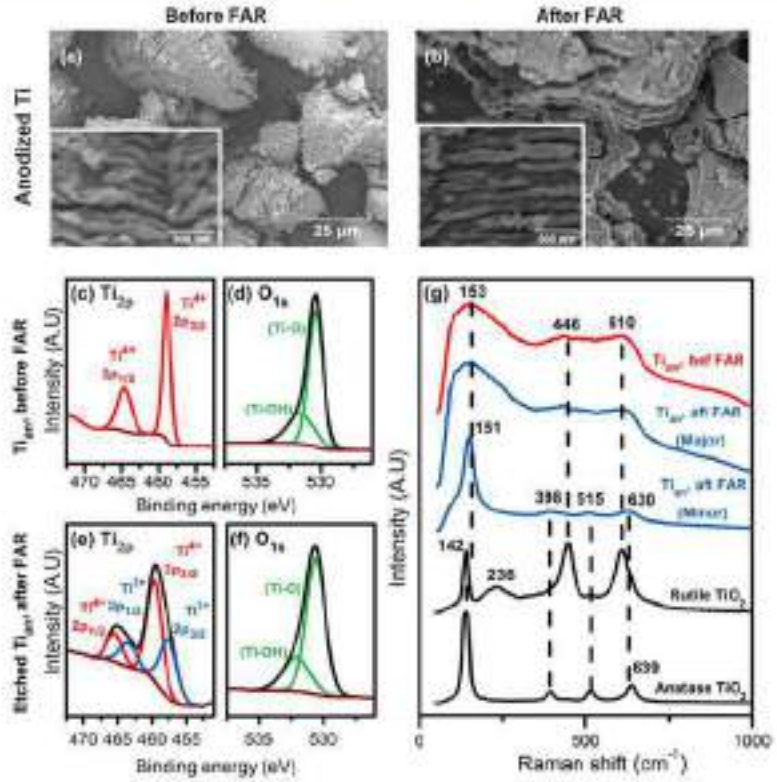

Figure 1. Characterization of Ti anodized for 3 min in 0.2 M KCl ($Ti_{ox,\ 3\ min}$). SEM images of $Ti_{ox,\ 3\ min}$ (a) before FAR and (b) after FAR at −1.0 V vs RHE. The insets are the magnified images of Ti_{ox} before and after FAR. XPS analyses of (c)−(d) $Ti_{ox,\ 3\ min}$ before FAR and (e)−(f) $Ti_{ox,\ 3\ min}$ after FAR at −1.0 V vs RHE after its surface was etched with an Ar^+ ion beam. (g) Raman spectra of TiO_2 standards and $Ti_{ox,\ 3\ min}$ before and after FAR at −1.0 V vs RHE. The peak intensities in the Raman spectra of $Ti_{ox,\ 3\ min}$ before FAR and $Ti_{ox,\ 3\ min}$ after FAR (major) were ~5× smaller than those in the Raman spectrum of $Ti_{ox,\ 3\ min}$ after FAR (minor) and have been rescaled here for clarity.

phosphoric acid electrolyte at 80 °C.[16] Adegoke et al. reported a FE_{CH_3OH} of 11.9% for FAR on In_2O_3 nanoparticles at an applied cell voltage of 3.5 V in a two-electrode electrolyzer.[17] While FAR activity has been observed in these scattered reports, the key active sites and mechanistic pathways are still unclear. These voids of knowledge severely limit research efforts to improve FAR to CH_3OH.

Recently, it was shown that the anatase phase of TiO_2 could electroreduce non-aromatic carboxylic acids, such as oxalic acid, to their corresponding aldehydes and finally to alcohols.[11] Through adsorption and density functional theory (DFT) studies, it was proposed that significant interaction of the carboxylic acid with the catalyst surface is necessary for electron transfer from the electrode to the LUMO of the molecule. Interestingly, HCOOH could not be reduced. Thus, new approaches that capitalize on this finding are clearly needed. Herein, we put forth another strategy to improve the electroreduction of carboxylic acids using the Ti^{3+} and oxygen vacancy sites of TiO_2 (hereon denoted as TOVs), which can be created by applying a negative voltage on the material. We propose that TOVs aid in C−O bond scission by directly stripping O atoms from the reactants, giving rise to new pathways for the reduction of carboxylic acids. In this respect, TiO_2 is an appealing catalyst for C−O bond scission, as the strong Ti−O bond lowers the activation energy of the C−O bond cleavage.[18]

On the basis of the above discussion, we anodized titanium (Ti_{ox}), an earth-abundant and relatively inexpensive element, so as to introduce TOVs to its surface. Ti_{ox} exhibits significant electrocatalytic activity for FAR to CH_3OH. We quantitatively assess the impact of varying the amount of TOVs on Ti_{ox} for CH_3OH production using electron paramagnetic resonance (EPR) spectroscopy and cyclic voltammetry (CV). These experimental findings, coupled with DFT calculations, allow us to elucidate the catalytic pathway for FAR to CH_3OH, determine that the critical active sites are the TOVs, and provide quantitative guidelines for the future enhancement of FAR catalysts.

2. RESULTS AND DISCUSSION

2.1. Formation and Characterization of Ti^{3+} and Oxygen Vacancies on Anodized Ti. Our strategy for forming TOVs is as follows: Ti discs were first anodized at +0.25 A/cm^2 in a 0.2 M KCl solution for 3 min ($Ti_{ox,\ 3\ min}$). Scanning electron microscopy (SEM) revealed that the $Ti_{ox,\ 3\ min}$ catalyst surface consisted of particles with grooves of 1.5−2 μm long (Figure 1a). The discs were then reduced in-situ during FAR at a representative potential of −1.0 V vs RHE to produce TOVs (all potentials reported hereafter are referenced to the RHE). No significant changes to the catalyst surface after FAR could be discerned by SEM (Figure 1b).

X-ray photoelectron spectroscopy (XPS) analysis of a freshly prepared $Ti_{ox,\ 5\ min}$ catalyst (Figures 1c−f) revealed that the main surface Ti species is Ti^{4+} (in TiO_2), as indicated by its $2p_{3/2}$ and $2p_{1/2}$ peaks at 458.7 and 464.5 eV, respectively.[19] O_{1s} peaks observed at 530.4 and 531.6 eV correspond to the oxygen in TiO_2 (Ti−O) and surface hydroxyl groups (Ti−OH), respectively.[20] No changes in the XPS spectra were

https://doi.org/10.1021/acscatal.1c01725
ACS Catal. 2021, 11, 8467−8475

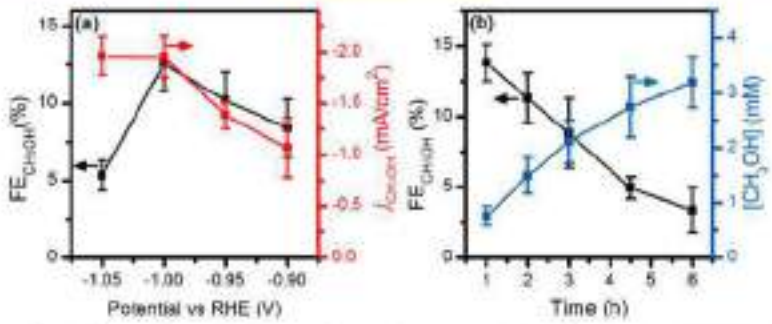

Figure 2. Formic acid reduction (FAR) using $Ti_{an,\ 3\ min}$ electrocatalysts in the 0.1 M K_2SO_4 electrolyte with 0.5 M HCOOH added (pH ~ 2.6). (a) Faradaic efficiency, FE (%), and partial current density, j (mA/cm^2), of CH_3OH obtained during 60 min of FAR at different applied potentials. (b) FE (%) and accumulated concentrations (mM) of CH_3OH production from FAR for 6 h at −1.0 V vs RHE. Arrows are included to guide the eye to the respective graph axes.

observed for the $Ti_{an,\ 3\ min}$ catalyst after it had been used for FAR at −1.0 V (Figures S1a−c). However, XPS analysis of its subsurface, which was exposed after 30 min of Ar^+ ion etching, revealed peaks at 457.6 and 463.4 eV. These can be respectively assigned to the $2p_{3/2}$ and $2p_{1/2}$ peaks of Ti^{3+}, indicating the reduction of Ti^{4+} to TOVs during FAR.[21] We note here that TOVs were not observed on the surface of the pre-etched catalyst, as they would have rapidly oxidized to Ti^{4+} after electrolysis and during sample transfer.[22] Ultraviolet−visible diffuse reflectance spectroscopy of Ti_{an} after FAR further confirmed the presence of Ti^{3+}, based on its characteristic absorption peak between 400 to 800 nm (Figure S2).[23]

X-ray diffraction (XRD) of the $Ti_{an,\ 3\ min}$ catalyst before and after FAR at −1.0 V showed no well-defined crystalline anatase or rutile TiO_2 XRD peaks, suggesting that it was XRD-amorphous (Figure S3). In contrast, Raman spectroscopy of the $Ti_{an,\ 3\ min}$ catalyst revealed TiO_2 peaks (Figure 1g and Table S4). Before FAR, Raman bands at 153, 446, and 610 cm^{-1} corresponding to rutile TiO_2 were recorded.[24] These bands were broadened and shifted, indicating lattice disorder and defects in $Ti_{an,\ 3\ min}$.[19] Note that rutile TiO_2 was detected by Raman spectroscopy, but not by XRD because of the absence of long-range order in the $Ti_{an,\ 3\ min}$ catalyst.[25,26]

The crystallography of the $Ti_{an,\ 3\ min}$ catalyst remained largely unchanged after FAR at −1.0 V (blue-colored Raman spectrum in Figure 1g, denoted as "major"). However, we also observed Raman bands at 151, 398, 515, and 630 cm^{-1} on a few spots of the $Ti_{an,\ 3\ min}$ catalyst (spectrum denoted as "minor"). These bands can be ascribed to anatase TiO_2.[24] These results suggest that a portion of amorphous $Ti_{an,\ 3\ min}$ crystallized to anatase TiO_2 during FAR, which is in agreement with previous works on the electrochemical behavior of amorphous TiO_2 nanotubes in water.[27,28]

2.2. Electrocatalytic Activity of Ti_{an} for FAR to CH_3OH.

The FAR activities of Ti_{an} were evaluated using a three-electrode setup, with a Ag/AgCl (saturated KCl) and graphite rod respectively employed as the reference and counter electrodes. Chronoamperometry was performed in 0.1 M K_2SO_4 electrolyte with 0.5 M HCOOH (pH 2.6) at potentials from −0.90 to −1.05 V using $Ti_{an,\ 3\ min}$ catalysts. HCOOH was reduced to CH_3OH with an optimal FE_{CH_3OH} of 12.6% and a j_{CH_3OH} of −2 mA/cm^2 at −1.0 V (Figure 2a, Table S5, and ^{1}H NMR spectroscopy and gas chromatography data in Figure S4; all reported current densities were normalized to the geometric surface area of the electrode). No CH_3OH was detected in the absence of electrochemical potentials, which shows that it was generated electrochemically.

Methane (CH_4) and formaldehyde (CH_2O) were detected as minor FAR products (FE_{CH_4} = 1.4% and FE_{CH_2O} = 0.1% at −1.0 V). Hydrogen gas from the parasitic hydrogen evolution reaction (HER) formed the bulk of the remaining products. To assess if CH_4 was a product of either CH_3OH or CH_2O reduction, we reduced 5 mM of the latter two molecules in 0.1 M K_2SO_4 at −1.0 V on a $Ti_{an,\ 3\ min}$ catalyst (Table S6). No CH_4 was detected, indicating that it was formed from the reduction of HCOOH. While CH_2O is a known precursor of CH_3OH, only small amounts of CH_3OH were obtained during CH_2O electrolysis.[6] This observation will be further explained in Section 2.4.

Trace amounts (3−14 ppm) of carbon monoxide (CO) were also detected during FAR. They were likely formed from HCOOH dehydration over the TOVs (Table S7), which is in agreement with previous works by Iwasawa et al. where in situ experimental and theoretical studies were used to model HCOOH dehydration to CO on TOVs.[29,30]

The catalytic stability was assessed by performing a 6 h HCOOH electrolysis on $Ti_{an,\ 3\ min}$ at −1.0 V (Figure 2b and Section S3.4). CH_3OH was formed throughout the entire period, although its rate of formation decreased from 11.6 to 4.6 μmol/h·cm^2. We also noted that FE_{CH_3OH} decreased from 13.8 to 3.4%. Based on the Pourbaix diagram of TiO_2, the dissolution of TiO_2 to Ti^{2+} can occur at pH 2.6 and −1.0 V (or −1.15 V vs SHE).[31] We thus hypothesize that the decrease in the activity and selectivity of CH_3OH is due to catalyst layer dissolution of Ti_{an} during prolonged electrolysis. This was verified by SEM imaging of the catalysts, which showed the loss of Ti_{an} after 6 h of FAR. Inductively coupled plasma-optical emission spectrometry (ICP-OES) analysis also detected 8.6 ppm of Ti in the electrolyte after 6 h of FAR at −1.0 V. This corresponds to 0.103 mg of Ti, which is ~7% loss of the Ti_{an} powder that was initially formed on a $Ti_{an,\ 3\ min}$ catalyst (1.45 mg). Interestingly, while the dissolution of the Ti_{an} catalysts could be lowered at a higher electrolyte pH (pH 4.5 and 5.8, adjusted using KOH), the amount of CH_3OH formed decreased significantly. This suggests that the active species for FAR to CH_3OH is HCOOH rather than $HCOO^-$ (the pK_a of HCOOH is 3.6−3.8).[32]

To close this section, we note that FAR to CH_3OH cannot be extended to other metal electrodes, even if they have been anodized (Table S10). This was exemplified using Sn and Cr electrodes, which were previously reported to exhibit FAR

https://doi.org/10.1021/acscatal.1c01725
ACS Catal. 2021, 11, 8467−8475

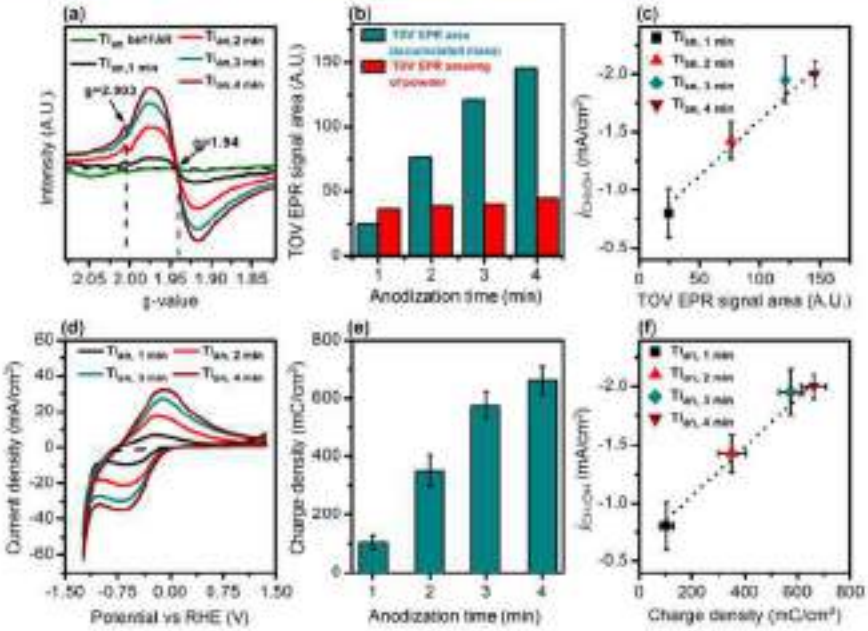

Figure 3. (a) EPR spectra of Ti_{as} samples (anodized over 1, 2, 3, and 4 min) after they were used as catalysts for 60 min of FAR at −1.0 V vs RHE. The catalyst before FAR had been anodized for 3 min. (b) EPR signal areas of TOVs on Ti_{as} samples (anodized for 1, 2, 3, and 4 min) (dark cyan bar) and EPR signal areas normalized to the mass of Ti_{as} samples (red bar). (c) Dependence of j_{CH3OH} on the amount of TOVs based on EPR signal areas (dotted lines are included to guide the eye). (d) Cyclic voltammograms (cathodic sweep first) of the Ti_{as} samples after 60 min of FAR at −1.0 V vs RHE. Scan rate: 50 mV/s. The electrolyte used was 0.1 M K_2SO_4 with 0.5 M HCOOH. (e) Anodic peak areas (mC/cm²; from −0.85 to 1.35 V vs RHE) corresponding to the amount of TOVs on the Ti_{as} samples (anodized over 1, 2, 3, and 4 min). (f) Dependence of j_{CH3OH} on the amount of TOVs based on anodic peak areas (dotted lines are included to guide the eye).

activity.[15,16] At −1.0 V, no CH_3OH was detected from either the polished or anodized Sn discs, while insignificant amounts of CH_3OH were observed on a polished Cr disc (FE_{CH3OH} = 0.07% and j_{CH3OH} = −0.08 mA/cm²) and anodized Cr (FE_{CH3OH} = 0.005% and j_{CH3OH} = −0.007 mA/cm²).

2.3. Identification of the Active Sites for FAR to CH_3OH. In this section, we evaluate our proposition that TOVs are the active sites for FAR to CH_3OH. The paramagnetic TOVs in the Ti_{as} samples can be quantified using EPR spectroscopy.[33] Ti discs were first anodized at +0.25 A/cm² in a 0.2 M KCl solution for 1, 2, 3, and 4 min and then used for FAR. Three discs were studied at each anodization time. The Ti_{as} layers were removed from the discs for EPR analysis.

The EPR spectra of the Ti_{as} catalysts before and after FAR are shown in Figure 3a. Before FAR, no EPR signals from Ti^{3+} or OVs were observed. After 60 min of FAR at −1.0 V, the Ti_{as} samples exhibited a broad EPR signal at g = 1.94, which can be assigned to paramagnetic Ti^{3+} centers that are trapped on defects in amorphous titanium.[34,35] The peak at g = 2.003 is attributed to the presence of OVs.[35] Since Ti^{3+} and OVs are concurrently formed, we shall use both their EPR signals to quantify the amount of TOVs present.

We found that the mass of Ti_{as} powder formed and the EPR signal for the TOVs both increased by ~5× when the anodization time of the Ti foil was increased from 1 to 4 min (Figure 3b and Table S11). More importantly, we observed a positive correlation between the amount of TOVs and j_{CH3OH}: extending the anodization time for the Ti_{as} catalyst from 1 to 4 min increased the amount of TOVs on the catalyst by ~5×, which led to a 2.5× higher j_{CH3OH} from FAR (Figure 3c). However, the mass-normalized EPR signal areas of the TOVs are relatively constant across all anodization times, which indicates that the quantity of TOVs present per unit mass of the Ti_{as} catalyst is similar (Figure 3b).

We also recorded cyclic voltammograms of the Ti_{as} samples after FAR at −1.0 V to determine if the TOVs are accessible for electrolysis (Figure 3d). The broad oxidation peak observed from −0.85 to 1.35 V can be assigned to the oxidation of the TOVs to Ti^{4+}.[37] The population of TOVs on the catalysts can be estimated using the integrated charges in this peak (Figure 3e and Table S12) and was also found to be positively correlated with j_{CH3OH} (Figure 3f). This complements the findings from the EPR analysis. Overall, our EPR and CV results show that the amount of TOVs is correlated to CH_3OH production. Assuming that all available TOVs on a $Ti_{as,\ 3\ min}$ catalyst are active, the average turnover frequency (TOF) of CH_3OH formation at −1.0 V was determined to be 8.5×10^{-4} s^{-1} (Section S7.2).

We also performed experiments on crystalline anatase and rutile TiO_2 samples (0.15−1 μm in particle size) which were drop-casted on a Ti disc at −1.0 V (Section S4.3 and Figure S3). No TOVs were observed from the voltammograms of rutile and anatase TiO_2 particles after FAR. Interestingly, these catalysts reduce HCOOH to CH_3OH with a FE_{CH3OH} of <0.2% and j_{CH3OH} of −0.05 mA/cm². These observations further verify the role of TOVs as active sites for FAR to CH_3OH.

Additionally, we note that Ti_{as} catalysts which were anodized for longer times exhibited poorer selectivities for the HER; for example, the FEs for H_2 decreased from 87% on $Ti_{as,\ 3\ min}$ to 70% on $Ti_{as,\ 4\ min}$ (Table S14). Thus, to sum up, increasing the number of TOV sites in Ti_{as} improves the

https://doi.org/10.1021/acscatal.1c01725
ACS Catal. 2021, 11, 8467−8475

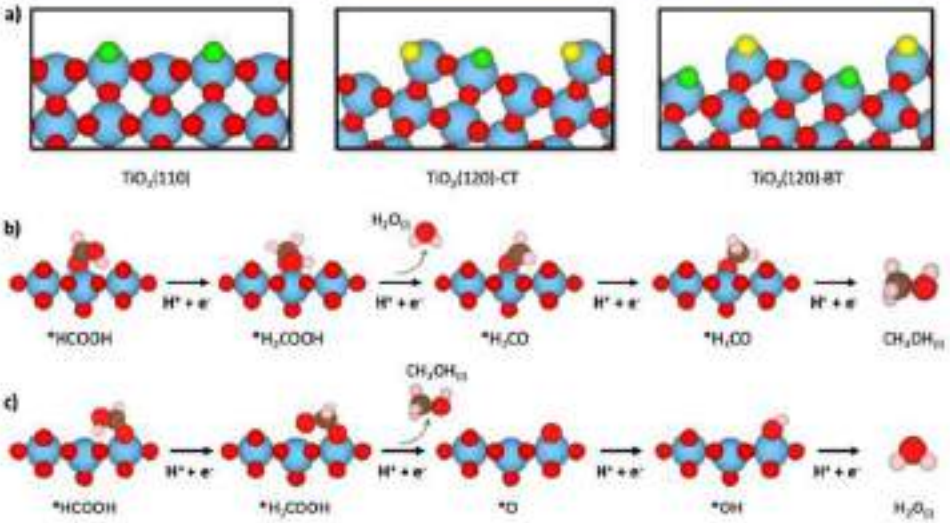

Figure 4. (a) Schematics of the slab models used in this work. Ti atoms are shown in blue, O atoms are shown in red, bridge site oxygen atoms (O_{2c}) are shown in green, and edge site oxygen atoms ($E\text{-}O_{2c}$) are shown in yellow. The lowest-energy pathway for FAR to CH_3OH at (b) CUS sites and (c) on TOVs. In panels (b) and (c), the Ti, O, C, and H atoms are shown in blue, red, brown, and pink, respectively.

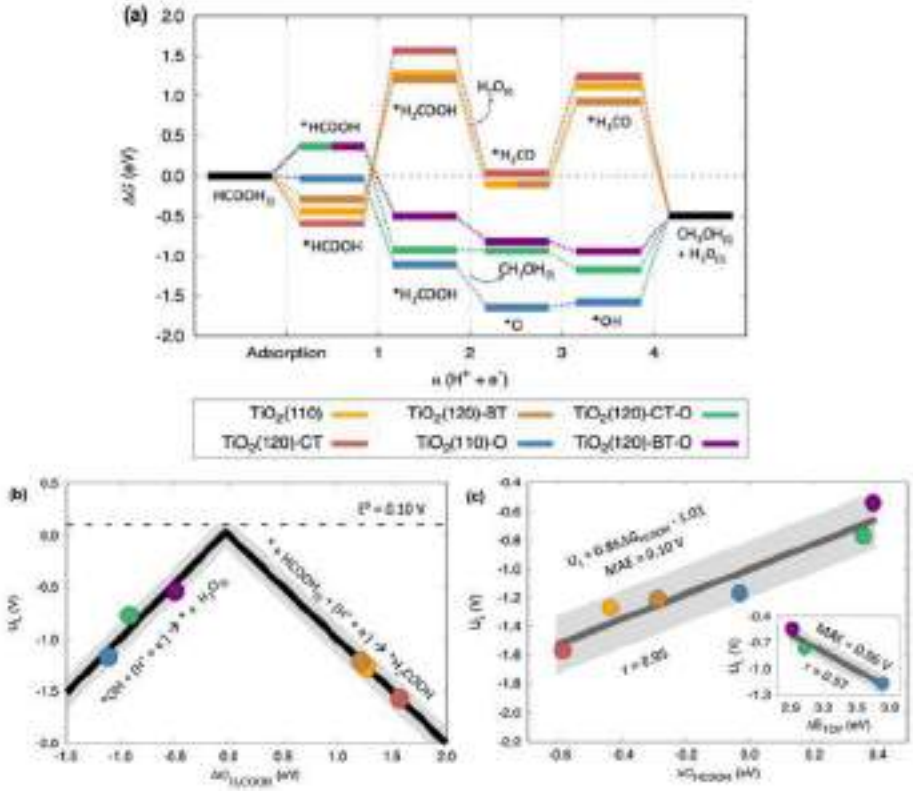

Figure 5. (a) Free-energy diagrams at 0 V *vs* RHE for FAR to CH_3OH at CUS and TOV sites. The intermediates and active sites are shown in Figure 4. (b) Volcano plot correlating the onset potential for FAR with the adsorption energy of $*H_2COOH$. The dashed line corresponds to the calculated equilibrium potential (0.10 V vs RHE, it is 0.11 V vs RHE in experiments[10]). Gray bands of ±0.16 V around the black lines correspond to ±2MAE (MAE: mean absolute error) of the scaling relation between $*H_2COOH$ and *OH. (c) Calculated onset potential as a function of the adsorption free energy of formic acid. The MAE and the Pearson regression coefficient (r) are also provided together with a linear regression in dark gray and a light gray zone of ±2MAE. The inset shows the calculated onset potential as a function of the oxygen vacancy formation energy at TOV sites. The color code for each active site is the same in all panels and is shown at the center of the figure.

selectivity for CH_3OH from FAR, while suppressing the competing HER.

2.4. Mechanistic Pathway for FAR to CH_3OH. We will now interplay theory and experiments to probe the role of TOVs as active sites and elucidate the FAR reaction pathway

https://doi.org/10.1021/acscatal.1c01725
ACS Catal. 2021, 11, 8467−8475

to CH_3OH. We first modeled the most stable bulk structure of TiO_2, i.e., the rutile phase. After optimizing its geometry, we modeled its most stable surface termination, $TiO_2(110)$. This surface has alternating rows of coordinatively unsaturated (CUS) and bridge sites (Figure 4a). CUS sites have undercoordinated Ti atoms that are available to interact with the adsorbates, while bridge sites do not. Conversely, bridge sites have twofold-coordinated oxygen atoms (O_{2c}), which are known to leave TOVs on TiO_2.[38] To incorporate the heterogeneity of amorphous Ti_{am} as observed from our XRD and Raman experiments, we also modeled the following two stepped surfaces: CUS-terminated $TiO_2(120)$ (denoted $TiO_2(120)$-CT) and bridge-terminated $TiO_2(120)$ (denoted $TiO_2(120)$-BT). These surfaces have alternating rows of CUS and bridge sites (with their corresponding O_{2c}) and a unique type of O_{2c} located at edge sites (denoted E-O_{2c}).

To determine if TOVs could be formed on the stepped TiO_2 surfaces, we calculated the oxygen vacancy formation energies ($\Delta E_{TOV} = E_{slab-TOV} + \frac{1}{2}E_{O2} - E_{slab}$, where $E_{slab-TOV}$ is the energy of the slab with an oxygen vacancy, E_{O2} is the corrected total energy of gas-phase molecular oxygen,[18,39,40] and E_{slab} is the energy of the pristine slab). Values of 3.04 and 2.93 eV were obtained for O_{2c} at $TiO_2(120)$-CT and $TiO_2(120)$-BT, respectively, while on $TiO_2(110)$ it was 3.75 eV. These results lead us to conclude that TOVs are more facilely formed on stepped TiO_2 surfaces. This is in line with our experimental results, where the formation of TOVs was observed on amorphous Ti_{am} but not on highly crystalline rutile and anatase TiO_2 particles (Section S4.3). Furthermore, the values of ΔE_{TOV} for E-O_{2c} were found to be around 0.3 eV more unstable in both cases, indicating that TOVs are more favorably formed on O_{2c} rather than E-O_{2c} on these surfaces.

Next, we determined the most favorable pathway for FAR to CH_3OH on CUS sites and TOVs (Tables S15–S16 and Figures S12–S17). On both sites, the hydrogenation of *HCOOH results in the formation of $*H_2COOH$, but the pathways bifurcate from that point on. On CUS sites, $*H_2COOH$ is hydrogenated to produce $*H_2CO + H_2O_{(l)}$ (Figure 4b; note that $*H_2CO$ is adsorbed formaldehyde). This is similar to a previously proposed mechanism for FAR to CH_3OH on Cr, where $*H_2COOH$ is formed initially and splits into $*CHO + H_2O$. *CHO then undergoes hydrogenation to form CH_3OH via a $*H_2CO$ intermediate.[16] In contrast, on the TOVs the protonation of $*H_2COOH$ results in the direct formation of CH_3OH and the filling of the TOV with *O (Figure 4c).

Free-energy diagrams for FAR on the different surface sites were made to facilitate the quantitative analysis of both pathways (Figure 5a). The pathways at the CUS sites (denoted as $TiO_2(110)$, $TiO_2(120)$-CT, and $TiO_2(120)$-BT) show that the hydrogenation of HCOOH to $*H_2COOH$ is the potential-limiting step. The calculated onset potentials are −1.27, −1.57, and −1.21 V at CUS sites for $TiO_2(110)$, $TiO_2(120)$-CT, and $TiO_2(120)$-BT, respectively. In contrast, the reduction of HCOOH on TOVs (denoted $TiO_2(110)$-O, $TiO_2(120)$-CT-O, and $TiO_2(120)$-BT-O) proceeds via the exothermic formation of $*H_2COOH$. The potential-limiting step is the protonation of *OH to form $H_2O_{(l)}$, which regenerates the TOV and restarts the catalytic cycle. The onset potentials are −1.17, −0.77, and −0.54 V for $TiO_2(110)$-O, $TiO_2(120)$-CT-O, and $TiO_2(120)$-BT-O, respectively. Clearly, the onset potentials at TOVs are considerably lower than those at CUS sites, which can be attributed to the favorable formation of $*H_2COOH$ and the opening of a different catalytic pathway. These results highlight the following two key findings: (i) based on their lower onset potentials, we identify TOVs at steps as the most active sites for FAR to CH_3OH, and (ii) adsorbed formaldehyde ($*H_2CO$) is not part of the FAR reaction pathway on TOVs but is a key intermediate during FAR on CUS sites.

We also determined if the sizable difference of FAR activities between CUS sites and TOVs could be observed on anatase TiO_2. A similar conclusion was obtained: the calculated onset potentials were −1.75 and −0.58 V on anatase $TiO_2(101)$ without and with TOVs, respectively (denoted as A-$TiO_2(101)$ and A-$TiO_2(101)$-O, respectively; Tables S15–S16 and Figures S18–S19). This reaffirms our findings that TOVs on TiO_2 are the active sites for CH_3OH production.

Figure 5b condenses the activity trends in a Sabatier-type activity plot, using the adsorption energy of $*H_2COOH$ (ΔG_{H_2COOH}) as a descriptor. CUS sites are on the weak-binding (right) leg of the volcano, where the formation of $*H_2COOH$ is potential-limiting. TOVs are on the strong-binding (left) leg, where *OH hydrogenation is potential-limiting. We found that the onset potential (U_L) at the peak lies close to the equilibrium potential (E_0) when $\Delta G_{H_2COOH} \approx 0$. This indicates that (i) it is thermodynamically feasible to synthesize nearly ideal FAR electrocatalysts and (ii) $\Delta G_{H_2COOH} \approx 0$ is a simple guiding principle for the computational selection of promising FAR catalysts. Accordingly, optimal catalysts for FAR should feature a free energy of adsorption close to 0 eV for $*H_2COOH$.

In the search for complementary guiding principles, we found that the free energy of adsorption of HCOOH can also be used as a descriptor for FAR activity: the weaker the binding energy of *HCOOH, the more positive the U_L (Figure 5c). This descriptor is useful because the adsorption energy of HCOOH can be calculated with DFT or measured experimentally.[41,42] The correlation in Figure 5c shows that HCOOH adsorbs strongly on CUS sites and weakly on TOVs, while the opposite is true for the next intermediate, $*H_2COOH$. Thus, weakly bound $*H_2COOH$ on CUS sites is reduced to CH_3OH through a high-overpotential pathway, while strongly bound $*H_2COOH$ on TOVs reduces to CH_3OH via a low-overpotential pathway (Figure 5a). We note, however, that the correlation in Figure 5c is to be taken with caution because if the *HCOOH adsorption energy is too weak, it might not adsorb at all, and no activity will be observed.

Additionally, we found that ΔE_{TOV} is inversely correlated with U_L (inset of Figure 5c). Hence, surface sites with more positive TOV formation energies have simultaneously more stable *OH adsorption energies. This is justified by the following facts: (i) ΔE_{TOV} is the additive inverse of the oxygen adsorption energy at the vacancy ($\Delta E_O = -\Delta E_{TOV}$), (ii) *OH and *O adsorption energies are linearly related by the so-called scaling relations,[18] and (iii) $U_L = \Delta G_{OH}$ on TOVs since *OH hydrogenation is the potential-limiting step of FAR to CH_3OH. Therefore, TOV formation energies may be used as quantitative criteria for the design of FAR catalysts.

We further found that *H is more weakly bound on TOVs than on CUS sites (Tables S15 and S16). Since TiO_2 lies on the weak-binding arm in the Sabatier plot for HER,[43] weakening *H on TOVs should lead to a poorer HER activity

https://doi.org/10.1021/acscatal.1c01725
ACS Catal. 2021, 11, 8467−8475

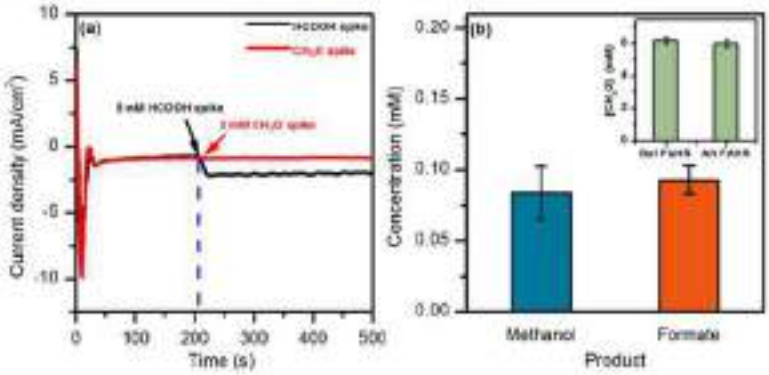

Figure 6. (a) Spike tests of HCOOH (black line) and CH_2O (red line) in 0.1 M K_2SO_4 at −1.0 V vs RHE on a $Ti_{ox,\ 3\ min}$ catalyst. (b) CH_3OH and HCOOH concentrations after formaldehyde reduction (FAHR) at −1.0 V vs RHE on a $Ti_{ox,\ 3\ min}$ catalyst. The inset graph shows the CH_2O concentrations before and after FAHR at −1.0 V vs RHE based on UV−vis measurements using the chromotropic acid method. The increase in CH_3OH and HCOOH concentrations is attributed to the Cannizzaro disproportionation of CH_2O.

on Ti_{ox}. This is in excellent agreement with our experimental observations. Interestingly, the adsorption free energy of *H scales linearly with that of *HCOOH (Figure S10). Therefore, we expect a higher FAR activity and a lower *H coverage (or poorer HER) when *HCOOH is weakly adsorbed on the surface.

We now use experiments to assess the reaction pathway predicted by the computational analysis (shown in Figure 5a). Based on our calculations, CH_2O is not an intermediate species during FAR to CH_3OH on TOVs. We verified this experimentally by performing HCOOH and CH_2O spike tests on $Ti_{ox,\ 3\ min}$ during chronoamperometry at −1.0 V (Figure 6a). While the HCOOH spike (0.1 M K_2SO_4 with 5 mM HCOOH, pH 3.5) generated higher current densities, CH_2O (0.1 M K_2SO_4 with 5 mM CH_2O; adjusted with H_2SO_4 to pH 3.5) was electrochemically inert. We further electrolyzed 5 mM CH_2O (nominal concentration) on a $Ti_{ox,\ 3\ min}$ catalyst at potentials from −0.95 to −1.05 V (Table S17). Interestingly, we detected similar amounts of CH_3OH and HCOOH at all potentials. For example, we detected 0.08 mM CH_3OH and 0.09 mM HCOOH after CH_2O electrolysis at −1.0 V (Figure 6b, Tables S17 and S18, and Section S7.3). This strongly suggests that the CH_3OH observed was formed through the Cannizzaro disproportionation reaction of CH_2O ($2CH_2O + OH^- \rightarrow HCOO^- + CH_3OH$) rather than an electrocatalytic reduction.[44] The electrochemical inertness of CH_2O on the $Ti_{ox,\ 3\ min}$ catalyst also allows us to rule out CUS sites as the active sites.

Lastly, CO and CO_2 might be possible intermediates for FAR to CH_3OH.[45] However, we did not detect CH_3OH when we reduced CO and CO_2 at −1.0 V in 0.1 M K_2SO_4 (the pH was adjusted to 2.6 with H_2SO_4) (Table S17). This excludes both molecules as active intermediates.

Collectively, we have elucidated that strongly reducing TOVs on Ti_{ox} are the active sites for FAR to CH_3OH. The mechanistic pathway proceeds through a direct reduction of HCOOH on Ti_{ox}, whereas previously recognized intermediates for CH_3OH production, such as $*H_2CO$, can be ruled out.[16] Our results show that aliphatic carboxylic acids can be directly electroreduced to alcohols under ambient conditions using only water as the H source. This contrasts with the conventional reduction of carboxylic acids using stoichiometric reagents such as $LiAlH_4$, which leads to a large production of Li and Al waste byproducts.[46]

3. CONCLUSIONS

In this work, we exemplify the use of Ti_{ox} for electrocatalytic FAR to CH_3OH. Characterization studies indicate that the Ti_{ox} catalyst is highly amorphous and bears TOV sites during electrocatalytic FAR. The optimum FE_{CH3OH} and j_{CH3OH} obtained for FAR on $Ti_{ox,\ 3\ min}$ samples were 12.6% and −2 mA/cm², respectively. A detailed examination of the Ti_{ox} catalyst using EPR spectroscopy and CV indicates that the increase in CH_3OH production is correlated with the amount of TOVs in the catalyst. DFT calculations showed that the most favorable reaction pathway is through the protonation of a $*H_2COOH$ intermediate to produce CH_3OH and *O, filling the previously formed vacancy. Subsequent hydrogenation to *OH and $H_2O_{(l)}$ regenerates the TOV, completing the catalytic cycle. In addition, the adsorption energies of *HCOOH and $*H_2COOH$, as well as the formation energy of TOVs can be used as complementary descriptors to guide the design of enhanced FAR catalysts.

In a broader context, our work illustrates how we can rationally design an electrocatalyst for the reduction of a highly stable organic functional group, which in this case is the carboxylic acid group. By introducing enhanced catalytic sites such as TOVs to anodized Ti, a non-noble and earth-abundant element, the carboxylic acid group can be favorably reduced to produce a valuable alcohol. Apart from showing the feasibility of CH_3OH synthesis under ambient conditions from CO_2 reduction via tandem electrocatalysis, this work provides an alternative route for valorizing longer-chain aliphatic acids to valuable alcohols, such as *n*-propanol.

■ ASSOCIATED CONTENT

Supporting Information

The Supporting Information is available free of charge at https://pubs.acs.org/doi/10.1021/acscatal.1c01725.

Detailed experimental and theoretical procedures; characterization methods; gas-phase and liquid-phase corrections; specific free energy values, including ZPE and TS corrections; and the coordinates of the optimized slabs (PDF)

https://doi.org/10.1021/acscatal.1c01725
ACS Catal. 2021, 11, 8467−8475

AUTHOR INFORMATION

Corresponding Authors

Boon Siang Yeo − *Department of Chemistry, National University of Singapore, Singapore 117543; Solar Energy Research Institute of Singapore, National University of Singapore, Singapore 117574;* orcid.org/0000-0003-1609-0867; Email: chmyeos@nus.edu.sg

Federico Calle-Vallejo − *Department of Materials Science and Chemical Physics & Institute of Theoretical and Computational Chemistry (IQTCUB), University of Barcelona, 08028 Barcelona, Spain;* Email: f.calle.vallejo@ub.edu

Authors

Wei Jie Teh − *Department of Chemistry, National University of Singapore, Singapore 117543; Solar Energy Research Institute of Singapore, National University of Singapore, Singapore 117574*

Oriol Piqué − *Department of Materials Science and Chemical Physics & Institute of Theoretical and Computational Chemistry (IQTCUB), University of Barcelona, 08028 Barcelona, Spain;* orcid.org/0000-0002-6995-5927

Qi Hang Low − *Department of Chemistry, National University of Singapore, Singapore 117543; Solar Energy Research Institute of Singapore, National University of Singapore, Singapore 117574*

Weihan Zhu − *Department of Chemistry, National University of Singapore, Singapore 117543; Solar Energy Research Institute of Singapore, National University of Singapore, Singapore 117574*

Complete contact information is available at: https://pubs.acs.org/10.1021/acscatal.1c01725

Notes

The authors declare no competing financial interest.

ACKNOWLEDGMENTS

We acknowledge the National University of Singapore (R143-000-B52-114 and R143-000-A64-114) for financial support of this project. Q.H.L. thanks the Solar Energy Research Institute of Singapore (SERIS) for financial support. F.C.-V. acknowledges funding from Spanish MICIUN RYC-2015-18996 and RTI2018-095460-B-I00, María de Maeztu MDM-2017-0767 grants, and partly by Generalitat de Catalunya (2017SGR13). O.P. thanks the Spanish MICIUN for an FPI PhD grant (PRE2018-083811). We are thankful to Red Española de Supercomputación (RES) for supercomputing time at CENITS (QS-2020-2-0021). The use of supercomputing facilities at SURFsara was sponsored by NWO Physical Sciences, with financial support by NWO.

REFERENCES

(1) Rauche, K.; Plass, L.; Wernicke, H. J.; Bertau, M. Methanol for Renewable Energy Storage and Utilization. *Energy Technol.* **2016**, *4* (1), 193−200.

(2) Dalena, F.; Senatore, A.; Marino, A.; Gordano, A.; Basile, M.; Basile, A. Methanol Production and Applications: An Overview. In *Methanol: Science and Engineering*; Basile, A., Dalena, F., Eds.; Elsevier B.V.: Amsterdam, The Netherlands, 2018; pp 3−28.

(3) Ott, J.; Gronemann, V.; Pontzen, F.; Fiedler, E.; Grossmann, G.; Kersebohm, D. B.; Weiss, G.; Witte, C. Methanol. In *Ullmann's Encyclopedia of Industrial Chemistry*; Ullmann, F., Gerhartz, W., Yamamoto, Y. S., Campbell, F. T., Pfefferkorn, R., Rounsaville, J. F., Eds.; Wiley-VCH Verlag GmbH & Co. KGaA: Weinheim, Germany, 2012; pp 8−9.

(4) Rumayor, M.; Dominguez-Ramos, A.; Irabien, A. Innovative Alternatives to Methanol Manufacture: Carbon Footprint Assessment. *J. Cleaner Prod.* **2019**, *225*, 426−434.

(5) Hatsukade, T.; Kuhl, K. P.; Cave, E. R.; Abram, D. N.; Feaster, J. T.; Jongerius, A. L.; Hahn, C.; Jaramillo, T. F. Carbon Dioxide Electroreduction Using a Silver-Zinc Alloy. *Energy Technol.* **2017**, *5* (6), 955−961.

(6) Low, Q. H.; Loo, N. W. X.; Calle-Vallejo, F.; Yeo, B. S. Enhanced Electroreduction of Carbon Dioxide to Methanol Using Zinc Dendrites Pulse-Deposited on Silver Foam. *Angew. Chem., Int. Ed.* **2019**, *58* (8), 2256−2260.

(7) He, Y.; Jiang, W. J.; Zhang, Y.; Huang, L. B.; Hu, J. S. Pore-Structure-Directed CO_2 Electroreduction to Formate on SnO_2/C Catalysts. *J. Mater. Chem. A* **2019**, *7* (31), 18428−18433.

(8) White, J. L.; Bocarsly, A. B. Enhanced Carbon Dioxide Reduction Activity on Indium-Based Nanoparticles. *J. Electrochem. Soc.* **2016**, *163* (6), H410−H416.

(9) Pander, J. E.; Lum, J. W. J.; Yeo, B. S. The Importance of Morphology on the Activity of Lead Cathodes for the Reduction of Carbon Dioxide to Formate. *J. Mater. Chem. A* **2019**, *7* (8), 4093−4101.

(10) Dean, J. A. Section 6: Thermodynamic Properties. In *Lange's Handbook of Chemistry*; Dean, J. A., Lange, N. A., Eds.; McGraw-Hill: Knoxville, TN, 1999; pp 6.1−6.147.

(11) Sadakiyo, M.; Hata, S.; Fukushima, T.; Juhász, G.; Yamauchi, M. Electrochemical Hydrogenation of Non-Aromatic Carboxylic Acid Derivatives as a Sustainable Synthesis Process: From Catalyst Design to Device Construction. *Phys. Chem. Chem. Phys.* **2019**, *21* (11), 5882−5889.

(12) Bondue, C. J.; Calle-Vallejo, F.; Figueiredo, M. C.; Koper, M. T. M. Structural Principles to Steer the Selectivity of the Electrocatalytic Reduction of Aliphatic Ketones on Platinum. *Nat. Catal.* **2019**, *2* (3), 243−250.

(13) Ledezma-Yanez, I.; Gallent, E. P.; Koper, M. T. M.; Calle-Vallejo, F. Structure-Sensitive Electroreduction of Acetaldehyde to Ethanol on Copper and Its Mechanistic Implications for CO and CO_2 Reduction. *Catal. Today* **2016**, *262*, 90−94.

(14) Schouten, K. J. P.; Kwon, Y.; Van Der Ham, C. J. M.; Qin, Z.; Koper, M. T. M. A New Mechanism for the Selectivity to C_1 and C_2 Species in the Electrochemical Reduction of Carbon Dioxide on Copper Electrodes. *Chem. Sci.* **2011**, *2* (10), 1902−1909.

(15) Russell, P. G.; Kovac, N.; Srinivasan, S.; Steinberg, M. The Electrochemical Reduction of Carbon Dioxide, Formic Acid, and Formaldehyde. *J. Electrochem. Soc.* **1977**, *124* (9), 1329−1338.

(16) Kotoulas, L.; Kyriacou, G. Conversion of Carbon Dioxide to Methanol through the Reduction of Formic Acid on Chromium. *J. Chem. Technol. Biotechnol.* **2017**, *92* (7), 1794−1800.

(17) Adegoke, K. A.; Radhakrishnan, S. G.; Gray, C. L.; Sowa, B.; Morais, C.; Reyess, P.; Rohwer, E. R.; Comminges, C.; Kokoh, K. B.; Roduner, E. Highly Efficient Formic Acid and Carbon Dioxide Electro-Reduction to Alcohols on Indium Oxide Electrodes. *Sustainable Energy Fuels* **2020**, *4* (8), 4030−4038.

(18) Su, H. Y.; Ma, X.; Sun, K.; Sun, C.; Xu, Y.; Calle-Vallejo, F. Trends in C-O and N-O Bond Scission on Rutile Oxides Described Using Oxygen Vacancy Formation Energies. *Chem. Sci.* **2020**, *11* (16), 4119−4124.

(19) Zhou, Y.; Chen, C.; Wang, N.; Li, Y.; Ding, H. Stable Ti^{3+} Self-Doped Anatase-Rutile Mixed TiO_2 with Enhanced Visible Light Utilization and Durability. *J. Phys. Chem. C* **2016**, *120* (11), 6116−6124.

(20) Wale, L. E.; Borg, A.; Johansson, E. M. J.; Plogmaker, S.; Rensmo, H.; Uvdal, P.; Sandell, A. Mixed Dissociative and Molecular Water Adsorption on Anatase TiO_2(101). *J. Phys. Chem. C* **2011**, *115* (19), 9545−9550.

(21) Syres, K. L.; Thomas, A. G.; Flavell, W. R.; Spencer, B. F.; Bondino, F.; Malvestuto, M.; Preobrajenski, A.; Grätzel, M. Adsorbate-Induced Modification of Surface Electronic Structure:

Pyrocatechol Adsorption on the Anatase TiO_2 (101) and Rutile TiO_2 (110) Surfaces. *J. Phys. Chem. C* **2012**, *116* (44), 23515−23525.
(22) Wierzbicka, E.; Zhou, X.; Denisov, N.; Yoo, J. E.; Fehn, D.; Liu, N.; Meyer, K.; Schmuki, P. Self-Enhancing H_2 Evolution from TiO_2 Nanostructures under Illumination. *ChemSusChem* **2019**, *12* (9), 1900−1905.
(23) Zhang, Z.; Hedhili, M. N.; Zhu, H.; Wang, P. Electrochemical Reduction Induced Self-Doping of Ti^{3+} for Efficient Water Splitting Performance on TiO_2 Based Photoelectrodes. *Phys. Chem. Chem. Phys.* **2013**, *15* (37), 15637−15644.
(24) Balachandran, U.; Eror, N. G. Raman Spectra of Titanium Dioxide. *J. Solid State Chem.* **1982**, *42* (3), 276−282.
(25) Yanagisawa, K.; Ovenstone, J. Crystallization of Anatase from Amorphous Titania Using the Hydrothermal Technique: Effects of Starting Material and Temperature. *J. Phys. Chem. B* **1999**, *103* (37), 7781−7787.
(26) Zhang, G.; Huang, C.; Zhou, L.; Ye, L.; Li, W.; Huang, H. Enhanced Charge Storage by the Electrocatalytic Effect of Anodic TiO_2 Nanotubes. *Nanoscale* **2011**, *3*, 4174−4181.
(27) Aijo, J. K.; Thankamonianamma, M.; Puigdollers, J.; Anuroop, R.; Pradeep, B.; Shripathi, T.; Philip, R. R. Rapid Room Temperature Crystallization of TiO_2 Nanotubes. *CrystEngComm* **2017**, *19* (12), 1585−1589.
(28) Nair, S. B.; Aijo, J. K.; Menon, S. S.; Bahman, H.; Joseph, J. A.; Shaji, S.; Philip, R. R. Influence of Electrochemical Reduction of Selfdoping on the Low Temperature Crystallization and Photocatalytic Activities of TiO_2 Nanotubes. *Semicond. Sci. Technol.* **2019**, *34* (9), 095023.
(29) Morikawa, Y.; Takahashi, I.; Aizawa, M.; Namai, Y.; Sasaki, T.; Iwasawa, Y. First-Principles Theoretical Study and Scanning Tunneling Microscopic Observation of Dehydration Process of Formic Acid on a TiO_2(110) Surface. *J. Phys. Chem. B* **2004**, *108* (38), 14446−14451.
(30) Aizawa, M.; Morikawa, Y.; Namai, Y.; Morikawa, H.; Iwasawa, Y. Oxygen Vacancy Promoting Catalytic Dehydration of Formic Acid on TiO_2(110) by in situ Scanning Tunneling Microscopic Observation. *J. Phys. Chem. B* **2005**, *109* (40), 18831−18838.
(31) McCafferty, E. Thermodynamics of Corrosion: Pourbaix Diagrams. In *Introduction to Corrosion Science*; Springer: New York, NY, 2010; p 110.
(32) Wang, X.; Fu, H.; Du, D.; Zhou, Z.; Zhang, A.; Su, C.; Ma, K. The Comparison of pKa Determination between Carbonic Acid and Formic Acid and Its Application to Prediction of the Hydration Numbers. *Chem. Phys. Lett.* **2008**, *460* (1−3), 339−342.
(33) Fu, G.; Zhou, P.; Zhao, M.; Zhu, W.; Yan, S.; Yu, T.; Zou, Z. Carbon Coating Stabilized Ti^{3+}-Doped TiO_2 for Photocatalytic Hydrogen Generation under Visible Light Irradiation. *Dalton Trans.* **2015**, *44* (28), 12812−12817.
(34) Wierzbicka, E.; Osuagwu, B.; Denisov, N.; Fehn, D.; Meyer, K.; Schmuki, P. Light-Induced in-situ Ti^{3+} Formation in TiO_2 Nanosheets for Photocatalytic Hydrogen Evolution. *IOP Conf. Ser.: Mater. Sci. Eng.* **2020**, *908* (1), 012001.
(35) Chiesa, M.; Paganini, M. C.; Livraghi, S.; Giamello, E. Charge Trapping in TiO_2 Polymorphs as Seen by Electron Paramagnetic Resonance Spectroscopy. *Phys. Chem. Chem. Phys.* **2013**, *15* (24), 9435−9447.
(36) Sarkar, A.; Khan, G. G. The Formation and Detection Techniques of Oxygen Vacancies in Titanium Oxide-Based Nanostructures. *Nanoscale* **2019**, *11* (8), 3414−3444.
(37) Ghicov, A.; Tsuchiya, H.; Hahn, R.; Macak, J. M.; Muñoz, A. G.; Schmuki, P. TiO_2 Nanotubes: H^+ Insertion and Strong Electrochromic Effects. *Electrochem. Commun.* **2006**, *8* (4), 528−532.
(38) Yamamoto, Y.; Kasamatsu, S.; Sugino, O. Scaling Relation of Oxygen Reduction Reaction Intermediates at Defective TiO_2 Surfaces. *J. Phys. Chem. C* **2019**, *123* (32), 19486−19492.
(39) Calle-Vallejo, F.; Martínez, J. I.; García-Lastra, J. M.; Mogensen, M.; Rossmeisl, J. Trends in Stability of Perovskite Oxides. *Angew. Chem., Int. Ed.* **2010**, *49* (42), 7699−7701.
(40) Granda-Marulanda, L. P.; Rendón-Calle, A.; Builes, S.; Illas, F.; Koper, M. T. M.; Calle-Vallejo, F. A Semiempirical Method to Detect and Correct DFT-Based Gas-Phase Errors and Its Application in Electrocatalysis. *ACS Catal.* **2020**, *10*, 6900−6907.
(41) Campbell, C. T.; Sellers, J. R. V. Enthalpies and Entropies of Adsorption on Well-Defined Oxide Surfaces: Experimental Measurements. *Chem. Rev.* **2013**, *113* (6), 4106−4135.
(42) Rumptz, J. R.; Campbell, C. T. Adhesion Energies of Solvent Films to Pt(111) and Ni(111) Surfaces by Adsorption Calorimetry. *ACS Catal.* **2019**, *9* (111), 11819−11825.
(43) Laursen, A. B.; Varela, A. S.; Dionigi, F.; Fanchiu, H.; Miller, C.; Trinhammer, O. L.; Rossmeisl, J.; Dahl, S. Electrochemical Hydrogen Evolution: Sabatier's Principle and the Volcano Plot. *J. Chem. Educ.* **2012**, *89* (12), 1595−1599.
(44) Birdja, Y. Y.; Koper, M. T. M. The Importance of Cannizzaro-Type Reactions during Electrocatalytic Reduction of Carbon Dioxide. *J. Am. Chem. Soc.* **2017**, *139* (5), 2030−2034.
(45) Schizodimou, A.; Kotoulas, I.; Kyriacou, G. Electrochemical Reduction of Formic Acid through Its Decarbonylation in Phosphoric Acid Solution. *Electrochim. Acta* **2016**, *210*, 236−239.
(46) Harinath, A.; Bhattacharjee, J.; Panda, T. K. Facile Reduction of Carboxylic Acids to Primary Alcohols under Catalyst-Free and Solvent-Free Conditions. *Chem. Commun.* **2019**, *55* (10), 1386−1389.

https://doi.org/10.1021/acscatal.1c01725
ACS Catal. 2021, 11, 8467−8475

Chapter 4

Interplay of C Atoms and Transition Metal Systems

4.1 Introduction

Transition metals (TMs) are of great relevance in industrial heterogeneous catalysis. In fact, late TMs are often involved in heterogeneous catalysts[154] for a large variety of industrially relevant reactions such as ammonia synthesis or the Fischer-Tropsch process,[155] among others. On the other hand, early TMs are too active for such purposes, adsorbing molecules too strongly according to *Le Sabatier* principle.[11] However, the carburization of these metals lowers their catalytic activity, forming TM carbides (TMCs), which have been proposed as viable replacements of late TMs in catalysis and offer unique catalytic properties.[156,157] The main drawback of these systems as catalysts is that, during the course of the reaction, they gradually get deactivated. The main reason for such deactivation is the presence of poisoning agents, where carbon excels among others.[158,159] It is usual that C species formed on the surface of the TM catalyst agglomerate as carbon deposits, covering the catalysts and preventing the access of reactants to the surface active sites, effectively poisoning it.[160] Despite this, in some cases, a small amount of C can tune the catalytic activity and selectivity of the TM catalyst. For instance, the presence of subsurface C in Pd catalysts favors selective alkyne hydrogenation to olefins while suppressing hydrogenation to alkanes.[161] Moreover, subsurface C is key in the synthesis of carbon nanotubes (CNT) and graphene.[162,163] Motivated by these results, the aim of this work is to obtain a detailed and broad atomistic view of C interaction with TM surfaces, including thermodynamic, kinetic, and even dynamic aspects of their presence and possible impact.

4.2 Investigating the Presence of Subsurface C in *fcc* Transition Metals

Introduction As an initial approach, we first tackled the interaction of C atoms with *fcc* TM surfaces. We obtained the adsorption (E_{ads}) and absorption energies (E_{abs}) of C atoms on/in the (111) surface of *fcc* TMs, which corresponds to their most stable surface termination.[41] To explore the kinetics involved in the penetration of C atoms into these surfaces, we calculated the sinking energy barriers. For completeness, we also modelled M_{79} TM nanoparticles to investigate the effect of low-coordinated sites on C ad/absorption. The data obtained allowed us to investigate the thermodynamic and kinetic aspects regarding the presence of subsurface C in *fcc* TMs. Note that the presence of subsurface C has been observed before for group 10 TMs,[164] but in this work we point out its existence also for group 11 TMs. Hence, we show here that the existence of subsurface C is a general feature to be considered for *fcc* TMs. Finally, dynamic simulations allowed us to estimate the lifetimes of atomic C species at the surface and subsurface regions of these TMs.

This work led to the publication of two research articles.[61,165] The manuscripts are included at the end of this section. In the following pages, a summary of them is provided. My contributions to the research articles were: (a) Calculation of C ad/absorption energies for all the slabs and NPs, (b) determination of surface, subsurface, sinking, and emerging energy barriers for all the slabs, (c) calculation of sinking energy barriers for all the NPs, and (d) analysis and figure assembly of the parts corresponding to (a), (b), and (c). I was not involved in the kMC modelling and simulations. The supporting information for "*Subsurface carbon: a general feature of noble metals*" can be found in Appendix F. The optimized geometries were removed from this document to save space but can be found online at: https://doi.org/10.1002/anie.201813037. The supporting information for "*Towards understanding the role of carbon atoms on transition metal surfaces: implications for catalysis*" can be found in Appendix G.

Results Initially, C atoms at surface and subsurface regions were optimized on (111) surface slab models of *fcc* TMs, alongside with the sinking energy barriers. Figure 28 shows these calculated E_{ads}, E_{abs}, and the sinking energy barriers are shown for the earliest five *fcc* TMs, on their most stable sites in surface and subsurface regions, namely

the *hcp* and *fcc* three-atom surface hollow sites and the tetrahedral subsurface (*tss*) and octahedral subsurface (*oss*) sites.

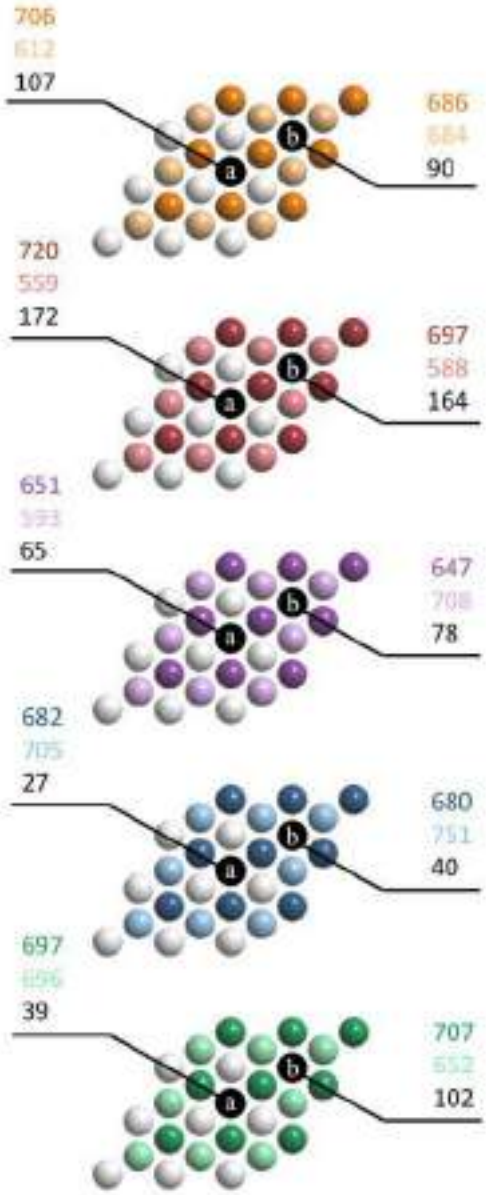

Figure 28. In descending order, Rh, Ir, Ni, Pd, and Pt adsorption (E_{ads}, in dark colours) and subsurface absorption (E_{abs}, in light colours) energies, in kJ mol^{-1}, on the (111) surface (a) *hcp* and subsurface *tss* sites, respectively, and (b) *fcc* and *oss* sites, respectively. Carbon sinking energy barriers on each site are shown in black. This figure corresponds to Figure S11 in the supporting information of reference 61 and is included here to facilitate the reading of this thesis.

Results show that C atoms are clearly most stable at the surface than at the subsurface only of Rh and Ir (111) surfaces and have to surmount high-energy sinking barriers to penetrate the surface. On the other hand, Ni, Pd, and Pt (111) surfaces feature

competitive or preferential C subsurface stability together with low-energy sinking barriers, as reported previously.[164] Moreover, as shown in Figure 29, the most noble TMs, those of group 11 (Cu, Ag, and Au), also showed competitive or higher stability of subsurface C compared to surface situations.

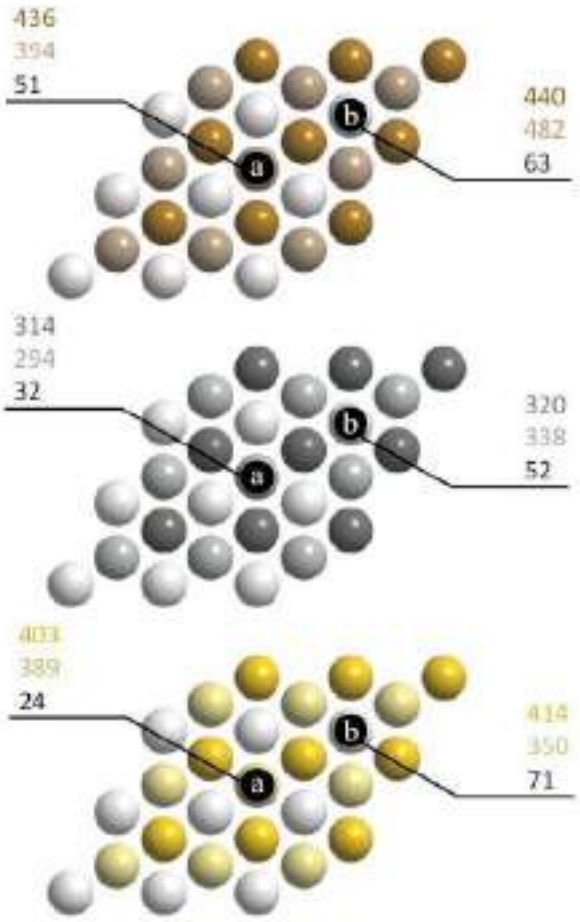

Figure 29. In descending order, Cu, Ag, and Au adsorption (E_{ads}, in dark colours) and subsurface absorption (ΔE_{abs}, in light colours) energies, in kJ mol^{-1}, on (111) surface (a) *hcp* and subsurface *tss* sites, respectively, and (b) *fcc* and *oss* sites, respectively. Carbon sinking energy barriers on each site are shown in black. This figure corresponds to Figure 1 in reference 61 and is included here to facilitate the reading of this thesis.

For Cu, the *fcc* and *hcp* surface sites have akin stability, but the subsurface *oss* site is more stable than the *fcc* surface site by 42 kJ mol^{-1}. For Ag, the surface *fcc* site is 18 kJ mol^{-1} less stable than the subsurface *oss* site. For Au, the surface *fcc* site is more stable than the subsurface *tss* site by 25 kJ mol^{-1}. The key driver subsurface stability appears to be a compromise between the energetic cost of subsurface deformation to accommodate

C atoms within constrained space and the increased C bonding saturation. At full monolayer coverage, estimates show that the surface or subsurface preferred stability prevails, but with reduced E_{ads} and E_{abs}. The sinking energy barriers are within 32-63 kJ mol^{-1} for Cu and Ag, hence, non-negligible but easy to overcome at catalytic working temperatures. Barriers for Au range from 24 to 71 kJ mol^{-1}.

These results triggered a more detailed study on this subject. We further modelled metal nanoparticles of 79 atoms (M_{79} NPs), and so within the scalable regime,[166] for Cu, Ag, and Au, to inspect the effect of lower-coordinated sites such as the edges and corners of these NPs on the ad/absorption energies and sinking energy barriers. The results, shown in Figure 30, feature many similarities to the extended surfaces, with caveats.

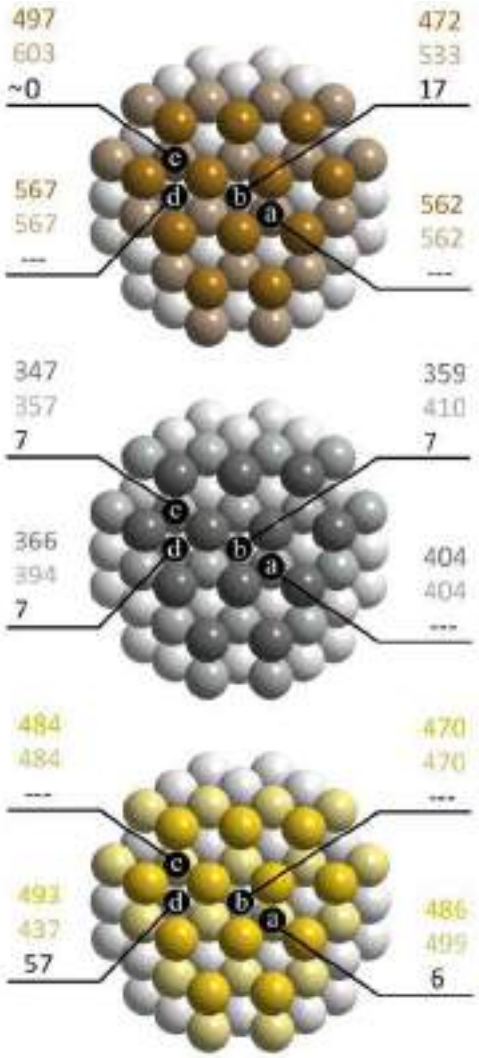

Figure 30. In descending order, Cu_{79}, Ag_{79}, and Au_{79} adsorption (E_{ads}, in dark colours) and subsurface absorption (E_{abs}, in light colours) energies, in kJ mol^{-1}, on diverse (111) facet sites. Carbon diffusion energy barriers on each site are shown in black. Dashed lines are present when in-plane situations are found, *i.e.*, adsorption and absorption lead to a common final stable situation (E_{ads} and E_{abs} values are identical). This figure corresponds to Figure 2 in reference 61 and is included here to facilitate the reading of this thesis.

Many *hcp*/*tss* and *fcc*/*oss* sites on Cu_{79} and Ag_{79} show increased E_{ads} and E_{abs}, ranging 32-59 kJ mol^{-1} for the adsorption cases and 61-72 kJ mol^{-1} for the absorption cases. For Au_{79}, the increase in E_{abs} is larger, within 87-100 kJ mol^{-1}, than for E_{ads}, ranging 79-83 kJ mol^{-1}. Small size effects and the proximity to low-coordinated sites can justify the increment of the adsorption strengths. For subsurface cases, the much larger increment is related to a larger and easier deformability of vicinal metal atoms to stabilize and accommodate the subsurface C atom. This is shown by a deformation/attachment energies balance, in which attachment energies are larger for Cu, Ag, and Au NPs than on the (111) surfaces counterparts, by up to 123, 91, and 104 kJ mol^{-1}, respectively, while featuring similar deformation energies for surface and subsurface situations. Hence, low-coordinated sites allow for larger deformations, without affecting the structural energy of the site.

For Cu_{79}, E_{abs} increases by 209 kJ mol^{-1} with respect to the (111) extended surface for corner *tss*, which is the most stable site for C on Cu_{79}. A similar stabilization of subsurface C is seen for edge *tss* on Au_{79} with an E_{abs} increase of 110 kJ mol^{-1}, with respect to the Au (111) situation. Hence, subsurface C at edge *tss* is the most stable situation in Au_{79}. On Ag_{79}, similarly to what is observed for the Ag (111) slab, the centre *oss* site remains the most stable situation. Thus, low-coordination sites do not only preserve the preference of C atoms for subsurface in Cu and Ag, but also promote subsurface occupancy in Au systems. Moreover, the sinking energy barriers essentially vanish, hinting for a kinetic easy entrance of C adatoms into the subsurface region of NPs. Very low barriers of nearly zero to 17 kJ mol^{-1} are found at corner *tss* and central *oss* sites for Cu_{79}, of 7 kJ mol^{-1} for almost all situations of Ag_{79}, and a barrier of only 6 kJ mol^{-1} for the edge *hcp* site of Au_{79}.

A further issue is whether such subsurface C occupancy is thermodynamically driven. To this end, phase diagrams for all *fcc* TMs (111) surfaces have been obtained, taking into account the turning conditions of pristine surfaces to become early C-containing, either on surface (C^{sur}) or in subsurface (C_{sub}). Phase diagrams in Figure 31, show that C adatoms would be thermodynamically stable on Rh, Ir, and Pt (111) surfaces, subsurface in Ni and Pd (111) surfaces, and thermodynamically unstable on Cu, Ag, and Au (111) surfaces at regular catalytic temperature working conditions. Hence, on the latter, the existence of subsurface C isolated species would be only kinetically driven, and to be considered only during the course of the reaction, even though the final state of these C atoms would be aggregated in graphite or amorphous carbon phases. However,

the thermodynamic stability can be achieved on low-coordinated sites of the Cu_{79} NP, see Figure 32.

Note that this has important implications for catalysis, since, in those situations were C atoms have a thermodynamic preference for surface sites and high sinking energy barriers, carbon will act as a poisoning agent, blocking the active sites where the reactants would adsorb and eventually aggregating on top of the catalysts when the C coverage increases. On the other hand, in those situations where C atoms prefer to accommodate in subsurface sites, they will not poison the catalyst, but they can modify the electronic structure of the surface, affecting the on-going catalysis.

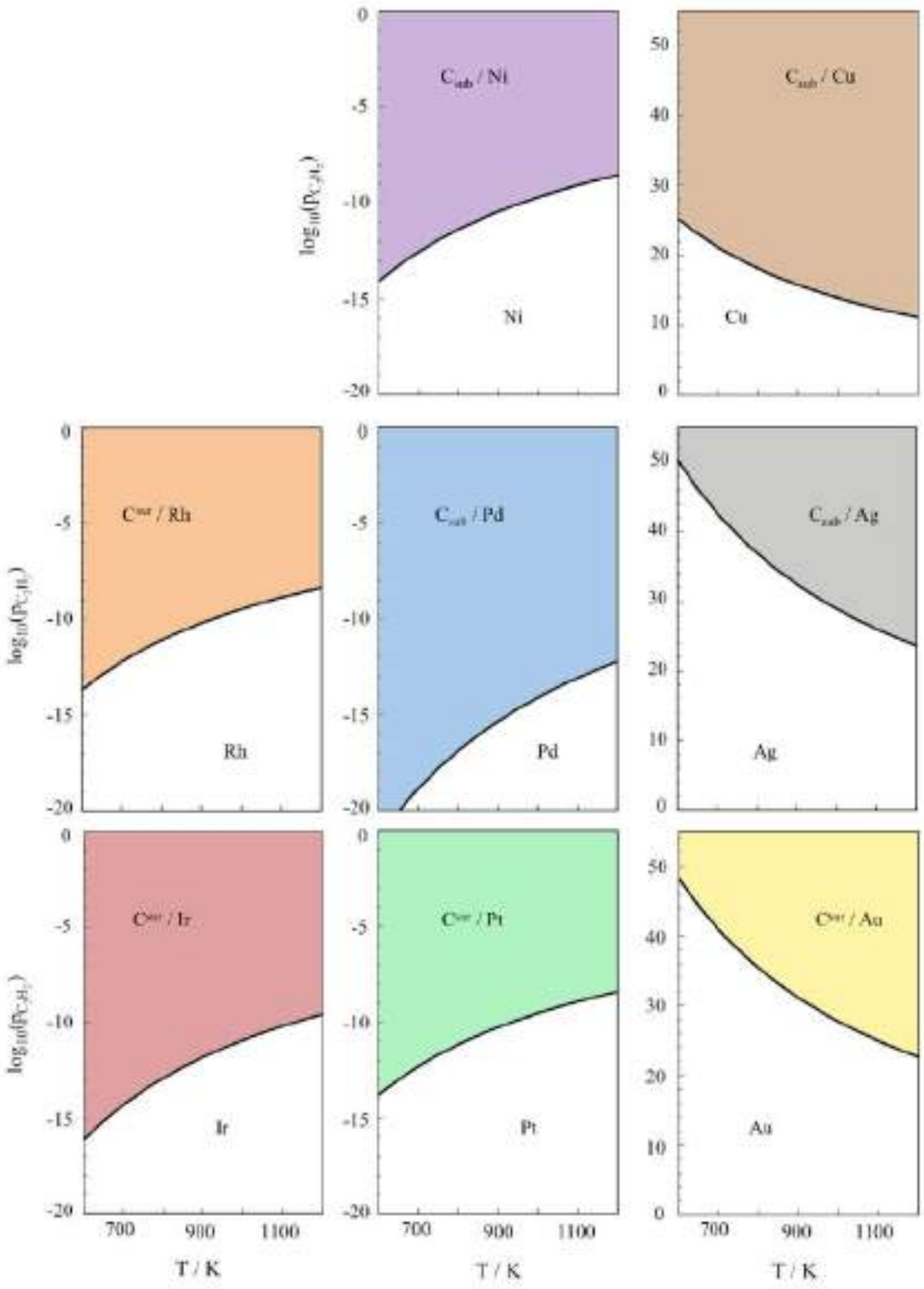

Figure 31. Phase diagrams for *fcc* TMs (111) surfaces (TM = Rh, Ir, Ni, Pd, Pt, Cu, Ag, and Au) depending on the acetylene partial pressure (in Pa), and the temperature (T, in K). Diagrams are obtained for a constant partial pressure of H_2, equal to 10^{-7} Pa. The white region belongs to a pristine metal phase, and the colored regions belong to phases with C adatoms adsorbed (C^{sur}) or absorbed (C_{sub}). This figure corresponds to Figure S9 in the supporting information of reference 61 and is included here to facilitate the reading of this thesis.

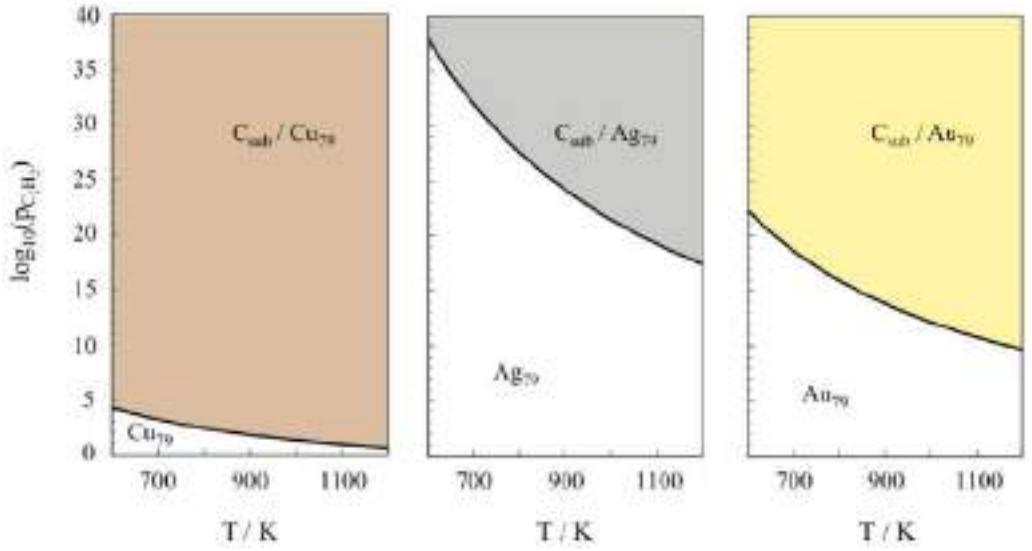

Figure 32. Phase diagrams for TM_{79} nanoparticle models (TM = Cu, Ag, and Au) in the same conditions as in Figure 31. This figure corresponds to Figure S10 in the supporting information of reference 61 and is included here to facilitate the reading of this thesis.

To go one step further, we investigated the dynamic aspects of the surface/subsurface C stability on *fcc* TM (111) surfaces. Diffusion energy barriers along the surface and through the subsurface were calculated, joining our already calculated sinking (and emerging) energy barriers. This way, a complete diffusion map of C atoms in *fcc* TM (111) surfaces was obtained. This data was later used by a coworker, MSc. Biel Martínez, to perform kinetic Monte Carlo (kMC) simulations on surface models to obtain information on the frequency of diffusion events, and, by that, of the surface structure under working conditions and on the lifetime of such surface and subsurface C species.

Results showed that, at 300 K, C atoms are almost all the time at the surface for Rh, Ir, Pt, and Au (111) surfaces; and almost all the time only in subsurface for Ni, Pd, Cu, and Ag (111) surfaces, in agreement with the energetic preference shown by the DFT calculations reported above. On the other hand, increasing the temperature has a relevant effect on some of the surfaces. For instance, for the Ag (111) surface, raising the temperature decreases the subsurface C concentration, while for the Pt (111) surface the amount of C in subsurface increases from 2% at 300 K to 13% at 700 K. Thus, at catalytic working temperatures there is a non-negligible amount of subsurface C in Pt that can affect the on-going surface catalysis. Interestingly, it is observed that surface and subsurface diffusion processes are much more frequent than those corresponding to sinking/emerging diffusions. Moreover, the quantification of C atom lifetimes at less

stable sites also provides compelling information. For those metals with preferential subsurface C stability, one can expect the emergence of one C atom to the surface each μs per $Å^2$, which lasts at the surface for a significant time, almost 1 ms in the case of Ag (111). This effect is very relevant for catalysis since the frequent emergence of C atoms can condition the surface activity of the on-going catalytic processes. For metals where C prefers surface sites, the presence of subsurface C does not condition as much the catalysis in progress, since the main effects will be a consequence of C adatoms.

Conclusions These results, together with additional data and analyses shown in the research articles below, lead to the following conclusions:

- There is both thermodynamic and kinetic evidence on the presence of subsurface C species in both group 10 and 11 TM systems. Such evidence has been found in both extended surfaces and low-coordinated sites of metallic NPs.
- C thermodynamic preference for subsurface sites is enhanced at low-coordinated sites of NPs. Moreover, the sinking energy barriers of C atoms at these NP sites are nearly 0 eV. The malleability of these sites is key for C accommodation.
- C surrounding metal atoms show electron deficiency or partial positive charge, which will affect their catalytic properties.
- kMC simulations at 300 K essentially predict the same behavior extracted from static DFT calculations, C atoms spend most of the time around their most stable ad/absorption site.
- At higher temperatures other less stable ad/absorption sites become populated, such as subsurface sites at Pt (111) and Rh (111) surfaces, and surface sites at Ag (111) surface.
- In general, surface and subsurface diffusion dominate the kinetics, with sinking/emerging processes being less frequent.
- For Ag (111) surface, C emerging processes are triggered by annealing. The raised C atom can then bias the on-going catalytic processes occurring at the surface.
- These results indicate that the role of surface and subsurface C species in simulation models of some of the *fcc* TMs should be reconsidered.

Heterogeneous Catalysis

International Edition: DOI: 10.1002/anie.201813037
German Edition: DOI: 10.1002/ange.201813037

Subsurface Carbon: A General Feature of Noble Metals

Oriol Piqué[+], Iskra Z. Koleva[+], Francesc Viñes, Hristiyan A. Aleksandrov,* Georgi N. Vayssilov, and Francesc Illas*

Abstract: *Carbon moieties on late transition metals are regarded as poisoning agents in heterogeneous catalysis. Recent studies show the promoting catalytic role of subsurface C atoms in Pd surfaces and their existence in Ni and Pt surfaces. Here energetic and kinetic evidence obtained by accurate simulations on surface and nanoparticle models shows that such subsurface C species are a general issue to consider even in coinage noble-metal systems. Subsurface C is the most stable situation in densely packed (111) surfaces of Cu and Ag, with sinking barriers low enough to be overcome at catalytic working temperatures. Low-coordinated sites at nanoparticle edges and corners further stabilize them, even in Au, with negligible subsurface sinking barriers. The malleability of low-coordinated sites is key in the subsurface C accommodation. The incorporation of C species decreases the electron density of the surrounding metal atoms, thus affecting their chemical and catalytic activity.*

Late transition metals, including coinage (Ni, Cu, Ag, Au) and Pt-group (Pt, Pd, Rh, Ir, Re, Os) metals, are in widespread use as heterogeneous catalysts[1] for many reactions of industrial interest.[2,3] The systems simplicity, triggered by the applications importance, has prompted research aimed at their catalytic activity improvement, desirably coupled with a materials cost reduction. Nanostructuration strategies have been contemplated for that purpose.[4,5] The rational design of novel metal and alloy catalysts, backed up by precise ab initio quantum chemistry calculations on suited catalyst models, has meant as well a great leap forward in the quest for new, improved activity transition metal catalysts.[5,6]

Transition-metal catalysts are typically employed as shape-defined supported metal nanoparticles (NPs), for example, Au NPs on TiO_2 for low temperature carbon monoxide oxidation,[3] or Pd NPs on Al_2O_3 for exhaust gas treatments.[7] The high catalytic performance of such noble metal NPs is inherent to 1) the exposure of facets other than most stable one, and so, chemically more active, and 2) the exhibition of even lower-coordinated sites such as NPs edges and corners, more prone to attach molecules onto;[8] other effects can also play a key role, for example 3) quantum confinement,[9] 4) strong metal–support interactions,[9] 5) nanoparticle flexibility,[10] and 6) nano-polymorphism.[11] Still, the main drawback of such catalysts is that, in the course of the catalysed reaction, these get gradually deactivated over time and use. Besides NP sintering, the origin of this activity loss is the presence of poisoning agents, where carbon excels among others.

Carbon poisoning normally implies C_x moieties, usually generated as a side, undesired product of the on-going catalysed reaction, typically involving organic reagents. At low C coverage, C atoms can strongly adsorb on the catalyst low-coordinated sites, restricting the reagent adsorption upon and/or chemically modifying the very nature of the active sites.[12–14] At high C coverage, monolayers and multilayers of graphene can emerge on top of the metal surface, and even surround and contain metal NPs, structurally fully blocking its active sites.[15,16] However, recent experiments and computational simulations have changed the paradigm of low C content from a poison to a promoter role, as subsurface C in Pd catalysts favours the selective alkyne hydrogenation to olefins,[17] and its presence at low-coordination regions of metal NPs is explained by density functional theory (DFT) based simulations.[14]

Subsurface C has been shown to bias the selectivity of other substitutional or interstitial carbon residues,[18] displaying higher reactivity towards surface O and H adatoms than surface C.[19] The subsurface moieties mediated chemistry is non-exclusive to Pd. Interstitial C is well-known in Ni surfaces and NPs,[16] and recently justified on Pt systems,[20] all belonging to Group 10 of the periodic table. Motivated by these results, a question mark arises: Is such subsurface atom induced chemistry a singularity or a common feature otherwise? In the latter assumption, such effect has been often disregarded, focusing on the vicinal C-perturbing/blocking poisoning picture, which should in fact include the subsurface interaction situation.

Herein we show that the existence of subsurface C is a general feature to be considered. This is confirmed by inspecting its energetic and kinetic stability on most noble metals, namely, Group 11 Cu, Ag, and Au. By means of accurate DFT-based ab initio calculations we give arguments of the competitive, often higher stability of subsurface C compared to surface situations, and its kinetic feasibility by

[*] Prof. O. Piqué,[+] Dr. F. Viñes, Prof. Dr. F. Illas
Departament de Ciència de Materials i Química Física & Institut de Química Teòrica i Computacional (IQTCUB)
Universitat de Barcelona
c/ Martí i Franquès 1, Barcelona 08028 (Spain)
E-mail: francesc.vines@ub.edu
Prof. I. Z. Koleva,[+] Prof. H. A. Aleksandrov, Prof. Dr. G. N. Vayssilov
Faculty of Chemistry and Pharmacy, University of Sofia
1126 Sofia (Bulgaria)
E-mail: haa@chem.uni-sofia.bg
[+] These authors contributed equally to this work.
Supporting information and the ORCID identification number(s) for the author(s) of this article can be found under: https://doi.org/10.1002/anie.201813037.

overcoming small subsurface sinking energy barriers, with indications of subsurface C being a near-surface entity. DFT results are obtained on periodic supercell slab models suited to describe single-crystal (111) extended surfaces, but also on well-shaped NP models of 79 atoms, a NP size within the scalable regime, and, therefore, representative of larger NPs.[8] For comparison, the surface and subsurface situations are modelled at the (111) surfaces of the other five face-centred cubic (*fcc*) transition metals (Ni, Pd, Pt, Rh, Ir). Further details and definitions are present in the Supporting Information.

The calculated C adsorption (E_{ads}) and absorption (E_{abs}) energies on Cu, Ag, and Au (111) surface slab models for hexagonal close-packed (*hcp*) and *fcc* surface, and tetrahedral subsurface (*tss*) and octahedral subsurface (*oss*) sites, which are the most stable sites, are shown in Figure 1. For Cu, the *hcp* and *fcc* sites have similar stability, 436–440 kJ mol^{-1}, but in the subsurface *oss* site C is more stable by 42 kJ mol^{-1}. For Ag, the surface *fcc* site (E_{ads} of 320 kJ mol^{-1}) is 18 kJ mol^{-1} less stable than the subsurface *oss* site (E_{ads} of 338 kJ mol^{-1}). For Au (111) the surface *fcc* site (E_{ads} of 414 kJ mol^{-1}) is more stable than the subsurface *tss* by 25 kJ mol^{-1}. The main factor for the subsurface stability seems to be a balance between the

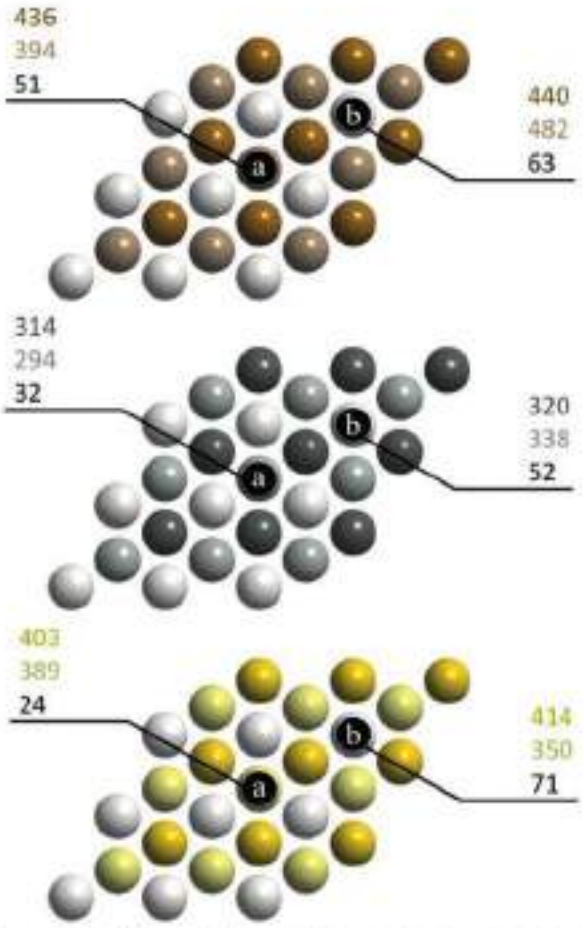

Figure 1. Cu (top), Ag (middle), and Au (bottom) adsorption (E_{ads}, in dark colours) and subsurface absorption energies (E_{abs}, in light colours), in kJ mol^{-1}, on (111) surface a) *hcp* and *tss* sites, respectively, and b) *fcc* and *oss* sites, respectively. Carbon diffusion energy barriers on each site are shown in black.

increased C bonding saturation and the subsurface deformation energetic cost to accommodate C atoms within the constrained subsurface space (see the Supporting Information for a discussion of the deformation energies, E_{def}, and Table S1). Moreover, the higher chemical activity of gold compared to silver is explained due to a silver deeper *d*-band centre, as found in equivalent DFT simulations,[21,22] plus a weaker C–Ag coupling, which prevents antibonding states being above Fermi level, and so, destabilizing the C interaction towards Ag.[23,24] Estimates at a full monolayer coverage (Supporting Information, Table S6), show that the surface or subsurface preferential stability prevails, although with reduced E_{ads} and E_{abs}.

A last critical point to tackle is the kinetic hindrance. Subsurface sinking energies displayed in Figure 1 reveal that barriers are within 32 and 63 kJ mol^{-1} for both Cu and Ag (111) surfaces, and, therefore, non-negligible, yet easy to overcome at catalyst working temperatures. For Au (111) the barriers range from 24 to 71 kJ mol^{-1}. The E_{ads}, E_{abs}, and sinking energy barrier values are in line with previous calculations,[20,25] and here well-reproduced for all *fcc* TMs (111) surfaces (Supporting Information, Figure S11). Furthermore, the further penetration of the C atom has been also considered yet discarded (see discussion in the Supporting Information). In general terms Group 11 (Cu, Ag, Au) *fcc*→*oss* sinking barriers are comparable yet higher than Group 10 (Ni, Pd, Pt), despite of the similar stability of the subsurface C. The kinetic hindrance in the former group could explain the lower experimental solubility of C (see discussion in the Supporting Information).

The above results apply for subsurface C suitability on Cu and Ag surfaces under operating conditions. A remaining aspect towards a more holistic picture view is the C interaction in/on lower-coordinated sites, such as edges and corners of metal NPs. This is fully explored on the (111) facets of M_{79} metal NP models (Supporting Information, Figure S2), and E_{ads}, E_{abs}, and subsurface sinking barriers are shown in Figure 2. One immediately detects similarities to extended surfaces, with caveats. Many *fcc*/*oss* and *hcp*/*tss* sites featuring both surface and subsurface states on Ag_{79} and Cu_{79} reveal increased E_{ads} and E_{abs} ranging 32–59 kJ mol^{-1} for the adsorption situations and 61–72 kJ mol^{-1} for the absorption situations. For the Au NP the increase of E_{abs} is in general notably higher (87–100 kJ mol^{-1}) than for E_{ads} (79–83 kJ mol^{-1}). Remaining small size effects and the still close proximity to low-coordinated sites can explain the increment of adsorptive situations. In the case of subsurface accommodation, the much larger increment is directly linked to a larger flexibility and deformability of vicinal metal atoms to accommodate and further stabilize the subsurface C moiety. This is clearly highlighted by the deformation and attachment energies balance (Supporting Information, Table S2), where attachment energies can be higher than on the (111) extended surfaces counterparts, by up to 123, 91, and 104 kJ mol^{-1}, for Cu, Ag, and Au NPs, respectively, accompanied by similar deformation energies for surface and subsurface situations. Thus, the low-coordinated sites allow for such deformation, beneficial for the C binding, without compromising the structural energy of the site.

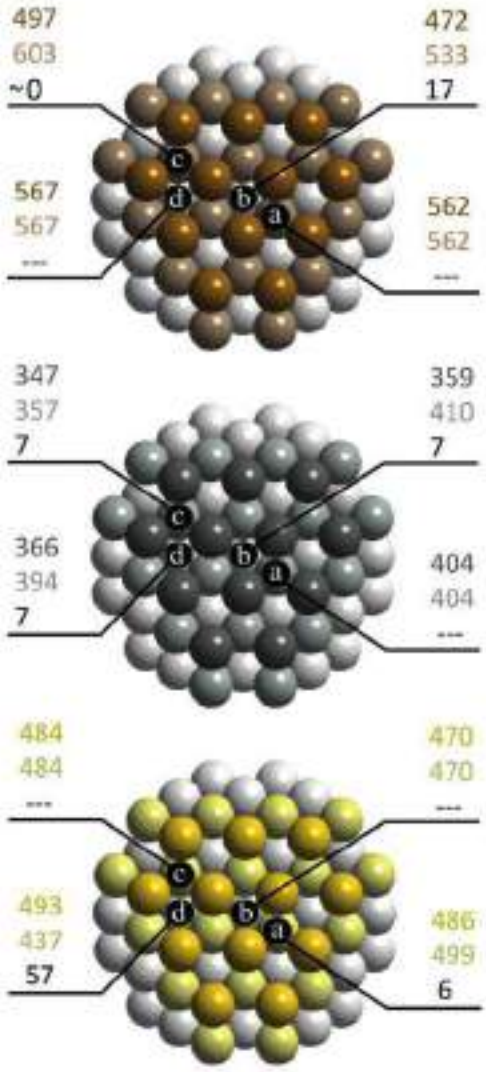

Figure 2. Cu_{79} (top), Ag_{79} (middle), and Au_{79} (bottom) C adsorption (E_{ads}, in dark colours) and subsurface absorption energies (E_{abs}, in light colours), in kJ mol^{-1}, on diverse (111) facet sites. Carbon diffusion energy barriers on each site are shown in black. Dashed lines are present when in-plane situations are found, that is, adsorption and absorption lead to a common final stable situation (E_{ads} and E_{abs} values are identical).

For the Cu_{79} NP, E_{abs} increases by 209 kJ mol^{-1} with respect the (111) slab model for corner *tss*, which becomes the most stable site for C on Cu_{79}. Analogous stabilization of subsurface C is observed on edge *tss* on Au_{79} with an E_{abs} increase of 110 kJ mol^{-1}, with respect to the Au (111) reference. Thus, subsurface C at edge *tss* site becomes the most stable situation in Au_{79}, although only 6 kJ mol^{-1} more stable than the edge *fcc* location. On Ag_{79}, similarly to Ag (111) surface, the centre *oss* site remains the most stable situation, but only 6 kJ mol^{-1} more stable than the edge *hcp* and *tss* locations. Therefore, low-coordination sites not only preserve the C preference for subsurface in Cu and Ag, but also foster subsurface occupancy even in Au systems. However, at a nearly full coverage situation (Supporting Information, Table S6), the subsurface stability is lost for the NP models, favouring surface situations which can involve the clustering of C atoms, see the example on Cu_{79} shown in the Supporting Information, Figure S12.

The most prominent feature on all the low-coverage cases is that the energy barriers, E_b, for the subsurface diffusion essentially vanish, and so, there is a kinetic free entrance for C adatoms to the subsurface region at the NPs edge and corner regions. Reduced barriers of essentially zero to 17 kJ mol^{-1} are found to occupy corner *tss* and central *oss* sites in Cu_{79}, of 7 kJ mol^{-1} in all situations of Ag_{79} but for the edge *hcp*/*tss* case, and a reduced barrier of only 6 kJ mol^{-1} for the entrance towards the edge *hcp* site in Au_{79}. This energy barrier lowering located at under-coordinated sites was also earlier found for Pd NPs.[14] Moreover, it has been found that low-coordination sites geometrically approach the surface and subsurface minima of the ad/absorbed C atom (see discussion in Supporting Information and Figures S3 and S4).

A further question is whether such subsurface C occupancy would be thermodynamically driven. To this end, phase diagrams have been acquired for all *fcc* TMs (111) surfaces, considering the turning conditions of pristine surfaces to become early C-containing, either on surface (C^{ad}) or in subsurface (C_{sub}). The details on phase-diagram construction, equalling the chemical potential of C, $\mu(C)$, to be half of that of acetylene (C_2H_2) minus hydrogen (H_2) molecular gases,[26] thus emulating alkyne hydrogenation conditions,[17] are given in the Supporting Information. The phase diagrams in the Supporting Information, Figure S9, show that, at regular catalytic temperature working conditions, C adatoms would be thermodynamically stable on Rh, Ir, and Pt (111) surfaces, subsurface on Ni and Pd (111) surfaces, and thermodynamically unstable on Cu, Ag, and Au (111) surfaces. This highlights that, on the latter, the isolated C adatom existence would be only dynamically and/or kinetically prompted, and to be considered only on the course of the reaction, even though the final state of such C moieties would be aggregate in graphite or amorphous carbon phases. However, note that the thermodynamic stability is reachable on low-coordinated sites of the Cu_{79} NP (Supporting Information, Figure S10). In any case, the ex situ subsurface C detection on Cu, Ag, and Au regular surfaces does not seem feasible, and a challenging task in situ (for example, see the discussion based on ambient pressure X-ray photoemission spectroscopy (APXPS)[27] in the Supporting Information), where indirect approaches through modified surface activity or site specific surface science techniques seem more feasible for the detection of subsurface C species in noble-metal systems.

Furthermore, to estimate the changes in the electronic structure of the three metals upon adsorption or absorption of C, we calculated the difference between the 3*s* core levels of metal centres around C and the corresponding centres in the pristine models before C insertion (Table 1; Supporting Information, Table S6). In all cases, there is a stabilization of the metal core level energies, suggesting a decrease of the electron density, and hence, a partial positive charge on those metal atoms. The core levels of surface atoms bound to C on Cu and Au (111) surfaces are stabilized by 0.63–0.94 and 0.65–0.89 eV, respectively, while for the Ag (111) surface this interval is 0.27–0.55 eV. For the subsurface atoms this stabilization appears to be smaller, for example, for the *oss*

Table 1: Shifts (in eV) of the 3*s* core levels (positive values correspond to stabilization) and of the *d*-band centres ε_d of the metal atoms bound to the carbon with respect to the corresponding metal atoms in the pristine (111) slab model.

		3*s* Core-level shifts			ε_d		
		Cu	Ag	Au	Cu	Ag	Au
fcc		0.94	0.55	0.89	−0.90	−0.40	−0.79
oss	Surf	0.63	0.27	0.65	−0.64	−0.24	−0.63
	Subs	0.46	0.08	0.13	−0.47	−0.07	−0.13
hcp		0.96	0.56	0.88	−0.92	−0.41	−0.79
tsi	Surf	0.65	0.30	0.69	−0.65	−0.25	−0.66
	Subs	0.61	0.18	0.54	−0.60	−0.11	−0.43

position of the Au slab the energy decrease is 0.65 and 0.13 eV for surface and subsurface Au atoms, respectively. Along the same line, the metal reactivity change is measured by the *d*-band centre shift of the metal atoms bound with the C atom with respect to the same atomic values on the corresponding pristine model. The obtained values reveal the same trend as the 3*s* core levels (Table 1; Supporting Information, Table S6). For instance, for Cu, Ag, and Au (111) surfaces with C at *fcc* or *hcp* positions, the shift of *d*-band centres to lower energies is 0.90/0.92, 0.40/0.41, and 0.79/0.79 eV, thus making the sites a priori less chemically active. The values for the slab and NP models are comparable. Again, the effect of subsurface C is weaker than that of the C atoms on the metal surface.

The density of states (DOS) difference plots for 5*d* states of Au metal centres bound to C at *oss* position of the Au (111) and at *hcp* edge of the NP are shown with solid lines in Figures 3a and b, respectively (the DOS plots for Cu and Ag are provided in the Supporting Information, Figures S5 and S6). For both slab and NP models there is an increase of DOS in the −7.5 to −4.0 eV region upon C absorption; while in the −3 to −1 eV region, closer to the Fermi level, a strong depletion of DOS is observed. This picture is in agreement with the stabilization of these metal centres, concluded from the analysis of the previous characteristics. Interestingly, when considering these metal-atom DOS plots in the same geometry while removing the C atom (see the dashed lines in Figure 3a,b), the opposite trend is observed: 5*d* DOS increases strongly close to the Fermi level and decreases at lower energies. Finally, in Figures 3c–f the charge density difference for some of the C-containing Au models is visualized (see also the Supporting Information, Figures S7 and S8 for the other C positions and metals). These figures confirm that there is a depletion of electron density from the metal centres around C (blue regions) and a rearrangement of electron density at those centres, likely due to a rehybridization of their frontier orbitals.

In summary, the present findings provide compelling energetic plus kinetic evidence that subsurface C species are to be considered in coinage metal systems, from extended surfaces to low-coordinated sites present in metallic NPs, under working catalytic temperature conditions. In the case of low-coordinated sites such as NPs edges and corners, subsurface positions are the most stable situation at low C concentrations, even in gold, to the point of subsurface C being a thermodynamically viable phase in Cu low-coordinated sites. On extended (111) facets/surfaces, subsurface C is dynamically and kinetically envisaged on Cu and Ag systems. These results broaden the subsurface C chemistry, so as to be considered a general aspect of late transition metal systems.

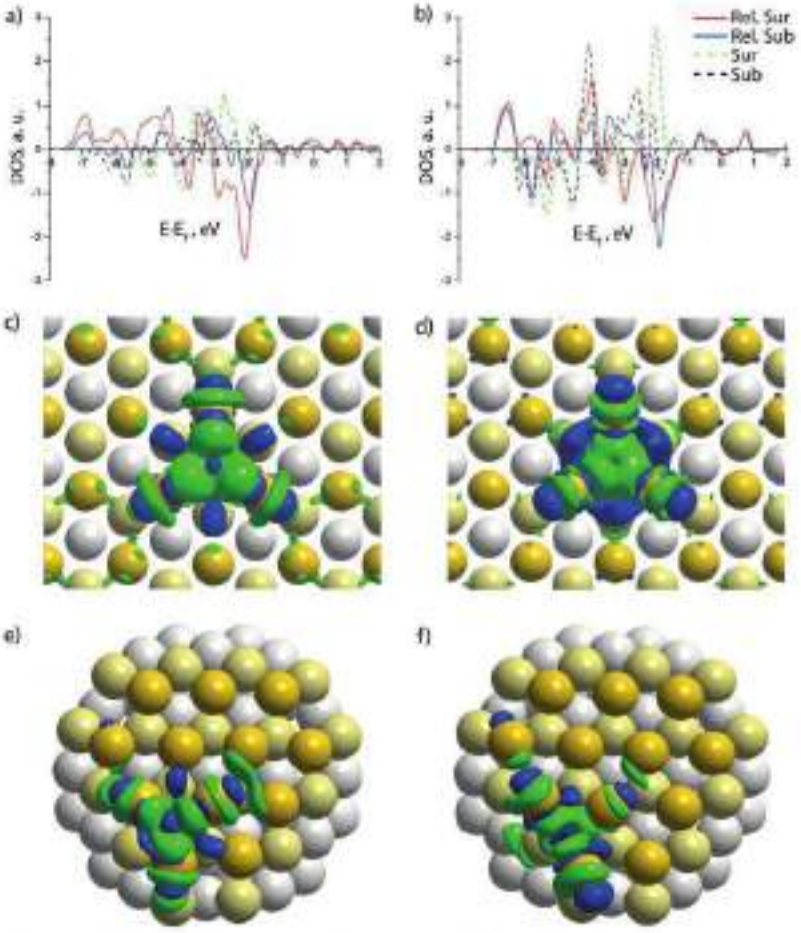

Figure 3. Difference in the density of states plots of Au 5*d* states for metal centres bound to C and corresponding Au atoms in a) the pristine model for C in *oss* position on Au (111) surface and b) C in *hcp* edge position on Au_{79} NP. Red solid line for surface Au atoms; blue solid line for subsurface Au atoms; dashed lines belong to difference between single point calculations for the corresponding structures after removal of C and the corresponding atoms in the pristine optimized structure: green dashed line belongs to surface Au atoms; black to subsurface Au atoms. The plots are normalized with respect to the number of gold atoms around the carbon. c)–f) Charge density difference for surface *fcc* (c) and subsurface oss (d) positions of C on Au(111) slab model; surface *fcc* edge (e) and *oss* edge (f) positions of C on Au NP; green regions indicate the increase of the electron density due to C addition, and blue regions the electron density depletion.

The malleability of low-coordinated sites at surfaces, edges, and corners appears to be the key aspect in the subsurface site C accommodation. Furthermore, this aspect does explain the easy sinking of surface C species to near surface situations, with low diffusion energy barriers, from almost vanishing at NPs edges and corners. The experimental in situ identification of such C species is challenging, although its presence may explain previously observed peculiar surface chemical activities of coinage metals with C impurities, and, furthermore, introduces itself as an aspect to be regarded in the future when studying heterogeneously catalysed processes by transition metal systems. The analysis of electronic structure changes in the C surrounding metal atoms reveals electron deficiency at those centres, indicating a partial positive charge that will affect their chemical and catalytic properties.

Acknowledgements

The authors are thankful to the *Ministerio de Economía y Competitividad* (MEC) for the CTQ2015-64618-R FEDER grant, and F.V. in particular for the *Ramón y Cajal* (RYC-2012-10129) research contract. Authors thank the *Generalitat de Catalunya* for its partial support through 2017SGR13 and XROTC grants. Financial support from Spanish MINECO through the Excellence *María de Maeztu* program (grant MDM-2017-0767) is also fully acknowledged. Acknowledgments are placed towards EU Horizon 2020 NOMAD Center of Excellence (No. 676580) and Materials Networking (No. 692146), and by the European Regional Development Fund and the Operational Program "Science and Education for Smart Growth" under contract UNITe No. BG05M2OP001-1.001-0004-C01. F.I. acknowledges additional support from 2015 ICREA Academia Award. Authors are thankful to *Red Española de Supercomputación* (RES) for the Picasso supercomputing time (QCM-2018-1-0005 and QCM-2018-2-0008). H.A.A. and I.Z.K. are thankful to the Bulgarian National Science Fund (project DN-09/5). I.Z.K. is grateful to Operational programme "Science and Education for Smart Growth", project BG05M2OP001-2.009-0028.

Conflict of interest

The authors declare no conflict of interest.

Keywords: density functional calculations · extended surfaces · metal nanoparticles · noble metals · subsurface carbon

How to cite: *Angew. Chem. Int. Ed.* **2019**, *58*, 1744–1748
Angew. Chem. **2019**, *131*, 1758–1762

[1] J. Greeley, J. K. Nørskov, M. Mavrikakis, *Annu. Rev. Phys. Chem.* **2002**, *53*, 319.
[2] A. J. Medford, A. Vojvodic, J. S. Hummelshøj, J. Voss, F. Abild-Pedersen, F. Studt, T. Bligaard, A. Nilsson, J. K. Nørskov, *J. Catal.* **2015**, *328*, 36.
[3] M. Haruta, S. Tsubota, T. Kobayashi, H. Kageyama, M. J. Genet, B. Delmon, *J. Catal.* **1993**, *144*, 175.
[4] F. Zaera, *ChemSusChem* **2013**, *6*, 1797.
[5] J. K. Nørskov, T. Bligaard, J. Rossmeisl, C. H. Christensen, *Nat. Chem.* **2009**, *1*, 37.
[6] S. M. Kozlov, G. Kovács, R. Ferrando, K. M. Neyman, *Chem. Sci.* **2015**, *6*, 3868.
[7] F. Viñes, A. Desikusumastuti, T. Staudt, A. Görling, J. Libuda, K. M. Neyman, *J. Phys. Chem. C* **2008**, *112*, 16539.
[8] F. Viñes, J. R. B. Gomes, F. Illas, *Chem. Soc. Rev.* **2014**, *43*, 4922.
[9] S. J. Tauster, *Acc. Chem. Res.* **1987**, *20*, 389.
[10] H. A. Aleksandrov, S. M. Kozlov, S. Schauermann, G. N. Vayssilov, K. M. Neyman, *Angew. Chem. Int. Ed.* **2014**, *53*, 13371; *Angew. Chem.* **2014**, *126*, 13589.
[11] B. K. Min, C. M. Friend, *Chem. Rev.* **2007**, *107*, 2709.
[12] S. M. Davis, G. A. Somorjai, *The Chemical Physics of Solid Surfaces and Heterogeneous Catalysis*, Elsevier, Amsterdam, The Netherlands, **1983**.
[13] S. Vajda, M. J. Pellin, J. P. Greeley, C. L. Marshall, L. A. Curtiss, G. A. Ballentine, J. W. Elam, S. Catillon-Mucherie, P. C. Redfern, F. Mehmood, P. Zapol, *Nat. Mater.* **2009**, *8*, 213.
[14] F. Viñes, C. Loschen, F. Illas, K. M. Neyman, *J. Catal.* **2009**, *266*, 59.
[15] S. K. Sengar, B. R. Mehta, R. Kumar, V. Singh, *Sci. Rep.* **2013**, *3*, 2814.
[16] H. A. Aleksandrov, N. Pegios, R. Palkovits, K. Simeonov, G. N. Vayssilov, *Catal. Sci. Technol.* **2017**, *7*, 3339.
[17] D. Teschner, J. Borsodi, A. Wootsch, Z. Révay, M. Hävecker, A. Knop-Gericke, S. D. Jackson, R. Schlögl, *Science* **2008**, *320*, 86.
[18] A. Rinaldi, J.-P. Tessonnier, M. E. Schuster, R. Blume, F. Girgsdies, Q. Zhang, T. Jacob, S. B. Abd Hamid, D. S. Su, R. Schlögl, *Angew. Chem. Int. Ed.* **2011**, *50*, 3313; *Angew. Chem.* **2011**, *123*, 3371.
[19] M. Maciejewski, A. Baiker, *Pure Appl. Chem.* **1995**, *67*, 1879.
[20] P. Janthon, F. Viñes, J. Sirijaraensre, J. Limtrakul, F. Illas, *Catal. Sci. Technol.* **2017**, *7*, 807.
[21] Y. Santiago-Rodríguez, J. A. Herron, M. C. Curet-Arana, M. Mavrikakis, *Surf. Sci.* **2014**, *627*, 57.
[22] B. W. J. Chen, D. Kirvassilis, Y. Bai, M. Mavrikakis, *J. Phys. Chem. C* **2018**, https://doi.org/10.1021/acs.jpcc.7b11629.
[23] B. Hammer, J. K. Nørskov, *Adv. Catal.* **2000**, *45*, 71.
[24] A. Notario-Estévez, S. M. Kozlov, F. Viñes, F. Illas, *Chem. Commun.* **2015**, *51*, 5602.
[25] S. P. Liu, M. Zhao, W. Gao, Q. Jiang, *ChemSusChem* **2017**, *10*, 387–393.
[26] D. Teschner, Z. Révay, J. Borsodi, M. Hävecker, A. Knop-Gericke, R. Schlögl, D. Milroy, S. D. Jackson, D. Torres, P. Sautet, *Angew. Chem. Int. Ed.* **2008**, *47*, 9274–9278; *Angew. Chem.* **2008**, *120*, 9414–9418.
[27] M. Favaro, H. Xiao, T. Cheng, W. A. Goddard III, J. Yano, E. J. Crumlin, *Proc. Natl. Acad. Sci. USA* **2017**, *114*, 6706.

Manuscript received: November 14, 2018
Accepted manuscript online: December 7, 2018
Version of record online: January 4, 2019

Applied Surface Science 513 (2020) 145765

Contents lists available at ScienceDirect

Applied Surface Science

journal homepage: www.elsevier.com/locate/apsusc

Full Length Article

Towards understanding the role of carbon atoms on transition metal surfaces: Implications for catalysis

Biel Martínez, Oriol Piqué, Hèctor Prats, Francesc Viñes*, Francesc Illas

Departament de Ciència de Materials i Química Física & Institut de Química Teòrica i Computacional de la Universitat de Barcelona (IQTCUB), c/Martí i Franquès, 1-11, Barcelona, Spain

ARTICLE INFO

Keywords:
Transition metal catalysts
Subsurface carbon
Density functional theory
Kinetic Monte Carlo
Thermodynamics and kinetics
Dynamics

ABSTRACT

Carbon moieties, in a low coverage regime being reduced to C adatoms, are a rock-in-the-shoe for heterogeneously catalyzed processes involving carbon-containing species. Their presence affects the performance of Transition Metal (*TM*) based industrial catalysts, often resulting in poisoning. Recent studies on the C adatom thermodynamic stability revealed that both surface and subsurface C atoms may coexist, indicating additional poisoning mechanisms, yet also new catalytic promoting mechanisms. The present work provides a systematic study of the potential dynamic relevance of such subsurface C atoms in the most stable (111) surface of all *fcc* TMs at low C coverages. This relies on evaluating the composition at thermodynamic equilibrium and the time scale of the different involved processes by means of Density Functional Theory (*DFT*) and kinetic Monte Carlo (*kMC*) simulations, respectively. These DFT and kMC simulations highlight the relevant role of subsurface C atoms for Ag and Pd, and a fast C mobility for Au and Pt, which might be important factors contributing to poisoning or opening new reactive path mechanisms, especially relevant at high temperature working conditions.

1. Introduction

Transition Metals (*TMs*) are crucial in many heterogeneously catalyzed industrial chemical processes with huge relevance in the modern mankind society development. The production of ammonia, for instance, is to date mostly carried out through the Haber-Bosch process, using Fe as a catalyst [1]. Specifically, due to their established moderate chemical activity [2], TMs deliver a good compromise between affordable reaction energy barriers and moderate binding strengths of the involved reaction species —*i.e.*, fulfilling *Le Sabatier* principle— and, hence, are broadly employed in heterogeneous catalysis [3]. Nevertheless, research endeavors are continuously undertaken to develop novel or improved catalysts involving TMs as indispensable components, either as active phase, as supports, forming alloys, or even in the limit of isolated single atoms, the so-called Single Atom Catalysts (*SACs*). Among the TMs used in heterogeneous catalysis, those with face-centered cubic (*fcc*) crystal structure are prominent, *e.g.* in the hydrogen production, catalyzed by Ni [4], the generation of nitric acid through the Ostwald process using Pt or Rh as catalysts [5], methanol synthesis using large supported Cu nanoparticles [6], or the partial oxidation of methane to carbon monoxide, achievable using Ni, Ru, Rh, Pd, Ir, or Pt [7].

Many of the aforementioned industrially relevant processes involve carbon-containing species. In fact, all the organic and fine chemistry industries handle, generically, carbon rich molecules. During the formation or breaking of chemical bonds, some intermediate species can eventually escape from the sought catalytic cycle through side secondary reactions, resulting in C_x moieties attached to the catalyst surface. These carbon residues can eventually lead to coke formation, which would poison the catalyst by blocking the active surface metal sites [8]. This is indeed a frequent problem on *fcc* TM surfaces, where poisoning by carbon species have been reported for a wide variety of catalytic processes [9–11], thus reducing or even jeopardizing the catalytic activity over time, and ultimately, requiring costly catalyst regeneration steps.

Typically, poisoning occurs at high carbon coverage, θ_C, where different complex structures are found going from carbon filaments to graphene, graphite, or amorphous carbon [12,13]. At very low θ_C, C remains mostly isolated, normally as surface adatoms [13]. Recent works studied the thermodynamic and kinetic stability of such C atoms on most-stable (111) surfaces of *fcc* TMs and realistic nanoparticle models, revealing for a number of the studied cases a rather unexpected higher stability at subsurface sites [14,15]. So far, this extended surprising feature has not been taken into account in the computational

*Corresponding author.
E-mail address: francesc.vines@ub.edu (F. Viñes).

https://doi.org/10.1016/j.apsusc.2020.145765
Received 16 December 2019; Received in revised form 20 January 2020; Accepted 12 February 2020
Available online 13 February 2020
0169-4332/

models previously used to simulate catalytic processes on such surfaces. The consideration of the presence of subsurface carbon might well lead to a change of paradigm in our understanding of the catalytic activity and reactivity of a variety of metal surfaces that can experience this phenomenon. Indeed, there are experimental and theoretical works that already underline the pivotal role of such C species on tuning the catalytic activity, reactivity, and selectivity of Pd catalysts [16,17].

Here we go one step further investigating the dynamic aspects of surface/subsurface C stability on all *fcc* TM (111) surfaces. To this end we perform kinetic Monte Carlo (*kMC*) simulations, with rates obtained from Density Functional Theory (*DFT*) based calculations, aimed at gaining information of the surface structure under realistic working conditions over time. This information is likely to be relevant for the determination of the potential role of surface or subsurface C species, aside, with the aim to ascertain whether the lifetime of such species falls in the reaction rate time-lapse, and, therefore, should be considered as a potential catalytic role-player.

2. Computational details

The DFT based calculations have been carried out for suitable periodic models of the *fcc* TM (111) surfaces (TM = Ni, Cu, Rh, Pd, Ag, Ir, Pt, and Au) using the Vienna *Ab Initio* Simulation Package (*VASP*) [18], and employing the Perdew-Burke-Ernzerhof (*PBE*) form of the exchange and correlation functional [19], shown to be one of the most accurate choices for a wide variety of TM systems and properties, including the atomic and electronic structure of bulk and low Miller index surfaces [20–23]. The (111) surface has been chosen since it is the most stable surface and, according to the Wulff construction minimizing the surface energy [21,24], the most exposed in large supported nanoparticles in the *fcc* TM real catalysts.

The adsorption of atomic C has been studied on the highest symmetry sites, including top, bridge, and three-fold hollow sites —*fcc*, having a subsurface metal atom two layers underneath, and hexagonal close-packed (*hcp*), having a metal atom in the immediate subsurface layer—, being hollow sites the most preferred by C species. As far as subsurface sites are concerned, several non-equivalent sites have been sampled with the C atom in between the first and second atomic metal layers, finding that the only relevant adsorption sites are the *fcc* subsurface —also known as octahedral subsurface site, *oss*— and the *hcp* subsurface —known as tetrahedral subsurface site, *tss*—. The energy barriers for diffusion, E_b, of C species along the (111) surface, along the (111) subsurface, and in between the surface and subsurface regions have been obtained using the Climbing Image Nudged Elastic Band (*CI-NEB*) method [25].

To represent the TM (111) surfaces, a $p(3\times3)$ supercell with six atomic layers, containing a total of 54 metal atoms, has been used. The three uppermost layers have been allowed to fully relax, whereas the three bottommost layers were fixed at optimized bulk crystal positions to simulate bulk rigidity. Such models are wide enough so to deliver converged results up to few tenths of an eV —below *c.a.* 0.04 eV— for absorption and adsorption energies [15]. The valence electron density was expanded in a plane wave basis set, with a kinetic energy cutoff of 415 eV. In the self-consistent field method, a suitable smearing algorithm has been used to enhance the convergence procedure, yet final energies have been extrapolated to 0 K. The reported energies account for the Zero Point Energy (*ZPE*) term, calculated within the harmonic approximation. The frequency calculations have been computed from diagonalization of the corresponding block of the Hessian matrix with elements computed from finite displacements of analytic gradients; a value of 0.01 Å was considered for all the atoms relaxed during the structural optimization or the Transition State (TS) search location. The sampling of the reciprocal space has been carried out following a $3\times3\times1$ Monkhorst-Pack k-points grid [26]. The E_b for the sinking-emerging processes have been extracted from literature [14], yet here including the ZPE term.

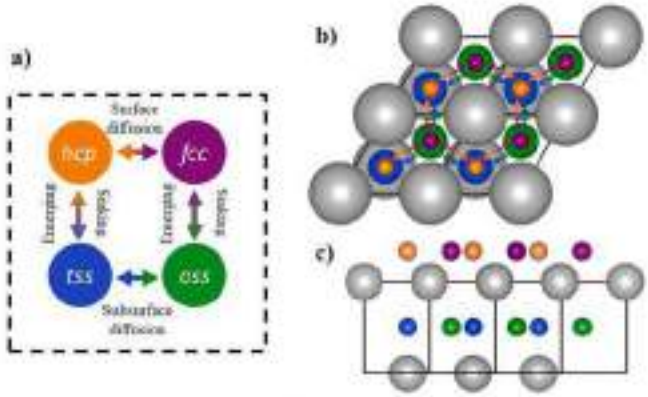

Fig. 1. Schematic representation of the employed lattice unit cell indicating the considered active sites, and their connectivity: (a) representation of the adsorption sites included in the unit cell, and the eight different diffusion processes accounted for in the kMC simulations, (b) top view of a $p(2\times2)$ supercell. Black spheres denote metal atoms, and the unit cell units are represented with black lines. Colored smaller (larger) spheres denote surface (subsurface) sites following the notation in (a), and colored lines show the connectivity between sites within the same layer, and (c) side view of (b), where colored lines show the sinking/emerging channels of the lattice. (For interpretation of the references to colour in this figure legend, the reader is referred to the web version of this article.)

A Python-based kMC code has been written to correctly propagate the system configurations by means of the widely used rejection-free Variable Step Size Method (*VSSM*) [27]. The different TM (111) surfaces are represented in the kMC framework as a two-dimensional periodic lattice, where each adsorption site corresponds to a point in the lattice. The latter is built by replicating $L\times L$ times the $p(1\times1)$ primitive unit cell, which contains two surface sites (i.e., one *fcc* and one *hcp*), and two subsurface sites (i.e., one *oss* and one *tss*), as shown in Fig. 1. Periodic boundary conditions were included in the kMC simulations to emulate the extended character of the surface at the atomic scale. As the purpose here is to study the low θ_C real situations, the kMC simulations have been performed in the θ_C range of 1−9 at% and a temperature, T, range of 300−700 K. Note that θ_C at% is defined as the percentage of carbon atoms per lattice surface lattice sites, being these the sum of the *hcp* and *fcc* hollows in the unit cell. At this low-coverage regime, the effect of possible lateral interactions, not accounted in this kMC model, is irrelevant, even more when they have been seen to be rather anecdotic, if any, during the simulations, as just very rarely C atoms are located vicinal to each other. A total of eight types of diffusion processes have been considered for the present kMC simulations, which involve the reversible surface and subsurface diffusions from *fcc* to *hcp* and from *tss* to *oss*, respectively, as well as the reversible sinking/emerging processes from *hcp* to *tss* and from *fcc* to *oss*.

For diffusion processes at solid surfaces, the adsorbed species only contribute to the vibrational partition function, and the rate constant can be obtained from Transition State Theory (*TST*) as:

$$k = \frac{k_B T}{h}\frac{Q_{TS}}{Q}e^{-\frac{E_b}{k_B T}}, \tag{1}$$

where E_b is the energy barrier including the ZPE term, h the Planck constant, k_B the Boltzmann constant, and Q_{TS} and Q the vibrational partition functions at the TS and at the initial state, respectively, which can be computed as:

$$Q = \prod_{i=1}^{3N}\frac{1}{1-e^{-\frac{i\nu h}{k_B T}}}, \tag{2}$$

for energies already including the ZPE term, where N is the number of relaxed atoms, and the product runs for the $3N$ vibrational frequencies, ν_i. Note that our reaction model involves diffusion processes with very dissimilar E_b values. In order to speed up the kMC

Table 1
Total number of carbon atoms, N_C, and lattice size $p(N\times N)$, and total number of sites, n_{sites}, as a function of θ_C.

	θ_C/ML				
	1	3	5	7	9
n_C	98	150	160	126	162
$p(N\times N)$	$p(70\times70)$	$p(50\times50)$	$p(40\times40)$	$p(30\times30)$	$p(30\times30)$
n_{sites}	19,600	10,000	6400	3600	3600

simulations, the difference in time scales has been handled by manual scaling the rate constants of the fastest processes by some appropriate factor $\alpha < 1$, while ensuring that this scaling does not alter the final outcome of the simulation. This solution has been successfully applied in many previous kMC studies [28–31]. Here, we applied α, so that $\log_{10}(\alpha) = -6$, -2, and -3 for surface diffusion in Cu, Ni, and Rh, respectively; and $\log_{10}(\alpha) = -2$ for Pt *hcp*↔*tss* processes. Additional details regarding the manually scaling and the validation of the kMC code are provided in the Supplementary Material (*SM*).

The chosen θ_C is simulated by initially repeating the lattice unit cell and adding an appropriate number of C atoms at random positions, see Table 1. All kMC simulations have been carried out until the system reached the equilibrium, plus $5{\cdot}10^6$ extra steps for production, from which the overall macroscopic properties have been extracted. First, the mean percentage of C atoms at each site have been determined. Moreover, the average waiting time between an emerging event and its subsequent emerging in a given surface area through either *fcc* or *hcp* site, $\tilde{t}_{em}$, in units of time per surface area, has been computed as the quotient between the total production time, t_p, and the number of emerging processes, n_{em}, occurred through a *fcc* or an *hcp* site, times the area A of the simulation cell:

$$\tilde{t}_{em} = \frac{t_p}{(n_{em})A}. \tag{3}$$

Another interesting property is the average lifetime of a C atom in a given region, lt_r, where r relates to being surface or subsurface, or on a given site type, lt_j, where j = *hpc*, *fcc*, *tss*, or *oss*, which can be calculated from the kMC simulations as:

$$lt_r = \frac{1}{n_C}\sum_{i=1}^{n_C}\frac{t_r^i}{n_r^i}, \tag{4}$$

$$lt_j = \frac{1}{n_C}\sum_{i=1}^{n_C}\frac{t_j^i}{n_j^i}, \tag{5}$$

where n_C is the number of carbon atoms, t_r^i and t_j^i are the time spent for the i^{th} atom in the region r and the site type j, respectively, and n_r^i and n_j^i are the number of processes experienced by the i^{th} atom that drove it to the region r and the site type j, respectively. Obtaining these aforementioned properties allows one to reach not only a complete analysis of the equilibrium state but also a deeper analysis on the time scales of the equilibrium fluctuations, that could very well be a key factor on the surface chemistry of a significantly carbided surface.

3. Results and discussion

The relative energetic stability of C at the different adsorption sites, as well as the energy barriers for sinking/emerging processes, have been taken from the previous work by Piqué et al. [14]. Here we have performed additional DFT calculations at the same level of theory to obtain the energy barriers for surface and subsurface diffusion, as well as to include the ZPE term, which was previously neglected. Figs. 2 and 3

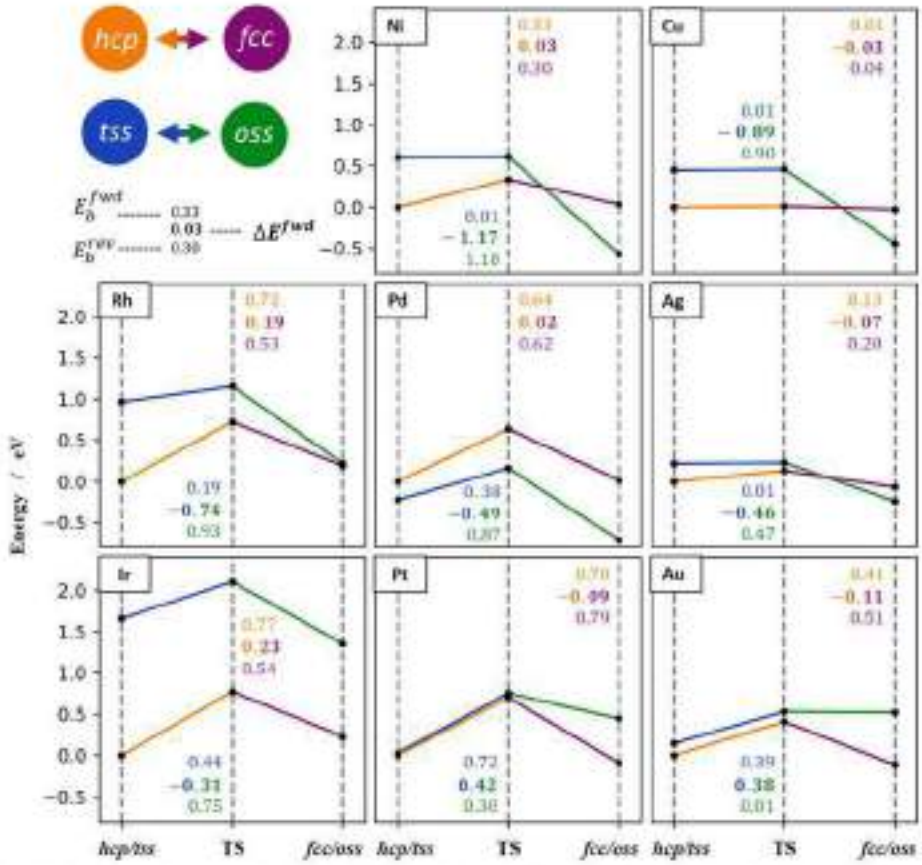

Fig. 2. Energy profiles for *hcp*↔*fcc* surface and *tss*↔*oss* subsurface diffusions of an isolated C atom for the eight studied *fcc* transition metal (111) surfaces. The left top-most panel contains a description of the processes and indicates the meaning of the numerical values in the rest of panels.

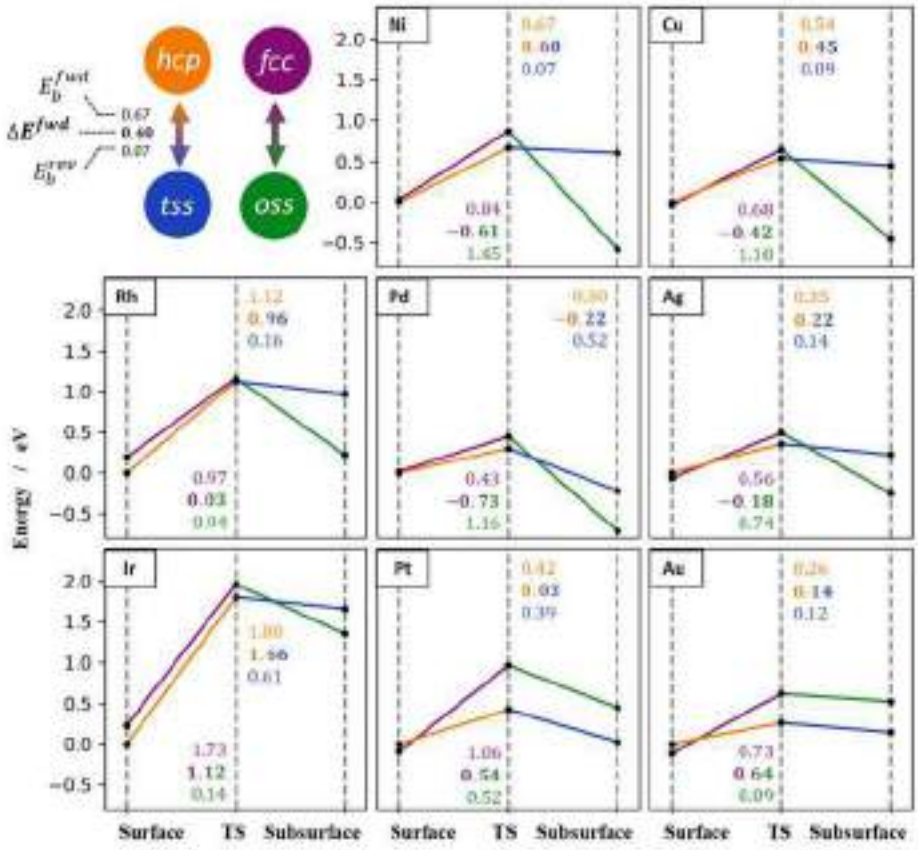

Fig. 3. Energy profiles for *hcp*↔*tss* and *fcc*↔*oss* sinking/emerging processes of an isolated C atom for the eight studied *fcc* transition metal (111) surfaces. Diffusion energy barriers were initially obtained from literature [14] but here include the ZPE term. The topmost left panel is as in Fig. 2.

show the energy profiles for all diffusion processes with the energy barriers for both forward and reverse directions, while values of the relative stability of C atoms on the different adsorption sites are reported in Table S1 of the SM. The most stable region for a C atom on Ni, Cu, Pd, and Ag is subsurface, specifically oss, understandable just in terms of cavity space as compared to *ss*. In fact, *oss* is found to be more stable than *ss* for all the studied transition metals except for Pt and Au. On the contrary, C prefers the surface region on Rh, Ir, Pt, and Au, with both *fcc* and *hcp* sites featuring similar adsorption energies. As one moves along a TM series and up a group in the periodic table, the metal atomic radii decreases, and the C subsurface stability compared to the surface stability increases, since metals with smaller radius allow for extra space within their voids.

The E_b values for surface diffusion range from 0.04 for Cu to 0.79 eV for Pt, suggesting a likely surface C adatoms mobility at working conditions. Surprisingly, subsurface diffusion does not imply much larger energy barriers, which range from 0.39 for Au to 1.18 eV for Ni. Note that the diffusion across the subsurface region implies an elongation of the three-fold hollow sites metal-metal bonds involved in the C crossing pathway. At first sight, one would argue that this deformation has an energy cost that could largely increase the E_b values. However, the TS structure appears to be stabilized by the surrounding metal atomic coordination shell, which compensates the structural distortion destabilization. Interestingly, C atoms diffuse more easily when the surface chemical activity is small, this is, when moving along a TM series and down a group, being weakly bonded to a specific site, which happens to be a common trend of adsorbed diffusing species on transition metals [32].

In general, sinking/emerging processes present higher E_b compared to surface/subsurface diffusions, as the former imply an increase of the surface metal-metal bonds of the three surface metal atoms conforming the hollow sites along the C atom crossing pathway [15,33], but without being much stabilized by coordination. The sinking energy barriers range from 0.26 to 1.80 eV for Au and Ir *hcp*→*tss* cases, respectively. On the other hand, the emerging energy barriers range from only 0.07 to 1.45 eV, both belonging to Ni, but for *tss*→*hcp* and *oss*→*fcc*, respectively. In general, the sinking/emerging energy barriers decrease while going down a group of the periodic table, due to a combination of larger interstices and malleability of the metals [15]. Note that the high subsurface C stability does not necessarily imply a smaller E_b for the C sinking. For instance, C is very stable at the oss site of both Ni and Ag, but their corresponding sinking energy barriers are 0.84 and 0.43 eV, respectively. Thus, dynamic simulations are necessary to shed light into whether the sinking/emerging E_b values are determining, i.e. large enough to prevent the exchange of C atoms between surface and subsurface sites under working conditions.

To have a deeper insight into the overall dynamic process of C atoms at these surfaces, we carried out kMC simulations under *operando* conditions, and calculated several macroscopic properties such as the percentage of total C at the surface and subsurface regions, with results reported in Fig. 4. The kMC simulations show that, at 300 K, C atoms are almost only at the surface for Rh, Ir, Pt, and Au; and almost only in the subsurface for Ni, Cu, Pd, and Ag, in agreement with the relative energetic stability predicted by the DFT calculations. Indeed, the 100% surface situation is found for Ir, whereas a 100% of subsurface C is found for Pd. Hence, in the low θ_C regime, the large number of empty sites enables the location of all C atoms in their thermodynamically most stable adsorption sites. Tables S2–S9 of the SM summarize the percentage of C atoms in all four different types of adsorption sites at all temperature values considered. The kMC simulations allow us to keep track of the preferred paths for the C atoms within the lattice. In general, there is a drastically larger preference for the sinking/emerging processes to occur through a *hcp* site, which is also in agreement with the smaller E_b values, see Fig. 3. The reason is that C at *tss* sites is

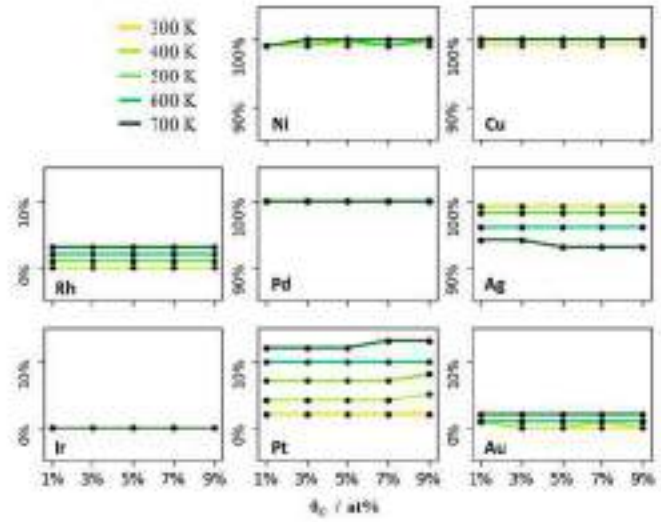

Fig. 4. Percentage subsurface C for the studied *fcc* TM (111) surfaces as a function of the total θ_C and in the temperature ranges of 300–700 K.

generally less stable than at oss, and, hence, features lower emerging barriers. In addition, the subsurface metal atom stabilizes the TS for sinking through a coordination effect. Overall, the C motion is mainly composed by diffusion steps either at the surface or across subsurface, connected through sinking/emerging processes involving *hcp* and *tss* sites. Thus, the occupation of *oss* sites, which are the most stable sites in the subsurface, is not reached through a direct sinking from a *fcc* surface site, but rather from a *hcp*→*tss* sinking followed by a *tss*→*oss* subsurface diffusion.

The effect of θ_C on the amount of C present at the surface or subsurface sites is negligible, even for the θ_C of 9 at%. However, the effect of temperature is relevant in some of the studied surfaces, leading to an increase of the C population in the less stable sites. This effect is especially prominent for Ag and Pt. In the case of Ag, there is a decrease of subsurface C concentration by increasing the temperature, which represents up to a 7% of the total C released to the surface at 700 K. This suggests that upon annealing, C containing Ag (111) samples would feature a segregation of C towards the surface, rather than increasing solubility of C within the material. In the case of Pt, the amount of C in subsurface sites increases from 2% at 300 K to 13% at 700 K, thus becoming an important factor to take into consideration when dealing with Pt catalysts in presence of C moieties and also when modeling organic chemistry reactions on Pt (111) terraces at working conditions. Note that these unexpected results cannot be anticipated by inspection of the DFT energy profiles alone, and may be very relevant in the catalytic activity of these transition metal surfaces at high working temperatures.

The presence of subsurface C can affect the surface chemical activity in different ways, such as increasing or reducing the adsorption strength of particular molecules. The subsurface C stability in Pd (111) at all operating conditions explains the observed C_1 promoting role of Pd catalysts in alkyne dehydrogenation reactions [34,35]. Moreover, for cases where C atoms are preferentially located at the surface, the sinking of C atoms to the subsurface might be followed by their diffusion and posterior emerging to other regions, either C-containing or C-free. This process can be enhanced with the temperature, especially in the case of Pt, Rh, and Au. In particular, this can explain the double-layer model as detected on Pt (111) [36], consisting of a graphene-like layer, with C atoms connecting it to the Pt(111) surface [37]. Alternatively, for cases where C prefers to be in the subsurface region, the surface would be apparently clean, yet C atoms would remain trenched at the *oss* sites. Apart from the possible perturbing effect on the expected surface activity, their possible emergence could imply these C

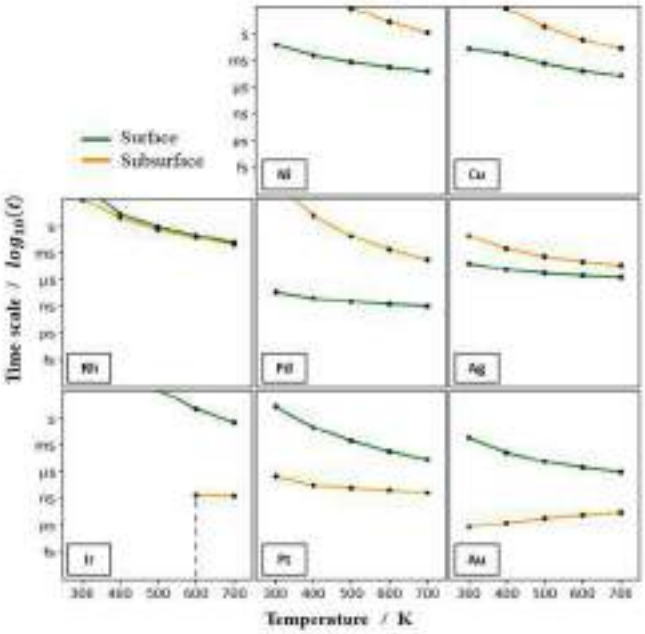

Fig. 5. Mean lifetime of a C atom on the or subsurface regions as a function of temperature, *T*. All values have been computed for θ_C = 1 at%. Note that for Ir no subsurface sites were populated below 600 K in the performed simulations.

atoms being involved in the on-going reaction, a point which may well be the case for Ag, and for Ni and Cu to a lesser extent, at high temperatures.

In order to quantify the occurrence probability of processes involving emerging C atoms, we have to consider the emergence feasibility and the lifetime of C species at the surface and on subsurface sites. Fig. 5 displays the average lifetime of C atoms at surface and subsurface regions in the range of studied temperatures and θ_C = 1 at%. Note that, as stated above, results for this quantity are independent of the C coverage. Obviously, longer lifetimes are obtained for the most stable regions, which are rarely below the μs even at 700 K. This indicates that, once the system is at equilibrium, there are very few sinking and emerging processes. Interestingly, when they occur, the lifetime of the C on the new, less stable situation, is generally still in the range of the ps to ms, which cannot be neglected as surface reaction steps are comprised at these time scales. Note that both lt_{surf} and lt_{sub} decrease when increasing the temperature and while going down a group, in agreement with the decrease in sinking/emerging energy barriers.

Let us analyze in more detail the systems for which C prefers a subsurface site; *i.e.* Ni, Cu, Pd, and Ag. All of them present lt_{surf} below 1 s, and even below 1 ms at 700 K. Thus, when the exposure time is larger than lt_{surf}, one would expect that all C atoms go subsurface. Since catalytic cycles may operate well beyond this ms time scale, one can confirm that a migration of C from surface to subsurface sites in these metal surfaces will occur under realistic *operando* catalytic conditions, which may introduce changes in the performance of the catalyst. In addition, the effect of surface C does not have to be misregarded, given that reaction steps occur in the fs to ms scales frame where as-generated surface C atoms can be present.

Fig. 6 shows the mean lifetimes for the C atoms on the different types of adsorption sites, as well as the average waiting time between two consecutive emerging processes, t_{em}, at 300 and 700 K, and θ_C = 1 at%. The obtained results for all the other studied operating conditions can be found in Tables S10-S17 of the SM, together with some hints to ease the interpretation of Fig. 6. In general, the simulations show that C lifetimes at particular sites are many orders of magnitude lower than lifetimes at surface or subsurface, indicating that intra-layer diffusion processes are dominant. This alters the static image that one could get

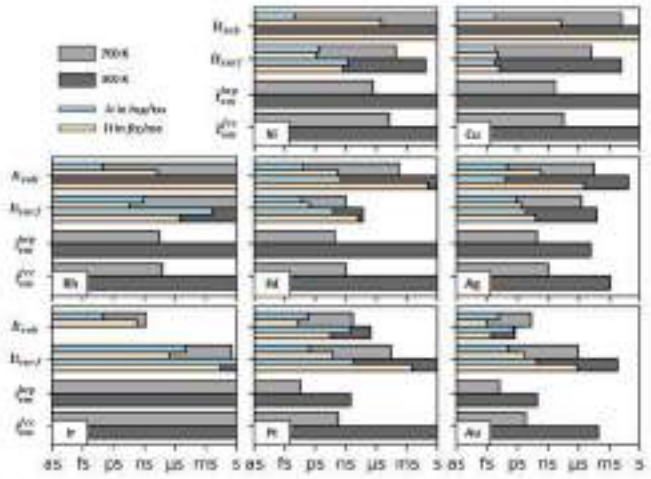

Fig. 6. Mean lifetime of C in the different regions; lt_{surf} and lt_{sub}, and in the four different adsorption/absorption sites, lt_{fcc}, lt_{hcp}, lt_{tss}, and lt_{oss} as well as the average waiting time between two consecutive emerging processes through either *fcc*, $\bar{t}_{em}^{fcc}$, or *hcp*, $\bar{t}_{em}^{hcp}$. All values have been computed at 300 K (dark grey) and 700 K (light grey), and θ_C = 1 at%. For lt_{surf} and lt_{sub}, a decomposition in terms of *hcp/tss* and *fcc/oss* sites is provided in light blue and orange insight each grey bar. See the SM for further details on the interpretation of the bars.

from the systems when analyzing Fig. 4 and suggests that there is a continuous diffusion of C atoms within the same metal layer. Before going into details for the different cases, a rough analysis of the results in Fig. 6 predicts that C at Ir (111) can be regarded as an example of a rather static system, with large waiting times, and long lifetimes on specific site, almost as much as the overall surface or subsurface lifetimes. On the other hand, Pt and Au show short waiting times, and comparable high and easy mobilities. Finally, Ni, Cu, Rh, Pd, and Ag are in between the two previous scenarios. These behaviors quite correlate to what is expected from the energy profiles and energy barrier values shown in Figs. 2 and 3.

For the systems where carbon is found to be more stable at subsurface, namely Ni, Cu, Pd, and Ag, $\bar{t}_{em}$ is in the ns and s range, normally ns for *tss*→*hcp* transitions. This couples to lt_{surf} values ranging from fs to ns, large enough to allow the interaction of the emerging C with available adsorbates with possible concomitant effects on the ongoing surface catalyzed process. Although the emergence of C at 300 K is in the seconds time frame, $\bar{t}_{em}$ clearly drops to µs or ns when the system is annealed to 700 K, even though this reduces lt_{surf}, which still is slightly below the ms time scale. This result indicates that, on the average, one can expect the emergence of one C atom to the surface each µs per Å^2, and lasting at the surface for a substantial time, almost 1 ms in the case of Ag. Obviously, a frequent and long C presence can clearly condition the surface activity and the on-going processes, which underlines the C subsurface chemistry as a factor to be considered when working with Ni, Cu, Pd, and Ag surfaces, especially critical in the case of Ag, as an apparently clean surface at 300 K could contain C trenched subsurface that may emerge when the surface is heated at the working conditions.

For the systems where C is found to prefer surface sites (Rh, Ir, Pt, and Au) the presence of subsurface C might not critically condition the on-going catalysis, as the main influence will come from surface C adatoms. In these cases, the only effect of subsurface C presence would be to facilitate the mobility of carbon around the lattice and, eventually, emerge on C-free or C-containing areas of the surface; *i.e.* it could open another channel to move C contamination to all possible sites in the lattice. Moreover, the emergence of subsurface C atoms may imply another front of attack in the catalytic reaction, which can be important e.g. on Pt, given then enhanced C solubility, see Fig. 4. For Ir, however, the presence of subsurface C, only detectable at high temperatures, is merely testimonial. Not only the sinking processes are rarely occurring, but also the diffusion at surface, with time scales above the µs even at 700 K. Rh partially populates subsurface at the equilibrium at 700 K, but the lt_{sub} is above the seconds timeframe even at 700 K, which implies that, even if subsurface is partially populated, such carbon atoms would be trapped inside, neither moving nor emerging to other surface areas. However, they can locally perturb the electronic density of the Rh metal atoms immediately above, and, eventually, their chemical activity and reactivity.

For Au, kMC simulations predict a substantial reduction of both $\bar{t}_{em}$ and lt_{sf}, similar to Pt. This translates into a much more dynamic equilibrium as compared to the other cases, with a continuous exchange of C atoms between surface and subsurface, especially at 700 K, where this exchange is below the ps time scale. As shown in Fig. 4, however, the subsurface population only reaches considerable values for Pt, slightly above 10% of the total carbon at 700 K, while only 2–3% for Au. Surface C moieties, then, are anyway expected, yet the extra disorder effect caused by the opening of the subsurface diffusion channel will certainly be present in Au and mainly in Pt surfaces when exposed to low coverages of surface C.

4. Conclusions

By means of kMC simulations with rates derived from periodic DFT calculations and TST, the present work assesses the dynamic mobility of C atoms on all *fcc* TM (111) surfaces under working conditions of low C coverage; θ_C = 1–9 at% and working temperatures ranging 300–700 K. Overall, the macroscopic kinetic properties obtained from the kMC simulations are in agreement with the predictions made from the static DFT energy landscape. For instance, kMC simulations show that at 300 K C atoms spend most of the time around the thermodynamically most stable adsorption sites, with little effect of the θ_C. These sites are subsurface *oss* for Ni, Cu, Pd, and Ag, and surface *fcc* for Rh, Ir, Pt, and Au.

In some cases, however, other adsorption sites start to become populated at higher temperatures. For instance, subsurface sites for Pt and Rh, and surface sites for Ag. This is an unexpected conclusion, which possibly cannot be anticipated by inspection of the DFT energy profiles alone, and that may have relevant impact in the catalytic activity of these transition metal surfaces at high temperature. Present kMC simulations also show that, in general, surface and subsurface diffusions dominate the kinetics, with sinking/emerging processes being much less frequent, and, surprisingly, occurring involving the channel connecting surface *hcp* and subsurface *tss* sites. In the case of Ag, and to a lesser extent Pd, emerging processes are triggered by annealing, and the thus raised C atoms can vary or bias on-going catalytic processes occurring on these surfaces. For Au and Pt, C mobility has been seen to be considerably higher than for the rest of the studied surfaces. Even if the C is mainly found at surface, it can diffuse through the subsurface region to other areas, either C-free or C-containing, and even imply a new reaction mechanism with a C attack from subsurface. Even though the study is focused on (111) *fcc* surfaces, it is likely that such effects can be present in other surface terminations, even in TMs with different crystallographic structure. The present results highlight the need of reconsidering the role of both surface and subsurface carbon moieties in the simulation models, a factor which has been, hitherto, mostly neglected.

CRediT authorship contribution statement

Biel Martínez: Methodology, Software, Validation, Formal analysis, Investigation, Data curation, Writing - original draft, Writing - review & editing, Visualization. **Oriol Piqué:** Methodology, Investigation. **Hèctor Prats:** Formal analysis, Data curation, Supervision. **Francesc Viñes:** Conceptualization, Methodology, Resources, Writing - original draft, Writing - review & editing, Supervision, Project administration, Funding acquisition. **Francesc Illas:** Resources, Writing - review & editing, Funding acquisition.

Declaration of Competing Interest

The authors declare that they have no known competing financial interests or personal relationships that could have appeared to influence the work reported in this paper.

Acknowledgements

The present work was financially supported by the Spanish Ministerio de Ciencia y Universidades (MICIUN) RTI2018-095460-B-I00 and María de Maeztu MDM-2017-0767 grants and, in part, by Generalitat de Catalunya (grants 2017SGR13 and XRQTC). O.P. thanks the Spanish MICIUN for a PhD grant (PRE2018-083811). F.I. acknowledges additional support from the 2015 ICREA Academia Award for Excellence in University Research.

Appendix A. Supplementary material

Supplementary data to this article can be found online at https://doi.org/10.1016/j.apsusc.2020.145765.

References

[1] J.W. Erisman, M.A. Sutton, J. Galloway, Z. Klimont, W. Winiwarter, How a century of ammonia synthesis changed the world, Nat. Geosci. 1 (2008) 636–639.
[2] L. Vega, B. Martínez, F. Viñes, F. Illas, Robustness of surface activity electronic structure-based descriptors of transition metals, Phys. Chem. Chem. Phys. 20 (2018) 29548–29554.
[3] A.J. Medford, A. Vojvodic, J.S. Hummelshøj, J. Voss, F. Abild-pedersen, F. Studt, T. Bligaard, A. Nilsson, J.K. Nørskov, From the Sabatier principle to a predictive theory of transition-metal heterogeneous catalysis, J. Catal. 328 (2015) 36–42.
[4] H.F. Abbas, M.A.W. Wan Daud, Hydrogen production by methane decomposition: a review, Int. J. Hydrog. Energy. 35 (2010) 1160–1190.
[5] J. Van Hooreo, A century of chemical dynamics traced through the nobel prizes. 1909: Wilhelm Oswald, J. Chem. Educ. 79 (2002) 146–148.
[6] K.J. Smith, R.B. Anderson, The higher alcohol synthesis over promoted Cu/ZnO catalysts, Can. J. Chem. Eng. 61 (1983) 40–45.
[7] P.D.F. Vernon, M.L.H. Green, A.K. Cheetham, A.T. Ashcroft, Partial oxidation of methane to synthesis gas, Catal. Lett. 6 (1990) 181–186.
[8] C.H. Bartholomew, Carbon deposition in steam reforming and methanation, Catal. Rev.-Sci. Eng. 24 (1982) 67–112.
[9] H. Ren, M.P. Humbert, C.A. Menning, J.G. Chen, Y. Idra, U.G. Singh, W.C. Cheng, Inhibition of coking and CO poisoning of Pt catalysts by the formation of Au/Pt bimetallic surfaces, Appl. Catal. A 375 (2010) 303–309.
[10] P. Albers, J. Pietsch, S.F. Parker, Poisoning and deactivation of palladium catalysts, J. Mol. Catal. A Chem. 173 (2001) 275–286.
[11] J.C. Rodríguez, E. Rosen, J.L.G. Fierro, J. Santamaría, A. Monzón, Deactivation by coking and poisoning of spinel type Ni catalysts, Catal. Today 37 (1997) 255–265.
[12] R.T.K. Baker, M.A. Barber, P.S. Harris, F.S. Feates, R.J. Waite, Nucleation and growth of carbon deposits from the nickel catalyzed decomposition of acetylene, J. Catal. 26 (1972) 51–62.
[13] C.J. Weststrate, A.C. Kazakova, E.T.R. Rosen, M.W.G.M. Verhoeven, I.M. Clédel, A.M. Saib, J.W. Niemantsverdriet, Atomic and polymeric carbon on Co(0001): surface reconstruction, graphene formation, and catalyst poisoning, J. Phys. Chem. C. 116 (2012) 11575–11583.
[14] O. Piqué, I.Z. Koleva, F. Viñes, H.A. Aleksandrov, G.N. Vayssilov, F. Illas, Subsurface carbon: a general feature of noble metals, Angew. Chem. Int. Ed. 58 (2019) 1744–1748.
[15] P. Janthon, F. Viñes, J. Sirijaraensre, J. Limtrakul, F. Illas, Carbon dissolution and segregation in platinum, Catal. Sci. Technol. 7 (2017) 807–816.
[16] D. Teschner, J. Borsodi, A. Wootsch, Z. Révay, M. Hävecker, A. Knop-Gericke, S.D. Jackson, R. Schlögl, The roles of subsurface carbon and hydrogen in palladium-catalyzed alkyne hydrogenation, Science 320 (2008) 86–89.
[17] A.J. Du, S.C. Smith, X.D. Yao, G.Q. Lu, Catalytic effects of subsurface carbon in the chemisorption of hydrogen on a Mg(0001) surface: An ab-initio study, J. Phys. Chem. B 110 (2006) 1814–1819.
[18] G. Kresse, J. Furthmüller, Efficient iterative schemes for ab initio total-energy calculations using a plane-wave basis set, Phys. Rev. B 54 (1996) 169–186.
[19] J.P. Perdew, K. Burke, M. Ernzerhof, Generalized gradient approximation made simple, Phys. Rev. Lett. 77 (1996) 3865–3868.
[20] J. Paier, M. Marsman, G. Kresse, Why does the B3LYP hybrid functional fail for metals? J. Chem. Phys. 127 (2007) 1–10.
[21] L. Vega, J. Ruvireta, F. Viñes, F. Illas, Jacob's ladder as sketched by Escher: Assessing the performance of broadly used density functionals on transition metal surface properties, J. Chem. Theory Comput. 14 (2018) 395–403.
[22] P. Janthon, S.M. Kozlov, F. Viñes, J. Limtrakul, F. Illas, J. Chem. Theory Comput. 9 (2013) 1631–1640.
[23] P. Janthon, S. Luo, S.M. Kozlov, F. Viñes, J. Limtrakul, D.G. Truhlar, F. Illas, J. Chem. Theory Comput. 10 (2014) 3832–3839.
[24] J. Ruvireta, L. Vega, F. Viñes, Cohesion and coordination effects on transition metal surface energies, Surf. Sci. 664 (2017) 45–49.
[25] G. Henkelman, U. Bas P., H. Jónsson, A climbing image nudged elastic band method for finding saddle points and minimum energy paths and minimum energy paths, J. Chem. Phys. 113 (2000) 9901–9904.
[26] H.J. Monkhorst, J.D. Pack, Special points for Brillouin-zone integrations, Phys. Rev. B. 13 (1976) 5188–5192.
[27] A.P.J. Jansen, An introduction to kinetic Monte Carlo simulations of surface reactions, Lecture Notes in Physics vol. 856, Springer-Verlag, Heidelberg, Germany, 2012.
[28] H. Prats, S. Posada-Pérez, J.A. Rodriguez, R. Sayós, F. Illas, Kinetic monte carlo simulations unveil synergic effects at work on bifunctional catalysts, ACS Catal. 9 (2019) 9117–9126.
[29] L. Yang, A. Ranjan, J.T. Muckerman, Density functional kinetic monte carlo simulation of water-gas shift reaction on Cu/ZnO, J. Phys. Chem. C 117 (2013) 3414–3425.
[30] S. Piccinin, M. Stamatakis, CO oxidation on Pd(111): A first-principles-based kinetic monte carlo study, ACS Catal. 4 (2014) 2143–2152.
[31] H. Prats, L. Álvarez, F. Illas, R. Sayós, Kinetic monte carlo simulations of the water gas shift reaction on Cu(111) from density functional theory based calculations, J. Catal. 333 (2016) 217–226.
[32] A.U. Nilekar, J. Greeley, M. Mavrikakis, A simple rule of thumb for diffusion on transition-metal surfaces, Angew. Chem. Int. Ed. 45 (2006) 7046–7049.
[33] F. Viñes, C. Loschen, F. Illas, K.M. Neyman, Edge sites as a gate for subsurface carbon in palladium nanoparticles, J. Catal. 266 (2009) 59–63.
[34] F. Studt, F. Abild-Pedersen, T. Bligaard, R.Z. Sørense, C.H. Christensen, J.K. Nørskov, On the role of surface modifications of palladium catalysts in the selective hydrogenation of acetylene, Angew. Chem. Int. Ed. 47 (2008) 9299–9302.
[35] A. Rinaldi, J.-P. Tessonnier, M.E. Schuster, R. Blume, F. Girgsdies, Q. Zhang, T. Jacob, S.B. Abd Hamid, D.S. Su, R. Schlögl, Dissolved carbon controls the initial stages of nanocarbon growth, Angew. Chem. Int. Ed. 50 (2011) 3313–3317.
[36] H. Zi-Pu, D.F. Ogletree, M.A. van Hove, G.A. Somorjai, Leed theory for incommensurate overlayers: Application to graphite on Pt(111), Surf. Sci. 180 (1987) 433–458.
[37] F. Viñes, K.M. Neyman, A. Görling, Carbon on Platinum substrates: From carbidic to graphitic phases on the (111) surface and on nanoparticles, J. Phys. Chem. A. 2009, 113, 11963–11975.

4.3 Charting the Atomic C Interaction with Transition Metal Surfaces

Introduction In the previous section we assessed the interactions of atomic C with the (111) surfaces or facets of *fcc* TM systems and investigated the presence of absorbed subsurface C species in them. In this section we expand the previous work by delivering a broad, detailed, and holistic atomic view of the interaction of C with TM surfaces. This time, by performing DFT calculations on proper surface slab models, we study the stability of C atoms on the Miller surfaces with index order of 1 of all those TMs featuring a *fcc*, *bcc*, or *hcp* bulk crystallographic structure, see Figure 33 and Figure 34.

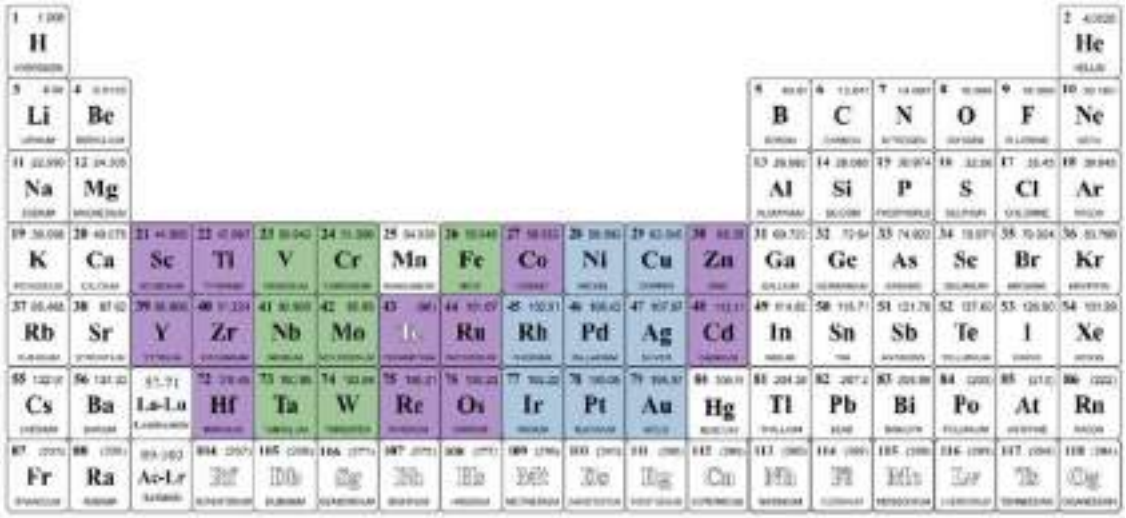

Figure 33. Periodic table with *fcc* TMs coloured in blue, *bcc* TMs in green, and *hcp* TMs in purple.

For such surfaces, most stable surface and subsurface sites are identified and their bond strength is seized to obtain a thermodynamic picture. Furthermore, all sorts of C diffusion energy barriers, E_b, are explored, including surface, subsurface, sinking, and emerging diffusion energy barriers for each metal surface, denoted E_{sur}, E_{sub}, E_{sink}, and E_{emer}, respectively. A schematic depiction of the different studied barrier types is shown in Figure 35.

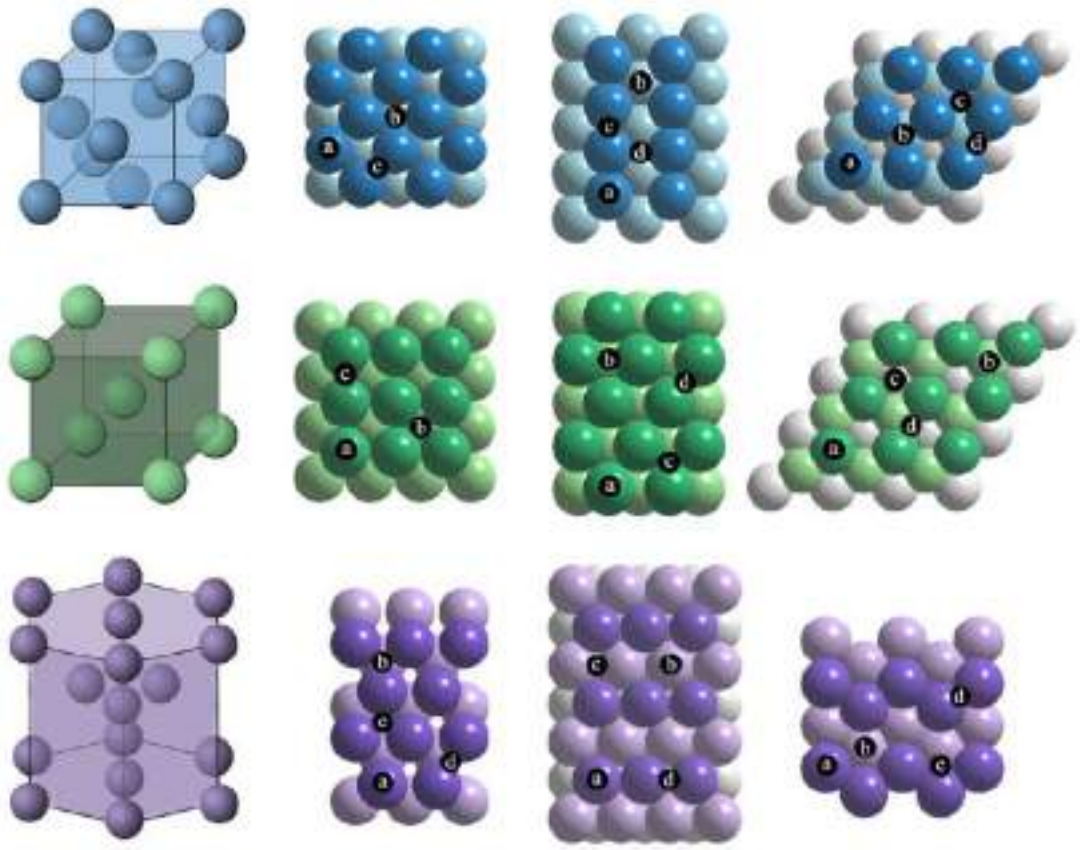

Figure 34. Depiction of positions studied for each surface termination of each crystallographic structure. In blue, from left to right, *fcc* unit cell, and (001), (011), and (111) surfaces. In green, from left to right, *bcc* unit cell, and (001), (011), and (111) surfaces. In purple, from left to right, *hcp* unit cell, and (0001), (10$\bar{1}$0), and (11$\bar{2}$0) surfaces. Positions depicted for *fcc* (001) correspond to a) Top, b) Hollow, c) Bridge; for *fcc* (011) a) Top, b) Hollow, c) BridgeS, d) BridgeL; for *fcc* (111) a) Top, b) Hollow *hcp*, c) Hollow *fcc*, d) Bridge. Positions depicted for *bcc* (001) correspond to a) Top, b) Hollow, c) Bridge; for *bcc* (011) a) Top, b) Hollow, c) HollowT, d) Bridge; for *bcc* (111) a) Top, b) Hollow *hcp*, c) Hollow *fcc*, d) Bridge. Positions depicted for *hcp* (0001) correspond to a) Top, b) Hollow, c) HollowE, d) Bridge; for *hcp* (100) a) Top, b) Hollow, c) BridgeL, d) BridgeS; for *hcp* (110) a) Top, b) Hollow, c) BridgeL, d) BridgeS.

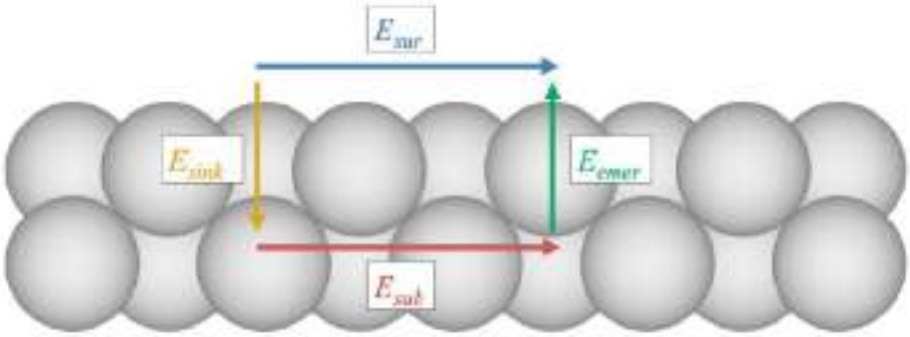

Figure 35. Schematic depiction of the different diffusion barrier types studied in this work: Surface diffusion (E_{sur} – blue), subsurface diffusion (E_{sub} – red), sinking diffusion (E_{sink} – yellow), and emerging diffusion (E_{emer} – green).

This systematic study provides a navigation chart of the C tendency to poison surface active sites, to aggregate into C_n moieties, to sink into the subsurface, plus provides insights on the possible formation of TMCs. The obtained amount of data allows for further analysis based on machine learning algorithms, aimed at defining subgroup kinds of similar behavior in terms of C bond strength and diffusivity, the primary physicochemical descriptors characterizing these, as well as multivariable regressions of adsorption and diffusion properties as a matter of physicochemical descriptors.

This work led to the elaboration of a research article, which is not yet published. The manuscript is included at the end of this section. In the following pages, a summary of it is given. My contribution to the research article was: (a) Calculation of all ad/absorption energies, (b) calculation of around 60% of the diffusion energy barriers, (c) performance of the descriptor analysis, including the multivariable regressions, (d) implementation of the ML algorithms, both for clustering and regressions, and (e) writing an initial draft of the paper. The supporting information for this manuscript can be found in Appendix H.

Results We first start by showing the results for the most stable position adsorption E_{ads}, or absorption, E_{abs}, energy values for each surface termination of each metal; therefore, presenting three values per metal, *versus* the C height, h, computed as the vertical distance between the C atom and the TM surface plane. To have clearly defined references, an in-plane case is shown at zero h, together with the graphite cohesive energy, E_{coh}. As shown in Figure 36, the display is divided into four different quadrants, implying four different behaviors of C atoms when interacting with TM surfaces, depending on whether an adsorption or absorption situation is preferred, and whether the interaction of C with the TM is stronger or weaker than the C-C interaction in graphite.

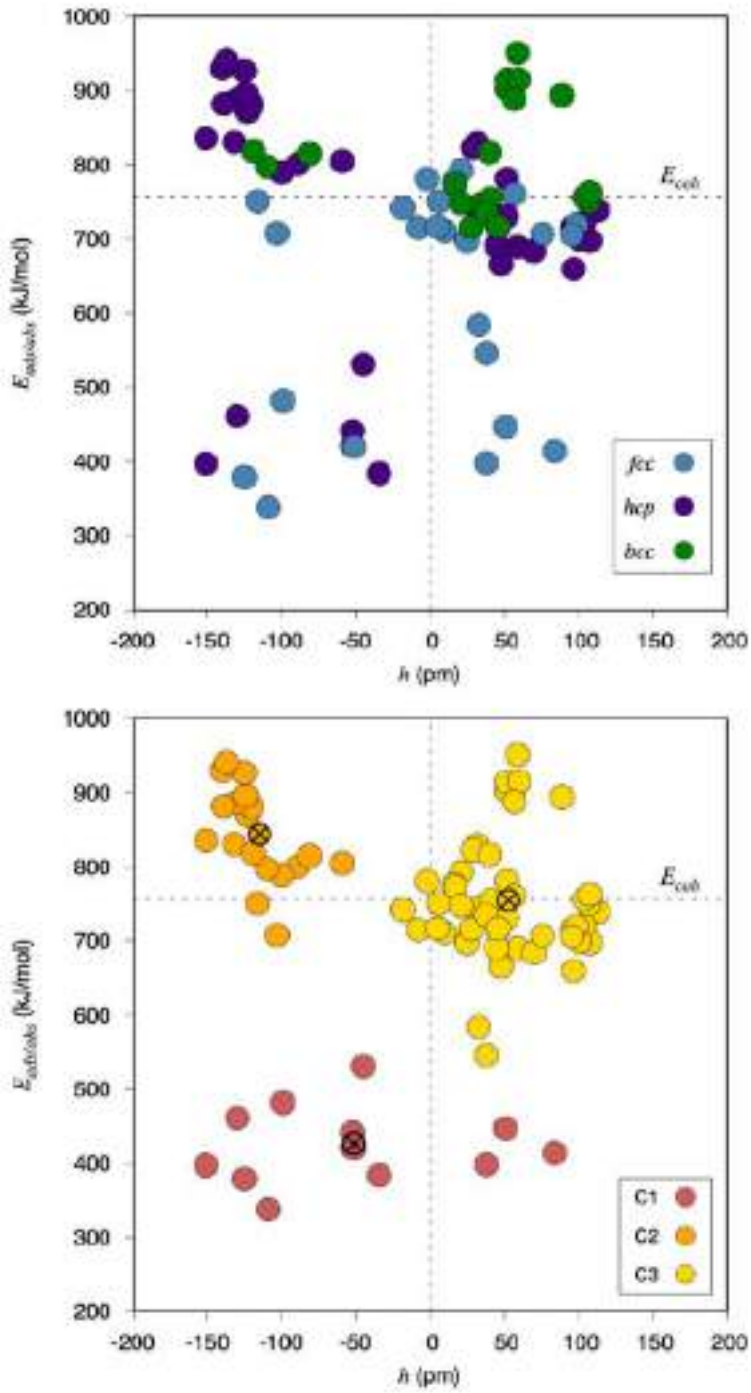

Figure 36. Most stable $E_{ads/abs}$ situations on every TM surface with respect h. In the top panel, values in blue correspond to *fcc* TMs, green to *bcc* TMs, and purple to *hcp* TMs. In the bottom panel, three different colors are used to mark off the three different clusters determined through a KM analysis, with centers marked crossed.

In the top panel of Figure 36, the data is color-coded according to the TM crystallographic structure. We discover that that virtually all *bcc* values are beyond the surface limit with $E_{ads/abs}$ values higher than E_{coh}. These findings are consistent with these

metals proclivity to form TMCs.[157] However, note that the majority of the points denote surface positions, implying that the carburization of *bcc* TMs is a non-trivial process, which probably includes a crystallographic reconstruction. Most of the values for *fcc* TMs are found in the lower portion of the plot, indicating that C has a stronger affinity for other C atoms than for these metals. This is consistent with the known fact of *fcc* TMs being poisoned as a result of the formation of graphite layers on their surfaces, which blocks their surface active sites. There are six *fcc* values in the subsurface region that are readily visible: The two upper-most correspond to Ni and Pd (111), in agreement with prior calculations and experiments that confirm the existence of carbide phases of these TMs.[164] Furthermore, the four lowest values correspond to Cu (111), Ag (111), Ag (011), and Au (011), showing that C has a tendency to penetrate such surfaces, as discussed in section 4.2.[61] Concerning *hcp* TMs, we notice that their values are dispersed, as their position in the Periodic Table. Even yet, grouping is observed in the subsurface, highly bonded C area, where C appears to present a propensity to penetrate such TMs.

On the other hand, a KM analysis was conducted utilizing the data from Figure 36, which can be found in the bottom panel of the figure. We were able to identify three different clusters by using the elbow method. First cluster groups data points with a weak interaction with TM surfaces compared to the graphite E_{coh}. In these scenarios, C atoms would thermodynamically tend to combine into graphite, formed on the surface, eventually poisoning the catalyst surface by site-blocking. On the other hand, the second group of data is characterized by a very strong interaction with TM surfaces, and a distinct preference for the subsurface region. This would imply TMs and surfaces suitable for their carburization. Finally, cluster number three includes the majority of data points where C atoms display an interaction with TM surfaces of a comparable strength to the cohesive energy of graphite and a distinct preference for staying at the surface. It is in such scenarios where a subtle imbalance in the interaction strengths and kinetics may ultimately determine whether such C isolated moieties exist as such at low C concentrations, or they eventually merge to create graphitic layers on the catalyst surface.

Aside from these investigations, another key aspect resides in the search of descriptors of the ad/absorption energy values. We examined different descriptors presented in the literature to linearly correlate ad/absorption energies with them. Precisely, surface energy, γ,[70] work function, ϕ,[71] *d*-band center, ε_d,[73] corrected *d*-band center, ε_d^W,[74] and the highest Hilbert transform *d*-band peak, ε_u,[75] were analyzed. Their

independent assessment shows that the linear adjustment adequacy decreases as $\varepsilon_d > \varepsilon_d^W > \varepsilon_u > \gamma > \phi$. A further evaluation of the most effective descriptor, ε_d, by evaluating one regression line for each crystallographic structure, as shown in Figure 37, indicates that crystal packing is a key aspect regarding the C interaction with TM surfaces. We notice that linear trends are only rational for *hcp* and *fcc* structures, with regression coefficients, R, of 0.94 and 0.90, respectively. The *bcc* TMs trend line is not representative, with a regression coefficient of 0.09, indicating that there is no correlation.

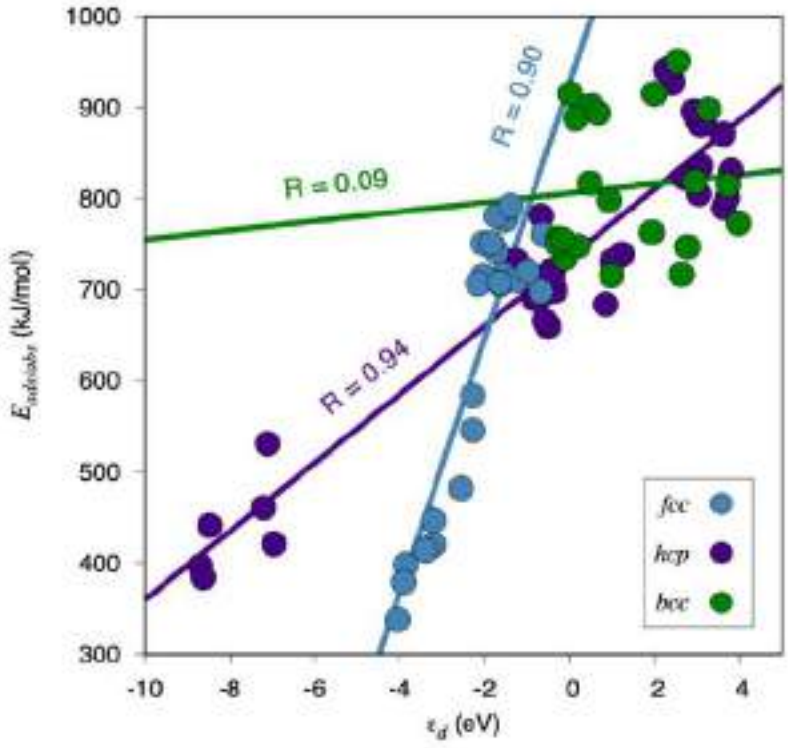

Figure 37. Most stable $E_{ads/abs}$ situations with respect to ε_d, and the corresponding linear correlations. Values in blue correspond to *fcc* TMs, green to *bcc* TMs, and purple to *hcp* TMs.

We then investigate the effect of aggregating descriptors by performing multivariable regressions. Figure 38 shows that combining ε_d with γ results to a better correlation than using them separately. Moreover, one may build higher-degree combinations such as having $\gamma \cdot \varepsilon_d$ terms or even squared values for each descriptor, which would be second-degree combinations, or even third-degree combinations, including, *e.g.*, $\gamma^2 \cdot \varepsilon_d$ or ε_d^3 terms. When these are accounted for, one observes a gradual enhancement of the multivariable adjustment, as seen by an increase of the R value up to 0.90. These findings strongly suggest that when seeking for adsorption and/or absorption energy

descriptors, one should not be restricted to finding the perfect one, as it may not exist, as the interaction is influenced by multiple surface properties at the same time. Hence, one may look for combinations of descriptors, each of them providing a separate piece of information about the metal surface one works with.

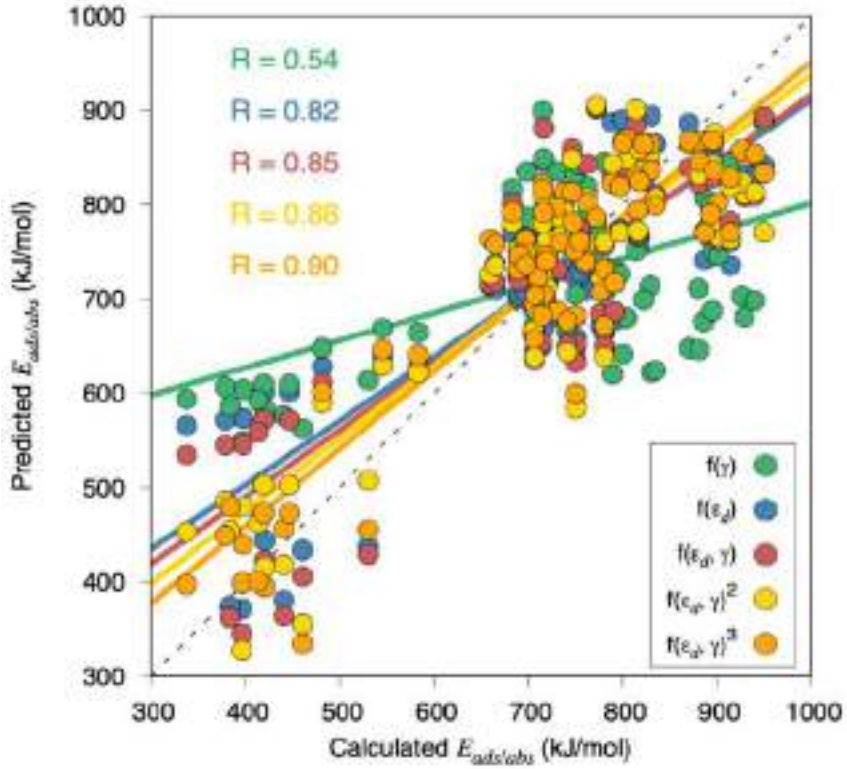

Figure 38. Most stable $E_{ads/abs}$ situations *vs.* the predicted $E_{ads/abs}$ from different linear, multivariable, and polynomial regressions involving γ, ε_d, or a combination of them. The black dashed line represents a perfect correlation.

This study set the groundwork for a more in-depth multi-variable analysis, feasible by using machine learning (ML) techniques. To this end, the E_{ads} or E_{abs} values of the most stable positions are expressed as a function of the above-mentioned descriptors (ε_d, ε_d^W, ε_u, γ, and ϕ), but also taking into account the crystallographic structure (CS) of the TM, given the variant behaviors of *fcc*, *hcp*, and *bcc* TMs, and also including the surface coordination number (CN),[167] and the bulk shortest interatomic distance, δ.[168] Aside from that, the number of TM *d* electrons, n_d, is also accounted for. Last, the number of TM atoms neighboring the C atom is determined, CN_{site}, to represent the different adsorption or absorption sites, allowing for site specificity.

With this set of descriptors, we performed a random forest regression (RFR), evaluating its performance in terms of mean absolute error (MAE) minimization. We

found out that three features become key from the analysis; unsurprisingly, ε_d and γ, as discussed above, but also the site coordination, CN_{site}, which delivers site-specificity to the analysis. Results show a training set MAE of 13.7 ± 0.9 kJ·mol^{-1}, with a test set MAE accuracy of 39.1 ± 8.9 kJ·mol^{-1}. The learning curve of this model is shown in Figure 39. While the test set accuracy is insufficient to use this ML model to make quantitative forecasts, the most interesting aspect is that the RFR algorithm allows us to capture the importance of each key feature. In this case, the importance factors are of 0.6, 0.3, and 0.1 for ε_d, γ, and CN_{site}, respectively, in accordance with the prior descriptor analysis but with the addition of site-specificity.

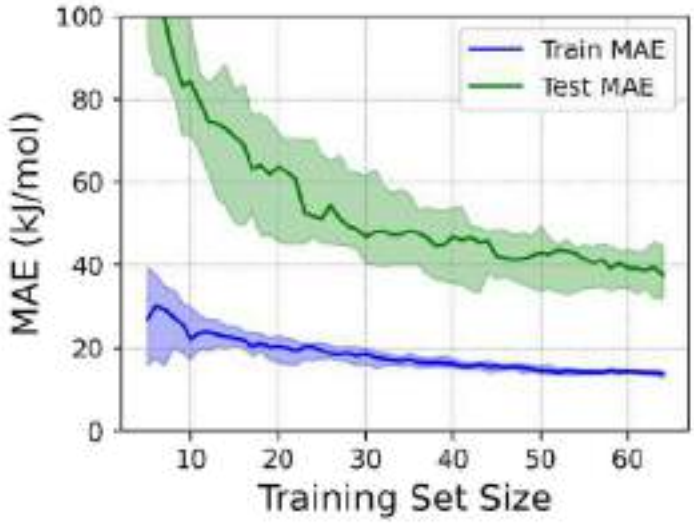

Figure 39. MAE evolution for training (blue) and the test (green) sets as a function of the number of samples contained in the training set for the prediction of $E_{ads/abs}$ using a RFR algorithm. Colored areas around the lines account for the error dispersion resulting from the cross validation.

After finding the primary physicochemical descriptors using the RFR algorithm, we now perform a KM analysis aimed at the descriptors. This three-dimensional grouping is depicted in the top panel of Figure 40. The components of the three resulting clusters have been projected onto the $E_{ads/abs}/h$ space in the bottom panel of Figure 40. Interestingly, one observes that the clusters observed in the bottom panel of Figure 36 and the clusters obtained from the descriptors essentially coincide, with the only exception of one case for each cluster. This finding indicates that the descriptors are well suited to define $E_{ads/abs}$ and h. Moreover, the analysis allows for quantifying the average values for each descriptor in each of the clusters.

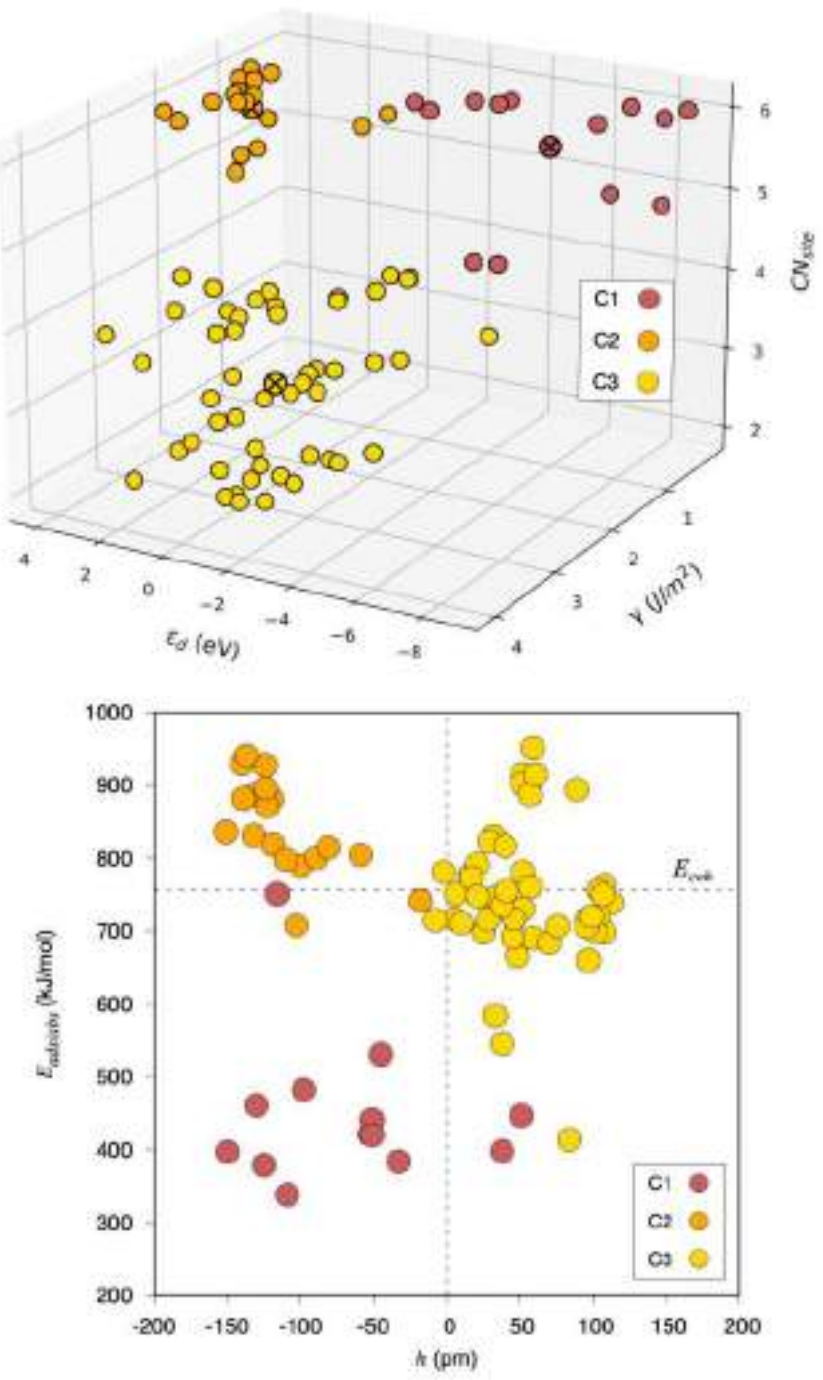

Figure 40. In the top panel, the three-dimensional KM clustering of the most important features extracted from the RFR, namely e_d, g, and CN_{site}. In the bottom panel, a quadrant plot as in Figure 36, but showing the clusters from the top panel projected in the $E_{ads/abs}/h$ space.

Because the above analyses focused just on the energetic stability, obtaining a holistic overview would require exanimating the C moieties diffusion kinetics on all the studied TMs. Hence, we gathered a total of 324 diffusion energy barriers, comprising surface, subsurface, sinking, and emerging diffusions. This large quantity of data can also be depicted and analyzed in a four-quadrant plot, in a similar way as done for the

thermodynamics in Figure 36. Therefore, Figure 41 shows the $\log_{10}(E_{sub}/E_{sur})$ *vs.* $\log_{10}(E_{sink}/E_{emer})$, having 81 points (the same amount of explored TM surfaces). It is worth noting that the zero value for $\log_{10}(E_{sub}/E_{sur})$ implies that $E_{sub} = E_{sur}$, and so, equally feasible surface and subsurface diffusions. Similarly, the zero value for $\log_{10}(E_{sink}/E_{emer})$ implies that surface C sinking diffusion is kinetically as feasible as the subsurface C emerging. These two zero values depict the four quadrants in Figure 41. Values greater than zero for $\log_{10}(E_{sub}/E_{sur})$, located in the right side of the plot, imply that E_{sub} values are larger than E_{sur}, and thus, for these cases, C atoms would diffuse more easily along the surface than through the subsurface. For $\log_{10}(E_{sub}/E_{sur})$ values smaller than zero, the opposite behavior is expected. When it comes to $\log_{10}(E_{sink}/E_{emer})$ values, data above the zero limit indicate that emerging is favored over sinking, implying a preferential location on the surface. On the other hand, values below zero imply a preference towards C sinking into the subsurface region.

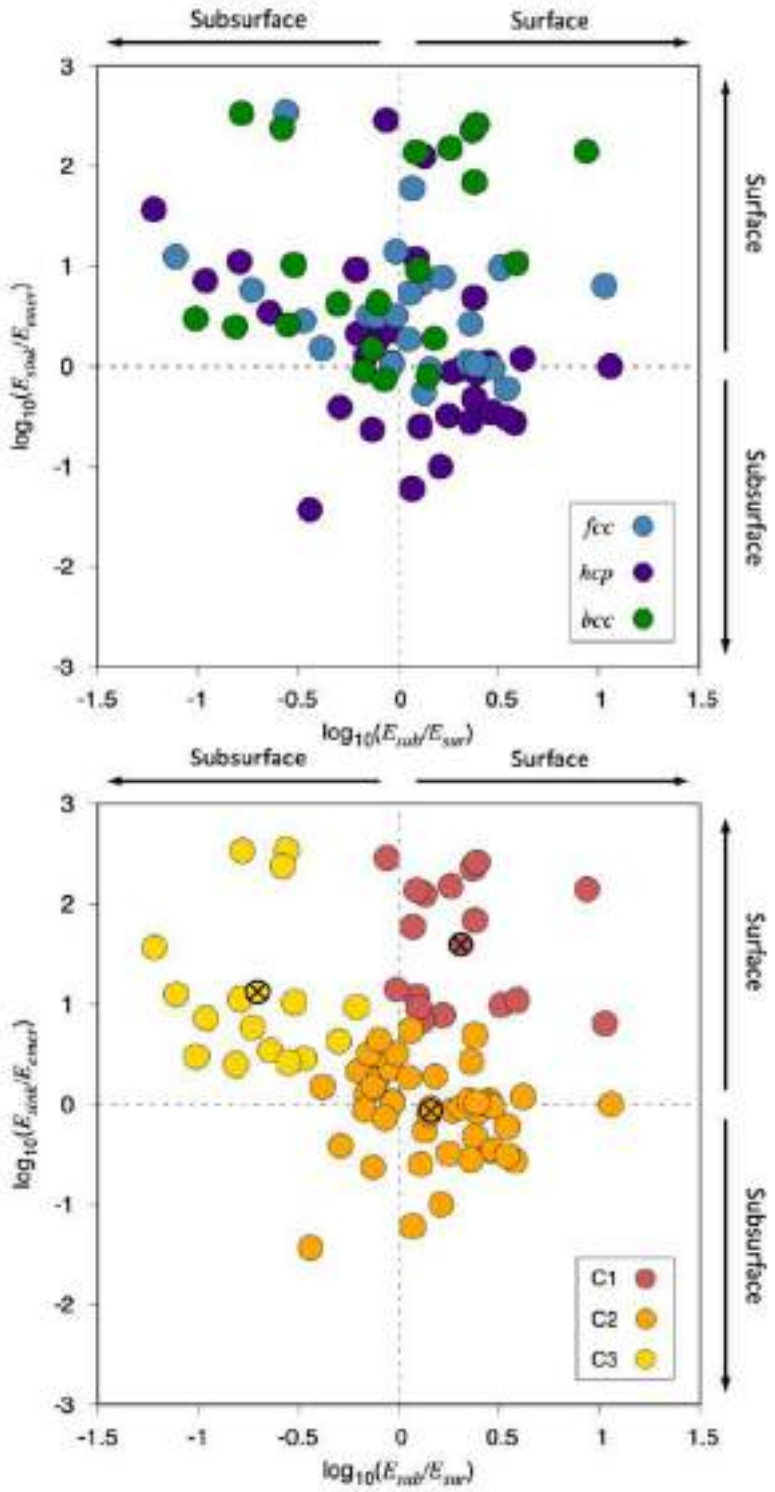

Figure 41. The base 10 logarithm of E_{sub}/ E_{sur} with respect the base 10 logarithm of E_{sink}/E_{emer}. In the top panel, values in blue correspond to *fcc* TMs, green to *bcc* TMs, and purple to *hcp* TMs. In the bottom panel, three different colors are used to mark off the three different clusters determined through a KM analysis.

The top panel of Figure 41 shows data colored according to the crystallographic structure of the TM, revealing that *fcc* and *bcc* TMs data points behave similarly, being dispersed on the top half of the plot, indicating that for these metals E_{sink} is often larger

than E_{emer}, and pointing for a kinetically allowed surface presence of C adatoms. Still, few cases are at the early bottom part of the plot. These cases correspond to *fcc* (111) surface models, precisely, to Ni, Pd, Pt, Cu, Ag, and Au, where the above situation reverses, indicating a more difficult emergence towards the surface of dissolved C atoms in the subsurface. Aside, neither *fcc* nor *bcc* TMs show a distinct preference between E_{sur} and E_{sub}, with every surface being somehow unique in this aspect. Last, *hcp* TMs display sizable dispersion, but are primarily found in the bottom right part of the plot. This quadrant gathers scenarios with an E_{sink} barrier lower than E_{emer}, and E_{sub} being greater than E_{sur}. Therefore, one observes that the majority of *hcp* TMs feature kinetically favorable penetration of isolated C atoms to the subsurface region, but with restricted diffusion through the subsurface, since the diffusion along the surface is preferred.

Moreover, the bottom panel shows the three-cluster KM analysis. There, Cluster 1 groups values of the right-upper quadrant, implying E_{emer} barriers lower than E_{sink}, and E_{sur} lower than E_{sub}. These features indicate a certain preference for C atoms to be located on the surface and diffusing along it. Beyond that, Cluster 3 also fits nicely in one quadrant, but now showing an easier C emergence than sinking, but, more importantly, with E_{sub} values sensibly smaller than E_{sur} ones. This quadrant refers to certain TM surfaces where C diffuses more easily through the subsurface region. In this regard, C species would move around in the subsurface region, and only emerge from time to time. Last, Cluster 2 contains the most abundant group, showing in general well balanced E_{sub}/E_{sur} and E_{sink}/E_{emer} ratios near unity. Its general behavior would be that all diffusion processes should be regarded as feasible, indicating a somewhat free mobility on the surface, through the subsurface region, and with exchange of C atoms in between surface and subsurface sites.

The attention is now placed into finding descriptors of the diffusion energy barriers. The ones used for ad/absorption energies, these are ε_d, ε_d^W, ε_u, γ, and ϕ, deliver poor results. This can be regarded as natural, since such descriptors were developed to seize the interaction strength, not the heights of energy barriers. Alternatively, we also tested the most stable position ad/absorption energy as a descriptor, as shown in Figure 42, inspired by the work of Nilekar and colleagues,[169] who observed that the diffusion energy barrier depends on the adsorption strength of the adsorbed species, being a twelve per cent of the latter, with an R of 0.85. Our analysis displays the same trend for the four different diffusion processes here analyzed, indicating that the stronger the ad/absorption energy, the larger the diffusion energy barrier, and in all the cases with similar slopes of

approximately 0.16. However, the regression coefficients are still quite unsatisfactory, being at most 0.45 for E_{sur} energy barriers.

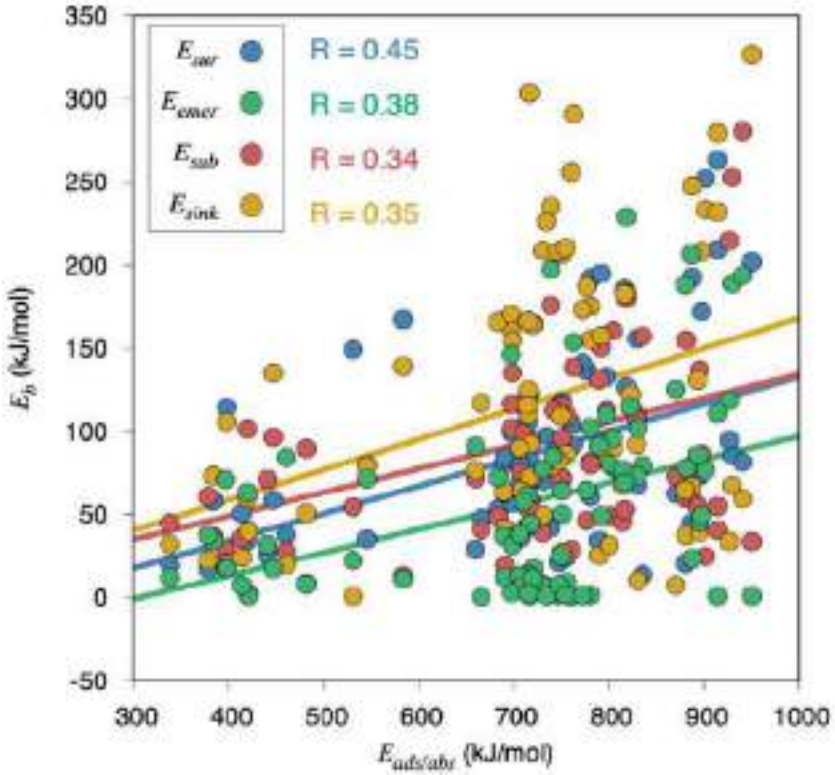

Figure 42. Linear evolutions of the different E_b diffusion energy barriers —E_{sur}, E_{sub}, E_{sink}, and E_{emer}— with respect to most stable initial position E_{ads} or E_{abs}.

Another widely used linear correlation for energy barriers are Brønsted–Evans–Polanyi (BEP) relations, linearly expressing the reaction step energy barrier with the step energy variation, ΔE.[56,57,58] In this study we do not deal with reaction steps, as we analyze diffusion processes, but the same fundamentals apply. BEP relations were investigated, but only for C sinking and emerging processes, as for surface and subsurface diffusions ΔE equals zero. Figure 43 shows the BEP analysis with a fairly good correlation for E_{sink}, with a R of 0.83; however, the regression for E_{emer} shows more dispersion, with a smaller R of 0.63.

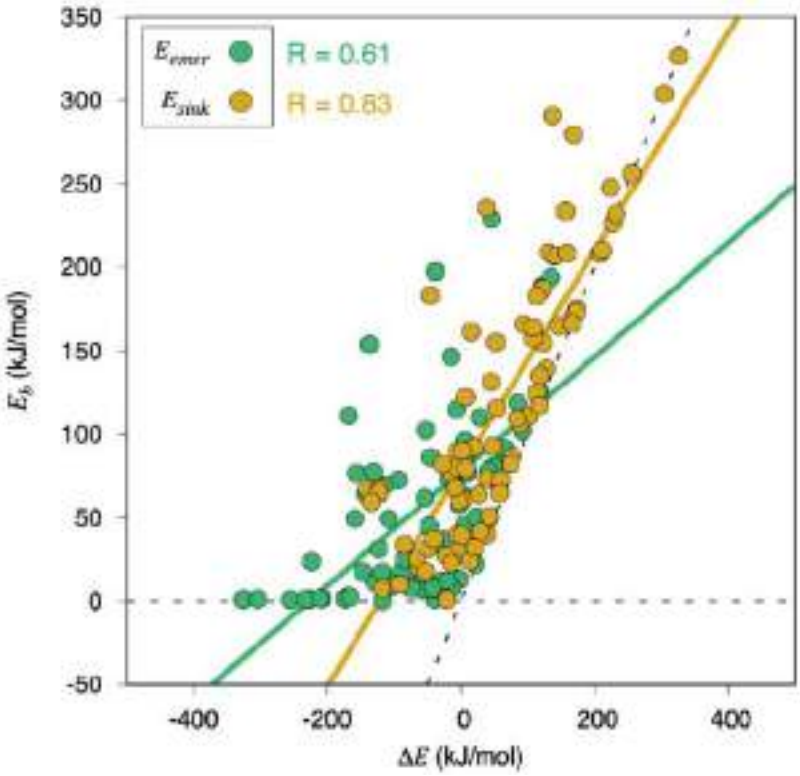

Figure 43. BEP linear evolutions of E_b with respect to ΔE, and the corresponding linear correlations for each explored barrier type. Dashed lines define latest TS limit, where $E_b = \Delta E$, or earliest TS limit, where $E_b = 0$ regardless of ΔE.

Given the best correlations observed for E_{sink} as described by γ and ΔE, we performed a multivariable regression involving combinations of ΔE and γ up to a second order degree, since third degree yielded no improvement, shown in Figure 44. We observe that the combination of both factors is beneficial, with an enhanced R of 0.86, while the incorporation of higher-order descriptors translates into a mild improvement. As discussed in the thermodynamic analysis, this highlights that the description of kinetic processes should be tackled considering a combination of different descriptors, grasping the different aspects that influence the kinetic energy barriers.

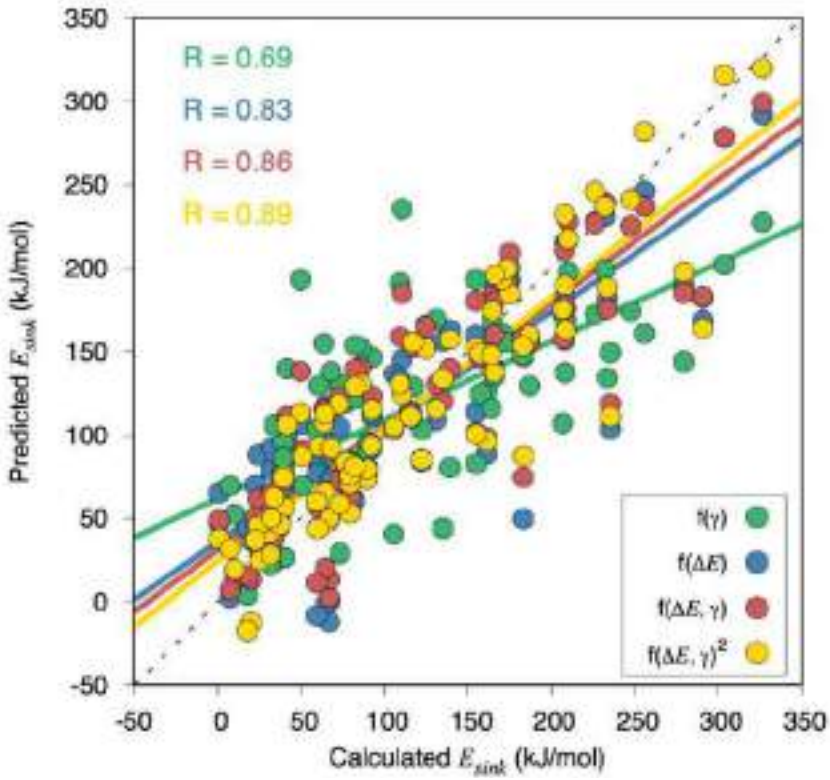

Figure 44. Calculated E_{sink} *vs.* the predicted E_{sink} from different linear, multivariable, and polynomial regressions involving γ, Δ*E*, or different degrees of combinations of them. The black dotted line represents the ideal correlation.

Finally, we applied a RFR to locate key descriptors governing such processes. The features used are the same as for the thermodynamic analysis, but now adding most stable position $E_{ads/abs}$ and Δ*E*. Moreover, the barrier type, BT —E_{sur}, E_{sub}, E_{sink}, *or* E_{emer}—, and the coordination number of the initial and final sites, named CN_{IS} and CN_{FS}, respectively, are also included. We identify the key features as Δ*E*, $E_{ads/abs}$, ϕ, CN_{FS}, and CN_{IS}. Results show a MAE of 32.6 ± 2.3 kJ·mol^{-1} for the test set, while the training set delivers a MAE of 13.1 ± 0.4 kJ·mol^{-1}. The learning curve of this model is shown in Figure 45. Compared to the thermodynamic analysis, the RFR offers more accuracy for diffusion energy barriers, which get closer to the usual DFT accuracy of 10-20 kJ·mol^{-1}, although this is far from a model that performs quantitative estimations. Features importance is acquired from the RFR algorithm, with values of 0.43, 0.27, 0.15, 0.09, and 0.06, for Δ*E*, $E_{ads/abs}$, ϕ, CN_{FS}, and CN_{IS}, respectively. Notice that *ΔE* is the most dominant feature, as expected from the previous analysis, and particularly true for E_{sink} and E_{emer}, although it is not as important as ε_d was for $E_{ads/abs}$. The next in the line is the most stable position $E_{ads/abs}$, also in accordance with the above discussion. It is worth noting that the two most relevant

descriptors are thermodynamic parameters, which can be used to estimate energy barriers. The other factors affecting the kinetic barriers are, unexpectedly, ϕ, and CN_{IS} and CN_{FS}, which reveals that the coordination of the sites involved in the diffusion play a minor role in the height of the barriers.

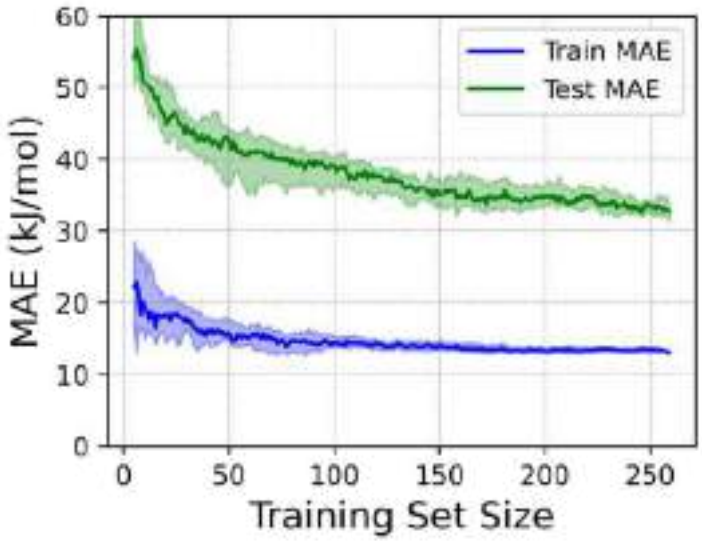

Figure 45. MAE evolution for training (blue) and the test (green) sets as a function of the number of samples contained in the training set for the prediction of E_b using a RFR algorithm. Colored areas around the lines account for the error dispersion resulting from the cross validation.

Conclusions These results, together with additional data and analyses shown in the research article below, lead to the following conclusions:

- Both thermodynamic and kinetics maps on atomic C interplay with TM surfaces are provided. The results presented are in line with experimental observations regarding carbide formation and C poisoning tendency.
- Descriptor analyses for ad/absorption energies show that *d*-band center is the most successful one at correlating $E_{ads/abs}$. We observe that this correlation is only valid for *fcc* and *hcp* TMs, while it presents significant deviations for *bcc* TMs.
- We identify $E_{ads/abs}$ and ΔE, in the cases of sinking and emerging diffusions, as the most relevant descriptors for diffusion energy barriers.
- Clustering analyses through the KM algorithm reveal three different types of TM thermodynamic and kinetic behavior towards C atoms.
- Random forest regressions show that, both for the gained thermodynamic and kinetic data, a combination of descriptors yield to a better description of minima

and energy barriers, although the accuracy is so far only valid for a rapid qualitative assessment.

- This work underscores the need of looking for a few number of descriptors biasing the interaction strength and diffusion possibilities, rather than trying to get a single perfect descriptor, which may not be the wisest option as different physicochemical aspects do indeed affect such processes.

Charting the Atomic C Interaction with Transition Metal Surfaces

Oriol Piqué,[a,†] Iskra Z. Koleva,[b,†] Albert Bruix,[a] Francesc Viñes,[*,a] Hristiyan A. Aleksandrov,[*,b] Georgi N. Vayssilov,[b] and Francesc Illas[a]

[a] *Departament de Ciència de Materials i Química Física & Institut de Química Teòrica i Computacional (IQTCUB), Universitat de Barcelona, c/ Martí i Franquès 1, 08028 Barcelona, Spain*

[b] *Faculty of Chemistry and Pharmacy, University of Sofia, 1126 Sofia, Bulgaria*

*Emails: francesc.vines@ub.edu and haa@chem.uni-sofia.bg

Abstract

Carbon interaction with transition metal (TM) surfaces is a relevant topic in heterogeneous catalysis, either for its poisoning capability, for the recently attributed promoter role when incorporated in subsurface, or for the formation of early transition metal carbides, which are increasingly used in catalysis. Herein we present a high-throughput systematic study, adjoining thermodynamic *plus* kinetic evidence obtained by extensive density functional calculations on surface models (324 diffusion barriers located on 81 TM surfaces in total), which provides a navigation map of these interactions in a holistic fashion. Correlation between previously proposed electronic descriptors and ad/absorption energies has been tested, with *d*-band centre being found the most suitable one, although machine learning protocols underscore also the importance of the surface energy and the site coordination number. Descriptors have also been tested for diffusion barriers, with ad/absorption energies and the difference in energy between minima being the most appropriate ones. Furthermore, multivariable, polynomial, and random forest regressions show that both thermodynamic and kinetic data are better described when using a combination of different descriptors. Therefore, looking for a single perfect descriptor may not be the best quest, while combining different ones may be a better path to follow.

Keywords: Carbon Atoms, Transition Metal Surfaces, Adsorption, Absorption, Diffusion, Descriptors, Machine Learning, Phase Diagrams

† Both authors equally contributed

Table of Contents

A complete roadmap is provided, including both thermodynamic and kinetic aspects, on the C interaction with 81 different transition metal surfaces.

Introduction

Nowadays, transition metals (TMs) are ubiquitous in many areas of science and technology, from Solid State Physics through Applied Chemistry up to Materials Science, with relevance in diverse industrial fields, such as Nanotechnology and Heterogeneous Catalysis. In fact, late TMs, including noble coinage (Ni, Cu, Ag, Au) and Pt-group (Pt, Pd, Rh, Ir, Re, Os) metals, are in widespread use as heterogeneous catalysts[1] for a large diversity of reactions of industrial interest, *e.g.* ammonia synthesis, exhaust gas treatments, or the Fischer-Tropsch reaction, to name just a few.[2,3] However, early TMs are far too active for such purposes according to *Le Sabatier* principle,[4] adsorbing chemical moieties too strongly. Their heterogeneous catalysis interest though lies into the TM carbides (TMCs) formation, since the carburization of these metals diminishes their chemical activity, to the point of making TMCs viable replacements of the above-commented late TMs in catalysis,[5] featuring improved catalytic performances, selectivities, or poison resistances compared to Pt-group TMs.[6,7]

The relative simplicity of TM systems and the industrial importance of their applications has prompted state-of-the-art research aimed at unveiling their catalytic activity improvement, desirably coupled with materials cost reduction, as the one achieved

when using Earth-abundant TMCs. To this end nanostructuration, alloys usage, even the design of nanoalloys have been contemplated as plausible strategies.[8,9] The rational design of novel metal and alloy catalysts, backed up by precise *ab initio* quantum chemistry calculations on proper catalyst models, has meant a great leap forward in the quest for new, improved activity TM catalysts.[9,10]

Still, however, one main drawback of such catalysts is that, in the course of the catalysed reaction, these get gradually deactivated over time and use, with the concomitant loss in efficiency and economic profit. The origin of this loss is the presence of poisoning agents, where carbon excels among others.[11,12] Thus, the interaction of C with TMs is indeed a fundamental field of study in Heterogeneous Catalysis. Historically, from the catalytic deactivation processes point of view, it is quite usual that carbon entities, going from C atoms to small C_n aggregates, are formed on the TM catalyst surface due to secondary reactions of the on-going surface catalysed process, generally involving organic molecules. These carbon entities can spread through the surface and eventually agglomerate forming diverse types of carbon deposits, from graphene through graphite, up to amorphous C aggregates. These surface carbon structures can cover the catalyst, *de facto* restricting the access of reactants to the TM catalytic surface active sites, and effectively poisoning it.

Despite this, recent experiments and computational simulations have changed the paradigm view of the low C content from a poisoner to a promoter role. For instance, subsurface C into Pd catalysts appears to favour the selective alkyne hydrogenation to olefins,[13] and its presence, explained by simulations based on density functional theory (DFT), shows how such subsurface C can be easily present at the surfaces of late TM surfaces and nanoparticles (NPs).[14-17] Moreover, subsurface C plays an important role in the synthesis of graphene and carbon nanotubes (CNT), where segregation of C atoms diluted in pre-molten or molten TMs appears when cooling down the system, which induces the growth of graphene layers, even CNTs.[18,19]

Furthermore, subsurface C has been found to bias the appearance of other substitutional or interstitial carbon residues in Pd,[20] which may display even higher reactivity towards surface O and H adatoms than surface C,[21] and to act as a gate opener for H absorption.[22] Such subsurface moieties mediated chemistry is non-exclusive to neither C nor Pd. Indeed, subsurface C has been proposed to be a key player in the electrochemical conversion of CO_2 on Cu surfaces,[23] and interstitial C in Au NPs has been found to affect the metal electronic structure, being the ultimate responsible of the three-times increment of the

measure turnover frequency in the chemoselective hydrogenation of 3-nitrostyrene.[24] Apart from subsurface C, it is worth mentioning that, subsurface O can also affect the on-going surface activity, see *e.g.* the recent key role of subsurface O on Cu (111) surface in CO_2 capture and activation applications, with critical implications in environmental chemistry.[25] Subsurface chemistry has often been ignored, but is now growingly attracting attention within the scientific community, seen as a change of paradigm in what surface chemical activity is concerned.[26]

Motivated by these results, the primal aim of this work is to deliver, for the first time, a broad, detailed, and holistic atomistic view of the interaction of C with TM surfaces. This is achieved by studying, by *ab initio* DFT calculations on proper surface slab models, the stability of C atoms on the Miller surfaces with index order of 1 for all those TMs featuring a face-centred cubic (*fcc*), body-centred cubic (*bcc*), or hexagonal close-packed (*hcp*) bulk crystallographic structure —see Figs. S1 and S2 of Section S1 of the Electronic Supplementary Information (ESI). For such surfaces, most stable surface and subsurface sites are identified and their bond strengths seized, so as to gain thermodynamic pictures and stability phase diagrams, as done earlier for *fcc* TM (111) surfaces.[15] Furthermore, all sorts of C diffusion energy barriers, E_b, are explored, including surface, subsurface, sinking, and emerging diffusion energy barriers for each metal surface, denoted E_{sur}, E_{sub}, E_{sink}, and E_{emer}, respectively —see Fig. S3 in Section S1 of the ESI for a depiction of the different barrier types. This systematic study will provide a navigation chart of the C tendency to poison surface active sites, to aggregate into C_n moieties, and will also provide insights on the possible formation of TMCs. Finally, the acquired amount of data allows for further analysis based on artificial intelligence (AI) and machine-learning (ML) regression algorithms, addressed at defining subgroup types of similar behaviour concerning C bond strength and diffusivity, the main physicochemical descriptors defining these, as well as regressions of adsorptive and diffusive properties as a function of physicochemical descriptors.

Computational Details

Present DFT calculations have been performed using the Vienna *ab initio* simulation package (VASP) code,[27] imposing periodic symmetry. Relaxed geometries and total energies were acquired using the Perdew-Burke-Ernzerhof (PBE) exchange-correlation functional,[28] known to accurately describe TMs bulks and surfaces and also the interaction of C with them.[16,29] Moreover, previous works show that relative stabilities and diffusion

energy barriers, E_b, are rather unbiased by the used exchange-correlation functional, with small variations between 1-5 kJ mol^{-1} depending on the used functional.[16] The valence electrons density was expanded in a plane wave basis set with a 415 eV cutoff for the kinetic energy, while the projector augmented wave method was used to describe the interactions between core and valence electrons.[30] Calculations were carried out non spin-polarized except for magnetic Ni, Co, and Fe TMs. Geometry optimizations were performed until all forces acting on relaxed atoms became lower than 0.03 eV Å^{-1}, and the electronic convergence threshold was set to 10^{-6} eV.

The TMs most stable surfaces with Miller index with maximum order of 1 have been modelled using slabs, generally including most stable surfaces, with no step defects. These are the (001), (011), and (111) Miller indices surfaces of *fcc* and *bcc* TMs; and the (0001), (10$\bar{1}$0), and (11$\bar{2}$0) of *hcp* TMs, following Miller-Bravais indices notation for *hcp* metals, being a total number of 81 modelled surfaces.[29] The simulation of extended surfaces has been performed using supercell slab models constructed from previously PBE optimized bulks,[31,32] see Fig. S2 in Section S1 of the ESI for a depiction of the explored adsorption/absorption sites. The supercell size depends on the specific surface termination being modelled; (3×3) supercells composed of 54 atoms were used for *fcc* (111), *hcp* (10$\bar{1}$0), *bcc* (001), and *bcc* (111) surfaces, while (2×2) supercells composed of 48 atoms were used for *fcc* (001), *fcc* (011), *hcp* (0001), *hcp* (11$\bar{2}$0), and *bcc* (011) surfaces. All surface slab models contain six atomic layers; with nine atoms per layer for (3×3) slabs or eight atoms per layer for (2×2) slabs. Consequently, the adsoprtion/absorption of one C atom implies a similar coverage of $^1/_9$ or $^1/_8$ monolayers (ML), respectively, defined as the number of C atoms with respect the number of surface metal atoms on one side of the slab.

After optimization of the pristine surfaces one C atom was adsorbed/absorbed with the three bottom layers of the slab fixed, while the other three upper layers were allowed to relax during the geometry optimization together with the interacting adsorbed/absorbed C atom, a procedure known as 3+3 approximation. The reciprocal space was sampled with 3×3×1 Γ-centred Monkhorst Pack[33] **k**-point grid and calculations were performed using a Gaussian smearing of 0.2 eV energy width to speed up convergence, yet final energies were extrapolated to 0 K (no smearing).

The adsorption/absorption energies, Eads/abs have been calculated as

$$E_{ads/abs} = -E_{C/metal} + E_C + E_{metal} \quad (1),$$

where $E_{C/metal}$ is the total energy of the metal slab with the C atom either adsorbed or

absorbed, E_C is the energy of the isolated carbon atom in vacuum, and E_{metal} is the energy of the optimized clean TM substrate. Within this definition, stable adsorption/absorption correspond to positive $E_{ads/abs}$ values. Zero-point energies imply negligible variations between the stability of the different sampled sites, below 0.1 kJ·mol^{-1} according to test calculations, and so have been disregarded in the final analysis.

The surface, subsurface, sinking, and emerging E_b, these are, the E_{sur}, E_{sub}, E_{sink}, and E_{emer}, were determined by using the climbing image nudged elastic band (CI-NEB) procedure using four images in between initial and final states.[34] The approximate transition state (TS) geometries were posteriorly refined using a Quasi-Newton optimization algorithm until forces acting on atoms were under 0.03 eV Å^{-1}. All TS were characterized by vibrational frequency analysis performed *via* construction and diagonalization of the corresponding block of the Hessian matrix, with elements estimated by analytical gradients from finite displacements of 0.03 Å length, certifying their saddle point nature with only one imaginary frequency. The E_b values were calculated subtracting the TS energy from the initial diffusive energy state.

As far as the AI algorithms used in the analysis are concerned, the group analysis was carried out using the k-means (KM) approach, as implemented in the *sklearn* python library.[35] The number of clusters for each case was determined using the elbow method,[36] consisting in the evaluation of the cluster inertia (or distortion) curve shape —defined as the sum of squared distances of samples to their closest cluster center plotted against the number of clusters, and selecting the elbow of the curve, *i.e.* the minimum number of clusters that already yields a sought accuracy. This number of clusters is then used in the cluster groups descriptions, see more details in Section S2 of the ESI. KM clustering was used to define subgroup types of TMs with similar activity with respect C atoms, or similar diffusions. KM was also used to correlate these subgroups with the main descriptors defining these.

Concerning the tested ML regression algorithms, those were also implemented using the *sklearn* python library. Aside, $E_{ads/abs}$ and E_b magnitudes were correlated with a list of TM features or physicochemical descriptors, commented in the forthcoming sections, using three different ML regression models: multivariable linear regression (MLR), decision tree regression (DTR), and random forest regression (RFR). Models were refined by removing unnecessary features using the leave-one-out procedure, and hyperparameters were tuned by conducting a grid search involving different parameter combinations and selecting the best preforming ones.

Results and Discussion

1. Thermodynamic Analysis

1.1. Energy landscape

Let us first start with an analysis of the thorough study of C interaction with the explored 81 transition metal surface models, so as to provide a general view of the C interaction with TMs. A full list of adsorption and absorption energies of the gained minima is present in Tables S1-S3 of Section S3 in the SI. For a better readability, the top panel of Fig. 1 shows a summarized overview of the results displaying the most stable position adsorption, E_{ads}, or absorption, E_{abs}, energy values for each surface termination of each metal —thus presenting three different values per metal— *versus* the C height, h, defined as the vertical distance between the C atom and the TM surface plane in each particular position, compiled in Tables S4-S6 of Section S3 of the ESI. So as to have clear defined references, an in-plane situation is shown at zero h, along with the graphite cohesive energy, E_{coh}, obtained from the literature and obtained through equivalent optimizations as the ones here presented in terms of employed DFT exchange-correlation functional, plane-wave cutoff, **k**-points density, etc.[37] As can be seen in Fig. 1, the display defines four different quadrants, which imply four different behaviors of C atoms when interacting with TMs surfaces, depending on whether an adsorption or absorption situation is preferred, and whether the interaction of C with the TM is stronger or weaker compared to that in graphite.

A first analysis can be carried out with the data color-coded according to the TM crystallographic structure; this is, *fcc*, *hcp*, or *bcc*. At first glimpse, one notices that nearly all *bcc* values are found to be above the surface limit, implying a preferential adsorption, except for three cases —V, Nb, and Ta (011) surfaces, all being group V of the Periodic Table— where carbon prefers to lie subsurface. The $E_{ads/abs}$ above E_{coh} implies that C has more affinity for *bcc* TMs than for other C atoms, a feature that happens in many cases, and in the above-commented subsurface cases, demonstrating a clear thermodynamic tendency for C to penetrate these metal surfaces. These results are indeed in perfect agreement with these metals propensity to form TMCs.[5] However, since the majority of points imply surface positions, the carburization of *bcc* TMs, implying the interstitial placement of C, appears to be a non-trivial process. Notice that *bcc* crystallographic structures are perfect templates to place C in their octahedral interstitials, thus featuring the final rocksalt crystallographic structure of TMCs. Therefore, crystal reconstruction appears not to be a restricting aspect in many of these cases exhibiting rocksalt TMCs, such as VC,

NbC, TaC, CrC, δ-MoC, and FeC,[5] although, for other more stable polymorphs, when necessary, the C incorporation is likely to involve a crystallographic phase transition. Previous studies on Zn oxidation and other TMs hydrogenation reflect a preferential subsurface stabilization of O and H atoms, including superficial crystallographic reconstructions,[38] featured at higher atomic coverages, and so, such type of mechanisms could well explain the eventual subsurface incorporation of C to form TMCs, even when implying a crystal transformation.

Going beyond *bcc* TMs, *fcc* TM values are found in their majority in the lower part of the panel, *i.e.* adsorption or absorption energies weaker than in graphite, meaning that C has more clustering affinity than for these metals. This is in fair agreement with the known fact of *fcc* TMs being poisoned due to the formation of graphene/graphite layers on them, blocking their surface active sites. Nevertheless, this preference to form graphene layers may be interesting in the context of nanotechnology, *e.g.* in graphene synthesis from chemical vapor deposition or segregation.[18] There are a couple of cases —Ni and Rh (001)— where the C interaction is above the graphite limit, which presents them as a the least favorable for graphene synthesis, and more favorable concerning carbide formation, although their preference is on the surface, or in-plane. Note, however, that such strongly attached C can block still active sites, or perturb the very chemical nature of nearby metal surface atoms. Finally, there are six *fcc* values that are clearly in the subsurface region: The two upper-most data points correspond to Ni and Pd (111), in agreement with previous calculations and experiments that certify the existence of carbide phases of these TMs.[16] Moreover, the four lowest values correspond to Cu (111), Ag (111), Ag (011), and Au (011); indicating, as recently showed in the literature, that C has a tendency to penetrate subsurface on such noble metals.[15]

Last but not least, and regarding *hcp* TMs, their values are scattered, as is their position in the Periodic Table. Still, grouping is observed in the subsurface, highly attached C region, where C appears to present a tendency to penetrate such TMs. In fact, these values correspond to Sc, Y, Ti, Zr, Hf, Zn, and Cd. The first five belong to groups III and IV of the Periodic Table, known to display a very high chemical activity and a propensity to form rocksalt TMCs. Thus, clearly the high absorption energy could well contribute in compensating the energy demands for an eventual phase transition towards a rocksalt structure. On the other hand, Zn and Cd are d^{10} elements, with an *a priori* low chemical activity according to *d*-band center arguments, see below. However, the strong interaction

calculated here is in line with the existence of such carbides, as reported in previous studies.[39]

The data in Fig. 1 has been used to carry out a KM clustering to better understand how this data can be grouped within the $E_{ads/abs}$ and h space. As shown in the bottom panel of Fig. 1, the existence of three different clusters is best detected once the elbow method is applied, see Fig. S4 of Section S4 of the ESI. Data points in the first cluster, C1, have in common a rather weak interaction with the TM surfaces compared to the graphite E_{coh}, with the group centre or centroid —marked by a fictionalcrossed point in Fig. 1— located at an E_{abs} of 424 kJ·mol^{-1}, and with a h of -52 pm below the surface level. For these systems, C atoms would thermodynamically tend to merge into graphitic C aggregates on the surface, eventually poisoning the catalyst surface by site-blocking. However, at low C concentrations, there could be C adatoms or interstitial C atoms, affecting the electronic structure of the surrounding metal atoms, particularly, when their mobility and eventual aggregation would be hindered, see below.

The second cluster, C2, is, on the contrary, characterized by a very strong interaction between C and the TM surfaces, and a general clear preference for the subsurface region, reflected in the centroid being located at an E_{abs} of 843 kJ·mol^{-1}, and h of -117 pm. This implies that these TMs and surfaces are suitable for their carburization, with the sole exception of Ni and Pd (111) surfaces, which feature an E_{abs} smaller than E_{coh}, and so, similarly to C1 members, would imply an eventual formation of surface aggregated carbonaceous structures, particularly when kinetically allowed, in perfect agreement with the reported graphene growth by segregation reported on both surfaces.[40,41]

Finally, the third cluster, C3, groups most of the data points, where C atoms display an interaction with TM surfaces of similar strength to the cohesive energy of graphite, plus and general clear preference for staying at the surface. This is reflected with the group center located at E_{ads} of 753 kJ·mol^{-1}, very close to the E_{coh} of graphite of 757 kJ·mol^{-1}, and a height as well of 53 pm. It is in such situations where the subtle imbalance of interaction strengths and kinetic movement inhibition may finally determine whether such C isolated moieties exist as such at low C concentrations, or they eventually merge forming graphitic layers on the catalyst surface, and such imbalance could be potentially affected by the DFT uncertainty of ca. 20 kJ·mol^{-1}. Even if this is a general trend, there are situations where C atoms have a significant affinity for TM surfaces, but now generally preferring to stay on the surface, thus occupying active sites that would be no longer be available for any other reactants, acting as poisons by site-blocking, exemplified by the

subset of points with an E_{ads} larger than 850 kJ·mol^{-1}. The exposed KM clustering allows defining thus certain general behaviors, but is not exempt of singularities; apart from the above, a couple of outliers can be caught from a visual inspection, for instance, Cu (001) and Cu (011) are points that could belong to Cluster 1, although the inertia calculation assigns them to Cluster 3.

Aside from the previous analysis, we inspected suitable reaction conditions at which such C moieties can be present on the inspected TM surfaces. To this end, thermodynamic phase diagrams have been built for the different studied TM surfaces, considering pressure and temperature working conditions that would turn pristine TM surfaces into early C-containing surfaces, either having C on surface or subsurface. To this end, acetylene (C_2H_2) is considered as a carbon source, and the TM surface and molecular chemical potentials are equaled, see completed details on the phase diagram construction procedure found in the literature.[15,42,43] Fig. 2 shows the exemplary phase diagrams corresponding to all *fcc* TMs (111) surfaces, since such TM surfaces are most relevant to Heterogeneous Catalysis, but all the other phase diagrams for *fcc*, *hcp*, and *bcc* surfaces can be found in Figs. S5-S7 of Section S5 of the ESI. Focusing on the cases revealed on Fig. 2, the shown lines define, for each metal, temperatures, T, and C_2H_2 partial pressures, $p_{C_2H_2}$, where C atoms adsorbed or absorbed would be thermodynamically equally stable to a pristine TM surface case, see other details in the literature.[15] Any T and $p_{C_2H_2}$ conditions above the shown curves imply a preference of having C adsorbed, C^{sur}, or absorbed, C_{sub}, while conditions below the curve imply a preferential TM pristine surface situation. In this particular case, C^{sur} moieties are expected for Pd, Ir, Rh, and Pt (111) surfaces, and C_{sub} for Ni (111) at, *e.g.*, a standard working $p_{C_2H_2}$ of 10^5 Pa, and a regular catalytic working temperature of 600 K. Only Cu, Ag, and Au display their nobility in this aspect, Ag being the most C-resisting one, known and explained by the Ag deeper *d*-band center,[44] joined to a weaker C–Ag coupling, which prevents antibonding states being above the Fermi level, eventually destabilizing the C interaction towards Ag.[45] In any case, Cu and Ag (111) surface would prefer to incorporate such C moieties, while surface C would be observed on Au (111) surfaces.

The Group XI —Cu, Ag, and Au— nobility is also shown in (001) and (011) TM surfaces, see Fig. S5 of Section S5 of the ESI, revealing an enhancement of the surface chemical activity for (011) and (001) surfaces, being the latter the most chemically active, to the point of Cu (001) surfaces being C-poisoned at standard conditions of pressure and

working temperatures above *ca.* 750 K. The rest of *fcc* TMs behave similarly among them, featuring systematically C^{sur} situations on (001) surfaces and most of (011) surfaces, with the exception of Ag, Au, and Pd (011) surfaces, where C_{sub} would be preferred.

When addressing *hcp* TMs, see Fig. S6 of Section S5 of the ESI, three different behaviors are found: Late TMs with d^{10} electronic configuration, these are, Group XII Zn and Cd, behave like noble Group XI elements, thus not being C-poisoned at standard working conditions. Other late TMs, like Group VII (Re, Tc), Group VIII (Ru, Os), and Group IX Co display a chemical affinity more similar to *fcc* Pt-group TMs, while early TMs such as Group III (Sc, Y) and Group IV (Ti, Zr, and Hf) show a high affinity towards C. As can be seen in Fig. S6, regardless of the exposed surface, C_{sub} situations are preferred for the very early Groups III and IV TMs (Sc, Y, Ti, Zr, and Hf), and very late XII TMs (Zn, Cd), whereas C^{sur} situations are preferred on middle and late TMs of Groups VII (Re, Tc), VIII (Ru, Os), and IX (Co). The sole exceptions are Ti and Hf $(10\bar{1}0)$ surfaces, where C^{sur} moieties are more stable. Finally, *bcc* TMs, belonging to early Groups V (V, Nb, Ta), VI (Cr, Mo, W), and VIII (Fe) reveal a high affinity towards C, see Fig. S7 of Section S5 of the ESI, going for a C-moiety presence in any working conditions, and only avoiding them at ultrahigh vacuum conditions and high temperatures. Such C moieties are systematically C^{sur} for (001) and (111) surfaces, and as well for (011) surfaces, with the exception of Group V TMs (V, Nb, Ta), where C_{sub} are more stable, going for the C incorporation within the TM.

1.2. Descriptors of C behaviour at TMs surfaces

The above trends seem to point out that the chemical activity is somewhat influenced by the position along the *d* series of the Periodic Table. Thus, an important aspect resides in the search for descriptors of the ad/absorption energies accounting for the observed trends. Here, different descriptors proposed in the literature, either energetic or electronic, are evaluated so as to linearly correlate ad/absorption energies with them. In particular, surface energy, γ,[46] work function, ϕ,[47] *d*-band center, ε_d,[48] corrected *d*-band center, ε_d^W,[49] and the highest Hilbert transform *d*-band peak, ε_a,[50] are considered —details on their correct calculation can be found in the literature.[29,44] Briefly, the description of their independent evaluations —see Figs. S8-S12 in Section S6 of the ESI for all the analyses details— reveals that the linear adjustment adequacy decreases in the order $\varepsilon_d > \varepsilon_d^W > \varepsilon_a > \gamma > \phi$. In the case of *d*-band center based descriptors, it is clear that any attempt of improvement on

ε_d is detrimental; still, the expected trend is captured, in the sense that the higher in energy is ε_d, ε_d^W, or ε_u, the stronger the C attachment is. Likewise, the larger the surface energy, γ, the stronger the attachment energy of C; although the correlation on this energy-based descriptor is poorer when compared to those based on the electronic structure. Finally, the work function, ϕ, is a very bad descriptor; not only because of the very small regression coefficient, R, of 0.17, but also because one would expect that the larger the work function, the stronger the bonding, as a result of a TM→C charge transfer, observed in late TMs, and expected for earlier and more reducing TMs. However, the observed trend in Fig. S12 of Section S6 of the ESI is just the opposite.

Given the above analysis, ε_d could be regarded as the most successful descriptor, at least, when describing the exhibited thermodynamic data. The most stable $E_{ads/abs}$ *vs.* ε_d results are shown in Fig. 3 grouping results as per the different featured crystallographic structures. Notice that an evaluation with one regression line for each type of surface termination, shown in Fig. S13 of Section S6 of the ESI, reveals that the trends for the three surfaces of each crystallographic have similar slopes, and such slopes are very different for the different examined crystal structures. These results reinforce the consideration of crystal packing as a determining aspect concerning the C interaction with TM surfaces. Focusing on Fig. 3, however, one readily notices that linear trends can only be valid for *hcp* and *fcc* structures, which present regression coefficients, *R*, of 0.94 and 0.90 respectively. On the other hand, the *bcc* TMs trend line is not representative, presenting a poor regression coefficient of solely 0.09; showing that there is no correlation in these cases. This puts the accent in that the ε_d descriptor, typically tested on coinage and Pt-group TMs,[48] all featuring to *fcc* and *hcp* close packed situations, does not account for a possible packing effect that can translate in changes on the TM surface chemical activity.

Still, the trends based on energetic and electronic structure descriptors, *e.g.* on ε_d and γ, pave the way to inspect whether there exists combined effects of them, tackled here by evaluating them through multivariable regressions. As shown in Fig. 4, combining ε_d with γ leads to a better correlation than using them alone. Furthermore, one could make combinations of a larger degree, *e.g.* having $\gamma \cdot \varepsilon_d$ terms or even squared values for each descriptor, which would be second degree combinations, or even third degree combinations; including, *e.g.*, $\gamma^2 \cdot \varepsilon_d$ or ε_d^3 terms. By considering these, one observes a gradual improvement of the multivariable adjustment, as observed by an increase of the *R* value up to 0.90, and the approach of the adjustment to the ideal one. These observations

strongly suggest that, when looking for adsorption and/or absorption energy descriptors, one should not restrain to finding the perfect one, as it may well not exist, as the interaction is simultaneously influenced by different surface properties. Thus, one should look for combinations of descriptors, each of them bringing a different piece of information of the metal surface one works with.

The above analysis indeed laid the foundations for a proper and deeper multi-variable analysis, feasible by applying different AI machine learning (ML) regression methodologies. To this end, the E_{ads} or E_{abs} values of most stable positions are expressed as a function of the above-introduced descriptors (ε_d, ε_d^W, ε_σ, γ, and ϕ), but regarding as well the crystallographic structure (CS) of the TM case, given the different behaviors of *fcc*, *hcp*, and *bcc* TMs, and including as well the surface coordination number (CN), retrieved from the literature,[51] so as to differentiate the different studied surfaces for the same metal, plus the bulk shortest interatomic distance, δ,[31,32] as a geometry measure distinct for every TM, even when having the same CS and CN. Aside, the number of TM *d* electrons, n_d, are accounted, as they represent a natural trend across the *d* series. Finally, to represent the different adsorption or absorption sites, the number of TM atoms neighboring the C atom are defined, CN_{site}, allowing for site specificity. This accounts for a total of ten descriptors related to the TM surface. Note that, since the same adsorbing or absorbing moiety is regarded always, this is, C atoms, no descriptors from the ad/absorbed species are necessary.[52]

Within this set of descriptors and features, we evaluated three different ML algorithms, including MLR, DTR, and RFR, see details of them in Section S7 of the ESI, and explicative images of the DTR procedure in Figs. S14 and S15 in Section S7 of the ESI. A first analysis, using all the aforementioned features and default parameters of the algorithms —*e.g.* 100 trees in RTR, and a maximal number of allowed features to be used in each tree to be equal to the total number of considered features— provided by the *sklearn* python library was performed using a shuffle split cross validation (CV) employing 20 splits for the set of the 81 surfaces with C in its most stable position. For the CV, for each size of the training set, a number of random data points are taken which represent 80% of the data set. The remaining 20% are random points also taken, but to be used for the test set.

The analysis results, in terms of mean absolute error (MAE) ± standard deviation, yielded test set values of 66.7 ± 12.5, 49.1 ± 8.4, and 43.5 ± 8.4 kJ·mol^{-1} for MLR, DTR, and RFR, respectively, for the largest training set size. Thus, focusing on RFR, the

regression algorithm that delivered the smaller error, one can successively remove those features that were less relevant in terms of minimizing the test set MAE. To this end, we used the leave-one-out procedure, which consists in removing one feature at a time and assessing the impact on the test set MAE to decide whether it is worth including or not. In this case, three parameters emerge as most relevant from the analysis; not surprisingly, ε_d and γ, as outlined above, but also the number of metal atoms neighboring the adsorbed or absorbed C, *i.e.* the site coordination, CN_{site}, which brings site-specificity to the analysis.

Once the candidate descriptors are shortlisted according to the leave-one-out approach, the RFR algorithm hyperparameters were tuned by performing CV evaluations on different combinations of parameters and selecting those that minimized the MAE, exemplified in Fig. 5 by the learning curve of RFR, displaying the training and test errors when increasing the number of samples in the training set. Results showed that, by using ε_d, γ, and CN_{site} only as input features, a RFR with 50 decision trees considering two features for each split already provided a very good training set MAE of 13.7 ± 0.9 kJ·mol^{-1}, although the test set MAE accuracy is of 39.1 ± 8.9 kJ·mol^{-1}. Notice, still that curves are not converged, and lower MAEs could expected by widening and diversifying the number of cases, usign, *e.g.* vicinal surfaces or sites at nanoparticle models, or even when differentiating adsorption from absorption situations.

Notice that the obtained final accuracy for the test set is still far from using such a ML model to carry out forecasts in a quantitative fashion, where, desirably, one would require MAEs below the DFT accuracy, estimated to be *ca.* 20 kJ·mol^{-1}. However, still, it can be useful for a rapid evaluation and qualitative assessment. Further than that, the most interesting factor is that, from the RFR algorithm, one can seize the importance of each key feature. In this case, the importance factors are 0.6, 0.3, and 0.1 for ε_d, γ, and CN_{site}, respectively, quite in line to the above discussion referring to ε_d as the main descriptor, but weighting the importance as well of γ, as already above detected in the descriptor analysis, where combinations of them were found to improve the regression quality, see Fig. 4. Still, their definition is somewhat modulated by the site coordination, a feature not identified in the previous analysis.

After having isolated the main physicochemical descriptors through the RFR method, one could well carry out a KM analysis as done in Fig. 1, but now identifying similarities in the descriptor space instead of on the target $E_{ads/abs}$ and h properties. This three-dimensional grouping is shown in Fig. 6 (top panel). The components of these three

clusters have been projected into the $E_{ads/abs}/h$ space in Fig. 6 (bottom panel). Surprisingly, one observes that clusters in $E_{ads/abs}/h$ space shown in Fig. 1 mostly coincide with gained clusters in descriptors space, with only few exeptions. Pd (111) surface of Cluster 1, appearing in Cluster 2; the Pd (011) surface of Cluster 2, appearing in Cluster 3, and the Au (111) surface of Cluster 3, appearing in Cluster 1. In any case, the resulting grouping underscores that groups of systems with similar $E_{ads/abs}$ and h also exhibit similar descriptor values. From the values in Table 1, one notes that, even when accounting for the standard deviation, the feature average values mostly do not overlap with each other for the different clusters, indicating that their representation is mostly unique, which reinforces that such descriptor values are key in defining the features groups shown in Fig. 1.

2. Influence of Kinetics

2.1. The energy barriers landscape

The above analysis dealt only with the energetic stability and, therefore, to reach a holistic overview would require analyzing the C moieties diffusion kinetics on all the studied TMs, as, *e.g.*, the subsurface presence may be kinetically hindered when the sinking energy barrier, E_{sink}, would be too large, and the same applies to the possible C emergence for E_{emer}, hindering an eventual surface coke formation from subsurface C atoms. Aside, coke formation could be as well hindered by surface diffusion, governed by the E_{sur} kinetic energy barrier, E_b. Finally, we evaluate here the possible diffusion at the subsurface level, defined by E_{sub}, and questioning whether lateral diffusion preferentially happens on the surface. Notice that such barrier information has been found valuable in a catalytic context, *e.g.*, serve to obtain the mean lifetimes of such species, and so, in which time frame they can affect the surface on-going catalyzed process, as recently demonstrated on *fcc* (111) surfaces by kinetic Monte Carlo simulations.[17]

The four different types of diffusion barriers, illustrated in Fig. S3 of Section S1 of the ESI, have been obtained by CI-NEB algorithm and properly characterized by vibrational analysis. For each TM type of surface, different diffusive paths have been investigated, including non-trivial ones for certain complicated diffusions. The explored paths are listed in Tables S7-S9 of Section S8 of the ESI. For each case, the lowest E_b values have been collected, accounting for a total of 324 diffusion energy barriers, summarized along their diffusion path in Table S10 of Section S8 of the ESI. Notice that mean values, including standard deviation, reveal, as expected, E_{sur} diffusion energy barriers of 86.7 ± 55.8 kJ·mol^{-1}, being slightly lower than E_{sub}, of 94.5 ± 63.1 kJ·mol^{-1}. Still, the difference is not

excessively large, and already at this stage one could envisage that surface and subsurface diffusions are similarly possible. This striking finding can be easily explained, as, on one hand, surface diffusion TSs get stabilized thanks to a more freedom of flexibility of surface metal atoms; however, subsurface diffusion TSs get stabilized thanks to a higher metal coordination, see Figs. S16-S18 of Section S8 of the ESI. Other than that, sinking energy barriers, E_{sink}, have a sensibly larger value of 117.1 ± 79.0 kJ·mol^{-1}, while emerging energy barriers, E_{emer}, are noticeably smaller, of the order of 57.9 ± 56.3 kJ·mol^{-1}, succinctly implying that is more difficult for C adatoms to dissolve in the metal matrix than to segregate towards the surface.

Still, the large standard deviation of the points expresses a great variety of situations. For instance, the largest E_{sur} of 263.2 kJ·mol^{-1} corresponds to Ta (001) surface, where such C atoms would be rather immobile, at variance with Cu (111), where, with an E_{sur} of 8.4 kJ·mol^{-1}, C atoms would be rather mobile; a point that favors the observed graphene synthesis by deposition on such surfaces.[18,53] Even if subsurface diffusion is less favored, quite inhibited, *e.g.* on W (111), with an E_{sub} of 303.7 kJ·mol^{-1}, it is rather easy on Zn $(10\bar{1}0)$ surface, with an E_{sub} of 2.4 kJ·mol^{-1} only. Similarly, one can think that C sinking into the subsurface region is quite difficult, and it is indeed on W (001), with an E_{sink} of 326.6 kJ·mol^{-1}, while C sinking through the Zn $(11\bar{2}0)$ surface is essentially barrierless, with an E_{sink} of 0.8 kJ·mol^{-1}. Finally, C emergence to the surface is rather easy on Co $(10\bar{1}0)$ surface, with an E_{emer} of 0.8 kJ·mol^{-1}, while it can be quite difficult on Ta (011), where C segregation would be rather impeded with an E_{emer} of 229.0 kJ·mol^{-1}.

This large set of data, which can be quite different, can also be gathered and analysed in a four-quadrant plot, in a similar fashion as done for the thermodynamics in Fig. 1. To do so, Fig. 7 shows the $\log_{10}(E_{sub}/E_{sur})$ *vs.* $\log_{10}(E_{sink}/E_{emer})$, having thus 81 points corresponding to the same amount of explored TM surfaces. Thus, zero value for $\log_{10}(E_{sub}/E_{sur})$ implies that $E_{sub} = E_{sur}$, and so, surface and subsurface diffusion are kinetically equally feasible. Likewise, zero value for $\log_{10}(E_{sink}/E_{emer})$ implies that surface C sinking diffusion is kinetically as likely as the subsurface C emerging. These two zero values delimit the four quadrants in Fig. 7. Values larger than zero for $\log_{10}(E_{sub}/E_{sur})$ implies that E_{sub} values are higher than E_{sur}, and hence, for these cases, C atoms would diffuse more easily along the surface than through the slab subsurface region, points located on the right side of the zero limit. The opposite behavior is expected for $\log_{10}(E_{sub}/E_{sur})$ smaller than zero, located on the left side. When it concerns

$\log_{10}(E_{sink}/E_{emer})$ values, data above the zero limit imply that emerging is preferred over sinking, *i.e.* a preferential location on the surface. On the contrary, values below zero imply a preference towards C penetrating the subsurface region.

The top panel of Fig. 7 features data colored depending on the crystallographic structure of the TM, revealing that *fcc* and *bcc* TMs data points behave similarly, being dispersed on the top half of the plot, implying that for such metals E_{sink} is often larger than E_{emer}, and going for a kinetically allowed surface presence of C adatoms. Still, few cases are the early bottom part of the plot. These belong to *fcc* (111) Ni, Pd, Pt, Cu, Ag, and Au (111) surface models, where the above situation reverses, implying a more difficult segregation towards the surface of dissolved C atoms in the bulk metal matrix. Notice that the (111) surface termination is the most stable and abundant one on such TM metals,[29,51] and so such subsurface C effect should not be discarded on any on-going surface catalyzed process. Aside, neither *fcc* nor *bcc* TMs show a clear preference between E_{sur} and E_{sub}, with every metal being somehow unique in this regard. Finally, *hcp* TMs show sizable dispersion, but are mainly found in the bottom right part of the quadrants plot. This quadrant gathers situations with an E_{sink} barrier lower than E_{emer}, and E_{sub} being larger than E_{sur}. Hence, one observes that most of *hcp* TMs feature kinetically favorable penetration of isolated C atoms towards the subsurface region, but with restricted diffusion along the subsurface, as the diffusion across the surface is preferred.

Furthermore, the bottom panel shows the KM analysis again using three clusters as derived from Fig. 1. There, it is clear that Cluster 1 fits values of the right-upper quadrant, implying E_{emer} barriers smaller than E_{sink}, and E_{sur} smaller than E_{sub}. Altogether, these features imply a certain preference for C atoms to be located on the surface, and diffusing over it, as shown by the cluster centre, where E_{sub} is two times larger than E_{sur}, and E_{sink} 39.8 times larger than E_{emer}. Beyond that, Cluster 3 also nicely fits one quadrant, but now implying an easier C emergence compared to the sinking, but, more importantly, featuring E_{sub} values sensibly smaller than E_{sur} ones, as shown by the cluster centre, located at a point where E_{sur} values are five times larger than E_{sub}, and E_{sink} 12.8 times larger than E_{emer}. This quadrant points out certain TM surfaces where C diffuses more easily going through the subsurface region, probably due to the aforementioned stabilization of the diffusion TS states by a higher coordination. In this sense, C moieties would move around in the subsurface region, and only emerge from time to time, as if they were the targets of a whack-a-mole game. Finally, Cluster 2 contains the most numerous group, displaying, in general, well balanced E_{sub}/E_{sur} and E_{sink}/E_{emer} ratios near unity, as shown by the center,

being the ratios 1.4 and 0.9, respectively. Only a certain preference is found for a surface diffusion over the subsurface one, but, aside from that, the general behavior would be that all diffusion processes should be regarded feasible, implying a somewhat free mobility on the surface, through the subsurface region, and with exchange of C atoms in between surface and subsurface sites.

2.2. Descriptors controlling the energy barriers

Similar to the analysis carried out for the adsorption and absorption energies, the attention is now placed into finding descriptors of the diffusion energy barriers. The ones used for the thermodynamic minima, these are ε_d, ε_d^W, ε_{ss}, γ, and ϕ, are listed in Figs. S19-S23 of Section S9 of the ESI. There, even when using different regressions for each barrier type, the obtained results were unsatisfactory, reaching, at most, a regression coefficient R of 0.69 for E_{sink} *vs.* γ. Still, the limited applicability of such descriptors can be though as natural as such descriptors were developed and applied to seize the interaction strength, not the heights of energy barriers. Still, trends are regularly observed, *i.e.* the larger the ε_d, ε_d^W, or ε_{ss} the larger the E_b, and so it applies for γ, and ϕ, although for these inverse trends are observed for E_{emer} and E_{sub}, respectively.

In any case, the previous discussion underscores the point of similar trends achieved for adsorption or absorption energies, and diffusion energy barriers. Within this context, one has to remark the work of Nilekar and colleagues[54], who showed in their seminal work that the diffusion energy barrier depends on the adsorption strength of the adsorbed moiety, being indeed basically a twelve per cent of the latter, with an R of 0.85. Fig. 8 shows this trend for the four different diffusion processes here studied, revealing that, indeed, the stronger the adsorption or absorption energy, the larger the diffusion energy barrier, and in all the cases with similar slopes of *ca.* 0.16. However, the regression coefficients, R, are still quite modest, being at most 0.45 for E_{sur} energy barriers.

Another extended linear correlation used for energy barriers are Brønsted–Evans–Polanyi (BEP) relations, linearly expressing a reaction step energy barrier with the step energy variation, ΔE.[55-57] In this work we do not deal with reaction steps, as we are focusing on diffusion processes, but the same principle applies. To this end, the BEP relations were analyzed, yet only for C sinking and emerging processes, as surface and subsurface diffusions feature a ΔE of zero. Fig. 9 shows their BEP analysis with a fairly good correlation for E_{sink}, with a regression coefficient R of 0.83; however, the regression

for E_{emer} shows more dispersion, with a lower R of 0.63. Notice that for sinking process, the linear regression is close to the limit of a very late TS, where $E_b = \Delta E$, signaled in Fig. 9 with a dashed black line. Another regression constrain is an earliest TS situation, where E_b equals zero regardless of the value of ΔE. Still, there is also a number of cases located in between, so no evident trend can be claimed. At variance with the description of $E_{ads/abs}$ with respect to ε_d, the BEP correlation coefficients when splitting the data into different crystallographic groups does not substantially improve the outcome, indicating this time that the crystal structure is not a determining factor in the BEP correlations for neither E_{sink} nor E_{emer}; see Figs. S24 and S25 in Section S9 of the ESI.

Mimicking the above analysis of E_{ads} or E_{abs} dependence on ε_d and γ, and given the best correlations observed for E_{sink} as described by γ and ΔE, we carried out a multivariable regression involving combinations of ΔE and γ descriptors up to a second order degree —since third degree yielded no improvement— shown in Fig. 10. There, as happened in the thermodynamic evaluation in Fig. 4, one observes that *i)* the combination of both factors is beneficial, with an improved R of 0.86, while *ii)* the incorporation of descriptors higher orders translates into a mild improvement. As happened with the thermodynamic analysis, this underscores that the description of kinetic processes should be tackled considering a combination of different descriptors, instead of looking for a single, determining one, as appears that different aspects influence the kinetic energy barriers.

Thus, following the same procedure as for the thermodynamic analysis, we applied here different machine learning (ML) regression algorithms to have tools to forecast diffusion energy barriers and locate key descriptors governing such processes. Note that now the data set is four times larger —324 E_b values— than the 81 cases of E_{ads} or E_{abs}. The features and descriptors used are the same of the thermodynamic analysis, but now adding most stable position $E_{ads/abs}$ and ΔE. Moreover, the barrier type, BT —E_{sur}, E_{sub}, E_{sink}, or E_{emer}—, and the CN of the initial and final sites, named CN_{IS} and CN_{FS}, respectively, are also included. The target goal here is to predict E_b, and to this end MLR, DTR, and RFR have been used. A first analysis was carried out following the procedure and hyperparameters used for the thermodynamic data, yielding MAEs of 34.3 ± 2.4, 42.5 ± 4.7, and 33.1 ± 2.8 kJ·mol^{-1} for MLR, DTR, and RFR, respectively. Again, RFR is posed as the best performing ML algorithm.

By refining the number of descriptors by means of the leave-one-out procedure, the less relevant features were removed, and left only those that had a significant enough impact in

terms of error minimization, which are ΔE, $E_{ads/abs}$, ϕ, CN_{FS}, and CN_{IS}, with weights of 0.43, 0.27, 0.15, 0.09, and 0.06, respectively. Notice how ΔE is the most important feature, as expected from the BEP analysis, and particularly true for E_{sink} and E_{emer} barriers, although is not as predominant as ε_d was for $E_{ads/abs}$. The next in the list is indeed the most stable position $E_{ads/abs}$, in line with the above discussion where it was found to affect the barrier heights. Notice that the two most important descriptors are thermodynamic parameters, which can be used to estimate kinetic energy barriers. Other factors affecting the energy barriers are, unexpectedly, ϕ, even if by scratch does not show good linear correlations with the kinetic data, and CN_{IS} and CN_{FS}, which shows that the coordination number of the sites involved in the diffusion play minor, yet still relevant role in the height of the barriers.

As a last step, we selected the best performing hyperparameters of the RFR algorithm by performing CV evaluations on different combinations of parameters and choosing those that lead to minimal MAE, see the learning curve in Fig. 11. Results showed that, by using only ΔE, $E_{ads/abs}$, ϕ, CN_{FS}, and CN_{IS} as the input features, a RFR with 30 decision trees which considers three features for each split, see Fig. 11, provided the best accuracy, with a MAE of 32.6 ± 2.3 kJ·mol^{-1} for the test set, while the training set offers a MAE of solely 13.1 ± 0.4 kJ·mol^{-1}. The dimensionality reduction in Fig. 7 avoids using a KM clustering in the feature space, also because different features are simultaneously affecting the different E_b values. Other than that, the analysis done in Fig. 11 can actually be carried out differentiating the four different diffusive processes. This has been done and discussed in Figs. S26-S29 and Table S11 of Section S10 of the ESI. Briefly, RFR persisted as the best performing algorithm, with MAEs very similar to that obtained when considering all E_b altogether, with best performance found for E_{sur} barriers, with a test set MAE of 25.2 ± 6.6 kJ·mol^{-1}, and the less accurate case being E_{sub}, with a test set MAE of 38.2 ± 7.1 kJ·mol^{-1}. Compared to the thermodynamic data, the RFR offers more accuracy for diffusion energy barriers, which get closer to the typical DFT accuracy of 10-20 kJ·mol^{-1}, although one is still far from achieving an accuracy that would support quantitative estimations. However, the main descriptors affecting the C diffusions have been unfolded, and estimates can be argued upon them, allowing for a rapid qualitative assessment and sieving process.

Conclusions

In this work, by performing high-throughput periodic DFT calculations on proper slab models of 81 TM surfaces using the PBE *xc* functional, we provide compelling thermodynamic *plus* kinetic information on the interplay of C atom on and in TM surfaces, providing detailed information of adsorption and absorption minima sites and energies, and diffusive energy barriers along surface and subsurface regions, as well as in between both regions, summarized in Table S12 of Section S11 of the ESI. The provided thermodynamic and kinetic results are in line with experimental observations regarding carbide formation in *bcc* and early *hcp* TMs, also revealing the possibility of a surface reconstruction, being the key step of such process in some of the cases. Moreover, results are also in line with the well-known tendency of C to form graphene layers on top of *fcc* TMs surfaces, effectively poisoning them for heterogeneous catalysis purposes. Thermodynamic phase diagrams have been built for all the explored surfaces, delimiting temperature and ethylene partial pressure working conditions at which the presence of C atoms would be favorable.

Further than that, electronic and energetic descriptors have been analyzed on ad- and absorptive minima and energy barriers, where the *d*-band center has been found to be the most successful one when correlating ad/absorption energies, in a particular reliable fashion for *hcp* and *fcc* TMs, whereas presenting significant deviations *bcc* TMs. For diffusion energy barriers, the adsorption or absorption strength of the departing minimum, and the difference in energy between minima, ΔE, in the cases of sinking and emerging diffusions. Finally, k-means clustering has been used to delimit three types of TM thermodynamic and kinetic behavior towards C atoms, while machine learning random forest regression revealed that, both for the gained thermodynamic and kinetic data, a combination of descriptors yields to a better description of minima and energy barriers, although the accuracy is so far only valid for a rapid qualitative assessment. In any case, the analysis underscores the need of looking for a few number of descriptors biasing the interaction strength and diffusion possibilities, rather than trying to get a single perfect descriptor, which may not be the wisest option as different physicochemical aspects do indeed affect such processes.

Acknowledgments

The authors are thankful to the *Ministerio de Economía y Competitividad* (MEC) for the RTI2018-095460-B-I00 and *María de Maeztu* MDM-2017-0767 grants, to the *Generalitat de Catalunya* for the 2017SGR13 grant, and to the COST Action CA18234. Authors are

thankful to *Red Española de Supercomputación* (RES) for the supercomputing time (QCM-2018-1-0005, QCM-2018-2-0008, QCM-2019-1-0017, QS-2019-3-0017, QS-2020-1-0013). The study was also supported by the project EXTREME, funded by the Bulgarian Ministry of Education and Science, D01-76/30.03.2021 through the programme "European Scientific Networks". I. Z. K. is grateful to L'Oréal-UNESCO For Women in Science National Fellowship Program, 2020. H. A. A. is grateful to European Regional Development Fund and the Operational Program "Science and Education for Smart Growth" under contract UNITe No. BG05M2OP001-1.001-0004-C01. O. P. thanks the Spanish MICIUN for a PhD grant (PRE2018-083811). A. B. thanks *Generalitat de Catalunya* for his Beatriu de Pinós grant (2018BP00190). Authors are also thankful for insightful scientific discussions with MSc. Raúl Santiago.

Author Contributions

O. P. carried out the ad/absorption minima calculations and more than half of the transition states locations, analyzed the descriptors correlations, took care of the ML regressions and KM clustering, and made an initial draft of the manuscript. I. Z. K. carreid out *ca.* half of the transition states and assembled phase diagrams. A. B. assisted with the ML regressions and KM clustering. F. V. and H. A. A. conceived the research and revised the manuscript. H. A. A., G. N. V., and F. I. supervised the research and helped revising the manuscript. All authors discussed, commented, and revised the manuscript.

Competing Interests

The Authors declare no Competing Financial or Non-Financial Interests.

Data Availability

The energetic and geometric data gained from the density functional calculations is found in the Supplemental Material. Further data are are available from the corresponding author upon reasonable request.

Table 1. Average values for ε_d, γ, and CN, for each of the clusters shown in Fig. 6, plus their standard deviation.

	ε_d / eV	γ / J·m^{-2}	CN_{site}
C1	-0.1 ± 1.7	2.6 ± 0.7	3.0 ± 0.9
C2	-5.4 ± 2.5	0.7 ± 0.3	5.5 ± 0.8
C3	2.5 ± 1.7	1.6 ± 0.5	5.8 ± 0.4

Fig. 1. Most stable $E_{ads/ads}$ situations on every TM surface with respect to h. In the top panel, values in blue correspond to *fcc* TMs, green to *bcc* TMs, and purple to *hcp* TMs. In the bottom panel, three different colors are used to mark off the three different clusters determined through a KM analysis, with centers marked crossed.

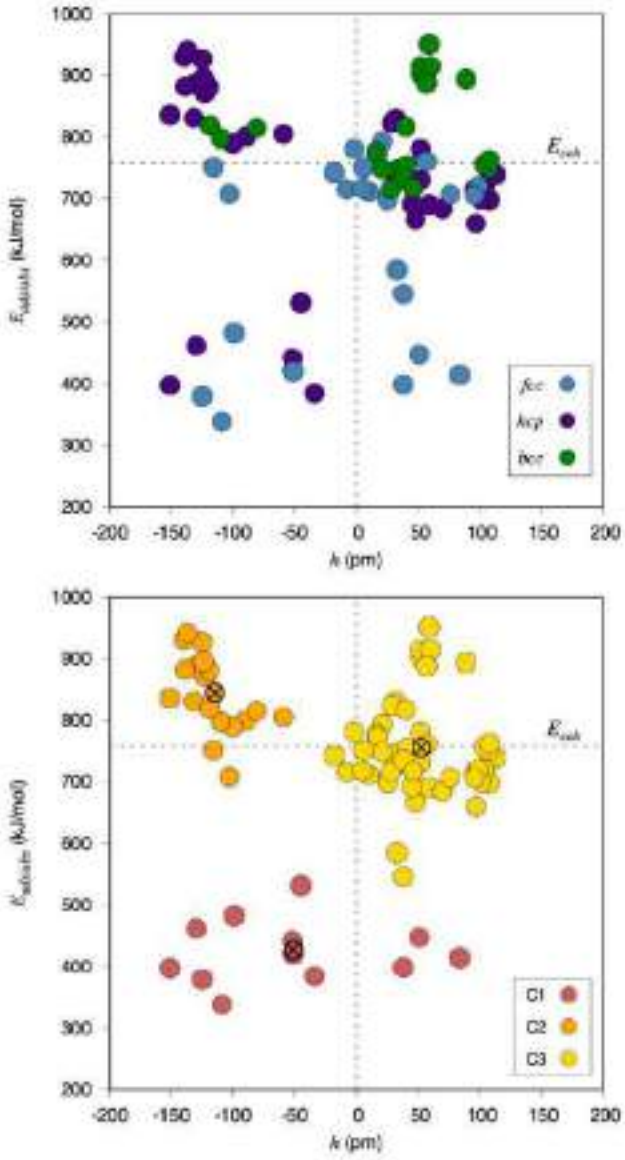

Fig. 2. Phase diagrams for *fcc* TMs (111) surfaces as a function of the acetylene partial pressure, $p_{C_2H_2}$, and temperature, T. Diagrams are obtained for a constant partial pressure of H_2, $p_{H_2} = 10^{-7}$ Pa. Regions above or below each curve indicate conditions at which the C-containing or pristine surfaces, respectively, are thermodynamically preferred.

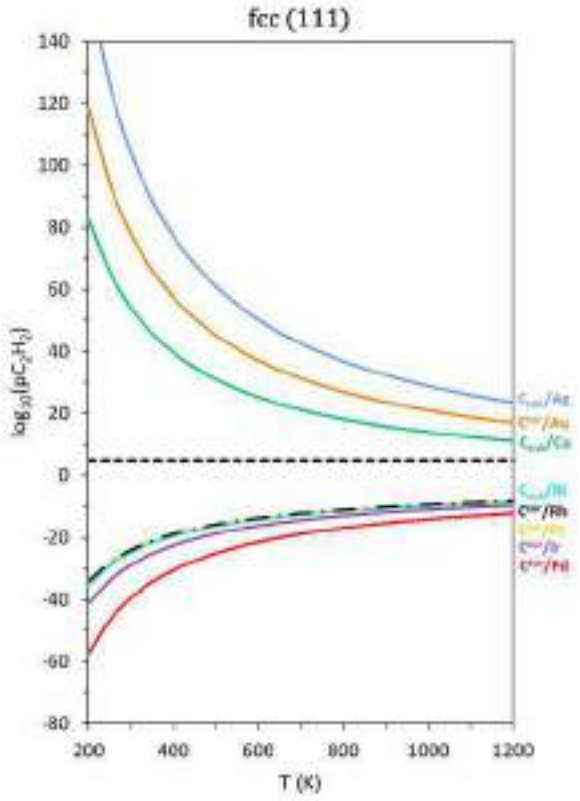

Fig. 3. Most stable $E_{adsorbs}$ situations with respect to ε_d, and the corresponding linear correlations. Values in blue correspond to *fcc* TMs, green to *bcc* TMs, and purple to *hcp* TMs.

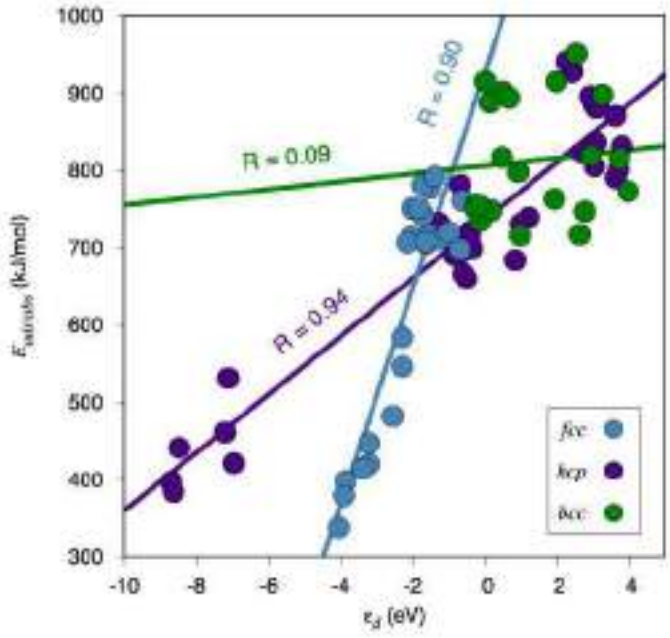

Fig. 4. Most stable $E_{ads/abs}$ situations *vs.* the predicted $E_{ads/abs}$ from different linear, multivariable, and polynomial regressions involving γ, ε_d, or a combination of them. The black dashed line represents a perfect correlation.

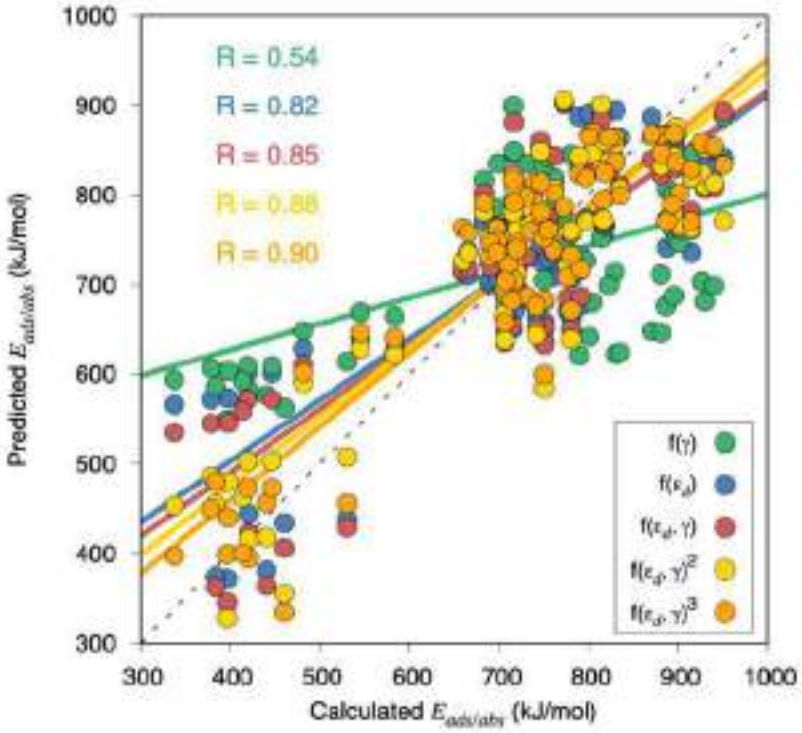

Fig. 5. MAE evolution for training (blue) and the test (green) sets as a function of the number of samples contained in the training set for the prediction of $E_{ads/abs}$ using a RFR algorithm. Colored areas around the lines account for the error dispersion resulting from the cross validation using 20 runs.

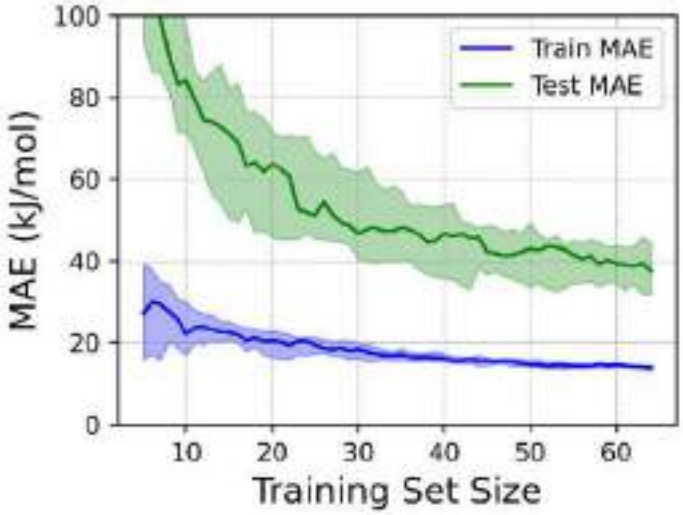

Fig. 6. Top panel: the three-dimensional KM clustering of the most important features extracted from the RFR, namely ε_d, γ, and CN_{sto}. Bottom panel: a quadrant plot as in Fig. 1, but showing the clusters from the top panel projected in the E_{adsorb}/h space.

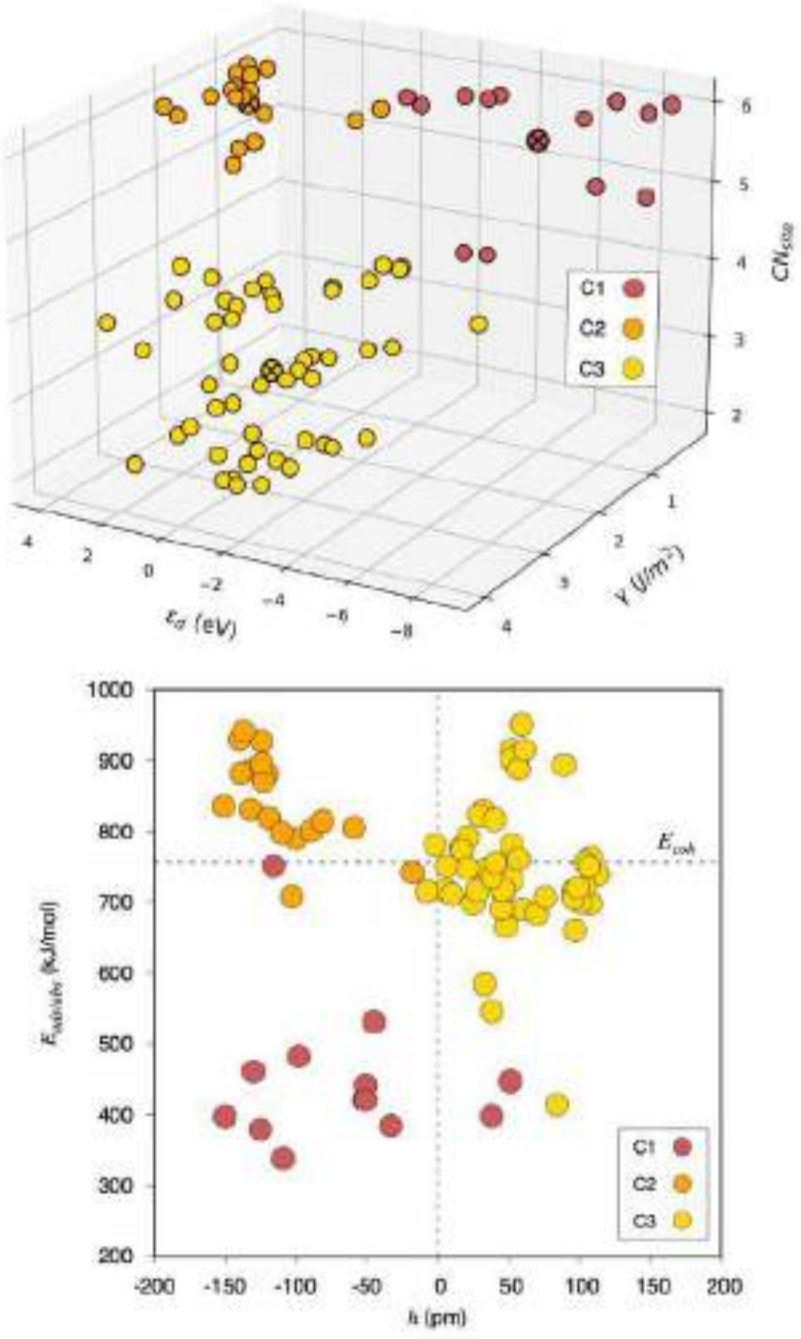

Fig. 7. The base 10 logarithm of E_{sub}/E_{sur} with respect to the base 10 logarithm of E_{sink}/E_{emer}. In the top panel, values in blue correspond to *fcc* TMs, green to *bcc* TMs, and purple to *hcp* TMs. In the bottom panel, three different colors are used to mark off the three different clusters determined through a KM analysis.

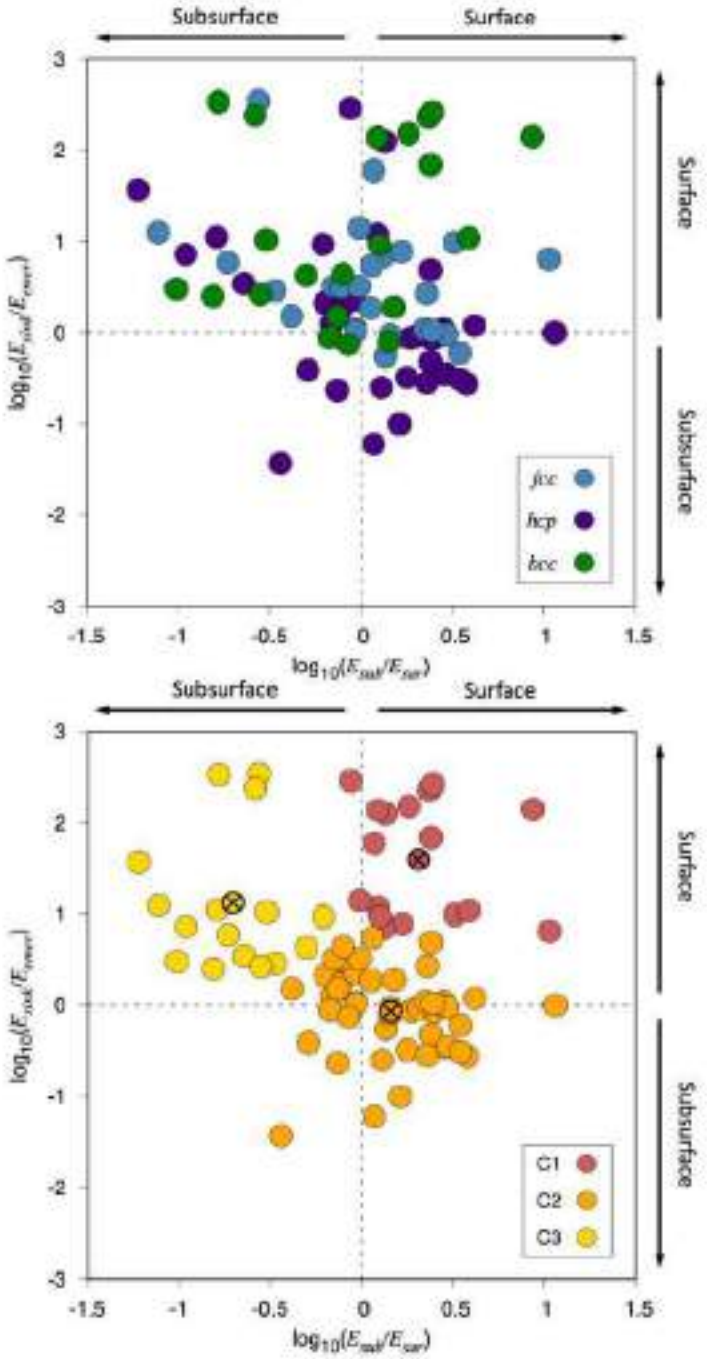

Fig. 8. Linear evolutions of the different E_b diffusion energy barriers —E_{sur}, E_{sub}, E_{sink}, and E_{emer}— with respect to most stable initial position E_{sub} or E_{abs}.

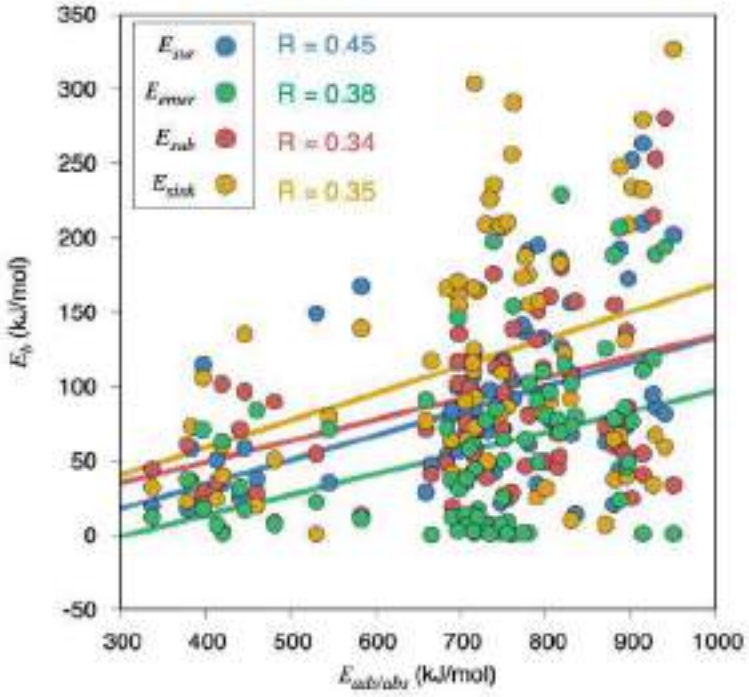

Fig. 9. BEP linear evolutions of E_b with respect to ΔE, and the corresponding linear correlations for each explored barrier type. Dashed lines define latest TS limit, where $E_b = \Delta E$, or earliest TS limit, where $E_b = 0$ regardless of ΔE.

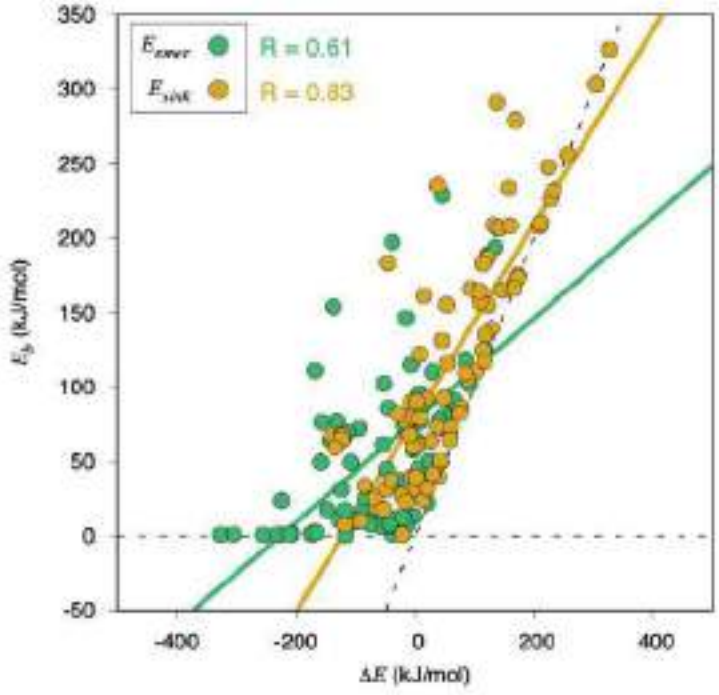

Fig. 10. Calculated E_{sink} *vs.* the predicted E_{sink} from different linear, multivariable, and polynomial regressions involving γ, ΔE, or different degrees of combinations of them. The black dotted line represents the ideal correlation.

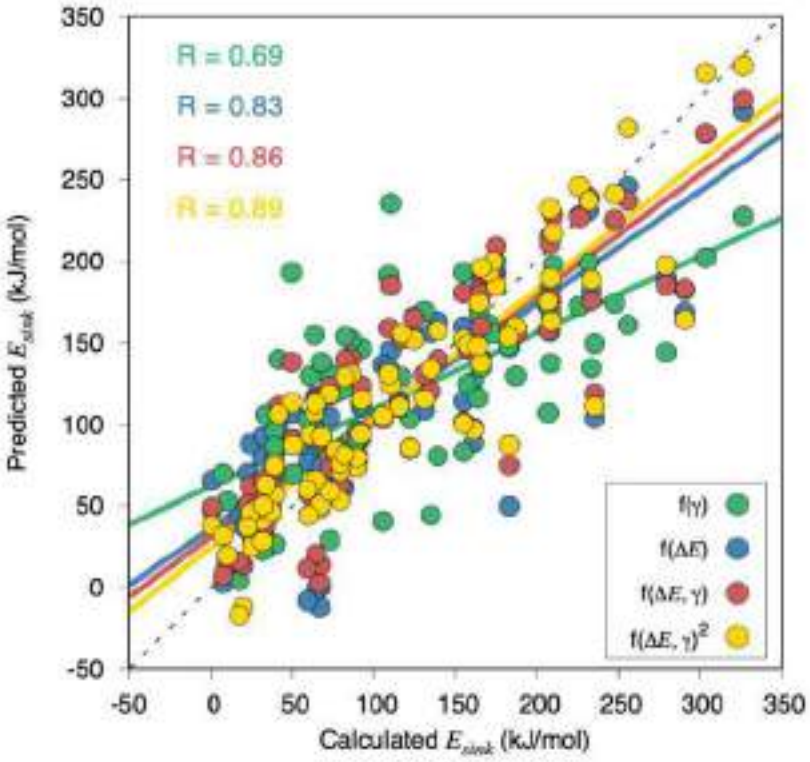

Fig. 11. MAE evolution for training (blue) and the test (green) sets as a function of the number of samples contained in the training set for the prediction of E_b using a RFR algorithm. Colored areas around the lines account for the error dispersion resulting from the cross validation using 20 runs.

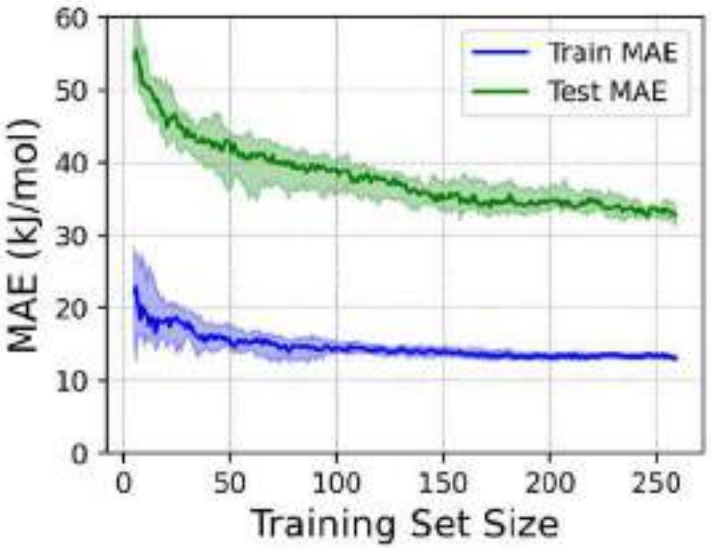

References

1 J. Greeley, J. K. Nørskov and M. Mavrikakis, *Annu. Rev. Phys. Chem.*, 2002, **53**, 319–348.

2 A. J. Medford, A. Vojvodic, J. S. Hummelshøj, J. Voss, F. Abild-Pedersen, F. Studt, T. Bligaard, A. Nilsson and J. K. Nørskov, *J. Catal.*, 2015, **328**, 36–42.

3 M. Haruta, S. Tsubota, T. Kobayashi, H. Kageyama, M. J. Genet and B. Delmon, *J. Catal.*, 1993, **144**, 175–192.

4 P. Sabatier, *La catalyse en chimie organique* (Béranger, Paris, France, 1920, 2nd edn.)

5 M. G. Quesne, A. Roldán, N. H. de Leeuw and C. R. A. Catlow, *Phys. Chem. Chem. Phys.*, 2018, **20**, 6905–6916.

6 H. H. Hwu and J. G. Chen, *Chem. Rev.*, 2005, **105**, 185-212.

7 R. B. Levy and M. Boudart, *Science*, 1973, **181**, 547-549.

8 F. Zaera, *ChemSusChem*, 2013, **6**, 1797–1820.

9 J. K. Nørskov, T. Bligaard, J. Rossmeisl and C. H. Christensen, *Nat. Chem.*, 2009, **1**, 37–46.

10 S. M. Kozlov, G. Kovács, R. Ferrando and K. M. Neyman, *Chem. Sci.*, 2015, **6**, 3868–3880.

11 S. M. Davis and G. A. Somorjai, *The Chemical Physics of Solid Heterogeneous Catalysis: Fundamental Studies of Heterogeneous Catalysis* (Elsevier, Amsterdam, Netherlands, 1982, 1st edn.).

12 S. Vajda, M. J. Pellin, J. P. Greeley, C. L. Marshall, L. A. Curtiss, G. A. Ballentine, J. W. Elam, S. Catillon-Mucherie, P. C. Redfern, F. Mehmood and P. Zapol, *Nat. Mater.*, 2009, **8**, 213–216.

13 D. Teschner, J. Borsodi, A. Wootsch, Z. Révay, M. Hävecker, A. Knop-Gericke, S. D. Jackson and R. Schlögl, *Science*, 2008, **320**, 86–89.

14 F. Viñes, C. Loschen, F. Illas and K. M. Neyman, *J. Catal.*, 2009, **266**, 59–63.

15 O. Piqué, I. Z. Koleva, F. Viñes, H. A. Aleksandrov, G. N. Vayssilov and F. Illas, *Angew. Chem. Int. Ed.*, 2019, **58**, 1744–1748.

16 P. Janthon, F. Viñes, J. Sirijaraensre, J. Limtrakul and F. Illas, *Catal. Sci. Technol.*, 2017, **7**, 807–816.

17 B. Martínez, O. Piqué, H. Prats, F. Viñes and F. Illas, *Appl. Surf. Sci.*, 2020, **513**, 145765.

18 A. Reina, S. Thiele, X. Jia, S. Bhaviripudi, M. S. Dresselhaus, J. A. Schaefer and J. Kong, *Nano Res.*, 2009, **2**, 509–516.

19 J.-M. Aguiar-Hualde, Y. Magnin, H. Amara and C. Bichara, *Carbon*, 2017, **120**, 226–232.

20 A. Rinaldi, J.-P. Tessonnier, M. E. Schuster, R. Blume, F. Girgsdies, Q. Zhang, T. Jacob, S. B. Abd Hamid, D. S. Su and R. Schlögl, *Angew. Chem. Int. Ed.*, 2011, **50**, 3313–3317.

21 M. Maciejewski and A. Baiker, *Pure Appl. Chem.*, 1995, **67**, 1879–1884.

22 K. M. Neyman and S. Schauermann, *Angew. Chem. Int. Ed.*, 2010, **49**, 4743–4746.

23 S. P. Liu, M. Zhao, W. Gao and Q. Jiang, *ChemSusChem*, 2017, **10**, 387–393.

24 Y. Sun, Y. Cao, L. Wang, X. Mu, Q. Zhao, R. Si, X. Zhu, S. Chen, B. Zhang, D. Chen and Y. Wan, *Nat. Commun.*, 2020, **11**, 4600.

25 M. Favaro, H. Xiao, T. Cheng, W. A. Goddard, J. Yano and E. J. Crumlin, *Proc. Natl. Acad. Sci.*, 2017, **114**, 6706–6711.

26 T. Chen, C. Foo and S. C. E. Tsang, *Chem. Sci.*, 2021, **12**, 517–532.

27 G. Kresse and J. Furthmüller, *Comput. Mater. Sci.*, 1996, **6**, 15–50.

28 J. P. Perdew, K. Burke and M. Ernzerhof, *Phys. Rev. Lett.*, 1996, **77**, 3865–3868.

29 L. Vega, J. Ruvireta, F. Viñes and F. Illas, *J. Chem. Theory Comput.*, 2018, **14**, 395–403.

30 G. Kresse and D. Joubert, *Phys. Rev. B*, 1999, **59**, 1758–1775.

31 P. Janthon, S. Luo, S. M. Kozlov, F. Viñes, J. Limtrakul, D. G. Truhlar and F. Illas, *J. Chem. Theory Comput.*, 2014, **10**, 3832–3839.

32 L. Vega and F. Viñes, *J. Comput. Chem.*, 2020, **41**, 2598–2603.

33 H. J. Monkhorst and J. D. Pack, *Phys. Rev. B*, 1976, **13**, 5188–5192.

34 G. Henkelman, B. P. Uberuaga and H. Jónsson, *J. Chem. Phys.*, 2000, **113**, 9901–9904.

35 F. Pedregosa, G. Varoquaux, A. Gramfort, V. Michel, B. Thirion, O. Grisel, M. Blondel, P. Prettenhofer, R. Weiss, V. Dubourg, J. Vanderplas, A. Passos, D. Cournapeau, M. Brucher, M. Perrot and E. Duchesnay, *J. Mach. Learn Res.*, 2011, **12**, 2825-2830.

36 Z. Chaker, P. Chervy, Y. Boulard, S. Bressanelli, P. Retailleau, M. Paternostre and T. Charpentier, *J. Phys. Chem. B*, 2021, **125**, 9454-9466.

37 X. Jiang, C. Ärhammar, P. Liu, J. Zhao and R. Ahuja, *Sci. Rep.*, 2013, **3**, 1877.

38 H. Matsushima, A. Taranovskyy, C. Haak, Y. Gründer and O. M. Magnussen, *J. Am. Chem. Soc.*, 2009, **131**, 10362–10363.

39 A. Tsouloucha, I. S. K. Kerkines and A. Mavridis, *J. Phys. Chem. A*, 2003, **107**, 6062–6072.

40 H. S. Mok, A. Ebnonnasir, Y. Murata, S. Nie, K. F. McCarty, C. V. Ciobanu and S. Kodambaka, *Appl. Phys. Lett.*, 2014, **104**, 101606.

41 W. Zhao, S. M. Kozlov, O. Höfert, K. Gotterbarm, M. P. A. Lorenz, F. Viñes, C. Papp, A. Görling and H.-P. Steinrück, *J. Phys. Chem. Lett.*, 2011, **2**, 759-764.

42 D. Teschner, Z. Révay, J. Borsodi, M. Hävecker, A. Knop-Gericke, R. Schlögl, D. Milroy, S. D. Jackson, D. Torres and P. Sautet, *Angew. Chem. Int. Ed.*, 2008, **47**, 9274-9278.

43 J. Rogal and K. Reuter, Educational Notes RTO-EN-AVT-142, 2007, **2**, 1-18.

44 L. Vega, B. Martínez, F. Viñes and F. Illas, *Phys. Chem. Chem. Phys.*, 2018, **20**, 20548–20554.

45 B. W. J. Chen, D. Kirvassilis, Y. Bai and M. Mavrikakis, *J. Phys. Chem. C*, 2019, **123**, 7551–7566.

46 H. Zhuang, A. J. Tkalych and E. A. Carter, *J. Phys. Chem. C*, 2016, **120**, 23698–23706.

47 H. B. Michaelson, *J. Appl. Phys.*, 1977, **48**, 4729–4733.

48 B. Hammer and J. K. Nørskov, *Surf. Sci.*, 1995, **343**, 211–220.

49 A. Vojvodic, J. K. Nørskov and F. Abild-Pedersen, *Top. Catal.*, 2014, **57**, 25–32.

50 H. Xin, A. Vojvodic, J. Voss, J. K. Nørskov and F. Abild-Pedersen, *Phys. Rev. B*, 2014, **89**, 115114.

51 J. Ruvireta, L. Vega and F. Viñes, *Surf. Sci.*, 2017, **664**, 45–49.

52 C. S. Praveen and A. Comas-Vives, *ChemCatChem*, 2020, **12**, 4611.

53 L. Gao, R. Guest and N. P. Guisinguer, *Nano Lett.*, 2010, **10**, 3512–3516.

54 A. U. Nilekar, J. Greeley and M. A. Mavrikakis, *Angew. Chem. Int. Ed.*, 2006, **45**, 7046–7049.

55 J. L. C., Fajín, F. Viñes, M. N. D. S. Cordeiro, F. Illas and J. R. B. Gomes, *J. Chem. Theory Comput.*, 2016, **12**, 2121–2126.

56 J. N. Brønsted, *Chem. Rev.*, 1928, **5**, 231−338.

57 M. G. Evans, M. Polanyi, *Trans. Faraday Soc.*, 1938, **34**, 11−24.

Conclusions

In this thesis, density functional theory (DFT) calculations were used to understand and improve the electrocatalytic reduction of CO_2 (CO_2RR) to valuable commodities and investigate the interactions of C atoms with transition metal (TM) surfaces and nanoparticles (NPs). Although the individual conclusions resulting from each of the studies featured in this thesis have been already discussed at the end of each section, some general conclusions are outlined here along with possible future directions for the research here presented.

From the modelling point of view, the work presented in this thesis shows that DFT calculations on periodic systems are a useful tool to describe the interactions of TM surfaces with ad/absorbed atoms and molecules, to unveil the mechanistic information of electrocatalytic reactions, and to assess the catalytic activity of different materials towards a certain reaction. The computational models used in this thesis were able to describe the underlying cause of key observations from experiments and to predict and identify the characteristics of active catalytic surfaces. In general, we have shown that:

- Square four-atom islands on top of Cu(100) terraces are suggested as the active sites responsible for ethanol evolution on OD-Cu.
- The active sites for CO_2RR are different for each C_2 product. The product selectivity of Cu electrodes is dictated by the site-specific formation of either ethylene oxide or acetaldehyde. Highly undercoordinated sites are the active sites for the electroreduction of acetaldehyde, moderately coordinated sites are active towards the electroreduction of ethylene oxide, and highly coordinated sites are dedicated to the evolution of H_2.
- In CuAg composite electrocatalysts, when there is excess *CO, an alternative pathway to reduce CO_2 selectively to ethanol is opened. This pathway does not proceed via *CO dimerization but through the coupling of *CO + *CH_x (x = 1, 2) species.
- Certain sites at catalytic surfaces are inactive because of their inability to stabilize certain adsorbates. They can become active via the opening of an alternative pathway that circumvents the formation of such problematic species.

- FAR to CH_3OH can be performed successfully using anodized titanium. Oxygen vacancies located at steps are the active sites responsible for the formation of methanol.
- There is thermodynamic, kinetic, and dynamic evidence on the presence of subsurface C species on the (111) surface of groups 10 and 11 TM systems. The role of surface and subsurface C species in simulation models of some of the *fcc* TMs should be reconsidered.
- The *d*-band center is identified as the most successful descriptor of ad/absorption energies of atomic C at TM surfaces. $E_{ads/abs}$ and ΔE are the most relevant descriptors for diffusion energy barriers.
- ML regressions show that a combination of descriptors yield a better description of minima and energy barriers. This underscores the need for seeking a few descriptors biasing the interaction strength and diffusion possibilities, rather than trying to get a single perfect descriptor, which may not be the wisest option as different physicochemical aspects do indeed affect such processes.

As future directions to continue the research exposed in this thesis, I suggest:

- Calculate the CO_2RR pathway to C_2 products using the new solvation method proposed by Rendón-Calle *et al.*,[117] and observe the similarities and/or differences with the present results. Moreover, it would be interesting to explore how to include cation effects in such method.
- Inspect the possible effects of the presence of subsurface C at Cu surfaces on the activity and selectivity of CO_2RR.
- Since a large overpotential was found for EOR on Cu, a study featuring calculations for EOR on different TMs is worthwhile.
- Adding an HCOOH-producing co-catalyst to anodized titanium may be of interest. Experimental observations may be necessary first as to observe the behavior of such catalytic system.
- Calculate all the ad/absorption energies of *O, *N, and *H, together with the corresponding diffusion barriers on all the same systems. This would increase the size of the data set together with its variety. Predictions for other atomic species could be made.

List of Publications

Part of this thesis:

O. Piqué, F. Viñes, F. Illas, F. Calle-Vallejo. Elucidating the structure of ethanol-producing active sites at oxide-derived Cu electrocatalysts, *ACS Catal.*, 10, 10488-10494 (2020)

O. Piqué, M. Löffler, I. Katsounaros, F. Calle-Vallejo. Computational-experimental study of the onset potentials for CO_2 reduction on polycrystalline and oxide-derived copper electrodes, *Electrochim. Acta*, 380, 138247 (2021)

O. Piqué, Q. H. Low, A. D. Handoko, B. S. Yeo, F. Calle-Vallejo. Selectivity map for the late stages of CO and CO_2 reduction to C_2 species on copper electrodes, *Angew. Chem. Int. Ed.*, 60, 10784-10790 (2021)

L. R. L. Ting, **O. Piqué**, S. Y. Lim, M. Tanhaei, F. Calle-Vallejo, B. S. Yeo. Enhancing CO_2 electroreduction to ethanol on copper-silver composites by opening an alternative catalytic pathway, *ACS Catal.*, 10, 4059-4069 (2020)

W. J. Teh, **O. Piqué**, Q. H. Low, W. Zhu, F. Calle-Vallejo, B. S. Yeo. Toward efficient tandem electroreduction of CO_2 to methanol using anodized titanium, *ACS Catal.*, 11, 8467-8475 (2021)

O. Piqué, I. Z. Koleva, F. Viñes, H. A. Aleksandrov, G. N. Vayssilov, F. Illas. Subsurface carbon: a general feature of noble metals, *Angew. Chem. Int. Ed.*, 58, 1744-1748 (2019)

B. Martínez, **O. Piqué**, H. Prats, F. Viñes, F. Illas. Towards understanding the role of carbon atoms on transition metal surfaces: implications for catalysis, *Appl. Surf. Sci.*, 513, 145765 (2020)

O. Piqué, I. Z. Koleva, A. Bruix, F. Viñes, H. A. Aleksandrov, G. N. Vayssilov, F. Illas. Charting the atomic C interaction with transition metal surfaces, *J. Mater. Chem. A*, Submitted (2022).

Other Publications:

B. Garlyyev, J. Fitchner, **O. Piqué**, O. Schneider, A. S. Bandarenka, F. Calle-Vallejo. Revealing the nature of active sites in electrocatalysis, *Chem. Sci.*, 10, 8060-8075 (2019)

O. Piqué, F. Illas, F: Calle-Vallejo. Designing water splitting catalysts using rules of thumb: advantages, dangers, and alternatives, *Phys. Chem. Chem. Phys.*, 22, 6797-6803 (2020)

M. Retuerto, L. Pascual, **O. Piqué**, P. Kayser, M. A. Salam, M. Mokhtar, J. A. Alonso, M. Peña, F. Calle-Vallejo, S. Rojas. How oxidation state and lattice distortion influence the oxygen evolution activity in acid of iridium double perovskites, *J. Mater. Chem. A*, 9, 2980-2990 (2021)

I. Mangoufis-Giasin, **O. Piqué**, P. Khanipour, K. J. J. Mayrhofer, F. Calle-Vallejo, I. Katsounaros. Different promoting roles of ruthenium for the oxidation of primary and secondary alcohols on PtRu electrocatalysts, *J. Catal.*, 400, 166-172 (2021)

References

1 K. J. Laider, *Pure Appl. Chem.*, 1996, **68**, 149–192.

2 B. A. Averill, J. A. Moulijn, R. A. van Santen and P. W. N. M. van Leeuwen, *Catalysis: An Integrated Approach*, Elsevier, Amsterdam, 1999.

3 J. N. Armor, *Catal. Today*, 2011, **163**, 3–9.

4 Z. Ma and F. Zaera, in *Encyclopedia of Inorganic and Bioinorganic Chemistry*, John Wiley & Sons, Ltd., Hoboken, 2014.

5 C. Geantet, J. Afonso, M. Breysse, N. Allali and M. Danot, *Catal. Today*, 1996, **28**, 23–30.

6 A. Clearfield and D. S. Thakur, *Appl. Catal.*, 1986, **26**, 1–26.

7 C. M. Domínguez, P. Ocón, A. Quintanilla, J. A. Casas and J. J. Rodriguez, *Appl. Catal. B*, 2014, **144**, 599–606.

8 A. P. E. York, J. B. Claridge, A. J. Brungs, S. C. Tsang and M. L. H. Green, *Chem. Commun.*, 1997, 39–40.

9 G. C. Bond, *Metal-Catalysed reactions of hydrocarbons*, Springer, New York, 2005.

10 J. M. Thomas and W. J. Thomas, *Principles and practice of heterogeneous catalysis*, VCH, Weinheim, 1996.

11 P. Sabatier, *La catalyse en chimie organique*, Béranger, Paris, 1920.

12 G. C. Bond, *Heterogeneous catalysis: Principles and applications*, Clarendon Press, Oxford, 1974.

13 Y. Yang, M. Luo, W. Zhang, Y. Sun, X. Chen and S. Guo, *Chem*, 2018, **4**, 2054–2083.

14 J. O. M. Bockris, *Int. J. Hydrog. Energy*, 2013, **38**, 2579–2588.

15 S. Gu, B. Xu and Y. Yan, *Annu. Rev. Chem. Biomol. Eng.*, 2014, **5**, 429–454.

16 Z. W. Seh, J. Kibsgaard, C. F. Dickens, I. Chorkendorff, J. K. Nørskov and T. F. Jaramillo, *Science*, 2017, **355**, eaad4998.

17 M. K. Debe, *Nature*, 2012, **486**, 43–51.

18 V. R. Stamenkovic, D. Strmcnik, P. P. Lopes and N. M. Markovic, *Nat. Mater.*, 2017, **16**, 57–69.

19 M. Luo and S. Guo, *Nat. Rev. Mater.*, 2017, **2**, 1–13.

20 M. Born and J. R. Oppenheimer, *Ann. Phys.*, 1927, **84**, 457.

21 D. R. Hartree, *Math. Proc. Camb. Philos. Soc.*, 1928, **24**, 111–132.

22 C. Møller and M. S. Plesset, *Phys. Rev.*, 1934, **46**, 618–622.

23 H. J. Monkhorst, *Int. J. Quantum Chem.*, 1977, **12**, 421–432.

24 B. M. Austin, D. Y. Zubarev and W. A. Lester, *Chem. Rev.*, 2012, **112**, 263–288.

25 P. Hohenberg and W. Kohn, *Phys. Rev.*, 1964, **136**, B864–B871.

26 W. Kohn and L. J. Sham, *Phys. Rev.*, 1965, **140**, A1133–A1138.

27 S. H. Vosko, L. Wilk and M. Nusair, *Can. J. Phys.*, 1980, **58**, 1200–1211.

28 J. P. Perdew, K. Burke and M. Ernzerhof, *Phys. Rev. Lett.*, 1996, **77**, 3865–3868.

29 J. Tao, J. P. Perdew, V. N. Staroverov and G. E. Scuseria, *Phys. Rev. Lett.*, 2003, **91**, 146401.

30 J. P. Perdew, M. Ernzerhof and K. Burke, *J. Chem. Phys.*, 1996, **105**, 9982–9985.

31 I. de P. R. Moreira, F. Illas and R. L. Martin, *Phys. Rev. B*, 2002, **65**, 155102.

32 M. Fischer, F. O. Evers, F. Formalik and A. Olejniczak, *Theor. Chem. Acc.*, 2016, **135**, 257.

33 S. Jana, K. Sharma and P. Samal, *J. Chem. Phys.*, 2018, **149**, 164703.

34 P. Mori-Sánchez, A. J. Cohen and W. Yang, *J. Chem. Phys.*, 2006, **125**, 201102.

35 A. J. Cohen, P. Mori-Sánchez and W. Yang, *Science*, 2008, **321**, 792–794.

36 P. Mori-Sánchez, A. J. Cohen and W. Yang, *Phys. Rev. Lett.*, 2008, **100**, 146401.

37 J. Hubbard and B. H. Flowers, *Proc. Math. Phys. Eng. Sci.*, 1963, **276**, 238–257.

38 V. I. Anisimov and O. Gunnarsson, *Phys. Rev. B*, 1991, **43**, 7570–7574.

39 C. Loschen, J. Carrasco, K. M. Neyman and F. Illas, *Phys. Rev. B*, 2007, **75**, 035115.

40 G. Kresse and J. Furthmüller, *Phys. Rev. B*, 1996, **54**, 11169–11186.

41 L. Vega, J. Ruvireta, F. Viñes and F. Illas, *J. Chem. Theory Comput.*, 2018, **14**, 395–403.

42 J. L. C. Fajín, M. N. D. S. Cordeiro, J. R. B. Gomes and F. Illas, *J. Chem. Theory Comput.*, 2012, **8**, 1737–1743.

43 D. R. Hamann, M. Schlüter and C. Chiang, *Phys. Rev. Lett.*, 1979, **43**, 1494–1497.

44 D. Vanderbilt, *Phys. Rev. B*, 1990, **41**, 7892–7895.

45 G. Kresse and D. Joubert, *Phys. Rev. B*, 1999, **59**, 1758–1775.

46 F. Bloch, *Z. Physik*, 1929, **57**, 545–555.

47 L. Granda-Marulanda, A. Rendon-Calle, S. Builes, F. Illas, M. T. M. Koper and F. Calle-Vallejo, *ACS Catal.*, 2020, **10**, 6900–6907.

48 D. R. Lide, *CRC Handbook of Chemistry and Physics*, CRC Press, Boca Raton, 2005.

49 Q. Li, Y. Ouyang, S. Lu, X. Bai, Y. Zhang, L. Shi, C. Ling and J. Wang, *Chem. Commun.*, 2020, **56**, 9937–9949.

50 Z.-D. He, S. Hanselman, Y.-X. Chen, M. T. M. Koper and F. Calle-Vallejo, *J. Phys. Chem. Lett.*, 2017, **8**, 2243–2246.

51 F. Calle-Vallejo and M. T. M. Koper, *Angew. Chem. Int. Ed.*, 2013, **52**, 7282–7285.

52 J. K. Nørskov, J. Rossmeisl, A. Logadottir, L. Lindqvist, J. R. Kitchin, T. Bligaard and H. Jónsson, *J. Phys. Chem. B*, 2004, **108**, 17886–17892.

53 G. Jerkiewicz, *ACS Catal.*, 2020, **10**, 8409–8417.

54 I. Mangoufis-Giasin, O. Piqué, P. Khanipour, K. J. J. Mayrhofer, F. Calle-Vallejo and I. Katsounaros, *J. Catal.*, 2021, **400**, 166–172.

55 A. Bagger, L. Arnarson, M. H. Hansen, E. Spohr and J. Rossmeisl, *J. Am. Chem. Soc.*, 2019, **141**, 1506–1514.

56 J. L. C. Fajín, F. Viñes, M. N. D. S. Cordeiro, F. Illas and J. R. B. Gomes, *J. Chem. Theory Comput.*, 2016, **12**, 2121–2126.

57 J. N. Brønsted, *Chem. Rev.*, 1928, **5**, 231–338.

58 M. G. Evans and M. Polanyi, *Trans. Faraday Soc.*, 1938, **34**, 11–24.

59 J. Rogal and K. Reuter, *Educational Notes RTO-EN-AVT-142*, 2007, **2**, 1.

60 M. K. Gilson and K. K. Irikura, *J. Phys. Chem. B*, 2010, **114**, 16304–16317.

61 O. Piqué, I. Z. Koleva, F. Viñes, H. A. Aleksandrov, G. N. Vayssilov and F. Illas, *Angew. Chem. Int. Ed.*, 2019, **58**, 1744–1748.

62 H. Eyring, *Chem. Rev.*, 1935, **17**, 65–77.

63 M. G. Evans and M. Polanyi, *Trans. Faraday Soc.*, 1935, **31**, 875–894.

64 J. W. McIver Jr. and A. Komornicki, *J. Am. Chem. Soc.*, 1972, **94**, 2625–2633.

65 A. Komornicki, K. Ishida, K. Morokuma, R. Ditchfield and M. Conrad, *Chem. Phys. Lett.*, 1977, **45**, 595–602.

66 H. B. Schlegel, *J. Comput. Chem.*, 2003, **24**, 1514–1527.

67 G. Henkelman, B. P. Uberuaga and H. Jónsson, *J. Chem. Phys.*, 2000, **113**, 9901–9904.

68 F. Pedregosa, G. Varoquaux, A. Gramfort, V. Michel, B. Thirion, O. Grisel, M. Blondel, P. Prettenhofer, R. Weiss, V. Dubourg, J. Vanderplas, A. Passos, D. Cournapeau, M. Brucher, M. Perrot and E. Duchesnay, *J. Mach. Learn Res.*, 2011, **12**, 2825–2830.

69 Z. Chaker, P. Chervy, Y. Boulard, S. Bressanelli, P. Retailleau, M. Paternostre and T. Charpentier, *J. Phys. Chem. B*, 2021, **125**, 9454–9466.

70 H. Zhuang, A. J. Tkalych and E. A. Carter, *J. Phys. Chem. C*, 2016, **120**, 23698–23706.

71 H. B. Michaelson, *Int. J. Appl. Phys.*, 1977, **48**, 4729–4733.

72 F. Calle-Vallejo, N. G. Inoglu, H.-Y. Su, J. I. Martínez, I. C. Man, M. T. M. Koper, J. R. Kitchin and J. Rossmeisl, *Chem. Sci.*, 2013, **4**, 1245–1249.

73 B. Hammer and J. K. Nørskov, *Surf. Sci.*, 1995, **343**, 211–220.

74 A. Vojvodic, J. K. Nørskov and F. Abild-Pedersen, *Top. Catal.*, 2014, **57**, 25–32.

75 H. Xin, A. Vojvodic, J. Voss, J. K. Nørskov and F. Abild-Pedersen, *Phys. Rev. B*, 2014, **89**, 115114.

76 N. Govindarajan, J. M. García-Lastra, E. J. Meijer and F. Calle-Vallejo, *Curr. Opin. Electrochem.*, 2018, **8**, 110–117.

77 T. Bligaard and J. K. Nørskov, *Electrochim. Acta*, 2007, **52**, 5512–5516.

78 H. Li, Y. Li, M. T. M. Koper and F. Calle-Vallejo, *J. Am. Chem. Soc.*, 2014, **136**, 15694–15701.

79 F. Calle-Vallejo, J. Tymoczko, V. Colic, Q. H. Vu, M. D. Pohl, K. Morgenstern, D. Loffreda, P. Sautet, W. Schuhmann and A. S. Bandarenka, *Science*, 2015, **350**, 185–189.

80 J. K. Nørskov, T. Bligaard, J. Rossmeisl and C. H. Christensen, *Nat. Chem.*, 2009, **1**, 37–46.

81 F. Calle-Vallejo, J. I. Martínez, J. M. García-Lastra, E. Abad and M. T. M. Koper, *Surf. Sci.*, 2013, **607**, 47–53.

82 F. Calle-Vallejo, J. I. Martínez, J. M. García-Lastra, J. Rossmeisl and M. T. M. Koper, *Phys. Rev. Lett.*, 2012, **108**, 116103.

83 F. Calle-Vallejo, D. Loffreda, M. T. M. Koper and P. Sautet, *Nat. Chem.*, 2015, **7**, 403–410.

84 F. Calle-Vallejo and M. T. M. Koper, *ACS Catal.*, 2017, **7**, 7346–7351.

85 B. Garlyyev, J. Fichtner, O. Piqué, O. Schneider, A. S. Bandarenka and F. Calle-Vallejo, *Chem. Sci.*, 2019, **10**, 8060–8075.

86 N. S. Lewis and D. G. Nocera, *PNAS*, 2006, **103**, 15729–15735.

87 O. S. Bushuyev, P. D. Luna, C. T. Dinh, L. Tao, G. Saur, J. van de Lagemaat, S. O. Kelley and E. H. Sargent, *Joule*, 2018, **2**, 825–832.

88 D. Gao, R. M. Arán-Ais, H. S. Jeon and B. Roldan Cuenya, *Nat. Catal.*, 2019, **2**, 198–210.

89 Y. Y. Birdja, E. Pérez-Gallent, M. C. Figueiredo, A. J. Göttle, F. Calle-Vallejo and M. T. M. Koper, *Nature Energy*, 2019, **4**, 732–745.

90 A. D. Handoko, F. Wei, Jenndy, B. S. Yeo and Z. W. Seh, *Nat. Catal.*, 2018, **1**, 922–934.

91 Y. Hori, A. Murata, R. Takahashi and S. Suzuki, *J. Am. Chem. Soc.*, 1987, **109**, 5022–5023.

92 Y. Hori, A. Murata and R. Takahashi, *J. Chem. Soc., Faraday Trans. 1*, 1989, **85**, 2309–2326.

93 Y. Hori, R. Takahashi, Y. Yoshinami and A. Murata, *J. Phys. Chem. B*, 1997, **101**, 7075–7081.

94 M. Gattrell, N. Gupta and A. Co, *J. Electroanal. Chem.*, 2006, **594**, 1–19.

95 R. Kortlever, J. Shen, K. J. P. Schouten, F. Calle-Vallejo and M. T. M. Koper, *J. Phys. Chem. Lett.*, 2015, **6**, 4073–4082.

96 C. W. Li and M. W. Kanan, *J. Am. Chem. Soc.*, 2012, **134**, 7231–7234.

97 C. W. Li, J. Ciston and M. W. Kanan, *Nature*, 2014, **508**, 504–507.

98 A. Verdaguer-Casadevall, C. W. Li, T. P. Johansson, S. B. Scott, J. T. McKeown, M. Kumar, I. E. L. Stephens, M. W. Kanan and I. Chorkendorff, *J. Am. Chem. Soc.*, 2015, **137**, 9808–9811.

99 Y. Hori, I. Takahashi, O. Koga and N. Hoshi, *J. Mol. Catal. A Chem.*, 2003, **199**, 39–47.

100 I. Ledezma-Yanez, E. P. Gallent, M. T. M. Koper and F. Calle-Vallejo, *Catal. Today*, 2016, **262**, 90–94.

101 E. Bertheussen, A. Verdaguer-Casadevall, D. Ravasio, J. H. Montoya, D. B. Trimarco, C. Roy, S. Meier, J. Wendland, J. K. Nørskov, I. E. L. Stephens and I. Chorkendorff, *Angew. Chem. Int. Ed.*, 2016, **55**, 1450–1454.

102 Y. Lum and J. W. Ager, *Nat. Catal.*, 2019, **2**, 86–93.

103 O. Piqué, F. Viñes, F. Illas and F. Calle-Vallejo, *ACS Catal.*, 2020, **10**, 10488–10494.

104 O. Piqué, M. Löffler, I. Katsounaros and F. Calle-Vallejo, *Electrochim. Acta*, 2021, **380**, 138247.

105 E. Pérez-Gallent, G. Marcandalli, M. C. Figueiredo, F. Calle-Vallejo and M. T. M. Koper, *J. Am. Chem. Soc.*, 2017, **139**, 16412–16419.

106 A. Murata and Y. Hori, *BCSJ*, 1991, **64**, 123–127.

107 M. R. Singh, Y. Kwon, Y. Lum, J. W. Ager and A. T. Bell, *J. Am. Chem. Soc.*, 2016, **138**, 13006–13012.

108 W. J. Durand, A. A. Peterson, F. Studt, F. Abild-Pedersen and J. K. Nørskov, *Surf. Sci.*, 2011, **605**, 1354–1359.

109 J. H. Montoya, C. Shi, K. Chan and J. K. Nørskov, *J. Phys. Chem. Lett.*, 2015, **6**, 2032–2037.

110 P. Khanipour, M. Löffler, A. M. Reichert, F. T. Haase, K. J. J. Mayrhofer and I. Katsounaros, *Angew. Chem. Int. Ed.*, 2019, **58**, 7273–7277.

111 M. Löffler, P. Khanipour, N. Kulyk, K. J. J. Mayrhofer and I. Katsounaros, *ACS Catal.*, 2020, **10**, 6735–6740.

112 S. Hanselman, M. T. M. Koper and F. Calle-Vallejo, *ACS Energy Lett.*, 2018, **3**, 1062–1067.

113 Y. Pang, J. Li, Z. Wang, C.-S. Tan, P.-L. Hsieh, T.-T. Zhuang, Z.-Q. Liang, C. Zou, X. Wang, P. De Luna, J. P. Edwards, Y. Xu, F. Li, C.-T. Dinh, M. Zhong, Y. Lou, D. Wu, L.-J. Chen, E. H. Sargent and D. Sinton, *Nat. Catal.*, 2019, **2**, 251–258.

114 X. Chang, A. Malkani, X. Yang and B. Xu, *J. Am. Chem. Soc.*, 2020, **142**, 2975–2983.

115 J. Hussain, H. Jónsson and E. Skúlason, *ACS Catal.*, 2018, **8**, 5240–5249.

116 A. A. Peterson, F. Abild-Pedersen, F. Studt, J. Rossmeisl and J. K. Nørskov, *Energy Environ. Sci.*, 2010, **3**, 1311–1315.

117 A. Rendón-Calle, S. Builes and F. Calle-Vallejo, *Appl. Catal. B*, 2020, **276** 119147.

118 X. Nie, M. R. Esopi, M. J. Janik and A. Asthagiri, *Angew. Chem. Int. Ed.*, 2013, **52**, 2459–2462.

119 K. J. P. Schouten, Y. Kwon, C. J. M. van der Ham, Z. Qin and M. T. M. Koper, *Chem. Sci.*, 2011, **2**, 1902–1909.

120 W. Luo, X. Nie, M. J. Janik and A. Asthagiri, *ACS Catal.*, 2016, **6**, 219–229.

121 D. Torres, N. Lopez, F. Illas and R. M. Lambert, *J. Am. Chem. Soc.*, 2005, **127**, 10774–10775.

122 K. J. P. Schouten, E. Pérez Gallent and M. T. M. Koper, *ACS Catal.*, 2013, **3**,

1292–1295.

123 S. Nitopi, E. Bertheussen, S. B. Scott, X. Liu, A. K. Engstfeld, S. Horch, B. Seger, I. E. L. Stephens, K. Chan, C. Hahn, J. K. Nørskov, T. F. Jaramillo and I. Chorkendorff, *Chem. Rev.*, 2019, **119**, 7610–7672.

124 O. Piqué, Q. H. Low, A. D. Handoko, B. S. Yeo and F. Calle-Vallejo, *Angew. Chem. Int. Ed.*, 2021, **60**, 10784–10790.

125 H. Li, F. Calle-Vallejo, M. J. Kolb, Y. Kwon, Y. Li and M. T. M. Koper, *J. Am. Chem. Soc.*, 2013, **135**, 14329–14338.

126 F. Calle-Vallejo, J. I. Martínez, J. M. García-Lastra, P. Sautet and D. Loffreda, *Angew. Chem. Int. Ed.*, 2014, **53**, 8316–8319.

127 Y. Hori, I. Takahashi, O. Koga and N. Hoshi, *J. Phys. Chem. B*, 2002, **106**, 15–17.

128 W. Tang, A. A. Peterson, A. S. Varela, Z. P. Jovanov, L. Bech, W. J. Durand, S. Dahl, J. K. Nørskov and I. Chorkendorff, *Phys. Chem. Chem. Phys.*, 2011, **14**, 76–81.

129 R. Kas, R. Kortlever, A. Milbrat, M. T. M. Koper, G. Mul and J. Baltrusaitis, *Phys. Chem. Chem. Phys.*, 2014, **16**, 12194–12201.

130 D. Ren, B. S.-H. Ang and B. S. Yeo, *ACS Catal.*, 2016, **6**, 8239–8247.

131 S. Lee, G. Park and J. Lee, *ACS Catal.*, 2017, **7**, 8594–8604.

132 E. L. Clark, C. Hahn, T. F. Jaramillo and A. T. Bell, *J. Am. Chem. Soc.*, 2017, **139**, 15848–15857.

133 D. Higgins, A. T. Landers, Y. Ji, S. Nitopi, C. G. Morales-Guio, L. Wang, K. Chan, C. Hahn and T. F. Jaramillo, *ACS Energy Lett.*, 2018, **3**, 2947–2955.

134 T. T. H. Hoang, S. Verma, S. Ma, T. T. Fister, J. Timoshenko, A. I. Frenkel, P. J. A. Kenis and A. A. Gewirth, *J. Am. Chem. Soc.*, 2018, **140**, 5791–5797.

135 Z. Chang, S. Huo, W. Zhang, J. Fang and H. Wang, *J. Phys. Chem. C*, 2017, **121**, 11368–11379.

136 J. Wang, Z. Li, C. Dong, Y. Feng, J. Yang, H. Liu and X. Du, *ACS Appl. Mater. Interfaces*, 2019, **11**, 2763–2767.

137 Y. Lum and J. W. Ager, *Energy Environ. Sci.*, 2018, **11**, 2935–2944.

138 Y. C. Li, Z. Wang, T. Yuan, D.-H. Nam, M. Luo, J. Wicks, B. Chen, J. Li, F. Li, F. P. G. de Arquer, Y. Wang, C.-T. Dinh, O. Voznyy, D. Sinton and E. H. Sargent, *J. Am. Chem. Soc.*, 2019, **141**, 8584–8591.

139 J. Huang, M. Mensi, E. Oveisi, V. Mantella and R. Buonsanti, *J. Am. Chem. Soc.*, 2019, **141**, 2490–2499.

140 L. R. L. Ting, O. Piqué, S. Y. Lim, M. Tanhaei, F. Calle-Vallejo and B. S. Yeo, *ACS Catal.*, 2020, **10**, 4059–4069.

141 H. Okamoto, D. J. Chakrabarti, D. E. Laughlin and T. B. Massalski, *JPE*, 1987, **8**, 454.

142 K. Räuchle, L. Plass, H.-J. Wernicke and M. Bertau, *Energy Technol.*, 2016, **4**, 193–200.

143 M. Rumayor, A. Dominguez-Ramos and A. Irabien, *J. Clean. Prod.*, 2019, **225**, 426–434.

144 T. Hatsukade, K. P. Kuhl, E. R. Cave, D. N. Abram, J. T. Feaster, A. L. Jongerius, C. Hahn and T. F. Jaramillo, *Energy Technol.*, 2017, **5**, 955–961.

145 Q. H. Low, N. W. X. Loo, F. Calle-Vallejo and B. S. Yeo, *Angew. Chem. Int. Ed.*, 2019, **58**, 2256–2260.

146 J. E. Pander, J. W. J. Lum and B. S. Yeo, *J. Mater. Chem. A*, 2019, **7**, 4093–4101.

147 Y. He, W.-J. Jiang, Y. Zhang, L.-B. Huang and J.-S. Hu, *J. Mater. Chem. A*, 2019, **7**, 18428–18433.

148 J. L. White and A. B. Bocarsly, *J. Electrochem. Soc.*, 2016, **163**, H410.

149 J. A. Dean, *Lange's Handbook of Chemistry. Section 6: Thermodynamic Properties.*, McGraw-Hill, Knoxville, 1999.

150 P. G. Russell, N. Kovac, S. Srinivasan and M. Steinberg, *J. Electrochem. Soc.*, 1977, **124**, 1329.

151 K. A. Adegoke, S. G. Radhakrishnan, C. L. Gray, B. Sowa, C. Morais, P. Rayess, E. R. Rohwer, C. Comminges, K. B. Kokoh and E. Roduner, *Sustain. Energy Fuels*, 2020, **4**, 4030–4038.

152 W. J. Teh, O. Piqué, Q. H. Low, W. Zhu, F. Calle-Vallejo and B. S. Yeo, *ACS Catal.*, 2021, **11**, 8467–8475.

153 Y. Yamamoto, S. Kasamatsu and O. Sugino, *J. Phys. Chem. C*, 2019, **123**, 19486–19492.

154 J. Greeley, J. K. Nørskov and M. Mavrikakis, *Annu. Rev. Phys. Chem.*, 2002, **53**, 319–348.

155 A. J. Medford, A. Vojvodic, J. S. Hummelshøj, J. Voss, F. Abild-Pedersen, F. Studt, T. Bligaard, A. Nilsson and J. K. Nørskov, *J. Catal.*, 2015, **328**, 36–42.

156 R. B. Levy and M. Boudart, *Science*, 1973, **181**, 547–549.

157 M. G. Quesne, A. Roldan, N. H. de Leeuw and C. R. A. Catlow, *Phys. Chem. Chem. Phys.*, 2018, **20**, 6905–6916.

158 S. M. Davis and Somorjai, G. A., *The Chemical Physics of Solid Heterogeneous Catalysis: Fundamental Studies of Heterogeneous Catalysis*, Elsevier, Amsterdam, 1982.

159 S. Vajda, M. J. Pellin, J. P. Greeley, C. L. Marshall, L. A. Curtiss, G. A. Ballentine, J. W. Elam, S. Catillon-Mucherie, P. C. Redfern, F. Mehmood and P. Zapol, *Nat. Mater.*, 2009, **8**, 213–216.

160 D. J. Moodley, J. van de Loosdrecht, A. M. Saib, M. J. Overett, A. K. Datye and J. W. Niemantsverdriet, *Appl. Catal. A*, 2009, **354**, 102–110.

161 D. Teschner, J. Borsodi, A. Wootsch, Z. Révay, M. Hävecker, A. Knop-Gericke, S. D. Jackson and R. Schlögl, *Science*, 2008, **320**, 86–89.

162 A. Reina, S. Thiele, X. Jia, S. Bhaviripudi, M. S. Dresselhaus, J. A. Schaefer and J. Kong, *Nano Res.*, 2009, **2**, 509–516.

163 J.-M. Aguiar-Hualde, Y. Magnin, H. Amara and C. Bichara, *Carbon*, 2017, **120**, 226–232.

164 P. Janthon, F. Viñes, J. Sirijaraensre, J. Limtrakul and F. Illas, *Catal. Sci. Technol.*, 2017, **7**, 807–816.

165 B. Martínez, O. Piqué, H. Prats, F. Viñes and F. Illas, *Appl. Surf. Sci.*, 2020, **513**, 145765.

166 F. Viñes, J. R. B. Gomes and F. Illas, *Chem. Soc. Rev.*, 2014, **43**, 4922–4939.

167 J. Ruvireta, L. Vega and F. Viñes, *Surf. Sci.*, 2017, **664**, 45–49.

168 P. Janthon, S. (Andy) Luo, S. M. Kozlov, F. Viñes, J. Limtrakul, D. G. Truhlar and F. Illas, *J. Chem. Theory Comput.*, 2014, **10**, 3832–3839.

169 A. U. Nilekar, J. Greeley and M. Mavrikakis, *Angew. Chem. Int. Ed.*, 2006, **45**, 7046–7049.

Appendix A

Supporting Information for "Elucidating the Structure of Ethanol-Producing Active Sites at Oxide-Derived Cu Electrocatalysts"

Supplementary Information

Elucidating the Structure of Ethanol-Producing Active Sites at Oxide-Derived Cu Electrocatalysts

Oriol Piqué, Francesc Viñes, Francesc Illas, and Federico Calle-Vallejo*

Departament de Ciència de Materials i Química Física & Institut de Química Teòrica i Computacional (IQTCUB), Universitat de Barcelona, Martí i Franquès 1, 08028 Barcelona, Spain.

*Email: f.calle.vallejo@ub.edu

Table of contents

S1. Gas-phase corrections

The free energies of gas-phase molecules were estimated as: $G = E_{DFT} + ZPE - TS$. The ZPE (from vibrational frequency analyses) and TS values (from thermodynamic tables[1]) at 298.15K used for gas-phase species featured in this study are listed in Table S1. Since the PBE exchange-correlation functional does not describe correctly the free energy of $CO_{(g)}$ and $CO_{2(g)}$,[2-4] corrections to their formation energies of -0.24 and 0.19 eV were applied, respectively.

Table S1. Zero-point energy and entropy contributions to the free energies of gas-phase molecules. All values are in eV.

Molecule	ZPE	TS
CO_2	0.31	0.66
CO	0.14	0.61
H_2	0.27	0.40
C_2H_4	1.36	0.68
H_2O	0.57	0.58
CH_3CHO	1.47	0.82
C_2H_5OH	2.11	0.87

S2. Liquid-phase corrections

Some of the main products of CO_2 reduction on Cu such as water, ethanol, and acetaldehyde are formed in the liquid phase. Their free energies are estimated using the method described in Ref. 2, which is based on a correction to the TS values. The liquid-phase free energies of water, ethanol, and acetaldehyde were estimated using TS values of 0.67, 0.94, and 0.87 eV, respectively.

S3. Solvation contributions to the free energies

Solvation contributions to the free energies of the adsorbates (E_{sol} in $G = E_{DFT} + ZPE - TS + E_{sol}$) were modeled as an external correction depending on the chemical nature of the adsorbates. We used the values reported in previous works[2] and added a new correction for *OR adsorbates (see Table S2), which we approximate as 2/3 of the *ROH correction, where R represents a hydrocarbon chain. The 2/3 factor is justified by the fact that *ROH can, in principle, make three hydrogen bonds via *OH (two via the

O moiety and one via the H moiety in *OH), while *OR can only make two. The specific values used are listed in Table S2.

Table S2. Solvation corrections depending on the adsorbates' chemical nature. All values are provided in eV.

Functional group	Solvation Correction
*CO	-0.10
*OH	-0.50
*ROH	-0.38
*OR	-0.25

S4. Adsorption energies

The ZPE, TS_{vib}, solvation energy (E_{sol}), and the corresponding ΔG values obtained for the different adsorbates featured in this study are listed below. Only the most stabilizing possibility among the following three options appear in Table S3: solvated by water, interacting with K, or both. The most stable situation for each adsorbate (denoted MSS) is indicated below. *C_2O_2H is a special case where one functional group of the molecule interacts with the K atom and a solvation correction for the other group is included. Liquid acetaldehyde was considered when it was more stable than its adsorbed counterpart. Note that $2CO_{(g)}$ were used as a reference for the free energies in Table S3.

Table S3. Free energies of adsorption and its contributions for each species involved in CO_2 electroreduction to CO. All values are in eV.

Cu(100)	ZPE	TS_{vib}	MSS	ΔG
2 *CO	0.36	0.33	With K (-0.34)	-0.56
*C_2O_2H	0.69	0.26	K (-0.63) + Solvated (-0.38)	-0.06
*C_2O	0.34	0.19	With K (-0.31)	-0.98
*CHCO	0.60	0.24	With K (-0.34)	-0.70
*CHCHO	0.91	0.17	With K (-0.31)	-0.79
*CH_2CHO	1.21	0.20	Solvated (-0.25)	-1.05
*CH_3CHO	1.47	0.87	Liquid	-1.08
*CH_3CH_2O	1.83	0.30	Solvated (-0.25)	-1.48
*O	0.06	0.05	With K (-0.34)	-1.15
*OH	0.34	0.10	Solvated (-0.50)	-1.68

4AD@Cu(100)	ZPE	TS_{vib}	MSS	ΔG
2 *CO	0.37	0.38	Solvated (-0.20)	-0.66
*C_2O_2H	0.70	0.26	K (-0.55) + Solvated (-0.38)	-0.14
*C_2O	0.33	0.19	Solvated (-0.10)	-0.76
*CHCO	0.60	0.24	Solvated (-0.10)	-0.77
*CHCHO	0.90	0.17	Solvated (-0.25)	-1.03
*CH_2CHO	1.21	0.20	With K (-0.29)	-1.36
*CH_3CHO	1.48	0.32	Solvated (-0.25)	-1.22
*CH_3CH_2O	1.83	0.30	With K (-0.39)	-1.71
*O	0.06	0.05	With K (-0.04)	-0.76
*OH	0.35	0.09	Solvated (-0.50)	-1.81

Cu(111)	ZPE	TS_{vib}	MSS	ΔG
2 *CO	0.35	0.36	With K (-0.25)	-0.40
*C_2O_2H	0.71	0.31	K (-0.28) + Solvated (-0.38)	1.12
*C_2O	0.34	0.19	With K (-0.34)	-0.46
*CHCO	0.60	0.24	With K (-0.26)	-0.35
*CHCHO	0.90	0.18	With K (-0.37)	-0.44
*CH_2CHO	1.19	0.20	With K (-0.48)	-0.78
*CH_3CHO	1.47	0.87	Liquid	-1.08
*CH_3CH_2O	1.84	0.31	Solvated (-0.25)	-0.90
*O	0.07	0.04	With K (-0.42)	-0.74
*OH	0.34	0.08	Solvated (-0.50)	-1.04

4AD@Cu(111)	ZPE	TS_{vib}	MSS	ΔG
2 *CO	0.37	0.40	Solvated (-0.20)	-0.83
*C_2O_2H	0.71	0.25	K (-0.43) + Solvated (-0.38)	-0.17
*C_2O	0.34	0.19	With K (-0.18)	-0.82
*CHCO	0.61	0.23	Solvated (-0.10)	-0.86
*CHCHO	0.90	0.18	With K (-0.31)	-1.16
*CH_2CHO	1.21	0.25	With K (-0.36)	-1.59
*CH_3CHO	1.48	0.26	Solvated (-0.25)	-1.25
*CH_3CH_2O	1.84	0.32	Solvated (-0.25)	-1.69
*O	0.07	0.04	With K (-0.12)	-1.00
*OH	0.34	0.09	Solvated (-0.50)	-1.85

The direct coordinates of the systems appear in section S9. In Figures S1-S4 we show each adsorbate in their most stable situation (MSS). *C_2O_2, *C_2O_2H, *CHCHO and *CH_2CHO are bidentate and bind in bridge-to-bridge or bridge-to-top configurations. *CO, *C_2O, *CHCO, *CH_3CHO, *CH_3CH_2O, *O, and *OH are monodentate. Most of the latter adsorbates bind on bridge or top sites, except for *O and *C_2O, which bind at hollow sites. According to Figures S1-S4, adsorbate-cation stabilizing interactions are more frequent at flat terraces.

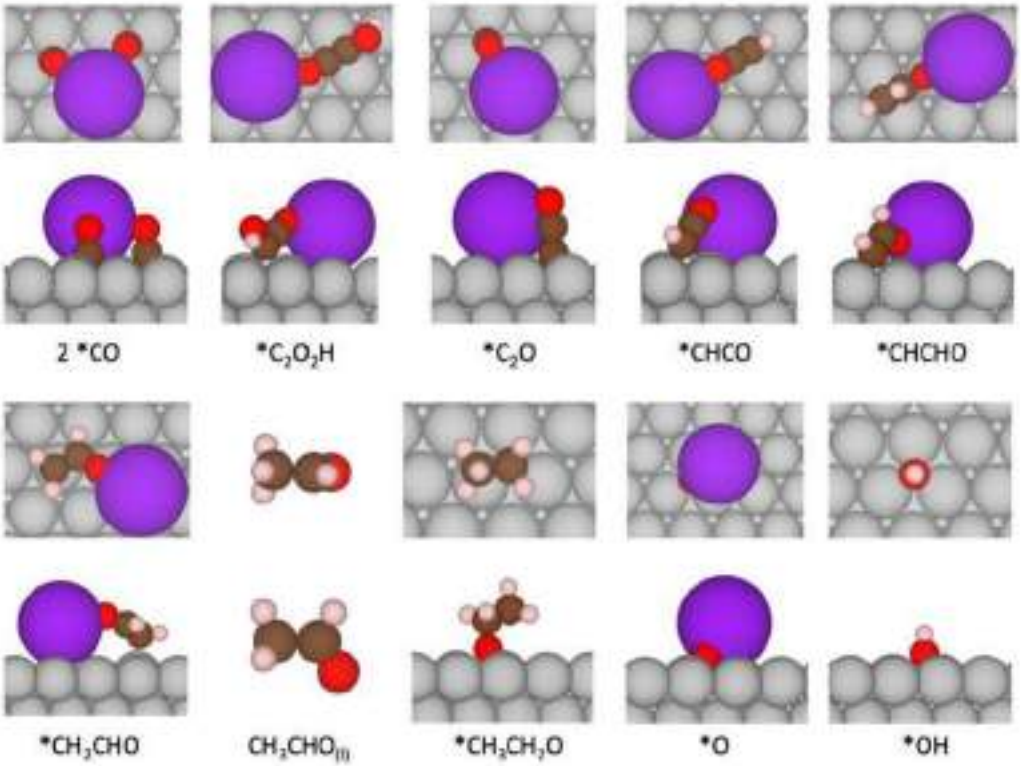

Figure S1. Most stable configurations for each adsorbate on Cu(111). Top and side views are provided in each case. Grey, brown, red, purple and pink represent Cu, C, O, K, and H atoms.

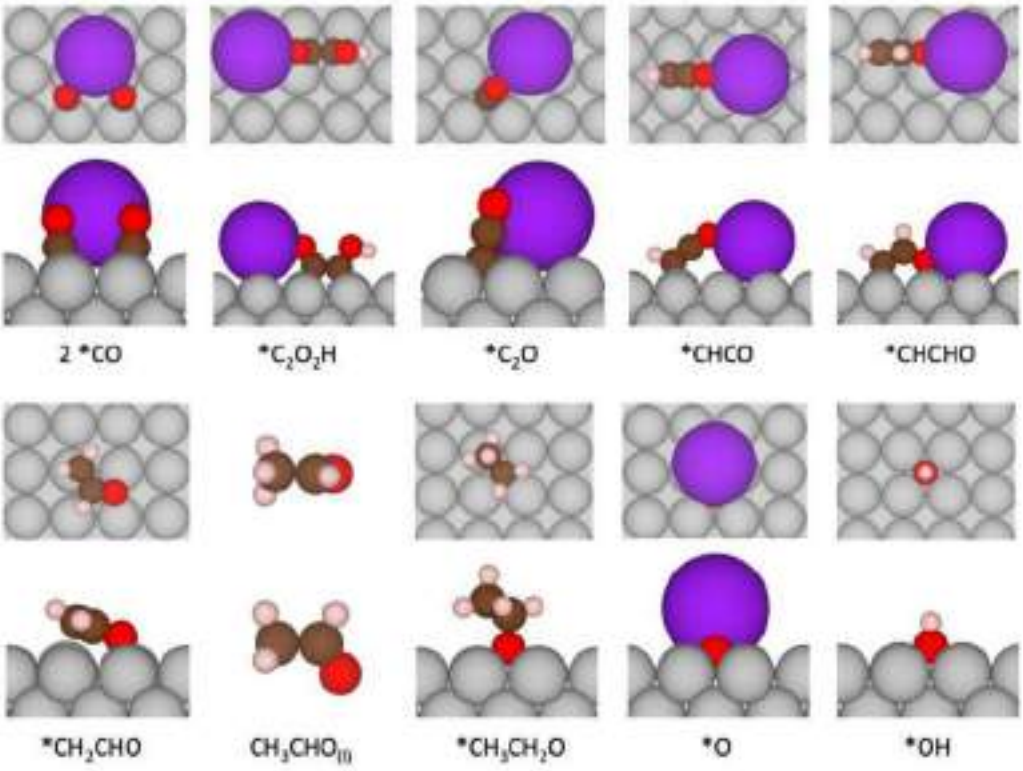

Figure S2. Most stable configurations for each adsorbate on Cu(100). Top and side views are provided in each case. Grey, brown, red, purple and pink represent Cu, C, O, K, and H atoms.

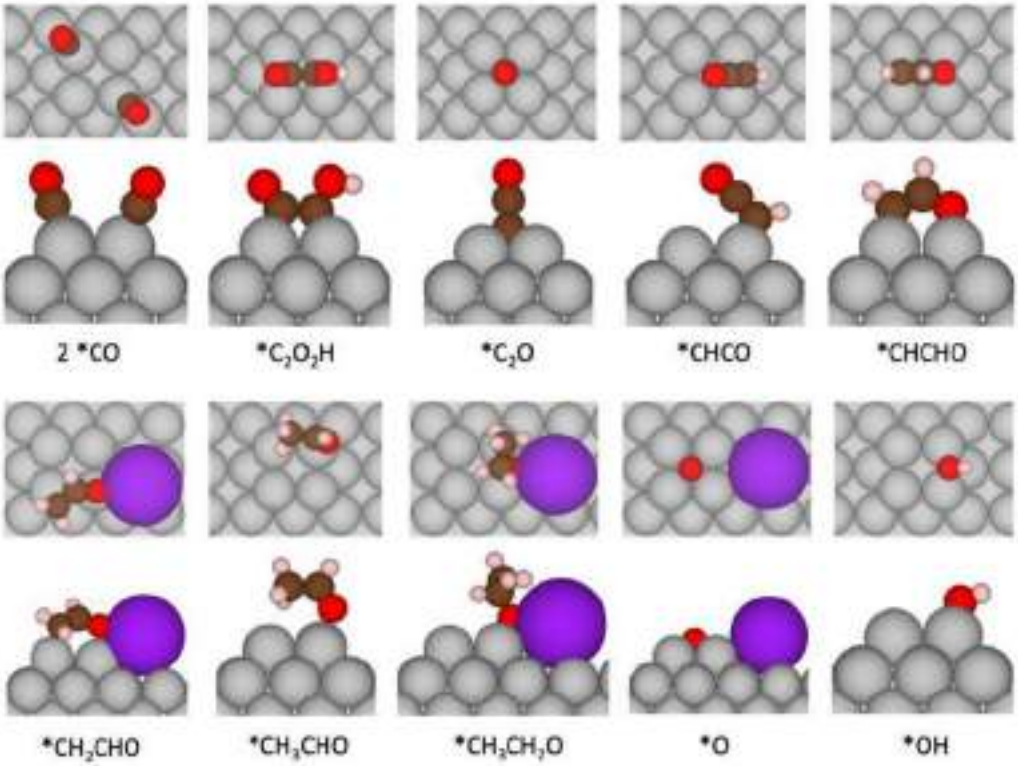

Figure S3. Most stable configurations for each adsorbate on 4AD@Cu(100). Top and side views are provided in each case. Grey, brown, red, purple and pink represent Cu, C, O, K, and H atoms.

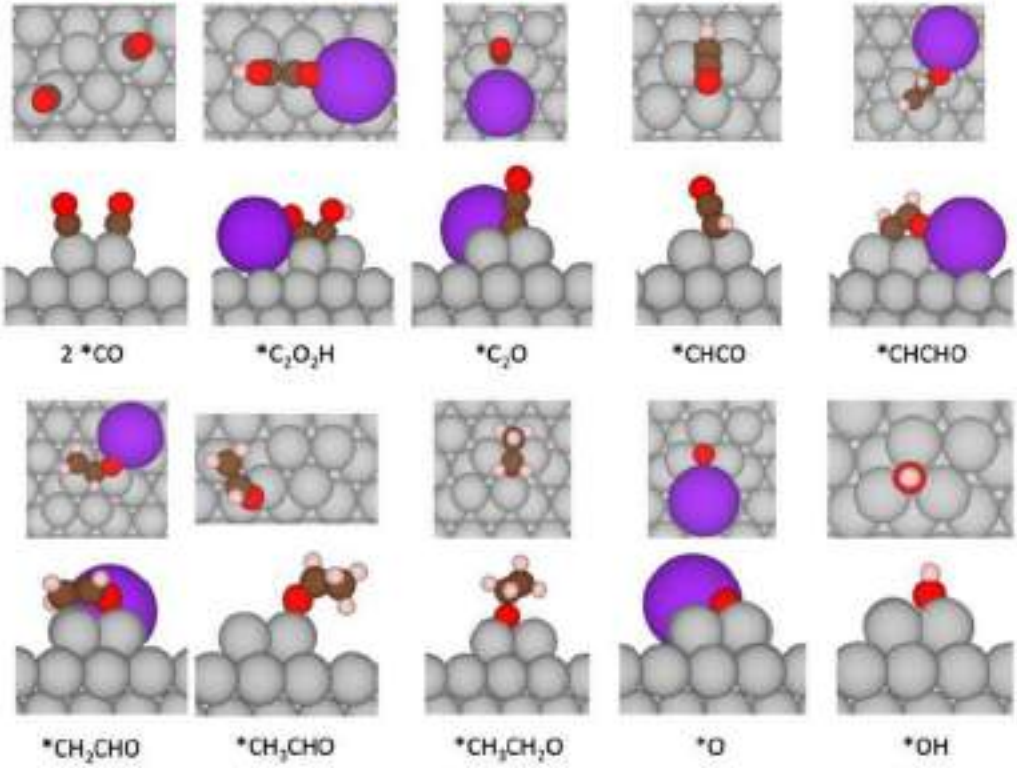

Figure S4. Most stable configurations for each adsorbate on 4AD@Cu(111). Top and side views are provided in each case. Grey, brown, red, purple and pink represent Cu, C, O, K, and H atoms.

Figure S5 shows the adsorption energies of 2*CO on the four studied models as a function of the coordination number of the active sites.

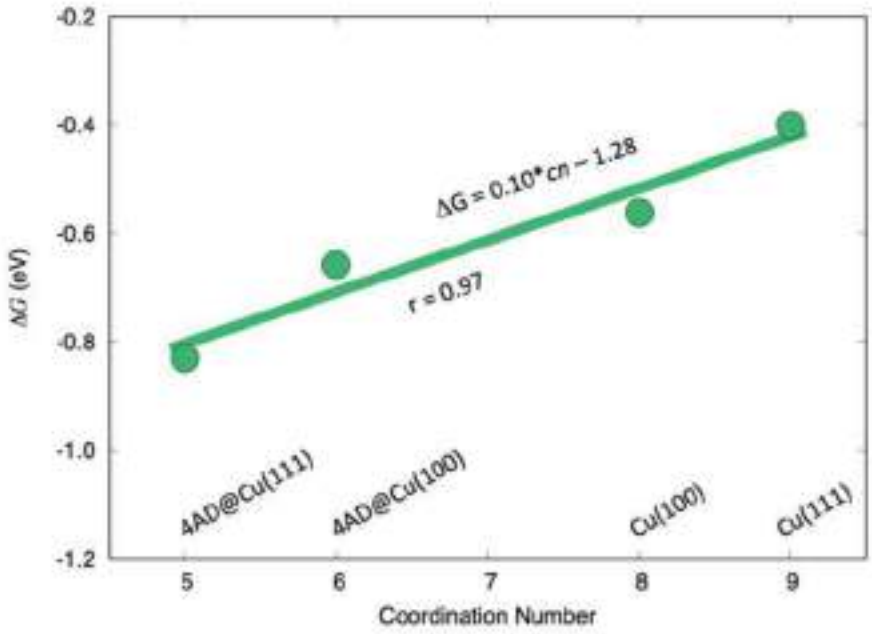

Figure S5. Adsorption free energies of 2*CO plotted as a function of the coordination number (*cn*) of the active sites. The least-squares linear fit and the regression coefficient are provided as insets.

S5. Stability of the 4-atom Cu islands

We analyzed the thermal and electrochemical stability of the Cu adatom clusters. To this end, we adsorbed 1, 2, 3, and 4 Cu adatoms on Cu(100) and Cu(111). A good indication of the thermal stability is the average adsorption energy of the clusters, defined as:

$$* + nCu^{2+} + 2ne^{-} \rightarrow * - nCu \quad \text{(S1)}$$

$$\Delta E_{ADS} = \left(E_{*_{-nCu}} - E_{*} - n\mu_{Cu^{2+}} \right) / n \quad \text{(S2)}$$

where $E_{*_{-nCu}}$ is the total energy of the system containing the Cu(100) or Cu(111) slabs and n Cu adatoms, E_* is the total energy of the pristine Cu(100) or Cu(111) slabs, and $\mu_{Cu^{2+}}$ is the chemical potential Cu^{2+} in solution, assessed by means of Strasser et al's method.[5] The results are shown in the second and third columns of Table S4.

Table S4. Average adsorption energies (ΔE_{ADS}, in eV/atom) of Cu clusters of 1-4 atoms on Cu(100) and Cu(111) surfaces, together with the corresponding deposition/dissolution potentials (U_{dd} in V vs RHE).

n	ΔE_{ADS} @ Cu(100)	ΔE_{ADS} @ Cu(111)	U_{dd} @ Cu(100)	U_{dd} @ Cu(111)
1	-0.13	0.11	0.07	-0.05
2	-0.29	0.01	0.14	-0.01
3	-0.33	-0.06	0.17	0.03
4	-0.41	-0.15	0.20	0.07

The adsorption energies are generally negative, indicating favorable adsorption of Cu^{2+} species in solution. As more adatoms are present (i.e. as n grows), the adsorption energies become more negative, given that more and more Cu-Cu bonds are made between the cluster and the surface, and also within the cluster. Most importantly, the adatoms adsorbed on Cu(100) are in each case more stable than those on Cu(111), because there are systematically more Cu-Cu bonds in the former compared to the latter: for instance, Cu atoms sit at fourfold and threefold hollow sites on Cu(100) and Cu(111), so at least for small clusters it is more stable to deposit on Cu(100) surfaces.

Furthermore, in the fourth and fifth columns of Table S4 we also evaluated the electrochemical stability of Cu clusters on Cu(111) and Cu(100) by normalizing the results of Equation S2 by the number of electrons transferred. This gives raise to the potentials for the deposition/dissolution of the Cu clusters (denoted U_{dd}). The clusters on Cu(100) dissolve at more positive potentials than those at Cu(111) and, as the cluster size grows, U_{dd} tends to the bulk dissolution potential of Cu of 0.34 V vs RHE.

From Table S4 we also conclude that the analyzed clusters are under cathodic protection when subjected to the typical potentials used for CO_2 and CO electrolysis ($U < -0.4$ V vs RHE). If OD-Cu catalysts are prepared by applying initially positive (oxidizing) potentials and then negative (reducing) potentials,[6,7] our results imply that the adatoms will likely be dissolved first and later redeposited. This analysis is a first approximation to be complemented by considerations on the surface oxidation of Cu.

S6. Cation effects

To model cation effects, we followed Janik *et al.*'s approach,[8] which we also used successfully in the past to capture cation effects.[9] Neutral K atoms are added but their low electronegativity makes them donate their *s* electron, so that they are effectively ionic in the calculations, whereas the lost electron is smeared within the metal slab (this

was verified by Bader charge analyses). For completeness, we performed DFT calculations subtracting one electron of the system on the most stable geometries featuring K atoms for Cu(100). In Table S5 we show the absolute value of the free energy differences for the most stable geometry with a K atom and the same geometry but withdrawing one electron from the system for all the studied adsorbates on Cu(100) ($\left|\Delta G_{Nv^-} - \Delta G_{Nv^- -1}\right|$). We can safely conclude that withdrawing one electron from the system has a small effect on the adsorption free energies, so that neutral slab calculations are suitable to capture cation effects.

Table S5. Absolute value of the free energy differences for the most stable geometry with a K atom (ΔG_{Nv^-}) and the same geometry but withdrawing one electron from the system ($\Delta G_{Nv^- -1}$) for all the studied adsorbates on Cu(100). All values are in eV.

Adsorbate	$\left\|\Delta G_{Nv^-} - \Delta G_{Nv^- -1}\right\|$
2 *CO	0.02
*C_2O_2H	0.01
*C_2O	0.07
*CHCO	0.00
*CHCHO	0.03
*CH_2CHO	0.05
*CH_3CHO	0.07
*CH_3CH_2O	0.03
*O	0.04
*OH	0.02

Because of steric hindrance, it is unlikely that a given adsorbate moiety be simultaneously water-solvated and cation-stabilized. Table S3 in the SI shows which interaction dominates for each adsorbate on each facet. To discern this, we performed calculations with different initial positions for the K atom around the adsorbate and kept the most stable geometry of all of them. Then, we compared the free energies of the most stable geometry with the K atom and the vacuum geometry plus the water solvation correction and kept the most stable one.

S7. Alternative pathways

In the article by Cheng et al,[10] the proposed pathway to ethylene proceeds as: 2*CO → *C_2O_2 → *COCOH → *COHCOH → *CCOH → *CHCOH → *CCH → *CCH_2 →

*$CHCH_2$ → * + C_2H_4, which coincides with ours up to *COCOH. We computed Cheng et al's pathway (deemed pathway I) based on previous results[2] on Cu(100) calculated in nearly the same way as in this work, except for the inclusion of cation effects and a slightly different plane-wave cutoff. Table S6 contains the formation energies of the intermediates in Pathway I and in our pathway (deemed pathway II), the missing intermediates are identical.

Table S6. Formation energies with respect to $2CO_{(g)}$, protons and electrons, of the CORR intermediates to C_2H_4 following two different pathways. N is the number of electrons transferred to $2CO_{(g)}$ to form the species. The free energies include solvation corrections but no cation effects. All values are in eV.

N	pathway I[10]	ΔG_I^f	pathway II[2]	ΔG_{II}^f	$\Delta G_{II}^f - \Delta G_I^f$
2	*COHCOH	-0.06	*CCO + H_2O	-0.80	-0.75
3	*CCOH + H_2O	0.09	*CHCO	-0.48	-0.57
4	*CHCOH	-0.42	*CHCHO	-0.64	-0.21
5	*CCH + H_2O	-0.37	*CH_2CHO	-0.88	-0.52
6	*CCH_2	-0.50	*O + C_2H_4	-0.87	-0.38
7	*$CHCH_2$	-0.63	*OH	-1.68	-1.04

The last column of Table S6 shows large, negative differences between the intermediates of both pathways for the same N, indicating that, at this level of theory, the intermediates in pathway II are more stable than those in pathway I. While some of the intermediates may be stabilized by cation effects (see Table S3), the differences in Table S6 are large enough for us to anticipate no variations in pathway II. Figure S6 provides a comparison between pathway I and pathway II.

Lum *et al.*[11] put to the test the notion that the oxygen atoms in the oxygenate products of CORR come exclusively from CO_2. The authors proposed a mechanism involving the simultaneous transfer of H^+ to the C end and OH^- to the CH end of an ethynyl intermediate (*C-CH) from water molecules in a Grotthuss chain. Later, Clark et al[12] pointed out that Lum et al's pathway is consistent with experiments but is not the most favorable one. They claim that the experimental observations can also be explained by the isotopic scrambling of acetaldehyde with water ($CH_3CHO + H_2O \leftrightarrow CH_3CH(OH_2)$),[13] which is a known intermediate of the CORR to ethanol.[14-16]

Acetaldehyde is formed in our pathway to ethanol, so that its scrambling is possible but would not appreciably change the free-energy diagrams. On the other hand, the pathway in the work of Lum *et al.*[11] branches from that of Cheng *et al.*,[10] which is

not the most stable pathway according to our free energy analysis (see Figure S6 and Table S6), so a direct comparison is not straightforward.

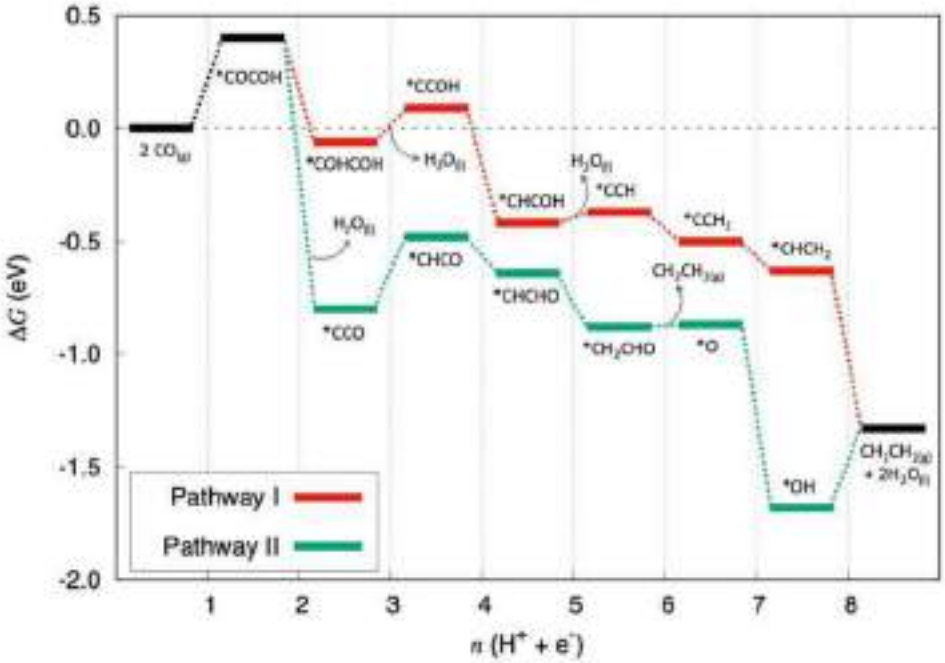

Figure S6. Free energy diagram for CO reduction to ethylene on Cu(100) via pathway I (red) and pathway II (green).

S8. CO coupling kinetics

In a common interpretation in electrochemistry, the symmetry factor (β) corresponds to the fraction of an electron that has been transferred up to the transition state in a cathodic reaction.[17] Here, we calculated the CO-CO coupling barrier, which implies the transfer of an electron ($*CO + *CO + e^- \rightarrow *C_2O_2^-$), whereas the proton is transferred subsequently ($*C_2O_2^- + H^+ \rightarrow *C_2O_2H$). Since $*C_2O_2$ is highly electronegative, the Bader charge analysis shows that it contains ~0.9 additional electrons with respect to gas-phase C_2O_2, while 2*CO contains nearly the same number of electrons as $2CO_{(g)}$. Therefore, we assumed $\beta \approx 0.9$ and, as a first approximation, the barrier was calculated in vacuum via the CI-NEB method.[18] The potential-dependent activation energy ($\Delta G_{act}(U)$) is given as:[2]

$$\Delta G_{act}(U) = \Delta G^{0}_{act} + \beta eU \qquad \text{(S3)}$$

where ΔG^{0}_{act} is the barrier calculated in vacuum. This is a special case applied to decoupled electron transfers of the more general method by Asthagiri *et al.*[19] for the

approximation of constant-potential electrochemical hydrogenation barriers. As there is no experimental evidence for the decoupling of other electrochemical steps during CORR to C_2 species, in terms of kinetics, here we only considered CO-CO coupling.

S10. References

(1) CRC Handbook of Chemistry and Physics. 85th ed.; Lide, D. R., Ed. CRC Press: Boca Raton, FL, 2005.

(2) Calle-Vallejo, F.; Koper, M. T. M. Theoretical Considerations on the Electroreduction of CO to C2 Species on Cu(100) Electrodes. *Angew. Chem.* **2013**, 125, 7423-7426.

(3) Peterson, A. A.; Abild-Pedersen, F.; Studt, F.; Rossmeisl, J.; Norskov, J. K. How Copper Catalyzes the Electroreduction of Carbon Dioxide into Hydrocarbon Fuels. *Energy Environ. Sci.* **2010**, 3, 1311-1315.

(4) Christensen, R.; Hansen,H. A.; Vegge, T. Identifying Systematic DFT Errors in Catalytic Reactions. *Catalysis Science & Technology* **2015**, 5, 4946-4949.

(5) Strasser, P.; Koh, S.; Greeley, J. Voltammetric Surface Dealloying of Pt Bimetallic Nanoparticles: An Experimental and DFT Computational Analysis. *Phys. Chem. Chem. Phys.* **2008**, 10, 3670–3683.

(6) Arán-Ais, R. M.; Scholten, F.; Kunze, S.; Rizo, R.; Roldan Cuenya, B. The Role of in Situ Generated Morphological Motifs and Cu(i) Species in C_{2+} Product Selectivity during CO_2 Pulsed Electroreduction. *Nat. Energy* **2020**, 5, 317–325.

(7) Khanipour, P.; Löffler, M.; Reichert, A. M.; Haase, F. T.; Mayrhofer, K. J. J.; Katsounaros, I. Electrochemical Real-Time Mass Spectrometry (EC-RTMS): Monitoring Electrochemical Reaction Products in Real Time. *Angew. Chem. Int. Ed.* **2019**, 58, 7273–7277.

(8) Akhade, S. A.; McCrum, I. T.; Janik, M. J. The Impact of Specifically Adsorbed Ions on the Copper-Catalyzed Electroreduction of CO_2. *J. Electrochem. Soc.* **2016**, 163, F477.

(9) Pérez-Gallent, E.; Marcandalli, G.; Figueiredo, M. C.; Calle-Vallejo, F.; Koper, M. T. M. Structure- and Potential-Dependent Cation Effects on CO Reduction at Copper Single-Crystal Electrodes. *J. Am. Chem. Soc.* **2017**, 139, 16412–16419.

(10) Cheng, T.; Xiao, H.; Goddard, W. A. Full Atomistic Reaction Mechanism with Kinetics for CO Reduction on Cu(100) from Ab Initio Molecular Dynamics Free-Energy Calculations at 298 K. *Proc. Natl. Acad. Sci.* **2017**, 114, 1795–1800.

(11) Lum, Y.; Cheng, T.; Goddard, W. A.; Ager, J. W. Electrochemical CO Reduction Builds Solvent Water into Oxygenate Products. *J. Am. Chem. Soc.* **2018**, 140, 9337–9340.

(12) Clark, E. L.; Wong, J.; Garza, A. J.; Lin, Z.; Head-Gordon, M.; Bell, A. T. Explaining the Incorporation of Oxygen Derived from Solvent Water into the Oxygenated Products of CO Reduction over Cu. *J. Am. Chem. Soc.* **2019**, 141, 4191–4193.

(13) Greenzaid, P.; Luz, Z.; Samuel, David. A Nuclear Magnetic Resonance Study of the Reversible Hydration of Aliphatic Aldehydes and Ketones. II. The Acid-Catalyzed Oxygen Exchange of Acetaldehyde. *J. Am. Chem. Soc.* **1967**, 89, 756–759.

(14) Ledezma-Yanez, I.; Gallent, E. P.; Koper, M. T. M.; Calle-Vallejo, F. Structure-Sensitive Electroreduction of Acetaldehyde to Ethanol on Copper and Its Mechanistic Implications for CO and CO_2 Reduction. *Catal. Today* **2016**, 262, 90–94.

(15) Schouten, K. J. P.; Kwon, Y.; Ham, C. J. M. van der; Qin, Z.; Koper, M. T. M. A New Mechanism for the Selectivity to C_1 and C_2 Species in the Electrochemical Reduction of Carbon Dioxide on Copper Electrodes. *Chem. Sci.* **2011**, 2, 1902–1909.

(16) Bertheussen, E.; Verdaguer-Casadevall, A.; Ravasio, D.; Montoya, J. H.; Trimarco, D. B.; Roy, C.; Meier, S.; Wendland, J.; Nørskov, J. K.; Stephens, I. E. L.; Chorkendorff, I. Acetaldehyde as an Intermediate in the Electroreduction of Carbon

Monoxide to Ethanol on Oxide-Derived Copper. *Angew. Chem. Int. Ed.* **2016**, 55, 1450–1454.

(17) Guidelli, R.; Compton, R. G.; Feliu, J. M.; Gileadi, E.; Lipkowski, J.; Schmickler, W.; Trasatti, S. Defining the Transfer Coefficient in Electrochemistry: An Assessment (IUPAC Technical Report). *Pure Appl. Chem.* **2014**, 86, 245–258.

(18) Henkelman, G., Uberuaga, B. P. & Jónsson, H. A climbing image nudged elastic band method for finding saddle points and minimum energy paths. *J. Chem. Phys.* **2000**, 113, 9901–9904.

(19) Nie, X.; Luo, W.; Janik, M. J.; Asthagiri, A. Reaction Mechanisms of CO_2 Electrochemical Reduction on Cu(111) Determined with Density Functional Theory. *J. Catal.* **2014**, 312, 108–122.

Appendix B

Supporting Information for "Computational-Experimental Study of the Onset Potentials for CO_2 Reduction on Polycrystalline and Oxide-Derived Copper Electrodes"

Supporting Information

Computational-Experimental Study of the Onset Potentials for CO_2 reduction on Polycrystalline and Oxide-Derived Copper Electrodes

Oriol Piqué,[1] Mario Löffler,[2,3] Ioannis Katsounaros,[2,*] and Federico Calle-Vallejo[1,*]

[1] Department of Materials Science and Physical Chemistry & Institute of Theoretical and Computational Chemistry (IQTCUB), University of Barcelona, Marti i Franquès 1, 08028 Barcelona, Spain.

[2] Helmholtz Institute Erlangen-Nürnberg for Renewable Energy (IEK-11), Forschungszentrum Jülich GmbH, Egerlandstr. 3, 91058 Erlangen, Germany.

[3] Department of Chemical and Biological Engineering, Friedrich-Alexander-Universität Erlangen-Nürnberg (FAU), Egerlandstr. 3, 91058 Erlangen, Germany

*Emails: i.katsounaros@fz-juelich.de, f.calle.vallejo@ub.edu

Table of contents

S1 Onset potential determination from mass ion signals

In electrochemical real-time mass spectrometry, mass ion signals are recorded as a response to an electrochemical excitation. Let us assume that such an electrochemical excitation leads to the occurrence of a reaction and the formation of a product at time $t = t_0$. As a result, the mass ion signal for that product rises from the background at a time $t = t_0 + \Delta t$. The finite response time Δt is caused by the transport of the product together with the electrolyte from the cell to the mass spectrometer through the tubings and the respective inlet system for each setup. The response time Δt can be determined from electrochemical pulse experiments by subtracting the time stamps of the electrochemical excitation and the mass spectrometer signature.

Moreover, when no electrochemical reaction takes place, the mean (μ) and standard deviation (σ) of the recorded background signal in the mass spectrometer are defined. We calculated the μ and σ from at least 100 data points, to have sufficient statistics as illustrated in Figure S1 over 50 seconds. If now, as depicted in Figure S1, a linear sweep voltammogram starts from a potential E_{start} (-0.4 V_{RHE} in the figure) at $t = t_0 = 0$, the mass spectrometer signal rises to $\mu+\sigma$ at time $t = \Delta t + t_1$, where t_1 is the time needed to reach the potential E_{onset} where the product is detected. Clark and Bell use the one-sigma level as "detection limit" [1]. The one-sigma level above the mean background signal ensures that natural fluctuations in the mass spectrometer signal are cancelled out. Knowing the t_1, the E_{onset} can be calculated using the sweep rate, υ, from the equation: $E_{onset} = E_{start} - t_1 \upsilon$, for a negative-going scan. The potential applied vs the Ag/AgCl reference electrode is calculated vs the reversible hydrogen electrode and post-corrected for the iR drop according to a previously described procedure [2].

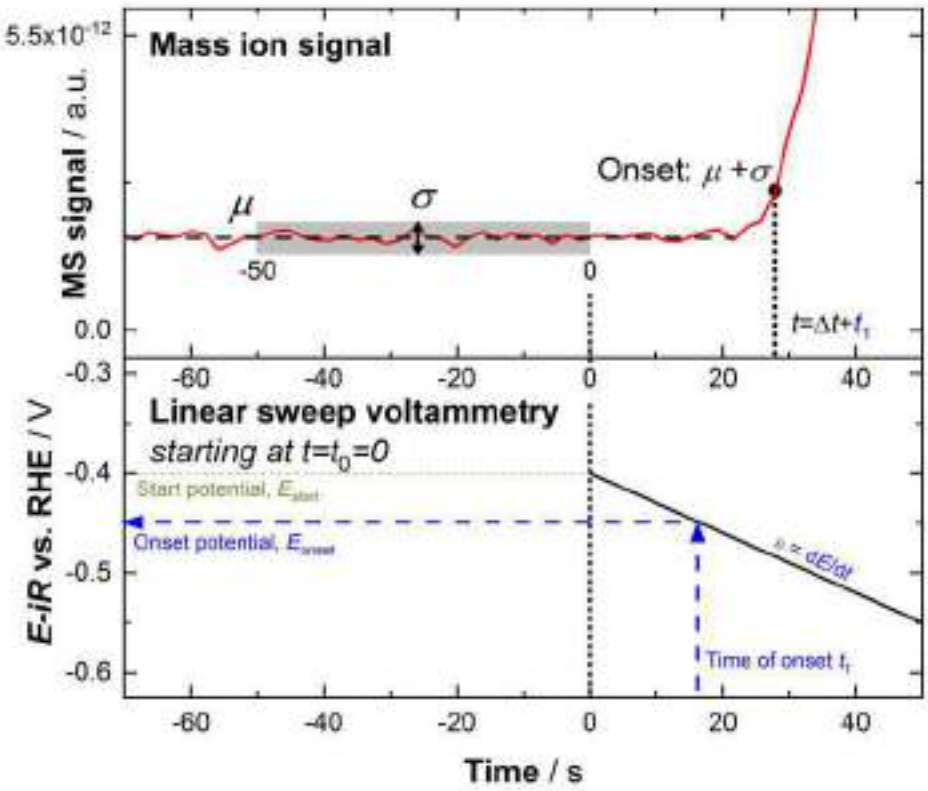

Figure S1. Determination of the onset potential from mass spectrometer signals resulting from the application of linear sweep voltammetry.

S2 Representative linear sweep voltammetry measurements

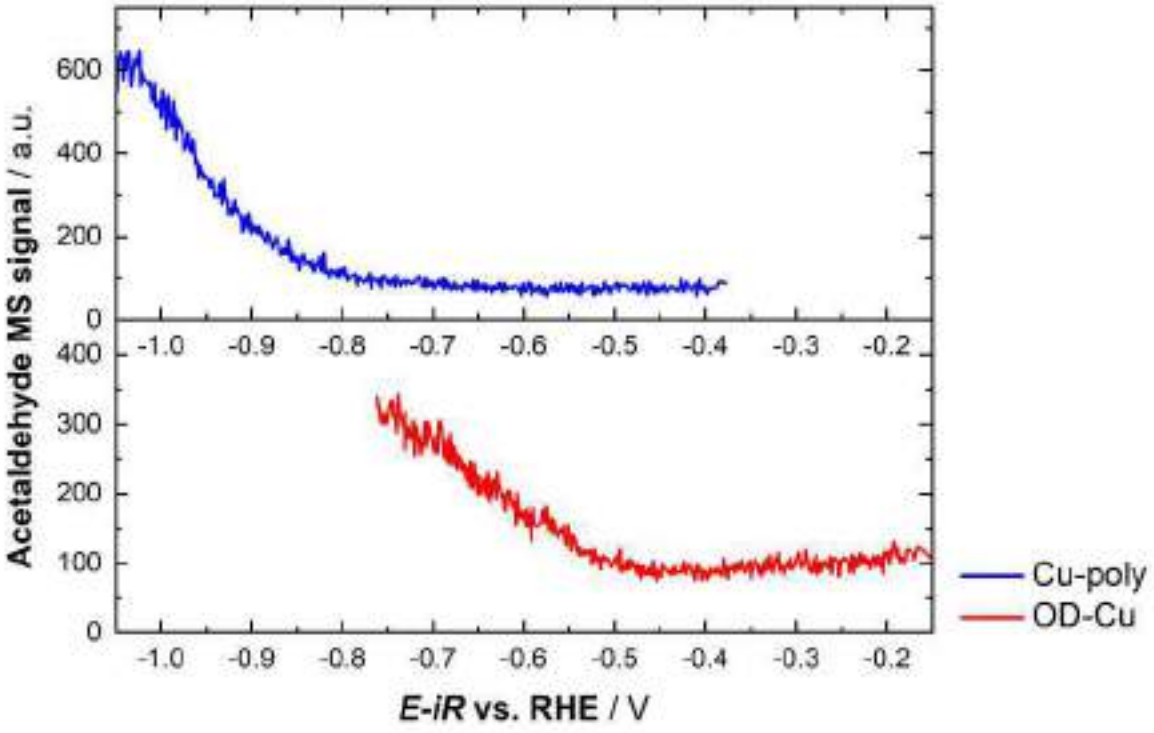

Figure S2. Representative linear sweep voltammetry measurements and mass spectrometry signals for acetaldehyde on polycrystalline (blue) and oxide-derived (red) copper.

S3 Gaseous phase corrections

The free energies of gaseous molecules were calculated as: $G \approx E_{DFT} + ZPE - TS$. The ZPE values were obtained from vibrational frequency analyses. The TS values were extracted from thermodynamic tables at 298.15 K and 1 atm [3]. The values used for all of the gases featured in this study are listed in Table S1. Because the PBE exchange-correlation functional does not describe correctly the free energy of $CO_{(g)}$ and $CO_{2(g)}$, corrections to their formation energies of -0.24 eV and 0.19 eV were applied, respectively, which are in line with those obtained in previous studies [4],[5],[6].

Table S1. Zero-point energy and entropy contributions to the free energies of gaseous molecules. All values are in eV.

Molecule	ZPE	TS
CO_2	0.31	0.66
CO	0.14	0.61
H_2	0.27	0.40
C_2H_4	1.36	0.68
H_2O	0.57	0.58
CH_3CHO	1.47	0.82
C_2H_5OH	2.11	0.87

S4 Liquid-phase corrections

For the products present in the liquid phase (namely water, ethanol, and acetaldehyde), the free energies were estimated using the method described in ref. [4], which is based on a correction added to the TS values. Specifically, TS values of 0.67 eV, 0.94 eV, and 0.87 eV were used to estimate the liquid-phase free energies of water, ethanol, and acetaldehyde, respectively.

S5 Solvation contributions to the free energies

Water-adsorbate interactions, deemed "solvation" corrections (E_{sol} in $G \approx E_{DFT} + ZPE - TS + E_{sol}$) were modeled as an external, ad hoc correction depending on the chemical nature of the adsorbates. We used the values reported in previous works [4,7]. The specific values used are listed in Table S2. These were obtained by calculating the difference in adsorption energies with and without water, using $\sqrt{3}\times\sqrt{3}$ Cu(111) cells covered with and without water and *OH, *COH, and *CO. The *OR correction was

approximated as 2/3 of that for *ROH, since, in principle, *ROH can make three hydrogen bonds with water (two accepting, two donating bonds), while *OR can only make two (two accepting bonds). Note that R represents a hydrocarbon chain. Values in Table S2 are commensurate with those in the literature [5,8].

Table S2. Stabilization provided by water-adsorbate interactions to the adsorption energies depending on the adsorbates' chemical structure. All values are given in eV.

Functional group	Solvation Correction
*CO	-0.10
*OH	-0.50
*ROH	-0.38
*OR	-0.25

S6 Adsorption energies

The respective ZPE, TS_{vib}, and solvation (E_{sol}) corrections, and ΔG values obtained for the different adsorbates featured in this study are a combination of data from previous works [7] and new calculations performed in this one. All the data are listed in Table S3. The most stable configuration (MSC) for each adsorbate is also indicated. $*C_2O_2H$ and *COOH are particular cases in which one part of the adsorbate interacts with the K atom and a solvation correction for the other group is included. Liquid acetaldehyde was considered when it was more stable than its adsorbed counterpart. Note that $2CO_{2(g)}$ and proton-electron pairs were used as the reference for the free energies in Table S3.

Table S3. Free energies of adsorption and their separate contributions for each species involved in CO_2 electroreduction to C_2 species. All values are in eV.

Cu(100)	ZPE	TS_{vib}	MSC	ΔG
2 *COOH	1.22	0.48	K + Solvated (-0.38)	0.05
2 *CO	0.36	0.33	With K	-0.15
$*C_2O_2H$	0.69	0.26	K + Solvated (-0.38)	0.36
$*C_2O$	0.34	0.19	With K	-0.56
*CHCO	0.60	0.24	With K	-0.28
*CHCHO	0.91	0.17	With K	-0.37
$*CH_2CHO$	1.21	0.20	Solvated (-0.25)	-0.64
$*CH_3CHO$	1.47	0.87	Liquid	-0.66
$*CH_3CH_2O$	1.83	0.30	Solvated (-0.25)	-1.06
*O	0.06	0.05	With K	-0.73
*OH	0.34	0.10	Solvated (-0.50)	-0.92

4AD@Cu(100)	ZPE	TS_{vib}	MSC	ΔG
2 *COOH	1.24	0.44	K + Solvated (-0.38)	-0.43
2 *CO	0.37	0.38	Solvated (-0.20)	-0.24
$*C_2O_2H$	0.70	0.26	K + Solvated (-0.38)	0.28
$*C_2O$	0.33	0.19	Solvated (-0.10)	-0.34
*CHCO	0.60	0.24	Solvated (-0.10)	-0.36
*CHCHO	0.90	0.17	Solvated (-0.25)	-0.61
$*CH_2CHO$	1.21	0.20	With K	-0.94
$*CH_3CHO$	1.48	0.32	Solvated (-0.25)	-0.81
$*CH_3CH_2O$	1.83	0.30	With K	-1.29
*O	0.06	0.05	With K	-0.34
*OH	0.35	0.09	Solvated (-0.50)	-1.40

Cu(111)	ZPE	TS_{vib}	MSC	ΔG
2 *COOH	1.22	0.46	K + Solvated (-0.38)	0.22
2 *CO	0.35	0.36	With K	0.02
$*C_2O_2H$	0.71	0.31	K + Solvated (-0.38)	1.16
$*C_2O$	0.34	0.19	With K	-0.04
*CHCO	0.60	0.24	With K	0.06
*CHCHO	0.90	0.18	With K	-0.02
$*CH_2CHO$	1.19	0.20	With K	-0.36
$*CH_3CHO$	1.47	0.87	Liquid	-0.66
$*CH_3CH_2O$	1.84	0.31	Solvated (-0.25)	-0.83
*O	0.07	0.04	With K	-0.32
*OH	0.34	0.08	Solvated (-0.50)	-0.96

4AD@Cu(111)	ZPE	TS_{vib}	MSC	ΔG
2 *COOH	1.24	0.44	K + Solvated (-0.38)	-0.59
2 *CO	0.37	0.40	Solvated (-0.20)	-0.41
$*C_2O_2H$	0.71	0.25	K + Solvated (-0.38)	0.24
$*C_2O$	0.34	0.19	With K	-0.40
*CHCO	0.61	0.23	Solvated (-0.10)	-0.45
*CHCHO	0.90	0.18	With K	-0.75
$*CH_2CHO$	1.21	0.25	With K	-1.17
$*CH_3CHO$	1.48	0.26	Solvated (-0.25)	-0.84
$*CH_3CH_2O$	1.84	0.32	Solvated (-0.25)	-1.28
*O	0.07	0.04	With K	-0.59
*OH	0.34	0.09	Solvated (-0.50)	-1.44

References

[1] E.L. Clark, A.T. Bell, Direct Observation of the Local Reaction Environment during the Electrochemical Reduction of CO2, J. Am. Chem. Soc. 140 (2018) 7012–7020. https://doi.org/10.1021/jacs.8b04058.

[2] M. Löffler, P. Khanipour, N. Kulyk, K.J.J. Mayrhofer, I. Katsounaros, Insights into Liquid Product Formation during Carbon Dioxide Reduction on Copper and Oxide-Derived Copper from Quantitative Real-Time Measurements, ACS Catal. 10 (2020)

6735–6740. https://doi.org/10.1021/acscatal.0c01388.

[3] D.R. Lide, CRC Handbook of Chemistry and Physics, 85th ed., CRC Press, Boca Raton, FL, 2005.

[4] F. Calle-Vallejo, M.T.M. Koper, Theoretical Considerations on the Electroreduction of CO to C2 Species on Cu(100) Electrodes, Angewandte Chemie International Edition. 52 (2013) 7282–7285. https://doi.org/10.1002/anie.201301470.

[5] A.A. Peterson, F. Abild-Pedersen, F. Studt, J. Rossmeisl, J.K. Nørskov, How copper catalyzes the electroreduction of carbon dioxide into hydrocarbon fuels, Energy Environ. Sci. 3 (2010) 1311–1315. https://doi.org/10.1039/C0EE00071J.

[6] R. Christensen, H. A. Hansen, T. Vegge, Identifying systematic DFT errors in catalytic reactions, Catalysis Science & Technology. 5 (2015) 4946–4949. https://doi.org/10.1039/C5CY01332A.

[7] O. Piqué, F. Viñes, F. Illas, F. Calle-Vallejo, Elucidating the Structure of Ethanol-Producing Active Sites at Oxide-Derived Cu Electrocatalysts, ACS Catal. 10 (2020) 10488–10494. https://doi.org/10.1021/acscatal.0c01880.

[8] A. Rendón-Calle, S. Builes, F. Calle-Vallejo, Substantial improvement of electrocatalytic predictions by systematic assessment of solvent effects on adsorption energies, Applied Catalysis B: Environmental. (2020) 119147. https://doi.org/10.1016/j.apcatb.2020.119147.

Appendix C

Supporting Information for "Selectivity Map for the Late Stages of CO and CO_2 Reduction to C_2 Species on Copper Electrodes"

S1 Experimental and computational methods

S1.1 Experimental methods

Preparation of electrodes

The surfaces of the copper single crystals were gently polished with 0.25 μm diamond slurry (Diapro, Struers). After rinsing thoroughly with deionized water, they were electropolished at 2 A cm^{-2} for 1 s (Autolab PGSTAT100) in an electrolyte consisting of 130 mL H_3PO_4 (85% w/w in H_2O, Sigma Aldrich), 20 mL H_2SO_4 (96%, VWR) and 60 mL deionized water. A platinum wire was used as counter electrode. The surfaces were then rinsed with deionized water and 0.1 mM $HClO_4$ (70%, Sigma Aldrich).[1],[2] The final acid rinsing step helps to restore the single crystal surface after exposure to oxygen from the surroundings.[3],[4]

Characterization of catalysts

The surfaces of the single crystals were characterized using cyclic voltammetry (CV). The scan rate was set to 50 mV s^{-1}. The electrolyte used was 0.1 M KOH (99.99%, Meryer) purged with N_2. The CV of the electrodes were also studied in CO-saturated 0.1 M potassium phosphate buffer solution (pH 7, cooled in ice bath). The cyclic voltammograms are presented in Figures S1 and S2 in Section S2.

The X-ray diffractograms of the Cu single crystals were measured using a Bruker D8 Discover goniometer equipped with a capillary focused IμS 2.0 Cu Kα X-ray source, 0.5 mm pinhole collimator, and a 5-axes Eulerian cradle. Vantec 500 with Xe microgap was used as a 2D area detector. The resulting 2D diffractograms were merged together and integrated with DIFFRAC.EVA software. The data is presented in Figures S3-S4 in Section S2.

Electrochemical Reduction of Ethylene Oxide

The electropolished Cu disks were used for the electrocatalytic reduction of ethylene oxide (EOR). The electrolyte was 0.1 M potassium phosphate buffer (pH = 7) made by mixing potassium phosphate monobasic (2.60 g) (≥99.0%, Sigma Aldrich) and potassium phosphate dibasic (7.06 g) (≥99.0%, Sigma Aldrich) in 500 mL of deionised water. A three-electrode configuration was used, where the working electrode was a

copper disk, the reference electrode was Ag/AgCl (saturated KCl, Pine) and the counter electrode was a graphite rod. The cathodic and anodic compartments were separated by an anion exchange membrane (AMV, AGC Asahi Glass). Online gas chromatography (GC) system (Agilent, 7890A) was used to analyze the gaseous product, while headspace-GC (Agilent, 7890B and 7697A) was used to analyze the liquid products. The electrolysis time was 40 min, with five aliquots of gas samples automatically injected and analyzed by GC at intervals of 493 s. Further details of our chromatography setups have been described in our previous work.[5] The electrolysis was controlled by a potentiostat (Gamry reference 600). The current interrupt mode was used to compensate for the iR drop. The potentials cited in this work are referenced to the reversible hydrogen electrode (RHE). The data is available in the main text, Table S2 and Figures S5-S6 of Section S2.

S1.2 Computational methods

The VASP code[6] with the PBE exchange-correlation functional[7] was used to perform the periodic DFT simulations. The projector augmented-wave (PAW) method[8] was used to describe the effect of the inner cores on the valence electron density. The Cu(100) and 4AD@Cu(100) surfaces were represented by a $4\sqrt{2}\times4\sqrt{2}$ R45° supercell slab consisting of 32 atoms per layer; Cu(111) and 4AD@Cu(111) were modeled as a 4×4 supercell with 16 atoms per layer; Cu(311) as a 2×2 supercell with 8 atoms per layer; and Cu(211) as a 3×1 supercell with 9 atoms per layer. 4AD denotes four Cu adatoms, so that 4AD@Cu(100) and 4AD@Cu(111) are Cu(100) and Cu(111) surfaces with four adatoms on top, forming an island. The dimensions of the supercells guarantee that lateral interactions between adsorbates are avoided. All slabs had four metal layers and were modeled with the PBE's converged lattice constant of 3.64 Å for Cu. The upper two layers and the adsorbates were allowed to relax in all directions, while the lower two layers were fixed at the bulk equilibrium distances. Smearing with an electronic temperature of 0.2 eV was used to facilitate convergence, and all total energies were extrapolated to 0 K. The plane wave cutoff was set to 450 eV. Iterative searches for minimum-energy structures were performed till the maximal force on any atom was below 0.05 $eV \cdot Å^{-1}$. The numerical integration in the reciprocal space was done using Monkhorst-Pack grids of 2×2×1 for Cu(100) and 4AD@Cu(100), 3×3×1 for Cu(111) and 4AD@Cu(111), 5×3×1 for Cu(311), and 4×5×1 for Cu(211). The distance in the vertical direction between

periodical images was larger than 13 Å and dipole corrections were applied. Boxes of 9 Å × 10 Å × 11 Å were used to calculate isolated molecules (H_2, H_2O, C_2H_4, C_2H_4O and C_2H_5OH), using an electronic temperature of 0.001 eV with further extrapolation to 0 K and considering the Γ-point only. The climbing-image nudged elastic band method[9] was used to find transition-state configurations. The latter were characterized by vibrational frequency calculations, ensuring that only one imaginary frequency along the reaction coordinate was obtained at the saddle point. The optimized geometries of all the minima and transition states featured in this work are provided in Section S10.

The reaction free energies were approximated as $\Delta G \approx \Delta E_{DFT} + \Delta ZPE - T\Delta S + \Delta E_{solvation}$, where ΔE_{DFT} is the reaction energy calculated with DFT, ΔZPE is the zero-point energy change between reactants and products, $T\Delta S$ is the overall entropy correction at 298.15 K, and $\Delta E_{solvation}$ is an external solvation correction applied to adsorbates. No solvation correction is needed for adsorbed ethylene oxide, as determined using the method provided in reference [10]. For *OH, an ad hoc correction of -0.50 eV was used; for $*CH_2CH_2OH$, a correction of -0.38 eV was used, and for $*OCH_2CH_3$, 2/3 of that value were used, as the oxygen atom in it can make two hydrogen bonds while that of $*CH_2CH_2OH$ can make three. These corrections are commensurate with previous works.[10],[11],[12] The values of ZPE and TS_{vib} were calculated from the vibrational frequencies obtained with DFT, within the harmonic approximation. For adsorbates, ΔS includes only vibrational entropies, whereas for free molecules, all entropy contributions were included and taken from standard thermodynamic tables.[13]

The computational hydrogen electrode was used to model proton-electron pairs.[14] The onset potential is defined as the largest positive reaction energy among the electrochemical steps at 0 V vs RHE ($U_{onset} = -\max\left(\Delta G_{C_2H_4O \to *OH}, \Delta G_{*OH \to H_2O}\right)/e^-$), see Equations 1 to 3 and Figure 1 in the main text. Gas-phase corrections were applied to the total energies of C_2H_4O and C_2H_4, to ensure that the experimental equilibrium potential of ethylene oxide reduction (0.81 V vs RHE) was matched by DFT. The semiempirical correction method can be found in reference [15]. Furthermore, the free energies of water and ethanol in the liquid phase were estimated using the method described in reference [11], which is based on a TS correction. The specific values of ZPE, TS, and gas and liquid-phase corrections are provided in Section S5. The ZPE, TS_{vib}, and ΔG values calculated in this work are provided in Section S6.

Generalized coordination numbers ($\overline{CN}$) are an extension of the conventional ones (cn) that includes the second coordination shell, namely the nearest neighbors of the nearest neighbors, and also the changes in the interatomic distances introduced by tensile strain.[16],[17] Table S11 shows the assessment of $\overline{CN}$ based on cn for the six sites in this study. The making of coordination-activity plots[16],[18] and selectivity maps[19] as a function of $\overline{CN}$ has been described in the stated references.

S2 Characterization of copper single crystals

Cyclic voltammetry (CV)

The cyclic voltammograms obtained for four different copper single crystal electrodes in 0.1 M KOH at 50 mV s^{-1} are presented in Figure S1. The peaks observed in the region between -0.30 to 0.20 V vs RHE are attributed to OH^- adsorption and desorption.[4],[20] The peaks between 0.30 to 0.45 V vs RHE correspond to the redox peaks of copper.[21],[22] There were no additional peaks in the CVs that could be assigned to contaminants, such as Pt[23] (Pt was used as the counter electrode during Cu electropolishing; note that Pt is thermodynamically stable when a negative bias is applied to it).[24]

The cyclic voltammograms obtained for four different copper single crystals electrodes in CO-saturated 0.1 M potassium phosphate buffer solution (pH 7, cooled in ice bath) are shown in Figure S2. The redox peak observed is the charge transfer peak due to the displacement of the adsorbed anions during CO adsorption on the catalyst surface.[25] We note that the charge transfer peak was not observed for Cu(111) in the scanned potential region. The scan rate used was 200 mV s^{-1}. The peak positions are shown in Table S1.

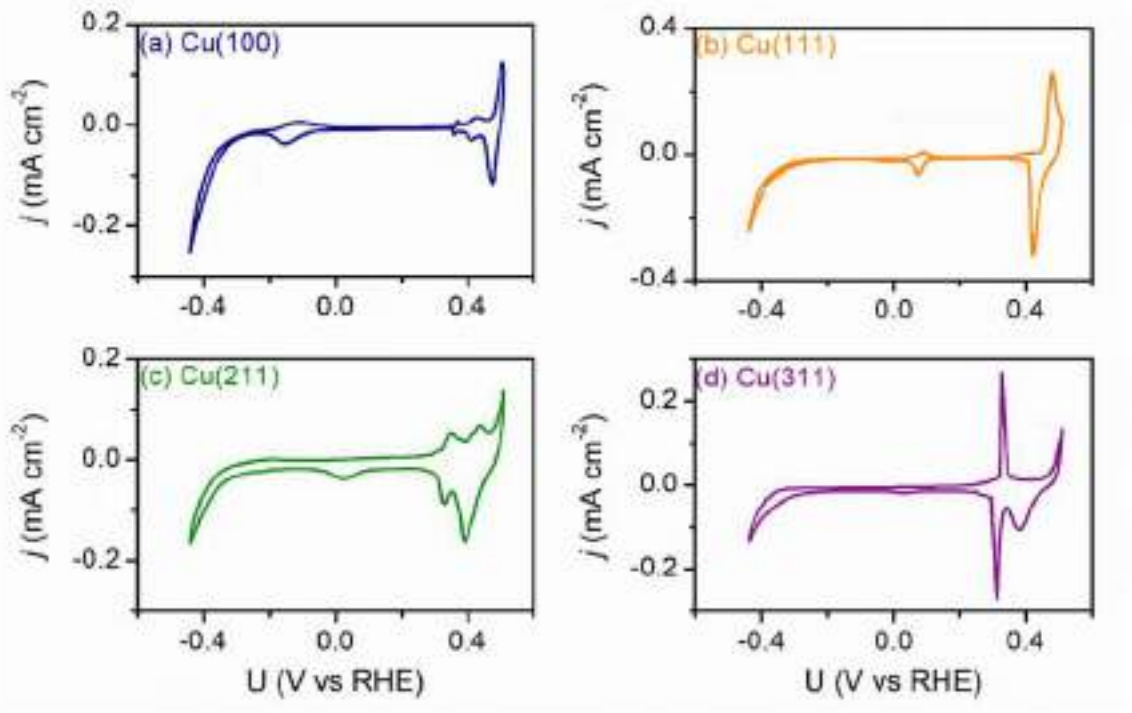

Figure S1. Cyclic voltammograms of Cu single crystals in 0.1 M KOH. (a) Cu(100). (b) Cu(111). (c) Cu(211). (d) Cu(311). The CV profiles of the single crystals for Cu(100) and Cu(111) are similar to those in previous studies.[4]

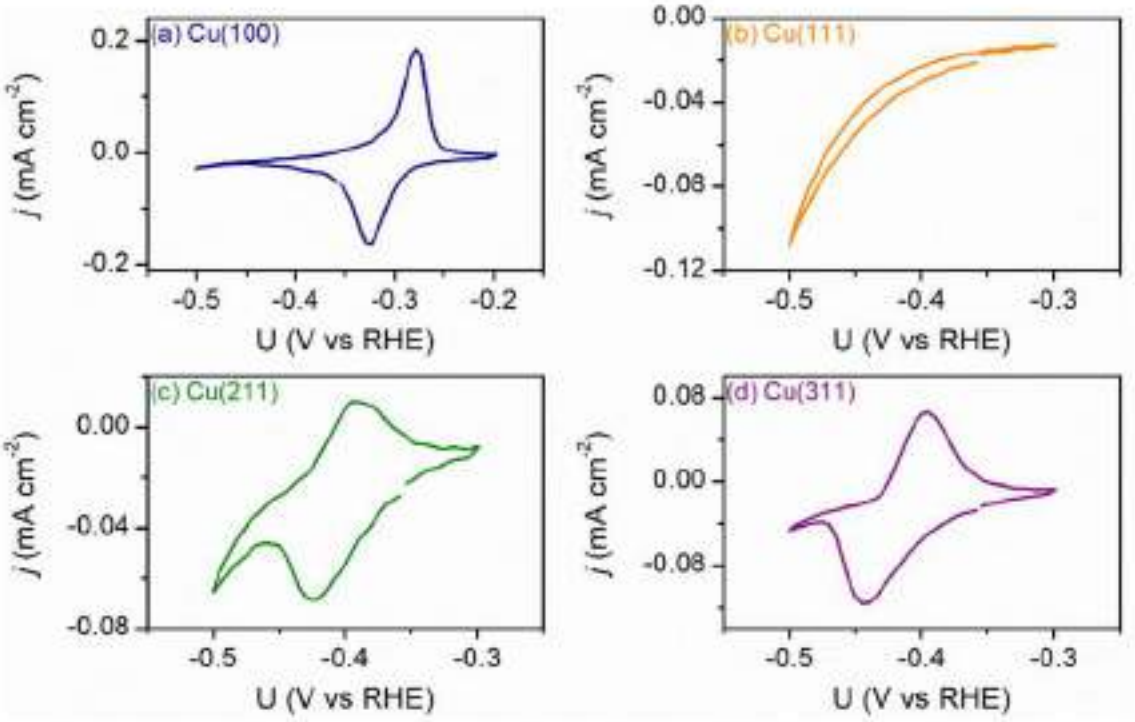

Figure S2. Cyclic voltammograms of Cu single crystals in CO-saturated 0.1 M potassium phosphate buffer solution (pH 7, cooled in ice bath). (a) Cu(100). (b) Cu(111). (c) Cu(211). (d) Cu(311). The CV profiles of the single crystals obtained are similar to previous study.[26]

Table S1. The charge transfer peak positions observed on different Cu single crystals in CO-saturated 0.1 M potassium phosphate buffer (pH 7, cooled in ice bath). The values are in the form of peak positions (oxidation peak, reduction peak). The literature values are obtained from Hori et al.[26]

Cu surface	Experimental (V vs RHE)	Experimental (V vs SHE)	Literature (V vs SHE)
Cu(100)	-0.28, -0.325	-0.68, -0.73	-0.68, -0.71 (small shoulder peak at -0.73)
Cu(111)	no peak	no peak	no peak
Cu(211)	-0.39, -0.42	-0.8, -0.83	-0.79, -0.82
Cu(311)	-0.40, -0.44	-0.80, -0.845	-0.80, -0.82

X-ray diffraction (XRD)

Cu single crystals (10 mm diameter), namely Cu(100), Cu(111) and Cu(311), were measured in 2θ scan mode at a fixed incoming angle (ω). The ω was set at the theoretical Bragg position of 25.19°, 21.65° and 44.99° corresponding to the Cu(200), Cu(111) and Cu(311) reflexions respectively while the detector recorded four frames at 18°, 36°, 54°, and 72° 2θ stationary positions for 300 seconds each. At the pre-set detector radius (420 mm), each recorded frame covers approximately 22° across 2θ and $\chi_{(detector)}$ range. Sample height alignment was made with the aid of a laser depth focusing system, while sample tilt was optimised by performing quick rocking curve (ω) and substrate tilt ($\chi_{(sample)}$) scans at narrow range of +2° to -2°. The resulting diffractograms from the 2θ scan mode show bright dots at the expected 2θ positions, indicating very strong texturing consistent of a single crystal. The data obtained are shown in Figure S3.

Specifically for Cu(211) single crystal, a gonio (coupled ω-2θ scan) was used to probe any possible reflexions. No reflexions were detected from wide range scan without substrate tilt. This is expected because (211) is a forbidden reflexion in the $Fm\bar{3}m$ space group, and no other planes or phases were detected. To demonstrate that the sample truly has a (211) orientation, wide range, off-axis gonio scans targeting Cu{111}, Cu{200}, and Cu{220} family of planes was done by setting the substrate tilt ($\chi_{(sample)}$) angle at the theoretical angles between the respective planes and the (211). These angles are respectively 19.5°, 35.3° and 30°, which can be calculated from the plane normal vectors' cross product. An illustration for intersecting (100) and (211) planes in a cubic system is shown in Figure S4.

The off-axis gonio scans of the tilted sample at the respective theoretical $\chi_{(sample)}$ angles detected sharp features at the expected 2θ positions for Cu(111) (and Cu(222)), Cu(200) and Cu(220) respectively, confirming the orientation of the single crystal to be (211).

Some scans show broad and diffuse humps around the main diffraction peak, which may originate from artefact reflection due to uneven sample height (X-ray shadowing effect) or slightly roughened surface (diffuse reflectance effect).

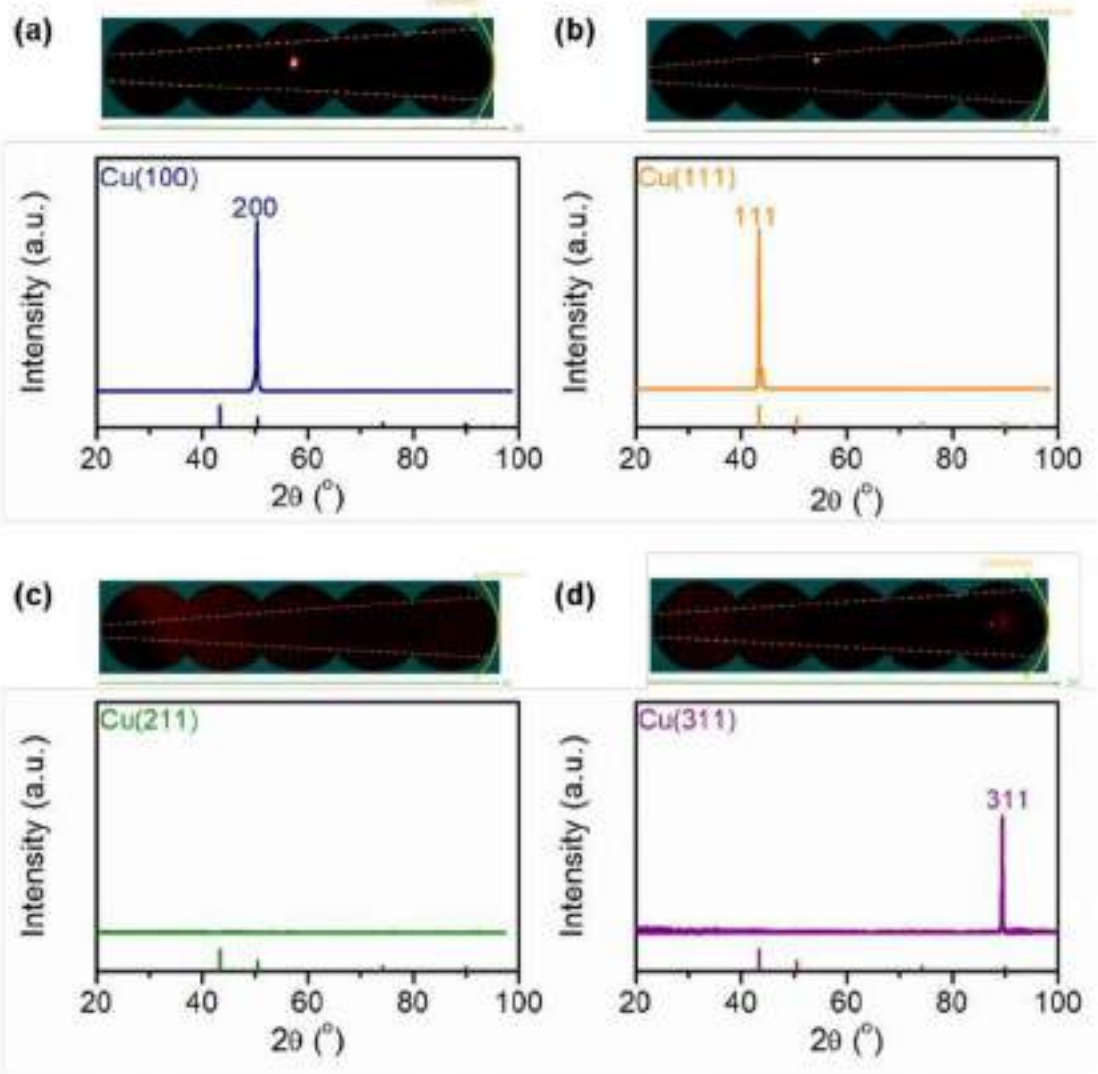

Figure S3. XRD analyses of copper single crystal facets: (a) Cu(100), (b) Cu(111), (c) Cu(211) and (d) Cu(311). (100) and (211) reflexions are absent in Cu(100) and Cu(211) respectively as they are forbidden reflexions in the $Fm\bar{3}m$ space group. The peaks are assigned according to standard XRD pattern PDF 00-004-0836. The 2D diffractograms obtained for each facets (on top of each XRD spectrum) showed significant reflexion texturing, which are characteristic of a single crystal. Small humps around the main diffraction peak on some samples may be caused by X-ray shadowing or diffuse reflectance effect.

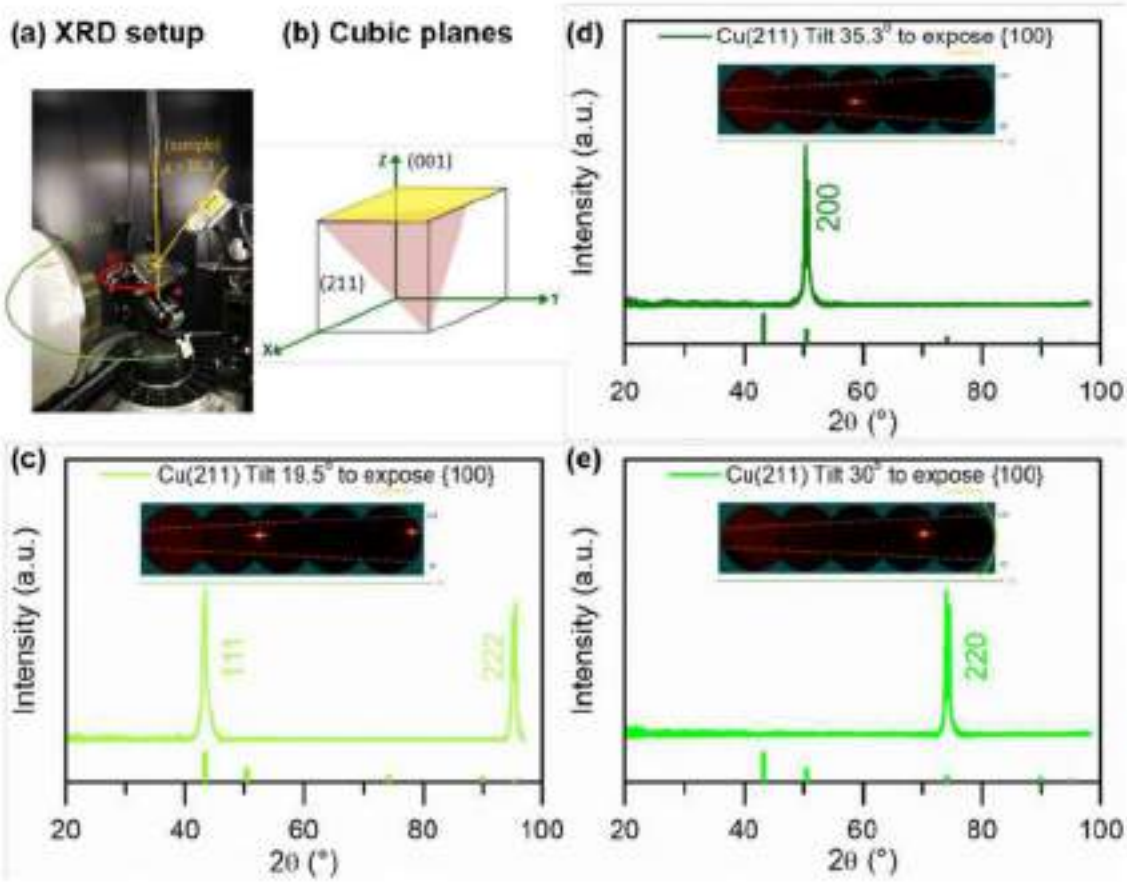

Figure S4. Off-axis XRD analysis setup of Cu(211) substrate. (a) Photograph of the XRD setup to observe Cu(200) reflexion in Cu(211) substrate by applying substrate tilt. The measurement axes (2θ, ω, and $\chi_{(sample)}$) are indicated. (b) Illustration of (211) and (100) planes in cubic system. The angle between (211) and (100) plane, determined from the cross product of the plane normal vectors, is 35.3°. The resulting 2D diffractograms (insets) and integrated intensities from the off-axis gonio (coupled ω-2θ) scan were shown when the sample is tilted at (c) $\chi = 19.5°$, (d) $\chi = 35.3°$ and (e) $\chi = 30°$. Strong reflexion spots were observed on the respective planes, indicating that these planes are highly textured, consistent of a bulk single crystal. The appearance of these reflexions when the sample is tilted at the theoretical angles confirmed the orientation of the single crystal to be (211).

S3 Electrolysis of ethylene oxide on copper catalysts

Protocol for onset potential determination for EOR

The onset potential of EOR to ethylene is defined as the potential in which the ethylene signal begins to be higher than the signal obtained at open circuit potential (OCP). For example: the signals obtained for ethylene at different applied potentials on Cu(100) are shown in Figure S5. Here, the onset potential was determined to be at -0.35 V vs RHE. The background ethylene signal at OCP was caused by trace ethylene 'contaminant' in the ethylene oxide feed.

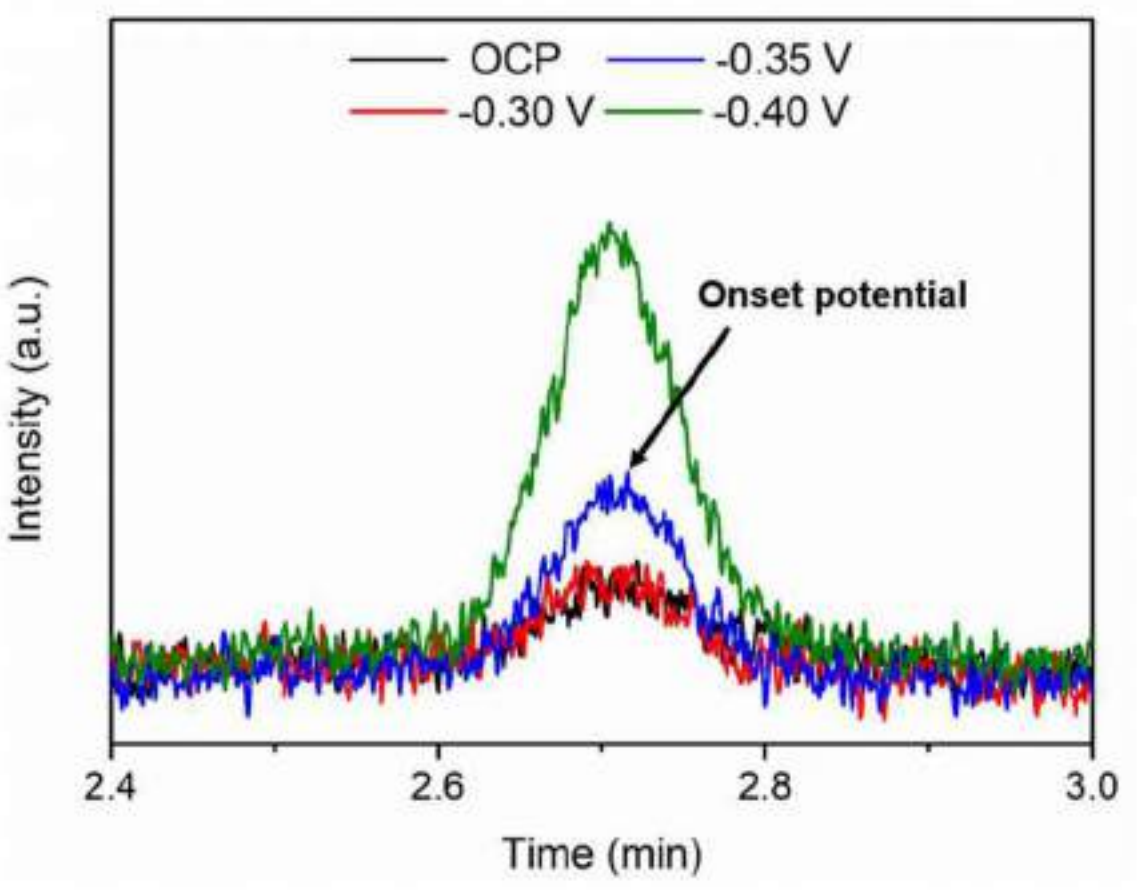

Figure S5. GC-FID signals of ethylene during EOR on Cu(100) at different applied potentials in 0.1 M potassium phosphate buffer solution (pH = 7).

Table S2. Results obtained for EOR under different applied potentials in 0.1 M potassium phosphate buffer solution using Cu(100), Cu(111), Cu(211) and Cu(311).

Catalyst	Potential (V vs RHE)	j_{total} (mA cm^{-2})	Faradaic Efficiency (%)		
			C_2H_4	H_2	Total
Cu (100)	-0.30	-0.1	N.D.	14.8	14.8
	-0.35	-0.2	0.04	54.0	54.0
	-0.40	-0.7	0.04	94.1	94.1
	-0.50	-1.0	0.06	100.1	100.2
Cu (111)	-0.45	-0.2	N.D.	79.3	79.3
	-0.50	-0.4	0.02	90.8	90.8
	-0.55	-0.8	0.01	91.0	91.0
Cu (211)	-0.45	-0.3	N.D.	96.5	96.5
	-0.50	-0.9	0.01	95.7	95.7
	-0.55	-1.3	0.01	96.4	96.4
Cu (311)	-0.40	-0.1	N.D.	89.4	89.4
	-0.45	-0.4	0.02	92.3	92.3
	-0.50	-0.5	0.02	99.1	99.1

Note: A small amount of ethane was observed on Cu(100) at -0.40 and -0.50 V vs RHE.

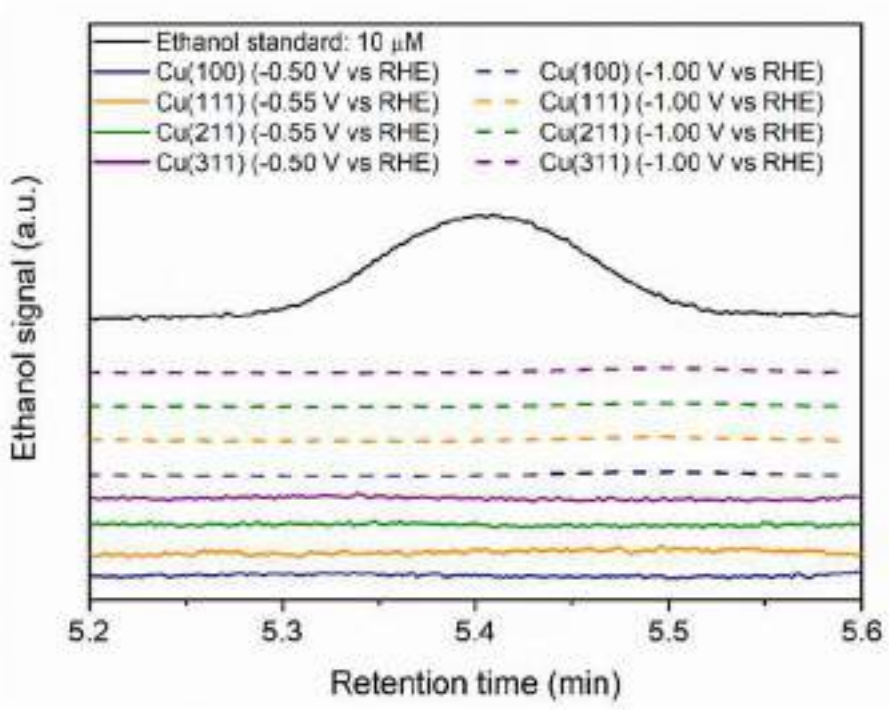

Figure S6. Comparison of ethanol signals obtained using GC-FID analyses for 10 μM ethanol standard and samples obtained after EOR at different applied potentials using Cu(100), Cu(111), Cu(211) and Cu(311) as electrocatalysts, respectively. The data shows that no ethanol was observed after EOR on all the copper single crystals used. This shows that ethylene is exclusively produced during EOR on Cu single crystals.

S4 Analysis of data from previous studies

The roughness factor of a surface can be taken as an approximation to the amount of edges / steps / undercoordinated defects present on it. Herein, we examine data from previous works on CO_2RR and COR on Cu catalysts. For each work, the ratio of the partial current densities of $j_{ethanol}$ and $j_{ethylene}$ of the catalysts studied was calculated (Tables S3-S8). We found that surfaces with higher roughness factors have generally larger $j_{ethanol}$ / $j_{ethylene}$ ratios. This finding is in agreement with the main results of this work demonstrating that steps, kinks and undercoordinated defects favor ethanol evolution.

Table S3. Partial current densities of ethylene ($j_{ethylene}$) and ethanol ($j_{ethanol}$) and the roughness factors obtained for different Cu surfaces in 0.1 M $KHCO_3$ electrolyte at -0.99 V vs RHE for CO_2 electrolysis. The data is taken from Ren et al.[27]

Catalyst	Roughness factor	j (mA/cm^2)		Ratio of $j_{ethanol}$ / $j_{ethylene}$
		C_2H_4	C_2H_5OH	
Electropolished copper	1	-0.41	N.D.	N.D.
0.2 μm film	1.5	-4.61	-0.84	0.18
1.7 μm film	4.7	-11.64	-2.70	0.23
3.6 μm film	5.5	-11.99	-5.73	0.48
8.8 μm film	11.3	-6.25	-1.48	0.24

Table S4. Partial current densities of ethylene ($j_{ethylene}$) and ethanol ($j_{ethanol}$) and the roughness factors obtained for different Cu surfaces at -1.05 V vs RHE in 0.1 M $KHCO_3$ electrolyte for CO_2 electrolysis. The data is taken from Ren et al.[28] Cu nanoparticles was formed via pulse electrodeposition. Cu nanocrystals (NC) were obtained by anodizing the obtained Cu nanoparticles for 10 (Cu NC-10) and 20 (Cu-NC-20) min respectively.

Catalyst	Roughness factor	j (mA/cm^2)		Ratio of $j_{ethanol}$ / $j_{ethylene}$
		C_2H_4	C_2H_5OH	
Electropolished copper	1	-1.66	-0.53	0.32
Cu nanoparticles	2.5	-4.72	-1.60	0.34
Cu NC-10 min	13	-10.66	-4.64	0.44
Cu NC-20 min	24	-6.78	-3.93	0.58

Table S5. Partial current densities of ethylene ($j_{ethylene}$) and ethanol ($j_{ethanol}$) and the roughness factors obtained for different Cu surfaces at -1.1 V vs RHE in 0.1 M $KHCO_3$ electrolyte for CO_2 electrolysis. The data is taken from Lum et al.[29] Cu foil: electropolished Cu. OD-Cu: Oxide-derived nanocrystalline copper. OD NW: Cu nanowire arrays. EC Cu: Electrochemically cycled Cu. EOD Cu: Electrodeposited Cu (I) oxide film.

Catalyst	Roughness factor	j (mA/cm^2)		Ratio of $j_{ethanol}$ / $j_{ethylene}$
		C_2H_4	C_2H_5OH	
Cu foil	1	-5.12	-1.76	0.34
OD Cu	103	-1.05	-0.74	0.71
OD NWs 150s	9.95	-4.10	-1.98	0.48
EC Cu	6.2	-4.15	-1.47	0.35
EOD Cu 100s	17	-4.29	-1.65	0.38

Table S6. Partial current densities of ethylene ($j_{ethylene}$) and ethanol ($j_{ethanol}$) and the roughness factors obtained for different Cu surfaces at -1.0 V vs RHE in 0.1 M $KHCO_3$ electrolyte for CO_2 electrolysis. The data is taken from Kwon et al.[30] KX (X=halides) cycled: The electropolished polycrystalline Cu is cycled in 4 mM of KX solution in 0.1 M $KHCO_3$ for three cycles between -1.1 and -0.9 V vs RHE at 20 mV s^{-1}.

Catalyst	Roughness factor	j (mA/cm^2)		Ratio of $j_{ethanol}$ / $j_{ethylene}$
		C_2H_4	C_2H_5OH	
Cu foil	1	-0.51	-0.14	0.28
KF cycled	1.7	-1.06	-0.51	0.48
KCl cycled	2.9	-1.43	-0.74	0.52
KBr cycled	2.3	-1.10	-0.56	0.51
KI cycled	1.3	-0.63	-0.24	0.38

Table S7. Partial current densities of ethylene ($j_{ethylene}$) and ethanol ($j_{ethanol}$) and the roughness factors obtained for different roughened Cu surfaces at -0.9 V vs RHE in 0.1 M $KHCO_3$ electrolyte for CO_2 electrolysis. The data is taken from Ren et al.[31] Cu-10: Electrodeposited Cu film at pH 10.5 for 10 min. CuO: Electrodeposited CuO film at pH 13.2 for 1 (CuO-1), 10 (CuO-10) and 60 min (CuO-60).

Catalyst	Roughness factor	j (mA/cm^2)		Ratio of $j_{ethanol}$ / $j_{ethylene}$
		C_2H_4	C_2H_5OH	
Cu-10	1.4	-0.019	-0.003	0.15
CuO-1	5	-0.445	-0.108	0.24
CuO-10	48	-6.812	-2.348	0.34
CuO-60	186	-9.869	-4.761	0.48

Table S8. Partial current densities of ethylene ($j_{ethylene}$) and ethanol ($j_{ethanol}$) and the roughness factors obtained for different Cu surfaces at -0.5 V vs RHE in 0.1 M KOH electrolyte for CO electrolysis. The data is taken from Li et al.[12] OD-Cu-1: Oxide-derived Cu was obtained from heating at 500 °C for one hour and electroreduced. OD-Cu-2: Oxide-derived Cu was obtained using the same method mentioned and reduced under H_2 atmosphere.

Catalyst	Roughness factor	j (mA/cm^2)		Ratio of $j_{ethanol}$ / $j_{ethylene}$
		C_2H_4	C_2H_5OH	
Cu nanoparticles	26	-0.047	-0.053	1.13
OD-Cu-1	135	-0.139	-0.388	2.79
OD-Cu-2	48	-0.192	-0.271	1.41

S5 Molecules

The free energies of gas-phase molecules were estimated as: $G = E_{DFT} + ZPE - TS$. The ZPE (from vibrational frequency analyses) and TS values (from thermodynamic tables)[13] at 298.15 K used for gas-phase species featured in this study are listed in Table S9. Gas-phase corrections of -0.17 and 0.04 eV were applied to the total energies of C_2H_4O and C_2H_4. These corrections are obtained using the semiempirical method described in reference [15], which is based on the difference between DFT-calculated and experimental formation energies. Corrections to the TS values of 0.09 and 0.07 eV were applied to estimate the liquid-phase energies of water and ethanol.[11]

Table S9. Zero-point energy and entropy contributions (in eV) to the free energies of gas-phase molecules.

Molecule	ZPE	TS
H_2	0.27	0.40
C_2H_4	1.36	0.68
H_2O	0.57	0.58
C_2H_4O	1.52	0.75
C_2H_5OH	2.11	0.87

S6 Adsorption energies

The ZPE, TS_{vib}, solvation energy (E_{sol}), and the corresponding ΔG values obtained for the different adsorbates featured in this study on all the six studied surface models are listed in Table S10. Note that $C_2H_4O_{(g)}$ was used as a reference for all the free energies.

Table S10. Free energies of adsorption and its contributions for all the possible intermediates involved in ethylene oxide reduction. All values are in eV.

Cu(111)	ZPE	TS_{vib}	E_{sol}	ΔG
$*OCH_2CH_2$	1.51	0.17	-	-0.12
$*OH + C_2H_{4(g)}$	0.34	0.08	-0.50	-1.65
$*CH_2CH_2OH$	1.79	0.33	-0.38	-0.65
$*CH_2CH_2O$	1.84	0.31	-0.25	-1.49

Cu(100)	ZPE	TS_{vib}	E_{sol}	ΔG
$*OCH_2CH_2$	1.50	0.21	-	-0.68
$*OH + C_2H_{4(g)}$	0.34	0.10	-0.50	-1.95
$*CH_2CH_2OH$	1.77	0.33	-0.38	-0.85
$*CH_2CH_2O$	1.83	0.30	-0.25	-1.73

Cu(311)	ZPE	TS_{vib}	E_{sol}	ΔG
$*OCH_2CH_2$	1.49	0.22	-	-0.40
$*OH + C_2H_{4(g)}$	0.36	0.09	-0.50	-2.07
$*CH_2CH_2OH$	1.78	0.31	-0.38	-1.08
$*CH_2CH_2O$	1.83	0.34	-0.25	-1.86

Cu(211)	ZPE	TS_{vib}	E_{sol}	ΔG
$*OCH_2CH_2$	1.50	0.20	-	-0.47
$*OH + C_2H_{4(g)}$	0.36	0.09	-0.50	-2.11
$*CH_2CH_2OH$	1.78	0.28	-0.38	-1.05
$*CH_2CH_2O$	1.82	0.25	-0.25	-1.84

4AD@Cu(100)	ZPE	TS_{vib}	E_{sol}	ΔG
$*OCH_2CH_2$	1.50	0.20	-	-1.03
$*OH + C_2H_{4(g)}$	0.35	0.09	-0.50	-2.09
$*CH_2CH_2OH$	1.77	0.36	-0.38	-1.09
$*CH_2CH_2O$	1.83	0.30	-0.25	-1.82

4AD@Cu(111)	ZPE	TS_{vib}	E_{sol}	ΔG
$*OCH_2CH_2$	1.49	0.21	-	-1.06
$*OH + C_2H_{4(g)}$	0.34	0.09	-0.50	-2.13
$*CH_2CH_2OH$	1.79	0.37	-0.38	-1.25
$*CH_3CH_2O$	1.84	0.32	-0.25	-1.95

In Figure S7, we show the weak correlation between *OH and $*OCH_2CH_2$ adsorption energies, to be considered when designing strategies to lower the calculated overpotentials.

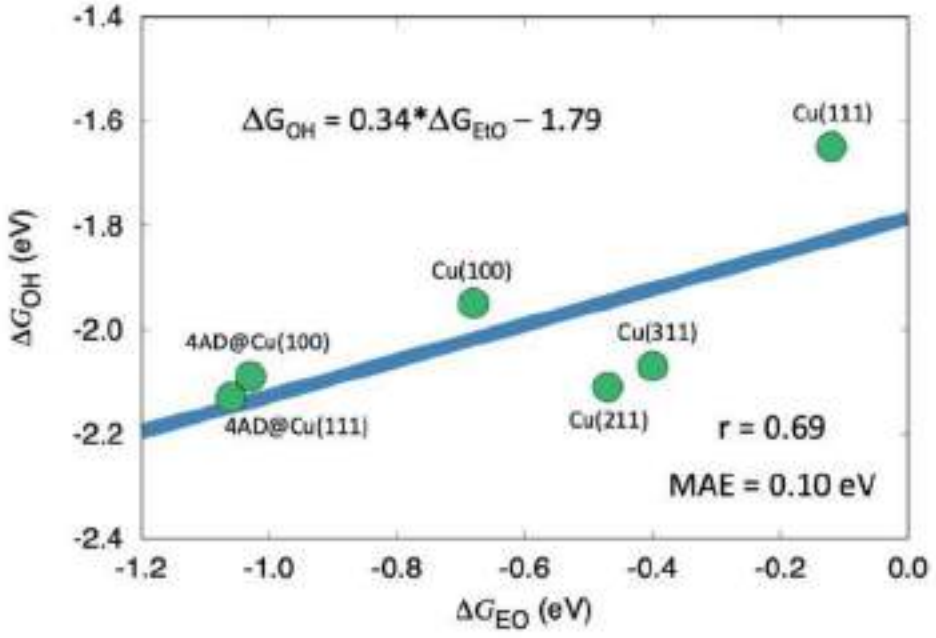

Figure S7. Adsorption free energy of *OH plotted against that of ethylene oxide (EO). In blue, the linear regression of the data. All data points are labelled to indicate the active site they represent. The Pearson regression coefficient, the mean absolute error (MAE), and the equation of the blue line are also provided.

S7 Generalized coordination numbers

Generalized coordination numbers ($\overline{CN}$) are the geometric descriptor used in this study.[16],[17] Usually, they are linearly correlated with adsorption energies. For a given surface site "i", $\overline{CN}$ is calculated arithmetically as:

$$\overline{CN}(i) = \sum_{j=1}^{n_i} \frac{cn(j)}{cn_{max}} \quad (1)$$

Conventional coordination numbers (cn) count the first nearest neighbors of the active sites "i", whereas $\overline{CN}$ weights every neighbor "j" by their respective coordination number ($cn(j)$). $\overline{CN}$ spans the same range as cn (i.e. 0-12), because the normalization factor cn_{max} is used. It corresponds to maximum number of first nearest neighbors in the bulk. For atop sites $cn_{max} = 12$. Note that if $cn(j) = 12$ for all n_i neighbors: $\overline{CN}(i) = cn(i)$. This means that conventional coordination is a particular case of the generalized one wherein all neighbors possess the bulk coordination. $\overline{CN}$ can be calculated for the sites in this study using Equation 1 (above) and the coordination number matrix provided in Table S11.

Table S11. Coordination number matrix for the sites under study on Cu electrodes.

Site	cn	3	4	5	6	7	8	9	10	11	12	$\overline{CN}$
Cu(111)	9	0	0	0	0	0	0	6	0	0	3	7.50
Cu(100)	8	0	0	0	0	0	4	0	0	0	4	6.67
Cu(311)	7	0	0	0	0	2	0	0	3	0	2	5.67
Cu(211)	7	0	0	0	0	2	0	2	1	0	2	5.50
4AD@Cu(100)	6	0	0	0	2	0	0	1	2	0	1	4.42
4AD@Cu(111)	5	0	0	0	2	0	0	0	2	0	1	3.67

S8 Double bridge configuration of adsorbed ethylene oxide at Cu(100)

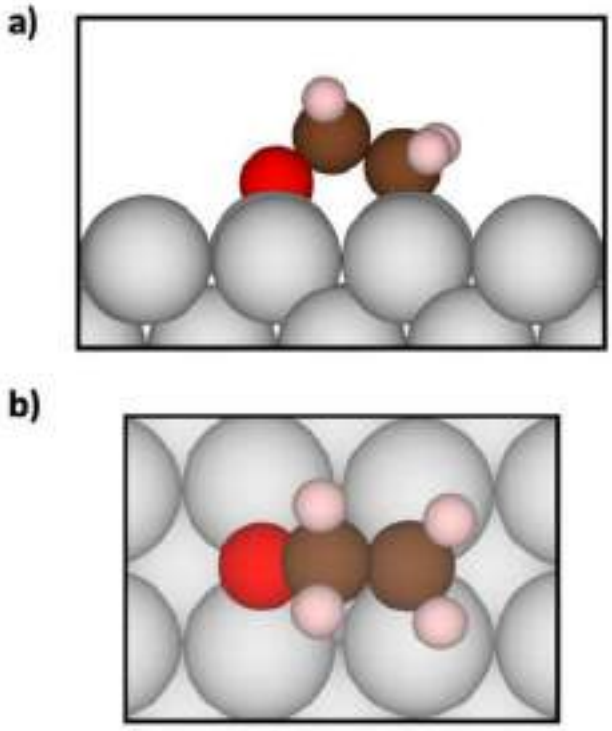

Figure S8. Double bridge configuration for ethylene oxide when adsorbed on Cu(100). a) Side view. b) Top view. Red, brown, pink, and grey spheres represent O, C, H, and Cu atoms, respectively.

S9 Free-energy diagrams

In Figure S9, we analyze the EOR on various Cu electrodes at two different potentials, namely 0 and 0.81 V vs RHE (the latter being the EOR equilibrium potential).

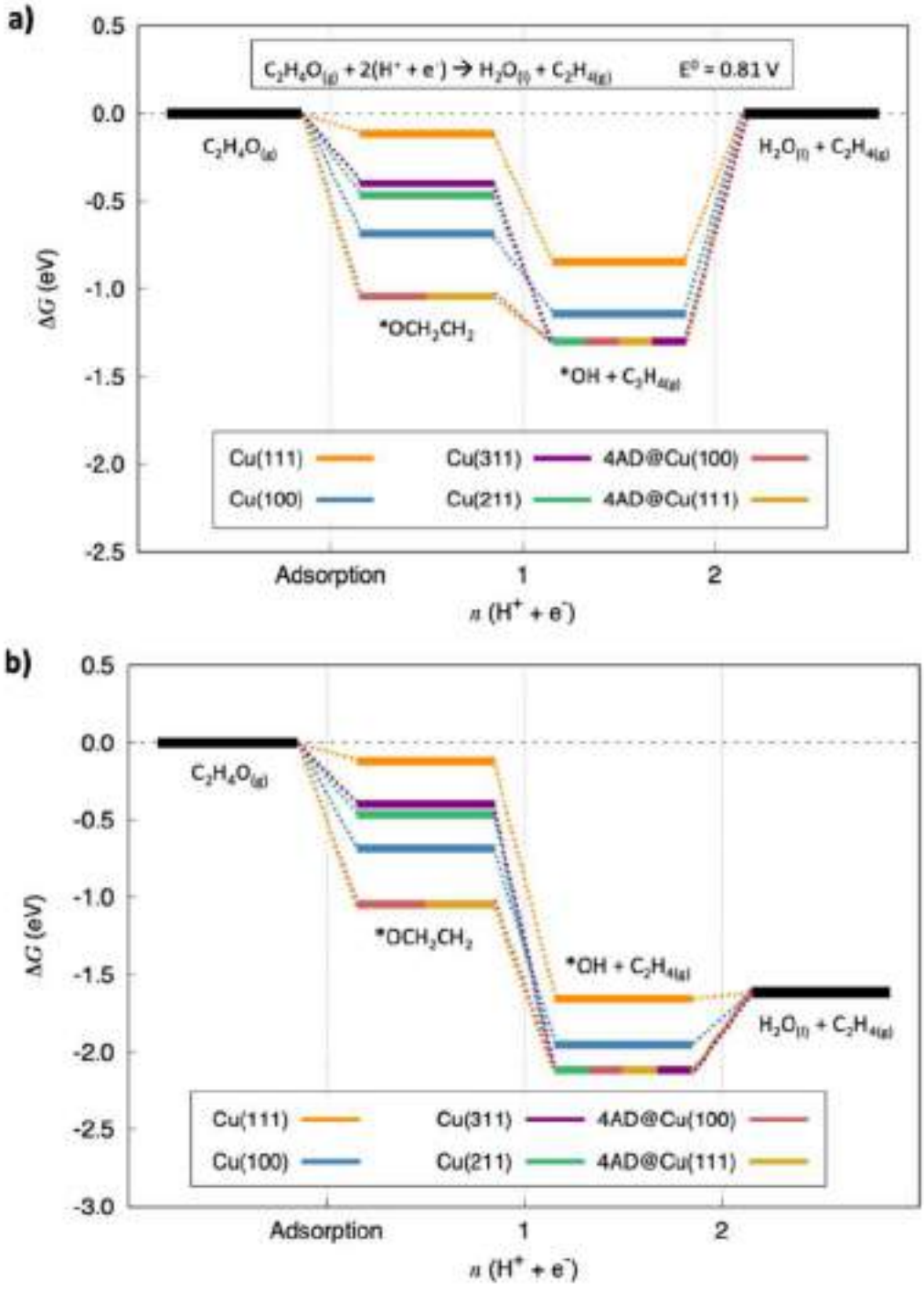

Figure S9. Free energy diagrams for the lowest-energy pathway for ethylene oxide reduction to ethylene at a) the equilibrium potential (0.81 V vs RHE) and b) 0 V vs RHE. The free energies of the intermediates with respect to ethylene oxide, protons and electrons are given for Cu(111) (orange), Cu(100) (blue), Cu(311) (purple), Cu(211) (green), 4AD@Cu(100) (red), and 4AD@Cu(111) (yellow).

In the following, we show the free-energy diagrams of the three different studied pathways for each surface model. In all cases, the most favourable pathway is Pathway 1 (in green). The least differences (calculated from Table S10) between the two most stable intermediates of the first hydrogenation, namely, *OH and *CH_3CH_2O, are 0.16, 0.22, 0.21, 0.27, 0.28, and 0.19 eV on Cu(111), Cu(100), Cu(311), Cu(211), 4AD@Cu(100), and 4AD@Cu(111), respectively.

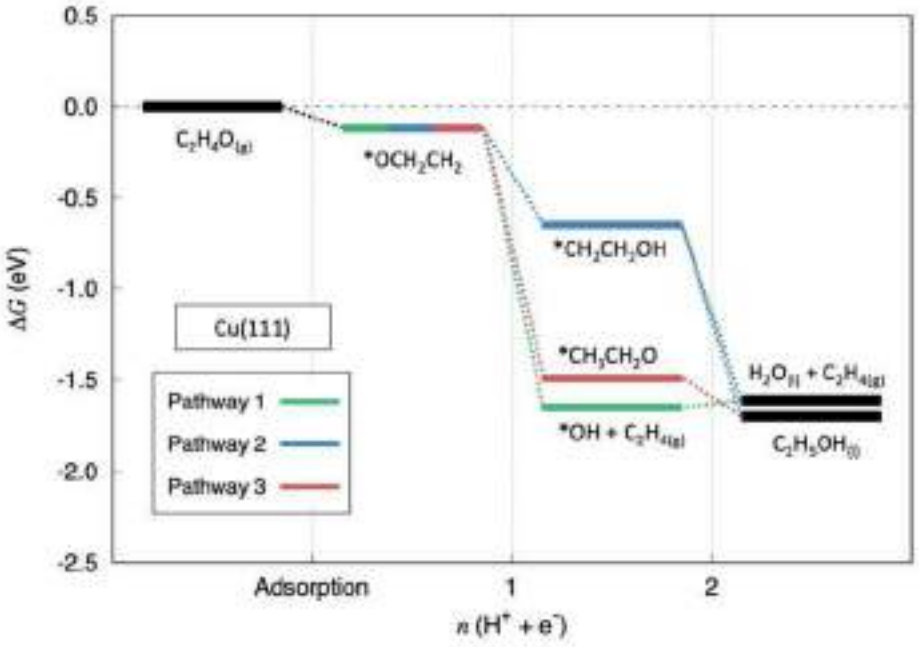

Figure S10. Free energy diagrams of the three studied pathways for ethylene oxide reduction to ethylene and ethanol on Cu(111).

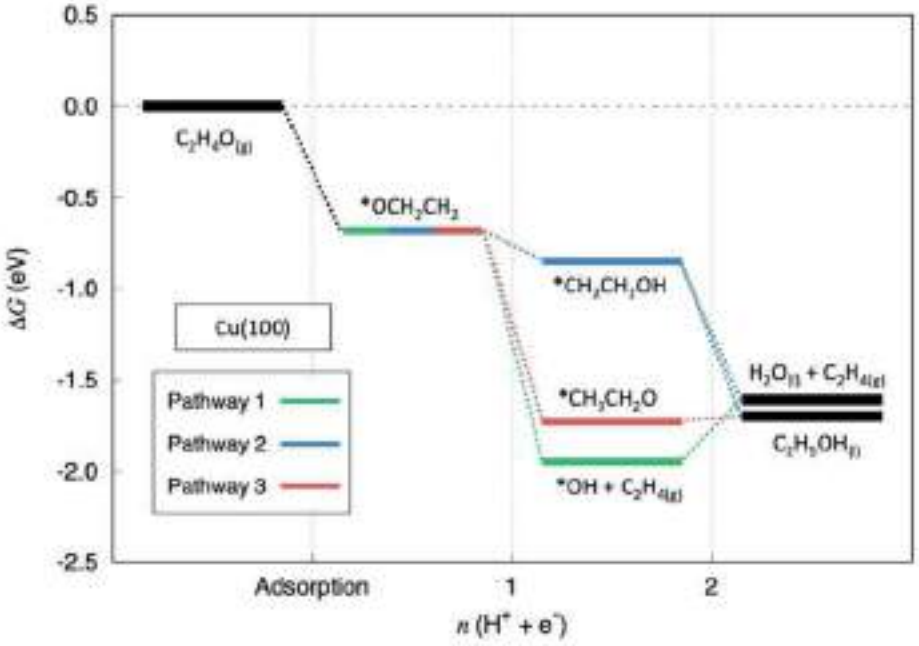

Figure S11. Free energy diagrams of the three studied pathways for ethylene oxide reduction to ethylene and ethanol on Cu(100).

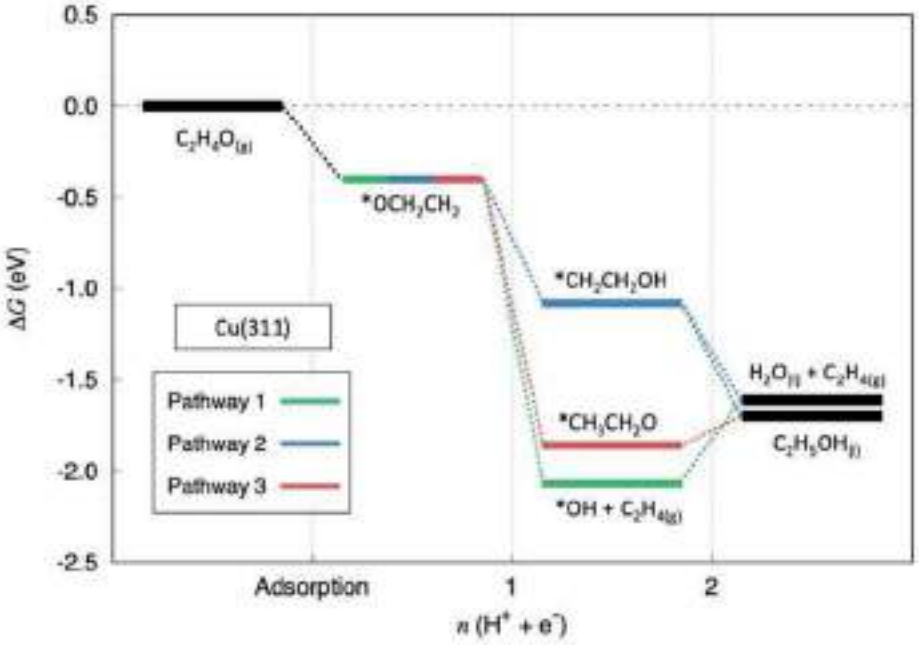

Figure S12. Free energy diagrams of the three studied pathways for ethylene oxide reduction to ethylene and ethanol on Cu(311).

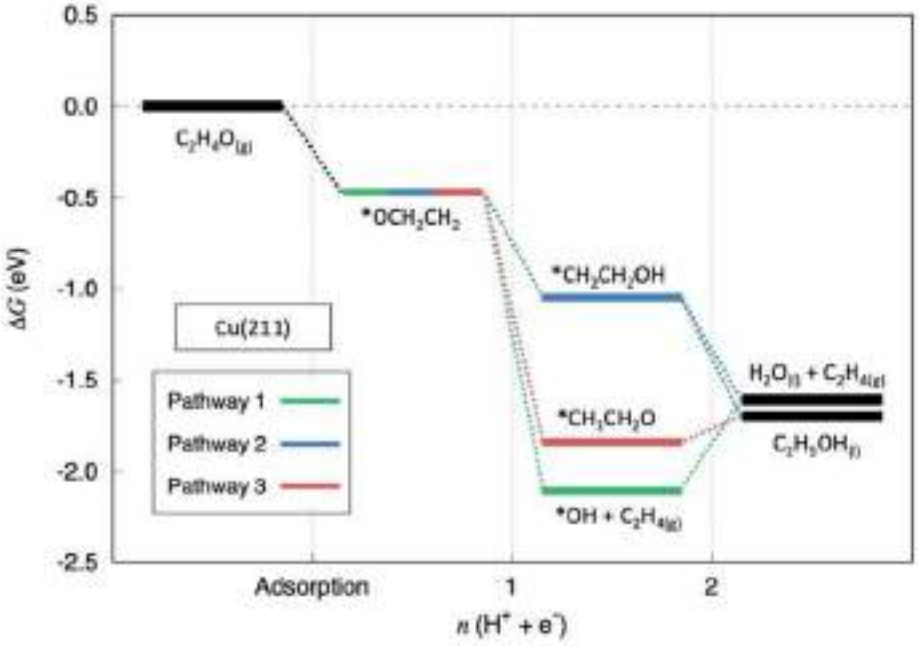

Figure S13. Free energy diagrams of the three studied pathways for ethylene oxide reduction to ethylene and ethanol on Cu(211).

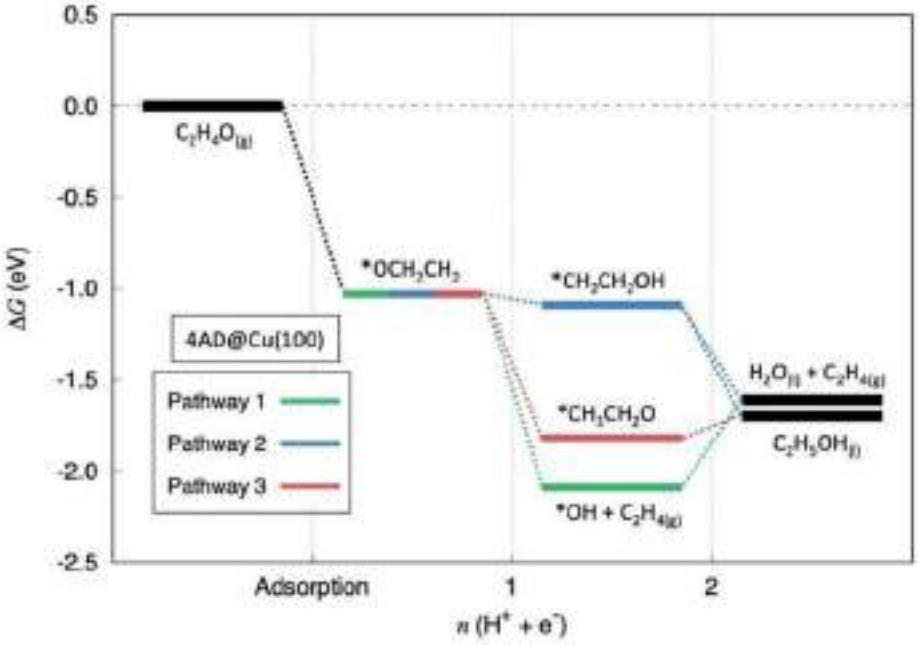

Figure S14. Free energy diagrams of the three studied pathways for ethylene oxide reduction to ethylene and ethanol on 4AD@Cu(100).

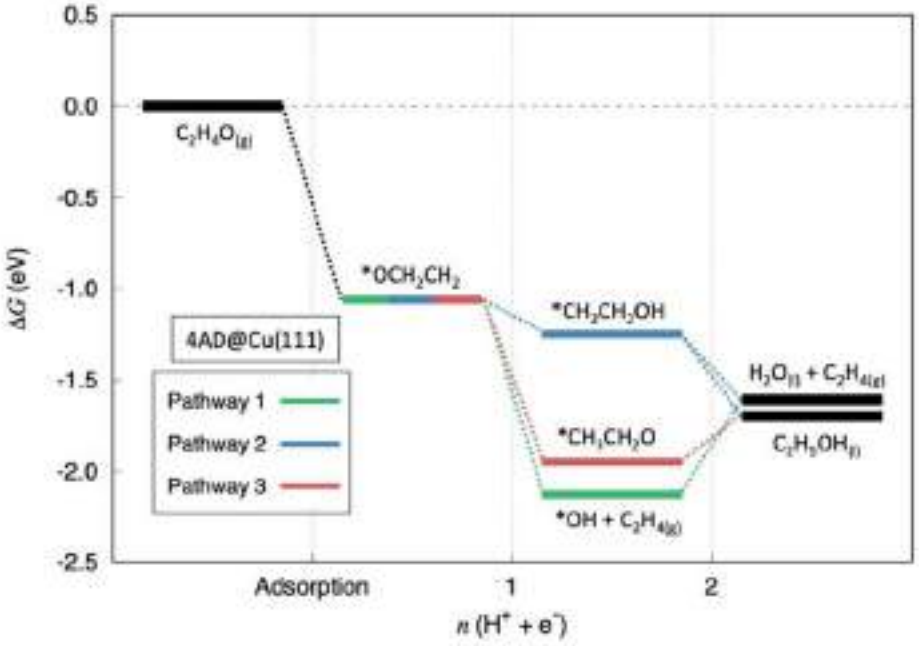

Figure S15. Free energy diagrams of the three studied pathways for ethylene oxide reduction to ethylene and ethanol on 4AD@Cu(111).

S11 References

[1] I. Takahashi, O. Koga, N. Hoshi, Y. Hori, *J. Electroanal. Chem.* **2002**, *533*, 135–143.

[2] H. Siegenthaler, K. Jüttner, *J. Electroanal. Chem.* **1984**, *163*, 327–343.

[3] J. L. Stickney, I. Villegas, C. B. Ehlers, *J. Am. Chem. Soc.* **1989**, *111*, 6473–6474.

[4] Y. Huang, A. D. Handoko, P. Hirunsit, B. S. Yeo, *ACS Catal.* **2017**, *7*, 1749–1756.

[5] Q. H. Low, N. W. X. Loo, F. Calle-Vallejo, B. S. Yeo, *Angew. Chem. Int. Ed.* **2019**, *58*, 2256–2260.

[6] G. Kresse, J. Furthmüller, *Phys. Rev. B* **1996**, *54*, 11169–11186.

[7] J. P. Perdew, K. Burke, M. Ernzerhof, *Phys. Rev. Lett.* **1996**, *77*, 3865–3868.

[8] G. Kresse, D. Joubert, *Phys. Rev. B* **1999**, *59*, 1758–1775.

[9] G. Henkelman, B. P. Uberuaga, H. Jónsson, *J. Chem. Phys.* **2000**, *113*, 9901–9904.

[10] A. Rendón-Calle, S. Builes, F. Calle-Vallejo, *Appl. Catal. B Environ.* **2020**, 119147.

[11] F. Calle-Vallejo, M. T. M. Koper, *Angew. Chem. Int. Ed.* **2013**, *52*, 7282–7285.

[12] A. A. Peterson, F. Abild-Pedersen, F. Studt, J. Rossmeisl, J. K. Nørskov, *Energy Environ. Sci.* **2010**, *3*, 1311–1315.

[13] D. R. Lide, *CRC Handbook of Chemistry and Physics*, CRC Press, Boca Raton, FL, **2005**.

[14] J. K. Nørskov, J. Rossmeisl, A. Logadottir, L. Lindqvist, J. R. Kitchin, T. Bligaard, H. Jónsson, *J. Phys. Chem. B* **2004**, *108*, 17886–17892.

[15] L. Granda-Marulanda, A. Rendon-Calle, S. Builes, F. Illas, M. T. M. Koper, F. Calle-Vallejo, *ACS Catal.* **2020**, *10*, 6900–6907.

[16] F. Calle-Vallejo, A. S. Bandarenka, *ChemSusChem* **2018**, *11*, 1824–1828.

[17] F. Calle-Vallejo, J. I. Martinez, J. M. Garcia-Lastra, P. Sautet, D. Loffreda, *Angew. Chem. Int. Ed.* **2014**, *53*, 8316–8319.

[18] F. Calle-Vallejo, M. D. Pohl, A. S. Bandarenka, *ACS Catal.* **2017**, *7*, 4355–4359.

[19] C. J. Bondue, F. Calle-Vallejo, M. C. Figueiredo, M. T. M. Koper, *Nat. Catal.* **2019**, *2*, 243–250.

[20] K. J. P. Schouten, E. P. Gallent, M. T. M. Koper, *J. Electroanal. Chem.* **2013**, *699*, 6–9.

[21] V. Maurice, H.-H. Strehblow, P. Marcus, *Surf. Sci.* **2000**, *458*, 185–194.

[22] J. Kunze, V. Maurice, L. H. Klein, H.-H. Strehblow, P. Marcus, *J. Electroanal. Chem.* **2003**, *554–555*, 113–125.

[23] P. Daubinger, J. Kieninger, T. Unmüssig, G. A. Urban, *Phys. Chem. Chem. Phys.* **2014**, *16*, 8392–8399.

[24] M. Pourbaix, J. Van Muylder, N. De Zoubov, *Platinum Met. Rev.* **1959**, *3*, 47–53.

[25] Y. Hori, H. Wakebe, T. Tsukamoto, O. Koga, *Surf. Sci.* **1995**, *335*, 258–263.

[26] Y. Hori, I. Takahashi, O. Koga, N. Hoshi, *J. Mol. Catal. Chem.* **2003**, *199*, 39–47.

[27] D. Ren, Y. Deng, A. D. Handoko, C. S. Chen, S. Malkhandi, B. S. Yeo, *ACS Catal.* **2015**, *5*, 2814–2821.

[28] D. Ren, N. T. Wong, A. D. Handoko, Y. Huang, B. S. Yeo, *J. Phys. Chem. Lett.* **2016**, *7*, 20–24.

[29] Y. Lum, B. Yue, P. Lobaccaro, A. T. Bell, J. W. Ager, *J. Phys. Chem. C* **2017**,

121, 14191–14203.
[30] Y. Kwon, Y. Lum, E. L. Clark, J. W. Ager, A. T. Bell, *ChemElectroChem* **2016**, *3*, 1012–1019.
[31] D. Ren, J. Fong, B. S. Yeo, *Nat. Commun.* **2018**, *9*, 925.
[32] C. W. Li, J. Ciston, M. W. Kanan, *Nature* **2014**, *508*, 504–507.

Appendix D

Supporting Information for "Enhancing CO_2 Electroreduction to Ethanol on Copper-Silver Composites by Opening an Alternative Catalytic Pathway"

Supporting Information

Enhancing CO_2 Electroreduction to Ethanol on Copper-Silver Composites by Opening an Alternative Catalytic Pathway

Louisa Rui Lin Ting,[1,2,†] Oriol Piqué,[3,†] Si Ying Lim,[1,2] Mohammad Tanhaei,[4] Federico Calle-Vallejo,[3,*] and Boon Siang Yeo[1,2,*]

[1] Department of Chemistry, National University of Singapore, 3 Science Drive 3, Singapore 117543.

[2] Solar Energy Research Institute of Singapore, National University of Singapore, 7 Engineering Drive 1, Singapore 117574.

[3] Departament de Ciència de Materials i Química Física & Institut de Química Teòrica i Computacional (IQTCUB), Universitat de Barcelona, Martí i Franquès 1, 08028 Barcelona, Spain.

[4] Institute of Materials Research and Engineering, Agency for Science, Technology and Research, 2 Fusionopolis Way, Singapore 138634.

* To whom correspondence should be addressed to: chmyeos@nus.edu.sg, f.calle.vallejo@ub.edu

† These authors contributed equally to this work.

Table of Contents

S1 Catalyst loading

Table S1. Loading of Cu_2O and Ag in catalysts used for CO_2 reduction.

Catalyst	Mass of Cu_2O nanowires per 1 mL of catalyst ink (mg)	Mass of Ag powder per 1 mL of catalyst ink (mg)
OD-Cu NW	1.0	0
Ag-20	N.A.	30.0
Ag-100	N.A.	30.0
Ag-1000	N.A.	30.0
$Cu(Ag\text{-}20)_5$	1.0	7.5
$Cu(Ag\text{-}20)_9$	1.0	13.5
$Cu(Ag\text{-}20)_{15}$	1.0	22.5
$Cu(Ag\text{-}20)_{20}$	1.0	30.0
$Cu(Ag\text{-}100)_{20}$	1.0	30.0
$Cu(Ag\text{-}1000)_{20}$	1.0	30.0
$Cu(Ag\text{-}20)_{20}$-S*	1.0	30.0

*For $Cu(Ag\text{-}20)_{20}$-S, 25 μL of 1 mg/mL Cu_2O nanowires and 25 μL of 30 mg/mL of 20 nm Ag powder were sequentially drop-casted onto the graphite substrate.

N.A.: Not applicable.

S2 Physical characterisation of catalysts

S2.1 Energy dispersive X-ray spectroscopy characterisation of $Cu(Ag\text{-}20)_{20}$

Table S2. Ag/Cu ratio of as-prepared $Cu(Ag\text{-}20)_{20}$, determined by energy dispersive X-ray spectroscopy (EDX).

Ag Content (atom %)	Cu Content (atom %)	Ag/Cu	Average Ag/Cu
27.28	1.67	16.3	
29.56	1.68	17.6	18± 2
31.70	1.59	19.9	

Table S3. Ag/Cu ratio of $Cu(Ag\text{-}20)_{20}$ after one hour of CO_2 reduction electrolysis at -1.1 V vs. RHE, determined by EDX.

Ag Content (atom %)	Cu Content (atom %)	Ag/Cu	Average Ag/Cu
18.60	0.97	19.2	
20.90	0.94	22.2	22± 2
15.86	0.67	23.7	

S2.2 Transmission electron microscopy of Cu(Ag-20)$_{20}$ after electrolysis

Transmission electron microscopy (TEM) was performed on Cu(Ag-20)$_{20}$ after CO_2 electrolysis (Figure S1). It showed that the dispersion process to prepare the TEM sample separated the Cu(Ag-20)$_{20}$ into its OD-Cu NW and Ag-20 components. High-resolution TEM analysis revealed pure Cu(111) and Ag(111) phases respectively for the separated OD-Cu NW and Ag-20 components of Cu(Ag-20)$_{20}$. Collectively, these evidences suggest that the Cu and Ag phases in the Cu(Ag-20)$_{20}$ composite did not alloy during the electrolysis.

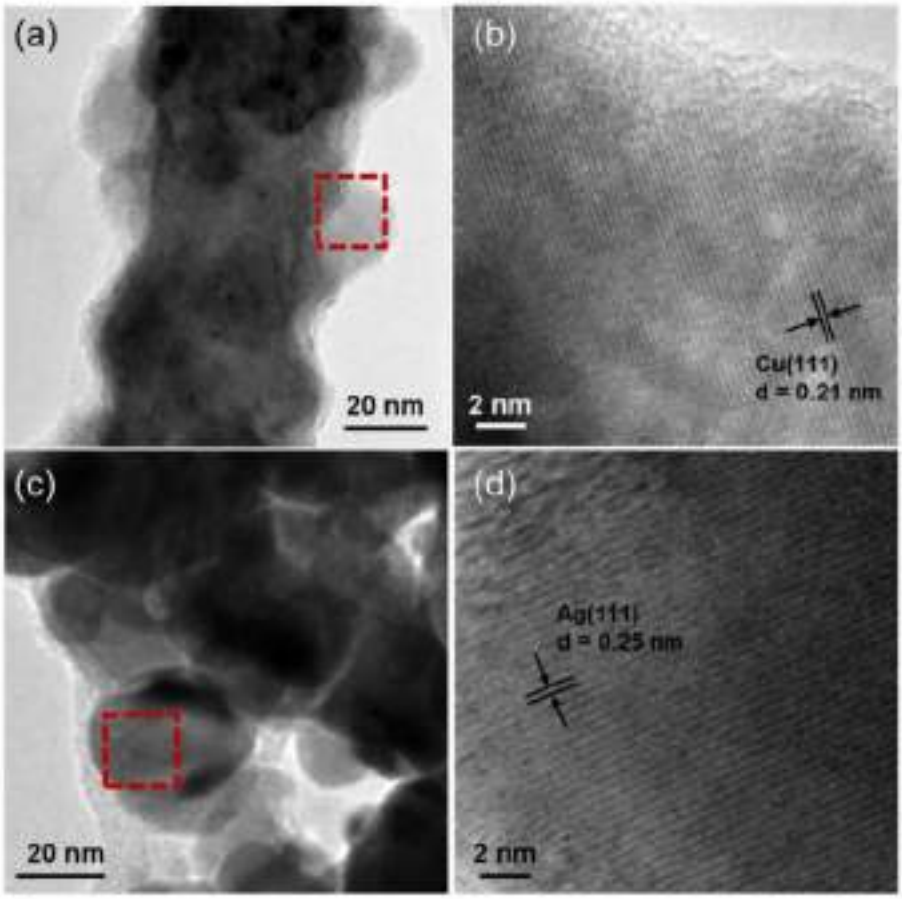

Figure S1. (a) TEM image of OD-Cu NW from Cu(Ag-20)$_{20}$ after electrolysis. (b) High-resolution TEM image of OD-Cu NW from Cu(Ag-20)$_{20}$ after electrolysis. The analysis region is indicated in red on (a). (c) TEM image of Ag-20 from Cu(Ag-20)$_{20}$ after electrolysis. (d) High-resolution TEM image of Ag-20 from Cu(Ag-20)$_{20}$ after electrolysis. The analysis region is indicated in red on (c).

S3 Electrochemical CO_2 reduction on OD-Cu NW, Ag-20, Cu(Ag-20)$_{20}$

The average total current density of each electrolysis was calculated by dividing the total charge passed by the electrolysis duration.

Table S4. Faradaic efficiencies and geometric partial current densities of products detected from CO_2 electroreduction on OD-Cu NW.

V vs. RHE		CO	$HCOO^-$	CH_4	C_2H_4	C_2H_5OH	CH_3CHO	Minor liquids*	H_2	Total
-0.9	FE (%)	11.2	20.7	1.0	7.0	2.0	0.6	3.1	54.5	100.1
	j (mA/cm^2)	-0.29	-0.59	-0.03	-0.21	-0.06	-0.02	-0.09	-1.49	-2.85
-1.0	FE (%)	12.1	13.0	2.1	19.7	5.7	8.0	6.5	29.2	96.2
	j (mA/cm^2)	-0.52	-0.55	-0.09	-0.84	-0.24	-0.34	-0.21	-1.24	-4.25
-1.1	FE (%)	6.9	3.3	14.5	20.1	7.3	5.1	2.8	36.2	96.2
	j (mA/cm^2)	-0.80	-0.39	-1.72	-2.35	-0.85	-0.59	-0.33	-4.29	-11.7
-1.2	FE (%)	1.2	2.7	20.1	6.3	3.0	2.9	0.5	58.4	95.0
	j (mA/cm^2)	-0.23	-0.54	-4.11	-1.30	-0.62	-0.62	-0.09	-11.5	-19.9

* "Minor liquids" include methanol, acetate, n-propanol, propionaldehyde, acetone, allyl alcohol.

Table S5. Faradaic efficiencies and geometric partial current densities of products detected from CO_2 electroreduction on Ag-20.

V vs. RHE		CO	$HCOO^-$	CH_4	C_2H_4	C_2H_5OH	CH_3CHO	Minor liquids*	H_2	Total
-0.9	FE (%)	90.6	0.9	0.01	N.D.	N.D.	N.D.	N.D.	2.1	93.6
	j (mA/cm^2)	-7.91	-0.08	-0.001	N.D.	N.D.	N.D.	N.D.	-0.19	-8.73
-1.0	FE (%)	90.7	2.3	0.01	N.D.	0.12	N.D.	N.D.	1.7	94.8
	j (mA/cm^2)	-10.8	-0.27	-0.001	N.D.	-0.01	N.D.	N.D.	-0.20	-11.9
-1.1	FE (%)	82.7	3.9	0.04	N.D.	0.1	N.D.	N.D.	7.3	94.1
	j (mA/cm^2)	-13.2	-0.62	-0.007	N.D.	-0.02	N.D.	N.D.	-1.17	-15.9
-1.2	FE (%)	68.1	8.4	0.3	N.D.	0.4	N.D.	N.D.	14.7	91.9
	j (mA/cm^2)	-12.5	-1.53	-0.05	N.D.	-0.07	N.D.	N.D.	-2.77	-18.4

* "Minor liquids" include methanol, acetate, n-propanol, propionaldehyde, acetone, allyl alcohol; N.D. = not detected.

Table S6. Faradaic efficiencies and geometric partial current densities of products detected from CO_2 electroreduction on $Cu(Ag\text{-}20)_{20}$.

V vs. RHE		CO	$HCOO^-$	CH_4	C_2H_4	C_2H_5OH	CH_3CHO	Minor liquids*	H_2	Total
-0.9	FE (%)	73.1	1.3	0.04	3.1	2.1	2.4	2.3	16.7	101.0
	j (mA/cm^2)	-7.71	-0.14	-0.004	-0.33	-0.22	-0.25	-0.22	-1.76	-10.5
-1.0	FE (%)	64.7	1.6	0.9	6.7	6.6	2.5	3.3	14.0	100.4
	j (mA/cm^2)	-9.28	-0.23	-0.14	-0.96	-0.94	-0.36	-0.48	-2.00	-14.3
-1.1	FE (%)	17.6	1.4	9.5	14.9	16.5	3.4	5.2	24.5	93.1
	j (mA/cm^2)	-4.42	-0.36	-2.39	-3.76	-4.14	-0.85	-1.32	-6.16	-25.1
-1.2	FE (%)	1.5	0.3	11.4	2.0	2.1	0.4	0.2	77.9	95.8
	j (mA/cm^2)	-0.86	-0.19	-6.52	-1.16	-1.19	-0.24	-0.13	-44.6	-57.2

* "Minor liquids" include methanol, acetate, n-propanol, propionaldehyde, acetone, allyl alcohol.

Table S7. Faradaic efficiencies and geometric partial current densities of products detected from CO_2 electroreduction on polished graphite discs.*

V vs. RHE		CO	$HCOO^-$	CH_4	C_2H_4	C_2H_5OH	CH_3CHO	Minor liquids*	H_2	Total
-0.9	FE (%)	1.1	2.3	N.D.	N.D.	N.D.	N.D.	N.D.	75.8	79.5
	j (mA/cm^2)	-0.006	-0.01	N.D.	N.D.	N.D.	N.D.	N.D.	-0.52	-0.67
-1.0	FE (%)	2.0	6.2	N.D.	N.D.	N.D.	N.D.	N.D.	79.3	87.5
	j (mA/cm^2)	-0.03	-0.08	N.D.	N.D.	N.D.	N.D.	N.D.	-1.01	-1.28
-1.1	FE (%)	4.1	9.3	N.D.	N.D.	N.D.	N.D.	N.D.	76.7	90.4
	j (mA/cm^2)	-0.08	-0.21	N.D.	N.D.	N.D.	N.D.	N.D.	-1.49	-1.98
-1.2	FE (%)	1.8	16.8	N.D.	N.D.	N.D.	N.D.	N.D.	71.0	89.7
	j (mA/cm^2)	-0.05	-0.54	N.D.	N.D.	N.D.	N.D.	N.D.	-2.29	-3.22

* "Minor liquids" include methanol, acetate, n-propanol, propionaldehyde, acetone, allyl alcohol; N.D. = not detected.

S4 Stability of CO_2 reduction on $Cu(Ag\text{-}20)_{20}$ at -1.1V vs RHE

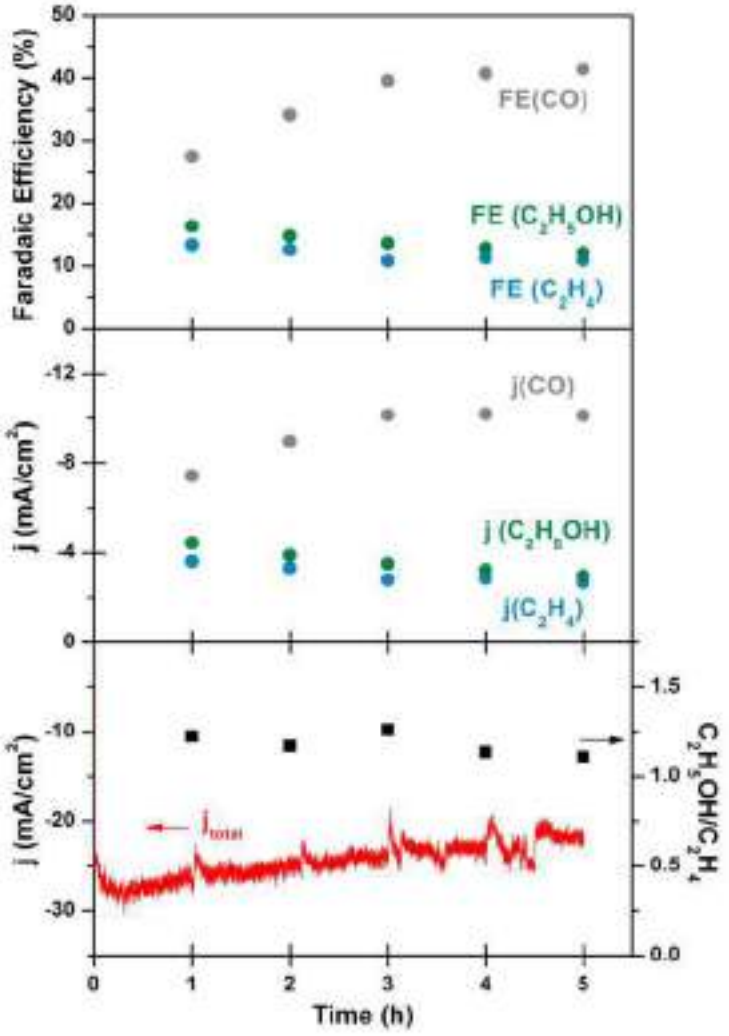

Figure S2. Five-hour stability measurement of electrochemical CO_2 reduction on $Cu(Ag\text{-}20)_{20}$ in CO_2-saturated 0.1 M $KHCO_3$. The potential applied was -1.1 V vs RHE.

The SEM and EDX mapping analyses of $Cu(Ag\text{-}20)_{20}$ after five hours of CO_2 reduction show that there is dissolution and re-deposition of Cu during the prolonged electrolysis (Figure S3). The detection of 0.1 ppm Cu from inductively coupled plasma-optical emission spectrometry (ICP-OES) analysis of the electrolyte also confirms the dissolution of Cu; Ag was not detected. This is consistent with the Ag/Cu ratio of 26±5 detemined by EDX (Table S8), and the increased CO production accompanying the decrease in ethanol and ethylene production (Figure S2).

Table S8. Ag/Cu ratio of $Cu(Ag\text{-}20)_{20}$ after five hours of CO_2 reduction electrolysis at -1.1 V vs. RHE, determined by EDX.

Ag Content (atom %)	Cu Content (atom %)	Ag/Cu	Average Ag/Cu
30.99	1.01	30.7	
19.99	0.75	26.7	26± 5
27.56	1.28	21.5	

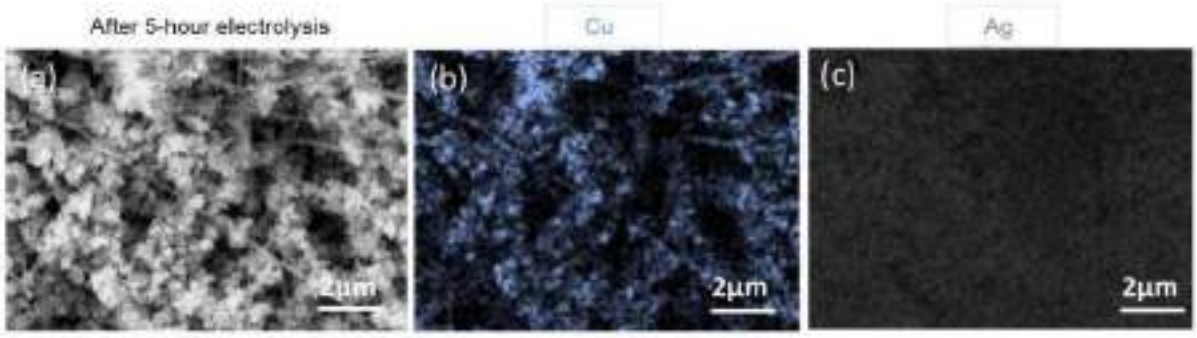

Figure S3. (a) SEM image and EDX mapping of (b) Cu and (c) Ag of $Cu(Ag\text{-}20)_{20}$ after 5-hour CO_2 electrolysis in 0.1 M $KHCO_3$ at -1.1 V vs RHE.

S5 Characterisation and electrochemical CO_2 reduction on $Cu(Ag\text{-}20)_5$, $Cu(Ag\text{-}20)_9$ and $Cu(Ag\text{-}20)_{15}$ at -1.1V vs RHE

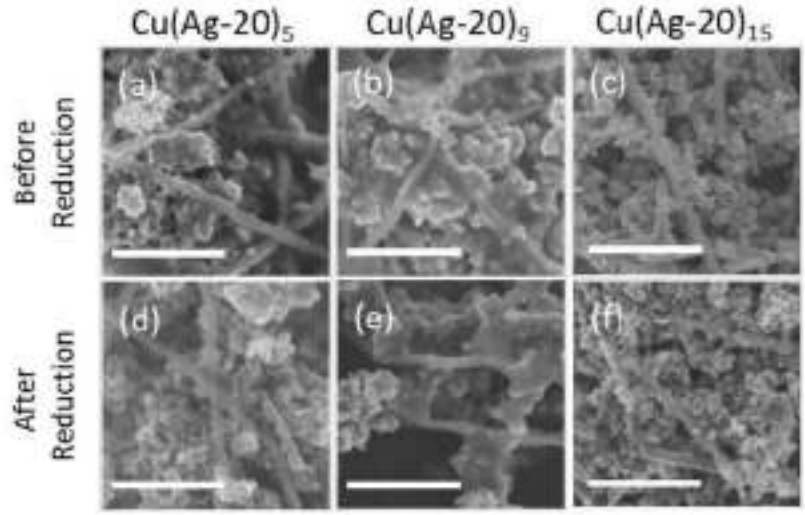

Figure S4. SEM images of $Cu(Ag\text{-}20)_5$, $Cu(Ag\text{-}20)_9$ and $Cu(Ag\text{-}20)_{15}$ before (a-c) and after (d-f) CO_2 reduction at -1.1V vs RHE. Each scale bar represents 1μm.

Table S9. Ag/Cu ratios of $Cu(Ag\text{-}20)_5$, $Cu(Ag\text{-}20)_9$ and $Cu(Ag\text{-}20)_{15}$ before and after CO_2 reduction, determined by EDX.

	$Cu(Ag\text{-}20)_5$	$Cu(Ag\text{-}20)_9$	$Cu(Ag\text{-}20)_{15}$
Before Reduction	4.2 ± 0.4	8.6 ± 1.6	15 ± 1
After Reduction	4.6 ± 0.4	9.0 ± 0.4	14 ± 1

X-ray photoelectron spectroscopy was performed on $Cu(Ag\text{-}20)_M$ composites and Ag-20 after they were used as catalysts for CO_2 reduction. Similar Ag 3d spectra for Ag-20 and the $Cu(Ag\text{-}20)_M$ composites were measured. This shows that the electronic structure of the two metallic phases in the composites was neither modified by the CO_2 electrolysis nor by the catalyst preparation process. Otherwise, there would have been a difference in binding energy shifts between the Ag 3d peaks of composites and Ag-20.[1-2]

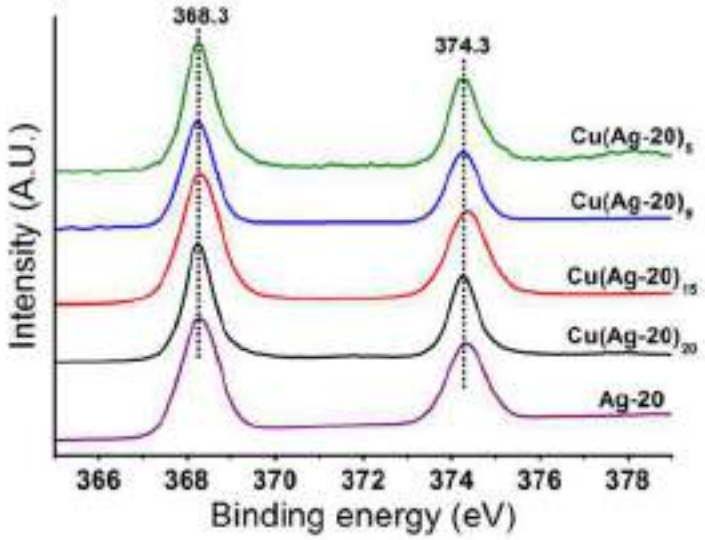

Figure S5. Ag 3d XPS spectra of Ag-20 and $Cu(Ag\text{-}20)_M$.

Table S10. Faradaic efficiencies and geometric partial current densities of products detected from CO_2 electroreduction on Cu(Ag-20)$_5$.

V vs. RHE		CO	$HCOO^-$	CH_4	C_2H_4	C_2H_5OH	CH_3CHO	Minor liquids*	H_2	Total
-0.9	FE (%)	62.4	2.5	0.02	1.7	0.6	1.5	2.1	24.1	94.9
	j (mA/cm^2)	-3.13	-0.12	-0.001	-0.09	-0.03	-0.07	-0.10	-1.21	-5.02
-1.0	FE (%)	35.1	1.9	1.7	15.5	6.7	5.8	6.4	27.2	100.4
	j (mA/cm^2)	-3.14	-0.17	-0.16	-1.39	-0.60	-0.52	-0.58	-2.42	-8.93
-1.1	FE (%)	24.2	2.2	9.0	15.0	10.6	6.2	4.1	21.3	92.6
	j (mA/cm^2)	-4.43	-0.38	-1.61	-2.96	-1.98	-1.10	-0.74	-3.80	-18.4
-1.2	FE (%)	6.7	1.3	13.2	3.8	4.6	1.1	0.9	59.3	90.9
	j (mA/cm^2)	-1.69	-0.43	-4.05	-1.03	-1.27	-0.26	-0.26	-19.3	-30.9

* "Minor liquids" include methanol, acetate, n-propanol, propionaldehyde, acetone, allyl alcohol.

Table S11. Faradaic efficiencies and geometric partial current densities of products detected from CO_2 electroreduction on Cu(Ag-20)$_9$.

V vs. RHE		CO	$HCOO^-$	CH_4	C_2H_4	C_2H_5OH	CH_3CHO	Minor liquids*	H_2	Total
-0.9	FE (%)	50.6	3.4	0.3	6.0	2.6	2.4	3.5	21.5	90.3
	j (mA/cm^2)	-3.04	-0.22	-0.03	-0.39	-0.18	-0.11	-0.23	-1.50	-6.27
-1.0	FE (%)	42.1	2.2	0.7	12.4	7.5	5.3	5.5	17.8	93.7
	j (mA/cm^2)	-4.69	-0.25	-0.08	-1.38	-0.84	-0.59	-0.62	-1.98	-11.1
-1.1	FE (%)	15.6	1.6	10.6	17.1	13.9	8.2	4.9	22.1	94.1
	j (mA/cm^2)	-3.39	-0.34	-2.24	-3.66	-2.98	-1.73	-1.05	-4.75	-21.4
-1.2	FE (%)	1.4	0.5	6.0	1.3	1.3	0.5	0.2	83.1	94.4
	j (mA/cm^2)	-0.54	-0.18	-2.29	-0.51	-0.49	-0.18	-0.09	-31.5	-37.9

* "Minor liquids" include methanol, acetate, n-propanol, propionaldehyde, acetone, allyl alcohol.

Table S12. Faradaic efficiencies and geometric partial current densities of products detected from CO_2 electroreduction on $Cu(Ag\text{-}20)_{15}$.

V vs. RHE		CO	$HCOO^-$	CH_4	C_2H_4	C_2H_5OH	CH_3CHO	Minor liquids*	H_2	Total
-0.9	FE (%)	60.8	1.3	0.03	4.2	2.3	2.6	2.3	23.0	96.4
	j (mA/cm²)	-5.25	-0.11	-0.003	-0.37	-0.19	-0.23	-0.20	-1.99	-8.64
-1.0	FE (%)	37.2	1.2	1.1	12.6	10.5	6.7	6.1	18.0	93.3
	j (mA/cm²)	-5.32	-0.17	-0.16	-1.80	-1.50	-0.95	-0.87	-2.57	-14.3
-1.1	FE (%)	16.7	1.3	12.9	17.0	14.9	5.1	4.4	24.9	97.2
	j (mA/cm²)	-3.84	-0.29	-2.96	-3.92	-3.44	-1.18	-1.00	-5.74	-23.0
-1.2	FE (%)	0.8	0.4	10.0	1.8	1.6	0.4	0.3	80.7	95.9
	j (mA/cm²)	-0.41	-0.22	-5.33	-0.96	-0.83	-0.22	-0.14	-43.2	-53.5

* "Minor liquids" include methanol, acetate, n-propanol, propionaldehyde, acetone, allyl alcohol.

S6 Characterisation and electrochemical CO_2 reduction on $Cu(Ag\text{-}100)_{20}$, $Cu(Ag\text{-}1000)_{20}$, Ag-100 and Ag-1000 at -1.1V vs RHE

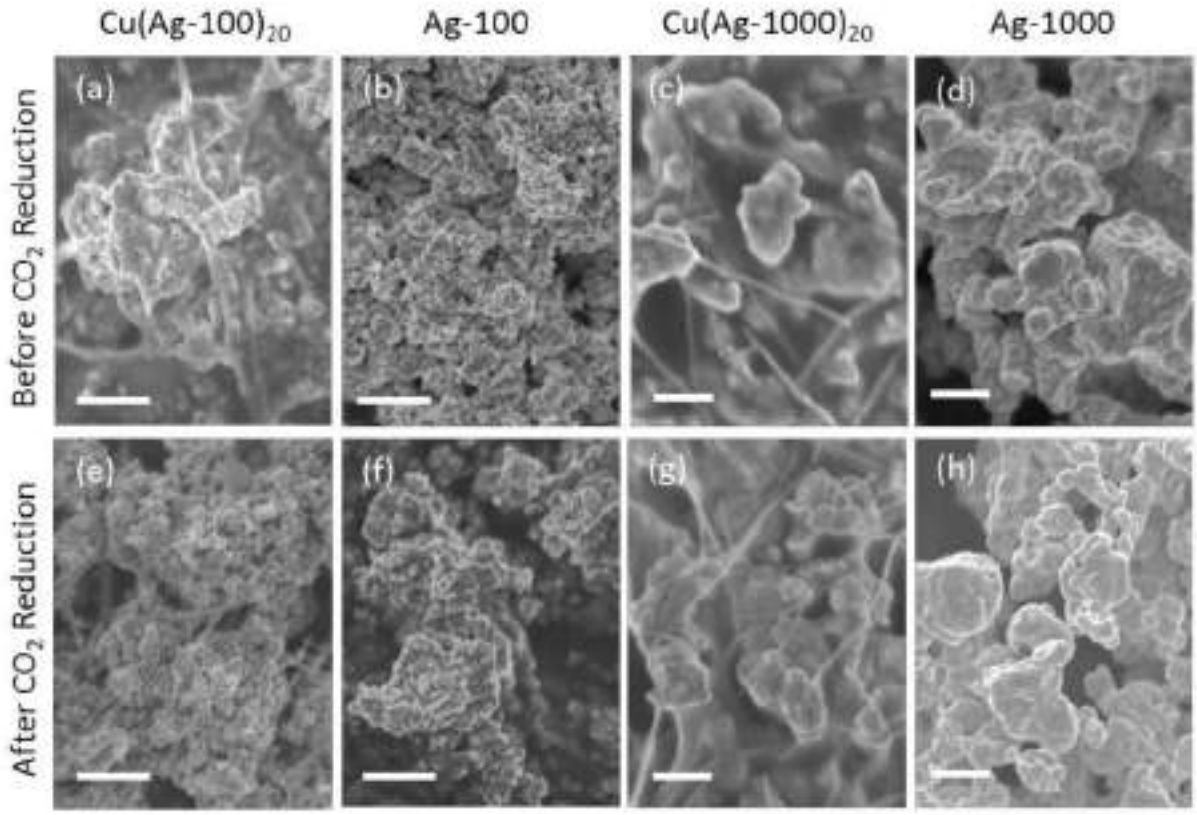

Figure S6. SEM images of $Cu(Ag\text{-}100)_{20}$, Ag-100, $Cu(Ag\text{-}1000)_{20}$ and Ag-1000 before (a-d) and after (e-h) CO_2 reduction at -1.1V vs RHE. Each scale bar represents 1μm.

Table S13. Ag/Cu ratios of $Cu(Ag\text{-}100)_{20}$ and $Cu(Ag\text{-}1000)_{20}$ before and after CO_2 reduction, determined by EDX.

	$Cu(Ag\text{-}100)_{20}$	$Cu(Ag\text{-}1000)_{20}$
Before Reduction	18 ± 1	20 ± 1
After Reduction	20 ± 2	19 ± 2

Table S14. Faradaic efficiencies and geometric partial current densities of products detected from CO_2 electroreduction on $Cu(Ag\text{-}100)_{20}$.

V vs. RHE		CO	$HCOO^-$	CH_4	C_2H_4	C_2H_5OH	CH_3CHO	Minor liquids*	H_2	Total
-0.9	FE (%)	37.1	2.5	0.06	7.2	3.1	4.2	3.4	33.5	91.0
	j (mA/cm^2)	-2.98	-0.20	-0.005	-0.58	-0.25	-0.34	-0.27	-2.69	-8.04
-1.0	FE (%)	52.5	1.3	1.2	9.7	5.6	3.2	4.2	18.0	95.7
	j (mA/cm^2)	-6.59	-0.16	-0.15	-1.21	-0.71	-0.40	-0.53	-2.26	-12.5
-1.1	FE (%)	14.1	1.2	9.6	16.9	13.5	3.9	4.3	27.1	90.6
	j (mA/cm^2)	-3.36	-0.29	-2.31	-4.04	-3.24	-0.93	-1.04	-6.47	-23.9
-1.2	FE (%)	1.5	0.6	9.4	1.4	1.4	0.3	0.3	79.0	93.8
	j (mA/cm^2)	-0.63	-0.24	-3.96	-0.61	-0.57	-0.14	-0.11	-33.3	-42.2

* "Minor liquids" include methanol, acetate, n-propanol, propionaldehyde, acetone, allyl alcohol

Table S15. Faradaic efficiencies and geometric partial current densities of products detected from CO_2 electroreduction on $Cu(Ag\text{-}1000)_{20}$.*

V vs. RHE		CO	$HCOO^-$	CH_4	C_2H_4	C_2H_5OH	CH_3CHO	Minor liquids*	H_2	Total
-0.9	FE (%)	46.7	4.9	0.08	2.3	0.81	1.0	1.2	36.7	93.6
	j (mA/cm^2)	-2.67	-0.28	-0.005	-0.13	-0.05	-0.06	-0.07	-2.10	-5.73
-1.0	FE (%)	45.3	2.9	1.8	10.5	3.5	3.8	4.0	23.2	94.9
	j (mA/cm^2)	-3.78	-0.24	-0.15	-0.88	-0.29	-0.32	-0.33	-1.94	-8.34
-1.1	FE (%)	5.5	1.3	12.4	16.5	7.2	2.6	2.3	44.8	92.6
	j (mA/cm^2)	-1.34	-0.32	-3.01	-4.03	-1.77	-0.64	-0.56	-10.9	-24.4
-1.2	FE (%)	1.4	0.9	11.7	2.3	1.4	0.7	0.2	73.0	91.6
	j (mA/cm^2)	-0.48	-0.31	-3.95	-0.79	-0.47	-0.23	-0.07	-24.7	-33.8

* "Minor liquids" include methanol, acetate, n-propanol, propionaldehyde, acetone, allyl alcohol

S6.1 Consideration of size effects for CO production on Ag powders

Smaller Ag particles could also have more active sites for producing CO. This, along with our observation from Section S5, may imply that ethanol enhancement from the use of smaller Ag particles in the composite could be due to the increased number of CO-producing sites, rather than a result of improved CO spillover from Ag to Cu. To study this effect, we performed control CO_2 reduction experiments on Ag-100 and Ag-1000. At −1.1 V vs RHE, their respective CO current densities of −10.8 and −9.5 mA/cm^2 were similar to the j_{CO} of −13.2 mA/cm^2 observed on Ag-20 at the same potential (Tables S5, S16-S17). The decrease in particle size from 2000 nm to 20 nm only resulted in a 0.4 × increase in j_{CO}. In comparison, j_{CO} values of Ag-1000 (−3.4 mA/cm^2), Ag-100 (−6.0 mA/cm^2) and Ag-20 (−7.9 mA/cm^2) at −0.9 V vs RHE differ by a factor of 2.3. This finding agrees with an earlier report that while 40 nm-sized Ag particles showed >3 times higher j_{CO} than 200 nm particles at smaller overpotentials, their activities were similar at more negative potentials.[3] Overall, we believe that at an applied potential of -1.1 V vs RHE, the enhancement of CO production on Ag particles due to size effects is less significant. Efficient migration of CO from Ag to Cu due to more Cu-Ag boundaries would be a more significant contributor to the enhanced ethanol production.

Table S16. Faradaic efficiencies and geometric partial current densities of products detected from CO_2 electroreduction on Ag-100.

V vs. RHE		CO	$HCOO^-$	CH_4	C_2H_4	C_2H_5OH	CH_3CHO	Minor liquids*	H_2	Total
-0.9	FE (%)	87.3	0.7	0.01	N.D.	N.D.	N.D.	N.D.	6.3	94.3
	j (mA/cm²)	-6.00	-0.05	-0.001	N.D.	N.D.	N.D.	N.D.	-0.43	-6.87
-1.0	FE (%)	87.2	2.2	0.01	N.D.	N.D.	N.D.	N.D.	2.4	91.8
	j (mA/cm²)	-9.31	-0.24	-0.001	N.D.	N.D.	N.D.	N.D.	-0.25	-10.7
-1.1	FE (%)	82.4	4.2	0.06	N.D.	0.3	0.1	N.D.	9.1	96.2
	j (mA/cm²)	-11.2	-0.57	-0.008	N.D.	-0.04	-0.01	N.D.	-1.23	-13.5
-1.2	FE (%)	46.8	4.9	0.02	N.D.	N.D.	N.D.	N.D.	45.6	97.3
	j (mA/cm²)	-9.81	-1.02	-0.004	N.D.	N.D.	N.D.	N.D.	-9.56	-21.0

* "Minor liquids" include methanol, acetate, n-propanol, propionaldehyde, acetone, allyl alcohol; N.D. = not detected.

Table S17. Faradaic efficiencies and geometric partial current densities of products detected from CO_2 electroreduction on Ag-1000.*

V vs. RHE		CO	$HCOO^-$	CH_4	C_2H_4	C_2H_5OH	CH_3CHO	Minor liquids*	H_2	Total
-0.9	FE (%)	82.5	1.1	0.02	N.D.	N.D.	N.D.	N.D.	5.3	89.0
	j (mA/cm²)	-3.43	-0.05	-0.001	N.D.	N.D.	N.D.	N.D.	-0.22	-4.15
-1.0	FE (%)	90.8	1.9	0.01	N.D.	N.D.	N.D.	N.D.	3.5	96.3
	j (mA/cm²)	-7.04	-0.14	-0.001	N.D.	N.D.	N.D.	N.D.	-0.27	-7.76
-1.1	FE (%)	80.4	5.1	0.03	N.D.	0.23	0.1	0.06	7.2	93.1
	j (mA/cm²)	-9.47	-0.60	-0.003	N.D.	-0.03	-0.01	-0.007	-0.84	-11.8
-1.2	FE (%)	46.7	6.0	0.1	N.D.	N.D.	N.D.	N.D.	43.6	96.4
	j (mA/cm²)	-8.16	-1.06	-0.009	N.D.	N.D.	N.D.	N.D.	-7.61	-17.5

* "Minor liquids" include methanol, acetate, n-propanol, propionaldehyde, acetone, allyl alcohol; N.D. = not detected.

S7 Electrochemical CO_2 reduction on $Cu(Ag\text{-}20)_{20}$-S

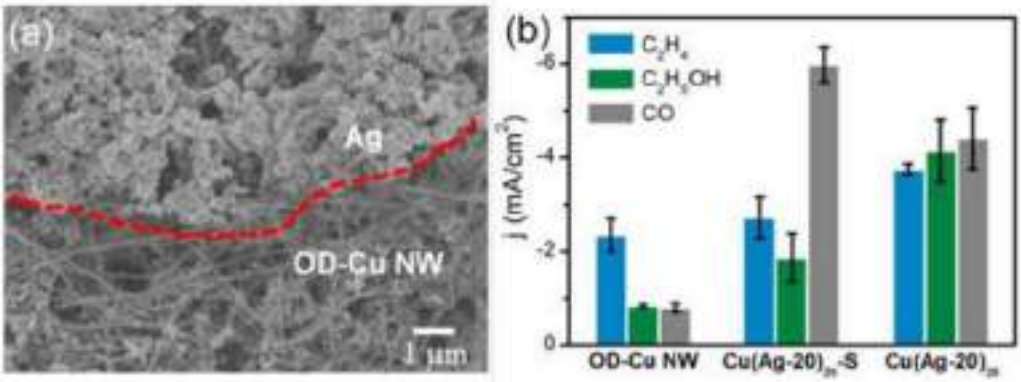

Figure S7. (a) SEM image of $Cu(Ag\text{-}20)_{20}$-S after CO_2 reduction at -1.1 V vs RHE. The red line highlights the distinct regions of OD-Cu NW nanowires and Ag particles in the sample. (b) Partial current densities of ethylene, ethanol and CO obtained at -1.1 V vs RHE for OD-Cu NW, $Cu(Ag\text{-}20)_{20}$-S and $Cu(Ag\text{-}20)_{20}$.

Table S18. Faradaic efficiencies and geometric partial current densities of products detected from CO_2 electroreduction on $Cu(Ag\text{-}20)_{20}$-S at -1.1V vs RHE.

	CO	$HCOO^-$	CH_4	C_2H_4	C_2H_5OH	CH_3CHO	Minor liquids*	H_2	Total
FE (%)	32.5	2.6	5.9	14.7	10.4	2.8	3.6	20.1	92.4
***j* (mA/cm²)**	-5.98	-0.48	-1.12	-2.72	-1.86	-0.52	-0.65	-3.74	-18.5

* Minor liquids include methanol, acetate, n-propanol, propionaldehyde, acetone, allyl alcohol.

S8 Electrochemical CO_2 reduction on Ag clusters on Cu foils

We have prepared Ag nanoclusters on Cu foil samples, by means of galvanic deposition of Ag (from aqueous 2 mM and 5 mM $AgNO_3$ solutions) on Cu foils electropolished in 85% phosphoric acid (+ 0.1A applied for 60s). The samples are labelled as "CuAg-Gx", where x is the concentration of $AgNO_3$ in mM used in the galvanic deposition. The deposition duration was 30s. CO_2 electrolysis was performed on electropolished Cu (EP-Cu), CuAg-G2 and CuAg-G5 at -1.1 V vs RHE in 0.1 M $KHCO_3$.

The surface Ag/Cu ratios of CuAg-G2 and CuAg-G5 after electrolysis were determined by XPS to be 1.7 and 2.2 respectively. From the SEM images of the CuAg-G2 and CuAg-G5 catalysts (post-electrolysis; Figure S8a, c), we determined the number of Ag clusters per unit area and measured their diameters in order to calculate the estimated total Cu-Ag boundary length (Figure S8b, d). Similar to the trend observed for the case of the CuAg composites prepared from OD-Cu NW and Ag powders, the ethanol enhancement (maximum of 3.8×) was greater than ethylene enhancement (maximum of 1.8×) (Figure S8e). However, due to the lower surface area of the Ag nanoclusters on Cu foils, the geometric partial current densities of ethanol and ethylene (Table S19) were lower than that on the CuAg composites.

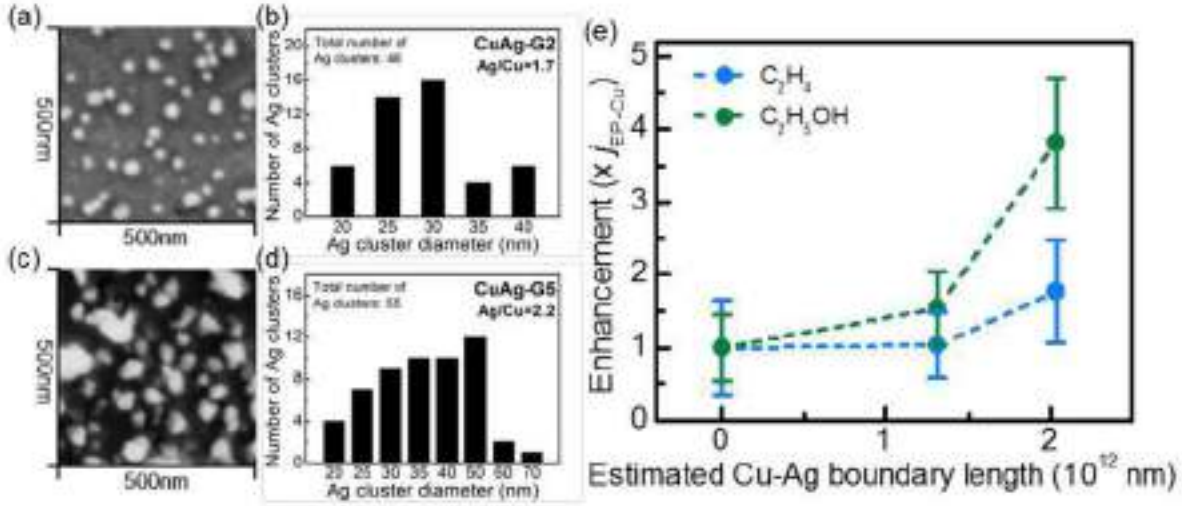

Figure S8. (a, c) SEM images, (b, d) number of Ag clusters and their respective diameters for CuAg-G2 (a, b) and CuAg-G5 (c, d). (e) Enhancement of ethanol and ethylene from CO_2RR on CuAg-G2 and CuAg-G5 compared with CO_2RR on electropolished Cu, plotted against the estimated Cu-Ag boundary length on the working electrode.

Table S19. Faradaic efficiencies and geometric partial current densities of products detected from CO_2 electroreduction on electropolished Cu, CuAg-G2 and CuAg-G5 at -1.1 V vs RHE.

Catalyst		CO	$HCOO^-$	CH_4	C_2H_4	C_2H_5OH	CH_3CHO	Other liquids*	H_2	Total
Electro-polished Cu	FE (%)	2.5	4.1	35.8	15.0	5.3	1.3	2.8	34.0	100.7
	j (mA/cm^2)	-0.21	-0.34	-3.25	-1.36	-0.52	-0.12	-0.26	-2.82	-8.85
CuAg-G2	FE (%)	20.3	2.3	16.1	15.8	9.2	8.4	10.9	9.0	92.1
	j (mA/cm^2)	-1.63	-0.20	-1.44	-1.39	-0.80	-0.73	-0.95	-0.77	-8.65
CuAg-G5	FE (%)	8.9	1.6	18.3	18.2	15.3	6.0	8.4	14.8	91.4
	j (mA/cm^2)	-1.15	-0.20	-2.47	-2.41	-1.99	-0.78	-1.10	-1.95	-13.21

*Other liquids include methanol, acetate, n-propanol, propionaldehyde, acetone, allyl alcohol.

S9 Electrochemical CO_2 reduction on Cu(Ag-20)$_{20}$-M

Metallic Cu nanowires were synthesised according to a published procedure.[4] The synthesised nanowires were washed with ethanol and dried under vacuum. XRD analysis (Figure S9a) confirmed that the nanowires contained Cu^0.

One milligram of Cu NW was ultrasonicated in 1 mL of solvent (75% H_2O, 20% ethanol, 5% Nafion) to form a homogeneous catalyst ink. 25 μL of this ink was dropcast onto polished graphite substrates and dried in a vacuum dessicator. Cu(Ag-20)$_{20}$-M samples was prepared in the same procedure, by ultrasonicating 1 mg of Cu NW with 34 mg of 20 nm Ag powder in 1 mL of solvent to form the ink. SEM analysis showed that the Cu NW had diameter of about 100-200 nm (Figure S9b), and that Cu NW and Ag powder was homogeneously mixed in Cu(Ag-20)$_{20}$-M (Figure S9c).

CO_2 electroreduction experiments were performed on Cu NW and Cu(Ag-20)$_{20}$-M samples at -1.1 V vs RHE in 0.1M $KHCO_3$ (Figure S9, Table S20). Addition of Ag to Cu NW improves the partial current density of ethanol by 10 times, while ethylene partial current density increased by only 4 ×. We also see that the enhancement effect on ethanol is higher on the metallic Cu system (~20×) than the oxide-derived Cu system (~5×).

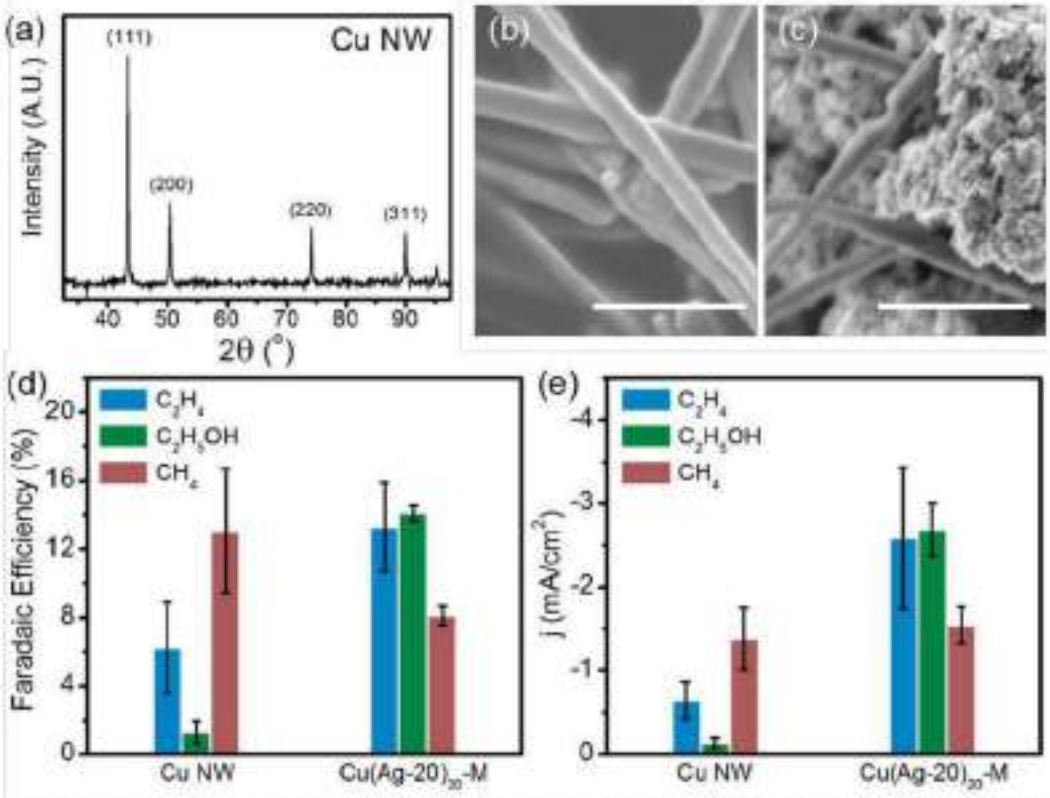

Figure S9. (a) XRD pattern of as-synthesised Cu nanowires. SEM images of (b) Cu NW and (c) Cu(Ag-20)$_{20}$-M after CO_2 reduction at -1.1 V vs RHE. The scale bar represents 1 μm. (d) Faradaic efficiencies and (e) partial current densities of ethylene, ethanol and methane obtained from CO_2 electrolysis at -1.1 V vs RHE for Cu NW and Cu(Ag-20)$_{20}$-M.

Table S20. Faradaic efficiencies and geometric partial current densities of products detected from CO_2 electroreduction on Cu NW and Cu(Ag-20)$_{20}$-M at -1.1 V vs RHE.*

Catalyst		H_2	$HCOO^-$	CO	CH_4	C_2H_4	C_2H_5OH	CH_3CHO	Minor liquids	Total
Cu NW	**FE (%)**	61.3	8.9	2.8	13.0	6.2	1.3	0.95	2.3	96.9
	***j* (mA/cm^2)**	-6.6	-0.95	-0.29	-1.4	-0.65	-0.13	-0.10	-0.24	-10.6
Cu(Ag-20)$_{20}$-M	**FE (%)**	18.1	1.2	29.4	8.1	13.3	14.1	1.3	6.0	92.8
	***j* (mA/cm^2)**	-3.5	-0.46	-5.4	-1.5	-2.6	-2.7	-0.24	-1.2	-19.1

* "Minor liquids" include methanol, acetate, n-propanol, propionaldehyde, acetone, allyl alcohol; N.D. = not detected

S10 CO reduction on OD-Cu NW and Cu(Ag-20)$_{20}$ catalysts

Table S21. Product distribution of CO reduction on OD-Cu NW in 0.1 M $KHCO_3$.

Applied Potential (V vs RHE)		CH_4	C_2H_4	C_2H_5OH	Minor liquids	H_2	Total
-0.75	FE (%)	0.1	1.4	0.9	1.3	82.2	85.9
	j (mA/cm^2)	-0.002	-0.02	-0.01	-0.01	-1.00	-1.21
-0.80	FE (%)	0.3	3.6	1.5	1.6	82.2	89.3
	j (mA/cm^2)	-0.004	-0.05	-0.02	-0.02	-1.18	-1.44
-0.90	FE (%)	1.6	1.9	0.8	0.6	88.5	93.5
	j (mA/cm^2)	-0.04	-0.04	-0.02	-0.01	-2.20	-2.43

* Minor liquids include n-propanol, acetaldehyde, propionaldehyde, acetone, allyl alcohol.

Table S22. Product distribution of CO reduction on Cu(Ag-20)$_{20}$ in 0.1 M $KHCO_3$.

Applied Potential (V vs RHE)		CH_4	C_2H_4	C_2H_5OH	Minor liquids	H_2	Total
-0.75	FE (%)	0.2	0.6	0.5	0.2	94.1	95.6
	j (mA/cm^2)	-0.01	-0.02	-0.01	-0.006	-2.58	-2.73
-0.80	FE (%)	0.5	1.7	0.7	0.7	88.3	91.9
	j (mA/cm^2)	-0.02	-0.06	-0.02	-0.02	-2.84	-3.19
-0.90	FE (%)	2.2	1.1	0.5	0.1	93.0	96.9
	j (mA/cm^2)	-0.16	-0.09	-0.04	-0.01	-7.20	-7.65

* Minor liquids include n-propanol, acetaldehyde, propionaldehyde, acetone, allyl alcohol.

S10.1 Estimation of CO flux from Fick's law

From Fick's law:

Diffusion flux, $J = -D\frac{c}{\Delta x}$

Where:

D is the diffusion coefficient of CO in water, -2.03 × 10^{-9} m^2/s

c is the concentration of CO in aqueous electrolyte, 1 mM (Derived from the room temperature solubility of CO in water, 0.028 g CO per kg H_2O)

Δx is the thickness of the diffusion layer, estimated to be 0.01cm

Therefore, the diffusion flux of CO during CO electrolysis was determined to be 2.0×10^{-9} mol cm^{-2} s^{-1}.

S10.2 Estimation of CO generation rate from Ag-20 at -1.1 V vs. RHE

We estimated the CO generation rate per unit electrode area from the j_{co} value of Ag-20 at -1.1 V, which was the potential that showed the highest $j_{ethanol}$ for CO_2 reduction on $Cu(Ag\text{-}20)_{20}$.

CO generation rate = $\frac{j_{CO}}{F\times n}$

Where

j_{CO} on Ag-20 at -1.1V = -13.2 mA cm^{-2}

F is the Faraday constant, 96485.3 C mol^{-1}

n = 2, the number of moles of electrons transferred to produce one mole of CO from CO_2

Therefor, CO generation rate = $\frac{0.0132\ A\ cm^{-2}}{96485.3\ C\ mol^{-1}\times2}$ = 6.8 × 10^{-8} mol cm^{-2} s^{-1}

S11 Acetaldehyde electrolysis on $Cu(Ag\text{-}20)_{20}$

One-hour electrolysis of 5 mM acetaldehyde (Sigma Aldrich, > 99.5%) in 0.1 M $KHCO_3$ at −25 $mAcm^{-2}$ was performed on $Cu(Ag\text{-}20)_{20}$. The products formed are shown in Table S23. The major product is ethanol.

Table S23. Product distributions of acetaldehyde electrolysis on $Cu(Ag\text{-}20)_{20}$ in N_2-saturated 0.1 M $KHCO_3$.

	H_2	C_2H6	C_2H_5OH	1-Butanol	Total
FE (%)	87.2	0.2	2.7	0.01	90.1
***j* (mA/cm²)**	-21.8	-0.04	-0.68	-0.003	-25.0

S12 Gas-phase corrections

The free energies of gas-phase molecules were estimated as: $G = E_{DFT} + ZPE - TS$. The ZPE (from vibrational frequency analyses) and TS values (from thermodynamic tables[5]) at 298.15 K used for gas-phase species featured in this study are listed in Table S24. The PBE exchange-correlation functional does not describe correctly the free energy of $CO_{(g)}$ and $CO_{2(g)}$[6-8]. Hence, corrections to the formation energy of -0.24 eV and 0.19 eV were applied, respectively.

Table S24. Zero-point energy and entropy contributions to free energy of gas-phase molecules. All values are in eV.

Molecule	ZPE	TS
CO_2	0.31	0.66
CO	0.14	0.61
H_2	0.27	0.40
C_2H_4	1.36	0.68
H_2O	0.57	0.58
CH_3CHO	1.47	0.82
C_2H_5OH	2.11	0.87

S13 Liquid-phase corrections

Some main products of CO_2 reduction on Cu such as water, ethanol, and acetaldehyde are formed in the liquid phase. Their free energies are estimated using the method described in Ref. 6, which is based on a correction to the TS values.[6] The liquid-phase free energies of water, ethanol, and acetaldehyde were estimated using TS values of 0.67 eV, 0.94 eV, and 0.87 eV, respectively.

S14 Solvation contributions to the free energies

Solvation contributions to the free energies were modelled as an external correction depending on the chemical nature of the adsorbates. We used the values tabulated in previous works,[6] and added a new correction for *OR adsorbates, which we approximate as 2/3 of the *ROH correction. Such correction is justified by the fact that the O atom in *OR is able to create hydrogen bonds with H atoms from water. The specific values used are listed in Table S25.

Table S25. Solvation corrections depending on the adsorbates' chemical nature.

Functional group	Solvation Correction (eV)
-CO	-0.10
*OH	-0.50
*ROH	-0.38
*OR	-0.25

S15 Adsorption energies, kinetic barriers and alloy formation energies

The ZPE, TS_{vib}, solvation energy (E_{sol}), and the corresponding ΔG values obtained for the different adsorbates featured in this study are listed below. For CO_2 electroreduction, $CO_{2(g)}$ was used as a reference. The specific values are listed in Table S26.

Table S26. Free energies of adsorption and its contributions for each species involved in CO_2 electroreduction to CO. All values are in eV.

Cu(111)	ZPE	TS_{vib}	E_{sol}	ΔG
*COOH	0.61	0.23	-0.48	0.43
*CO	0.17	0.15	-0.10	-0.07

Cu(211)	ZPE	TS_{vib}	E_{sol}	ΔG
*COOH	0.62	0.22	-0.48	-0.04
*CO	0.18	0.18	-0.10	-0.22

Ag-Cu	ZPE	TS_{vib}	E_{sol}	ΔG
*COOH	0.61	0.24	-0.48	0.47
*CO	0.16	0.28	-0.10	0.32

For the thermodynamic comparison between the coupling (*CH + *CO) and the dimerisation (*CO + *CO) pathways, 2 *CO were used as a reference. The specific values are listed in Table S27.

Table S27. ΔG and its contributions for each species involved in the electroreduction of 2 *CO to *CHCO. All values are in eV.

Cu(111)	ZPE	TS_{vib}	E_{sol}	ΔG
2 *CO	0.35	0.36	-0.20	0.00
$*C_2O_2H$	0.71	0.31	-0.48	1.36
$*C_2O$	0.34	0.19	-0.10	0.23
*CHCO	0.60	0.24	-0.10	0.26
*COH + *CO	0.63	0.31	-0.48	0.99
*CHOH + *CO	0.93	0.33	-0.48	1.00
*CH + *CO	0.51	0.20	-0.10	0.91

For the study of *CHCO electroreduction to ethanol, *CHCO was used as a reference. The specific values are listed in Table S28. Note that liquid species such as acetaldehyde and ethanol are not listed in the table since their values have been provided in a previous section.

Table S28. ΔG and its contributions for each species involved in *CHCO electroreduction to ethanol. All values are in eV.

Cu(111)	ZPE	TS_{vib}	E_{sol}	ΔG
*CHCO	0.60	0.24	-0.10	0.00
*CHCOH	0.90	0.19	-0.38	-0.01
*CHCHO	0.90	0.18	-0.25	-0.23
*CH_2CO	0.86	0.41	-0.10	-0.04
*CH_3CO	1.19	0.30	-0.10	-0.45
*CH_2COH	1.19	0.23	-0.38	0.03
*CH_2CHO	1.19	0.20	-0.25	-0.41
*$CHCH_2O$	1.17	0.18	-0.25	0.56
*CHCHOH	1.20	0.26	-0.38	-0.27
*CH_3COH	1.49	0.31	-0.38	-0.17
*O	0.07	0.04	0.00	-0.26
*CH_2CHOH	1.52	0.33	-0.38	-0.52
*OCH_2CH_2	1.51	0.17	-0.25	0.00
*CH_3CH_2O	1.84	0.31	-0.25	-1.13
*CH_3CHOH	1.81	0.30	-0.38	-0.46

In Figure S10 we provide all the pathways inspected for CH_xCO reduction to acetaldehyde, ethanol and ethylene.

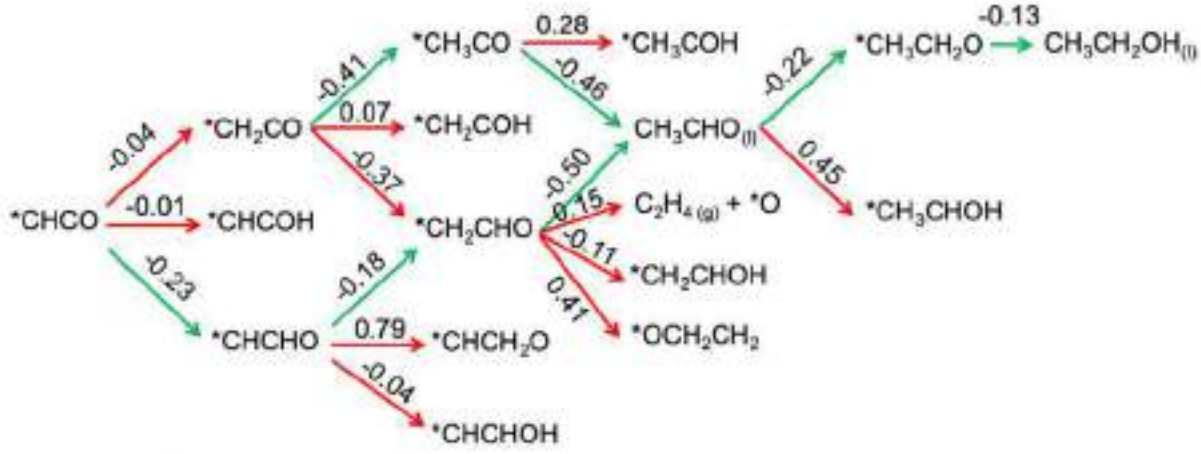

Figure S10. Pathways inspected for the production of ethanol and ethylene from *CHCO, including as well *CH_2CO, and *CH_3CO. The values over the arrows are the reaction free energies in eV. Green arrows lead, in each case, to the most stable intermediate, and red arrows are used for the least favorable intermediates.

Specific values obtained for the coupling of the species under study and for CO diffusion from Ag@Cu to Cu(111) are listed in Table S29.

Table S29. Coupling barriers via Langmuir-Hinshelwood (L-H) or Eley-Rideal (E-R) mechanisms on Cu(111), and CO diffusion barrier from Ag@Cu to Cu(111). All values are in eV.

Coupling on Cu(111)	L-H $\Delta G^{\ddagger}$	E-R $\Delta G^{\ddagger}$
CH + CO	0.70	1.40
CH_2 + CO	0.71	1.49
CH_3 + CO	1.20	---

Diffusion from Ag cluster to Cu(111)	$\Delta G^{\ddagger}$
CO	0.17

Furthermore, Figure S11 shows the alloy formation energies for various CuAg and CuAu alloys as a function of the alloy composition.

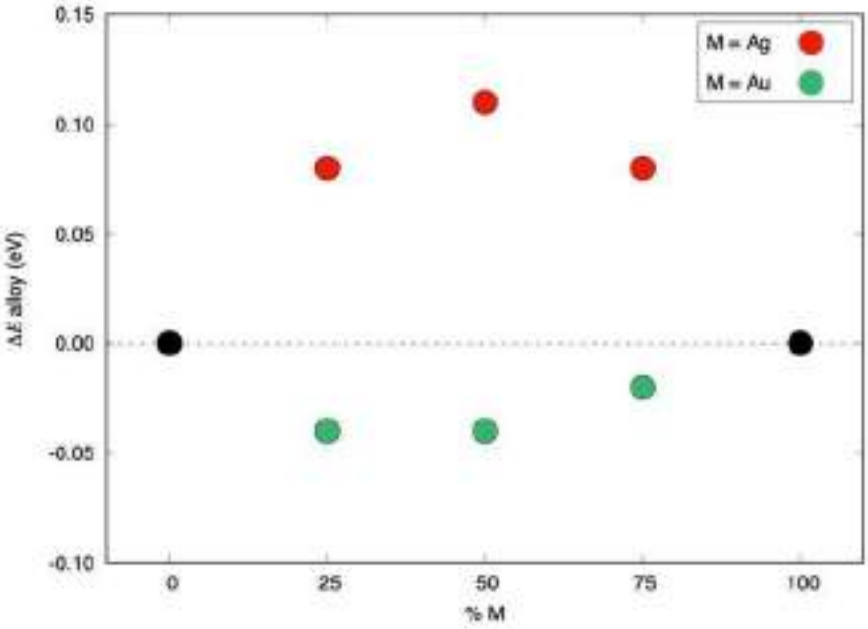

Figure S11. DFT-calculated alloy formation energies versus the % of M in CuM alloys. M = Ag (red), Au (green).

Finally, Table S30 shows the DFT adsorption energy of *CO and its variations in presence of co-adsorbed oxygen (both surface and subsurface) for Ag(111) and Cu(111).

Table S30. DFT-calculated *CO and *CO+*O adsorption energies on Ag(111) and Cu(111). All values are in eV.

Species	Ag(111)	Cu(111)
*CO	0.57	-0.19
*CO (with surface *O)	0.46	0.02
*CO (with subsurface *O)	0.52	-0.23

References

(1) Huang, J.; Mensi, M.; Oveisi, E.; Mantella, V.; Buonsanti, R., Structural Sensitivities in Bimetallic Catalysts for Electrochemical CO_2 Reduction Revealed by Ag–Cu Nanodimers. *J. Am. Chem. Soc.* **2019,** *141*, 2490-2499.

(2) Chang, Z.; Huo, S.; Zhang, W.; Fang, J.; Wang, H., The Tunable and Highly Selective Reduction Products on Ag@Cu Bimetallic Catalysts toward CO_2 Electrochemical Reduction Reaction. *J. Phys. Chem. C* **2017,** *121*, 11368-11379.

(3) Salehi-Khojin, A.; Jhong, H.-R. M.; Rosen, B. A.; Zhu, W.; Ma, S.; Kenis, P. J. A.; Masel, R. I., Nanoparticle Silver Catalysts that Show Enhanced Activity for Carbon Dioxide Electrolysis. *J. Phys. Chem. C* **2013,** *117*, 1627-1632.

(4) Kim, M. J.; Flowers, P. F.; Stewart, I. E.; Ye, S.; Baek, S.; Kim, J. J.; Wiley, B. J., Ethylenediamine Promotes Cu Nanowire Growth by Inhibiting Oxidation of Cu(111). *J. Am. Chem. Soc.* **2017,** *139*, 277-284.

(5) Lide, D. R., *CRC Handbook of Chemistry and Physics*. 85th ed.; CRC Press: Boca Raton, FL, 2005.

(6) Calle-Vallejo, F.; Koper, M. T. M., Theoretical Considerations on the Electroreduction of CO to C_2 Species on Cu(100) Electrodes. *Angew. Chem. Int. Ed.* **2013,** *52*, 7282-7285.

(7) Peterson, A. A.; Abild-Pedersen, F.; Studt, F.; Rossmeisl, J.; Norskov, J. K., How Copper Catalyzes the Electroreduction of Carbon Dioxide into Hydrocarbon Fuels. *Energy Environ. Sci.* **2010,** *3*, 1311-1315.

(8) Christensen, R.; Hansen, H. A.; Vegge, T., Identifying Systematic DFT Errors in Catalytic Reactions. *Catal. Sci. Technol.* **2015,** *5*, 4946-4949.

Appendix E

Supporting Information for "Toward Efficient Tandem Electroreduction of CO_2 to Methanol Using Anodized Titanium"

Supporting Information

Toward Efficient Tandem Electroreduction of CO_2 to Methanol using Anodized Titanium

Wei Jie Teh[a], Oriol Piqué[b], Qi Hang Low[a], Weihan Zhu[a], Federico Calle-Vallejo[b,], Boon Siang Yeo[a,*]*

[a] Department of Chemistry, National University of Singapore, 3 Science Drive 3, Singapore 117543 and Solar Energy Research Institute of Singapore, National University of Singapore, 7 Engineering Drive 1, Singapore 117574.

[b] Department of Materials Science and Chemical Physics & Institute of Theoretical and Computational Chemistry (IQTCUB), University of Barcelona, Martí i Franquès 1, 08028 Barcelona, Spain.

* To whom correspondence should be addressed: BSY (Email: chmyeos@nus.edu.sg) or FCV (Email: f.calle.vallejo@ub.edu).

Contents

S1. Experimental and computational methods

S1.1. Anodization of Ti substrate

A polycrystalline titanium disc (99.99%, Diameter: 15 mm, Goodfellow) was progressively polished using a SiC paper (Grit 1200, Struers), 15- and 3 μm diamond slurries (Diapro, Struers). The disc was then sonicated in ultrapure water (18 MΩ) to remove any residual diamond slurry. The polished Ti disc was anodized in 0.2 M KCl electrolyte (99.0%, Sigma-Aldrich) at 0.25 A/cm^2 at 1, 2, 3 or 4 min. A platinum wire was used as counter electrode. The anodized Ti foil will be referred to as Ti_{an}. The exposed electrode area was 0.785 cm^2. An Autolab PGSTAT 30 potentiostat (Eco Chemie) was used for controlling the electrochemistry.

S1.2. Preparation of control samples

The performance of the Ti_{an} catalyst for formic acid reduction (FAR) to methanol was compared against those of a polished Ti disc (0.785 cm^2) and commercial TiO_2 samples. 20 mg of commercial rutile (Sigma Aldrich, 99.9%, < 5 μm) or anatase (Sigma Aldrich, 99.8%, < 5 μm) TiO_2 was sonicated with 25 μL of Nafion® (5 % in aliphatic alcohols, Sigma Aldrich), 250 μL of ethanol (VWR chemicals, 99.97%) and 725 μL of ultrapure water. 25 μL of the catalyst ink was then dropcast onto a polished Ti disc and dried under a heat lamp, before being used for electrolysis.

S1.3. Electrochemical reduction of formic acid

FAR was conducted in 0.5 M HCOOH (Fluka, 98.0–100%) dissolved in aqueous 0.1 M K_2SO_4 (99.99%, Meryer) supporting electrolyte. A three-electrode configuration was used, with Ag/AgCl (saturated KCl, Pine) and graphite (Ted Pella) as the reference and counter electrodes, respectively. The cathodic (12 mL of 0.1 M K_2SO_4 + 0.5 M HCOOH) and anodic (8 mL of 0.1 M K_2SO_4) compartments were separated by a cation exchange membrane (CMV, AGC Asahi Glass).

A potentiostat (Gamry reference 600) was used to control the electrolysis of formic acid using chronoamperometry (CA). The current interrupt mode was used to compensate for the iR drop during CA measurements. The electrolysis period was 60 min. The potentials in this work are referenced to the reversible hydrogen electrode (RHE) using the average potential of the Ag/AgCl electrode ($E_{Ag/AgCl}$) (Equation 1).

$$E_{RHE} = E_{Ag/AgCl} + 0.197 + (0.059 \cdot pH) \quad (1)$$

The gaseous products (H_2, CO, CH_4) were detected from the cathodic compartment by an on-line gas chromatograph (GC, Agilent 7890A) with flame ionization detectors (FIDs) and a thermal conductivity detector (TCD). N_2 (Chemgas, 99.999 %) was used as the carrier gas. The measurements were made over the course of seven GC injections (intervals of 492 s between adjacent injections). To ensure that the reported data is from a system under equilibrium conditions, only measurements obtained from the 4th to 7th injections were used for analyses. Details of our chromatography setups have been described in our previous work.[1] Solutions at various pH values (2.6, 3.4, 4.5 and 5.8) were adjusted with KOH (99.99%, Sigma-Aldrich) for 6 h electrolysis experiments. After electrolysis, the liquid products were analyzed using headspace-GC (HS-GC, Agilent, 7890B and 7697A). The sample was equilibrated in an oven at 90 °C for 30 min, before its headspace was injected into the GC. An example of the HS-GC chromatogram obtained is shown in Figure S4.

The presence of methanol was also verified using ^{1}H nuclear magnetic resonance spectroscopy. 1 mL of catholyte was mixed with 50 µL internal standard, which consisted of 25 mM phenol (99.5%, Scharlau) and 5 mM dimethyl sulfoxide (DMSO, 99.9%, Quality Reagent Chemical). 540 µL of this mixture was further mixed with 60 µL D_2O (99.96 % D, Cambridge Isotope Lab), and transferred to a NMR sample tube. ^{1}H NMR spectroscopy was performed with a 500 MHz spectrometer (Avance 500, Bruker). The water suppression method was used. The spectrum was collected after 16 continuous scans. An example of the ^{1}H NMR spectrum obtained is shown in Figure S4.

Formaldehyde (CH_2O) concentrations were measured using the chromotropic acid method.[2] 1 mL of electrolyte was added into a 10 mL volumetric flask, followed by 0.14 mL of 5 % chromotropic acid disodium dihydrate solution (technical grade, Sigma-Aldrich). 5 mL of concentrated sulfuric acid (98%, Fisher-Scientific) was then added, with the flask placed in a cool water bath. The solution was topped up to the mark using 0.1 M K_2SO_4, left to stand for 15 min, and then analyzed using a Shimadzu UV-3600 UV-Vis-NIR spectrometer.

S1.4. Electrochemical reduction of formaldehyde

A three-electrode cell was used, with a cation exchange membrane to separate the anodic and cathodic compartments. Ag/AgCl (saturated KCl) and graphite were respectively employed as the reference and counter electrodes. A nominal amount (5 mM) of CH_2O (16% v/v, methanol-free, Sigma-Aldrich) was added into 14 mL of 0.1 M K_2SO_4 electrolyte. Before

CH_2O electrolysis, 1 mL of solution was extracted for HS-GC analysis for CH_3OH detection, while another 1 mL was extracted for formate detection using high-performance liquid chromatography (Agilent, HPLC−1260 Infinity Series; Aminex HPX-87H column; variable wavelength detector, and 0.5 mM H_2SO_4 mobile phase). The quantification process was repeated after 60 min of CH_2O electrolysis. The amount of HCOOH and CH_3OH formed from Cannizzaro disproportionation is based on the difference in HCOOH and CH_3OH concentrations before and after CH_2O electrolysis.[3] The amount of CH_2O present in the electrolyte was quantified using the chromotropic acid method.

S1.5. Characterization of catalysts

Scanning Electron Microscopy (SEM) (JEOL JSM-6701F, 5 keV) was employed to characterise the surface morphologies of the catalysts.

X-ray diffraction (XRD) analysis was used to determine the composition of the catalyst. The system used was a Bruker D8 Advance (Cu K_α 40 kV, 40 mA) with 2D Lynxeye XE PSD Counter detector, with the incoming signal fixed at 5°. The samples were loaded on a low background Si wafer (Diffraction free, p-type doped B, KMT corporation).

X-ray photoelectron spectroscopy (XPS) was used to analyse the surface composition of the Ti electrodes. XPS measurements were performed using a SPECS system with XR50 X-ray Mg K_α (1253.7 eV) source. Surface etching was done by Ar ion sputtering with an operation energy of 2.0 kV under an argon pressure of 10^{-5} mbar. The adventitious C_{1s} peak at 285.0 eV was used as reference for calibrating the binding energies.

Raman spectroscopy was performed using a confocal Raman microscope (Horiba Jobin Yvon) in an epi-illumination mode (top-down). A He-Ne laser with 633 nm wavelength (CVI Melles Griot) was used as the excitation source. The laser beam was focused on the samples using a dry objective lens (×50 Olympus MPlan N, numerical aperture 0.75). The back-scattered light was filtered through a 633 nm edge filter, before being directed into a spectrograph (iHR320) / charge-coupled device detector (Synapse CCD). The acquisition time of each spectrum was 30 s.

Diffuse Reflectance Spectroscopy (DRS) was performed using a Shimadzu UV-3600 UV-Vis-NIR spectrometer. The samples were placed on the sample holder for analysis, with $BaSO_4$ powder (Wako) as the reference.

Electron Paramagnetic Resonance (EPR) Spectroscopy was performed using a JEOL FA200 ESR spectrometer. The Ti_m layers were removed from the Ti substrates, weighed, and loaded into a 250 mm Wilmad Quartz (Cfq) EPR (Diam. 5mm) tube for analysis. The spectra were measured at a microwave frequency of approximately 9.207 GHz, microwave power of 1.0 mW, modulation frequency of 100 kHz, width of 1.0 mT, sweep time of 2 min and time constant of 0.1 s. All spectra were taken at room temperature. Mn^{2+} embedded in MgO was used as a reference for all experimental g values. All signal areas were taken using the numerical double integration of the EPR spectra peaks.[4,5]

Cyclic voltammetry was conducted on the samples after FAR. The electrolyte used was 0.1 M K_2SO_4 + 0.5 M HCOOH. The working electrode was scanned from –1.25 to 1.35 V vs RHE, at a scan rate of 50 mV/s. The TOV anodic peak area was measured from –0.85 to 1.35 V vs RHE.

Elemental analysis of the catholyte before and after FAR was performed using a Perkin Elmer Avio 500 Inductively Coupled Plasma-Optical Emission Spectrometer (ICP-OES).

S1.6. Computational methods

The VASP code was used to perform the DFT simulations.[6] The PBE exchange-correlation functional was used to estimate the total energies[7] and the projector augmented wave method was used to describe ion-electron interactions.[8] To help in localizing the *d* states of Ti atoms, a Hubbard U_{eff} of 5 eV was used, obtained in previous works through a linear-response method.[9] We used a plane-wave cutoff of 450 eV, k_BT = 0.2 eV (extrapolating total energies to 0 K), and the conjugate-gradient optimization algorithm until the maximal force on any atom was below 0.05 eV/Å.

The optimized bulk parameters were found to be a = 2.995 Å and b = 4.715 Å for the rutile phase, and a = 3.889 Å and b = 9.732 Å for the anatase phase. All TiO_2 slab models had 4 atomic layers, the two bottommost were fixed at the bulk equilibrium distances, whereas the topmost two and the adsorbates were fully allowed to relax. The TiO_2(110) slab contained 24 Ti and 48 O atoms, the TiO_2(120)-CT and TiO_2(120)-BT slabs had 39 Ti and 78 O atoms each, and the A-TiO_2(101) slab had 32 Ti and 64 O atoms. Those slabs avoid lateral interactions between adsorbates. The vertical distance between repeated images was at least 13 Å. Monkhorst-Pack[10] meshes of 4×6×1, 3×4×1, 3×4×1, and 3×5×1 for TiO_2(110), TiO_2(120)-CT,

TiO_2(120)-BT, and A-TiO_2(101), respectively, ensured convergence of the adsorption energies within 0.05 eV. Isolated molecules were calculated in boxes of 9 Å × 10 Å × 11 Å using k_BT = 0.001 eV and sampling the Γ-point only.

The reaction free energies were approximated as $\Delta G \approx \Delta E_{DFT} + \Delta ZPE - T\Delta S$, where ΔE_{DFT} is the DFT-calculated reaction energy, ΔZPE is the zero-point energy change and $T\Delta S$ is the entropy change at T = 298.15 K. ΔS only includes vibrational contributions for the adsorbates and all contributions for the free molecules. No explicit solvation was considered for two reasons: (I) the scope of this work is the identification of activity trends which, according to previous studies, remain intact after the inclusion of explicit solvation in TiO_2.[11] (II) Our systems are large, and the inclusion of explicit solvation would make this work intractable. However, we did perform implicit solvent calculations for the intermediates in the most favorable pathways on TiO_2(110) and TiO_2(110)-O.[12] In general, we observed a destabilization of all adsorbates by ~0.3 eV, in agreement with previous theoretical works.[13] The results are shown in Section S1.9.

The energetics of proton-electron pairs was evaluated using the computational hydrogen electrode approach.[14] The limiting potentials U_L were calculated based on the largest positive free energies of reaction: $U_L = -\Delta G_{max}/e^-$, where e^- is the charge of an electron. To ensure that the calculated and experimental equilibrium potentials agree, we corrected the total energies of liquids and gases using a semiempirical method.[15]

S1.7. Gas-phase corrections

The free energies of gas-phase molecules were estimated as: $G = E_{DFT} + ZPE - TS$. ZPE values were obtained from vibration frequency analyses and TS values were obtained from thermodynamic tables at T = 298.15 K, see Table S1. Moreover, corrections to the formation energies of 0.19, 0.04, 0.03, and 0.46 eV were applied to HCOOH, CH_3OH, CH_4, and O_2, respectively, following the method described by Granda-Marulanda et al.[15]

Table S1. Zero-point energy and entropy contributions to the free energies of gas-phase molecules. All values are in eV.

Molecule	ZPE	TS
H_2	0.27	0.40
H_2O	0.57	0.58
O_2	0.10	0.63
CH_4	1.19	0.58
CH_3OH	1.34	0.74
HCOOH	0.89	0.77

S1.8. Liquid-phase corrections

Formic acid, methanol, and water are in the liquid phase. Their free energies from gas-phase DFT calculations are approximated using the method described by Calle-Vallejo et al.,[16] which is based on TS corrections. Such corrections are for formic acid, methanol, and water –0.13, –0.04, and –0.09 eV, respectively.

S1.9. Implicit solvent calculations

Table S2. Free energies of adsorption of the intermediates involved in the most favorable pathway of FAR to methanol, with implicit solvent (ΔG_{sol}), without it (ΔG), and their absolute difference ($\Delta\Delta G$). All values are in eV.

TiO_2(110)	ΔG	ΔG_{sol}	$\Delta\Delta G$
*HCOOH	–0.44	–0.05	0.38
*H_2COOH	1.27	1.76	0.49
*H_2CO	–0.09	0.28	0.37
*H_3CO	1.12	1.45	0.32

TiO_2(110)-O	ΔG	ΔG_{sol}	$\Delta\Delta G$
*HCOOH	–0.03	0.18	0.21
*H_2COOH	–1.11	–0.57	0.54
*O + $CH_3OH_{(l)}$	–1.64	–1.63	0.02
*OH	–1.58	–1.24	0.34

S2. Characterization of catalysts

S2.1. X-ray photoelectron spectroscopy of Ti_{an}

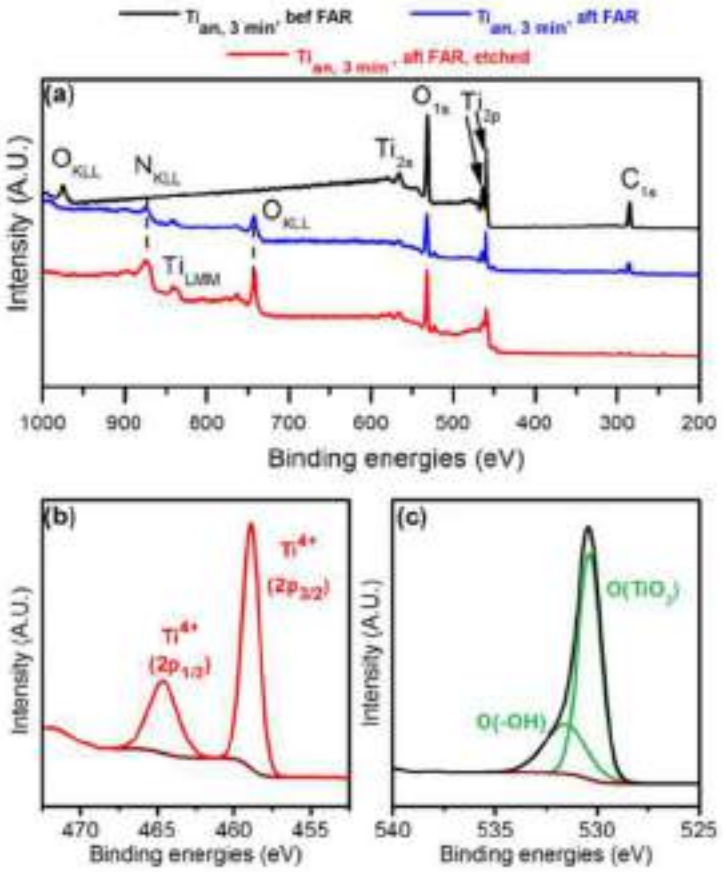

Figure S1. (a) XPS survey spectra of a $Ti_{an,\ 3\ min}$ catalyst before and after FAR at –1.00 V vs RHE. (b)-(c): Ti_{2p} and O_{1s} spectra of $Ti_{an,\ 3\ min}$ after FAR at –1.00 V vs RHE, before Ar^+ etching.

Table S3. Experimental (Exp) and literature (Lit) O_{1s} binding energies (BEs) of lattice TiO_2 (Ti-O) and surface hydroxyl groups (Ti-OH) in different forms of TiO_2.

Ti-O BEs (eV) (Exp)	Ti-OH BEs (eV) (Exp)	TiO_2 substrate	Ti-O BEs (eV) (Lit)	Ti-OH BEs (eV) (Lit)	References
530.4	531.6	Amorphous	530.5	531.8	17
		Anatase	530.5	531.5	18
		Rutile	530.1	531.7	19

S2.2. Diffuse reflectance spectroscopy of Ti_{an} catalyst

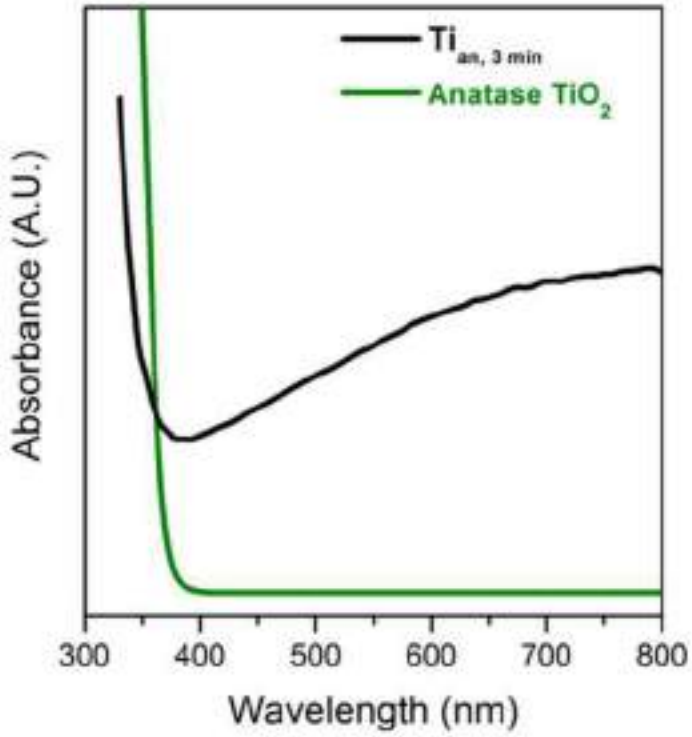

Figure S2. Diffuse reflectance spectroscopy (DRS) spectra of $Ti_{an,\ 3\ min}$ sample after FAR at –1.00 V vs RHE. For comparison, commercial anatase TiO_2 was also analyzed using DRS. The absorption region in the UV region (< 400 nm) is attributed to the 3.2 eV band gap transition in bulk TiO_2.[20] The absorption between 400 to 800 nm observed in the $Ti_{an,\ 3\ min}$ catalyst is attributed to TOVs, resulting in a continuous vacancy band of electronic states induced below the conduction band of TiO_2.[21]

S2.3. X-ray diffraction of Ti_{an} catalyst

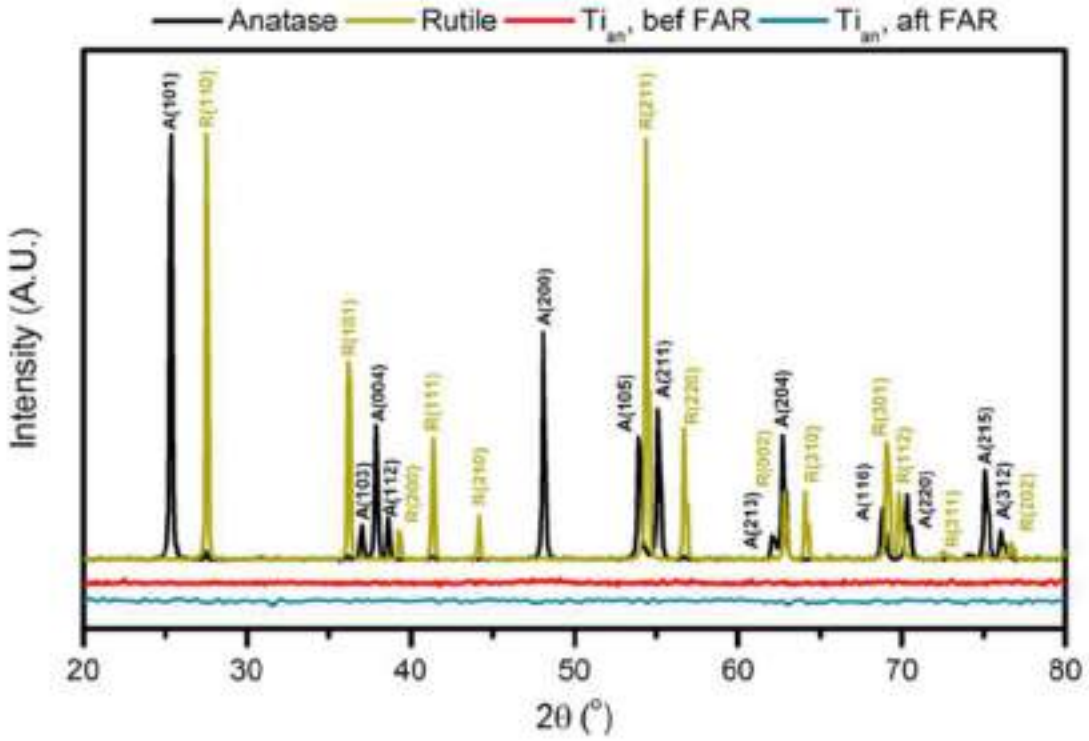

Figure S3. XRD analysis of $Ti_{an,\ 3\ min}$ powder before and after FAR at −1.00 V vs RHE. For comparison, crystalline anatase and rutile TiO_2 samples were also analyzed using XRD. No well-defined anatase or rutile TiO_2 XRD peaks were observed from the $Ti_{an,\ 3\ min}$ powder before and after FAR. This indicates that the anodized catalyst was XRD-amorphous.

S2.4. Raman spectroscopy of Ti_{an} catalyst

Table S4. Observed Raman shifts and peak assignments for titanium species shown in Figure 1g

Raman shift (cm^{-1}) of titanium species						
Ti_{an}, before electrolysis	Ti_{an}, after FAR electrolysis		Rutile TiO_2 standard	Anatase TiO_2 standard	Literature values	Peak assignment
	Major	Minor				
153	153	-	142	-	144	B_{1g} (Rutile)
-	-	-	236	-	235	Second-order Raman scattering
446	446	-	446	-	448	E_g (Rutile)
610	610	-	610	-	612	A_{1g} (Rutile)
-	-	151	-	142	147	E_g (Anatase)
-	-	398	-	398	398	B_{1g} (Anatase)
-	-	515	-	515	515	A_{1g}, B_{1g} (Anatase)
-	-	630	-	639	640	E_g (Anatase)

Literature values for rutile and anatase TiO_2 are taken from [22].

S3. Electrolysis on Ti_{an}

S3.1. Electrolysis of HCOOH on Ti_{an}

Table S5. Products obtained from the electrocatalytic FAR using $Ti_{an,\ 3\ min}$ catalysts at different applied potentials. Electrolysis were conducted for 60 min in 0.1 M K_2SO_4 + 0.5 M HCOOH.

Potential	**Products obtained**					**CH_3OH detected**
(V vs RHE)	CH_3OH	H_2	CH_4	CH_2O	Total	**(μM)**
–0.90	**8.4±1.9** *–1.07±0.29*	**77±10** *–9±4*	**1.7±0.9** *–0.15±0.04*	**0.41±0.07** *–0.019±0.003*	**87±11** *–10±4*	594±183
–0.95	**10.2±1.8** *–1.39±0.13*	**81±9** *–11±4*	**1.3±0.4** *–0.17±0.01*	**0.24±0.04** *–0.021±0.002*	**93±9** *–13±4*	771±135
–1.00	**12.6±1.8** *–1.95±0.20*	**77±3** *–12±2*	**1.4±0.3** *–0.20±0.03*	**0.14±0.04** *–0.019±0.001*	**91±4** *–14±2*	1122±188
–1.05	**5.3±1.0** *–1.96±0.19*	**88±8** *–29±7*	**0.8±0.2** *–0.23±0.05*	**0.06±0.01** *–0.024±0.005*	**94±8** *–31±7*	1231±93
No potential (pre-reduced Ti_{an})	N.D.	N.D.	N.D.	N.D.	-	N.D.

Numbers in bold are the Faradaic efficiencies in %, while numbers in italics are partial current densities in mA/cm^2. N.D.: Not detected.

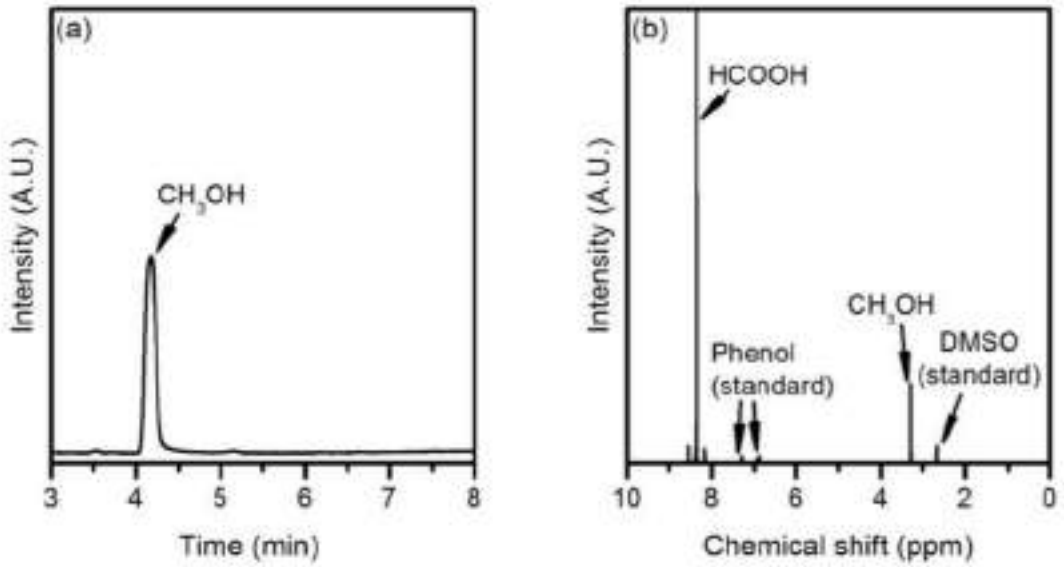

Figure S4. Detection of CH_3OH in the electrolyte using (a) HS-GC and (b) ^1H NMR. The electrolyte was analyzed after FAR, with FAR performed using $Ti_{an,\ 3\ min}$ catalysts biased at –1.00 V vs RHE.

S3.2. Electrolysis of FAR products on Ti_{an}

Table S6. Data obtained from the reduction of CH_3OH or CH_2O on a $Ti_{an,\ 3\ min}$ catalyst at –1.00 V vs RHE.

Reactant	Current density (mA/cm^2)	CH_4 detected (ppm)
CH_3OH	–5.1	N.D.
CH_2O	–1.9	N.D.

N.D.: Not detected.

S3.3. Production of CO from HCOOH

Table S7. Concentrations of CO detected from a $Ti_{an,\ 3\ min}$ catalyst in the presence of HCOOH.

Injection	CO detected (ppm)
	FAR, –1.00 V vs RHE
1	9.9
2	14.2
3	3.8
4	3.0
5	3.6
6	3.9
7	4.5

S3.4. Stability tests for FAR on Ti_{an}

Table S8. Stability test of $Ti_{an,\ 3\ min}$ at −1.00 V vs RHE for six hours. The electrolyte used was 0.1 M K_2SO_4 + 0.5 M HCOOH at pH 2.6.

Electrolyte pH	Time (h)	FE_{CH3OH} (%)	Accumulative CH_3OH concentrations (mM)
2.6	1	13.8 ± 1.3	0.8 ± 0.2
	2	11.3 ± 1.8	1.5 ± 0.3
	3	8.8 ± 2.5	2.1 ± 0.4
	4.5	4.9 ± 0.8	2.7 ± 0.6
	6	3.4 ± 1.6	3.2 ± 0.5

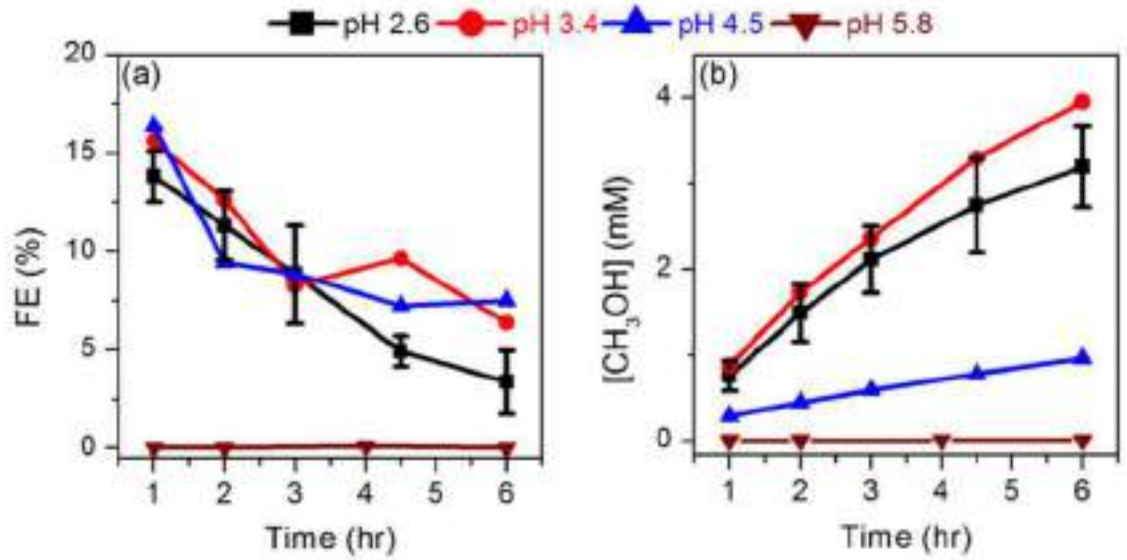

Figure S5. (a) Faradaic efficiencies (%) and (b) accumulated concentrations (mM) of CH_3OH after six hours FAR at –1.00 V vs RHE at various pH values. The pH values were adjusted using KOH.

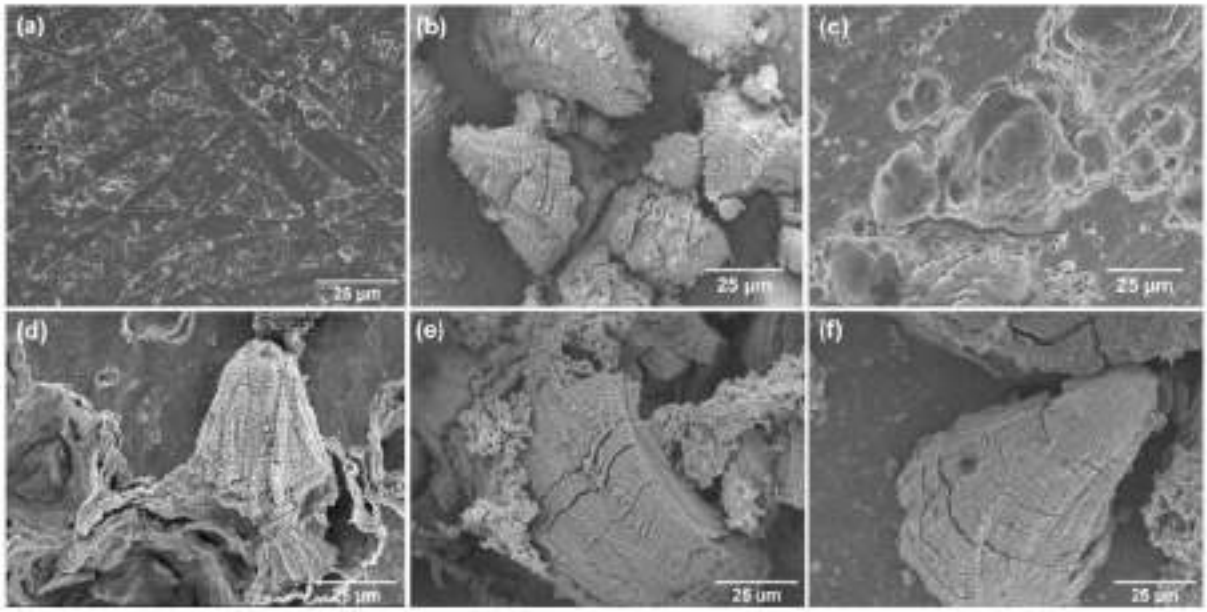

Figure S6. SEM images of (a) polished Ti disc, and (b) Ti disc anodized in 0.2 M KCl for 3 min ($Ti_{an,\,3\,min}$), before FAR. $Ti_{an,\,3\,min}$ after six hours of FAR at –1.00 V vs RHE at (c) pH 2.6, (d) pH 3.4, (e) pH 4.5, and (f) pH 5.8. Significant loss of $Ti_{an,\,3\,min}$ catalyst was observed after six hours of FAR at pH 2.6, and the amount of delaminated $Ti_{an,\,3\,min}$ catalyst decreases at higher pH.

Table S9. Elemental analyses of Ti content in 0.1 M K_2SO_4 electrolytes before and after they were used for 6 h of FAR at –1.00 V vs RHE. $Ti_{an,\ 3\ min}$ catalysts were used. The mass of dissolved Ti is calculated from the final electrolyte volume (12 mL). To verify that the Ti in the electrolyte is mainly from Ti_{an} and not from the underlying metallic Ti disc substrate, we performed FAR on a polished Ti disc electrode for 6 h. Only a very small amount of Ti (0.14 ppm) could be detected in the electrolyte.

Experiment	pH	Ti in the electrolyte (ppm)	Mass of dissolved Ti (mg)
Ti_{an}, before FAR	2.6	N.D	N.D
Ti_{an}, after 6 h FAR	2.6	8.56	0.103
	3.4	0.45	0.0050
	4.5	0.20	0.0024
	5.8	0.04	0.0005
Ti disc, after 6 h FAR	2.6	0.14	0.0016

N.D.: Not detected.

S3.5. FAR on other metal catalysts

Table S10. Activities of metal catalysts for FAR at –1.00 V vs RHE in 0.1 M K_2SO_4 + 0.5 M HCOOH.

Catalyst	Substrate	Current density (mA/cm^2)	FE_{CH3OH} (%)	j_{CH3OH} (mA/cm^2)	CH_3OH detected (μM)
Fe	Anodized (+0.25 A/cm^2 for 3 min in 0.2 M KCl)	–61	N.D.	N.D.	N.D.
Co		–56	N.D.	N.D.	N.D.
Cu		–216	N.D.	N.D.	N.D.
Zr		–13	N.D.	N.D.	N.D.
Sn		–13	N.D.	N.D.	N.D.
Cr		–100	0.005	–0.007	1.4
Ti		–14	12.6	–1.95	1122
Pd	Polished disc	–95	N.D.	N.D.	N.D.
Cr		–108	0.07	–0.08	22.6
Ti		–87	0.22	–0.12	62.3

N.D.: Not detected.

S4. Active site analysis of Ti_{an} for FAR

S4.1. Electron paramagnetic resonance analysis of Ti_{an}

Table S11. Mass of Ti_{an} (anodized at 1, 2, 3 and 4 min) catalyst powders removed from their disc substrates after they were used for electrocatalytic FAR; their TOV signals were measured using EPR spectroscopy. FAR was conducted for 60 min at −1.00 V vs RHE in 0.1 M K_2SO_4 + 0.5 M HCOOH. Three discs were studied at each anodization time. The TOV signal areas were taken from g =2.1 to g =1.81.

Anodization time (min)	Mass of powder from each substrate (mg)			Mass of accumulated powder from 3 substrates (mg)	TOV EPR signal area (A.U.)	Normalized TOV signal area/mg of powder (A.U.)	j_{CH3OH} (mA/cm²)
1	0.28	0.19	0.20	0.67	25	37	−0.80
2	0.60	0.76	0.60	1.96	76	39	−1.42
3	1.03	0.98	0.99	3.00	121	40	−1.95
4	1.00	1.17	1.05	3.22	146	45	−2.00
3 (Before FAR)		1.45		1.45	N.D.	N.D.	-

N.D.: Not detected.

S4.2. Cyclic voltammetry and double layer capacitances of Ti_{an}

Table S12. TOV anodic peak areas of Ti_{an} catalysts (anodized at 1, 2, 3 and 4 min) after FAR at –1.00 V vs RHE, measured using cyclic voltammetry. The TOV anodic peak area is taken from –0.85 V to 1.35 V vs RHE. The scan rate was 50 mV/s.

Anodization time/min	Anodic charge densities (mC/cm^2)
1	104 ± 26
2	351 ± 54
3	575 ± 47
4	661 ± 49

S4.3. FAR on control samples

Table S13. Faradaic efficiencies and partial current densities of products detected from electrocatalytic FAR on anatase and rutile TiO_2 dropcast on Ti discs. Experiments were conducted at –1.00 V vs RHE in 0.1 M K_2SO_4 + 0.5 M HCOOH for 60 min.

Sample		CH_3OH	H_2	CH_4	CH_2O	Total
Anatase TiO_2	**FE(%)**	0.18±0.04	90±2	0.021±0.003	N.D.	90±2
	***j*(mA/cm²)**	–0.05±0.01	–31±6	–0.008±0.002		–31±6
Rutile TiO_2	**FE(%)**	0.03±0.01	90±7	0.02±0.01	0.008±0.006	90±7
	***j*(mA/cm²)**	–0.05±0.02	–139±38	–0.03±0.02	–0.003±0.002	–139±38

N.D: Not detected.

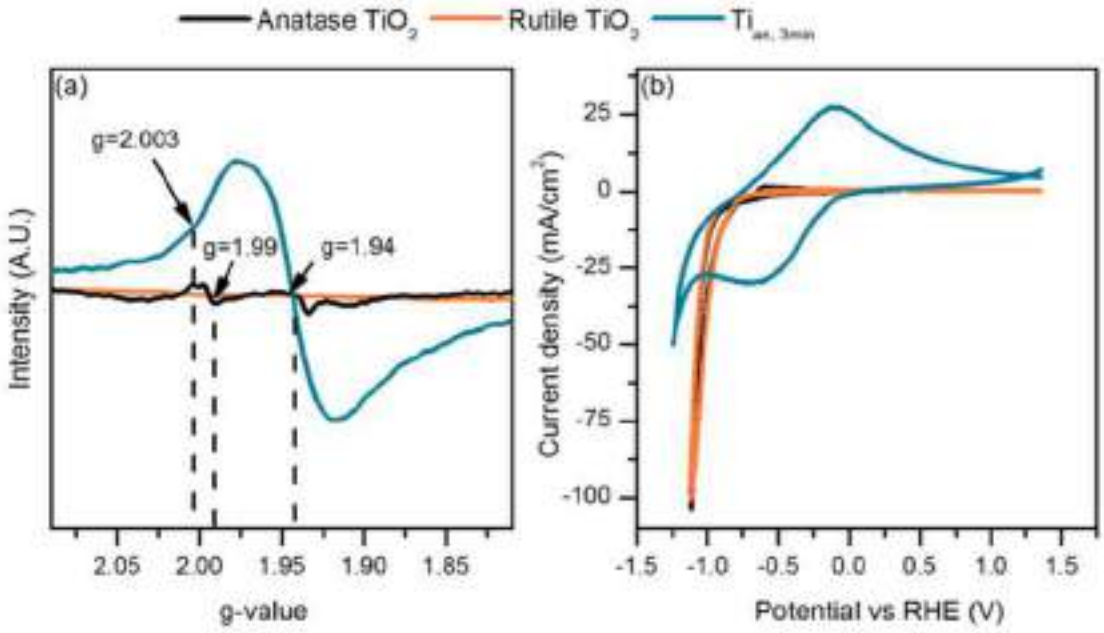

Figure S7. (a) Electron paramagnetic resonance (EPR) spectrum and (b) cyclic voltammogram (CV) of a $Ti_{an,\ 3\ min}$ catalyst, in comparison to those from control anatase and rutile TiO_2 samples. EPR spectroscopy and CV were conducted after 60 min FAR at –1.00 V vs RHE. The peak at g = 1.99 in the EPR spectrum of anatase TiO_2 corresponds to Ti^{3+} centres trapped in the TiO_2 lattice.[23] No Ti^{3+} signals were observed in the EPR spectrum of rutile TiO_2.

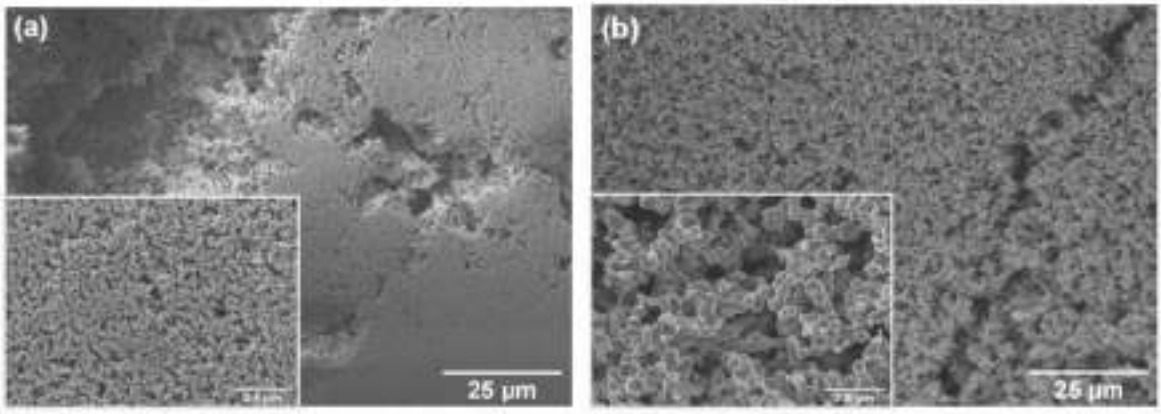

Figure S8. SEM images of crystalline (a) anatase and (b) rutile TiO_2 samples. The insets are the high magnification images of anatase and rutile TiO_2.

S4.4. FAR on Ti_{an} at different anodization times

Table S14. Faradaic efficiencies and partial current densities of products detected from FAR electroreduction on Ti_{an} (anodized for 1, 2, 3 and 4 min). Experiments were conducted at –1.00 V vs RHE for 60 min in 0.1 M K_2SO_4 + 0.5 M HCOOH.

Anodization time/min		CH_3OH	H_2	CH_4	CH_2O	Total
1	FE(%)	4.7±1.1	87±1	0.6±0.1	0.08±0.01	92±2
	j(mA/cm²)	–0.80±0.21	–11.8±0.5	–0.08±0.02	–0.011±0.002	–12.7±0.5
2	FE(%)	8.7±1.6	84±6	0.9±0.3	0.11±0.01	94±6
	j(mA/cm²)	–1.42±0.16	–14±5	–0.16±0.06	–0.019±0.004	–16±5
3	FE(%)	12.6±1.8	77±3	1.4±0.3	0.14±0.04	91±4
	j(mA/cm²)	–1.95±0.20	–12±2	–0.20±0.03	–0.019±0.001	–14±2
4	FE(%)	15.2±1.0	70±1	1.7±0.2	0.17±0.02	88±1
	j(mA/cm²)	–2.00±0.10	–9.8±0.3	–0.23±0.02	–0.023±0.002	–12.0±0.3

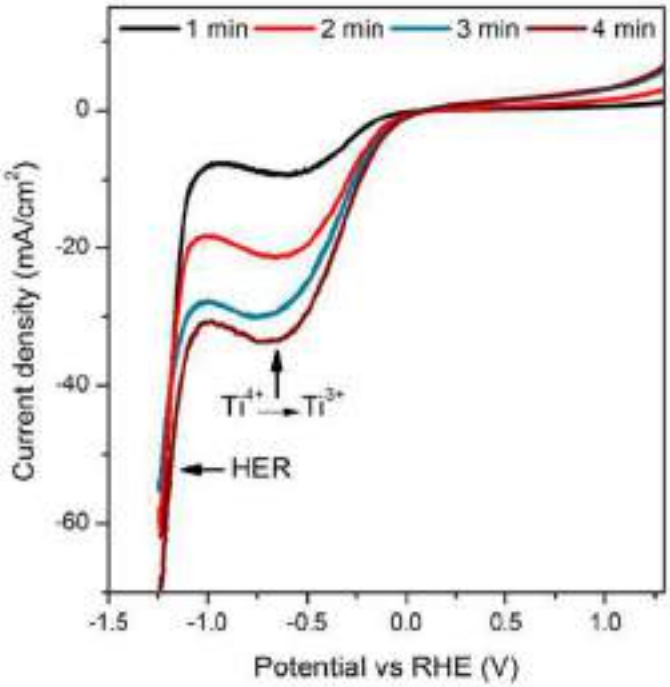

Figure S9. Linear sweep voltammograms of Ti_{an} (anodized for 1, 2, 3 and 4 min). The electrolyte used was 0.1 M K_2SO_4 + 0.5 M HCOOH (pH 2.6). The cathodic peak observed at –0.5 V vs RHE is assigned to the reduction of Ti^{4+} to Ti^{3+}, while the subsequent plunge in current at –1.25 V is assigned largely to the hydrogen evolution reaction.

S5. DFT calculations: tabulated data

S5.1. Adsorption energies

Tables S15a-d. Free energies of adsorption and their contributions for all the possible intermediates involved in the formic acid reduction to methanol at CUS sites. *H is also included. The ZPE, TS_{vib}, and the corresponding ΔG values obtained for the different adsorbates in this study on all the different surface models are listed. $HCOOH_{(l)}$, protons and electrons were used as a reference for all the free energies. All values are in eV.

(a)

TiO_2(110)	ZPE	TS_{vib}	ΔG
*HCOOH	0.93	0.26	–0.44
*H_2COOH	1.26	0.19	1.27
*CHO	0.42	0.20	1.72
*HCOH	0.79	0.19	1.70
*H_2CO	0.78	0.21	–0.09
*CH	0.40	0.04	1.63
*H_2COH	1.16	0.14	1.13
*H_3CO	1.09	0.19	1.12
*O + $CH_3OH_{(l)}$	0.09	0.03	4.37
*H	0.28	0.04	0.09

(b)

TiO_2(120)-BT	ZPE	TS_{vib}	ΔG
*HCOOH	0.93	0.26	–0.29
*H_2COOH	1.26	0.19	1.21
*CHO	0.42	0.20	1.65
*HCOH	0.79	0.19	1.75
*H_2CO	0.78	0.21	–0.10
*CH	0.40	0.04	3.01
*H_2COH	1.16	0.14	1.29
*H_3CO	1.09	0.19	0.92
*O + $CH_3OH_{(l)}$	0.09	0.03	3.94
*H	0.28	0.04	–0.09

(c)

TiO_2(120)-CT	ZPE	TS_{vib}	ΔG
*HCOOH	0.93	0.26	–0.59
*H_2COOH	1.26	0.19	1.57
*CHO	0.42	0.20	1.69
*HCOH	0.79	0.19	1.76
*H_2CO	0.78	0.21	0.03
*CH	0.40	0.04	2.09
*H_2COH	1.16	0.14	1.49
*H_3CO	1.09	0.19	1.24
*O + $CH_3OH_{(l)}$	0.09	0.03	4.54
*H	0.28	0.04	–0.21

(d)

A-TiO_2(101)	ZPE	TS_{vib}	ΔG
*HCOOH	0.93	0.26	–0.64
*H_2COOH	1.26	0.19	1.89
*CHO	0.42	0.20	1.75
*HCOH	0.79	0.19	2.18
*H_2CO	0.78	0.21	0.04
*CH	0.40	0.04	1.77
*H_2COH	1.16	0.14	1.23
*H_3CO	1.09	0.19	1.51
*O + $CH_3OH_{(l)}$	0.09	0.03	4.97
*H	0.28	0.04	0.69

Tables S16a-d. Free energies of adsorption and their contributions for all the possible intermediates involved in the formic acid reduction to methanol at TOV sites. *H is also included. The ZPE, TS_{vib}, and the corresponding ΔG values obtained for the different adsorbates in this study on all the different surface models are listed. $HCOOH_{(l)}$, protons and electrons were used as a reference for all the free energies. All values are in eV.

(a)

TiO_2(110)-O	ZPE	TS_{vib}	ΔG
*HCOOH	0.93	0.26	–0.03
*H_2COOH	1.26	0.19	–1.11
*CHO	0.42	0.20	0.62
*HCOH	0.79	0.19	1.06
*H_2CO	0.78	0.21	–0.99
*CH	0.40	0.04	1.91
*H_2COH	1.16	0.14	0.25
*H_3CO	1.09	0.19	–1.79
*O + $CH_3OH_{(l)}$	0.09	0.03	–1.64
*OH	0.35	0.09	–1.58
*H	0.28	0.04	0.16

(b)

TiO_2(120)-CT-O	ZPE	TS_{vib}	ΔG
*HCOOH	0.93	0.26	0.36
*H_2COOH	1.26	0.19	–0.92
*CHO	0.42	0.20	0.49
*HCOH	0.79	0.19	1.66
*H_2CO	0.78	0.21	0.23
*CH	0.40	0.04	2.56
*H_2COH	1.16	0.14	0.60
*H_3CO	1.09	0.19	–1.38
*O + $CH_3OH_{(l)}$	0.09	0.03	–0.93
*OH	0.35	0.09	–1.17
*H	0.28	0.04	0.56

(c)

TiO_2(120)-BT-O	ZPE	TS_{vib}	ΔG
*HCOOH	0.93	0.26	0.39
*H_2COOH	1.26	0.19	–0.50
*CHO	0.42	0.20	1.17
*HCOH	0.79	0.19	1.87
*H_2CO	0.78	0.21	0.49
*CH	0.40	0.04	2.74
*H_2COH	1.16	0.14	0.80
*H_3CO	1.09	0.19	–1.12
*O + $CH_3OH_{(l)}$	0.09	0.03	–0.82
*OH	0.35	0.09	–0.94
*H	0.28	0.04	0.80

(d)

A-TiO_2(101)-O	ZPE	TS_{vib}	ΔG
*HCOOH	0.93	0.26	–0.22
*H_2COOH	1.26	0.19	–0.32
*CHO	0.42	0.20	0.50
*HCOH	0.79	0.19	0.89
*H_2CO	0.78	0.21	0.30
*CH	0.40	0.04	1.83
*H_2COH	1.16	0.14	0.71
*H_3CO	1.09	0.19	–0.91
*O + $CH_3OH_{(l)}$	0.09	0.03	–1.35
*OH	0.35	0.09	–0.77
*H	0.28	0.04	1.10

S5.2. HER Suppression

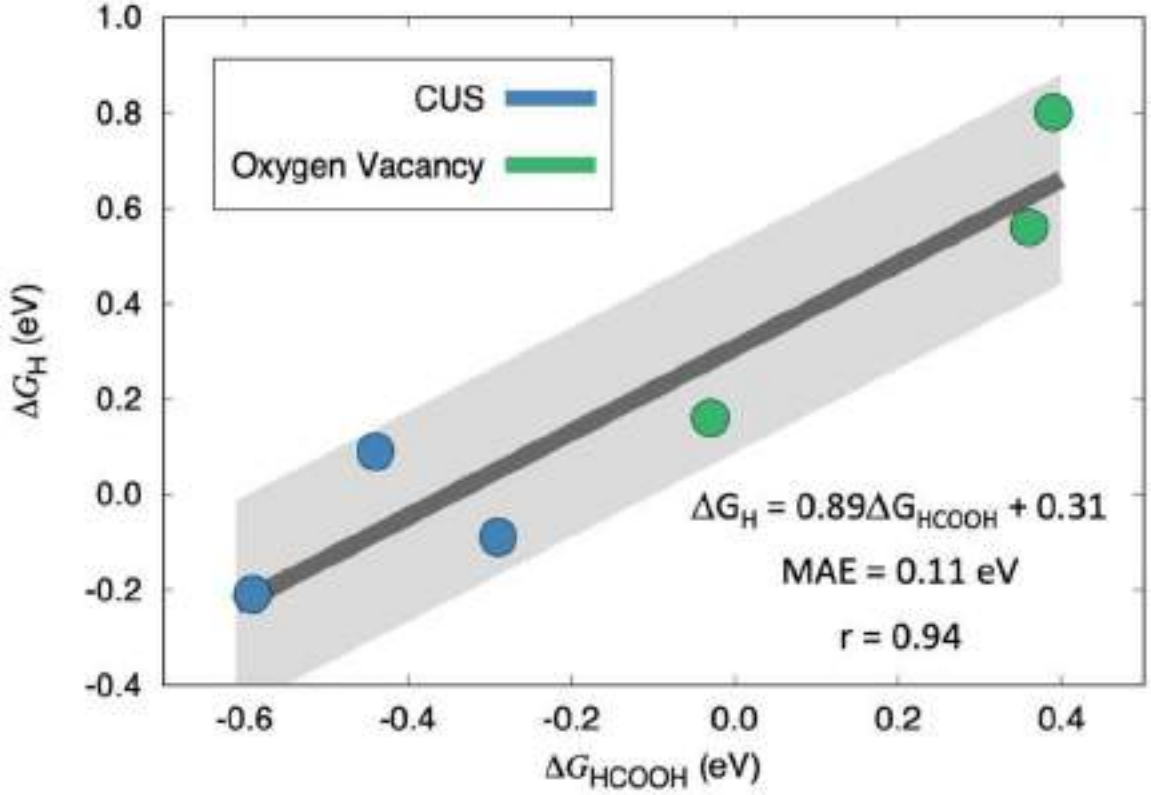

Figure S10. Adsorption-energy scaling relation for *HCOOH and *H. In dark gray we show the linear regression. A light gray zone of ± 2MAE (MAE: mean absolute error) is also shown. The equation, MAE, and Pearson regression coefficient (r) appear at the bottom. The data for CUS sites are shown in blue, while the data for the TOV sites are shown in green.

S6. Electrolysis of proposed FAR intermediates on Ti_{an}

Table S17. Data obtained from the electrocatalytic reduction of possible intermediates for FAR at various potentials using $Ti_{an,\ 3\ min}$ catalysts. Electrolysis were conducted for 60 min. The pH was adjusted to 2.6 using H_2SO_4 for CO, CO_2 and CH_2O experiments. After CH_2O reduction, we detected similar concentrations of CH_3OH and HCOOH. Thus, we conclude that CH_3OH and HCOOH is formed from the Cannizzaro disproportionation of CH_2O. Cannizzaro disproportionation likely occurs due to the higher local pH at the electrode during electrolysis.[3] The current densities observed during CH_2O reduction were attributed to the hydrogen evolution reaction.

Experimental condition	Potential (V vs RHE)	Current density (mA/cm^2)	Methanol detected (μM)	Formate detected (μM)
5 mM CH_2O (nominal concentration added) in 0.1 M K_2SO_4	–0.95	–1.7	59±20	59±12
	–1.00	–1.9	84±19	93±10
	–1.05	–2.4	113±30	119±27
CO in 0.1 M K_2SO_4	–1.00	–2.1	N.D.	N.D.
CO_2 in 0.1 M K_2SO_4	–1.00	–2.6	N.D.	N.D.

N.D- Not detected.

Table S18. CH_2O concentrations measured using the chromotropic acid method before and after CH_2O electrolysis at various potentials using $Ti_{an,\ 3\ min}$ catalysts.

Experimental condition	Potential (V vs RHE)	[CH_2O] (mM)	
		Before electrolysis	After electrolysis
CH_2O in 0.1 M K_2SO_4 (pH 2.6)	–0.95	5.8± 0.5	5.6± 0.5
	–1.00	6.2± 0.2	6.0± 0.2
	–1.05	6.3± 0.3	5.9± 0.5

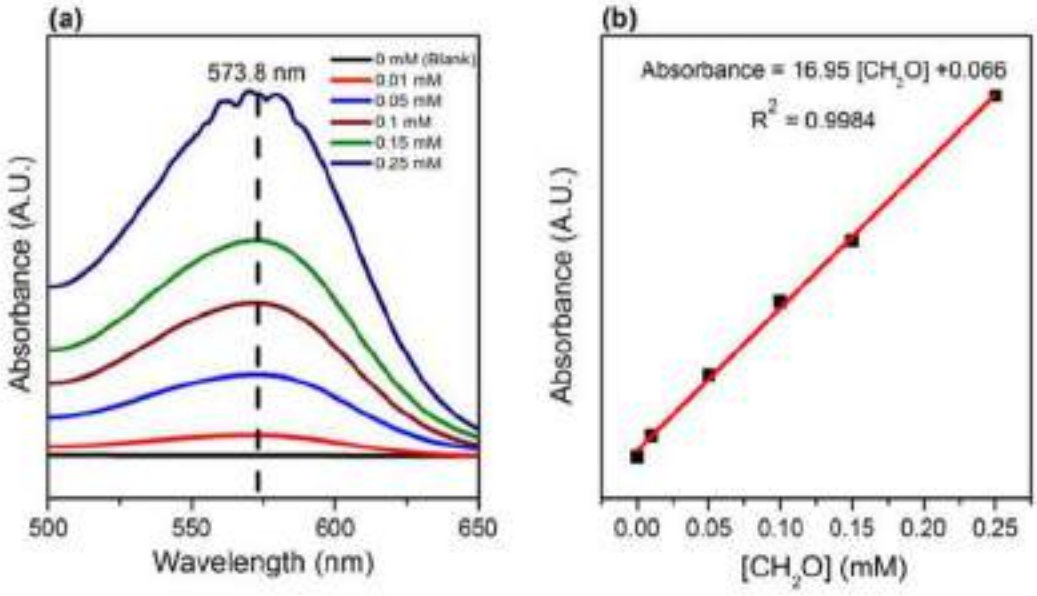

Figure S11. **(a)** UV-Vis spectra of various CH_2O concentrations measured using the chromotropic acid method. **(b)** Calibration plot of CH_2O concentrations.

S7. Experimental calculations

S7.1. Calculation of FAR equilibrium potential

FAR: $HCOOH + 4H^+ + 4e^- \rightarrow CH_3OH + H_2O$

Based on standard Gibbs free energies of formation at 25 °C and 1 atm,[24]
$\Delta G_{CH3OH\ (l)} = -166.6$ kJ/mol
$\Delta G_{H^+} = 0$ kJ/mol
$\Delta G_{H2O\ (l)} = -237.14$ kJ/mol
$\Delta G_{HCOOH\ (l)} = -361.4$ kJ/mol

$\Delta G_{FAR} = (-166.6 - 237.14) - (-361.4) = -42.3$ kJ/mol

$\Delta G = -nFE^\circ$, where n is the number of electrons utilized for FAR (4 e^-), F is the Faraday constant (96485 C/mol), and E° is the thermodynamic potential for FAR

$\therefore E^\circ = \frac{-42.3 \times 1000}{-(4 \times 96485)} = +0.11$ V

S7.2. Turnover frequency for CH_3OH production

The average turnover frequency (TOF) for formation of CH_3OH from TOVs was determined using the following formula:

$$\text{TOF} = \frac{No\ of\ moles\ of\ CH_3OH\ formed}{(No\ of\ moles\ of\ TOVs)\times(Time\ of\ reaction)}$$

$$HCOOH + 4H^+ + 4e^- \rightarrow CH_3OH + H_2O$$

For FAR on a $Ti_{an,\ 3\ min}$ catalyst (area = 0.785 cm^2) in 60 min (3600 s) at –1.0 V vs. RHE, j_{CH3OH} = –1.95 mA/cm^2 (Table S14):

$$\text{Charge} = \frac{1.95\times0.785\times3600}{1000} = 5.51\ C$$

$$\text{No of moles of electrons for FAR} = \frac{5.51}{96485} = 5.71 \times 10^{-5}\ \text{mol}$$

4 moles of electrons are used to reduce 1 mole of CH_3OH

$$\therefore \text{No of moles of } CH_3OH = \frac{5.71 \times 10^{-5}}{4} = 1.43 \times 10^{-5}\ \text{mol}$$

The population of TOVs was estimated using the charge densities measured from CV.

$$Ti^{3+} \rightarrow Ti^{4+} + e^-$$

For a $Ti_{an,\ 3\ min}$ catalyst, oxidation peak charge density = 0.575 C/cm^2 (Table S12)

$$\text{No of moles of electrons for TOVs oxidation} = \frac{0.575\times0.785}{96485} = 4.678 \times 10^{-6}\ \text{mol}$$

$$\therefore \text{No of moles of TOVs} = 4.678 \times 10^{-6}\ \text{mol}$$

$$\text{Average TOF} = \frac{1.43 \times 10^{-5}}{(4.678 \times 10^{-6})\times3600} = 8.5 \times 10^{-4}\ s^{-1}$$

S7.3. Cannizzaro disproportionation of CH_2O to CH_3OH and HCOOH

CH_2O is proposed to undergo Cannizzaro disproportionation: $2CH_2O + OH^- \rightarrow HCOO^- + CH_3OH$

Cannizzaro disproportionation of CH_2O is known to occur at pH 3, which is close to our experimental conditions (pH 2.6).[3] $HCOO^-$ is protonated to HCOOH at pH 2.6.

For CH_2O electrolysis at −1.00 V vs RHE:

Concentration of CH_2O ($[CH_2O]$) before electrolysis = 6.2 mM, $[CH_2O]$ after electrolysis = 6.0 mM

Difference in $[CH_2O]$ after electrolysis = 0.2 mM

[HCOOH] before electrolysis (background signal) = 28 μM

[HCOOH] after electrolysis = 121 μM

Difference in [HCOOH] after electrolysis = 93 μM

$[CH_3OH]$ before electrolysis (background signal) = 59 μM

$[CH_3OH]$ after electrolysis = 142 μM

Difference in $[CH_3OH]$ after electrolysis = 84 μM

Sum of CH_3OH and HCOOH concentrations= 93 + 84 = 177 μM (~ 0.2 mM)

The volumes of solutions analyzed using HPLC and HS-GC are the same (1 mL).

Due to an almost 1:1 molar ratio of CH_3OH and HCOOH, it is likely that CH_3OH is formed from the Cannizzaro disproportionation of CH_2O.

S8. Catalytic pathways and computed optimized geometries

The first hydrogenation of *HCOOH can result in the formation of three different intermediates: *H_2COOH, *CHO + H_2O, and *HCOHOH. The free-energy diagrams (Figures S12-S19) show that *H_2COOH is more stable than *CHO + H_2O in all the studied surfaces, both with and without TOVs. *HCOHOH was not included in the diagrams since we did not find any adsorption minimum for this intermediate on any of the model surfaces. In fact, we observed that *HCOHOH generally decomposes into *H and desorbed formic acid.

In Figures S12-S19 we provide the catalytic pathways inspected in this study, based on the energies reported in Tables S15-S16.

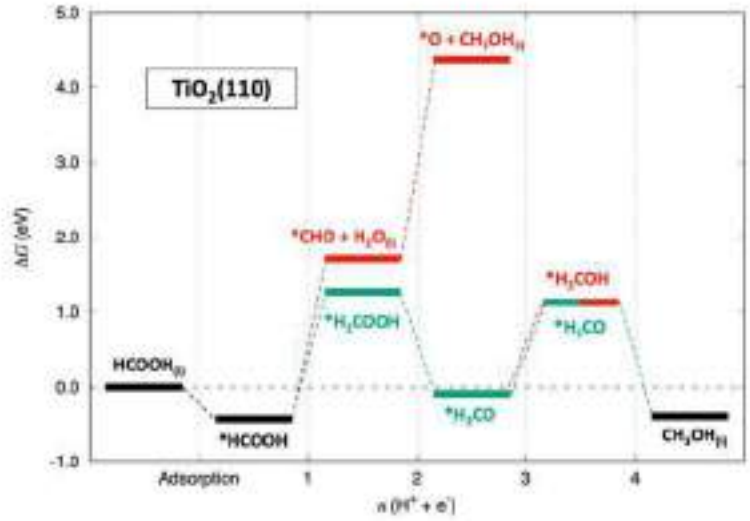

Figure S12. FAR pathways on TiO_2(110) sites. Species common to several pathways are shown in black, the most favorable species in green, and least favorable species in red.

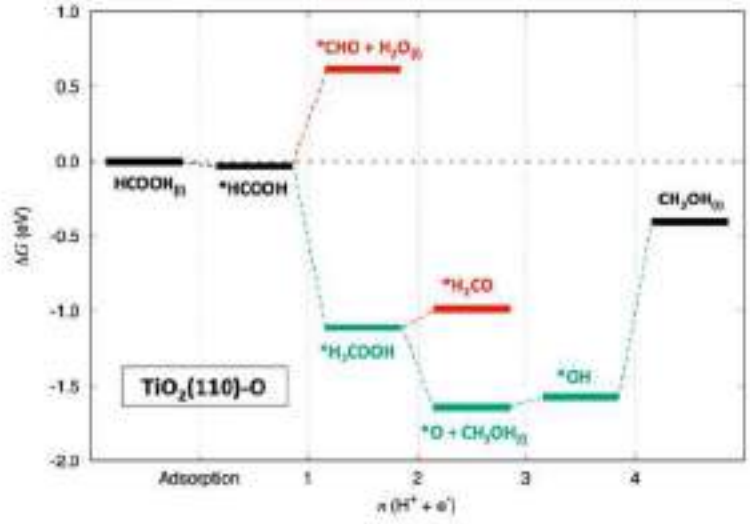

Figure S13. FAR pathways on TiO_2(110)-O sites. Species common to several pathways are shown in black, the most favorable species in green, and least favorable species in red.

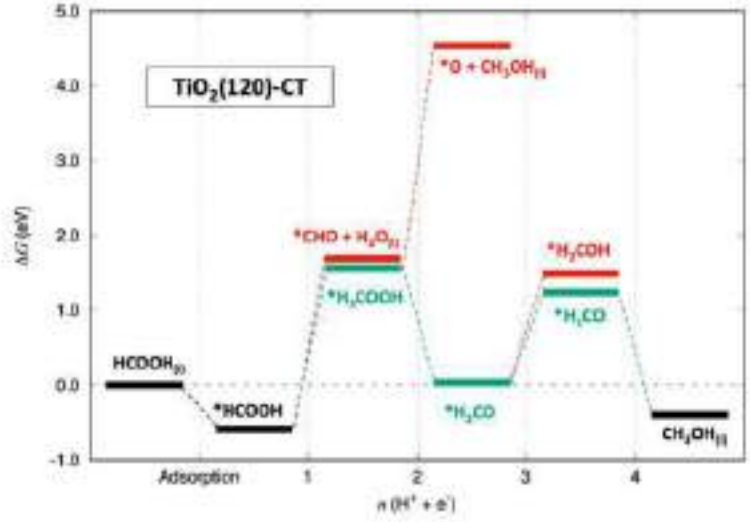

Figure S14. FAR pathways on TiO_2(120)-CT sites. Species common to several pathways are shown in black, the most favorable species in green, and least favorable species in red.

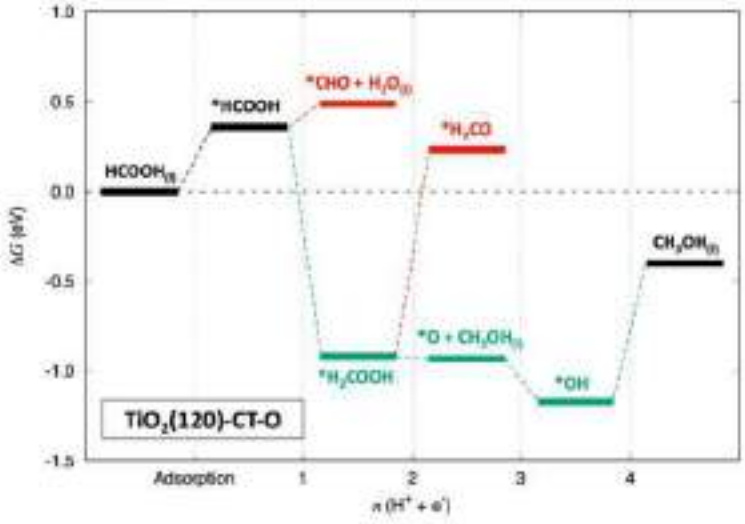

Figure S15. FAR pathways on TiO_2(120)-CT-O sites. Species common to several pathways are shown in black, the most favorable species in green, and least favorable species in red.

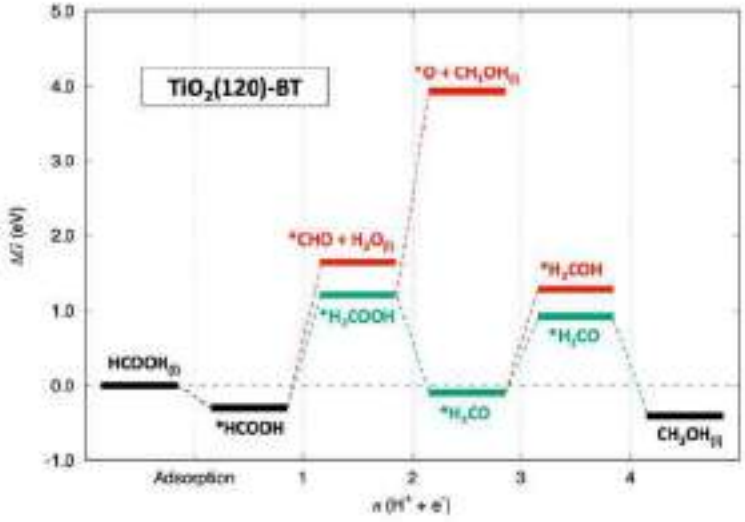

Figure S16. FAR pathways on TiO_2(120)-BT sites. Species common to several pathways are shown in black, the most favorable species in green, and least favorable species in red.

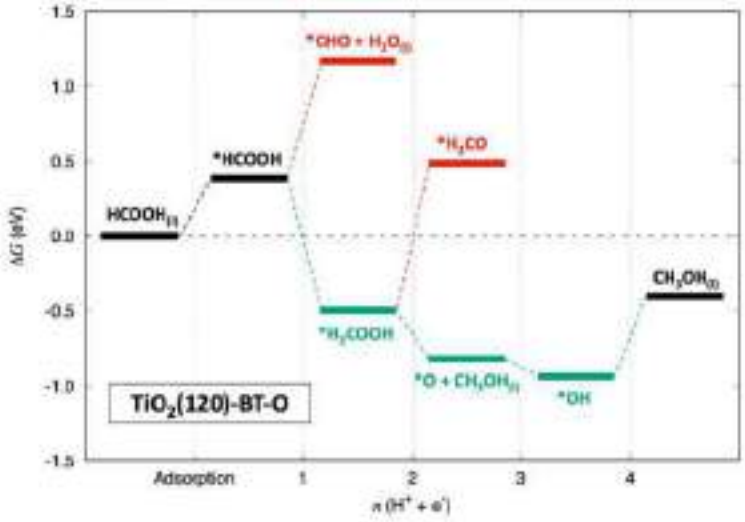

Figure S17. FAR pathways on TiO_2(120)-BT-O sites. Species common to several pathways are shown in black, the most favorable species in green, and least favorable species in red.

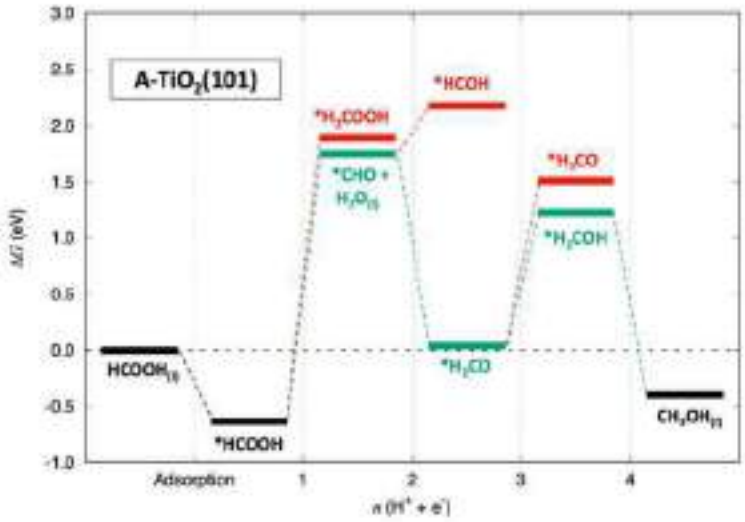

Figure S18. FAR pathways on A-TiO_2(101) sites. Species common to several pathways are shown in black, the most favorable species in green, and least favorable species in red.

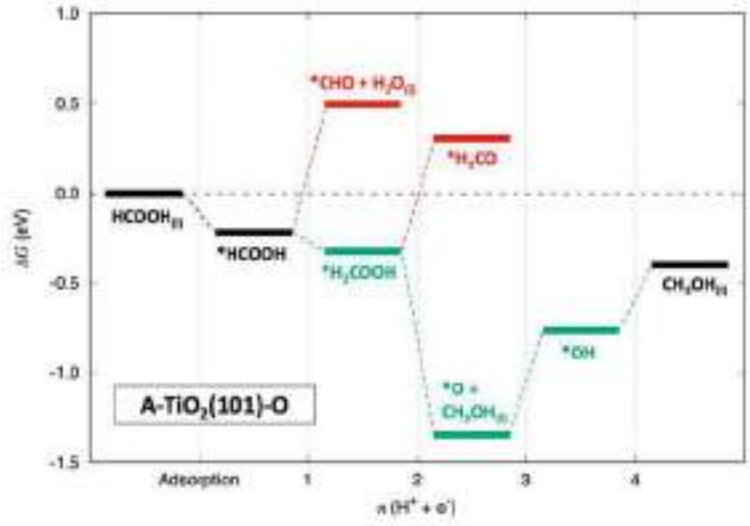

Figure S19. FAR pathways on A-TiO_2(101)-O sites. Species common to several pathways are shown in black, the most favorable species in green, and least favorable species in red.

S9. References

(1) Low, Q. H.; Loo, N. W. X.; Calle-Vallejo, F.; Yeo, B. S. Enhanced Electroreduction of Carbon Dioxide to Methanol Using Zinc Dendrites Pulse-Deposited on Silver Foam. *Angew. Chem., Int. Ed.* **2019**, *58* (8), 2256–2260.

(2) Shariati-Rad, M.; Irandoust, M.; Mozaffarinia, N. Response Surface Methodology in Spectrophotometric Determination of Formaldehyde Using Chromotropic Acid. *Anal. Bioanal. Chem. Res.* **2016**, *3* (2), 149–157.

(3) Birdja, Y. Y.; Koper, M. T. M. The Importance of Cannizzaro-Type Reactions during Electrocatalytic Reduction of Carbon Dioxide. *J. Am. Chem. Soc.* **2017**, *139* (5), 2030–2034.

(4) Strunk, J.; Vining, W. C.; Bell, A. T. A Study of Oxygen Vacancy Formation and Annihilation in Submonolayer Coverages of TiO_2 Dispersed on MCM-48. *J. Phys. Chem. C* **2010**, *114* (40), 16937–16945.

(5) Fu, G.; Zhou, P.; Zhao, M.; Zhu, W.; Yan, S.; Yu, T.; Zou, Z. Carbon Coating Stabilized Ti^{3+}-Doped TiO_2 for Photocatalytic Hydrogen Generation under Visible Light Irradiation. *Dalton Trans.* **2015**, *44* (28), 12812–12817.

(6) Kresse, G.; Furthmüller, J. Efficient Iterative Schemes for Ab Initio Total-Energy Calculations Using a Plane-Wave Basis Set. *Phys. Rev. B* **1996**, *54* (16), 11169–11186.

(7) Perdew, J. P.; Yang, W.; Burke, K.; Yang, Z.; Gross, E. K. U.; Scheffler, M.; Scuseria, G. E.; Henderson, T. M.; Zhang, I. Y.; Ruzsinszky, A.; Peng, H.; Sun, J.; Trushin, E.; Görling, A. Understanding Band Gaps of Solids in Generalized Kohn-Sham Theory. *Proc. Natl. Acad. Sci.* **2017**, *114* (11), 2801–2806.

(8) Kresse, G.; Joubert, D. From Ultrasoft Pseudopotentials to the Projector Augmented-Wave Method. *Phys. Rev. B* **1999**, *59* (3), 1758–1775.

(9) Xu, Z.; Rossmeisl, J.; Kitchin, J. R. A Linear Response DFT+U Study of Trends in the Oxygen Evolution Activity of Transition Metal Rutile Dioxides. *J. Phys. Chem. C* **2015**, *119* (9), 4827–4833.

(10) Monkhorst, H. J.; Pack, J. D. Special Points for Brillonin-Zone Integrations. *Phys. Rev. B* **2019**, *13* (12), 5188–5192.

(11) Siahrostami, S.; Vojvodic, A. Influence of Adsorbed Water on the Oxygen Evolution Reaction on Oxides. *J. Phys. Chem. C* **2015**, *119* (2), 1032–1037.

(12) Mathew, K.; Sundararaman, R.; Letchworth-Weaver, K.; Arias, T. A.; Hennig, R. G. Implicit Solvation Model for Density-Functional Study of Nanocrystal Surfaces and Reaction Pathways. *J. Chem. Phys.* **2014**, *140* (8), 084106.

(13) Briquet, L. G. V.; Sarwar, M.; Mugo, J.; Jones, G.; Calle-Vallejo, F. A New Type of Scaling Relations to Assess the Accuracy of Computational Predictions of Catalytic Activities Applied to the Oxygen Evolution Reaction. *ChemCatChem* **2017**, *9* (7), 1261–1268.

(14) Nørskov, J. K.; Rossmeisl, J.; Logadottir, A.; Lindqvist, L.; Kitchin, J. R.; Bligaard, T.; Jónsson, H. Origin of the Overpotential for Oxygen Reduction at a Fuel-Cell Cathode. *J. Phys. Chem. B* **2004**, *108* (46), 17886–17892.

(15) Granda-Marulanda, L. P.; Rendón-Calle, A.; Builes, S.; Illas, F.; Koper, M. T. M.; Calle-Vallejo, F. A Semiempirical Method to Detect and Correct DFT-Based Gas-Phase Errors and Its Application in Electrocatalysis. *ACS Catal.* **2020**, *10* (12), 6900–6907.

(16) Calle-Vallejo, F.; Koper, M. T. M. Theoretical Considerations on the Electroreduction of CO to C_2 Species on Cu(100) Electrodes. *Angew. Chem., Int. Ed.* **2013**, *52* (28), 7282–7285.

(17) Pouilleau, J.; Devilliers, D.; Garrido, F.; Durand-Vidal, S.; Mahé, E. Structure and Composition of Passive Titanium Oxide Films. *Mater. Sci. Eng., B* **1997**, *47* (3), 235–243.

(18) Walle, L. E.; Borg, A.; Johansson, E. M. J.; Plogmaker, S.; Rensmo, H.; Uvdal, P.; Sandell, A. Mixed Dissociative and Molecular Water Adsorption on Anatase TiO_2(101). *J. Phys. Chem. C* **2011**, *115* (19), 9545–9550.

(19) Kato, K.; Xin, Y.; Shirai, T. Structural-Controlled Synthesis of Highly Efficient Visible Light TiO_2 Photocatalyst via One-Step Single-Mode Microwave Assisted Reaction. *Sci. Rep.* **2019**, *9* (1), 1–9.

(20) Zhang, Z.; Hedhili, M. N.; Zhu, H.; Wang, P. Electrochemical Reduction Induced Self-Doping of Ti^{3+} for Efficient Water Splitting Performance on TiO_2 Based Photoelectrodes. *Phys. Chem. Chem. Phys.* **2013**, *15* (37), 15637–15644.

(21) Qiu, M.; Tian, Y.; Chen, Z.; Yang, Z.; Li, W.; Wang, K.; Wang, L.; Wang, K.; Zhang, W. Synthesis of Ti^{3+} Self-Doped TiO_2 Nanocrystals Based on Le Chatelier's Principle and Their Application in Solar Light Photocatalysis. *RSC Adv.* **2016**, *6* (78), 74376–74383.

(22) Balachandran, U.; Eror, N. G. Raman Spectra of Titanium Dioxide. *J. Solid State Chem.* **1982**, *42* (3), 276–282.

(23) Chiesa, M.; Paganini, M. C.; Livraghi, S.; Giamello, E. Charge Trapping in TiO_2 Polymorphs as Seen by Electron Paramagnetic Resonance Spectroscopy. *Phys. Chem. Chem. Phys.* **2013**, *15* (24), 9435–9447.

(24) Dean, J. A. Section 6: Thermodynamic Properties. In *Lange's Handbook of Chemistry.*; Dean, J. A., Lange, N. A., Eds.; McGraw-Hill: Knoxville, **1999**; pp 6.1-6.147.

Appendix F

Supporting Information for "Subsurface Carbon: a General Feature of Noble Metals"

Computational Methods

The DFT calculations have been carried out using the VASP code exploding periodic boundary conditions.[1] Relaxed geometries and total energies are acquired using the Perdew-Burke-Ernzerhof (*PBE*)[2] exchange-correlation functional, known to accurately describe TMs and also the interaction of C with them.[3,4] Valence electrons density is expanded in a plane wave basis set with a 415 eV cutoff for the kinetic energy. The projector augmented wave method was used to describe the interactions between core and valence electrons.[5] Unless stated otherwise, calculations are carried out non spin polarized. Geometry optimizations were performed until all forces acting on relaxed atoms became less than 0.03 eV $Å^{-1}$, and the electronic convergence threshold was set to $1 \cdot 10^{-6}$ eV.

The simulation of extended Cu, Ag, and Au (111) surfaces —and of Rh, Ir, Ni, Pd, and Pt (111) surfaces— is perfomed using a suited 54 metal atoms $p(3\times3)$ supercell slab model constructed from optimized bulks,[6] see Figure S1. The slab models contain six atomic layers with nine atoms per layer, and so the adsorption/absorption of one C atom implies a coverage of 1/9 monolayers (*ML*), defined as the number of C atoms per surface metal atoms. After optimization of the pristine surface the C was adsorbed/absorbed while the three bottom layers of the slab were kept fixed, while the other three upper layers were allowed to relax during geometry optimization, together with the adsorbed/absorbed carbon atom. The reciprocal space was sampled with 3×3×1 **Γ**-centred **k**-point grid and calculations were performed using a Gaussian smearing of 0.2 eV energy width to speed up convergence, yet final energies were extrapolated to 0 K (no smearing). The full coverage adsorption/absorption situations with 9 atoms, and therefore, a 9/9 ML coverage, have been computed likewise.

In addition, size scalable nanoparticle models of 79 atoms (M_{79}) have been used to compare extended surfaces to nanoparticles low-coordinated regions, *i.e.* edges and corners, see Figure S2. Briefly, such M_{79} nanoparticles have been calculated by placing them in a cubic box imposing a minimum distance of 10 Å in between translationally repeated nanoparticles and considering the Γ point only and optimizing the atomic positions. The same procedure was used to compute the energy of the isolated C atom, although an asymmetric box of 9×10×11 Å was used to certify the correct orbital occupancy (triplet state). The equilibrium Wulff shape of such *fcc* M_{79} nanoparticles consist of a cuboctahedral shape featuring eight (111) facets, and six rather small (001) facets. The adsorption, absorption, and sinking studies have been treated on the (111) facets in connection to the slab (111) surface model results. In this regard, the M_{79} nanoparticle features five layers, where the bottom two

were kept fixed during the C optimization procedures. For the full coverage investigation, six *hcp/tss* or seven *fcc/oss* C atoms have been placed on a given (111) facet of the M_{79} nanoparticle model, and computed likewise.

The surface→subsurface diffusion activation energy barriers were determined by scanning the potential energy profile along the line that connects the local minima of the surface and subsurface impurity atoms. Thus estimations of Transition States (*TS*s) were searched in a point-wise fashion along the path connecting adsorption and absorption configurations, where height of the carbon atom, defined with respect to the most distant frozen metal layer, was fixed, whereas all other degrees of freedom were allowed to fully relax. These approximate TSs were sequentially refined until forces acting on atoms were below 0.03 eV $Å^{-1}$. TSs have been characterized by vibrational frequency analysis, certifying their saddle point nature.

The adsorption/absorption energies are calculated as $E_{ads/abs} = -E_{C/metal} + E_C + E_{metal}$, where $E_{C/metal}$ is the total energy of the metal model with the C atom either adsorbed or absorbed, E_C is the energy of an isolated carbon atom, and E_{metal} is the energy of the optimized clean substrate: These are, the Cu, Ag, Au, Rh, Ir, Ni, Pd, or Pt (111) surface slab models, or Cu_{79}, Ag_{79}, or Au_{79} nanoparticles. With this definition, stable adsorption/absorption corresponds to positive $E_{ads/abs}$ values. The energy barriers, E_b, are calculated substracting the TS energy, from the surface adsorption energy state. The 3*s* of metal centres bound to C and C 1*s* core level energies have been acquired within the initial state approximation using the Fermi energy as a common reference.[7]

The more focused investigation on single crystal (111) surface slab models of Cu, Ag, and Au were chosen since *i)* they represent their most stable surface, and, actually, (111) facets are the majority of the NPs exposed area following the Wulff cuboctahedral shape of minimum surface tension,[8] and *ii)* the (111) surface is the highest packed possible surface for such face-centred-cubic (*fcc*) metals. Thus, the subsurface penetration across is thought as the most difficult possible, and, therefore, these systems are a conservative situation regarding subsurface occupancy. High symmetry surface and subsurface adsorption sites were optimized, considering multiple C connectivities, see Figure S1. The lowest minima were found for surface *fcc* and hexagonal close-packed (*hcp*) hollow sites, and their immediate octahedral (*oss*) and tetrahedral (*tss*) subsurface sites, respectively, which are discussed in the following. A complete set data is contained in Table S1.

Effect on Deformation Energies on Adsorption and Absorption Energies

The deformation energies are found to be a determining factor on the stabilization of C atoms at subsurface regions. This is clearly observed in the deformation energies, E_{def}, which are in the range of 29-96 kJ mol^{-1} for *oss* and *tss* sites, in average much larger than on the *fcc* and *hcp* surface sites, which range 8-36 kJ mol^{-1} —see Table S2. Accounting that so, the attachment energy of subsurface sites, E_{att}, is always larger than the equivalent surface sites by 25-74 kJ mol^{-1}, with the sole caveat of *oss* sites in Au(111), which display an attachment energy 43 kJ mol^{-1} less stable than immediately up surface *fcc* site. The above statements are well backed up by a small enlargement of site mean metal-metal distances, $\bar{d}$, with respect the bare surfaces —see Table S3— of 13-25 pm, whereas *oss* subsurface sites feature a similar enlargement of 18-20 pm, given their wider space, although *tss* subsurface sites do imply a much larger opening of the void by 35-41 pm to accommodate the C within, just affordable, to the point of being preferred, due to the larger attachment energies.

Comparison with Previous Calculations

Our E_{ads} and E_{abs} values on/in Cu (111) are in line with previous estimations of 458 and 490 kJ mol^{-1}.[9] The preference for *oss* in Cu compared to *tss*, 88 kJ mol^{-1} more stable, is similar to the one found previously in Ni, of 114 kJ mol^{-1}.[4] Furthermore, the similar stability of *oss* and *tss* in Ag (difference of 44 kJ mol^{-1}) is mirrored in Pd (42 kJ mol^{-1}), while the preference for *tss* in Au of 39 kJ mol^{-1} with respect *oss* was also found also in Pt (47 kJ mol^{-1}).[4] The calculated adsorption and absorption energies for Cu, Ag, and Au, ranging from 294 to 449 kJ mol^{-1}, are notably lower than ones calculated for Ni, Pd, and Pt, ranging from 650 to 746 kJ mol^{-1},[4] which is in agreement with the higher nobility of group 11 metals compared to group 10.

C Further Penetration Subsubsurface

A point of interest here is to determine whether such subsurface C penetrates further in the material. The E_{abs} in between the metal second and third layers —*tss*$_1$', *tss*$_2$', and *oss*'— subsubsurface sites reveal a preference for *oss*' sites for Cu and Ag (111), but *tss*$_2$' for Au (111), see Table S1. The results show that in Cu and Ag surfaces C is most stable in the subsurface region than in subsubsurface sites, with the E_{abs} being higher by 36 and 18 kJ mol^{-}

[1], respectively. Therefore, subsurface C seems to be a near-surface entity in Cu and Ag, and its quantity tied to the amount of exposed metal surface.

C Height and Near Surface Situations

Another type of minima corresponds to near surface situations, as seen by C height (*h*) measurements, see illustrations in Figure S3. For instance, both surface and subsurface C collapse into a single minimum, which is slightly subsurface for Cu_{79} *fcc/oss* and *hcp/tss*, and Ag_{79} *hcp/tss* edge sites. Such situations are also found on Au_{79} *hcp/tss* corner and *fcc/oss* centre sites, yet here, with C being above the metal surface layer; see distribution of C heights, *h*, for all the found minima in Figure S4 (*h* values are found in Tables S5). In general terms, Figure S4 illustrates how low-coordination sites featured in M_{79} NPs geometrically approach the surface and subsurface minima, with clear meetings in the just commented cases.

Subsurface C Experimental Evidence and Detection by X-ray Photoemission Means.

The subsurface C stability is in line with experimental C solubility measurements in molten metals. Despite C dissolution values on Cu, Ag, and Au can be rather small,[10] ranging 0.001 to 0.013 wt. % at ~1000 ºC, and therefore, smaller than on Ni (0.091 wt. %),[11] Pd (0.422 wt. %), and Pt (0.071 wt. %),[12] they are still present, measurable, and comparable. The experimental determination of late transition metal carbonyl carbido clusters,[13] where a carbon-centred hexanuclear Au octahedral cluster is stabilized using six diphenyl(2-pyridyl)phosphine ligands[14] further supports the C octahedral golden environment in particular, but the possible existence of interstitial C species in *tss* or *oss* positions on noble metals in general. Indeed, present simulations envision such carbide copper or silver clusters, yet not isolated.

As discussed, the subsurface C detection is cumbersome, even with high-resolution surface science techniques, such as the ambient pressure X-ray photoemission spectroscopy (APXPS). The core level binding energy estimates, obtained at the initial state approximation (see Table S9), are merely 0.4-0.6 eV higher than the gas phase CO_2 (g-CO_2) C 1*s* level, and so, likely masked by the prominent g-CO_2 APXPS peak, with a half-band width of ~0.5 eV according to recent experiments on Cu(111).[15] Given this, the direct detection of subsurface C species on Cu(111) becomes a challenging task, where indirect evidence through modified

surface activity appears more reachable. Notice that the shifts with respect to g-CO_2 rise up to detectable regions of 0.7-1.0 eV for Ag(111), and 1.2-1.7 eV for Au(111). However, still, the difference between surface *fcc*/*hcp* and *oss*/*tss* sites very small for Cu and Ag (111) surfaces, shift by up to 0.2 eV at most, slightly higher by 0.5 eV on *fcc*↔*oss* situations on Au(111). This situation is also observed on the C 1*s* surface/subsurface shifts obtained in metal M_{79} nanoparticle models, see Table S10.

Phase Diagram Generation

The pressure-temperature dependent phase diagrams shown in Figures S9 and S10 were created following a statistical thermodynamics approach from *ab initio* computed data.[16] Simplified, for each computed situation, one can acquire the adsorption or absorption free energy, ΔG^{ad} or ΔG^{ab}, respectively, as a function of the system temperature (T) and the gas pressure (p) it is exposed to. For simplification, the adsorption situation is exemplified in the following, although the procedure is equivalent for absorption situations. In our case, for the isolated C atom adsorption on the metal slab (111) surface model, containing 54 metal atoms, or the 79 metal atom NP, the formula is:

$$\Delta G^{ad}(T,p) \approx -\frac{1}{A}\{E^{total}(N_C,N_M) - E^{total}(0,N_M) - N_C(E_C^{total} + E_C^{ZPE}) - N_C\Delta\mu_C(T,p)\} \qquad (1),$$

where A is the system surface area, N_C the number of carbon atoms in the studied system —normally one in our case, except for full coverage situations which can go up to nine atoms—, N_M the number of metal atoms in the studied system —54 and 79 for slab and NP models, respectively—, and $\Delta\mu_C$ the carbon chemical potential variation of carbon.

Become aware of the negative sign in front of the equation, only introduced to turn most stable energies into the most positive ones. Moreover, the $\frac{1}{A}$ factor is not indispensable and it is only introduced to obtain surface free energy values. For our slab systems A has been calculated as the area of the exposed surface of the pristine slab, and for the NPs it has been estimated as the (111) facet area of the pristine NP, computed by dividing the (111) facet in triangles and adding up the resulting triangle areas. In addition, the zero-point energy (ZPE) term, E_C^{ZPE}, is included, see details below.

Notice that Equation 1 is valid for a system with an invariant number of substrate metal atoms, for a variant expression we refer to the literature.[16] In our case, the slab or nanoparticle models contain the same number of metal atoms, N_M, either pristine or having

one or more adsorbed/absorbed C atoms. Furthermore, note that equation 1 equals zero for the clean surface since in that case $N_C = 0$, and $E^{total}(N_C, N_M) = E^{total}(0, N_M)$.

The results presented here were obtained using $\mu_C = \frac{1}{2}(\mu_{C_2H_2} - \mu_{H_2})$, $E_C^{total} = \frac{1}{2}\left(E_{C_2H_2}^{total} - E_{H_2}^{total}\right)$, and $E_C^{ZPE} = \frac{1}{2}\left(E_{C_2H_2}^{ZPE} - E_{H_2}^{ZPE}\right)$ as a reference, as in the working catalytic experimental conditions it is not rigorous at all to consider a C atoms gas phase, and therefore is estimated as a lineal combination of chemical potentials of gas phase molecules. The usage of this reference implies that $\Delta\mu_C = \frac{1}{2}(\Delta\mu_{C_2H_2} - \mu\Delta_{H_2})$. Hence, to compute $\Delta\mu_C$, both C_2H_2 and H_2 —hereafter named *X* species— chemical potential variations are calculated as:

$$\Delta\mu_X(T,p) = -k_B T\left\{ln\left[\left(\frac{2\pi m_X}{h^2}\right)^{3/2}\frac{(k_B T)^{5/2}}{p_X}\right] + \ln\left(\frac{k_B T}{\sigma_X^{sym} B_{0,X}}\right) - \sum_{i=1}^{n} ln\left[1 - \exp\left(\frac{-\hbar\omega_{i,X}}{k_B T}\right)\right] + \ln\left(I_X^{spin}\right)\right\} \quad (2),$$

where h is the Planck constant, m_X is the mass of the *X* molecule, k_B is the Boltzmann constant, p_X is the partial pressure of the X species, σ_X^{sym} is the classical symmetry number of the *X* rigid molecule,[17] known as the number of different but indistinguishable arrangements of the molecule, B_0 is the rotational constant, calculated as $\frac{\hbar^2}{2I_X}$, where I_X is the moment of inertia of the molecule, $I_X = \sum_i m_i r_i^2$, where m_i is the mass of the atoms conforming the *X* molecule and r_i the distance of the i atom center to the molecular centre of mass, ω_i is each of the vibrational normal modes of the X molecule, and I_X^{spin} is the electronic spin degeneracy of the ground state, equal to one for the cases studied in this work, showing no degeneracy in the ground state.

To calculate the moments of inertia of H_2 and C_2H_2, these molecules were optimized using an asymmetric box of 9×10×11 Å carrying out **Γ** point optimizations. The distance of each atom to the molecular centre of mass can be obtained from the final geometries, and consequently, the moment of inertia. Moreover, vibrational frequency analysis within the harmonic approximation, carried out *via* construction and diagonalization of the Hessian matrix by finite displacements of 0.03 Å, were performed so as to obtain the fundamental vibrational modes of each molecule.

The first summand of the equation corresponds to the translational free energy, calculated as the translational partition function in the classical limit assuming an ideal behaviour of the gas phase. The second summand corresponds to the rotational free energy, calculated as the rotational partition function using the rigid rotator approximation and introducing the classical symmetry number as an approximation to the coupling between the rotational partition function and the nuclear spin degrees of freedom, which only holds for

linear molecules, see a more detailed explanation in the literature.[16] The third summand corresponds to the vibrational free energy, calculated as the vibrational partition function within the harmonic approximation, by writing the partition function as a sum over the harmonic oscillators of all n fundamental modes ω_i of the molecule; notice that in previous literature[16] there is a negative sign missing inside the exponential factor, here duly present. Finally, the fourth summand corresponds to the electronic and nuclear free energy, where the only term contributing significantly to the partition function is the possible spin degeneracy of the ground state.

Bringing it all together, ad/absorption free energies can be computed as function of T and p using equation 1 and 2. As demonstrated before, the ΔG^{ad} of the clean surface is zero; thus, if the ΔG^{ad} of the system with the adsorbate is positive, it is more stable than the clean surface, when negative less stable, and if zero it is equally stable to the clean surface, symbolizing a phase transition point in between pristine and C-containing phases.

Taking a look at Scheme 1 it can be seen that adsorption and absorption free energies depend linearly on the variation of the chemical potential, and that the clean surface ΔG does not. The most stable situation under a certain chemical potential corresponds to the one with the most positive ΔG, such situations highlited in Scheme 1 with thicker lines. The two C-containing situations exemplified in it, C^{sur} and C_{sub}, experience the same dependence on the chemical potential, hence, the most stable situation of the two will still be the most stable under any conditions of T and p. In the example, the point where C_{sub} and clean surface cross corresponds to the chemical potential in which these two situations are equally stable, this is, at ΔG^{ab} zero. The Scheme 1 is built at a constant temperature, *e.g.* could be at 600 K, and a constant p_{H_2} of 10^{-7} Pa, modelling limit ultra high vacuum conditions. This allows to find the corresponding $p_{C_2H_2}$ for a ΔG^{ab} of zero. Finding the temperatures and pressures that turn ad/absorption energies zero allows us to build a phase diagram by representing these points in a T-$p_{C_2H_2}$ plot, providing us the data for Figures S9 and S10.

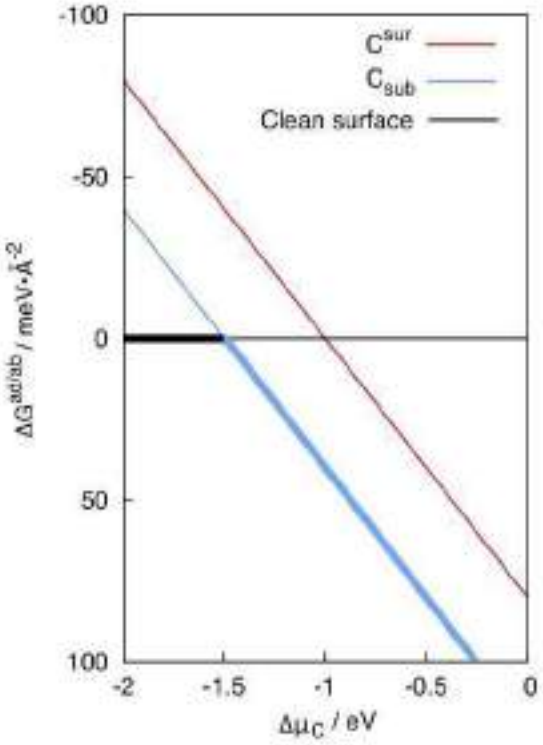

Scheme 1: Illustrative scheme showing the variation of the adsorption or absorpton free energies, $\Delta G^{ad/ab}$, across different variations of carbon chemical potential, $\Delta\mu_C$. Black line corresponds to the clean surface. Blue and red lines to C_{sub} and C^{sur} situations.

Figure S1: Top (top) and side (bottom) views of the employed models for C moieties on/in the (111) *fcc* metal surface; a) *top*, b) *hcp*, c) *fcc*, d) *bridge* e) *tss'*, f) *tss*, g) *oss* and h) *bss* sites. C atoms are shown as black spheres. Metal surface layer is depicted by dark gray spheres, whereas first and second subsurface layers by light-gray and white spheres, respectively.

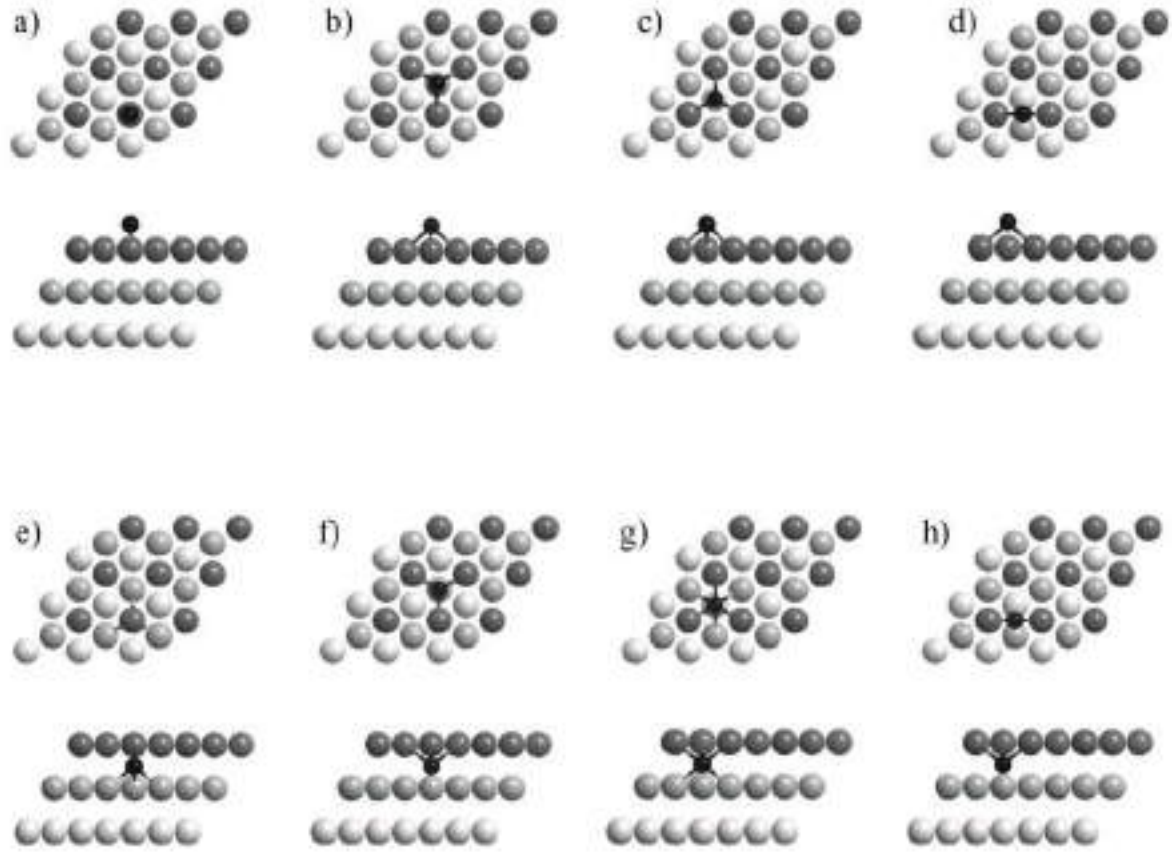

Figure S2: Top view of the M_{79} nanoparticle model for C moieties on/in the (111) facet, with the *hcp*/*tss* sites at; a) *edge* and c) *corner*, and the *fcc*/*oss* sites at; b) *center* and d) *edge* sites. Colour scheme as in Figure S1.

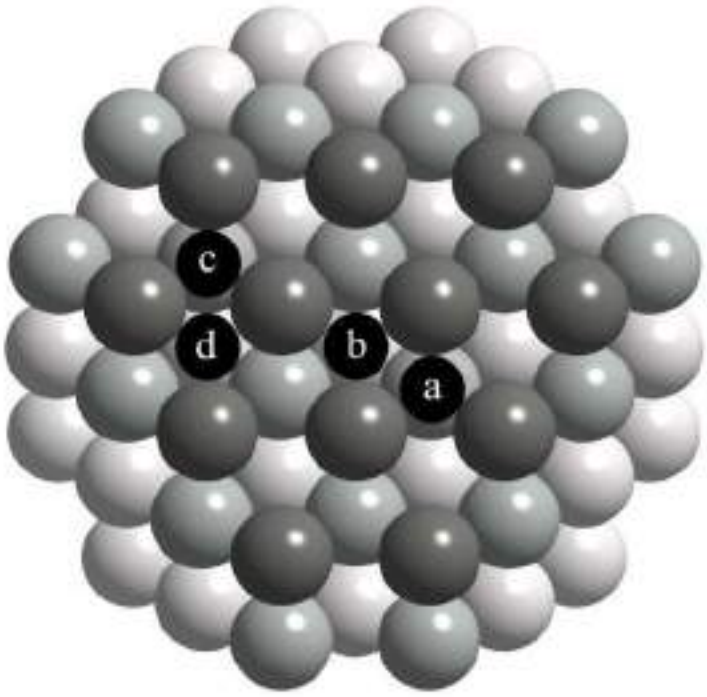

Figure S3: View of the C in-plane situations at a) *hcp/tss* edge of Ag_{79}, b) *fcc/oss* centre and c) *hcp/tss* corner of Au_{79}, and d) *hcp/tss* edge and e) *fcc/oss* edge of Cu_{79}. Color scheme as in Figure S1.

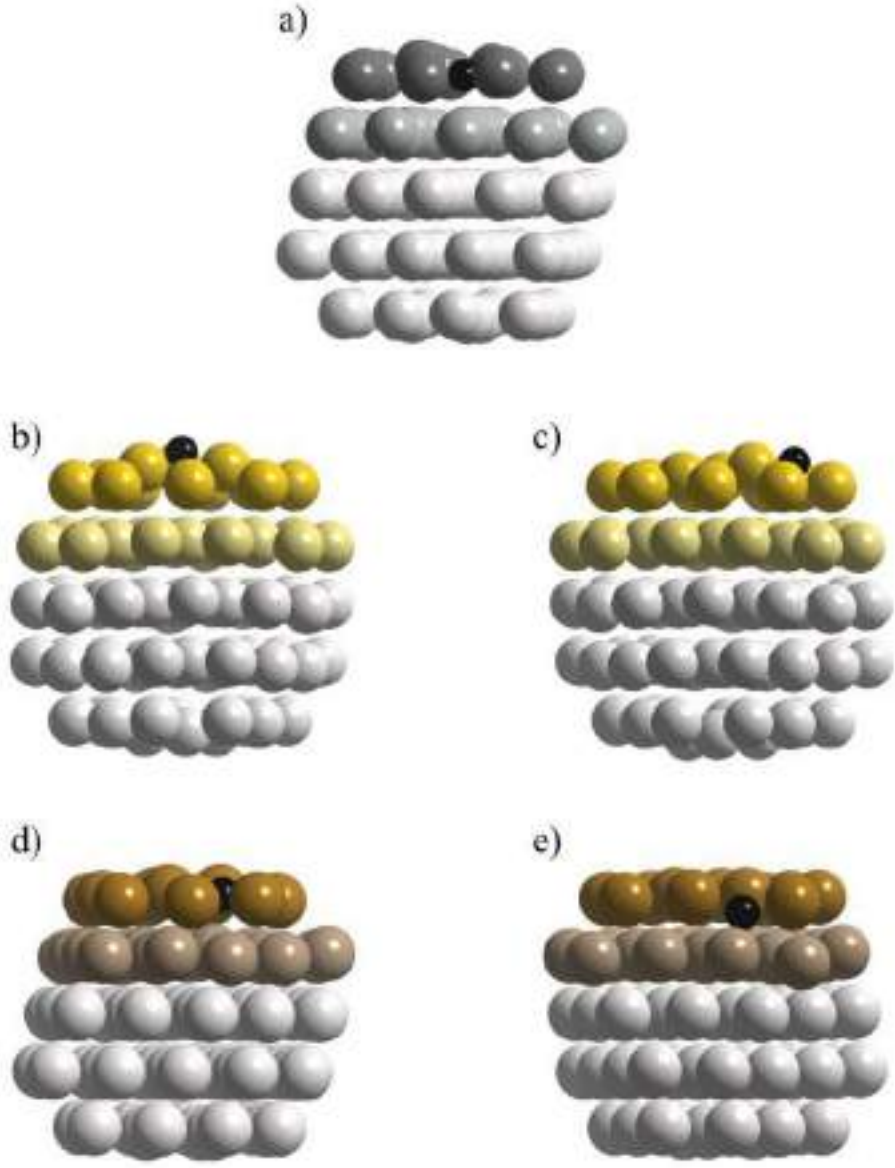

Figure S4. Adsorption (positive values, dark colours) and absorption (negative values, light colours) C heights (*h*, in pm) with respect the metal surface for the explored sites, as shown in Figures S1 and S2 of the Supporting Information, for Cu, Ag, and Au (111) surfaces (upper part) and for Cu_{79}, Ag_{79}, and Au_{79} NPs (bottom part). Site location **a**) top, **b**) *hcp*, **c**) *fcc*, **d**) *tss'*, **e**) *tss*, **f**) *oss*, **g**) *hcp* edge, **h**) *hcp* corner, **i**) *fcc* centre, **j**) *fcc* edge, **k**) *tss* edge, **l**) *tss* corner, **m**) *oss* centre, **n**) *oss* edge.

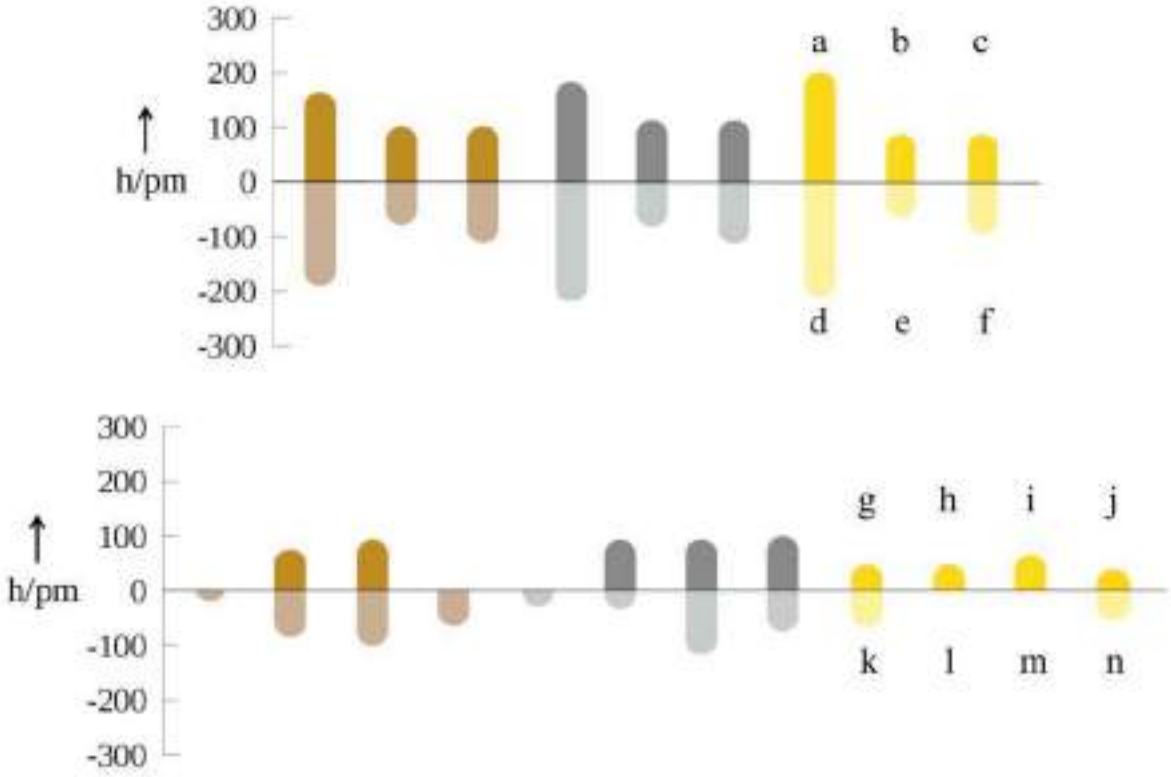

Figure S5. Projected DOS difference for Cu 3*d*, Ag 4*d*, and Au 5*d* states of TMs bound to C: a), c), and e) for *fcc/oss* sites, b), d), and f) for *hcp/tss* sites of Cu, Ag, and Au (111) surfaces, respectively; g) and h) *fcc*/oss and *hcp/tss* sites of the corresponding relaxed structure on Au (111) surface minus the pristine surface reference. Black line – *fcc/hcp* minus pristine, red and blue lines – surface and subsurface atoms bound to C, respectively, in structures with different *oss* and *tss* sites. Plots are normalized to the number of TMs around C.

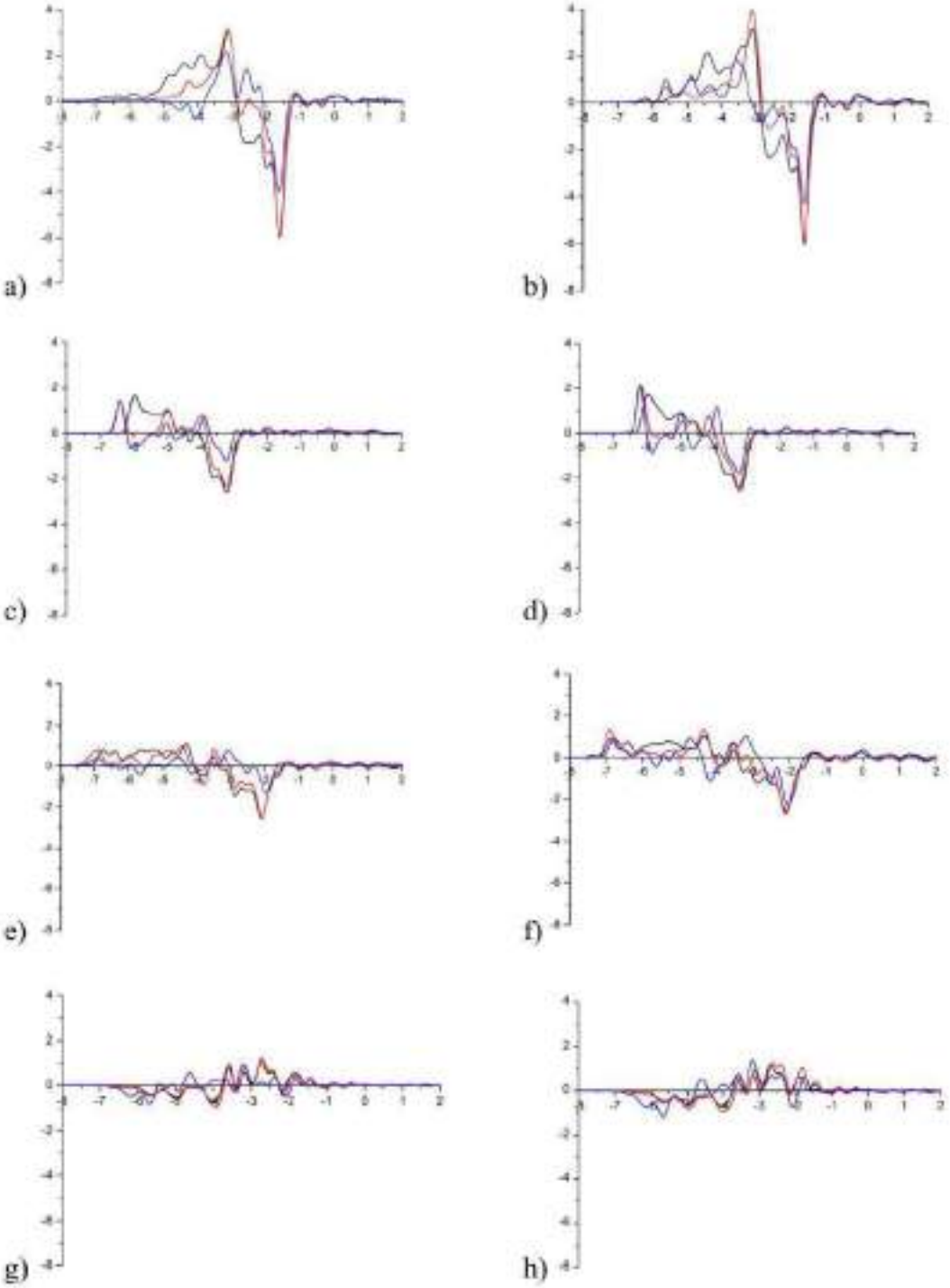

Figure S6. Difference in the density of states plots of Cu 3d, Ag 4d and Au 5d states for metal centers bound to C: a, e, m – *fcc* and *oss*; b, f, m – *fcc edge* and *oss edge*; c, g, n – *hcp edge* and *tss edge* sites; d, h, o – *hcp* corner and *tss* corner sites of Cu_{79}, Ag_{79} and Au_{79} nanoparticles, respectively; i, j, k and l – *hcp edge* and *tss* sites of the relaxed structure without C minus pristine. Black line – *fcc/fcc edge/hcp edge/hcp corner*; red line and blue line – surface and subsurface atoms bound to C, respectively in the structures with different *oss/oss edge/tss edge/tss corner* sites; m – cyan line for *fcc* site, black – *fcc edge*, red – surface atoms *oss edge* (C is coordinated only to surface atoms, since the fourth atom is not subsurface, but part of another (111) facet of the nanoparticle). The plots are normalized with respect to the number of metal atoms around the carbon.

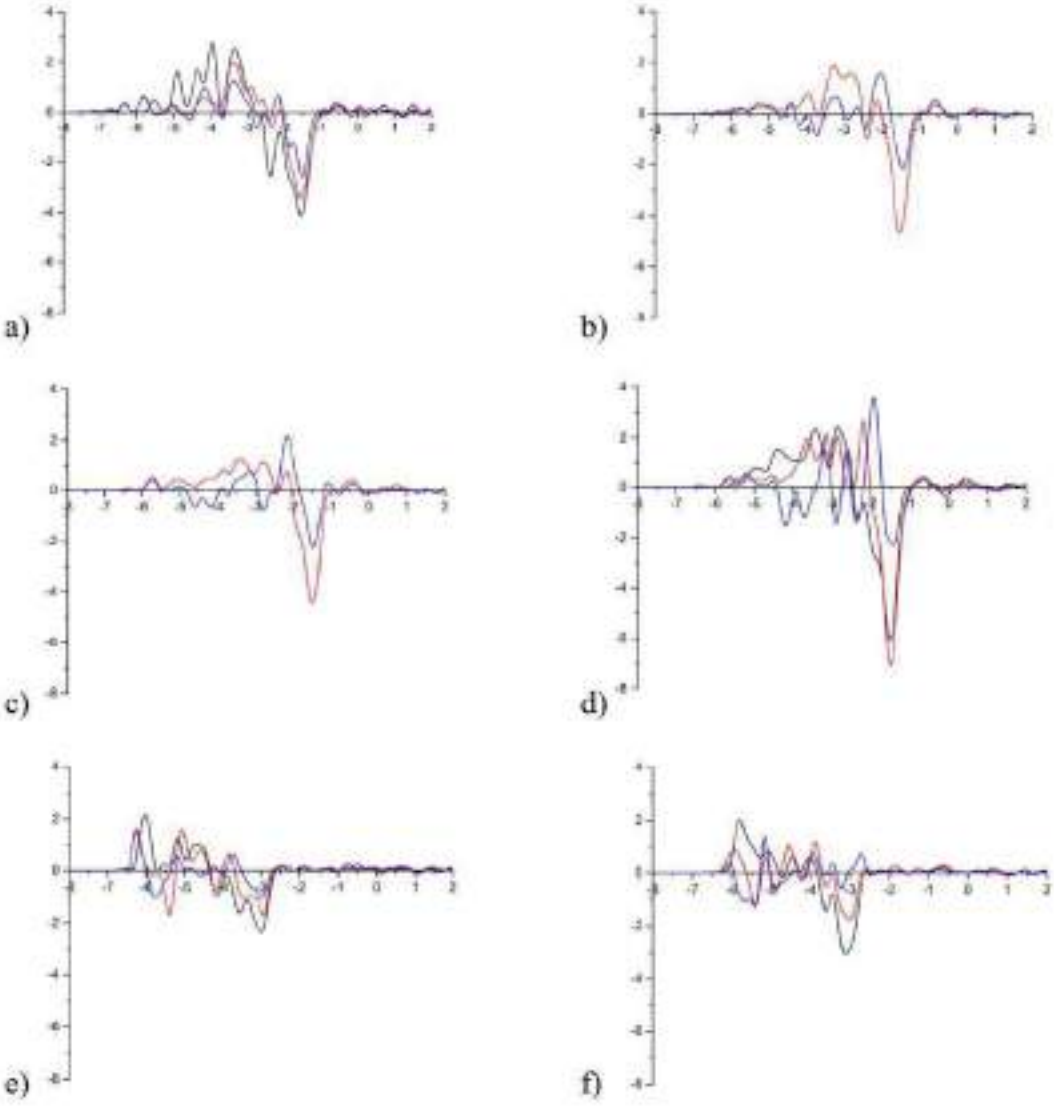

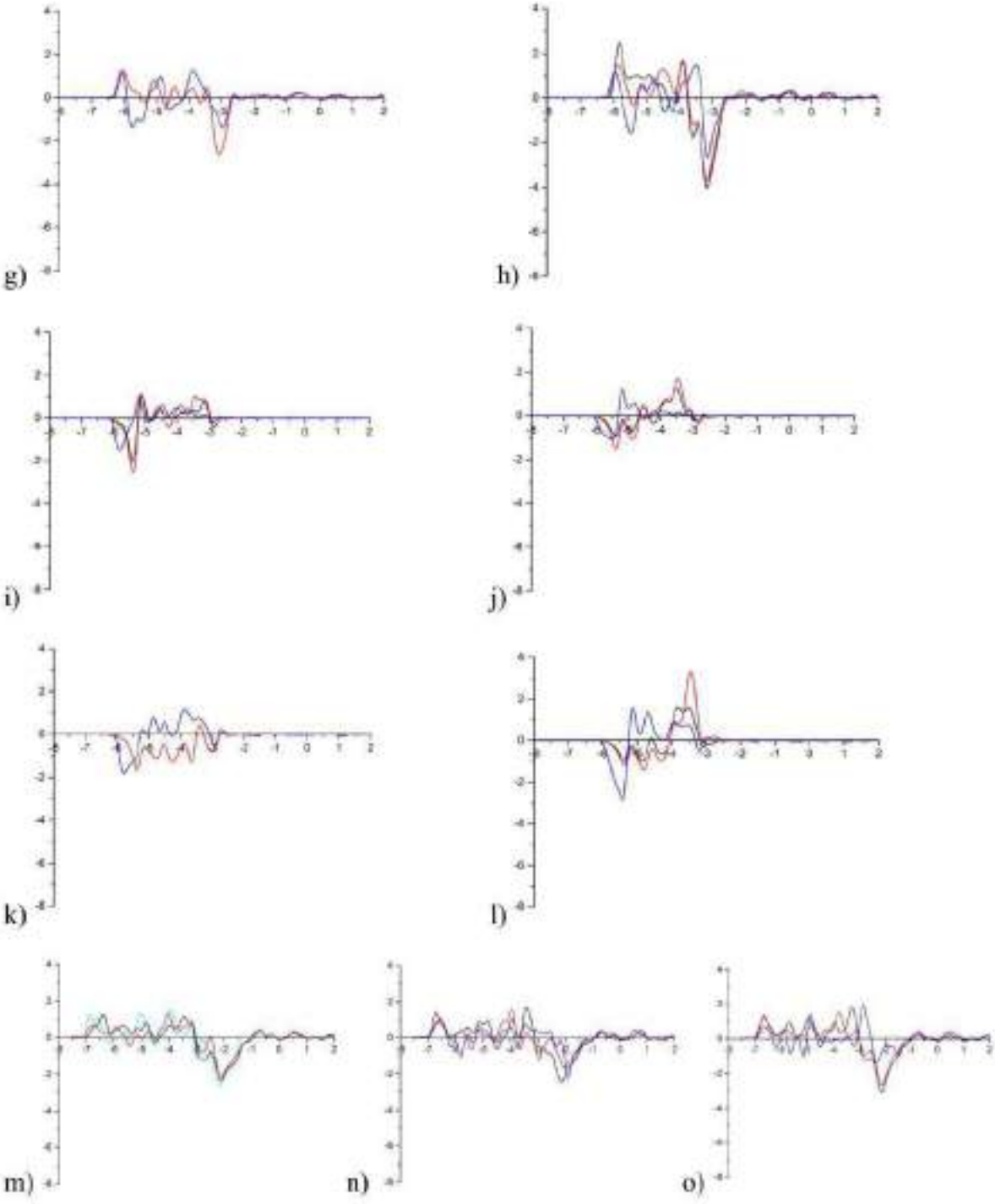
g)
h)
i)
j)
k)
l)
m)
n)
o)

Figure S7. Charge density difference for the various sites for C adsorption/absorption on (111) surfaces (first row – Cu; second – Ag; third – Au). Color scheme: green – increase of the electron density; blue – decrease of the electron density.

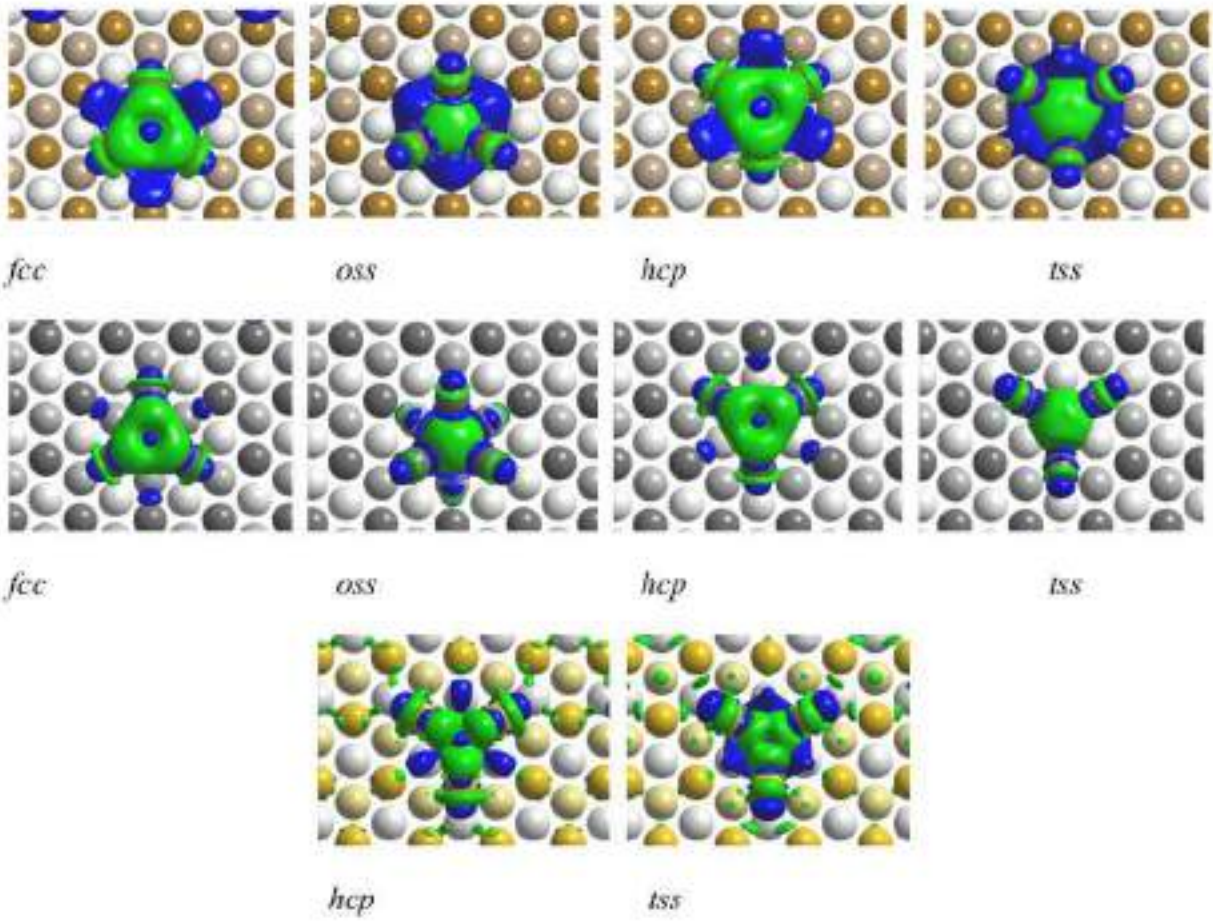

Figure S8. Charge density difference for various sites for C adsorption/absorption on M_{79} nanoparticles (first and second row – Cu; third and fourth – Ag; fifth and sixth – Au). Color scheme: green – increase of the electron density; blue – decrease of the electron density.

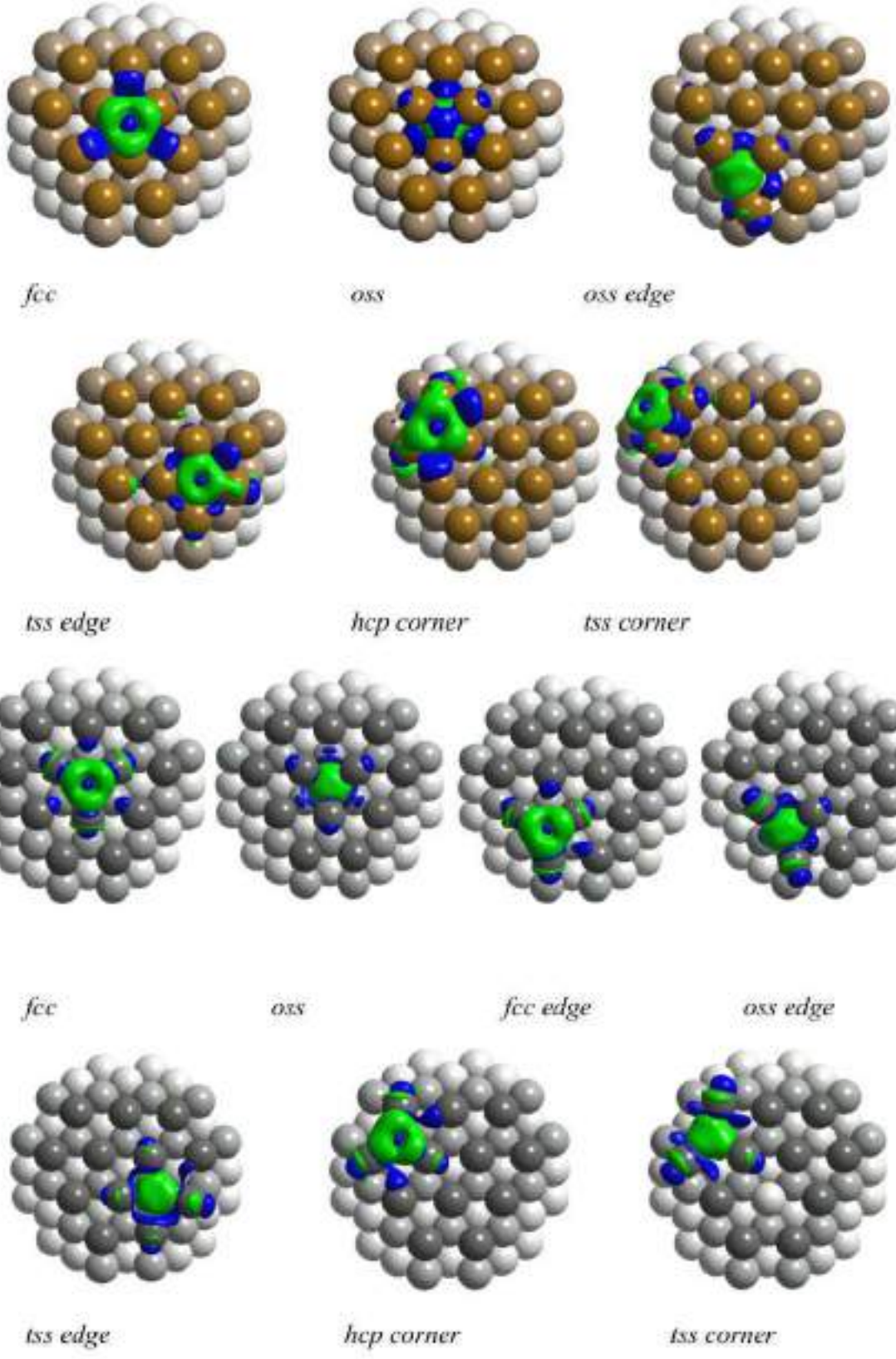

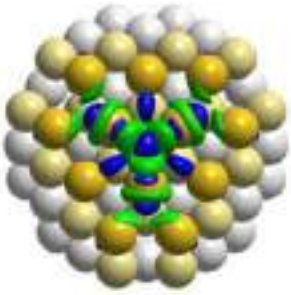

fcc

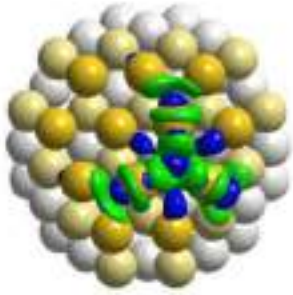

hcp edge

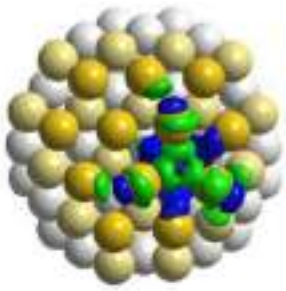

tss edge

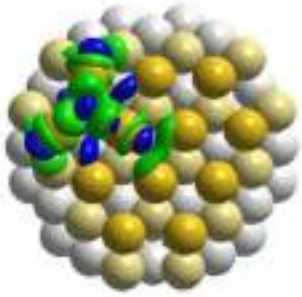

hcp corner

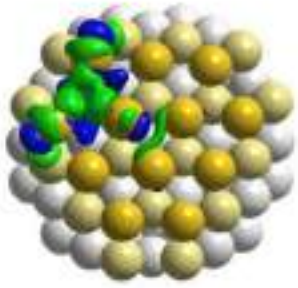

tss corner

Figure S9. Phase diagrams for *fcc* TMs (111) surfaces (TM = Rh, Ir, Ni, Pd, Pt, Cu, Ag, and Au) depending on the acetylene partial pressure ($p_{C_2H_2}$, in Pa), and the temperature (T). Diagrams are obtained for a constant partial pressure of H_2, $p_{H_2} = 10^{-7}$ Pa. The white region belongs to a pristine metal phase, and the colored regions belong to phases with C adatoms adsorbed (C^{sur}) or absorbed (C_{sub}).

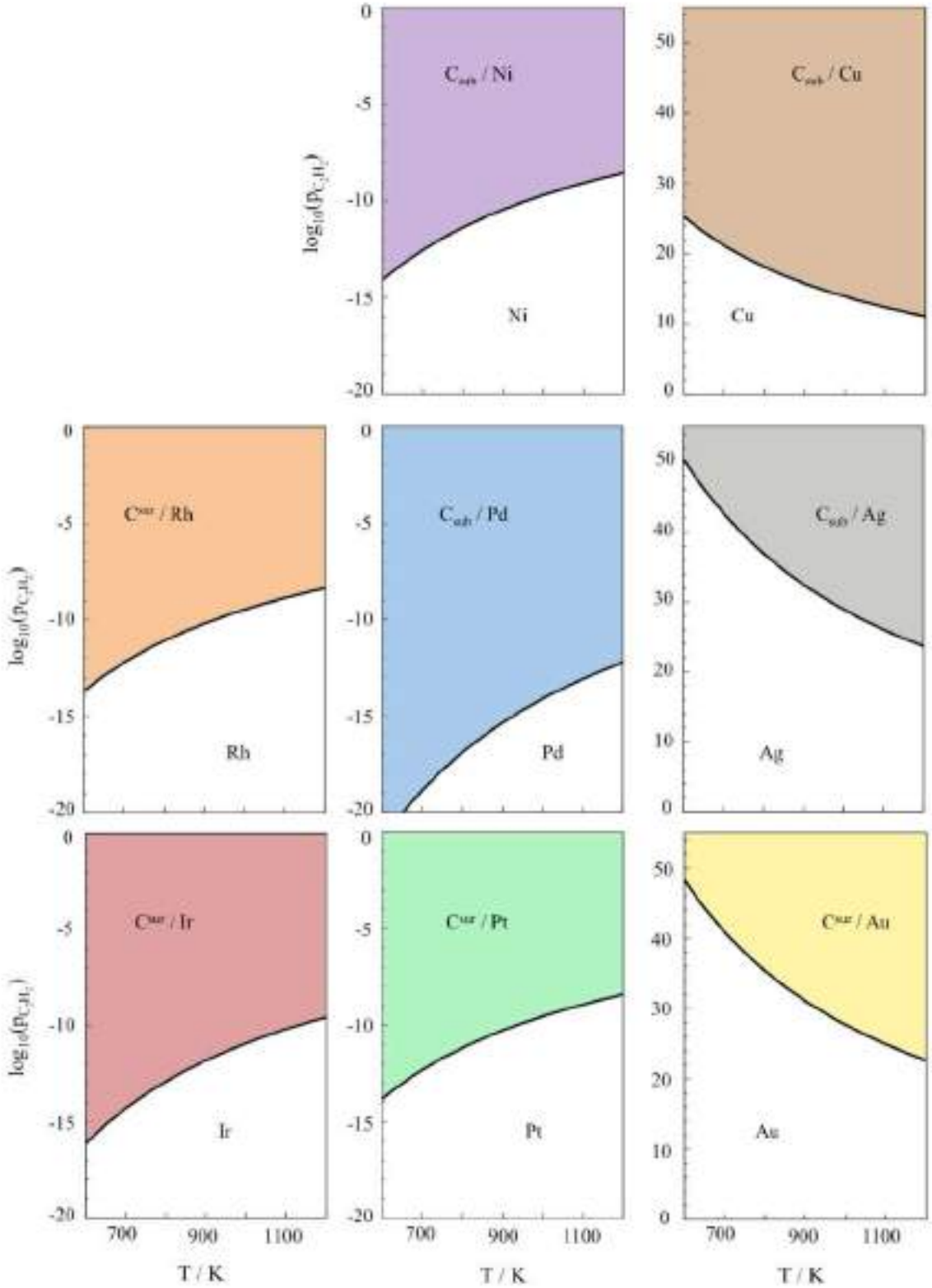

Figure S10. Phase diagrams for TM_{79} nanoparticle models (TM = Cu, Ag, and Au), in the same conditions as depicted in Figure S9.

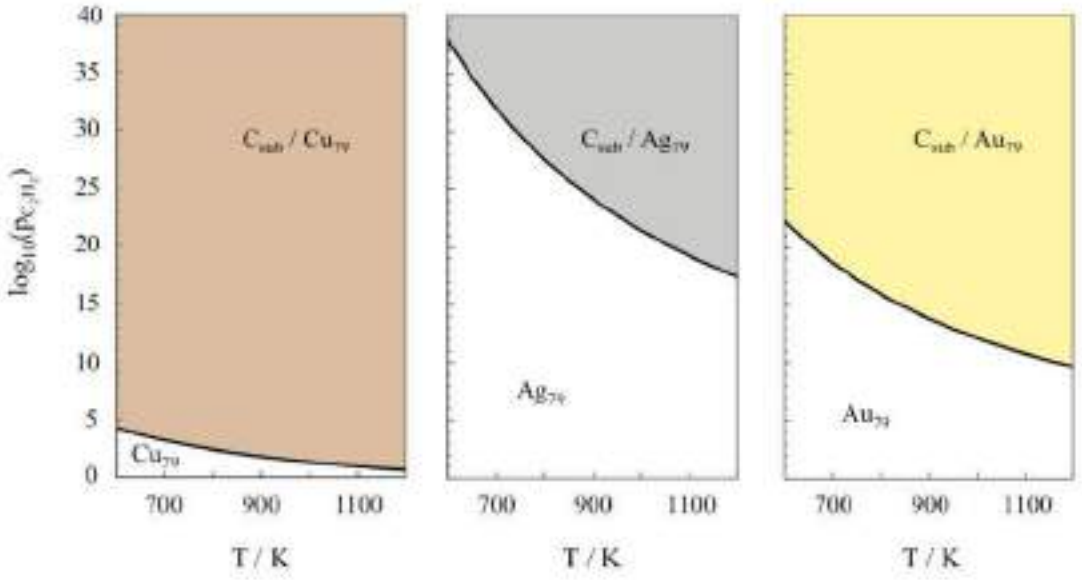

Figure S11. In descending order, Rh, Ir, Ni, Pd, and Pt adsorption (E_{ads}, in dark colours) and subsurface absorption (E_{abs}, in light colours) energies, in kJ mol^{-1}, on (111) surface (a) *hcp* and subsurface *tss* sites, respectively, and (b), *fcc* and *oss* sites, respectively. Carbon sinking energy barriers on each site are shown in black.

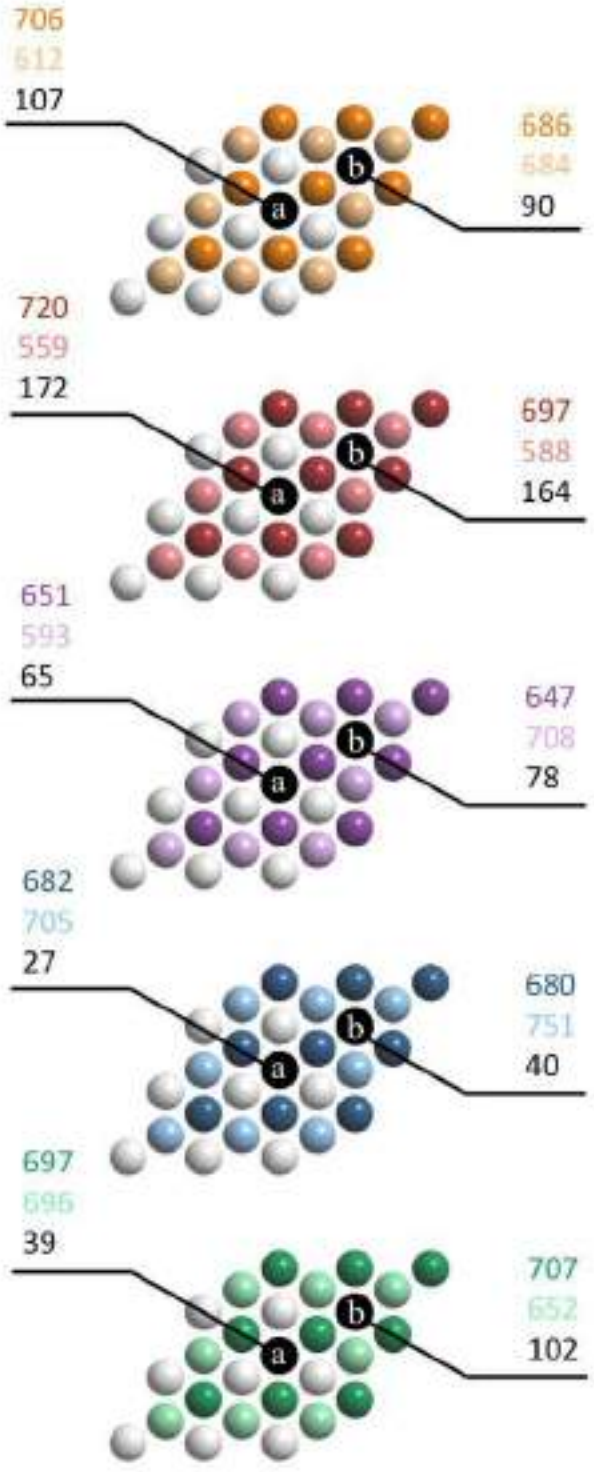

Figure S12: Top view of the C_{70} high coverage situation, revealing the formation of a C_6 aggregate. Colour coding as in Figure S3.

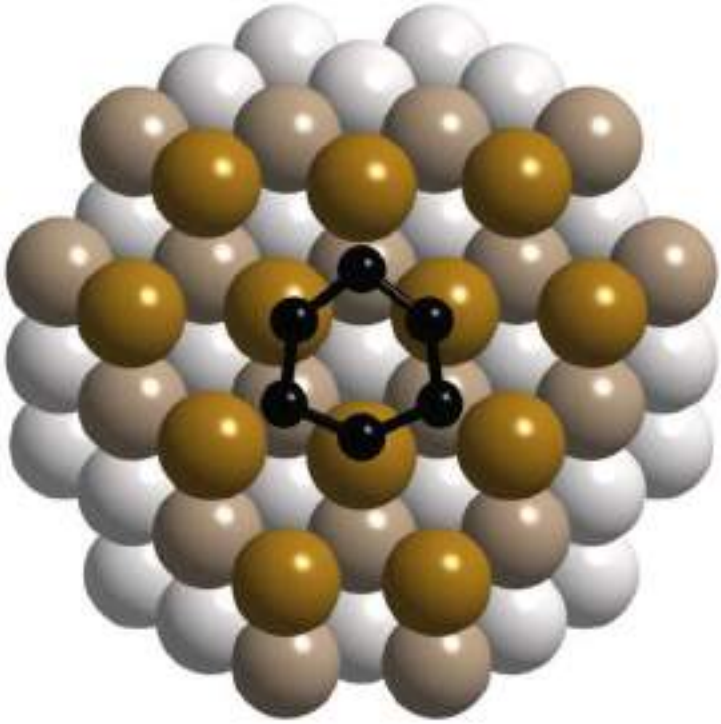

Table S1. Adsorption energies, E_{ads}, absorption energies, E_{abs}, deformation energies, E_{def}, and attachment/interaction energies, E_{att}, in kJ mol^{-1}, resulting from the optimization of the sites depicted in Figure S1.

	Cu(111)			Ag(111)			Au(111)		
	$E_{ads/abs}$	E_{def}	E_{att}	$E_{ads/abs}$	E_{def}	E_{att}	$E_{ads/abs}$	E_{def}	E_{att}
top	256			161			211		
tss'	383			268			310		
bridge	435			320			414		
bss	482			338			362		
fcc	440	10	450	320	8	328	414	26	440
oss	482	42	524	338	29	368	350	47	397
hcp	436	12	448	314	10	324	403	36	438
tss	394	96	489	294	63	357	389	74	463
oss[a]	446			316			294		
tss_1[a]	300			230			295		
tss_2[a]	351			255			305		

[a] – the site is subsubsurface

Table S2. Adsorption energies/absorption energies, $E_{ads/abs}$, deformation energies, E_{def}, and attachment energies, E_{att}, both in kJ mol^{-1}, resulting from the optimization of the sites depicted in Figure S2.

		Cu_{79}			Ag_{79}			Au_{79}		
		$E_{ads/abs}$	E_{def}	E_{att}	$E_{ads/abs}$	E_{def}	E_{att}	$E_{ads/abs}$	E_{def}	E_{att}
fcc	*centre*	472	27	499	359	28	387	470	65	535
	edge	567	58	626	366	18	384	493	43	536
oss	*centre*	533	47	580	410	29	439	470	65	535
	edge	567	58	626	394	46	440	437	95	532
hcp	*edge*	562	75	637	404	56	459	486	56	542
	corner	497	36	533	347	28	375	484	41	524
tss	*edge*	562	75	637	404	56	459	499	67	567
	corner	603	20	623	357	57	413	454	41	524

Table S3. Mean metal-metal distance, $\bar{d}$ and mean metal-metal distance, but prior to the C adsorption/absorption, $\bar{d}_{pr}$ in pm, for the optimized sites depicted in Figure S1 and Figure S2.

$\bar{d}$		**Cu(111)**	**Ag(111)**	**Au(111)**
fcc/oss		270/324	309/368	317/371
hcp/tss		272/332	311/374	320/370
$\bar{d}_{pr}$				
fcc/oss		257/305	294/350	295/351
hcp/tss		257/291	294/334	295/335
$\bar{d}$		**Cu_{79}**	**Ag_{79}**	**Au_{79}**
fcc/oss	*centre*	277/297	326/338	327/327
	edge	296/296	316/337	322/336
hcp/tss	*edge*	295/295	338/338	331/334
	corner	284/280	327/336	322/322
$\bar{d}_{pr}$				
fcc/oss	*centre*	252/277	289/318	281/324
	edge	250/274	288/315	284/319
hcp/tss	*edge*	252/254	289/291	286/294
	corner	249/250	286/288	284/290

Table S4. Initial state C 1*s* core level binding energy estimation, in eV, for the optimized sites depicted in Figure S1 and Figure S2.

C 1*s*		**Cu(111)**	**Ag(111)**	**Au(111)**
fcc/oss		266.4/266.6	266.8/267.0	267.2/267.7
hcp/tss		266.4/266.4	266.9/266.8	267.3/267.4
		Cu_{79}	**Ag_{79}**	**Au_{79}**
fcc/oss	*centre*	266.3/266.6	266.8/267.0	267.3/267.3
	edge	266.5/266.5	266.8/267.0	267.4/267.6
hcp/tss	*edge*	266.4/266.4	267.0/267.0	267.5/267.5
	corner	266.4/266.4	267.0/266.9	267.6/267.6

Table S5. The C height, *h*, with respect the bonded surface metals plane, for sites depicted in Figure S1 and Figure S2. All values are given in pm. Only a value is given when both surface and subsurface situations collapse in a single common minimum.

h		**Cu(111)**	**Ag(111)**	**Au(111)**
top/tss'		159/-182	183/-207	205/-204
bridge/bss		89/-99[a]	111[a]/-108[a]	96[a]/-61
fcc/oss		107/-98	112/-109	96/-87
hcp/tss		105/-72	111/-72	95/-58
		Cu_{79}	**Ag_{79}**	**Au_{79}**
fcc/oss	*centre*	89/-99	78/-108	60/60
	edge	-53/-53	95/-73	10/-39
hcp/tss	*edge*	-9/-9	-26/-26	32/-63
	corner	67/-76	82/-21	18/18

[a] – evolution towards a hollow position.

Table S6: Shift of the 3*s* core levels/*d* band centres, ε_d, of the metal atoms bound to the carbon with respect to the corresponding atoms in the pristine nanoparticles, in eV.

		3*s* core level shifts			**ε_d**		
		Cu	**Ag**	**Au**	**Cu**	**Ag**	**Au**
fcc		0.84	0.55	0.87	-0.93	-0.39	-0.79
fcc edge			0.57	0.91		-0.42	-0.78
oss	Surf	0.49	0.21		-0.61	-0.25	
	Subs	0.37	0.07		-0.35	-0.07	
oss edge	Surf	0.53	0.18	0.61	-0.55	-0.24	-0.54
	Subs	0.14	0.02		-0.13	0.00	
hcp		0.92		0.92			-0.82
hcp edge			0.63	1.04	-0.82	-0.45	-0.84
tss	Surf	0.39	0.28	0.58	-0.35	0.02	-0.26
	Subs	0.14	0.05	0.41	-0.07	-0.01	-0.29
tss edge	Surf	0.72	0.43	0.80	-0.54	-0.30	
	Subs	0.06	0.15	0.27	-0.07	-0.07	

Table S6: Mean adsorption and absorption energies, E_{ads} and E_{abs}, for most stable situations with a 9/9 ML coverage of C on Cu, Ag, and Au (111) surfaces, and to the equivalent situation on a (111) facet of Cu_{79}, Ag_{79}, and Au_{79} nanoparticle models.

$E_{ads/abs}$	**Cu(111)**	**Ag(111)**	**Au(111)**
fcc/oss	355/422	270/312	331/315
	Cu_{79}	**Ag_{79}**	**Au_{79}**
hcp/tss	612/575	579/362[a]	439/429

[a] – This case belongs to *fcc/oss*

References

[1] G. Kresse, J. Furthmüller, *Comput. Mater. Sci.* **1996**, *6*, 15.

[2] J. P. Perdew, K. Burke, M. Ernzerhof, *Phys. Rev. Lett.* **1996**, *77*, 3865.

[3] L. Vega, J. Ruvireta, F. Viñes, F. Illas, *J. Chem. Theory Comput.* **2018**, *14*, 395.

[4] P. Janthon, F. Viñes, J. Sirijaraensre, J. Limtrakul, F. Illas, *Catal. Sci. Technol.* **2017**, *7*, 807.

[5] P. E. Blöchl, *Phys. Rev. B*, **1994**, *50*, 17953.

[6] P. Janthon, S. Luo, S. M. Kozlov, F. Viñes, J. Limtrakul, D. G. Truhlar and F. Illas, *J. Chem. Theory Comput.* **2014**, *10*, 3832.

[7] L. Köhler, G. Kresse, *Phys. Rev. B*, **2004**, *70*, 165405.

[8] L. Vega, J. Ruvireta, F. Viñes, F. Illas, *J. Chem. Theory Comput.* **2018**, *14*, 395.

[9] Y. Santiago-Rodriguez, J. A. Herron, M. C. Curet-Arana, M. Mavrikakis, *Surf. Sci.* **2014**, *627*, 57.

[10] R. B. McLellan, *Scr. Mater*, **1969**, *3*, 389.

[11] J. J. Lander, H. E. Kern, A. L. Beach, *J. Appl. Phys.* **1952**, *23*, 1305.

[12] R. H. Siller, W. A. Oates, R. B. McLellan, *J. Less-Common Metals*, **1968**, *16*, 71.

[13] S. Takemoto, H. Matsuzaka, *Coord. Chem. Rev.* **2012**, *256*, 574.

[14] J.-H. Jia, Q.-M. Wang, *J. Am. Chem. Soc.* **2009**, *131*, 16634.

[15] M. Favaro, H. Xiao, T. Cheng, W. A. Goddard III, J. Yano, E. J. Crumlin, *Proc. Acad. Natl. Sci.* **2018**, 201701405.

[16] J. Rogal, K. Reuter, *Educational Notes RTO-EN-AVT-142*. **2007**, 2, 1.

[17] M. K. Gilson, K. K. Irikura, *J. Phys. Chem. B* **2010**, *114*, 16304.

Appendix F

Supporting Information for "Towards Understanding the Role of Carbon Atoms on Transition Metal Surfaces: Implications for Catalysis"

Towards Understanding the Role of Carbon Atoms on Transition Metal Surfaces: Implications for Catalysis

Biel Martínez[a], Oriol Piqué[a], Hèctor Prats[a], Francesc Viñes[a]*, Francesc Illas[a]

[a] *Departament de Ciència de Materials i Química Física & Institut de Química Teòrica i Computacional de la Universitat de Barcelona (IQTCUB), c/ Martí i Franquès, 1-11, Barcelona, Spain.*

*Corresponding author: francesc.vines@ub.edu

S1. Kinetic Monte Carlo Algorithm; Implementation and Validation

The in-house kinetic Monte Carlo (*kMC*) code has been developed using Python3, the *random* library package for the generation of random numbers, the Mersenne Twister as core generator, and relying on the widely used rejection-free Variable Step Size Method (*VSSM*). First, the simulation stopping conditions are chosen, and the system is initialized by randomly populating an empty lattice with C atoms up to the desired θ_C. Note that, even though in real experiments the initially populated sites are on surface, subsurface sites are also populated in our initial configurations. By this choice, the system is forced to explore all the sites before reaching equilibrium and allows one to gain information about the dynamics of the processes both at surface and subsurface regions already in the first steps of the kMC simulation, as is exposed afterwards in the computational workflow. Then, a list of all available diffusion processes on the different lattice sites is obtained. Next, two random numbers between 0 and 1 are generated, τ_1 and τ_2. The first is used to calculate a time interval Δt when no process occurs according to a Poisson distribution, which is inversely proportional to the sum of the rate constants of all the processes in the list:

$$\Delta t = \frac{1}{\sum_n k_n} \ln\left(\frac{1}{\tau_1}\right) \qquad (1).$$

The second random number is used to select the process i from the list with probability $P_i = k_i / \sum_n k_n$. Finally, the new configuration of the system is updated according to the chosen process, and the loop starts again by creating the new list of available events until the stopping criteria is reached.

In order to validate our in-house developed kMC code, a full analysis of its performance on a set of testing simulations was carried out. We show here a few relevant cases, *a*) with all processes with equal rate constants, *b*) with sinking processes four times faster than other remaining processes, and *c*) with emerging processes four times faster than the other remaining processes. The expected equilibrium results for these three sets are finding 50% of C atoms at

the surface and 50% on subsurface sites in case *a*), finding four times more C on the subsurface than on the surface in case *b*), and finding four times more C on the surface than on the subsurface in case *c*). Moreover, we have ensured that our kMC results does not depend on the initial configuration by, for each of the aforementioned cases, initializing the system in three different ways; *i*) with all C atoms initially placed at the surface, *ii*) with all C atoms initially placed at the subsurface, and *iii*) with all C atoms initially placed randomly over both the surface and the subsurface. Satisfactorily, all the kMC results for these sets of tests match, in all cases, the expected results, see Figure S1, indicating the correct functioning of the kMC code. Note that the macroscopic properties reported in the present study have been calculated using a single kMC replica, after carefully checking that the results are completely independent of the initial random number or the initial positions of the C atoms, and that running multiple kMC replicas provide virtually the same result.

As exposed in the manuscript, in some cases multiplicative $\alpha < 1$ factors were applied to manually scale the rate constants of the fastest and quasi-equilibrated processes, considered as such those that occur more than 10^6 times more often than the others, and the same number of times in both forward and reverse directions. To this end, a first kMC simulation without manually scaling was performed to determine whether there was a dominant process requiring an α factor. If this was the case, a bench of simulations was carried out with $\log_{10}(\alpha)$ values ranging from -0.5 to -6.0. The optimal α is taken as the highest, this is, closest to unity, value that enables to see all the non-dominant, yet still feasible, processes at least 10^3 times for every 10^6 KMC steps.

The manually scaling may affect the calculated mean lifetimes of C atoms at surface or subsurface, and does increase the mean lifetime of C atoms at the particular site types involving the dominant process; lt_j where j = *hpc*, *fcc*, *tss*, and *oss* sites, see their definition in the manuscript. Therefore, for those systems where α factors were used, additional kMC simulations were carried out by setting all $\alpha = 1$ to extract the correct lt. From the kMC simulation with the optimal α, or from the initial simulation when no α is needed, the time required to reach the equilibrium were extracted. As different temperatures and coverages were to be studied, we chose in these initial simulations the case that would require a longest time to reach the equilibrium, being this at the lowest temperature and with the largest number of C atoms in the system. This is at 300 K, and, as shown in Table 1, 9 at% of C coverage.

S2. Guide for the Interpretation of Figure 6

Given the importance and the quantity of information condensed in Figure 6, we considered relevant to provide some hints to ease the interpretation of the shown results. Figure 6 illustrates how dynamic the studied systems at 300 and 700 K are. For each of them, we computed $\bar{t}_{em}^{fcc}$ and $\bar{t}_{em}^{hcp}$, and also the lifetime of a C atom at a particular region or a particular site type. We do not show the average waiting time between two consecutive sinking processes, $\bar{t}_{sin}$, since they are essentially the same as $\bar{t}_{em}$. Time is plotted in logarithmic scale, to enable the comparison of time scales between systems and temperatures, and those processes involving time scales larger than seconds are truncated there.

First of all, one can extract the time scale involving the interlayer exchange of C atoms by checking how large $\bar{t}_{em}^{fcc}$ and $\bar{t}_{em}^{hcp}$ are. Comparison between systems and the effect of temperature can also be made. For example, one can see that for Ir $\bar{t}_{em}$ values are extremely large, and that temperature does not ease enough the C exchange between layers. One can also compare for example with Au, for which sinking/emerging channels are expected to be much more active. Also, the dominant channel in the sinking/emerging processes can be extracted by comparing $\bar{t}_{em}^{fcc}$ and $\bar{t}_{em}^{hcp}$ of a given system.

The same logic applies to lt_{surf} and lt_{sub}, and the same kind of comparisons can be made with the grey bars of the upper part of the plots. The information provided by these lifetimes is how long a C atom will remain in the surface (subsurface) once the emerging (sinking) has occurred. For example, one can see that for Ir there is no C at subsurface at 300 K, and at 700 K the partial population only lasts nanoseconds. At the surface, however, the lifetimes are extremely large. Comparing with Au, one can state that its higher $\bar{t}_{em}$ produce lower lifetimes, yet C lasts less in subsurface than in surface, as for Ir. Up to now, just by analyzing the length of the corresponding bars for $\bar{t}_{em}$ and lt_r, one can figure out how often a C atom is expected to be emerging or sinking, and the time it will spend in the newly adopted region.

The last set of data is the lifetime split for each site, plotted inside of the bar for each layer and temperature. The analysis of the site lifetimes allows to ultimately picture the dynamics of the systems. This decomposition reveals whether C atoms remain stuck in a given site or they are free to move around the same-layer sites. One can extract this information by comparing the layer lifetime and their corresponding site lifetimes. An example for the stuck situation would be subsurface C at Au at 300 K, since lifetimes in *tss* sites are in the same order of magnitude than lt_{ssb}; whereas an example of highly free C would be surface C at Cu, where the lifetime at the surface sites is many orders of magnitude below lt_{surf}.

Putting altogether, one can easily gain very valuable information on the mobility of C atoms in the studied systems by analyzing its corresponding bar plot in Figure 6. By checking $\bar{t}_{em}^{fcc}$ and $\bar{t}_{em}^{hcp}$ can extract how often will the emerging and sinking processes occur. Moreover, by evaluating lt_{surf} and lt_{mi}, one can determine for how much time will the C atoms last in each layer. Finally, by considering the site lifetimes, one can figure out if these atoms will remain stuck or will be diffusing along the layer during the time they stay there.

Figure S1. Validation simulations carried out for the in-house developed kMC code. A total of $15 \cdot 10^4$ KMC steps were performed with different sets of rate constants; all of them equal (black), sinking rate constants four times larger (green) and emerging rate constants four times larger (gray). For each of these sets, three initial conditions were chosen: *a*) with all C atoms at the surface, *b*) with all C atoms at the subsurface, and *c*) with all C atoms placed randomly over both the surface and the subsurface. Only the first 3000 kMC steps are plotted here, yet the average values have been extracted from the last 10^5 steps of the simulations.

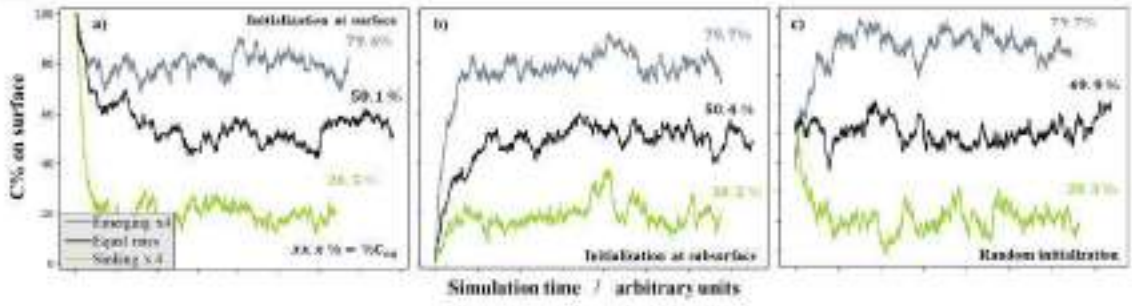

Table S1. Relative stability of a C atom referred to *hcp* on the different adsorption sites on (111) *fcc* transition metal surfaces.

site	Ag	Au	Cu	Ir	Ni	Pd	Pt	Rh
hcp	0.00	0.00	0.00	0.00	0.00	0.00	0.00	0.00
fcc	-0.07	-0.11	-0.04	0.23	0.03	0.02	-0.09	0.19
tss	0.22	0.14	0.45	1.66	0.60	-0.22	0.03	0.96
oss	-0.25	0.52	-0.46	1.35	-0.58	-0.71	0.45	0.22

Table S2. Percentage of C at surface and subsurface regions, and split in their respective *fcc*, *hcp*, *oss*, and *tss* sites, for **Ag**, for temperatures of 300, 400, 500, 600, and 700 K; and overall C coverages of 1, 3, 5, 7, and 9 at%.

Ag	T / K	% *fcc*	% *hcp*	% *oss*	% *tss*	% Sur	% Sub
1%	**300**	0.01	0.00	0.99	0.00	0.01	0.99
	400	0.01	0.01	0.99	0.00	0.02	0.99
	500	0.02	0.01	0.98	0.00	0.02	0.98
	600	0.03	0.01	0.96	0.00	0.04	0.96
	700	0.05	0.02	0.93	0.00	0.07	0.94
3%	**300**	0.00	0.01	0.99	0.00	0.01	0.99
	400	0.01	0.00	0.99	0.00	0.01	0.99
	500	0.02	0.01	0.98	0.00	0.02	0.98
	600	0.03	0.01	0.96	0.00	0.04	0.96
	700	0.05	0.02	0.93	0.00	0.07	0.94
5%	**300**	0.00	0.01	0.99	0.00	0.01	0.99
	400	0.01	0.00	0.99	0.00	0.01	0.99
	500	0.02	0.01	0.98	0.00	0.02	0.98
	600	0.03	0.01	0.96	0.00	0.04	0.96
	700	0.05	0.02	0.93	0.00	0.07	0.93
7%	**300**	0.01	0.00	0.99	0.00	0.01	0.99
	400	0.01	0.00	0.99	0.00	0.01	0.99
	500	0.02	0.01	0.98	0.00	0.02	0.98
	600	0.03	0.01	0.96	0.00	0.04	0.96
	700	0.05	0.02	0.93	0.00	0.07	0.93
9%	**300**	0.01	0.00	0.99	0.00	0.01	0.99
	400	0.01	0.00	0.99	0.00	0.01	0.99
	500	0.02	0.01	0.98	0.00	0.02	0.98
	600	0.03	0.01	0.96	0.00	0.04	0.96
	700	0.05	0.02	0.93	0.00	0.07	0.93

Table S3. Percentage of C at surface and subsurface regions, and split in their respective *fcc*, *hcp*, *oss*, and *tss* sites, for **Au**, for temperatures of 300, 400, 500, 600, and 700 K; and overall C coverages of 1, 3, 5, 7, and 9 at%.

Au	T / K	% *fcc*	% *hcp*	% *oss*	% *tss*	% Sur	% Sub
1%	**300**	0.98	0.02	0.00	0.01	1.00	0.01
	400	0.95	0.05	0.00	0.01	0.99	0.01
	500	0.92	0.08	0.00	0.01	0.99	0.01
	600	0.88	0.11	0.00	0.01	0.99	0.01
	700	0.84	0.14	0.00	0.02	0.98	0.02
3%	**300**	0.98	0.02	0.00	0.00	1.00	0.00
	400	0.95	0.05	0.00	0.00	1.00	0.00
	500	0.92	0.08	0.00	0.01	0.99	0.01
	600	0.88	0.11	0.00	0.01	0.99	0.01
	700	0.84	0.14	0.00	0.02	0.98	0.02
5%	**300**	0.98	0.02	0.00	0.00	1.00	0.00
	400	0.95	0.05	0.00	0.00	1.00	0.00
	500	0.91	0.08	0.00	0.01	0.99	0.01
	600	0.87	0.12	0.00	0.01	0.99	0.01
	700	0.84	0.15	0.00	0.02	0.98	0.02
7%	**300**	0.98	0.02	0.00	0.00	1.00	0.00
	400	0.95	0.05	0.00	0.01	1.00	0.01
	500	0.91	0.08	0.00	0.01	0.99	0.01
	600	0.87	0.12	0.00	0.01	0.99	0.01
	700	0.83	0.15	0.00	0.02	0.98	0.02
9%	**300**	0.98	0.02	0.00	0.00	1.00	0.00
	400	0.95	0.05	0.00	0.00	1.00	0.00
	500	0.91	0.09	0.00	0.01	0.99	0.01
	600	0.87	0.12	0.00	0.01	0.99	0.01
	700	0.83	0.16	0.00	0.02	0.98	0.02

Table S4. Percentage of C at surface and subsurface regions, and split in their respective *fcc*, *hcp*, *oss*, and *tss* sites, for **Cu**, for temperatures of 300, 400, 500, 600, and 700 K; and overall C coverages of 1, 3, 5, 7, and 9 at%.

Cu	T / K	% *fcc*	% *hcp*	% *oss*	% *tss*	% Sur	% Sub
1%	**300**	0.00	0.01	0.99	0.00	0.02	0.99
	400	0.00	0.00	1.00	0.00	0.00	1.00
	500	0.00	0.00	1.00	0.00	0.00	1.00
	600	0.00	0.00	0.99	0.01	0.00	1.00
	700	0.00	0.00	0.99	0.01	0.00	1.00
3%	**300**	0.00	0.01	0.99	0.00	0.01	0.99
	400	0.00	0.00	1.00	0.00	0.00	1.00
	500	0.00	0.00	0.99	0.01	0.00	1.00
	600	0.00	0.00	0.99	0.01	0.00	1.00
	700	0.00	0.00	0.99	0.01	0.00	1.00
5%	**300**	0.00	0.01	0.99	0.00	0.01	0.99
	400	0.00	0.00	1.00	0.00	0.00	1.00
	500	0.00	0.00	1.00	0.00	0.00	1.00
	600	0.00	0.00	0.99	0.01	0.00	1.00
	700	0.00	0.00	0.99	0.01	0.00	1.00
7%	**300**	0.00	0.01	0.99	0.00	0.01	0.99
	400	0.00	0.00	0.99	0.01	0.00	1.00
	500	0.00	0.00	1.00	0.00	0.00	1.00
	600	0.00	0.00	1.00	0.00	0.00	1.00
	700	0.00	0.00	1.00	0.00	0.00	1.00
9%	**300**	0.00	0.01	0.99	0.00	0.01	0.99
	400	0.00	0.00	1.00	0.00	0.00	1.00
	500	0.00	0.00	1.00	0.00	0.00	1.00
	600	0.00	0.00	1.00	0.00	0.00	1.00
	700	0.00	0.00	0.99	0.01	0.00	1.00

Table S5. Percentage of C at surface and subsurface regions, and split in their respective *fcc*, *hcp*, *oss*, and *tss* sites, for **Ir**, for temperatures of 300, 400, 500, 600, and 700 K; and overall C coverages of 1, 3, 5, 7, and 9 at%.

Ir	T / K	% *fcc*	% *hcp*	% *oss*	% *tss*	% Sur	% Sub
1%	**300**	0.01	0.99	0.00	0.00	1.00	0.00
	400	0.00	1.00	0.00	0.00	1.00	0.00
	500	0.01	0.99	0.00	0.00	1.00	0.00
	600	0.02	0.98	0.00	0.00	1.00	0.00
	700	0.03	0.97	0.00	0.00	1.00	0.00
3%	**300**	0.00	1.00	0.00	0.00	1.00	0.00
	400	0.01	0.99	0.00	0.00	1.00	0.00
	500	0.01	0.99	0.00	0.00	1.00	0.00
	600	0.02	0.98	0.00	0.00	1.00	0.00
	700	0.03	0.97	0.00	0.00	1.00	0.00
5%	**300**	0.01	0.99	0.00	0.00	1.00	0.00
	400	0.01	0.99	0.00	0.00	1.00	0.00
	500	0.01	0.99	0.00	0.00	1.00	0.00
	600	0.02	0.98	0.00	0.00	1.00	0.00
	700	0.03	0.97	0.00	0.00	1.00	0.00
7%	**300**	0.00	1.00	0.00	0.00	1.00	0.00
	400	0.01	0.99	0.00	0.00	1.00	0.00
	500	0.01	0.99	0.00	0.00	1.00	0.00
	600	0.02	0.98	0.00	0.00	1.00	0.00
	700	0.03	0.97	0.00	0.00	1.00	0.00
9%	**300**	0.01	0.99	0.00	0.00	1.00	0.00
	400	0.00	1.00	0.00	0.00	1.00	0.00
	500	0.01	0.99	0.00	0.00	1.00	0.00
	600	0.02	0.98	0.00	0.00	1.00	0.00
	700	0.03	0.97	0.00	0.00	1.00	0.00

Table S6. Percentage of C at surface and subsurface regions, and split in their respective *fcc*, *hcp*, *oss*, and *tss* sites, for **Ni**, for temperatures of 300, 400, 500, 600, and 700 K; and overall C coverages of 1, 3, 5, 7, and 9 at%.

Ni	T / K	% *fcc*	% *hcp*	% *oss*	% *tss*	% Sur	% Sub
1%	**300**	0.01	0.00	0.99	0.00	0.01	0.99
	400	0.01	0.00	0.99	0.00	0.01	0.99
	500	0.01	0.00	0.99	0.00	0.01	0.99
	600	0.00	0.01	0.99	0.00	0.01	0.99
	700	0.00	0.01	0.99	0.00	0.01	0.99
3%	**300**	0.00	0.01	0.99	0.00	0.01	0.99
	400	0.01	0.00	0.99	0.00	0.01	0.99
	500	0.00	0.01	0.99	0.00	0.01	0.99
	600	0.01	0.00	0.99	0.00	0.01	1.00
	700	0.00	0.00	1.00	0.00	0.00	1.00
5%	**300**	0.01	0.00	0.99	0.00	0.01	0.99
	400	0.01	0.00	0.99	0.00	0.01	0.99
	500	0.01	0.00	0.99	0.00	0.01	1.00
	600	0.00	0.01	1.00	0.00	0.01	1.00
	700	0.00	0.00	1.00	0.00	0.00	1.00
7%	**300**	0.01	0.00	0.99	0.00	0.01	0.99
	400	0.00	0.01	0.99	0.00	0.01	0.99
	500	0.01	0.00	0.99	0.00	0.01	0.99
	600	0.01	0.00	0.99	0.00	0.01	0.99
	700	0.00	0.01	1.00	0.00	0.01	1.00
9%	**300**	0.00	0.01	0.99	0.00	0.01	0.99
	400	0.01	0.00	0.99	0.00	0.01	0.99
	500	0.01	0.00	0.99	0.00	0.01	1.00
	600	0.00	0.01	1.00	0.00	0.01	1.00
	700	0.00	0.00	0.99	0.00	0.00	1.00

Table S7. Percentage of C at surface and subsurface regions, and split in their respective *fcc*, *hcp*, *oss*, and *tss* sites, for **Pd**, for temperatures of 300, 400, 500, 600, and 700 K; and overall C coverages of 1, 3, 5, 7, and 9 at%.

Pd	T / K	% *fcc*	% *hcp*	% *oss*	% *tss*	% Sur	% Sub
1%	**300**	0.00	0.00	1.00	0.00	0.00	1.00
	400	0.00	0.00	0.99	0.01	0.00	1.00
	500	0.00	0.00	0.99	0.01	0.00	1.00
	600	0.00	0.00	1.00	0.00	0.00	1.00
	700	0.00	0.00	1.00	0.00	0.00	1.00
3%	**300**	0.00	0.00	1.00	0.00	0.00	1.00
	400	0.00	0.00	0.99	0.01	0.00	1.00
	500	0.00	0.00	1.00	0.00	0.00	1.00
	600	0.00	0.00	0.99	0.01	0.00	1.00
	700	0.00	0.00	1.00	0.00	0.00	1.00
5%	**300**	0.00	0.00	0.99	0.01	0.00	1.00
	400	0.00	0.00	0.99	0.01	0.00	1.00
	500	0.00	0.00	0.99	0.01	0.00	1.00
	600	0.00	0.00	0.99	0.01	0.00	1.00
	700	0.00	0.00	0.99	0.01	0.00	1.00
7%	**300**	0.00	0.00	1.00	0.00	0.00	1.00
	400	0.00	0.00	0.99	0.01	0.00	1.00
	500	0.00	0.00	1.00	0.00	0.00	1.00
	600	0.00	0.00	0.99	0.01	0.00	1.00
	700	0.00	0.00	0.99	0.01	0.00	1.00
9%	**300**	0.00	0.00	0.99	0.01	0.00	1.00
	400	0.00	0.00	1.00	0.00	0.00	1.00
	500	0.00	0.00	1.00	0.00	0.00	1.00
	600	0.00	0.00	0.99	0.01	0.00	1.00
	700	0.00	0.00	1.00	0.00	0.00	1.00

Table S8. Percentage of C at surface and subsurface regions, and split in their respective *fcc*, *hcp*, *oss*, and *tss* sites, for **Pt**, for temperatures of 300, 400, 500, 600, and 700 K; and overall C coverages of 1, 3, 5, 7, and 9 at%.

Pt	T / K	% *fcc*	% *hcp*	% *oss*	% *tss*	% Sur	% Sub
1%	**300**	0.95	0.04	0.00	0.02	0.98	0.02
	400	0.89	0.07	0.00	0.04	0.96	0.04
	500	0.82	0.11	0.00	0.07	0.93	0.07
	600	0.77	0.14	0.00	0.10	0.91	0.10
	700	0.71	0.17	0.00	0.12	0.88	0.12
3%	**300**	0.95	0.03	0.00	0.02	0.98	0.02
	400	0.89	0.07	0.00	0.04	0.96	0.04
	500	0.82	0.11	0.00	0.07	0.93	0.07
	600	0.76	0.14	0.00	0.10	0.90	0.10
	700	0.71	0.17	0.00	0.12	0.88	0.12
5%	**300**	0.95	0.04	0.00	0.02	0.98	0.02
	400	0.88	0.07	0.00	0.04	0.96	0.04
	500	0.82	0.11	0.00	0.07	0.93	0.07
	600	0.76	0.14	0.00	0.10	0.90	0.10
	700	0.71	0.17	0.00	0.12	0.88	0.12
7%	**300**	0.94	0.04	0.00	0.02	0.98	0.02
	400	0.88	0.08	0.00	0.04	0.96	0.04
	500	0.81	0.12	0.00	0.07	0.93	0.07
	600	0.75	0.15	0.00	0.10	0.90	0.10
	700	0.70	0.17	0.00	0.12	0.87	0.13
9%	**300**	0.94	0.04	0.00	0.02	0.98	0.02
	400	0.88	0.08	0.00	0.05	0.96	0.05
	500	0.81	0.12	0.00	0.08	0.93	0.08
	600	0.75	0.15	0.00	0.10	0.90	0.10
	700	0.70	0.18	0.00	0.13	0.87	0.13

Table S9. Percentage of C at surface and subsurface regions, and split in their respective *fcc*, *hcp*, *oss*, and *tss* sites, for **Rh**, for temperatures of 300, 400, 500, 600, and 700 K; and overall C coverages of 1, 3, 5, 7, and 9 at%.

Rh	T / K	% *fcc*	% *hcp*	% *oss*	% *tss*	% Sur	% Sub
1%	**300**	0.00	1.00	0.00	0.00	1.00	0.00
	400	0.01	0.99	0.00	0.00	1.00	0.00
	500	0.02	0.98	0.01	0.00	0.99	0.01
	600	0.03	0.96	0.02	0.00	0.98	0.02
	700	0.04	0.93	0.03	0.00	0.97	0.03
3%	**300**	0.01	0.99	0.00	0.00	1.00	0.00
	400	0.01	0.99	0.00	0.00	1.00	0.00
	500	0.02	0.98	0.01	0.00	0.99	0.01
	600	0.03	0.96	0.02	0.00	0.98	0.02
	700	0.04	0.93	0.03	0.00	0.97	0.03
5%	**300**	0.00	1.00	0.00	0.00	1.00	0.00
	400	0.01	0.99	0.00	0.00	1.00	0.00
	500	0.02	0.98	0.01	0.00	0.99	0.01
	600	0.03	0.96	0.02	0.00	0.98	0.02
	700	0.05	0.93	0.03	0.00	0.97	0.03
7%	**300**	0.00	1.00	0.00	0.00	1.00	0.00
	400	0.01	0.99	0.00	0.00	1.00	0.00
	500	0.02	0.98	0.01	0.00	0.99	0.01
	600	0.03	0.95	0.02	0.00	0.98	0.02
	700	0.05	0.92	0.03	0.00	0.97	0.03
9%	**300**	0.01	0.99	0.00	0.00	1.00	0.00
	400	0.01	0.99	0.00	0.00	1.00	0.00
	500	0.02	0.98	0.01	0.00	0.99	0.01
	600	0.03	0.95	0.02	0.00	0.98	0.02
	700	0.05	0.92	0.03	0.00	0.97	0.03

Table S10. Time frequencies for an emerging process to happen through an *fcc* ($\bar{t}_{em}^{fcc}$) or an *hcp* site ($\bar{t}_{em}^{hcp}$), in s·Å^{-2}; plus mean lifetime of the C atom on surface, lt_{surf}, or in subsurface, lt_{sub}, as well as at each *fcc*, *hcp*, *oss*, or *tss* site, in units of seconds, for **Ag** at 300, 400, 500, 600, and 700 K, with a global C coverage of 1, 3, 5, 7, and 9 at%.

C	T / K	$\bar{t}_{em}^{fcc}$	$\bar{t}_{em}^{hcp}$	lt_{surf}^{fcc}	lt_{surf}^{hcp}	lt_{sub}^{fcc}	lt_{sub}^{hcp}	lt_{surf}	lt_{sub}
1%	**300**	-	8.30E-02	6.94E-11	6.82E-12	3.53E-06	6.69E-14	6.78E-05	8.62E-02
	400	2.26E-02	4.05E-04	1.43E-11	2.51E-12	4.81E-08	7.81E-14	1.34E-05	3.00E-03
	500	4.51E-04	1.53E-05	5.82E-12	1.45E-12	3.84E-09	8.91E-14	5.20E-06	4.02E-04
	600	3.07E-05	1.87E-06	3.31E-12	1.03E-12	7.41E-10	1.00E-13	2.82E-06	1.09E-04
	700	4.64E-06	4.18E-07	2.26E-12	8.31E-13	2.33E-10	1.12E-13	1.85E-06	4.12E-05
3%	**300**	-	5.55E-02	4.53E-11	4.46E-12	2.29E-06	4.60E-14	4.44E-05	5.19E-02
	400	4.65E-02	2.63E-04	9.34E-12	1.64E-12	3.15E-08	5.29E-14	8.73E-06	2.06E-03
	500	2.66E-04	9.76E-06	3.81E-12	9.45E-13	2.52E-09	6.09E-14	3.40E-06	2.64E-04
	600	2.05E-05	1.18E-06	2.16E-12	6.75E-13	4.85E-10	6.86E-14	1.85E-06	6.68E-05
	700	2.90E-06	2.73E-07	1.48E-12	5.43E-13	1.53E-10	7.61E-14	1.21E-06	2.66E-05
5%	**300**	3.46E+00	6.52E-02	4.24E-11	4.17E-12	2.18E-06	4.45E-14	4.15E-05	5.13E-02
	400	8.82E-03	2.48E-04	8.75E-12	1.54E-12	2.96E-08	5.16E-14	8.17E-06	1.96E-03
	500	2.50E-04	8.83E-06	3.57E-12	8.86E-13	2.37E-09	5.92E-14	3.22E-06	2.27E-04
	600	1.83E-05	1.05E-06	2.03E-12	6.34E-13	4.54E-10	6.68E-14	1.75E-06	5.99E-05
	700	2.71E-06	2.39E-07	1.39E-12	5.10E-13	1.43E-10	7.41E-14	1.15E-06	2.39E-05
7%	**300**	-	9.15E-02	5.40E-11	5.29E-12	2.73E-06	5.86E-14	5.23E-05	8.83E-02
	400	2.46E-02	2.90E-04	1.11E-11	1.95E-12	3.75E-08	6.88E-14	1.05E-05	2.18E-03
	500	3.20E-04	1.09E-05	4.53E-12	1.13E-12	3.02E-09	7.90E-14	4.10E-06	2.80E-04
	600	2.07E-05	1.28E-06	2.57E-12	8.08E-13	5.79E-10	8.91E-14	2.24E-06	7.23E-05
	700	3.40E-06	2.97E-07	1.76E-12	6.50E-13	1.82E-10	9.85E-14	1.46E-06	2.94E-05
9%	**300**	-	7.78E-02	4.19E-11	4.12E-12	2.11E-06	4.80E-14	4.07E-05	6.59E-02
	400	9.58E-03	2.21E-04	8.66E-12	1.52E-12	2.92E-08	5.65E-14	8.15E-06	1.70E-03
	500	2.69E-04	7.93E-06	3.53E-12	8.75E-13	2.34E-09	6.48E-14	3.20E-06	2.16E-04
	600	1.68E-05	9.52E-07	2.00E-12	6.28E-13	4.49E-10	7.18E-14	1.75E-06	5.55E-05
	700	2.82E-06	2.23E-07	1.37E-12	5.06E-13	1.42E-10	7.94E-14	1.14E-06	2.28E-05

Table S11. Time frequencies for an emerging process to happen through an *fcc* ($\bar{t}_{em}^{fcc}$) or an *hcp* site ($\bar{t}_{em}^{hcp}$), in s·Å^{-2}; plus mean lifetime of the C atom on surface, lt_{surf}, or in subsurface, lt_{sub}, as well as at each *fcc*, *hcp*, *oss*, or *tss* site, in units of seconds, for **Au** at 300, 400, 500, 600, and 700 K, with a global C coverage of 1, 3, 5, 7, and 9 at%.

C	T / K	$\bar{t}_{em}^{fcc}$	$\bar{t}_{em}^{hcp}$	lt_{surf}^{fcc}	lt_{surf}^{hcp}	lt_{sub}^{fcc}	lt_{sub}^{hcp}	lt_{surf}	lt_{sub}
1%	**300**	4.32E-01	4.36E-07	7.12E-07	9.08E-11	2.48E-15	4.07E-13	6.32E-03	5.86E-13
	400	5.30E-04	1.05E-08	3.92E-09	5.97E-12	1.40E-15	1.07E-13	1.44E-04	1.68E-12
	500	4.81E-06	1.11E-09	1.68E-10	1.12E-12	1.15E-15	4.71E-14	1.39E-05	6.36E-12
	600	2.89E-07	2.57E-10	2.07E-11	3.51E-13	1.02E-15	2.68E-14	2.86E-06	1.45E-11
	700	3.61E-08	9.09E-11	4.61E-12	1.50E-13	9.13E-16	1.78E-14	8.92E-07	2.62E-11
3%	**300**	2.69E-01	2.72E-07	4.60E-07	5.94E-11	1.14E-15	2.66E-13	3.94E-03	3.75E-13
	400	1.90E-04	6.52E-09	2.54E-09	3.90E-12	9.73E-16	7.01E-14	8.93E-05	1.23E-12
	500	3.42E-06	7.10E-10	1.11E-10	7.30E-13	7.77E-16	3.07E-14	8.89E-06	4.24E-12
	600	1.81E-07	1.62E-10	1.36E-11	2.31E-13	6.72E-16	1.76E-14	1.81E-06	9.97E-12
	700	2.40E-08	5.78E-11	3.03E-12	9.87E-14	6.03E-16	1.17E-14	5.68E-07	1.76E-11
5%	**300**	-	2.48E-07	4.41E-07	5.57E-11	1.14E-15	2.49E-13	3.59E-03	3.41E-13
	400	2.22E-04	5.97E-09	2.40E-09	3.67E-12	8.95E-16	6.54E-14	8.19E-05	1.14E-12
	500	2.92E-06	6.47E-10	1.05E-10	6.87E-13	7.14E-16	2.88E-14	8.11E-06	4.02E-12
	600	1.61E-07	1.49E-10	1.28E-11	2.17E-13	6.38E-16	1.65E-14	1.66E-06	9.33E-12
	700	2.27E-08	5.29E-11	2.84E-12	9.33E-14	5.67E-16	1.10E-14	5.21E-07	1.64E-11
7%	**300**	1.43E-01	2.89E-07	5.50E-07	7.07E-11	1.87E-15	3.17E-13	4.18E-03	4.99E-13
	400	2.67E-04	7.17E-09	3.02E-09	4.65E-12	1.10E-15	8.32E-14	9.82E-05	1.36E-12
	500	3.78E-06	7.89E-10	1.33E-10	8.74E-13	9.10E-16	3.67E-14	9.88E-06	5.04E-12
	600	2.12E-07	1.83E-10	1.63E-11	2.78E-13	7.92E-16	2.12E-14	2.04E-06	1.18E-11
	700	2.82E-08	6.58E-11	3.65E-12	1.19E-13	7.25E-16	1.41E-14	6.49E-07	2.13E-11
9%	**300**	2.23E-01	2.24E-07	4.33E-07	5.50E-11	1.03E-15	2.54E-13	3.25E-03	3.51E-13
	400	2.06E-04	5.32E-09	2.34E-09	3.62E-12	8.80E-16	6.50E-14	7.28E-05	1.10E-12
	500	3.03E-06	5.87E-10	1.03E-10	6.83E-13	7.13E-16	2.87E-14	7.35E-06	3.99E-12
	600	1.66E-07	1.38E-10	1.28E-11	2.17E-13	6.29E-16	1.66E-14	1.55E-06	9.45E-12
	700	2.25E-08	4.97E-11	2.86E-12	9.34E-14	5.69E-16	1.10E-14	4.90E-07	1.71E-11

Table S12. Time frequencies for an emerging process to happen through an *fcc* ($\bar{t}_{em}^{fcc}$) or an *hcp* site ($\bar{t}_{em}^{hcp}$), in s·Å^{-2}; plus mean lifetime of the C atom on surface, lt_{surf}, or in subsurface, lt_{sub}, as well as at each *fcc*, *hcp*, *oss*, or *tss* site, in units of seconds, for **Cu** at 300, 400, 500, 600, and 700 K, with a global C coverage of 1, 3, 5, 7, and 9 at%.

C	T / K	$\bar{t}_{em}^{fcc}$	$\bar{t}_{em}^{hcp}$	lt_{surf}^{fcc}	lt_{surf}^{hcp}	lt_{sub}^{fcc}	lt_{sub}^{hcp}	lt_{surf}	lt_{sub}
1%	**300**	2.64E+06	1.89E+04	1.94E-14	6.12E-15	5.44E+00	0.00E+00	1.89E-08	1.54E+05
	400	5.67E+01	1.68E+00	1.58E-14	6.66E-15	1.08E-03	6.41E-15	5.01E-09	7.15E+02
	500	1.09E-01	6.71E-03	1.47E-14	7.37E-15	6.82E-06	7.08E-15	5.05E-10	6.28E+00
	600	1.79E-03	1.73E-04	1.45E-14	8.10E-15	2.40E-07	7.70E-15	1.73E-10	2.23E-01
	700	9.73E-05	1.30E-05	1.46E-14	8.91E-15	2.25E-08	8.33E-15	1.84E-10	2.06E-02
3%	**300**	1.74E+06	1.22E+04	1.28E-14	4.07E-15	3.54E+00	0.00E+00	1.24E-08	1.01E+05
	400	3.60E+01	1.04E+00	1.04E-14	4.41E-15	7.06E-04	4.37E-15	3.37E-09	4.62E+02
	500	7.18E-02	4.14E-03	9.71E-15	4.87E-15	4.46E-06	4.82E-15	3.50E-10	4.09E+00
	600	1.17E-03	1.08E-04	9.48E-15	5.33E-15	1.57E-07	5.23E-15	1.16E-10	1.45E-01
	700	6.42E-05	8.13E-06	9.57E-15	5.81E-15	1.47E-08	5.66E-15	1.19E-10	1.34E-02
5%	**300**	4.42E+05	1.01E+04	1.20E-14	3.86E-15	3.32E+00	0.00E+00	1.17E-08	7.74E+04
	400	3.24E+01	9.37E-01	9.83E-15	4.19E-15	6.63E-04	4.31E-15	3.30E-09	4.26E+02
	500	6.64E-02	3.76E-03	9.16E-15	4.64E-15	4.17E-06	4.70E-15	3.37E-10	3.81E+00
	600	1.08E-03	9.72E-05	8.94E-15	5.06E-15	1.47E-07	5.11E-15	1.13E-10	1.36E-01
	700	5.95E-05	7.30E-06	8.96E-15	5.46E-15	1.38E-08	5.52E-15	1.13E-10	1.25E-02
7%	**300**	8.30E+05	1.28E+04	1.54E-14	5.01E-15	4.28E+00	4.02E-17	1.50E-08	9.69E+04
	400	4.10E+01	1.15E+00	1.25E-14	5.40E-15	8.42E-04	5.67E-15	4.28E-09	5.35E+02
	500	8.35E-02	4.51E-03	1.17E-14	5.94E-15	5.30E-06	6.24E-15	4.52E-10	4.82E+00
	600	1.39E-03	1.17E-04	1.13E-14	6.32E-15	1.87E-07	6.76E-15	1.44E-10	1.72E-01
	700	7.59E-05	8.86E-06	1.14E-14	6.93E-15	1.75E-08	7.31E-15	1.43E-10	1.59E-02
9%	**300**	1.00E+06	9.80E+03	1.20E-14	3.92E-15	3.26E+00	0.00E+00	1.17E-08	7.78E+04
	400	3.47E+01	8.46E-01	9.84E-15	4.26E-15	6.53E-04	4.67E-15	3.48E-09	4.07E+02
	500	6.53E-02	3.37E-03	9.13E-15	4.67E-15	4.12E-06	5.07E-15	3.63E-10	3.74E+00
	600	1.07E-03	8.62E-05	8.85E-15	4.99E-15	1.45E-07	5.51E-15	1.14E-10	1.33E-01
	700	5.77E-05	6.60E-06	8.87E-15	5.39E-15	1.36E-08	5.93E-15	1.14E-10	1.23E-02

Table S13. Time frequencies for an emerging process to happen through an *fcc* ($\bar{t}_{em}^{fcc}$) or an *hcp* site ($\bar{t}_{em}^{hcp}$), in s·Å^{-2}; plus mean lifetime of the C atom on surface, lt_{surf}, or in subsurface, lt_{sub}, as well as at each *fcc*, *hcp*, *oss*, or *tss* site, in units of seconds, for **Ir** at 300, 400, 500, 600, and 700 K, with a global C coverage of 1, 3, 5, 7, and 9 at%.

C	T / K	$\bar{t}_{em}^{fcc}$	$\bar{t}_{em}^{hcp}$	lt_{surf}^{fcc}	lt_{surf}^{hcp}	lt_{sub}^{fcc}	lt_{sub}^{hcp}	lt_{surf}	lt_{sub}
1%	300	-	-	3.39E-02	2.43E+02	-	-	-	-
	400	-	-	1.89E-04	1.46E-01	-	-	-	-
	500	-	-	8.72E-06	1.78E-03	-	-	-	-
	600	2.85E+03	7.13E+02	1.15E-06	9.63E-05	1.09E-09	1.73E-13	1.08E+01	2.19E-09
	700	1.23E+02	5.79E+00	2.77E-07	1.23E-05	1.87E-10	9.85E-14	3.69E-01	1.68E-09
3%	300	-	-	2.31E-02	1.59E+02	-	-	-	-
	400	-	-	1.29E-04	9.56E-02	-	-	-	-
	500	-	-	5.93E-06	1.16E-03	-	-	-	-
	600	-	6.23E+02	7.81E-07	6.30E-05	-	1.06E-13	1.13E+01	-
	700	4.81E+01	3.51E+00	1.88E-07	8.04E-06	1.36E-10	7.05E-14	2.43E-01	1.63E-09
5%	300	-	-	2.26E-02	1.49E+02	-	-	-	-
	400	-	-	1.26E-04	8.95E-02	-	-	-	-
	500	-	-	5.81E-06	1.09E-03	-	-	-	-
	600	-	5.00E+02	7.66E-07	5.91E-05	-	5.07E-14	9.21E+00	-
	700	2.66E+01	4.08E+00	1.84E-07	7.55E-06	6.59E-11	6.06E-14	2.43E-01	1.19E-09
7%	300	-	-	2.99E-02	1.89E+02	-	-	-	-
	400	-	-	1.67E-04	1.14E-01	-	-	-	-
	500	-	-	7.70E-06	1.38E-03	-	-	-	-
	600	4.45E+03	3.71E+02	1.02E-06	7.51E-05	2.27E-09	1.09E-13	6.79E+00	2.27E-09
	700	6.40E+01	4.46E+00	2.44E-07	9.59E-06	2.12E-10	8.33E-14	3.14E-01	2.54E-09
9%	300	-	-	2.44E-02	1.47E+02	-	-	-	-
	400	-	-	1.36E-04	8.85E-02	-	-	-	-
	500	-	-	6.29E-06	1.08E-03	-	-	-	-
	600	-	5.79E+02	8.31E-07	5.86E-05	-	6.92E-14	1.06E+01	-
	700	2.99E+01	2.91E+00	2.00E-07	7.46E-06	1.04E-10	7.59E-14	2.44E-01	1.87E-09

Table S14. Time frequencies for an emerging process to happen through an *fcc* ($\bar{t}_{em}^{fcc}$) or an *hcp* site ($\bar{t}_{em}^{hcp}$), in s·Å^{-2}; plus mean lifetime of the C atom on surface, lt_{surf}, or in subsurface, lt_{sub}, as well as at each *fcc*, *hcp*, *oss*, or *tss* site, in units of seconds, for **Ni** at 300, 400, 500, 600, and 700 K, with a global C coverage of 1, 3, 5, 7, and 9 at%.

C	T / K	$\bar{t}_{em}^{fcc}$	$\bar{t}_{em}^{hcp}$	lt_{surf}^{fcc}	lt_{surf}^{hcp}	lt_{sub}^{fcc}	lt_{sub}^{hcp}	lt_{surf}	lt_{sub}
1%	**300**	-	6.59E+08	5.61E-10	1.78E-09	3.46E+05	0.00E+00	5.84E-04	9.83E+08
	400	8.91E+05	3.76E+03	3.72E-11	8.88E-11	4.57E+00	0.00E+00	3.61E-05	1.29E+05
	500	3.84E+02	3.24E+00	7.70E-12	1.54E-11	5.73E-03	8.52E-15	6.64E-06	7.24E+02
	600	1.83E+00	3.12E-02	2.78E-12	4.98E-12	6.86E-05	9.43E-15	1.88E-06	2.02E+01
	700	3.82E-02	1.13E-03	1.38E-12	2.27E-12	2.98E-06	1.02E-14	6.71E-07	1.37E+00
3%	**300**	-	2.37E+08	3.72E-10	1.17E-09	2.17E+05	0.00E+00	3.90E-04	3.09E+08
	400	1.28E+06	2.24E+03	2.44E-11	5.81E-11	2.96E+00	0.00E+00	2.37E-05	7.96E+04
	500	2.92E+02	2.00E+00	5.03E-12	1.01E-11	3.72E-03	5.83E-15	4.37E-06	4.47E+02
	600	1.19E+00	1.95E-02	1.82E-12	3.26E-12	4.46E-05	6.40E-15	1.24E-06	1.28E+01
	700	2.40E-02	7.19E-04	9.02E-13	1.48E-12	1.94E-06	6.93E-15	4.45E-07	8.75E-01
5%	**300**	-	3.05E+08	3.56E-10	1.10E-09	2.11E+05	0.00E+00	3.72E-04	3.98E+08
	400	8.85E+05	2.03E+03	2.28E-11	5.43E-11	2.77E+00	0.00E+00	2.22E-05	7.33E+04
	500	2.67E+02	1.83E+00	4.71E-12	9.47E-12	3.49E-03	5.71E-15	4.11E-06	4.09E+02
	600	1.13E+00	1.74E-02	1.71E-12	3.05E-12	4.20E-05	6.22E-15	1.18E-06	1.16E+01
	700	2.30E-02	6.47E-04	8.46E-13	1.39E-12	1.83E-06	6.73E-15	4.27E-07	8.00E-01
7%	**300**	-	3.28E+08	4.57E-10	1.41E-09	2.60E+05	0.00E+00	4.80E-04	3.95E+08
	400	2.11E+06	2.52E+03	2.91E-11	6.91E-11	3.60E+00	0.00E+00	2.84E-05	8.76E+04
	500	3.30E+02	2.21E+00	5.99E-12	1.20E-11	4.45E-03	7.46E-15	5.25E-06	4.99E+02
	600	1.34E+00	2.13E-02	2.17E-12	3.87E-12	5.31E-05	8.22E-15	1.51E-06	1.44E+01
	700	3.04E-02	7.83E-04	1.07E-12	1.76E-12	2.32E-06	8.92E-15	5.54E-07	9.86E-01
9%	**300**	-	2.19E+08	3.61E-10	1.10E-09	1.98E+05	0.00E+00	3.75E-04	3.27E+08
	400	1.48E+06	1.86E+03	2.27E-11	5.39E-11	2.74E+00	1.50E-17	2.22E-05	6.12E+04
	500	3.41E+02	1.66E+00	4.65E-12	9.34E-12	3.45E-03	6.16E-15	4.10E-06	3.74E+02
	600	1.10E+00	1.57E-02	1.69E-12	3.01E-12	4.14E-05	6.67E-15	1.20E-06	1.07E+01
	700	2.35E-02	5.83E-04	8.36E-13	1.37E-12	1.80E-06	7.23E-15	4.36E-07	7.51E-01

Table S15. Time frequencies for an emerging process to happen through an *fcc* ($\bar{t}_{em}^{fcc}$) or an *hcp* site ($\bar{t}_{em}^{hcp}$), in s·Å^{-2}; plus mean lifetime of the C atom on surface, lt_{surf}, or in subsurface, lt_{sub}, as well as at each *fcc*, *hcp*, *oss*, or *tss* site, in units of seconds, for **Pd** at 300, 400, 500, 600, and 700 K, with a global C coverage of 1, 3, 5, 7, and 9 at%.

C	T / K	$\bar{t}_{em}^{fcc}$	$\bar{t}_{em}^{hcp}$	lt_{surf}^{fcc}	lt_{surf}^{hcp}	lt_{sub}^{fcc}	lt_{sub}^{hcp}	lt_{surf}	lt_{sub}
1%	**300**	1.95E+06	3.81E+03	1.44E-08	5.39E-11	9.63E-02	3.92E-10	4.31E-08	9.62E+04
	400	8.61E+00	1.61E-01	7.70E-11	2.32E-12	1.55E-05	7.90E-12	8.55E-09	1.54E+01
	500	1.02E-02	3.73E-04	7.02E-12	3.45E-13	8.11E-08	7.45E-13	3.47E-09	8.01E-02
	600	1.02E-04	6.51E-06	1.17E-12	9.72E-14	2.42E-09	1.53E-13	1.77E-09	2.37E-03
	700	3.83E-06	3.57E-07	3.06E-13	3.88E-14	1.95E-10	4.87E-14	1.02E-09	1.89E-04
3%	**300**	5.46E+05	2.55E+03	3.73E-09	3.40E-11	6.29E-02	2.67E-10	2.62E-08	6.28E+04
	400	5.69E+00	1.03E-01	6.78E-11	1.53E-12	1.02E-05	5.38E-12	7.39E-09	1.01E+01
	500	6.62E-03	2.36E-04	4.72E-12	2.25E-13	5.30E-08	5.06E-13	2.34E-09	5.23E-02
	600	6.89E-05	4.11E-06	7.70E-13	6.39E-14	1.58E-09	1.04E-13	1.12E-09	1.54E-03
	700	2.50E-06	2.26E-07	2.00E-13	2.54E-14	1.28E-10	3.32E-14	6.75E-10	1.24E-04
5%	**300**	3.59E+05	2.15E+03	2.32E-09	3.27E-11	5.92E-02	2.61E-10	2.32E-08	5.91E+04
	400	5.43E+00	9.13E-02	7.39E-11	1.39E-12	9.53E-06	5.26E-12	7.83E-09	9.47E+00
	500	6.00E-03	2.11E-04	4.26E-12	2.11E-13	4.97E-08	4.97E-13	2.17E-09	4.89E-02
	600	5.97E-05	3.66E-06	7.26E-13	5.86E-14	1.48E-09	1.01E-13	1.14E-09	1.45E-03
	700	2.31E-06	2.01E-07	1.99E-13	2.38E-14	1.20E-10	3.24E-14	6.79E-10	1.16E-04
7%	**300**	5.05E+05	2.68E+03	9.28E-09	4.06E-11	7.49E-02	3.45E-10	8.36E-08	7.48E+04
	400	8.12E+00	1.12E-01	8.26E-11	1.79E-12	1.21E-05	6.97E-12	7.52E-09	1.20E+01
	500	6.96E-03	2.58E-04	5.66E-12	2.68E-13	6.31E-08	6.57E-13	3.15E-09	6.21E-02
	600	7.74E-05	4.50E-06	1.00E-12	7.61E-14	1.88E-09	1.34E-13	1.57E-09	1.84E-03
	700	2.89E-06	2.44E-07	2.68E-13	3.03E-14	1.52E-10	4.29E-14	9.39E-10	1.47E-04
9%	**300**	8.85E+05	1.93E+03	3.37E-09	3.24E-11	5.83E-02	2.81E-10	1.35E-08	5.82E+04
	400	7.18E+00	8.01E-02	1.27E-10	1.39E-12	9.39E-06	5.68E-12	1.01E-08	9.32E+00
	500	6.07E-03	1.89E-04	4.45E-12	2.12E-13	4.90E-08	5.33E-13	2.22E-09	4.82E-02
	600	6.17E-05	3.30E-06	7.64E-13	5.91E-14	1.46E-09	1.10E-13	1.15E-09	1.42E-03
	700	2.16E-06	1.81E-07	2.00E-13	2.36E-14	1.18E-10	3.52E-14	7.17E-10	1.14E-04

Table S16. Time frequencies for an emerging process to happen through an *fcc* ($\bar{t}_{em}^{fcc}$) or an *hcp* site ($\bar{t}_{em}^{hcp}$), in s·Å^{-2}; plus mean lifetime of the C atom on surface, lt_{surf}, or in subsurface, lt_{sub}, as well as at each *fcc*, *hcp*, *oss*, or *tss* site, in units of seconds, for **Pt** at 300, 400, 500, 600, and 700 K, with a global C coverage of 1, 3, 5, 7, and 9 at%.

C	T / K	$\bar{t}_{em}^{fcc}$	$\bar{t}_{em}^{hcp}$	lt_{surf}^{fcc}	lt_{surf}^{hcp}	lt_{sub}^{fcc}	lt_{sub}^{hcp}	lt_{surf}	lt_{sub}
1%	**300**	-	1.06E-05	3.23E-03	5.84E-09	2.90E-11	2.69E-09	1.93E+01	3.74E-08
	400	3.60E-01	7.14E-08	1.19E-06	7.86E-11	1.08E-12	4.40E-11	9.38E-02	2.70E-08
	500	7.58E-04	3.39E-09	1.05E-08	5.82E-12	1.51E-13	3.67E-12	2.87E-03	1.66E-08
	600	1.44E-05	4.63E-10	4.40E-10	1.02E-12	4.06E-14	6.98E-13	1.98E-04	8.57E-09
	700	7.73E-07	1.12E-10	4.56E-11	2.89E-13	1.58E-14	2.10E-13	2.44E-05	4.44E-09
3%	**300**	-	6.49E-06	2.10E-03	3.85E-09	1.82E-11	1.80E-09	1.17E+01	2.46E-08
	400	3.20E-01	4.83E-08	7.93E-07	5.14E-11	7.03E-13	2.89E-11	6.01E-02	1.78E-08
	500	5.27E-04	2.22E-09	6.87E-09	3.82E-12	9.94E-14	2.42E-12	1.84E-03	1.11E-08
	600	8.82E-06	2.99E-10	2.89E-10	6.67E-13	2.68E-14	4.57E-13	1.28E-04	5.73E-09
	700	4.94E-07	7.28E-11	3.00E-11	1.90E-13	1.04E-14	1.38E-13	1.58E-05	2.97E-09
5%	**300**	-	8.09E-06	1.99E-03	3.58E-09	1.68E-11	1.65E-09	1.07E+01	2.24E-08
	400	1.89E-01	4.24E-08	7.38E-07	4.81E-11	6.58E-13	2.70E-11	5.45E-02	1.64E-08
	500	4.85E-04	2.03E-09	6.45E-09	3.59E-12	9.35E-14	2.27E-12	1.69E-03	1.06E-08
	600	8.03E-06	2.81E-10	2.73E-10	6.28E-13	2.51E-14	4.31E-13	1.19E-04	5.48E-09
	700	4.62E-07	6.69E-11	2.82E-11	1.79E-13	9.83E-15	1.30E-13	1.47E-05	2.85E-09
7%	**300**	-	9.30E-06	2.47E-03	4.54E-09	2.20E-11	2.09E-09	1.29E+01	3.17E-08
	400	4.26E-01	4.86E-08	9.46E-07	6.16E-11	8.45E-13	3.47E-11	6.72E-02	2.13E-08
	500	6.80E-04	2.56E-09	8.24E-09	4.59E-12	1.19E-13	2.92E-12	2.11E-03	1.36E-08
	600	1.05E-05	3.47E-10	3.48E-10	8.02E-13	3.20E-14	5.51E-13	1.48E-04	7.11E-09
	700	5.94E-07	8.51E-11	3.61E-11	2.29E-13	1.25E-14	1.67E-13	1.86E-05	3.70E-09
9%	**300**	-	5.98E-06	1.99E-03	3.53E-09	1.71E-11	1.63E-09	1.00E+01	2.32E-08
	400	3.21E-01	4.54E-08	7.39E-07	4.76E-11	6.70E-13	2.67E-11	5.05E-02	1.72E-08
	500	5.49E-04	1.95E-09	6.45E-09	3.57E-12	9.28E-14	2.27E-12	1.60E-03	1.08E-08
	600	8.33E-06	2.65E-10	2.73E-10	6.27E-13	2.51E-14	4.33E-13	1.14E-04	5.67E-09
	700	4.79E-07	6.56E-11	2.83E-11	1.79E-13	9.81E-15	1.30E-13	1.44E-05	2.94E-09

Table S17. Time frequencies for an emerging process to happen through an *fcc* ($\bar{t}_{em}^{fcc}$) or an *hcp* site ($\bar{t}_{em}^{hcp}$), in s·Å^{-2}; plus mean lifetime of the C atom on surface, lt_{surf}, or in subsurface, lt_{sub}, as well as at each *fcc*, *hcp*, *oss*, or *tss* site, in units of seconds, for **Rh** at 300, 400, 500, 600, and 700 K, with a global C coverage of 1, 3, 5, 7, and 9 at%.

C	T / K	$\bar{t}_{em}^{fcc}$	$\bar{t}_{em}^{hcp}$	lt_{surf}^{fcc}	lt_{surf}^{hcp}	lt_{sub}^{fcc}	lt_{sub}^{hcp}	lt_{surf}	lt_{sub}
1%	**300**	2.25E+07	6.31E+06	3.36E-06	5.12E-03	1.72E+01	0.00E+00	8.33E+01	1.07E+03
	400	3.09E+02	1.04E+02	2.09E-08	5.06E-06	1.78E-03	6.08E-13	2.20E-02	8.76E+00
	500	4.17E-01	1.66E-01	1.03E-09	8.29E-08	8.56E-06	2.28E-13	9.56E-04	4.75E-01
	600	5.17E-03	2.44E-03	1.43E-10	5.51E-09	2.50E-07	1.23E-13	1.04E-04	5.43E-02
	700	2.34E-04	1.22E-04	3.54E-11	8.12E-10	2.06E-08	8.06E-14	1.75E-05	8.63E-03
3%	**300**	1.59E+07	4.04E+06	2.29E-06	3.35E-03	9.30E+00	1.28E-13	5.46E+01	5.49E+02
	400	2.05E+02	6.73E+01	1.42E-08	3.31E-06	1.16E-03	4.01E-13	1.49E-02	5.70E+00
	500	2.64E-01	1.10E-01	7.00E-10	5.42E-08	5.59E-06	1.51E-13	6.50E-04	3.19E-01
	600	3.27E-03	1.59E-03	9.69E-11	3.60E-09	1.64E-07	8.14E-14	7.03E-05	3.67E-02
	700	1.46E-04	7.98E-05	2.41E-11	5.31E-10	1.34E-08	5.34E-14	1.18E-05	5.79E-03
5%	**300**	1.29E+07	3.27E+06	2.24E-06	3.13E-03	8.66E+00	8.10E-13	4.45E+01	6.15E+02
	400	1.81E+02	6.44E+01	1.39E-08	3.10E-06	1.11E-03	3.85E-13	1.46E-02	5.75E+00
	500	2.36E-01	1.03E-01	6.84E-10	5.09E-08	5.24E-06	1.43E-13	6.34E-04	3.11E-01
	600	2.94E-03	1.48E-03	9.46E-11	3.38E-09	1.54E-07	7.75E-14	6.81E-05	3.58E-02
	700	1.34E-04	7.51E-05	2.34E-11	4.99E-10	1.26E-08	5.07E-14	1.14E-05	5.54E-03
7%	**300**	1.45E+07	4.31E+06	2.99E-06	3.98E-03	1.10E+01	4.77E-13	5.67E+01	9.26E+02
	400	2.20E+02	7.74E+01	1.85E-08	3.95E-06	1.41E-03	4.83E-13	1.93E-02	8.05E+00
	500	2.90E-01	1.32E-01	9.07E-10	6.47E-08	6.63E-06	1.88E-13	8.39E-04	4.10E-01
	600	3.57E-03	1.90E-03	1.25E-10	4.30E-09	1.95E-07	1.00E-13	8.98E-05	4.66E-02
	700	1.63E-04	9.56E-05	3.10E-11	6.34E-10	1.60E-08	6.55E-14	1.49E-05	7.21E-03
9%	**300**	8.32E+06	3.91E+06	2.41E-06	3.10E-03	7.53E+00	1.04E-12	4.54E+01	6.40E+02
	400	1.52E+02	6.27E+01	1.51E-08	3.07E-06	1.08E-03	3.87E-13	1.57E-02	6.47E+00
	500	2.12E-01	1.03E-01	7.41E-10	5.04E-08	5.18E-06	1.47E-13	6.84E-04	3.34E-01
	600	2.68E-03	1.48E-03	1.02E-10	3.35E-09	1.52E-07	7.91E-14	7.24E-05	3.74E-02
	700	1.22E-04	7.45E-05	2.52E-11	4.95E-10	1.25E-08	5.18E-14	1.19E-05	5.75E-03

Appendix H

Supporting Information for "Charting the Atomic C Interaction with Transition Metal Surfaces"

Charting the Atomic C Interaction with Transition Metal Surfaces

Oriol Piqué,[a,†] Iskra Z. Koleva,[b,†] Albert Bruix,[a] Francesc Viñes,[*,a] Hristiyan A. Aleksandrov,[*,b] Georgi N. Vayssilov,[b] and Francesc Illas[a]

[a] *Departament de Ciència de Materials i Química Física & Institut de Química Teòrica i Computacional (IQTCUB), Universitat de Barcelona, c/ Martí i Franquès 1, 08028 Barcelona, Spain*

[b] *Faculty of Chemistry and Pharmacy, University of Sofia, 1126 Sofia, Bulgaria*

*e-mails: francesc.vines@ub.edu and haa@chem.uni-sofia.bg

Index of Sections

† Both authors equally contributed

Section S1: Models and Definitions

Fig. S1. Periodic table with *fcc* TMs coloured in blue, *bcc* TMs in green, and *hcp* TMs in purple.

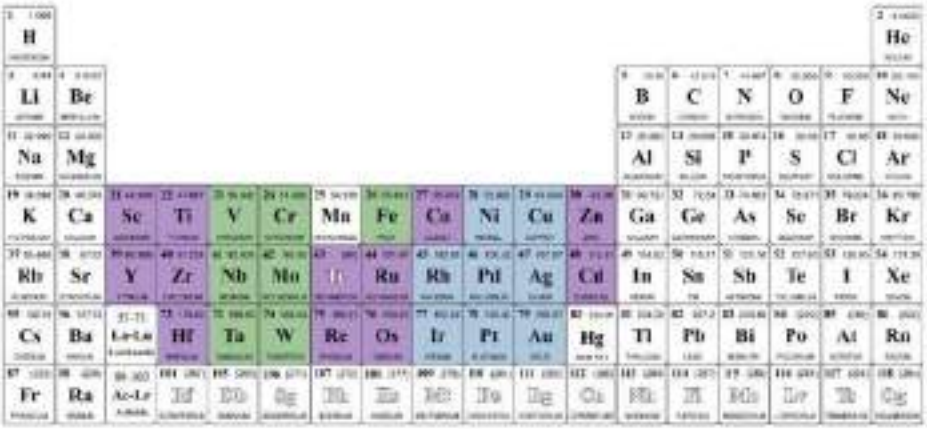

Fig. S2. Depiction of positions studied for each surface termination of each crystallographic structure. In blue, from left to right, *fcc* unit cell, and (001), (011), and (111) surfaces. In green, from left to right, *bcc* unit cell, and (001), (011), and (111) surfaces. In purple, from left to right, *hcp* unit cell, and (0001), $(10\bar{1}0)$, and $(11\bar{2}0)$ surfaces. Positions depicted for *fcc* (001) correspond to a) Top, b) Hollow, c) Bridge; for *fcc* (011) a) Top, b) Hollow, c) BridgeS, d) BridgeL; for *fcc* (111) a) Top, b) Hollow *hcp*, c) Hollow *fcc*, d) Bridge. Positions depicted for *bcc* (001) correspond to a) Top, b) Hollow, c) Bridge; for *bcc* (011) a) Top, b) Hollow, c) HollowT, d) Bridge; for *bcc* (111) a) Top, b) Hollow *hcp*, c) Hollow *fcc*, d) Bridge. Positions depicted for *hcp* (0001) correspond to a) Top, b) Hollow, c) HollowE, d) Bridge; for *hcp* (100) a) Top, b) Hollow, c) BridgeL, d) BridgeS; for *hcp* (110) a) Top, b) Hollow, c) BridgeL, d) BridgeS.

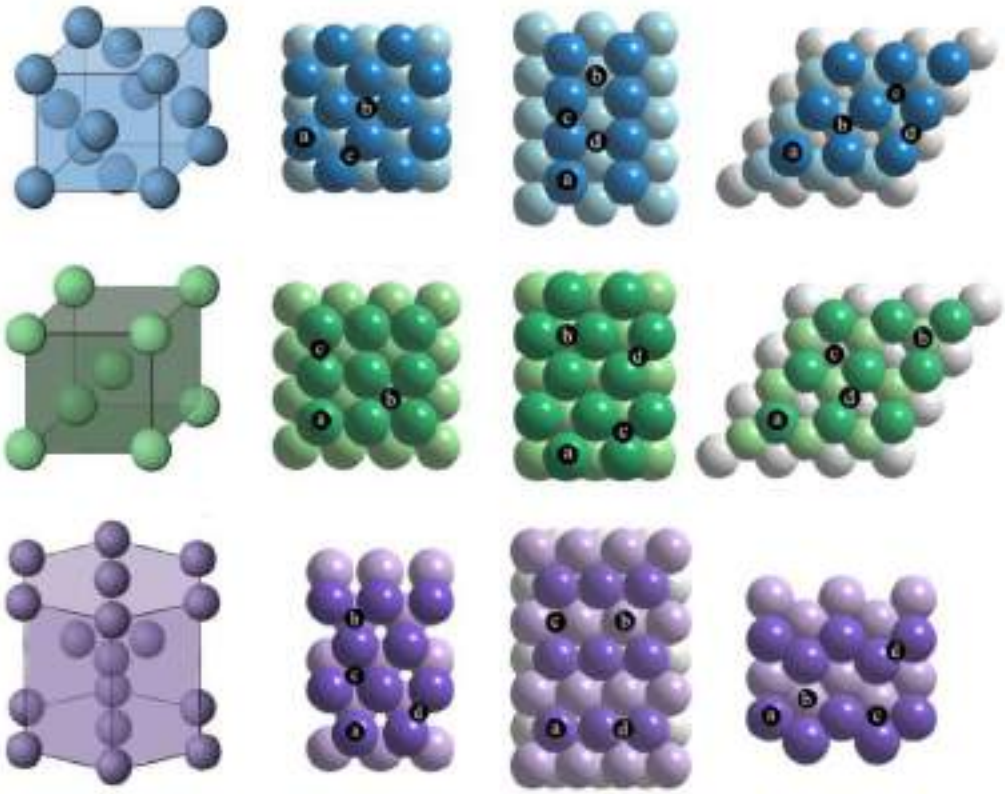

Fig. S3. Schematic depiction of the different diffusion barrier types studied in this work: Surface diffusion (E_{sur} – blue), subsurface diffusion (E_{sub} – red), sinking diffusion (E_{sink} – yellow), and emerging diffusion (E_{emer} – green).

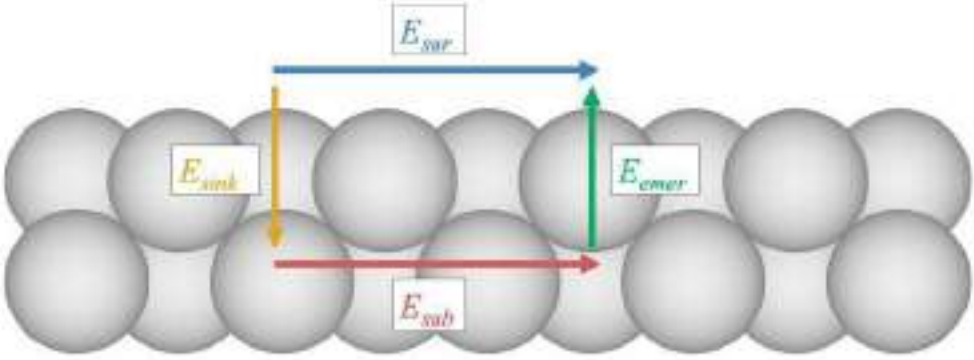

Section S2: K-means Clustering

The k-means (KM) algorithm has been used as implemented in the *sklearn* python library.[1] KM clusters data by splitting samples in n groups (clusters) of equal variance, where n is defined beforehand. The algorithm automatically finds n cluster centres which minimize the within-cluster sum-of-squares, also called inertia, see Eq. 1, in order to avoid compensation by negative displacement vectors from the centre, and as a way of preferentially gather those data points close to the cluster centre, and, at the same time, bias those located farther away.

$$\sum_{i=0}^{n} \min_{\mu_j \in C} \left(\|x_i - \mu_j\| \right)^2 \qquad (1),$$

where μ_j is the samples mean, also called cluster centroid, in the C disjoint clusters.

Inertia can be understood as a quantitative measure of how coherent clusters are, yet has some drawbacks. It assumes that clusters are isotropic and convex, and so, performs poorly with elongated clusters. Moreover, note that inertia is a non-normalized metric; *i.e.* one can just state that lower values are better, and zero optimal. In that regard, it does not perform well in high-dimensional spaces, where Euclidean distances tend to become inflated. Running a dimensionality reduction algorithm prior to the k-means analysis can help alleviating this problem.

However, that is not the case in the present study, and so this method is suited for the employed data, displayed two-dimensionally. Note that there exist other methodologies to find and define groups of similar behaviour, such as the subgroup discovery (SGD),[2] where a target variable is expressed as a function of a series of description features, which are Monte Carlo optimized to define regions of subgroups, as done *e.g.* in the past in the categorization of binary structures to rocksalt or zinc blende structures as a function of the atomic radii of valence s and p orbitals.[3] However, SGD defines fringe

conditions from which one expects one or another behaviour, while here KM defines centroids whose close data implies a similar behaviour.

Focusing on KM, notice that when n is exactly the number of data points, the minimum inertia of zero is achieved. Therefore, one needs to define a criterion to restrict to a small and useful n number. This has been done using the elbow method,[4] which consists in plotting the inertia as a function of n and picking the elbow of the curve as the suited number of clusters to use.

Section S3: Ad/Absorption Energies and Heights

Table S1. Adsorption, E_{ads}, and absorption, E_{abs}, energies of all different positions studied for (001), (011), and (111) surfaces of *fcc* TMs. All values are given in kJ mol^{-1}.

TM	(001) Position	E_{ads}	E_{abs}	(011) Position	E_{ads}	E_{abs}	(111) Position	E_{ads}	E_{abs}
Rh	Top	513	654	Top	523	560	Top	498	631
	Hollow	777	—	Hollow	633	—	Hollow *hcp*	706	612
	Bridge	638	613	BridgeS	651	658	Hollow *fcc*	686	684
	—	—	—	BridgeL	717	—	Bridge	—	—
Ir	Top	543	505	Top	577	412	Top	534	555
	Hollow	761	—	Hollow	600	—	Hollow *hcp*	720	559
	Bridge	656	527	BridgeS	697	530	Hollow *fcc*	697	588
	—	—	—	BridgeL	698	—	Bridge	—	—
Ni	Top	432	684	Top	423	610	Top	424	605
	Hollow	792	—	Hollow	697	—	Hollow *hcp*	651	593
	Bridge	582	612	BridgeS	578	708	Hollow *fcc*	647	708
	—	—	—	BridgeL	711	—	Bridge	—	—
Pd	Top	428	728	Top	438	646	Top	423	685
	Hollow	781	—	Hollow	685	—	Hollow *hcp*	682	705
	Bridge	599	695	BridgeS	613	748	Hollow *fcc*	680	751
	—	—	—	BridgeL	—	742	Bridge	—	—
Pt	Top	501	608	Top	531	542	Top	479	650

	Hollow	751	—	Hollow	616	—	Hollow *hcp*	697	696
	Bridge	642	677	BridgeS	662	661	Hollow *fcc*	707	652
	—	—	—	BridgeL	—	715	Bridge	—	—
Cu	Top	292	455	Top	266	459	Top	256	383
	Hollow	584	—	Hollow	546	438	Hollow *hcp*	436	394
	Bridge	419	442	BridgeS	—	538	Hollow *fcc*	440	482
	—	—	—	BridgeL	528	—	Bridge	—	—
Ag	Top	176	310	Top	170	317	Top	161	268
	Hollow	398	—	Hollow	364	—	Hollow *hcp*	314	294
	Bridge	250	311	BridgeS	—	379	Hollow *fcc*	320	338
	—	—	—	BridgeL	364	—	Bridge	—	—
Au	Top	238	329	Top	246	314	Top	211	310
	Hollow	447	—	Hollow	401	—	Hollow *hcp*	403	389
	Bridge	391	413	BridgeS	395	420	Hollow *fcc*	414	350
	—	—	—	BridgeL	—	417	Bridge	—	—

Table S2. Adsorption, E_{ads}, and absorption, E_{abs}, energies of all different positions studied for (001), (011), and (111) surfaces of *bcc* TMs. All values are given in kJ mol^{-1}.

TM	(001) Position	E_{ads}	E_{abs}	(011) Position	E_{ads}	E_{abs}	(111) Position	E_{ads}	E_{abs}
V	Top	431	—	Top	478	738	Top	364	599
	Hollow	898	—	Hollow	806	—	Hollow *hcp*	636	—
	Bridge	722	769	HollowT	—	815	Hollow *fcc*	773	—
	—	—	—	Bridge	769	—	Bridge	770	—
Nb	Top	436	—	Top	446	722	Top	353	550
	Hollow	902	—	Hollow	770	—	Hollow *hcp*	526	—
	Bridge	645	740	HollowT	—	798	Hollow *fcc*	636	—
	—	—	—	Bridge	636	—	Bridge	716	—
Ta	Top	404	—	Top	438	696	Top	373	539
	Hollow	915	—	Hollow	773	—	Hollow *hcp*	556	—
	Bridge	640	740	HollowT	—	819	Hollow *fcc*	619	—
	—	—	—	Bridge	645	—	Bridge	747	—

Cr	Top	540	—	Top	487	629	Top	421	544
	Hollow	915	—	Hollow	750	—	Hollow *hcp*	637	—
	Bridge	683	777	HollowT	—	666	Hollow *fcc*	729	—
	—	—	—	Bridge	659	—	Bridge	755	—
Mo	Top	512	—	Top	477	566	Top	450	508
	Hollow	888	—	Hollow	756	—	Hollow *hcp*	537	—
	Bridge	684	749	HollowT	—	679	Hollow *fcc*	620	—
	—	—	—	Bridge	668	—	Bridge	735	—
W	Top	522	—	Top	447	496	Top	416	412
	Hollow	951	—	Hollow	763	—	Hollow *hcp*	499	—
	Bridge	736	796	HollowT	—	626	Hollow *fcc*	576	—
	—	—	—	Bridge	672	—	Bridge	717	—
Fe	Top	526	—	Top	691	823	Top	495	673
	Hollow	817	—	Hollow	894	770	Hollow *hcp*	505	—
	Bridge	696	692	HollowT	—	849	Hollow *fcc*	728	—
	—	—	—	Bridge	821	—	Bridge	748	—

Table S3. Adsorption, E_{ads}, and absorption, E_{abs}, energies of all different positions studied for (0001), $(10\bar{1}0)$, and $(11\bar{2}0)$ surfaces of *hcp* TMs. All values are given in kJ mol^{-1}.

TM	(0001) Position	E_{ads}	E_{abs}	$(10\bar{1}0)$ Position	E_{ads}	E_{abs}	$(11\bar{2}0)$ Position	E_{ads}	E_{abs}
Sc	Top	—	739	Top	—	688	Top	—	794
	Hollow	753	—	Hollow	665	—	Hollow	841	—
	HollowE	—	871	BridgeS	—	801	BridgeL	—	—
	Bridge	—	—	BridgeL	752	—	BridgeS	—	882
Y	Top	—	736	Top	—	670	Top	—	755
	Hollow	739	—	Hollow	616	—	Hollow	781	—
	HollowE	—	831	BridgeS	—	790	BridgeL	—	—
	Bridge	—	—	BridgeL	724	—	BridgeS	—	836
Ti	Top	—	702	Top	—	705	Top	—	787
	Hollow	779	—	Hollow	688	—	Hollow	843	—
	HollowE	757	881	BridgeS	—	812	BridgeL	—	—
	Bridge	—	—	BridgeL	830	—	BridgeS	—	927
Zr	Top	—	728	Top	380	—	Top	—	792
	Hollow	776	—	Hollow	583	—	Hollow	808	—
	HollowE	747	887	BridgeS	—	805	BridgeL	—	—

	Bridge	—	—	BridgeL	799	—	BridgeS	—	930
Hf	Top	—	713	Top	382	636	Top	—	767
	Hollow	790	—	Hollow	517	—	Hollow	806	—
	HollowE	756	896	BridgeS	—	816	BridgeL	—	—
	Bridge	—	—	BridgeL	823	—	BridgeS	—	941
Tc	Top	468	—	Top	594	527	Top	—	626
	Hollow	698	567	Hollow	571	—	Hollow	690	—
	HollowE	684	669	BridgeS	751	608	BridgeL	—	—
	Bridge	—	—	BridgeL	781	—	BridgeS	607	664
Re	Top	490	525	Top	515	—	Top	—	591
	Hollow	732	—	Hollow	491	—	Hollow	684	—
	HollowE	739	701	BridgeS	694	600	BridgeL	—	—
	Bridge	—	—	BridgeL	731	—	BridgeS	623	584
Ru	Top	502	571	Top	555	—	Top	555	643
	Hollow	718	—	Hollow	538	—	Hollow	729	—
	HollowE	654	607	BridgeS	664	602	BridgeL	732	—
	Bridge	—	—	BridgeL	716	—	BridgeS	666	689
Os	Top	490	502	Top	576	576	Top	582	615
	Hollow	721	—	Hollow	504	—	Hollow	716	—
	HollowE	655	508	BridgeS	679	513	BridgeL	—	—
	Bridge	—	—	BridgeL	699	—	BridgeS	698	608
Co	Top	—	572	Top	465	550	Top	529	608
	Hollow	660	581	Hollow	523	—	Hollow	691	—
	HollowE	638	652	BridgeS	583	589	BridgeL	—	—
	Bridge	—	—	BridgeL	666	—	BridgeS	567	661
Zn	Top	—	421	Top	—	382	Top	—	491
	Hollow	—	438	Hollow	225	337	Hollow	509	—
	HollowE	397	461	BridgeS	—	421	BridgeL	—	—
	Bridge	—	—	BridgeL	—	413	BridgeS	—	531
Cd	Top	—	367	Top	183	345	Top	—	404
	Hollow	—	383	Hollow	157	290	Hollow	411	—
	HollowE	344	397	BridgeS	—	384	BridgeL	—	—
	Bridge	—	—	BridgeL	—	377	BridgeS	—	441

Table S4. C height, h, with respect to the TM surface plane, h^{surf} and h_{sub}, respectively, for all different positions studied for (001), (011), and (111) surfaces of *fcc* TMs. All values are given in pm.

TM	(001) Position	h^{surf}	h_{sub}	(011) Position	h^{surf}	h_{sub}	(111) Position	h^{surf}	h_{sub}
Rh	Top	170	-194	Top	169	-178	Top	169	-182
	Hollow	16	---	Hollow	47	—	Hollow *hcp*	96	-76
	Bridge	107	-95	BridgeS	115	-126	Hollow *fcc*	94	-108
	—	—	—	BridgeL	5	—	Bridge	—	—
Ir	Top	174	-189	Top	173	-176	Top	173	-184
	Hollow	57	—	Hollow	62	—	Hollow *hcp*	99	-76
	Bridge	108	-94	BridgeS	121	-120	Hollow *fcc*	97	-105
	—	—	—	BridgeL	25	—	Bridge	—	—
Ni	Top	164	-182	Top	162	-171	Top	164	-172
	Hollow	21	—	Hollow	37	—	Hollow *hcp*	95	-68
	Bridge	105	-71	BridgeS	110	-118	Hollow *fcc*	99	-102
	—	—	—	BridgeL	10	—	Bridge	—	—
Pd	Top	173	-202	Top	172	-187	Top	173	-187
	Hollow	1	—	Hollow	19	—	Hollow *hcp*	88	-70
	Bridge	98	-98	BridgeS	107	-135	Hollow *fcc*	80	-116
	—	—	—	BridgeL	—	-17	Bridge	—	—
Pt	Top	173	-190	Top	173	-185	Top	174	-189
	Hollow	6	—	Hollow	31	—	Hollow *hcp*	88	-75
	Bridge	107	-95	BridgeS	113	-69	Hollow *fcc*	76	-112
	—	—	—	BridgeL	—	-8	Bridge	—	—
Cu	Top	175	-192	Top	173	-181	Top	176	-182
	Hollow	33	—	Hollow	38	—	Hollow *hcp*	98	-72
	Bridge	101	-66	BridgeS	—	-111	Hollow *fcc*	100	-98
	—	—	—	BridgeL	17	—	Bridge	—	—
Ag	Top	194	-220	Top	192	-204	Top	195	-207
	Hollow	38	—	Hollow	37	—	Hollow *hcp*	104	-72

	Bridge	157	-86	BridgeS	—	-125	Hollow *fcc*	105	-109
	—	—	—	BridgeL	10	—	Bridge	—	—
Au	Top	186	-202	Top	185	-201	Top	187	-204
	Hollow	51	—	Hollow	15	—	Hollow *hcp*	79	-58
	Bridge	102	-85	BridgeS	72	-51	Hollow *fcc*	84	-87
	—	—	—	BridgeL	—	-9	Bridge	—	—

Table S5. C height, h, with respect to the TM surface plane, h^{sur} and h_{sub}, respectively, for all different positions studied for (001), (011), and (111) surfaces of *bcc* TMs. All values are given in pm.

TM	(001) Position	h^{sur}	h_{sub}	(011) Position	h^{sur}	h_{sub}	(111) Position	h^{sur}	h_{sub}
V	Top	175	—	Top	175	-44	Top	175	-175
	Hollow	56	—	Hollow	38	—	Hollow *hcp*	79	—
	Bridge	1	-119	HollowT	—	-81	Hollow *fcc*	17	—
	—	—	—	Bridge	1	---	Bridge	26	—
Nb	Top	185	—	Top	187	-50	Top	186	-172
	Hollow	52	—	Hollow	25	—	Hollow *hcp*	191	—
	Bridge	121	-17	HollowT	—	-110	Hollow *fcc*	20	—
	—	—	—	Bridge	120	—	Bridge	28	—
Ta	Top	188	—	Top	190	-53	Top	190	-186
	Hollow	52	—	Hollow	83	—	Hollow *hcp*	192	—
	Bridge	116	-10	HollowT	—	-119	Hollow *fcc*	204	—
	—	—	—	Bridge	125	—	Bridge	34	—
Cr	Top	168	—	Top	171	-182	Top	167	-170
	Hollow	61	—	Hollow	107	—	Hollow *hcp*	78	—
	Bridge	125	-1	HollowT	—	-90	Hollow *fcc*	35	—
	—	—	—	Bridge	118	—	Bridge	41	—
Mo	Top	177	—	Top	181	-44	Top	176	-179
	Hollow	57	—	Hollow	104	—	Hollow *hcp*	84	—
	Bridge	127	-2	HollowT	—	-96	Hollow *fcc*	43	—
	—	—	—	Bridge	125	—	Bridge	38	—
W	Top	183	—	Top	188	-45	Top	182	-181
	Hollow	59	—	Hollow	108	—	Hollow *hcp*	191	—
	Bridge	132	-4	HollowT	—	-98	Hollow *fcc*	52	—

	—	—	—	Bridge	130	—	Bridge	46	—
Fe	Top	160	—	Top	164	-91	Top	159	-182
	Hollow	40	—	Hollow	89	-96	Hollow *hcp*	186	—
	Bridge	9	-118	HollowT	—	-104	Hollow *fcc*	12	—
	—	—	—	Bridge	117	—	Bridge	21	—

Table S6. C height (h) with respect to the TM surface plane, h^{ver} and h_{sub}, respectively, for all different positions studied for (0001), $(10\bar{1}0)$, and $(11\bar{2}0)$ surfaces of *hcp* TMs. All values are given in pm.

TM	(0001) Position	h^{ver}	h_{sub}	$(10\bar{1}0)$ Position	h^{ver}	h_{sub}	$(11\bar{2}0)$ Position	h^{ver}	h_{sub}
Se	Top	—	-202	Top	—	-203	Top	—	-157
	Hollow	2	—	Hollow	33	—	Hollow	19	—
	HollowE	—	-123	BridgeS	—	-89	BridgeL	—	—
	Bridge	—	---	BridgeL	10	—	BridgeS	—	-139
Y	Top	—	-236	Top	—	-218	Top	—	-185
	Hollow	2	—	Hollow	26	—	Hollow	1	—
	HollowE	—	-132	BridgeS	—	-100	BridgeL	—	—
	Bridge	—	—	BridgeL	1	—	BridgeS	—	-151
Tl	Top	—	-57	Top	—	-187	Top	—	-98
	Hollow	43	—	Hollow	57	—	Hollow	38	—
	HollowE	98	-120	BridgeS	—	-47	BridgeL	—	—
	Bridge	—	—	BridgeL	32	—	BridgeS	—	-124
Zr	Top	—	-79	Top	197	—	Top	—	-108
	Hollow	17	—	Hollow	51	—	Hollow	31	—
	HollowE	96	-131	BridgeS	—	-59	BridgeL	—	—
	Bridge	—	—	BridgeL	23	—	BridgeS	—	-140
Hf	Top	—	-60	Top	199	-198	Top	—	-149
	Hollow	27	—	Hollow	202	—	Hollow	35	—
	HollowE	95	-124	BridgeS	—	-59	BridgeL	—	—
	Bridge	—	—	BridgeL	29	—	BridgeS	—	-137
Tc	Top	176	—	Top	172	-96	Top	—	-140
	Hollow	108	-86	Hollow	176	—	Hollow	59	—
	HollowE	111	-97	BridgeS	128	-74	BridgeL	—	—
	Bridge	—	—	BridgeL	52	—	BridgeS	126	-96
Re	Top	180	-79	Top	179	—	Top	—	-143
	Hollow	111	—	Hollow	186	—	Hollow	71	—

	HollowE	113	-100	BridgeS	124	-60	BridgeL	—	—
	Bridge	—	—	BridgeL	52	—	BridgeS	132	-100
Ru	Top	172	-182	Top	171	—	Top	169	-136
	Hollow	101	—	Hollow	182	—	Hollow	52	—
	HollowE	100	-95	BridgeS	111	-85	BridgeL	33	—
	Bridge	—	—	BridgeL	96	—	BridgeS	125	-95
Os	Top	176	-184	Top	174	-180	Top	172	-128
	Hollow	104	—	Hollow	185	—	Hollow	46	—
	HollowE	107	-94	BridgeS	121	-88	BridgeL	—	—
	Bridge	—	—	BridgeL	101	—	BridgeS	132	-87
Co	Top	—	-171	Top	160	-170	Top	77	-131
	Hollow	97	-85	Hollow	171	—	Hollow	45	—
	HollowE	101	-96	BridgeS	98	-84	BridgeL	—	—
	Bridge	—	—	BridgeL	48	—	BridgeS	112	-95
Zn	Top	—	-154	Top	—	-201	Top	—	-99
	Hollow	—	-25	Hollow	190	-198	Hollow	1	—
	HollowE	86	-130	BridgeS	—	-52	BridgeL	—	—
	Bridge	—	—	BridgeL	—	-47	BridgeS	—	-45
Cd	Top	—	-225	Top	217	-229	Top	—	-156
	Hollow	—	-42	Hollow	214	-225	Hollow	-41	—
	HollowE	95	-151	BridgeS	—	-33	BridgeL	—	—
	Bridge	—	—	BridgeL	—	-57	BridgeS	—	-51

Section S4: K-means Inertia

Fig. S4. Evolution of inertia as a function of the number of employed clusters in the $E_{ads/obs}$ *vs.* h quadrant plots. Within the elbow method, the optimal number of clusters would be three, belonging to the inflection point in the overall trend.

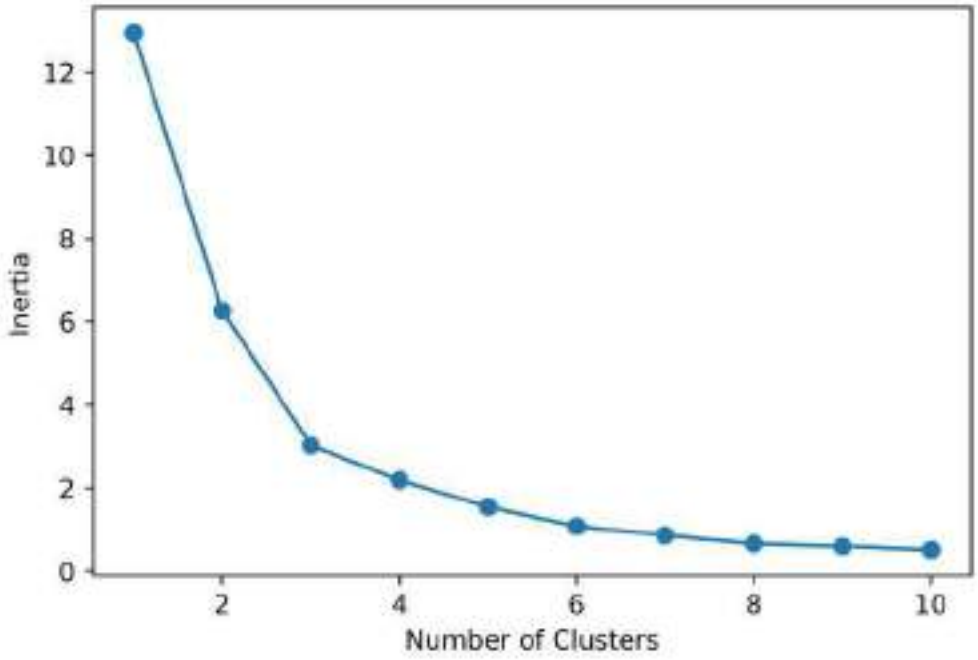

Section S5: Phase Diagrams

Fig. S5. Calculated phase diagrams for *fcc* TMs (001), (011), and (111) surfaces depending on the acetylene partial pressure, $p_{C_2H_2}$, and temperature, T. Diagrams are obtained for a constant partial pressure of H_2, $p_{H_2} = 10^{-7}$ Pa, and distinguish surface, C^{sur}, and subsurface, C_{sub}, situations. Regions above or below each curve indicate conditions at which the C-containing or pristine surfaces, respectively, are thermodynamically preferred.

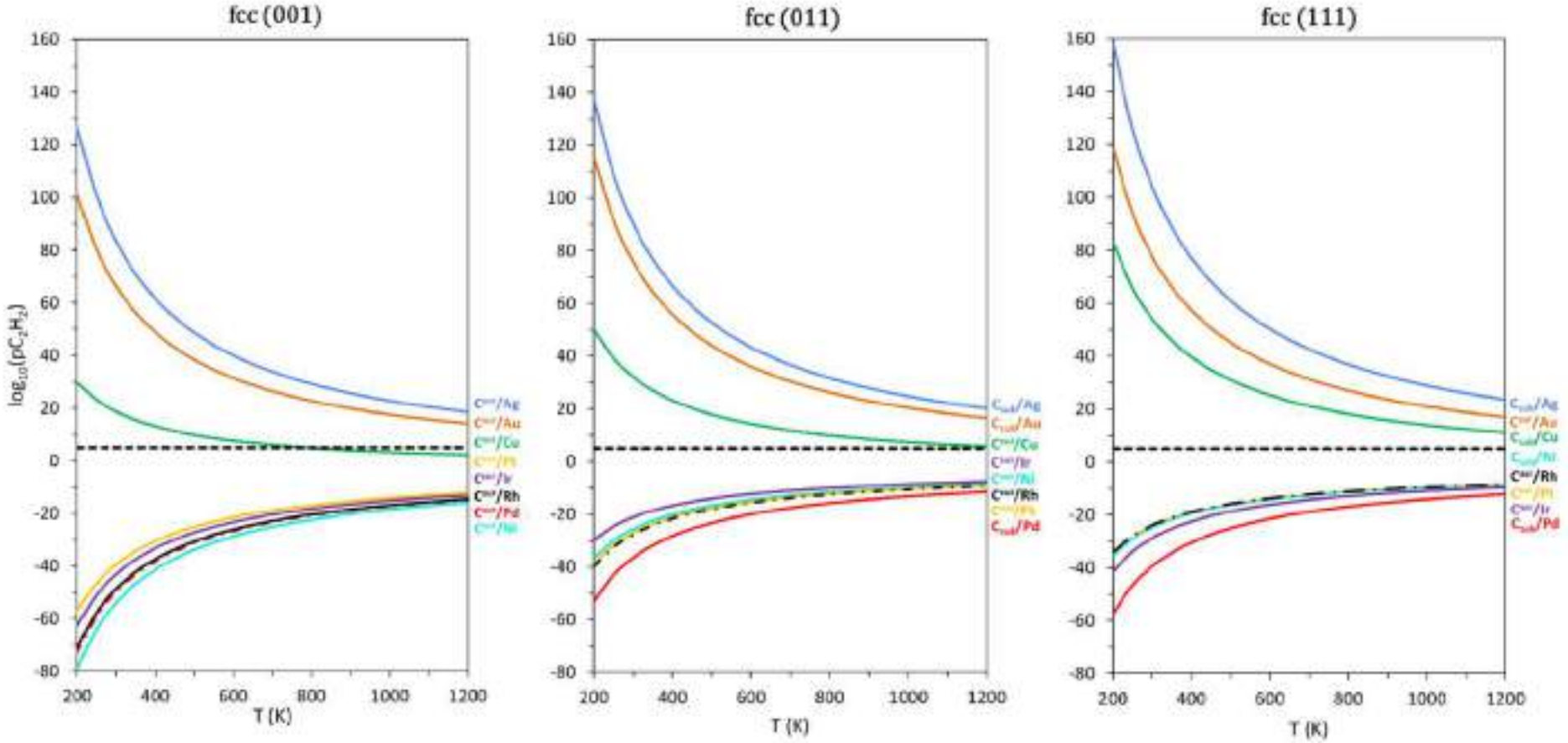

Fig. S6. Calculated phase diagrams for *hcp* TMs for (0001), $(10\bar{1}0)$, and $(11\bar{2}0)$ surfaces depending on the acetylene partial pressure, $p_{C_2H_2}$, and temperature, T. Diagrams are obtained for a constant partial pressure of H_2, $p_{H_2} = 10^{-7}$ Pa, and distinguish surface, C^{surf}, and subsurface, C_{sub}, situations. Regions above or below each curve indicate conditions at which the C-containing or pristine surfaces, respectively, are thermodynamically preferred.

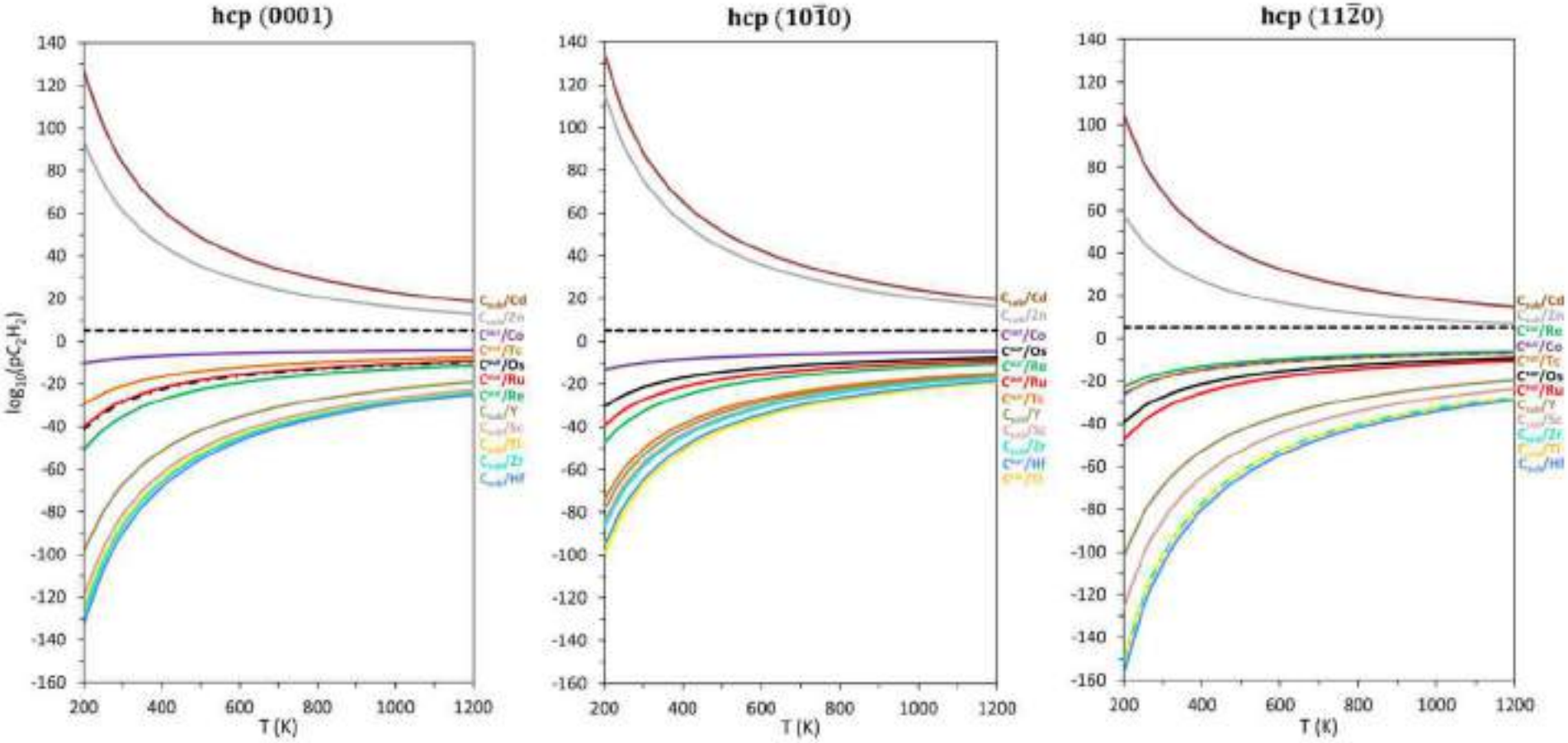

Fig. S7. Calculated phase diagrams for *bcc* TMs (001), (011), and (111) surfaces depending on the acetylene partial pressure, $p_{C_2H_2}$, and temperature, T. Diagrams are obtained for a constant partial pressure of H_2, $p_{H_2} = 10^{-7}$ Pa, and distinguish surface, C^{surf}, and subsurface, C_{sub}, situations. Regions above or below each curve indicate conditions at which the C-containing or pristine surfaces, respectively, are thermodynamically preferred.

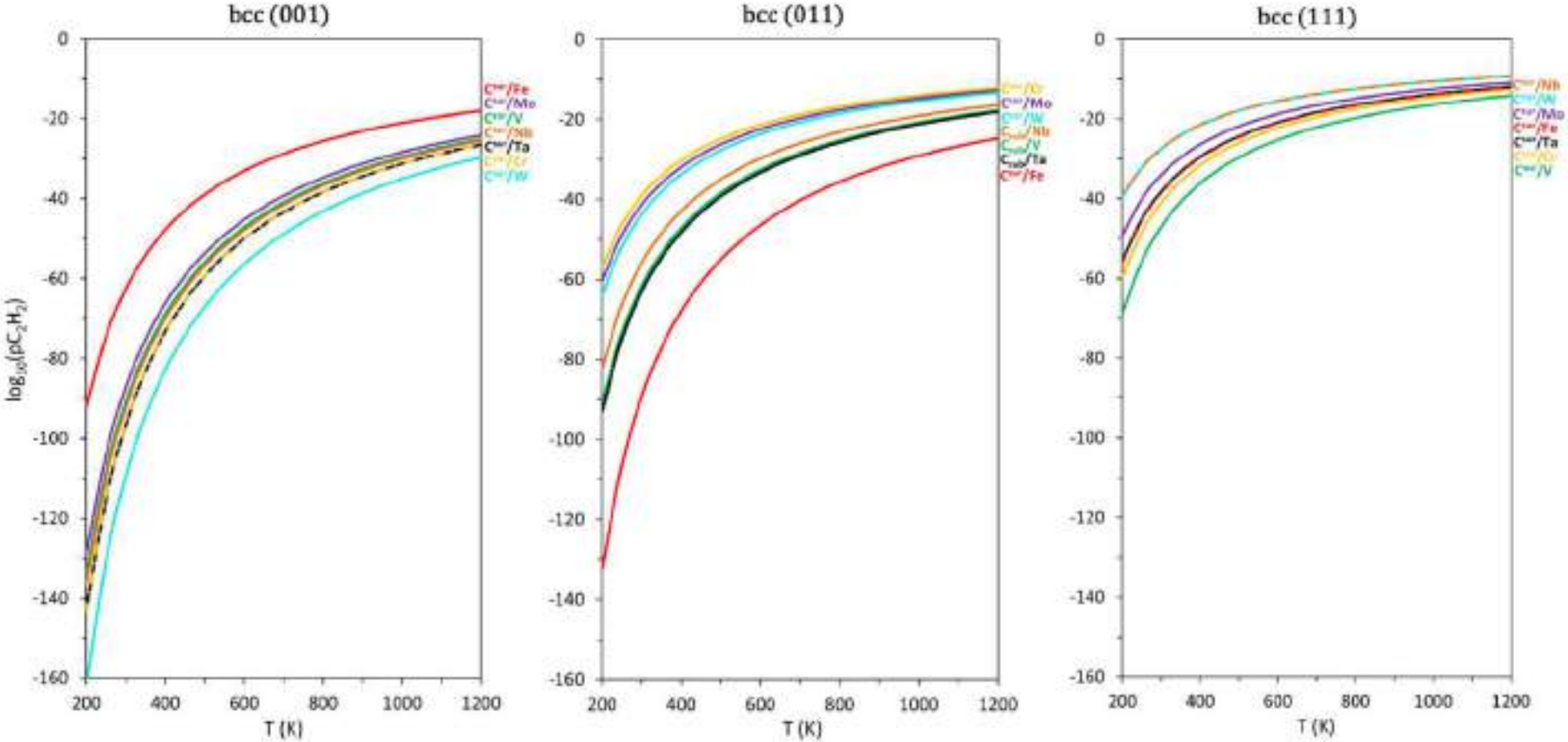

Section S6: Isolated Descriptors Evaluation

Fig. S8. Linear correlation between the *d*-band centre, ε_d, and most stable positions $E_{adsorbs}$. The regression coefficient, *R*, is displayed.

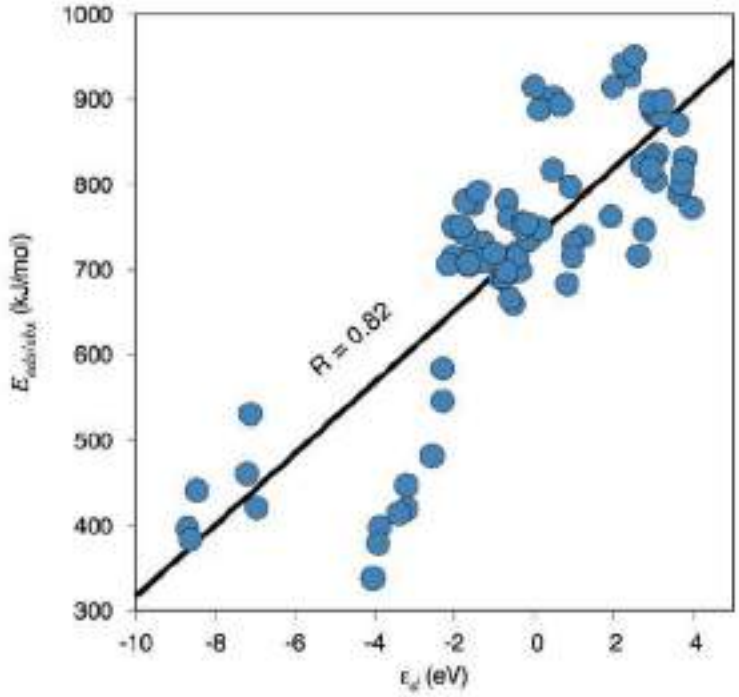

Fig. S9. Linear correlation between the width-corrected *d*-band centre, ε_d^W, and most stable positions $E_{adsorbs}$. The regression coefficient, *R*, is displayed.

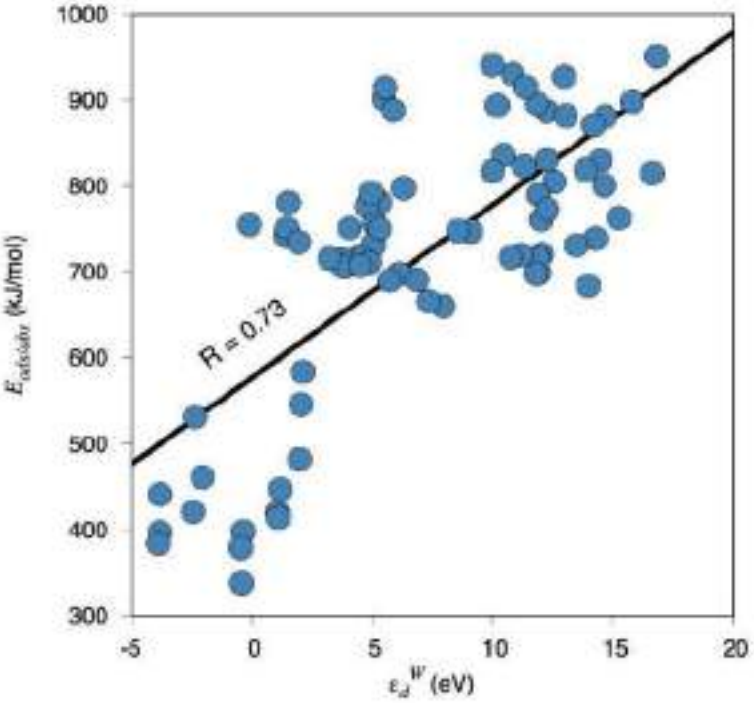

Fig. S10. Linear correlation between the maximum Hilbert peak, ε_h, and most stable positions $E_{adsorbs}$. The regression coefficient, R, is displayed.

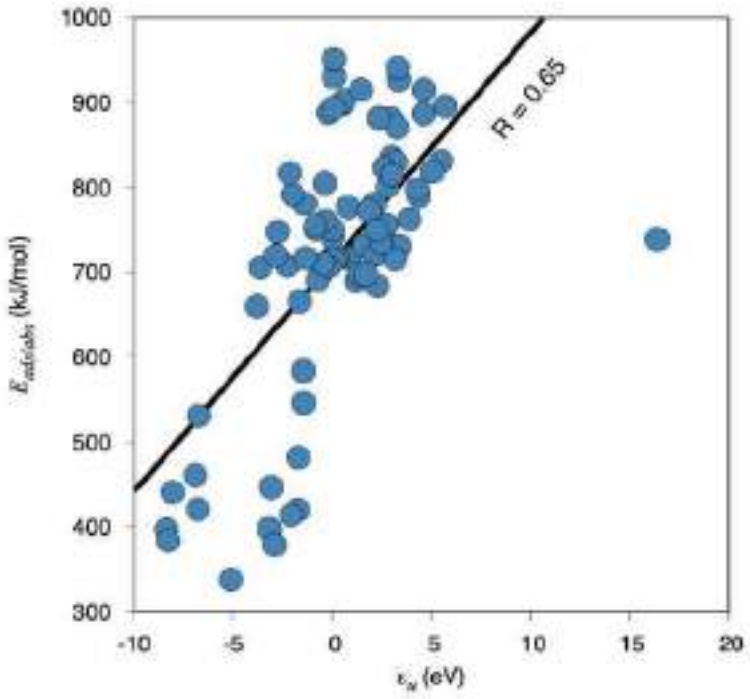

Fig. S11. Linear correlation between the surface energy, γ, and most stable positions $E_{adsorbs}$. The regression coefficient, R, is displayed.

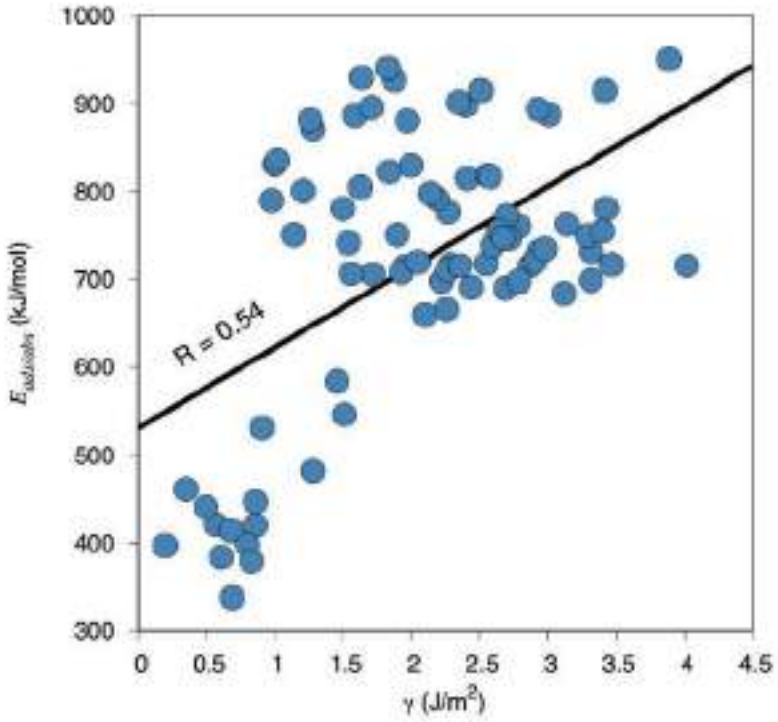

Fig. S12. Correlation between the surface work function, ϕ, and most stable positions $E_{adsorbs}$. The regression coefficient, R, is displayed.

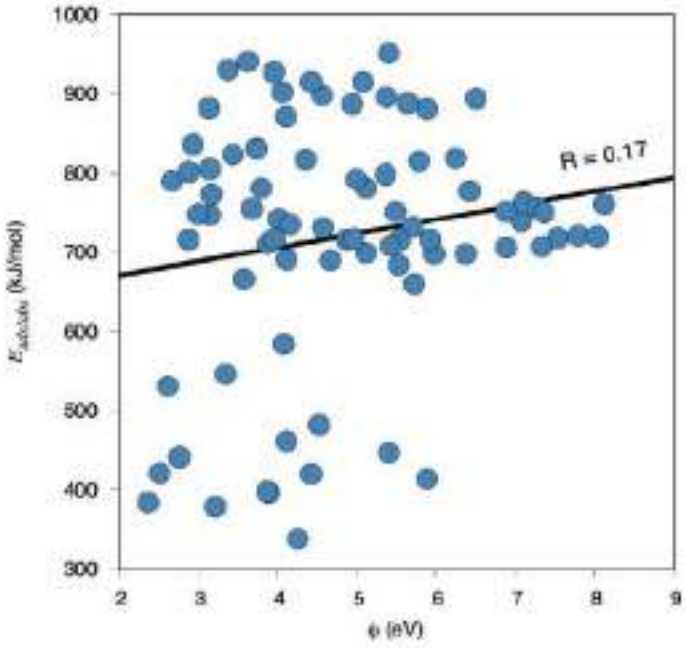

Fig. S13. Correlation between ε_d and most stable positions $E_{adsorbs}$. A regression line is shown for each of the nine different studied surfaces. Correlation coefficients of 0.91, 0.89, 0.93, 0.98, 0.93, 0.96, 0.41, 0.28, and 0.23 are found for *fcc* (001), *fcc* (011), *fcc* (111), *hcp* (0001), *hcp* (10$\bar{1}$0), *hcp* (11$\bar{2}$0), *bcc* (001), *bcc* (011), and *bcc* (111), respectively.

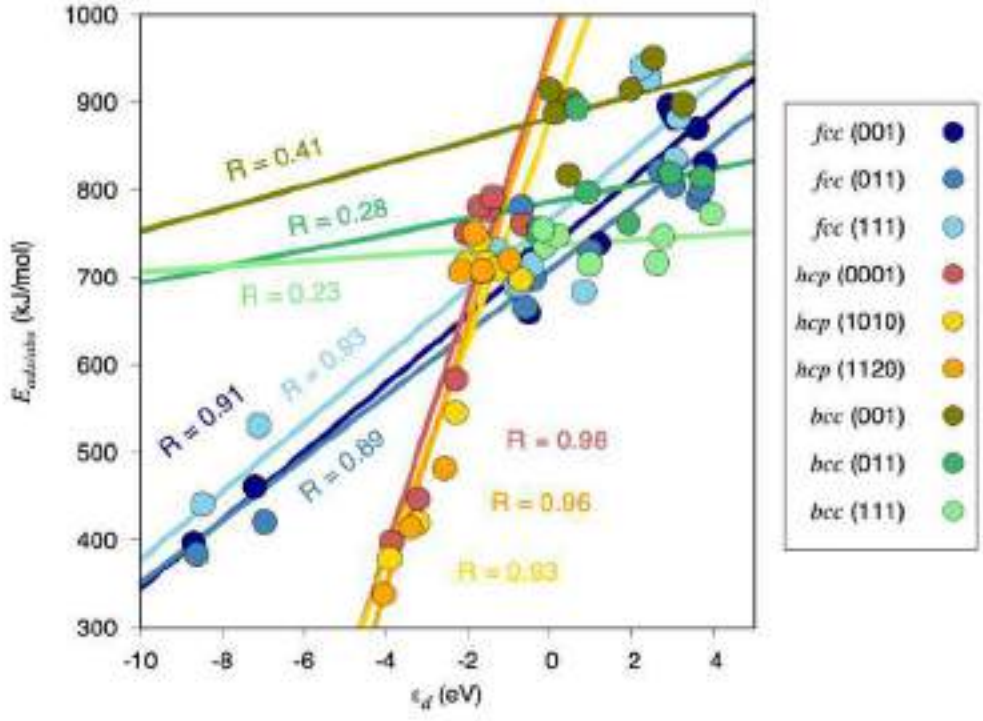

Section S7: Machine Learning Regression Algorithms

All the machine learning (ML) algorithms used in this work were applied as implemented in the *sklearn* Python library.[1] The multivariable linear regression (MLR) simply corresponds to the ordinary least squares linear regression but as a function of two or more variables. The decision tree regressor (DTR) is a supervised learning algorithm that has, as a goal, to build a model predicting the value of a target variable, in our case the E_{ads} or E_{abs}, through the learning of a set of binary rules derived from the data features, here the descriptors and surface features listed in the manuscript. For this DTR builds a model in the form of a tree structure featuring branches, nodes, and leaves. The order of the questions —known as decision nodes, which gives the name to the method— as well as their content is automatically determined and optimized by the algorithm, which looks for the homogeneity of y values in a found subset, and for that, uses the standard deviation of y values as an optimization criterion. During the training, the model learns any relationships between the data and the target variable, defining the best questions as well as their order to make the most accurate estimates possible. When predicting the dependent variable value of a new data point, this point is run completely through the entire tree branches by answering the node questions —posed as logic steps— until reaching the final answer leaf, with the target variable. Indeed, this variable value is just the average value of all points satisfying the same logic questions as the dependent point.

The complexity of the above explanation calls for an illustrative example so as to understand the basics of the procedure. Let us define a dependent variable target, y —which could be, *e.g.*, E_{ads}—, which depends on two features, x_1 and x_2 —*e.g.*, two descriptors, such as ε_d and γ. Fig. S14 displays a scatter plot of x_2 *vs.* x_1, and one could well imagine a three-dimensional plot, where y values would define the points heights in an orthogonal axis to x_1 and x_2. In it, dotted lines would delimit regions defined by the nodes, *e.g.*, a first one asking whether x_1 values is larger than 50, and second ones asking whether x_2 value is larger than 4 for x_1 values smaller than 50, or x_2 value being larger than 12 when x_1 is larger than 50. That leads to final four leaves, with different average y values, $\bar{y}$, see Fig. S15. For instance, when this is done for a training set, a test set value with $x_1 = 25$ and $x_2 = 12$ would yield an expected $\bar{y}$ value of 5.1. Notice that this is done for a very simplified, two-dimensional case, with y values depending on two variables, but is easily applied for the dependence on a higher number of variables.

Notice that, even if DTR is relatively easy to interpret, and requires little data preparation, the resulting tree is sensitive to the employed data, *i.e.* small variations on the data may be translated into a completely different built tree. To overcome this drawback, an ensemble of trees, *a.k.a.* a forest, can be used. This is indeed the basics of the random forest regression (RFR), where an ensemble of decision trees is grown. Each tree is assembled from a sample randomly drawn from the training set. For each

tree, when splitting each node, the best split can be found either from all the input features or for a random subset of features, *a.k.a. max_features*. These two sources of randomness help decreasing the variance of the estimator, since individual decision trees usually exhibit high variance and tend to overfit. The background idea is that, when a prediction is cast on a data set, *e.g.* the above commented x_1 and x_2 values, different $\bar{y}_i$ values are obtained for $i = 1 - N$, where N is the number of trees of the forest, a.k.a. *n_estimators*. Thus, the expected value of $\bar{y}$ is simply the average over the expected $\bar{y}_i$ values on the different N trees. By doing so, the predictive accuracy of the trees is narrowed, diluting possible extreme $\bar{y}$ forecasts. Notice that RFR becomes DTR for $i = 1$, and that the more the trees, the better the accuracy is, yet computationally more expensive. Aside, notice that accuracy decays with N, but results do not normally improve beyond a critical number of trees.

An appealing aspect of both DTR and RFR is the fact that the relative rank of a feature used as a decision node in a tree can be used to assess the relative importance of that feature with respect to the target variable predictions. For instance, features used at the top of the tree have a larger impact, since they affect the final prediction decision of a larger fraction of samples. Hence, the relative importance of the features can be estimated as the expected fraction of samples they contribute to.

Fig. S14. Exemplary scatter plot of values, shown as blue circles, of x_2 *vs.* x_1 variables, where black dotted lines represent the variable splitting decisions learned by the model. In light blue, the $\bar{y}$ average values for all those points belonging in each of the resulting sections inside the plot.

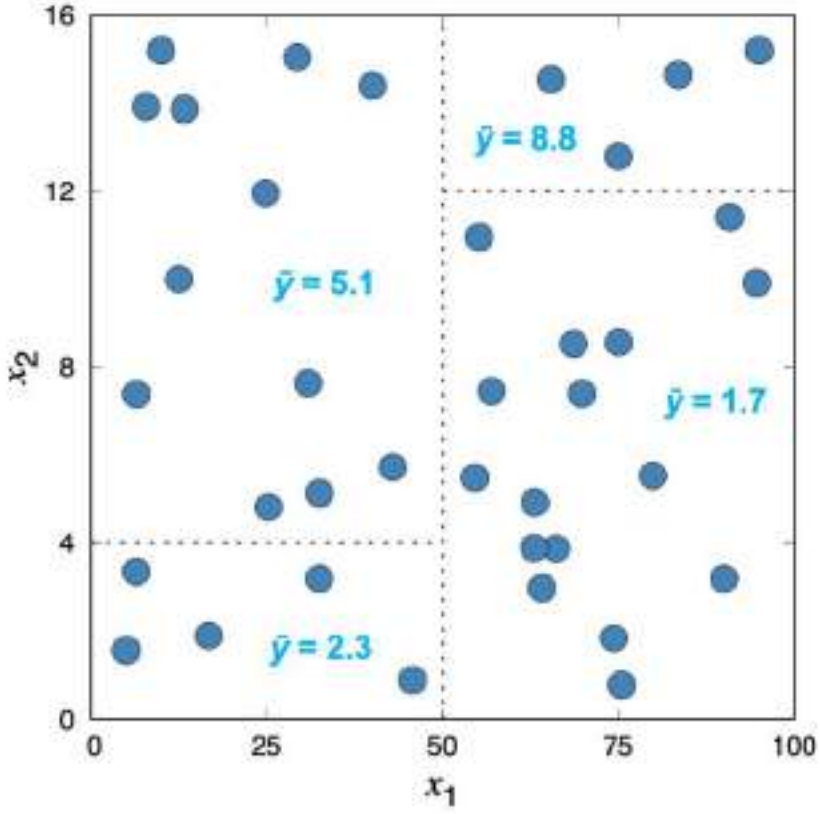

Fig. S15. Exemplary decision tree from data shown in Fig. S14.

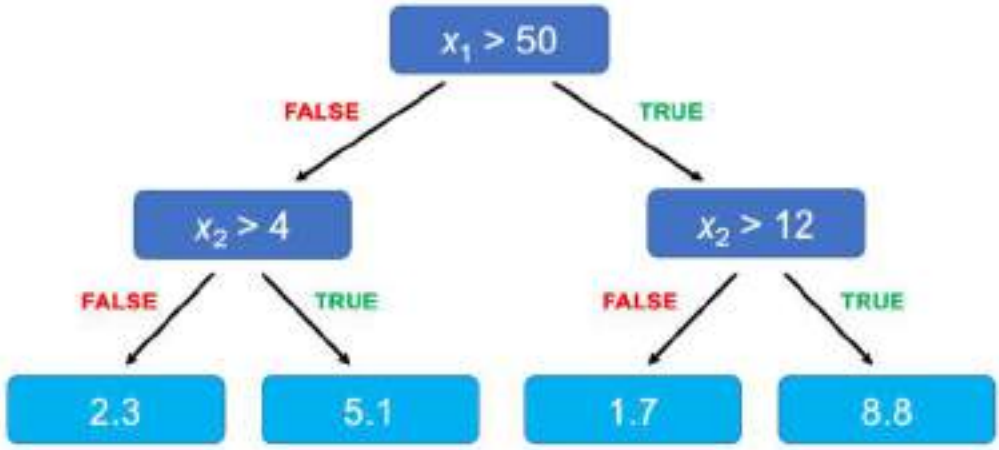

Section S8: Diffusion Energy Barriers

In order to evaluate the different diffusion E_b energy barriers, different paths have been explored for all the nine different TM surface types. Notice that, for some surfaces, and some sorts of diffusions, different paths have been evaluated, normally implying different adsorption or absorption minima. As an example of many, *fcc* (111) surfaces normally display two possible adsorption minima, Hollow *fcc* or Hollow *hcp*, see Fig. S2. C atoms can sink from these two adsorption minima towards two different absorption minima, these are, subsurface Hollow *fcc* or subsurface Hollow *hcp*. Since normally such surface minima are close in energy, we decided to evaluate both possible subsurface sinking paths to have a more complete description, although the final barrier used for a further evaluation was the lowest explored for a same process on the same surface.

Table S7. Explored paths for surface (E_{sur}), subsurface (E_{sub}), sinking (E_{sink}), and emerging (E_{emer}) diffusions on *fcc* TMs and their labelling. For each path, different minima stages are defined, with a subscript S to denote subsurface positions.

Surface	Barrier	Path 1	Path 2	Label Path 1	Label Path 2
(001)	E_{sur}	Hollow/Bridge/Hollow	—	a1	—
	E_{sub}	Top$_S$/Bridge$_S$/Top$_S$	Bridge$_S$/Top$_S$/Bridge$_S$	a2	a3
	E_{sink}	Hollow/Top$_S$	—	a4	—
	E_{emer}	Top$_S$/Hollow	—	a5	—
(011)	E_{sur}	BridgeS/Hollow/BridgeS	—	a6	—
	E_{sub}	BridgeL$_S$/Top$_S$/BridgeL$_S$	—	a7	—
	E_{sink}	BridgeS/BridgeL$_S$	Hollow/BridgeL$_S$	a8	a9
	E_{emer}	BridgeL$_S$/BridgeS	BridgeL$_S$/Hollow	a10	a11
(111)	E_{sur}	Hollow *fcc*/Hollow *hcp*/Hollow *fcc*	Hollow *hcp*/Hollow *fcc*/Hollow *hcp*	a12	a13
	E_{sub}	Hollow *fcc*$_S$/Hollow *hcp*$_S$/Hollow *fcc*$_S$	Hollow *hcp*$_S$/Hollow *fcc*$_S$/Hollow *hcp*$_S$	a14	a15
	E_{sink}	Hollow *fcc*/Hollow *fcc*$_S$	Hollow *hcp*/Hollow *hcp*$_S$	a16	a17
	E_{emer}	Hollow *fcc*$_S$/Hollow *fcc*	Hollow *hcp*$_S$/Hollow *hcp*	a18	a19

Table S8. Explored paths for surface (E_{sur}), subsurface (E_{sub}), sinking (E_{sink}), and emerging (E_{emer}) diffusions on *bcc* TMs and their labelling. For each path, different minima stages are defined, with a subscript S to denote subsurface positions.

Surface	Barrier	Path 1	Path 2	Label Path 1	Label Path 2
(001)	E_{sur}	Hollow/Bridge/Hollow	—	b1	—
	E_{sub}	Tops/Bridges/Tops	Bridges/Hollows/Bridges	b2	b3
	E_{sink}	Hollow/Tops	—	b4	—
	E_{emer}	Tops/Hollow	—	b5	—
(011)	E_{sur}	Hollow/Bridge/Hollow	—	b6	—
	E_{sub}	HollowTs/Hollow/HollowTs	—	b7	—
	E_{sink}	Hollow/HollowTs	—	b8	—
	E_{emer}	HollowTs/Hollow	—	b9	—
(111)	E_{sur}	Bridge/Hollow *fcc*/Bridge	Hollow *fcc*/Hollow *hcp*/Hollow *fcc*	b10	b11
	E_{sub}	Tops/Bridges/Tops	—	b12	—
	E_{sink}	Bridge/Tops	Hollow *fcc*/Tops	b13	b14
	E_{emer}	Tops/Bridge	Tops/Hollow *fcc*	b15	b16

Table S9. Explored paths for surface (E_{surf}), subsurface (E_{sub}), sinking (E_{sink}), and emerging (E_{emer}) diffusions on *hcp* TMs and their labelling. For each path, different minima stages are defined, with a subscript S to denote subsurface positions.

Surface	Barrier	Path 1	Path 2 ; 3 ; 4	Label Path 1	LabelS PathS 2 ; 3 ; 4
(0001)	E_{surf}	Hollow/HollowE/Hollow	HollowE/Hollow/HollowE	c1	c2
	E_{sub}	$HollowE_S$/$Hollow_S$/$HollowE_S$	—	c3	—
	E_{sink}	Hollow/$HollowE_S$	HollowE/$HollowE_S$	c4	c5
	E_{emer}	$HollowE_S$/Hollow	$HollowE_S$/HollowE	c6	c7
(10$\bar{1}$0)	E_{surf}	BridgeL/BridgeS/BridgeL	BridgeS/BridgeL/BridgeS	c8	c9
	E_{sub}	$BridgeS_S$/$BridgeL_S$/$BridgeS_S$	Top_S/$BridgeL_S$/Top_S	c10	c11
	E_{sink}	BridgeL/$BridgeS_S$	BridgeL/Top_S; BridgeS/Top_S	c12	c13 ; c13.2
	E_{emer}	$BridgeS_S$/BridgeL	Top_S/BridgeL ; Top_S/BridgeS	c14	c15 ; c15.2
(11$\bar{2}$0)	E_{surf}	Hollow/BridgeS/Hollow	BridgeS/BridgeL/BridgeS ; BridgeL/BridgeS/BridgeL	c16	c17 ; c17.2
	E_{sub}	$BridgeS_S$/$BridgeL_S$/$BridgeS_S$	Top_S/$BridgeL_S$/Top_S	c18	c19
	E_{sink}	Hollow/$BridgeS_S$	BridgeS/Top_S ; Hollow/Top_S ; BridgeL/$BridgeS_S$	c20	c21 ; c21.2 ; c21.3
	E_{emer}	$BridgeS_S$/Hollow	Top_S / $Bridge_S$; Top_S/Hollow ; $BridgeS_S$/BridgeL	c22	c23 ; c23.2 ; c23.3

Table S10. Calculated surface (E_{sur}), subsurface (E_{sub}), sinking (E_{sink}), and emerging (E_{emer}) diffusion energy barriers for all the TM surfaces featured in this work, along the associated diffusion paths defined in Tables S7-S9. All values are given in kJ mol^{-1}.

TM	Surface	E_{sur}	Path	E_{sub}	Path	E_{sink}	Path	E_{emer}	Path
Rh	(001)	136.7	a1	46.5	a2	187.2	a4	64.5	a5
	(011)	82.6	a6	95.7	a7	72.6	a8	13.4	a10
	(111)	68.6	a13	89.6	a14	90.0	a16	13.1	a18
Ir	(001)	104.8	a1	28.8	a3	256.0	a4	0.7	a5
	(011)	99.4	a6	116.6	a7	170.8	a8	2.8	a10
	(111)	74.4	a13	72.1	a14	164.2	a16	11.6	a18
Ni	(001)	195.1	a1	150.6	a2	157.6	a4	49.3	a5
	(011)	40.2	a6	98.7	a7	60.9	a8	57.8	a10
	(111)	36.2	a13	116.7	a14	64.5	a17	6.6	a19
Pd	(001)	192.1	a1	80.1	a2	155.1	a4	102.4	a5
	(011)	77.3	a6	112.7	a7	79.5	a8	84.7	a10
	(111)	71.6	a13	96.0	a14	27.3	a17	50.1	a19
Pt	(001)	117.8	a1	115.5	a3	207.0	a4	64.3	a5
	(011)	105.6	a6	119.6	a7	115.8	a8	61.6	a10
	(111)	80.2	a12	75.7	a15	39.4	a17	38.0	a19
Cu	(001)	167.4	a1	13.0	a2	139.3	a4	11.0	a5
	(011)	35.3	a6	79.7	a7	79.2	a9	71.6	a11
	(111)	8.4	a12	89.7	a14	50.7	a17	7.9	a19
Ag	(001)	114.5	a1	21.2	a3	105.8	a4	17.9	a5
	(011)	17.5	a6	60.9	a7	22.7	a8	37.5	a10
	(111)	19.5	a12	44.7	a14	32.2	a17	12.0	a19
Au	(001)	58.8	a1	96.5	a3	135.1	a4	17.4	a5
	(011)	34.6	a6	101.4	a7	59.9	a8	63.3	a10

	(111)	50.7	a12	35.8	a15	24.2	a17	7.4	a19
V	**(001)**	172.4	b1	86.3	b3	208.4	b4	49.4	b5
	(011)	67.9	b6	45.8	b7	68.0	b8	77.0	b9
	(111)	140.9	b11	173.5	b12	173.5	b14	1.3	b16
Nb	**(001)**	252.2	b1	24.8	b2	233.6	b4	76.6	b5
	(011)	132.8	b6	112.5	b7	82.0	b8	110.1	b9
	(111)	69.5	b10	166.2	b12	166.2	b13	2.4	b15
Ta	**(001)**	263.2	b1	40.7	b2	279.5	b4	111.1	b5
	(011)	126.6	b6	180.0	b7	183.3	b9	229.0	b9
	(111)	114.7	b10	208.1	b12	208.1	b13	1.4	b15
Cr	**(001)**	209.5	b1	54.9	b2	232.1	b4	1.0	b5
	(011)	90.9	b6	71.7	b7	109.4	b8	25.2	b9
	(111)	24.1	b10	210.2	b12	210.2	b13	1.5	b15
Mo	**(001)**	192.8	b1	58.8	b2	247.8	b4	23.6	b5
	(011)	86.5	b6	109.1	b7	86.4	b8	9.2	b9
	(111)	97.4	b10	226.3	b12	226.3	b13	1.0	b15
W	**(001)**	202.1	b1	33.7	b2	326.6	b4	1.0	b5
	(011)	92.0	b6	138.7	b7	290.9	b8	153.8	b9
	(111)	122.6	b10	303.7	b12	303.7	b13	1.2	b15
Fe	**(001)**	185.5	b1	52.8	b2	182.9	b4	69.2	b5
	(011)	73.4	b6	55.0	b7	131.1	b8	85.9	b9
	(111)	21.2	b10	82.3	b12	82.3	b13	7.6	b15
Sc	**(0001)**	62.5	c1	72.8	c3	7.5	c4	125.4	c6
	(10$\bar{1}$0)	96.2	c8	49.2	c10	31.5	c12	80.4	c14
	(11$\bar{2}$0)	64.7	c16	154.9	c18	37.5	c20	78.0	c22
Y	**(0001)**	67.6	c1	109.2	c3	10.2	c4	101.9	c8
	(10$\bar{1}$0)	34.5	c8	131.2	c10	25.3	c12	91.2	c14

	(11$\bar{2}$0)	13.7	c16	157.3	c18	79.5	c20	79.5	c22
	(0001)	20.7	c1	60.0	c3	64.7	c5	188.2	c7
Ti	**(10$\bar{1}$0)**	155.9	c8	107.4	c11	92.1	c13	73.6	c15
	(11$\bar{2}$0)	94.7	c16	214.8	c18	33.8	c20	118.6	c22
	(0001)	44.6	c1	78.9	c3	67.0	c5	206.6	c7
Zr	**(10$\bar{1}$0)**	78.0	c8	160.6	c10	89.8	c12	95.9	c14
	(11$\bar{2}$0)	85.8	c16	253.0	c18	67.3	c20	188.9	c22
	(0001)	73.6	c1	137.2	c3	39.5	c5	45.7	c8
Hf	**(10$\bar{1}$0)**	122.3	c8	114.9	c10	122.2	c12	114.9	c14
	(11$\bar{2}$0)	81.6	c16	280.5	c17	59.4	c20	193.9	c22
	(0001)	35.9	c1	102.0	c3	161.3	c5	146.3	c7
Tc	**(10$\bar{1}$0)**	60.9	c8	81.5	c11	175.3	c13	1.4	c15
	(11$\bar{2}$0)	80.9	c16	63.1	c18	63.7	c20	37.0	c22
	(0001)	41.9	c2	175.9	c3	235.5	c5	197.5	c7
Re	**(10$\bar{1}$0)**	46.8	c8	38.9	c10	208.8	c12	77.2	c14
	(11$\bar{2}$0)	53.2	c16	48.7	c19	165.9	c21.2	72.3	c23.2
	(0001)	72.3	c1	58.6	c3	92.6	c5	44.7	c7
Ru	**(10$\bar{1}$0)**	68.4	c8	11.1	c10	124.8	c12	11.1	c14
	(11$\bar{2}$0)	70.2	c17.2	7.7	c18	49.7	c21.3	6.9	c23.3
	(0001)	76.1	c1	46.5	c3	164.7	c5	17.7	c7
Os	**(10$\bar{1}$0)**	57.0	c8	135.2	c11	154.9	c13	31.4	c15
	(11$\bar{2}$0)	43.3	c16	53.8	c19	110.5	c21.2	9.1	c23.2
	(0001)	29.1	c1	71.8	c3	76.7	c5	91.0	c7
Co	**(10$\bar{1}$0)**	47.6	c8	41.0	c11	117.2	c13	0.4	c15
	(11$\bar{2}$0)	84.3	c16	19.3	c18	41.6	c20	12.1	c22
Zn	**(0001)**	37.5	c1	28.0	c3	20.0	c5	84.3	c7
	(10$\bar{1}$0)	40.1	c9	2.4	c11	40.0	c13.2	1.1	c15.2

	(11$\bar{2}$0)	149.2	c17	54.7	c19	0.8	c21	22.3	c23
	(0001)	22.7	c1	29.3	c3	17.9	c5	71.0	C7
Cd	**(10$\bar{1}$0)**	58.3	c9	36.6	c11	73.3	c13.2	34.3	c15.2
	(11$\bar{2}$0)	25.7	c17	71.2	c19	31.8	c21	31.8	c23

Fig. S16. Top (bottom image) and side (top image) views of exemplary TSs along the different paths explored on *fcc* TMs. Brown and grey spheres denote C and metal atoms, respectively.

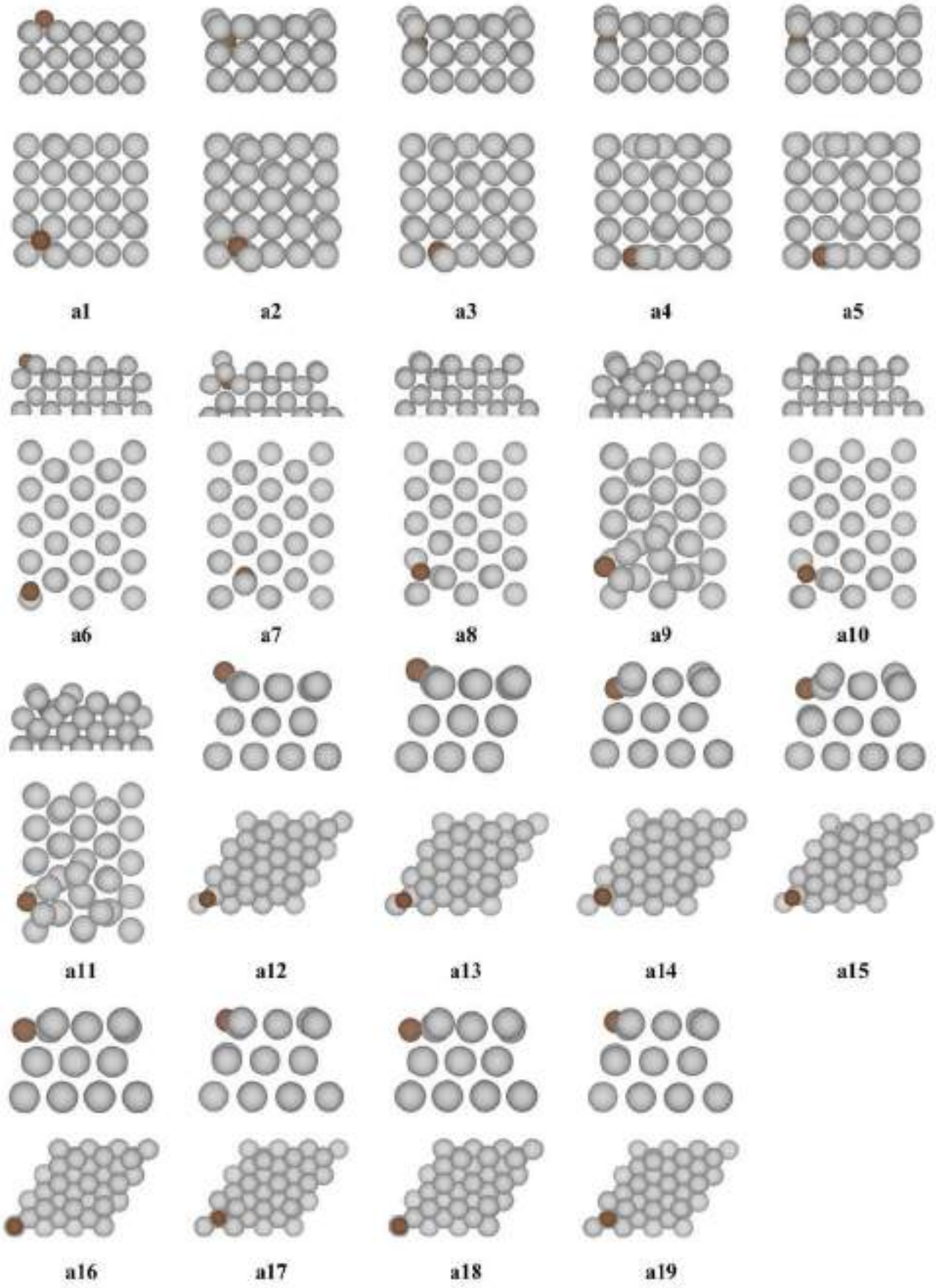

Fig. S17. Top (bottom image) and side (top image) views of exemplary TSs along the different paths explored on *bcc* TMs. Brown and grey spheres denote C and metal atoms, respectively.

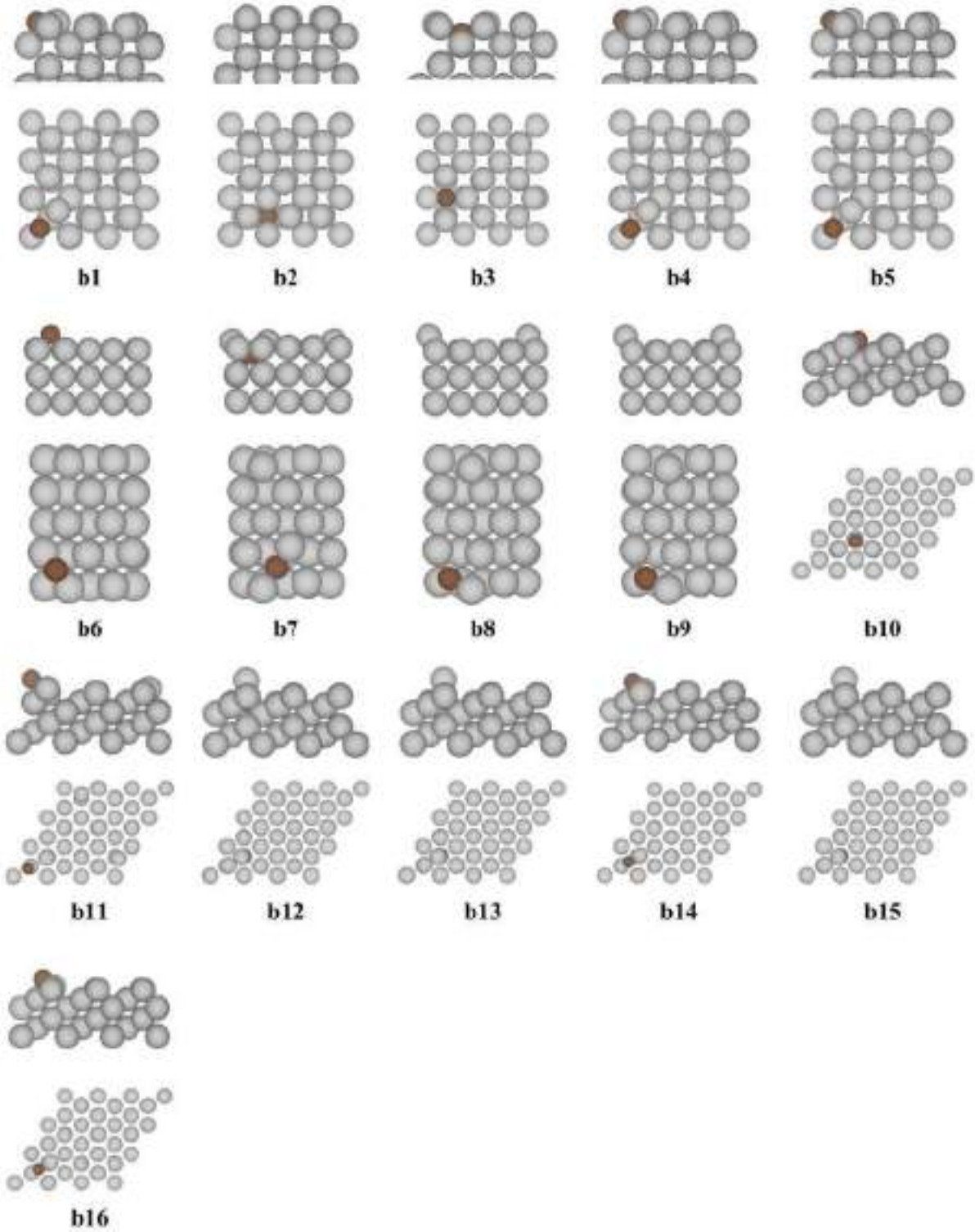

Fig. S18. Top (bottom image) and side (top image) views of exemplary TSs along the different paths explored on *hcp* TMs. Brown and grey spheres denote C and metal atoms, respectively.

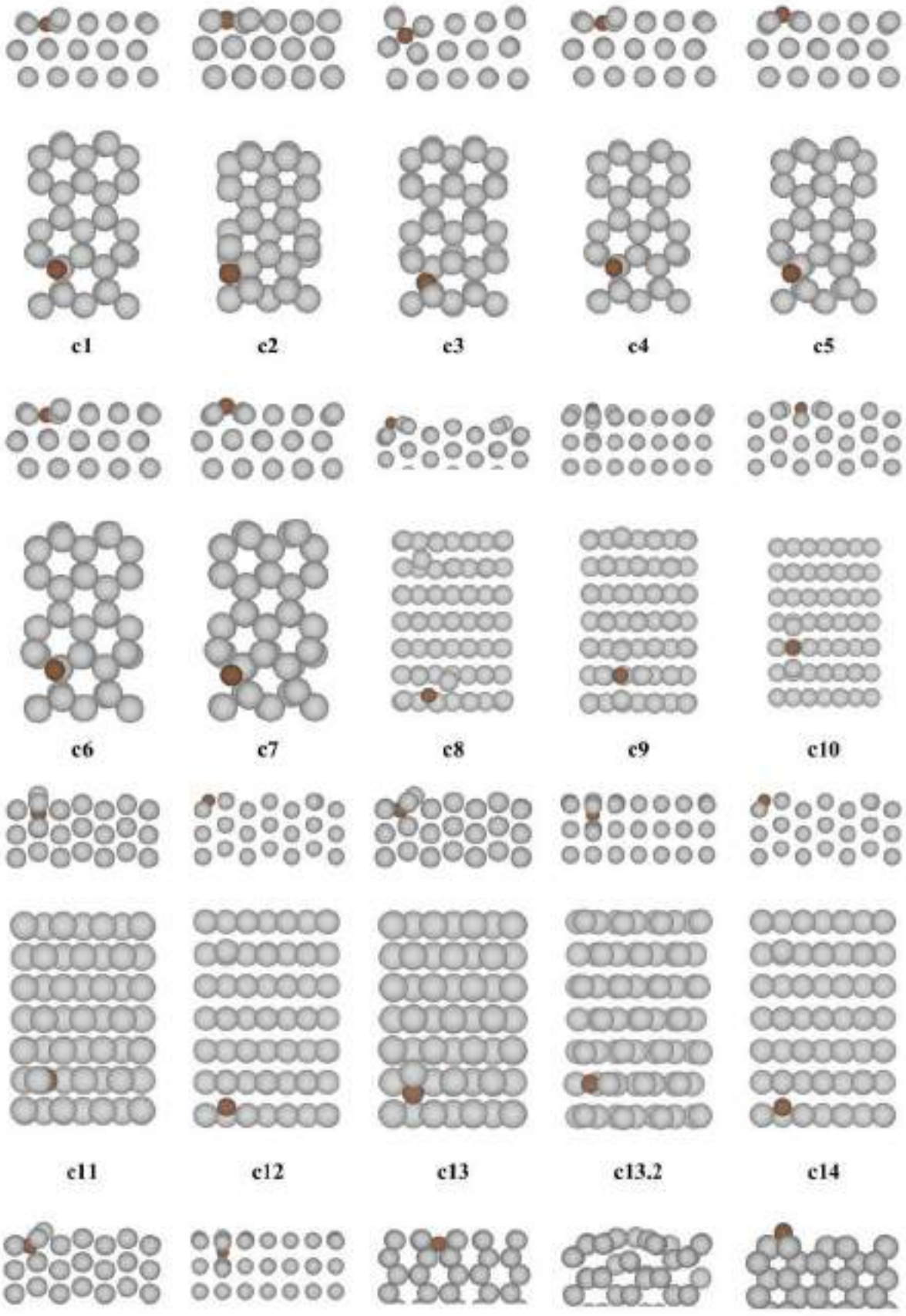

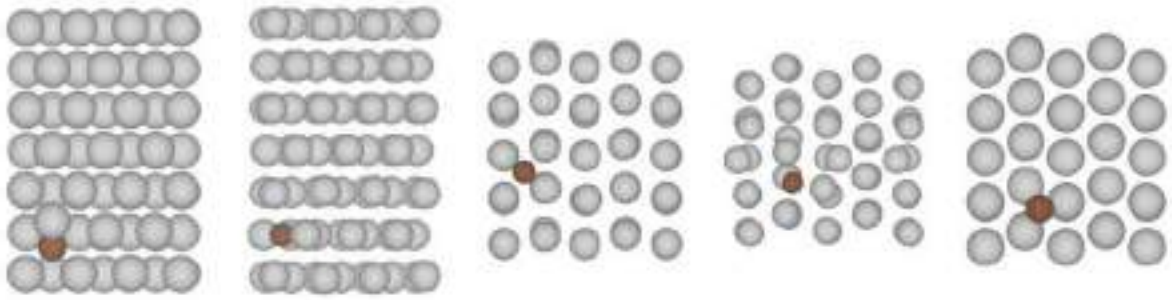

c15 c15.2 c16 c17 c17.2

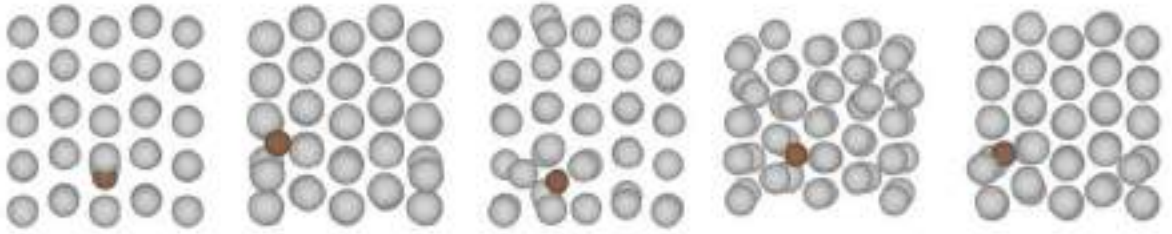

c18 c19 c20 c21 c21.2

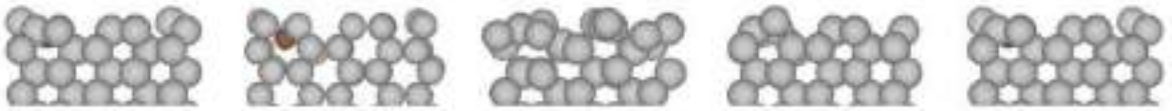

c21.3 c22 c23 c23.2 c23.3

Section S9: Diffusion Energy Barriers Isolated Descriptors

Fig. S19. Linear correlation between diffusion energy barriers, E_b, and the TM surface *d*-band centre, ε_d. The regression coefficient, *R*, is displayed.

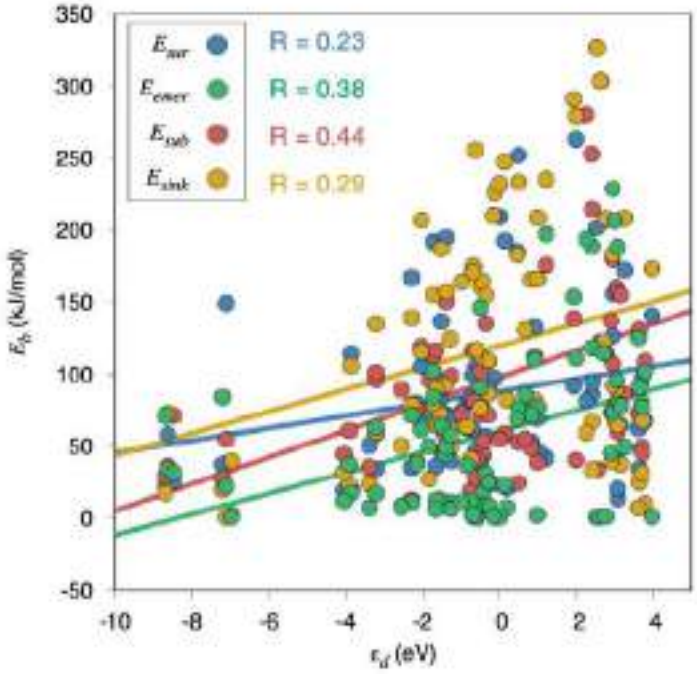

Fig. S20. Linear correlation between diffusion energy barriers, E_b, and the TM surface width-corrected *d*-band centre, ε_d^W. The regression coefficient, *R*, is displayed.

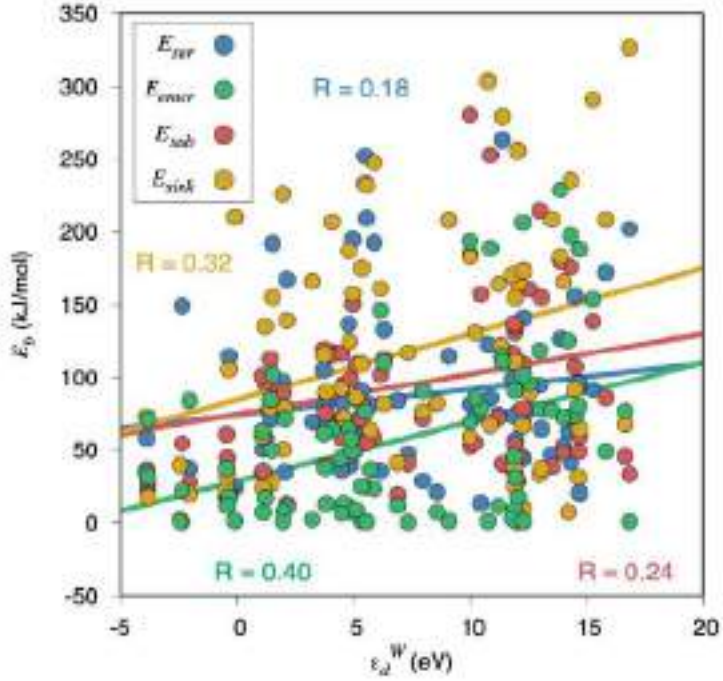

Fig. S21. Linear correlation between diffusion energy barriers, E_b, and the TM surface maximum Hilbert peak, ε_u. The regression coefficient, R, is displayed.

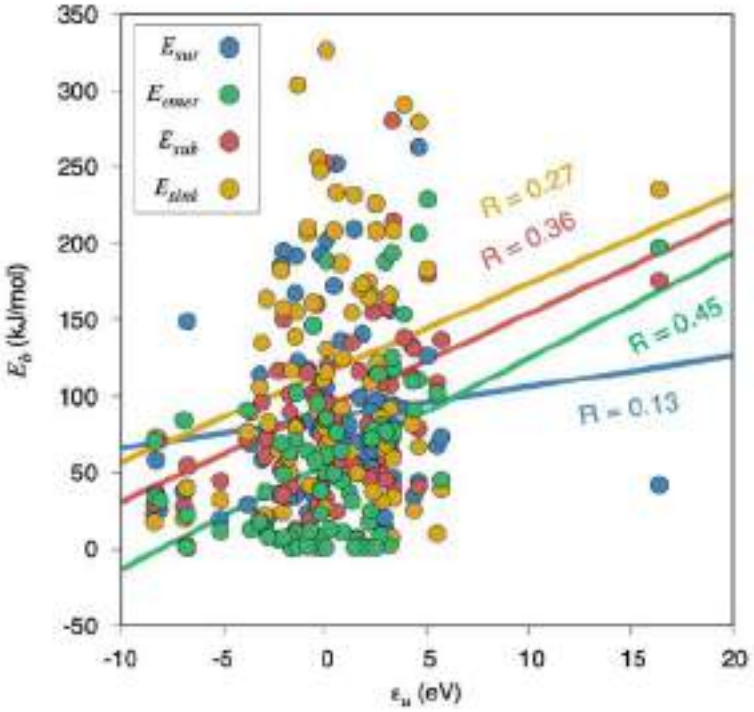

Fig. S22. Linear correlation between diffusion energy barriers, E_b, and the TM surface energy, γ. The regression coefficient, R, is displayed.

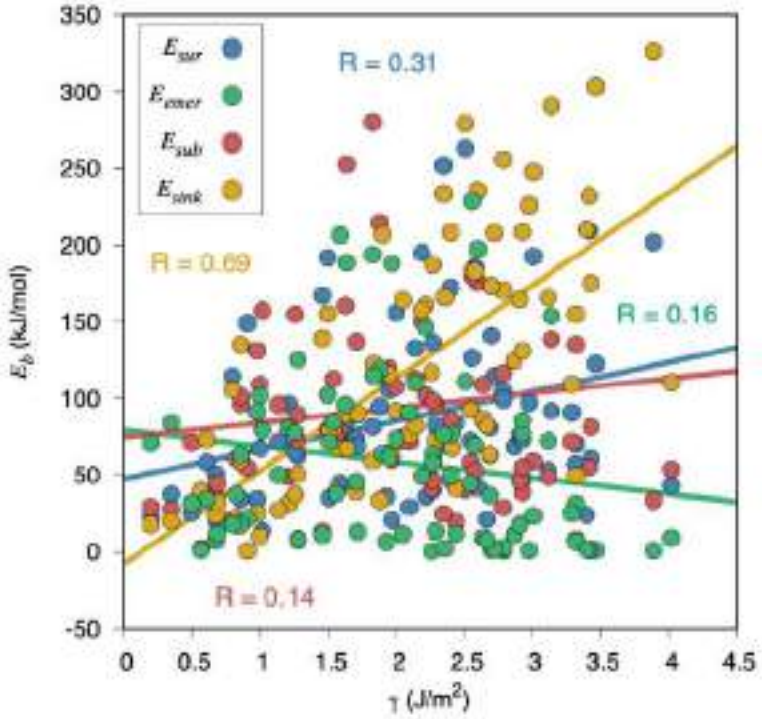

Fig. S23. Linear correlation between diffusion energy barriers, E_b, and the surface work function, ϕ. The regression coefficient, R, is displayed.

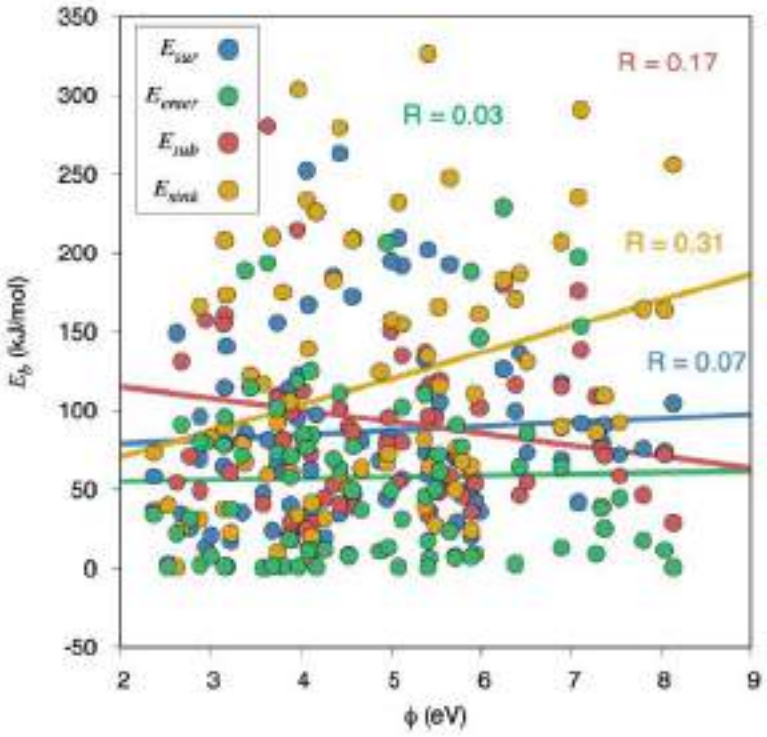

Fig. S24. BEP linear evolutions of E_{sink} with respect to ΔE, and the corresponding linear correlations for each explored barrier type, as a function of the TM crystal structure. Dashed lines define latest TS limit, where $E_b = \Delta E$, or earliest TS limit, where $E_b = 0$ regardless of ΔE.

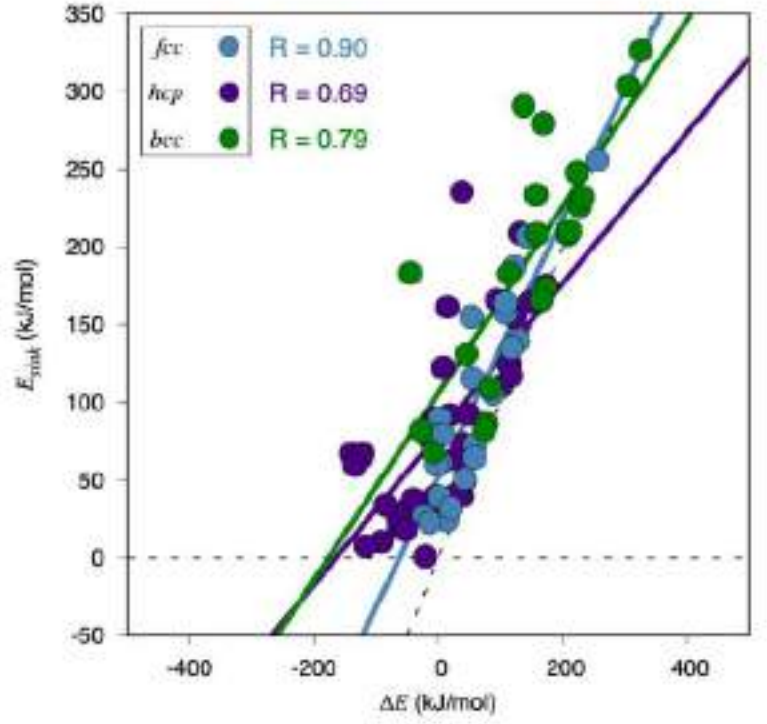

Fig. S25. BEP linear evolutions of E_{over} with respect to ΔE, and the corresponding linear correlations for each explored barrier type, as a function of the TM crystal structure. Dashed lines define latest TS limit, where $E_b = \Delta E$, or earliest TS limit, where $E_b = 0$ regardless of ΔE.

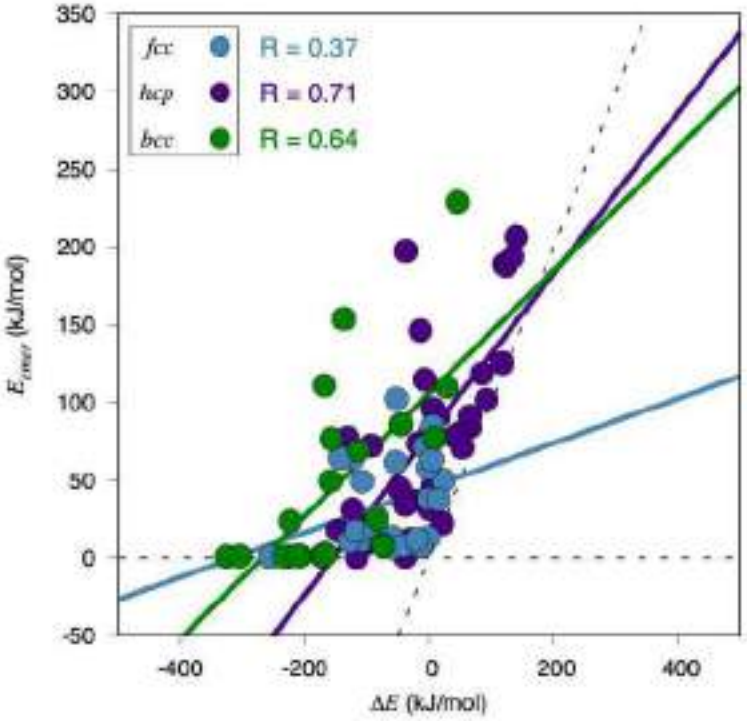

Section S10: Machine Learning Algorithms on Diffusion Energy Barriers

Fig. S26. MAE evolution for training (blue) and the test (green) sets as a function of the number of samples contained in the training set for the prediction of E_{tot} using a RFR algorithm. Coloured areas around the lines account for the error dispersion resulting from the cross validation using 20 runs. The training and test sets MAEs yield values of 25.2 ± 6.6 and 10.4 ± 0.8 kJ·mol^{-1}, respectively.

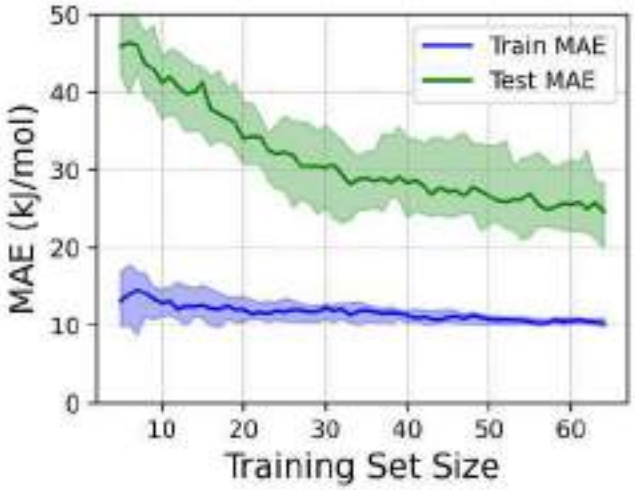

Fig. S27. MAE evolution for training (blue) and the test (green) sets as a function of the number of samples contained in the training set for the prediction of E_{sub} using a RFR algorithm. Coloured areas around the lines account for the error dispersion resulting from the cross validation using 20 runs. The training and test sets MAEs yield values of 38.2 ± 7.1 and 15.7 ± 1.1 kJ·mol^{-1}, respectively.

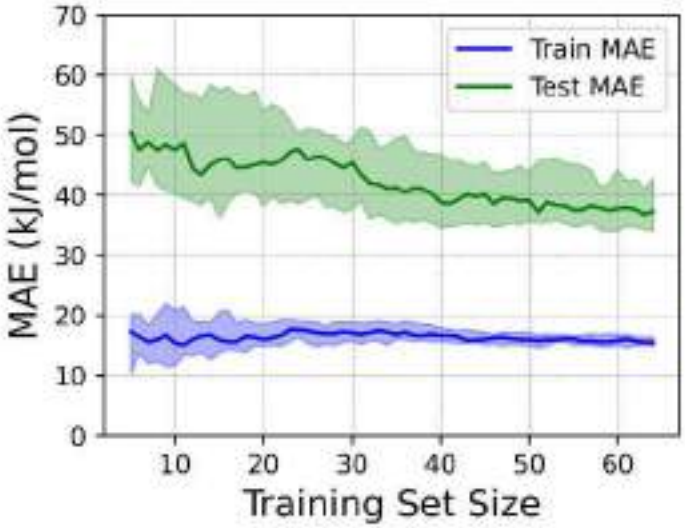

Fig. S28. MAE evolution for training (blue) and the test (green) sets as a function of the number of samples contained in the training set for the prediction of E_{sub} using a RFR algorithm. Coloured areas around the lines account for the error dispersion resulting from the cross validation using 20 runs. The training and test sets MAEs yield values of 30.3 ± 5.6 and 11.1 ± 0.8 kJ·mol^{-1}, respectively.

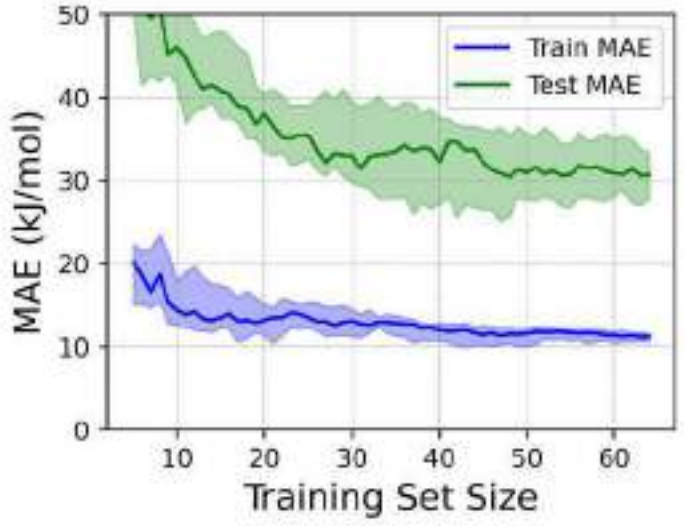

Fig. S29. MAE evolution for training (blue) and the test (green) sets as a function of the number of samples contained in the training set for the prediction of E_{emer} using a RFR algorithm. Coloured areas around the lines account for the error dispersion resulting from the cross validation using 20 runs. The training and test sets MAEs yield values of 28.4 ± 6.0 and 10.6 ± 0.9 kJ·mol^{-1}, respectively.

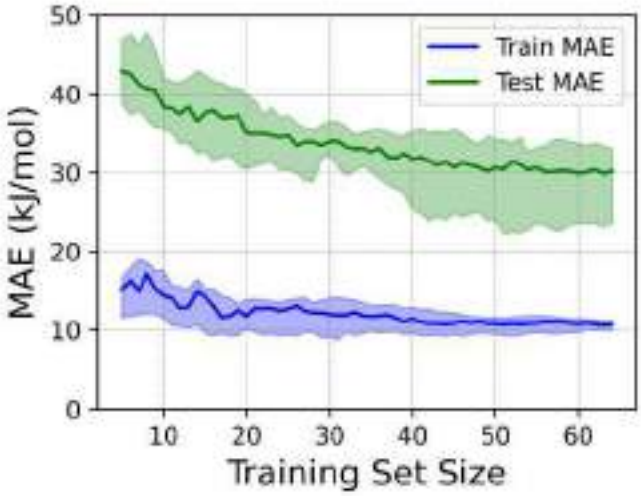

Table S11. Weight of the main features defining the Eb diffusion energy barriers, after applying the leave-one-out method on the RFR and MAE analysis shown in Figs. S27-S30.

	E_{sur}	E_{sub}	E_{sink}	E_{emer}
CN_{site}	0.174	0.138	—	—
CN_{FS}	0.316	0.021	—	—
ϕ	0.213	0.363	—	—
$E_{ads/abs}$	0.298	0.478	0.066	—
ΔE	—	—	0.603	0.628
δ	—	—	0.079	—
γ	—	—	0.251	—
ε	—	—	—	0.372

Section S11: Summary Table

Table S12. Summary table for all the surfaces studied in this work. It includes C preferred location (surface or subsurface), C preference for being isolated or grouped, C preferred diffusion (surface or subsurface), C preference for sinking or emerging, and to which of the thermodynamic and kinetic clusters each surface belongs.

TM	Surface	Preferred Location	C Cohesion or Isolation	Thermodynamic Cluster	Preferred Diffusion	Emergence or Sinking	Kinetic Cluster
Rh	(001)	Surface	Isolated	C3	Subsurface	Emerging	C3
	(011)	Surface	C Cohesion	C3	Surface	Emerging	C2
	(111)	Surface	C Cohesion	C3	Surface	Emerging	C1
Ir	(001)	Surface	Isolated	C3	Subsurface	Emerging	C3
	(011)	Surface	C Cohesion	C3	Surface	Emerging	C1
	(111)	Surface	C Cohesion	C3	Subsurface	Emerging	C1
Ni	(001)	Surface	Isolated	C3	Subsurface	Emerging	C2
	(011)	Surface	C Cohesion	C3	Surface	Emerging	C2
	(111)	Subsurface	C Cohesion	C2	Surface	Emerging	C1
Pd	(001)	Surface	Isolated	C3	Subsurface	Emerging	C2
	(011)	Surface	C Cohesion	C3	Surface	Sinking	C2
	(111)	Subsurface	C Cohesion	C2	Surface	Sinking	C2
Pt	(001)	Surface	C Cohesion	C3	Subsurface	Emerging	C2
	(011)	Surface	C Cohesion	C3	Surface	Emerging	C2
	(111)	Surface	C Cohesion	C3	Subsurface	Emerging	C2
Cu	(001)	Surface	C Cohesion	C3	Subsurface	Emerging	C3
	(011)	Surface	C Cohesion	C3	Surface	Emerging	C2
	(111)	Subsurface	C Cohesion	C1	Surface	Emerging	C1
Ag	(001)	Surface	C Cohesion	C1	Subsurface	Emerging	C3
	(011)	Subsurface	C Cohesion	C1	Surface	Sinking	C2
	(111)	Subsurface	C Cohesion	C1	Surface	Emerging	C2
Au	(001)	Surface	C Cohesion	C1	Surface	Emerging	C1
	(011)	Subsurface	C Cohesion	C1	Surface	Sinking	C2
	(111)	Surface	C Cohesion	C1	Subsurface	Emerging	C2

V	(001)	Surface	Isolated	C3	Subsurface	Emerging	C3
	(011)	Subsurface	Isolated	C2	Subsurface	Sinking	C2
	(111)	Surface	Isolated	C3	Surface	Emerging	C1
Nb	(001)	Surface	Isolated	C3	Subsurface	Emerging	C3
	(011)	Subsurface	Isolated	C2	Subsurface	Sinking	C2
	(111)	Surface	C Cohesion	C3	Surface	Emerging	C1
Ta	(001)	Surface	Isolated	C3	Subsurface	Emerging	C3
	(011)	Subsurface	Isolated	C2	Surface	Sinking	C2
	(111)	Surface	C Cohesion	C3	Surface	Emerging	C1
Cr	(001)	Surface	Isolated	C3	Subsurface	Emerging	C3
	(011)	Surface	C Cohesion	C3	Subsurface	Emerging	C2
	(111)	Surface	C Cohesion	C3	Surface	Emerging	C1
Mo	(001)	Surface	Isolated	C3	Subsurface	Emerging	C3
	(011)	Surface	C Cohesion	C3	Surface	Emerging	C1
	(111)	Surface	C Cohesion	C3	Surface	Emerging	C1
W	(001)	Surface	Isolated	C3	Subsurface	Emerging	C3
	(011)	Surface	Isolated	C3	Surface	Emerging	C2
	(111)	Surface	C Cohesion	C3	Surface	Emerging	C1
Fe	(001)	Surface	Isolated	C3	Subsurface	Emerging	C3
	(011)	Surface	Isolated	C3	Subsurface	Emerging	C2
	(111)	Surface	C Cohesion	C3	Surface	Emerging	C1
Sc	(0001)	Subsurface	Isolated	C2	Surface	Sinking	C2
	$(10\bar{1}0)$	Subsurface	Isolated	C2	Subsurface	Sinking	C2
	$(11\bar{2}0)$	Subsurface	Isolated	C2	Surface	Sinking	C2
Y	(0001)	Subsurface	Isolated	C2	Surface	Sinking	C2
	$(10\bar{1}0)$	Subsurface	Isolated	C2	Surface	Sinking	C2
	$(11\bar{2}0)$	Subsurface	Isolated	C2	Surface	Emerging	C2
Ti	(0001)	Subsurface	Isolated	C2	Surface	Sinking	C2
	$(10\bar{1}0)$	Surface	Isolated	C3	Subsurface	Emerging	C2

	(11$\bar{2}$0)	Subsurface	Isolated	C2	Surface	Sinking	C2
	(0001)	Subsurface	Isolated	C2	Surface	Sinking	C2
Zr	**(10$\bar{1}$0)**	Subsurface	Isolated	C2	Surface	Sinking	C2
	(11$\bar{2}$0)	Subsurface	Isolated	C2	Surface	Sinking	C2
	(0001)	Subsurface	Isolated	C2	Surface	Sinking	C2
Hf	**(10$\bar{1}$0)**	Surface	Isolated	C3	Subsurface	Emerging	C2
	(11$\bar{2}$0)	Subsurface	Isolated	C2	Surface	Sinking	C2
	(0001)	Surface	C Cohesion	C3	Surface	Emerging	C2
Tc	**(10$\bar{1}$0)**	Surface	Isolated	C3	Surface	Emerging	C1
	(11$\bar{2}$0)	Surface	C Cohesion	C3	Subsurface	Emerging	C2
	(0001)	Surface	C Cohesion	C3	Surface	Emerging	C2
Re	**(10$\bar{1}$0)**	Surface	C Cohesion	C3	Subsurface	Emerging	C2
	(11$\bar{2}$0)	Surface	C Cohesion	C3	Subsurface	Emerging	C2
	(0001)	Surface	C Cohesion	C3	Subsurface	Emerging	C2
Ru	**(10$\bar{1}$0)**	Surface	C Cohesion	C3	Subsurface	Emerging	C3
	(11$\bar{2}$0)	Surface	C Cohesion	C3	Subsurface	Emerging	C3
	(0001)	Surface	C Cohesion	C3	Subsurface	Emerging	C3
Os	**(10$\bar{1}$0)**	Surface	C Cohesion	C3	Surface	Emerging	C2
	(11$\bar{2}$0)	Surface	C Cohesion	C3	Surface	Emerging	C1
	(0001)	Surface	C Cohesion	C3	Surface	Sinking	C2
Co	**(10$\bar{1}$0)**	Surface	C Cohesion	C3	Subsurface	Emerging	C1
	(11$\bar{2}$0)	Surface	C Cohesion	C3	Subsurface	Emerging	C3
	(0001)	Subsurface	C Cohesion	C1	Subsurface	Sinking	C2
Zn	**(10$\bar{1}$0)**	Subsurface	C Cohesion	C1	Subsurface	Emerging	C3
	(11$\bar{2}$0)	Subsurface	C Cohesion	C1	Subsurface	Sinking	C2
	(0001)	Subsurface	C Cohesion	C1	Surface	Sinking	C2
Cd	**(10$\bar{1}$0)**	Subsurface	C Cohesion	C1	Subsurface	Emerging	C2
	(11$\bar{2}$0)	Subsurface	C Cohesion	C1	Surface	Emerging	C2

References

1 F. Pedregosa, G. Varoquaux, A. Gramfort, V. Michel, B. Thirion, O. Grisel, M. Blondel, P. Prettenhofer, R. Weiss, V. Dubourg, J. Vanderplas, A. Passos, D. Cournapeau, M. Brucher, M. Perrot and E. Duchesnay, *J. Mach. Learn Res.*, 2011, **12**, 2825-2830.

2 W. Duivesteijn, A. J. Feelders and A. Knobbe, *Data Min. Knowl. Discovery*, 2016, **30**, 47.

3 B. R. Goldsmith, M. Boley, J. Vreeken, M. Scheffler and L. M. Ghiringhelli, *New. J. Phys.*, 2017, **19**, 013031.

4 Z. Chaker, P. Chervy, Y. Boulard, S. Bressanelli, P. Retailleau, M. Patemostre and T. Charpentier, *J. Phys. Chem. B*, 2021, **125**, 9454-9466.